V. 121, NO. 3
MAY 2024

ACI STRUCTURAL JOURNAL

A JOURNAL OF THE AMERICAN CONCRETE INSTITUTE

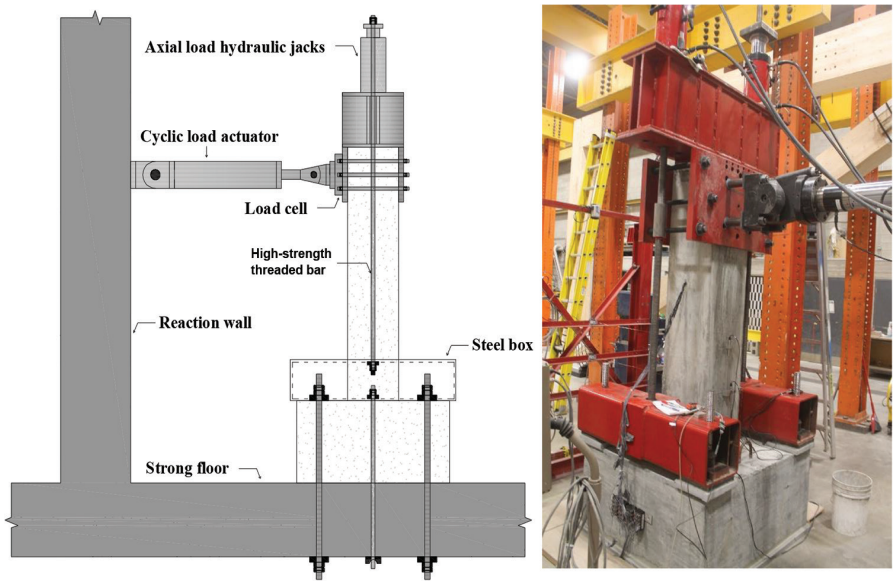

American Concrete Institute

ACI Structural Journal

May 2024, V. 121, No. 3

A JOURNAL OF THE AMERICAN CONCRETE INSTITUTE
AN INTERNATIONAL TECHNICAL SOCIETY

3 **Shear Test on Concrete Corbels: ACI 318-19 Formulas Evaluation**, by Bing Han and Yuan Huang

15 **Early-Age Cracking Resistance of Reinforced High-Strength Concrete**, by Chuyuan Wen, Dejian Shen, Yang Jiao, Ci Liu, and Ming Li

25 **Punching Shear Strength of Isolated Concrete Column Footings with Low Shear Span-Depth Ratios**, by Ngoc Hieu Dinh, Juok Noh, Kyoung-Kyu Choi, and Hong-Gun Park

43 **Design Tool for Finding Minimum Heights of Reinforced Concrete Beams and One-Way Slabs**, by Marc Sanabra-Loewe, David Garcia, Nikola Tošić, and Albert de la Fuente

57 **Impact of Confinement on Bar Anchorage in Relocated Plastic Hinges**, by Taylor J. Brodbeck, Zachary A. Shurow, Rudolf Seracino, and Mervyn J. Kowalsky

69 **Experimental Study of Concrete Columns Reinforced with Lap-Spliced Glass Fiber-Reinforced Polymer Bars under Seismic Load**, by Bahareh Nader Tehrani, Ahmed Sabry Farghaly, and Brahim Benmokrane

83 **Hysteresis Behavior of Glass Fiber-Reinforced Polymer-Reinforced Precast Concrete Tunnel Segments under Cyclic Load**, by Basil Ibrahim, Salaheldin Mousa, Hamdy M. Mohamed, and Brahim Benmokrane

97 **Numerical Analysis of Ultimate State of Reinforced Concrete Slabs under Low-Velocity Impact**, by Dandan Zheng, Masato Komuro, Norimitsu Kishi, and Tomoki Kawarai

109 **Interface Shear Capacity and Flexural Performance of Hybrid Beams**, by Ravi Singh, Yukihiro Sato, Hitoshi Sasaki, David Mukai, and Susumu Kono

119 **Post-Cracking Stiffness Model of Solid and Hollow Glass Fiber-Reinforced Polymer-Reinforced Concrete Members under Torsion**, by Ibrahim T. Mostafa, Salaheldin Mousa, Hamdy M. Mohamed, and Brahim Benmokrane

135 **Experimental Investigation of Deep Beams with High-Strength Headed Shear Reinforcement, Part I**, by Dhanushka K. Palipana and Giorgio T. Proestos

147 **Analytical Evaluation of Deep Beams with High-Strength Headed Shear Reinforcement, Part II**, by Dhanushka K. Palipana and Giorgio T. Proestos

Contents continued on next page

The *ACI Structural Journal* (ISSN 0889-3241) is published bimonthly by the American Concrete Institute. Publication office: 38800 Country Club Drive, Farmington Hills, MI 48331. Periodicals postage paid at Farmington, MI, and at additional mailing offices. Subscription rates: $199 per year, payable in advance. POSTMASTER: Send address changes to: *ACI Structural Journal*, 38800 Country Club Drive, Farmington Hills, MI 48331.

Canadian GST: R 1226213149.

Direct correspondence to 38800 Country Club Drive, Farmington Hills, MI 48331. Telephone: +1.248.848.3700. Facsimile (FAX): +1.248.848.3701. **Website: http://www.concrete.org.**

CONTENTS

159 **Seismic Performance of Gravity-Load-Designed Beam-Column Joints with Strain-Hardened Cementitious Composite**, by B. S. Sindu and Saptarshi Sasmal

173 **Shear Behavior of Precast Concrete Box Culverts Reinforced with Glass Fiber-Reinforced Polymer Bars under Concentrated Load**, by Ahmed Elnady, Salaheldin Mousa, and Brahim Benmokrane

187 **Cyclic Behavior of Beams with Double-Perimeter and Continuous-Stirrup Hoops**, by Yu-Chen Ou, Hermawan Sutejo, Jyun-Lin Huang, and Sheng-I Yen

201 **Modeling of Glass Fiber-Reinforced Polymer-Reinforced Squat Walls under Lateral Loading**, by Ju-Hyung Kim, Yail J. Kim, and Hong-Gun Park

215 **Reliability-Based Code Development for Carbon Fiber-Reinforced Polymer-Strengthened Circular Reinforced Concrete Columns**, by Juscelina Rosiane Ferreira, Peterson Araújo Quadros, and Sofia Maria Carrato Diniz

231 **Experimental Behavior of Concrete Corbels Reinforced with Glass Fiber-Reinforced Polymer Headed-End Bars**, by Matthew N. Allen and Ehab F. El-Salakawy

ON COVER: 121-S33, p. 72, Fig. 2—Schematic illustration of test setup.

Contributions to *ACI Structural Journal*

The *ACI Structural Journal* is an open forum on concrete technology and papers related to this field are always welcome. All material submitted for possible publication must meet the requirements of the "American Concrete Institute Publication Policy" and "Author Guidelines and Submission Procedures." Prospective authors should request a copy of the Policy and Guidelines from ACI or visit ACI's website at **www.concrete.org** prior to submitting contributions.

Papers reporting research must include a statement indicating the significance of the research.

The Institute reserves the right to return, without review, contributions not meeting the requirements of the Publication Policy.

All materials conforming to the Policy requirements will be reviewed for editorial quality and technical content, and every effort will be made to put all acceptable papers into the information channel. However, potentially good papers may be returned to authors when it is not possible to publish them in a reasonable time.

Discussion

All technical material appearing in the *ACI Structural Journal* may be discussed. If the discussion is received within four months of the paper's print publication, it will appear in the issue dated ten months from this journal's date. Discussion material received after specified dates will be considered individually for publication or private response. ACI Standards published in ACI Journals for public comment have discussion due dates printed with the Standard. Discussion should be complete and ready for publication, including finished, reproducible illustrations. Discussion must be confined to the scope of the paper and meet the ACI Publication Policy.

Follow the style of the current issue. Discussions should not exceed 1800-word equivalents (illustrations and tables count as 300 words each). References should be complete. Do not repeat references cited in original paper; cite them by original number. Numbering of additional references, figures, tables, and equations should follow sequentially from the original manuscript throughout the discussion. The discusser must indicate the month, year, volume number, issue number, authors' names, and manuscript number of the original manuscript. Closures responding to a single discussion should not exceed 1800-word equivalents in length, and to multiple discussions, approximately one half of the combined lengths of all discussions. Closures are published together with the discussions.

Discuss the paper, not some new or outside work on the same subject. Use references wherever possible instead of repeating available information.

Discussion offered for publication should offer some benefit to the general reader. Discussion which does not meet this requirement will be returned or referred to the author for private reply.

Send manuscripts to:
http://mc.manuscriptcentral.com/aci
Send discussions to:
Journals.Manuscripts@concrete.org

ACI STRUCTURAL JOURNAL TECHNICAL PAPER

Title No. 121-S28

Shear Test on Concrete Corbels: ACI 318-19 Formulas Evaluation

by Bing Han and Yuan Huang

The reinforced concrete corbel is widely used in assembled concrete structures as a convenient cantilever support member. In this paper, eight double-corbel specimens with the same design load capacity were obtained according to the strut-and-tie method (STM) in ACI 318-19. Corbels with different dimensional parameters were produced by varying the concrete compressive strength or shear span separately. The differences in actual bearing capacity and mechanical performance among the corbels were then compared to assess the accuracy and safety of the STM under the two variables. In addition, as the horizontal stirrups are not taken into consideration in the nominal design capacity of the STM, three non-stirrup corbel specimens were designed to investigate the effect of stirrups on the load-bearing capacity under different shear span-depth ratios. The results show that changing the concrete strength or shear span significantly affects the actual bearing capacity of the corbels, despite the design load capacity remaining constant. Increased compressive strength of the concrete or decreased shear span at the design stage results in a higher level of safety for the STM. The larger the shear span-depth ratio, the greater the strengthening effect of the stirrups on the corbels' bearing capacity.

Keywords: concrete compressive strength; horizontal stirrups; reinforced concrete corbel; shear span-depth ratio; strut-and-tie method (STM).

INTRODUCTION

Reinforced concrete corbels are widely used in assembled concrete structures for supporting crane beams and joists. As a typical D-zone member, the stress and strain distribution inside the corbels is quite complex.[1-3] The strain compatibility equation cannot be directly applied to load-bearing calculations as shear-type failure usually occurs in corbels.[4-7] The strut-and-tie method (STM) is employed to design the corbels and evaluate the bearing capacity. The STM can be traced back to 1899 or earlier.[8] Schlaich et al.[5] refined and improved the STM by applying it to the design of deep beams, corbels, and other D-zone members. The STM was later adopted by ACI Committee 318. The STM treats the corbel as an ideal truss, with the longitudinal steel bars acting as a tension tie and the inclined concrete acting as a compression strut. The tie and strut then transmit the force flow through the nodal connections, as shown in Fig. 1. The corbel is composed of three components: the tie, strut, and node. Based on the bearing strength of the individual components and then on the conditions for the force balance, the load-bearing capacity of a given corbel can be inversely calculated.

ACI 318-19[9] specifies that all components defined in the STM should be checked for strength. The corbel specimen reaches its ultimate load-bearing capacity when any components in the ties, struts, and nodes reach their ultimate strength. The capacity of the tension tie is calculated by

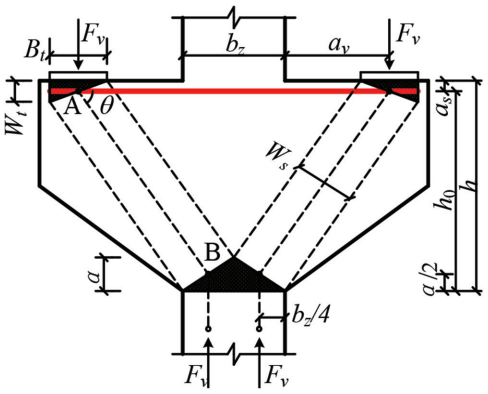

Fig. 1—Strut-and-tie method.

$$F_{tie} = f_y A_s \tag{1}$$

where f_y is the yield strength of the longitudinal bars; and A_s is the area of the longitudinal bars.

The angle (θ) between the tie and strut is calculated by

$$\theta = \arctan\frac{h_0 - a/2}{a_v + B_t/2} \tag{2}$$

where h_0 is the effective depth of the corbel section, which can be determined using Eq. (3), as specified in ACI 318-19 for normalweight concrete corbels; a_v is the shear span; B_t is the bearing width; and a is the equivalent height of the compression zone,[10] calculated by Eq. (4). ACI 318-19 specifies that θ is not less than 25 degrees.

$$h_0 \geq \max\left\{\begin{array}{c}\dfrac{V_u}{0.2\phi f_c' b}\\ \dfrac{V_u}{(480 + 0.08 f_c')b}\\ \dfrac{V_u}{1600\phi b}\end{array}\right\} \tag{3}$$

where V_u is the design shear load; ϕ is the strength reduction factor, taken as 0.75 (Reference 9); f_c' is the concrete

ACI Structural Journal, V. 121, No. 3, May 2024.
MS No. S-2022-236.R3, doi: 10.14359/51740455, received April 19, 2023, and reviewed under Institute publication policies.

cylindrical compressive strength, which can be calculated by converting the concrete cubic compressive strength according to the *fib* Model Code[11]; and b is the thickness of the corbel.

$$a = \frac{f_y A_s}{0.85 f_c' b} \tag{4}$$

The nominal capacity of the concrete compression strut is calculated by

$$F_{str} = 0.85\beta_c\beta_s f_c' w_s b \tag{5}$$

where β_c is the improvement coefficient of strength caused by local compression, taken as 1.0 in this test[12]; β_s is the effective strength coefficient for the concrete strut and is taken as 0.75 when the reinforcement rate of the stirrups passing through the strut satisfies Eq. (6)—otherwise, it is taken as 0.4 (Reference 9); and w_s is the width of the strut, calculated by Eq. (10).

$$\rho_{st} \geq \frac{0.0025}{\sin^2\theta} \tag{6}$$

The nominal compressive capacity of the nodal zone is calculated by

$$F_{no} = 0.85\beta_c\beta_n f_c' A_{no} \tag{7}$$

where β_n is the effective strength coefficient for the nodal zone, assigned a value of 1.0 for CCC nodes (nodes without ties, exemplified by Node B in Fig. 1) and 0.8 for CCT nodes (nodes with a single tie, as shown by Node A in Fig. 1); and A_{no} is the area of the bearing surfaces in the nodal zone. Nodes A and B both contain three bearing surfaces, and the area of each surface is calculated by

$$A_{no,A} = \begin{Bmatrix} A_{ba} \\ A_{be} \\ A_{inc} \end{Bmatrix} = \begin{Bmatrix} w_t b \\ B_t b \\ (w_t \cos\theta + B_t \sin\theta) b \end{Bmatrix} \tag{8}$$

$$A_{no,B} = \begin{Bmatrix} B_{ba} \\ B_{be} \\ B_{inc} \end{Bmatrix} = \begin{Bmatrix} ab \\ b_z b / 2 \\ (a\cos\theta + b_z \sin\theta / 2) b \end{Bmatrix} \tag{9}$$

where A_{ba} and B_{ba} are the areas of the surfaces perpendicular to the direction of the horizontal tie; A_{be} and B_{be} are the areas of the surfaces perpendicular to the direction of the vertical load; A_{inc} and B_{inc} are the areas of the surfaces perpendicular to the axis of the concrete strut; w_t is taken as two times the distance from the edge of the specimen to the center of the cross section of the longitudinal bars[9]; and b_z is the width of the column.

The width of the compression strut is taken from the minimum width of the contact surfaces between Node A and the strut or Node B and the strut, expressed by

$$w_s = \min\{(w_t\cos\theta + B_t\sin\theta), (a\cos\theta + b_z\sin\theta/2)\} \tag{10}$$

The bearing capacity of the individual components can be calculated according to Eq. (1) to (10). Then, the corresponding vertical loads can be inversely calculated based on the force balance conditions, and the minimum value is taken as the calculated load capacity of the corbel.

Scholars[13-16] have explored the effects of various factors on the load-bearing capacity of corbels. Kriz and Raths[13] investigated the relationship between corbels' bearing capacity and factors such as the shear span-depth ratio, reinforcement ratio of longitudinal bars, concrete strength, and so on. The test results showed that the load-bearing capacity increased with an increase in the longitudinal reinforcement ratio and concrete compressive strength but decreased with an increase in the shear span-depth ratio. Al-Shaarbaf et al.[14] explored the effects of factors such as the shear span-depth ratio, reinforcement ratio of horizontal stirrups, concrete strength, and concrete type on the load-bearing capacity of corbels. The test results indicated that increasing the area of horizontal stirrups enhanced the load-bearing capacity. Abdul-Razzaq et al.[15] analyzed experimental data to summarize the impact of various parameters on corbels' load-bearing capacity. They concluded that horizontal stirrups enhanced the corbels' ductility and were more effective in enhancing the corbels' bearing capacity than the vertical stirrups when the shear span-depth ratio was no more than one.[15] Hamoodi et al.[16] studied the effects of factors such as the compressive strength of the concrete containing recycled aggregate, the shear span-depth ratio, and the replacement ratio of the recycled aggregate on the corbels' bearing capacity. The test results showed that increasing the compressive strength of the concrete and decreasing the shear span-depth ratio improved the corbels' bearing capacity, while the variation in the replacement rate of the recycled aggregates had little effect. Additionally, various design methods for corbels have been studied and compared.[10,17,19,20] For instance, Khosravikia et al.[10] investigated the STM in AASHTO LRFD,[18] while Wilson et al.[17] and Abdul-Razzaq and Dawood[19] compared the accuracy of the shear-friction method (also referred to as the empirical method) and the STM method in ACI 318-14. Furthermore, Abdul-Razzaq and Dawood[20] proposed a new method that involves only placing steel bars in the struts and ties and removing the concrete through which they do not pass. The proposed corbels[20] were slightly lower in load-bearing capacity than conventional corbels designed by the STM but were also 13 to 52% lighter in weight.

To sum up, scholars have mainly studied the influence of various factors on the load-bearing capacity of corbels. Some researchers have also explored the accuracy of the STM or other methods by comparing corbels' calculated and tested bearing capacity. However, to the authors' knowledge, there is still a lack of research into the accuracy of the STM under the variations of a given factor, such as the concrete compressive strength and the shear span, specifically in the case of maintaining the same design load capacity. When the design load capacity is the same in engineering design, it is unknown whether the actual bearing capacity and mechanical properties of corbels designed by the STM are still the same if choosing different concrete strengths or shear spans. Research on this aspect is still lacking. Previous studies

Table 1—Design parameters of corbel specimens

ID	$f_{cu,de}$, MPa (ksi)	a_v, mm (in.)	h, mm (in.)	h_0, mm (in.)	Longitudinal bars, mm (in.)	Stirrups, mm (in.)	ρ_l, %	ρ_s, %
CY24-S0.57	30 (4.35)	200 (7.87)	375 (14.76)	350 (13.78)	4D16 (4D0.63)	2D10@100 (2D0.39@3.94)	0.766	0.449
CY54-S0.67	45 (6.53)	200 (7.87)	325 (12.80)	300 (11.81)	3D20 (3D0.79)	2D10@80 (2D0.39@3.15)	1.047	0.523
CY44-S0.73	60 (8.70)	200 (7.87)	300 (11.81)	275 (10.83)	4D18 (4D0.71)	2D10@70 (2D0.39@2.76)	1.233	0.571
CY54-S0.33	45 (6.53)	100 (3.94)	325 (12.80)	300 (11.81)	4D14 (4D0.55)	2D10@80 (2D0.39@3.15)	0.684	0.523
CY54-S0.80	45 (6.53)	300 (11.81)	400 (15.75)	375 (14.76)	4D18 (4D0.71)	2D10@80 (2D0.39@3.15)	0.904	0.558
CY54-S0.33*	45 (6.53)	100 (3.94)	325 (12.80)	300 (11.81)	4D14 (4D0.55)	0 (0)	0.684	0
CY54-S0.67*	45 (6.53)	200 (7.87)	325 (12.80)	300 (11.81)	3D20 (3D0.79)	0 (0)	1.047	0
CY54-S0.80*	45 (6.53)	300 (11.81)	400 (15.75)	375 (14.76)	4D18 (4D0.71)	0 (0)	0.904	0

Note: $f_{cu,de}$ is design cubic compressive strength of concrete; a_v is shear span; h and h_0 are overall depth and effective depth of corbels' section, respectively; ρ_l and ρ_s are reinforcement ratio of longitudinal bars and horizontal stirrups, respectively.

have shown that both concrete strength and shear span have a noticeable effect on the corbels' bearing capacity.[13-16] It is, therefore, necessary to investigate the effect of the two design parameters on the actual bearing capacity and mechanical performance of corbels with the same design load capacity. In addition, the nominal design capacity of the STM in ACI 318-19 does not take horizontal stirrups into consideration. However, the setting of horizontal stirrups not only strengthens the bearing capacity but may also change the failure pattern of the corbels with large shear span-depth ratios.[13-15,21] It is thus necessary to investigate the strengthening effect of horizontal stirrups on the bearing capacity of corbels for different shear span-depth ratios with the design of the STM.

This paper used the STM in ACI 318-19 to design eight double-corbel specimens with the same design load capacity. The concrete compressive strength or shear span was taken as the independent variable, and then different design parameters were produced for the corbels. Three non-stirrup corbel specimens with the corresponding shear span-depth ratios were included to help investigate the strengthening effect of horizontal stirrups. The accuracy of the STM was verified under parameter variations.

RESEARCH SIGNIFICANCE

The main objective of this paper is to assess the accuracy and safety of the STM in ACI 318-19 in designing corbels with the same design load capacity for varying concrete compressive strengths and shear span-depth ratios. The results can provide a reference for designers. In addition, this paper also investigates the strengthening effect of horizontal stirrups on the load-bearing capacity under different shear span-depth ratios, as the horizontal stirrups are not considered in the nominal design capacity of the STM.

EXPERIMENTAL INVESTIGATION

Design of corbel specimens

A total of eight double-corbel specimens were designed for this test. Regarding the common bearing magnitude of corbels and crane beams in engineering, the design load capacity for the specimens was 750 kN (168.61 kip).[22,23] Design parameters such as concrete strength, shear span, and reinforcement details are listed in Table 1. The design gradients for concrete cubic compressive strength were set at 30, 45, and 60 MPa (4.35, 6.53, and 8.70 ksi). Subsequently, the effective depths of 350, 300, and 275 mm (13.78, 11.81, and 10.83 in.) were selected by Eq. (3), corresponding to shear span-depth ratios of 0.57, 0.67, and 0.73, respectively. All three had a common shear span of 200 mm (7.87 in.) and a design bearing capacity of 750 kN (168.61 kip). The design gradients for the shear span were 100, 200, and 300 mm (3.94, 7.87, and 11.81 in.). The effective depths selected were 300, 300, and 375 mm (11.81, 11.81, and 14.76 in.), respectively, corresponding to the shear span-depth ratios of 0.33, 0.67, and 0.80. It is worth noting that the effective depth of the corbel with a shear span of 300 mm (11.81 in.) was selected as 375 mm (14.76 in.) rather than 300 mm (11.81 in.). The reasons are as follows: 1) if the effective depth were 300 mm (11.81 in.), the angle between the compression strut and the stirrups only in the horizontal direction would be 35 degrees, which is contrary to the rules specified in ACI 318-19, which requires the angle not to be less than 40 degrees; and 2) if the effective depth were 300 mm (11.81 in.), the clear spacing between the horizontal stirrups would be less than 40 mm (1.57 in.), making it difficult to place an internal concrete vibrator and potentially damaging the strain gauges on the reinforcements. Three non-stirrup corbel specimens were designed as the comparison specimens with the aforementioned shear span-depth ratios. The design parameters of the non-stirrup specimens were identical to the hooped specimens under the same shear span-depth ratio, except for the horizontal stirrups. The thickness of all corbels was 300 mm (11.81 in.). The reinforcement details are shown in Fig. 2. The longitudinal bars were welded to the transverse reinforcing bar to ensure sufficient anchoring resistance at the ends.[9] Strain gauges were applied to the longitudinal bars and stirrups at the vertical intersection between the corbels and the center column. The specimen names consist of two

Table 2—Mixture proportions

Concrete strength grade	Water, kg/m^3 (lb/yd^3)	Cement, kg/m^3 (lb/yd^3)	Gravel, kg/m^3 (lb/yd^3)	Sand, kg/m^3 (lb/yd^3)	Fly ash, kg/m^3 (lb/yd^3)	f_{cu}, MPa (ksi)	f_c', MPa (ksi)
C30	185 (312)	345 (582)	1195 (2015)	670 (1130)	0 (0)	38.6 (5.60)	23.8 (3.45)
C45	150 (253)	500 (843)	1188 (2003)	612 (1032)	0 (0)	65.3 (9.47)	54.2 (7.86)
C60	164 (277)	459 (774)	1086 (1831)	649 (1094)	114 (192)	59.7 (8.66)	44.2 (6.41)

Note: f_{cu} is actual cubic compressive strength of concrete blocks with dimensions of 150 x 150 x 150 mm (5.91 x 5.91 x 5.91 in.); f_c' is actual cylindrical compressive strength of blocks with ø150 x 300 mm (ø5.91 x 11.81 in.).

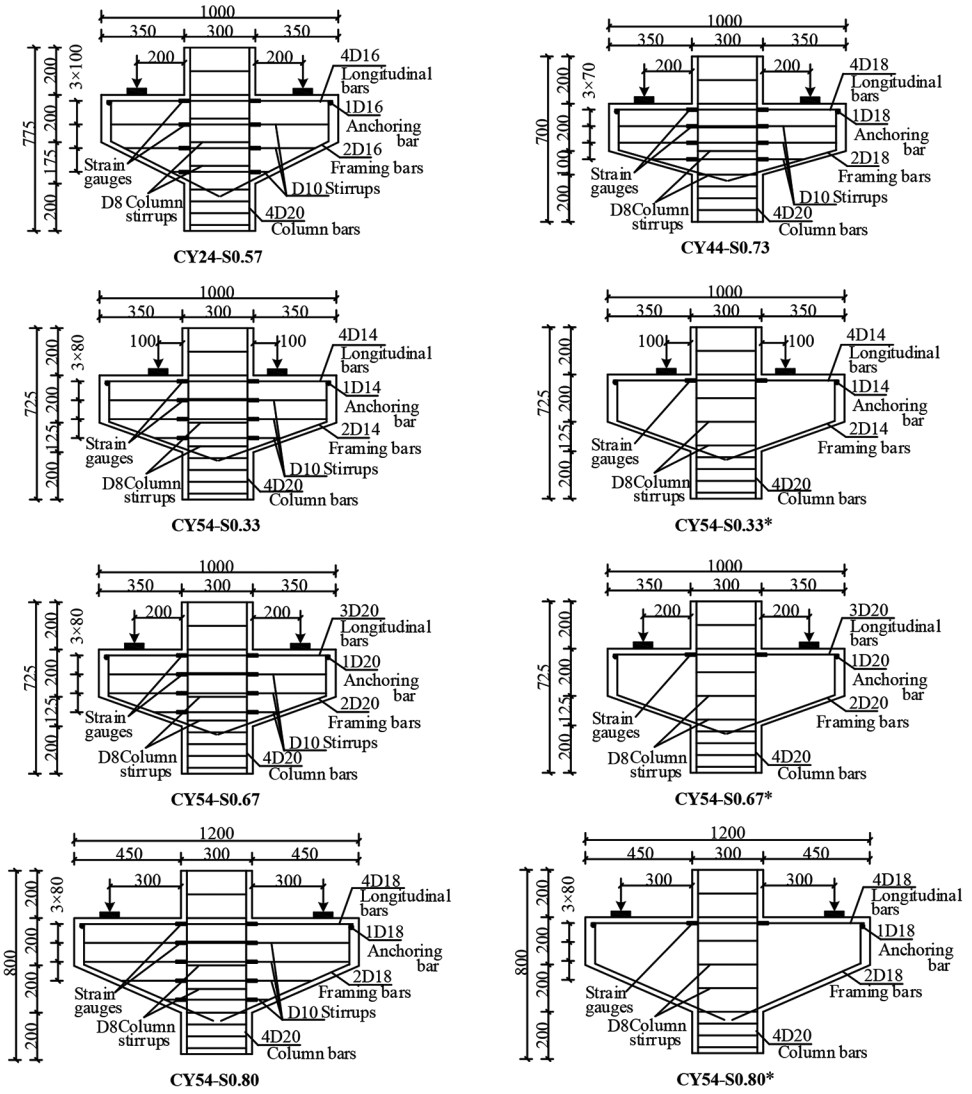

Fig. 2—Layout of reinforcements and position of strain gauges. (Note: All dimensions in mm; 1 mm = 0.039 in.)

parts: the first represents the tested cylindrical compressive strength of the concrete, and the second represents the shear span-depth ratio. The names of the non-stirrup specimens were labeled with an asterisk.

Material properties

The concrete composition and properties are listed in Table 2. Three ø150 x 300 mm (ø5.91 x 11.81 in., where ø represents the diameter of the cross section) cylindrical test blocks and three 150 mm (5.91 in.) cubic test blocks were reserved. The compressive strength of the blocks on the loading day was tested according to ASTM C39/C39M-17.[24] Both longitudinal bars and stirrups are HRB400 reinforcement, where HRB stands for hot-rolled ribbed bars, and 400 is the nominal yield strength in MPa. The properties of the steel bars were tested according to ASTM A370-17[25] and are listed in Table 3.

Note that the actual design load capacity ($F_{de,A}$) may differ from the initial design load capacity ($F_{de,P}$) due to various factors, such as the casting and curing environment in the laboratory. Therefore, the specimens have been designated based on their tested cylindrical compressive strength and shear span-depth ratio. In addition, small deviations exist between the measured and the design values of the reinforcing bar yield strength. However, the $F_{de,A}$ does not deviate significantly among specimens under the same

Table 3—Steel bar properties

Diameter, mm (in.)	A_s, mm^2 (in.^{2})	f_y, MPa (ksi)	f_u, MPa (ksi)	E_s, GPa (ksi)	ε_y, 10^{-6}
10 (0.39)	78.5 (0.12)	471 (68.31)	611 (88.62)	206 (29,878)	2286
14 (0.55)	153.9 (0.24)	452 (65.56)	610 (88.47)	206 (29,878)	2194
16 (0.63)	201.1 (0.31)	425 (61.64)	583 (84.56)	206 (29,878)	2063
18 (0.71)	254.5 (0.39)	492 (71.36)	612 (88.76)	206 (29,878)	2388
20 (0.79)	314.2 (0.49)	423 (61.35)	613 (88.91)	206 (29,878)	2053

Note: A_s is cross-sectional area of steel bars; f_y and f_u are yield strength and tensile strength, respectively; E_s is elastic modulus; ε_y is yield strain.

variable, as shown in Table 4. To improve the reliability of the test results, $F_{de,A}$ is used for the subsequent calculations, such as for the safety factors.

Test setup

The loading devices are shown in Fig. 3. A 5000 kN (1124 kip) hydraulic jack was used to apply vertical load. A spherical hinge support was placed at the top. Two linear variable differential transformers (LVDTs) were set at the base of the center column to monitor the vertical displacement. A data acquisition instrument was used to simultaneously acquire load, vertical displacement, and strain on reinforcements.

A preload of 30 kN (6.74 kip) was initially applied to eliminate any gaps between the devices and sand bedding. The vertical load was then applied in steps of 50 kN (11.24 kip), with a 3-minute interval required between each load step. Crack patterns were documented at each load step, and the crack width was measured using a crack observer with 0.02 mm (7.87×10^{-4} in.) accuracy. Crack width measurements were mainly taken near the intersections of the corbel and the column (for flexural cracks) and on the surface of the compression strut (for diagonal cracks).

EXPERIMENTAL RESULTS AND ANALYSIS

Failure mode and process

Two types of failure modes were distinguished, one for tension tie and compression strut (TT&CS) failure[9] and the other for diagonal splitting (DS) failure.[13] TT&CS was characterized by a slow rise in the load-bearing capacity after the longitudinal bars yielded until the inclined concrete was suddenly crushed. This failure type began after the longitudinal bars had yielded, which coincided with the failure mode defined by the STM for the yielding of the tie. DS failure was characterized by the sudden splitting of the concrete along the line from the support to the corbel root without yielding of the longitudinal bars. DS failure was triggered by the splitting and tension damage to the concrete instead of crushing. TT&CS failure occurred in all specimens except CY54-S0.80*, which had the largest shear span-depth ratio and no horizontal stirrup. The two typical failure patterns are shown in Fig. 4. The surfaces of the specimens with TT&CS failure were covered with small cracks and a main crushing

Table 4—Comparison between actual and initial design load

ID	$F_{de,P}$, kN (kip)	$F_{de,A}$, kN (kip)	$F_{de,A}/F_{de,P}$
CY24-S0.57	375 (84.30)	404 (90.82)	1.08
CY54-S0.67	375 (84.30)	416 (93.52)	1.11
CY44-S0.73	375 (84.30)	414 (93.07)	1.10
CY54-S0.33	375 (84.30)	467 (104.99)	1.25
CY54-S0.80	375 (84.30)	475 (106.78)	1.27
CY54-S0.33*	375 (84.30)	467 (104.99)	1.25
CY54-S0.67*	375 (84.30)	415 (93.30)	1.11
CY54-S0.80*	375 (84.30)	475 (106.78)	1.27

Note: $F_{de,P}$ and $F_{de,A}$ are initial design load capacity and actual design load capacity, respectively.

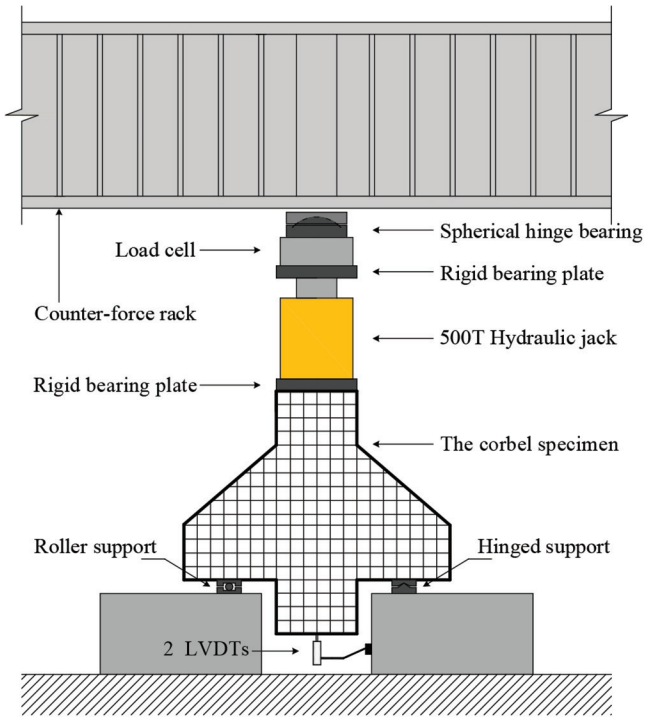

Fig. 3—Test setup.

crack; the surfaces of the specimen with DS failure had only a few small cracks and two major splitting cracks. The actual failure mode, predicted failure mode, first cracking load, load corresponding to the start of yielding and the complete yielding of the longitudinal bars, and ultimate load are listed in Table 5. Only the actual failure pattern of CY54-S0.80* differed from the prediction by the STM, which was mainly due to the premature damage caused by the lack of horizontal stirrups. CY54-S0.80 and CY54-S0.80* are taken as examples to illustrate the damage process under the two failure types.

For Specimen CY54-S0.80, the first flexural crack appeared at a load of 199 kN (44.74 kip) ($0.15V_t$, where V_t is the ultimate load) at the interface between the right corbel and the column and slowly propagated upwards. As the load increased to 399 kN (89.70 kip) ($0.30V_t$), the first diagonal crack appeared in the right corbel in a direction roughly parallel to the line from the inner side of the support to the

Table 5—Test results of corbels

ID	V_{cr}, kN (kip)	$V_{y,st}$, kN (kip)	$V_{y,al}$, kN (kip)	V_t, kN (kip)	ω_0, mm (in.)	Predicted failure modes	Actual failure modes
CY24-S0.57	99 (22.3)	446 (100.3)	475 (106.8)	492 (110.6)	0.20 (0.0079)	TT	TT&CS
CY54-S0.67	100 (22.5)	504 (113.3)	645 (145.0)	730 (164.1)	0.18 (0.0071)	TT	TT&CS
CY44-S0.73	126 (28.3)	575 (129.3)	754 (169.5)	754 (169.5)	0.13 (0.0051)	TT	TT&CS
CY54-S0.33	126 (28.3)	534 (120.0)	670 (150.6)	824 (185.2)	0.09 (0.0035)	TT	TT&CS
CY54-S0.80	100 (22.5)	601 (135.1)	662 (148.8)	662 (148.8)	0.23 (0.0091)	TT	TT&CS
CY54-S0.33*	149 (33.5)	470 (105.7)	611 (137.4)	658 (147.9)	0.12 (0.0047)	TT	TT&CS
CY54-S0.67*	123 (27.7)	448 (100.7)	550 (123.6)	611 (137.4)	0.19 (0.0075)	TT	TT&CS
CY54-S0.80*	125 (28.1)	—†	—†	445 (100.0)	0.41 (0.0161)	TT	DS

†Longitudinal bars did not yield when Specimen CY54-S0.80* was damaged.

Note: V_{cr} is first cracking load; $V_{y,st}$ and $V_{y,al}$ are load corresponding to start of yielding and complete yielding of longitudinal bars, respectively; V_t is ultimate load; ω_0 is crack width under serviceability limit state; TT is tension tie failure mode defined by STM; TT&CS is tension tie and compression strut failure mode; DS is diagonal splitting failure mode.

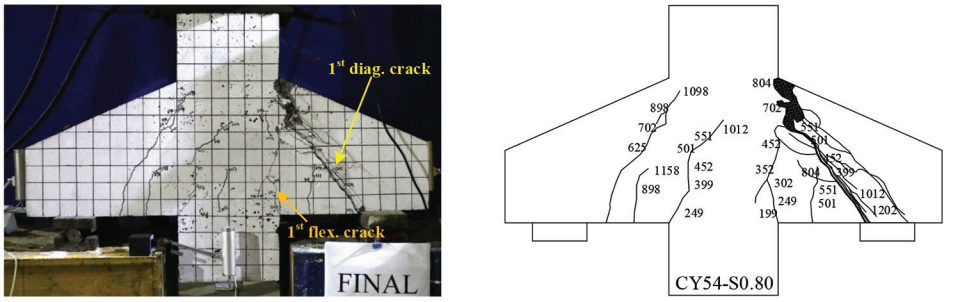

(a) CY54-S0.80 (tension tie and compression strut failure)

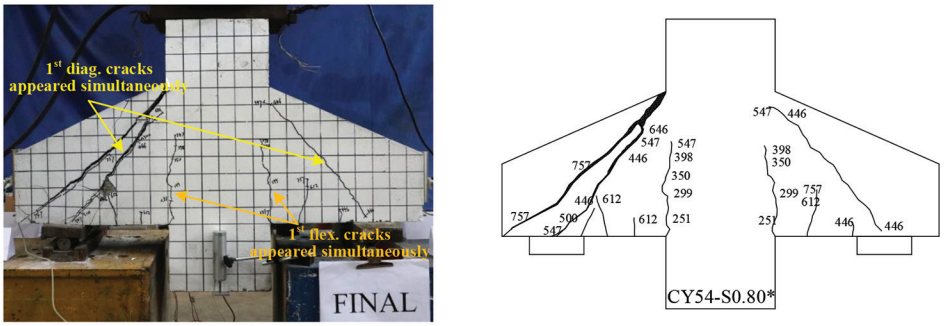

(b) CY54-S0.80* (diagonal splitting failure)

Fig. 4—Typical failure modes and crack distributions: (a) CY54-S0.80 (tension tie and compression strut failure); and (b) CY54-S0.80 (diagonal splitting failure). (Note: 1 kN = 0.225 kip.)*

corbel root. The width of the first diagonal crack was wider than that of the first flexural crack in subsequent loading steps. This is because the shear load tends to be transferred directly from the load point to the column point through the compression strut,[20] resulting in wider diagonal cracks on the strut with increased load. When the load increased to 625 kN (140.51 kip) ($0.47V_t$), a similar diagonal crack appeared in the left corbel. New parallel diagonal cracks then continued to appear. When the load increased to 1202 kN (270.22 kip) ($0.91V_t$), the longitudinal bars began to yield, and the diagonal cracks continued to develop and widen. When the load increased to 1324 kN (297.65 kip) ($0.99V_t$), all the longitudinal bars yielded. Soon after, a large diagonal crack suddenly appeared in the right corbel, accompanied by crushing and spalling of the concrete.

For Specimen CY54-S0.80*, two flexural cracks appeared simultaneously at a load of 251 kN (56.43 kip) ($0.28V_t$) at the corbel-column interface on the left and right sides. As the load increased to 446 kN (100.26 kip) ($0.50V_t$), two diagonal cracks first appeared simultaneously on the right and left corbels. When the load increased to 890 kN (200.08 kip) ($1.00V_t$), two diagonal cracks in the left corbel passed through the front and rear almost simultaneously, and the specimen lost the bearing capacity immediately. No yielding of the longitudinal bars occurred before the damage, and a little spalling of the concrete was observed. Due to the absence of horizontal stirrups, the load-bearing capacity of Specimen CY54-S0.80* was approximately 67% of that of CY54-S0.80.

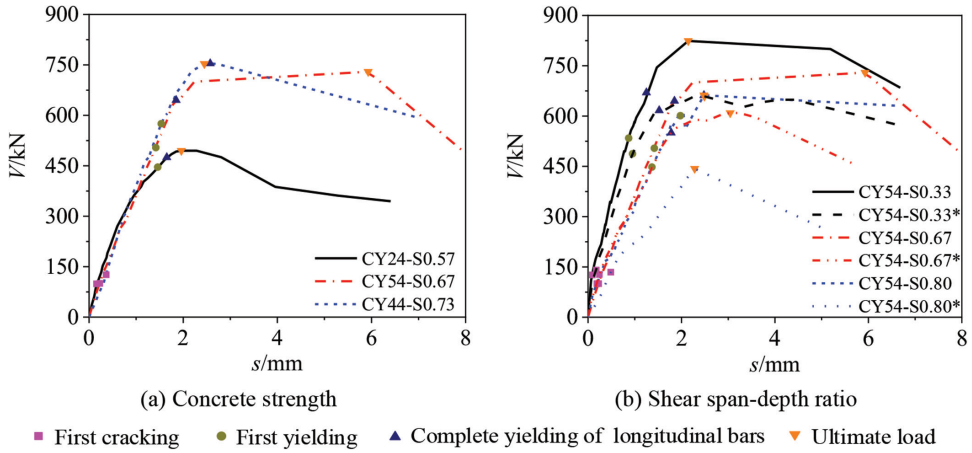

Fig. 5—Load-displacement curves and characteristic points under variables: (a) concrete strength; and (b) shear span-depth ratio.

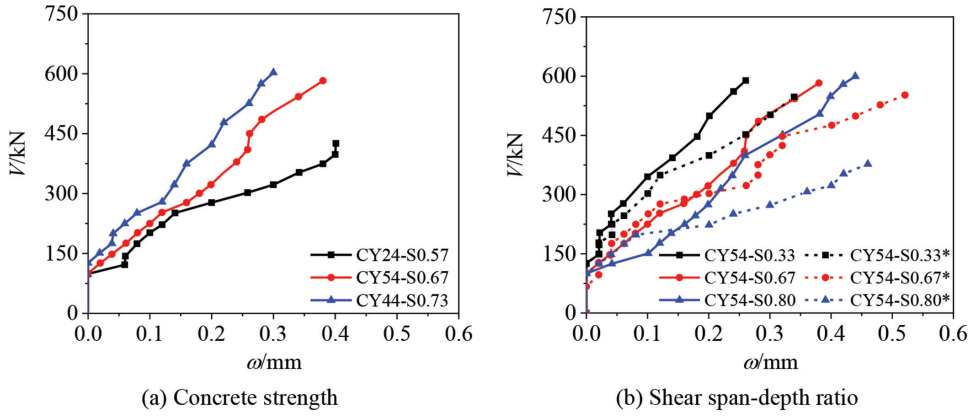

Fig. 6—Load-crack width curves under two variables: (a) concrete strength; and (b) shear span-depth ratio.

Load-displacement curves

The load-displacement curves are shown in Fig. 5. When the load increased to 20% of the peak, the corbel was cracked, and the slope of the curves began to decrease. When the load increased to approximately 70% of the peak, the longitudinal bars began to yield (except CY54-S0.80*), and the slope of the curve decreased at a faster pace. When the load was over 90% of the peak, all the longitudinal bars yielded, and the slope of the curves decreased even further. Due to the brittle character of the failure, the curves abruptly dropped off after reaching the peak.

According to the STM, if the compressive strength of the concrete is improved while keeping the design load capacity constant, the effective depth of the corbel section needs to be decreased, and the area of the longitudinal bars needs to be increased. As the shear span remains constant, improving the design value of concrete strength will cause an increase in the shear span-depth ratio for the corbels. Figure 5(a) shows that improving the compressive strength of the concrete has little effect on the stiffness of the specimens but significantly enhances the load-bearing capacity. The combined effect of increased compressive strength and increased area of longitudinal bars on the improvement in load-bearing capacity is greater than the reduction effect caused by the decreased section depth.

According to the STM, if the shear span is increased while keeping the design load capacity constant, the area of the longitudinal bars needs to be increased. Figure 5(b) shows that the vertical displacements of the specimens with larger shear span-depth ratios are more significant under the same load. The reason is that an increase in the shear span will aggravate the midspan deflection of the specimens.

In addition, Fig. 5(b) shows that the stiffness and load-bearing capacity of the hooped specimens are greater than those of the non-stirrup specimens. The discrepancy is particularly significant between CY54-S0.80 and CY54-S0.80*, which have the largest shear span-depth ratio. This phenomenon shows that the setting of horizontal stirrups can improve the stiffness of corbels, especially with a large shear span-depth ratio.

Crack width

Figure 6(a) shows that the cracks were thinner overall for the specimens with higher compressive strength at the same load. During the test, the widest cracks appeared on the surfaces of the compression strut. Improving the compressive strength of the concrete strengthens the compression strut.

Figure 6(b) shows that the specimens with larger shear spans have wider cracks at the same load. The crack width of the specimens equipped with horizontal stirrups was smaller

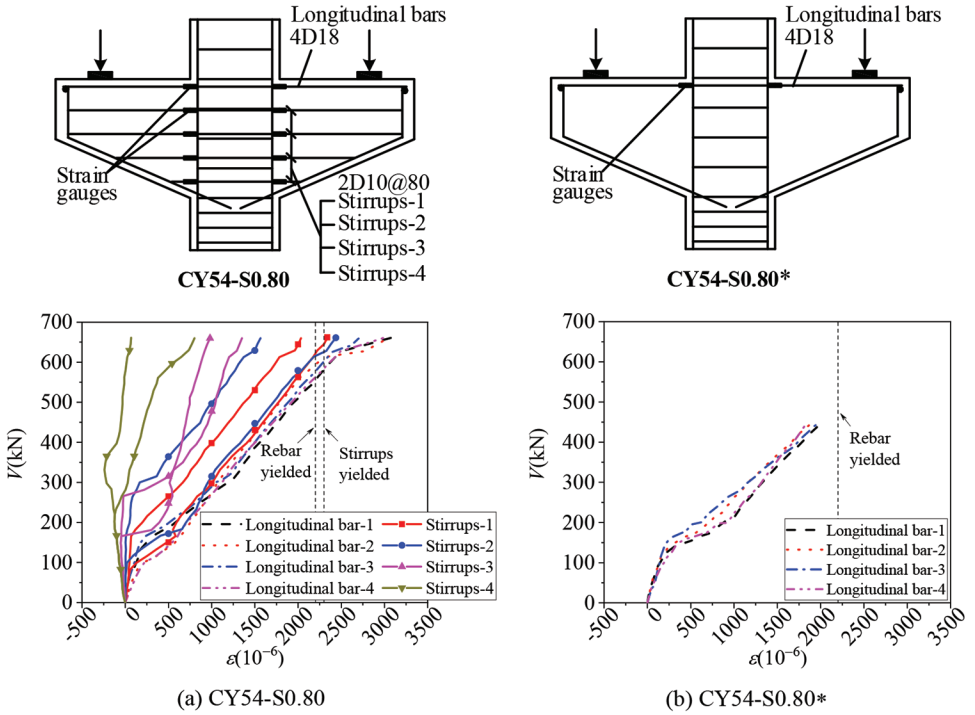

(a) CY54-S0.80 (b) CY54-S0.80*

Fig. 7—Strain development of longitudinal bars and stirrups: (a) CY54-S0.80; and (b) CY54-S0.80.*

than that of the non-stirrup specimens. The crack widths at the serviceability limit state are listed in Table 5. The load at the serviceability limit state was calculated by dividing the actual designed load by 1.4.[17,23] The larger the shear span-depth ratio, the more effectively the horizontal stirrups controlled the crack width. For example, the crack width of CY54-S0.80 under the serviceability limit state was approximately half that of CY54-S0.80*.

Strain on reinforcement

All the longitudinal bars in the corbel specimens except CY54-S0.80* yielded before failure. The typical strain trends of longitudinal bars and stirrups are shown in Fig. 7, and CY54-S0.80 and CY54-S0.80* are selected to show the difference. For CY54-S0.80, before cracking, the strain on longitudinal bars and stirrups developed slowly; the stress in stirrups-4 (the fourth layer of the horizontal stirrups, as shown in Fig. 7(a)) was initially compressive. The reason is the flexure of the specimen at the initial load stage, resulting in tension at the top and compression at the bottom. After cracking, the strain on the longitudinal bars in stirrups-1 (the first layer) and stirrups-2 (the second layer) developed at a noticeably faster rate. After all the longitudinal bars yielded, stirrups-1 and stirrups-2 successively yielded. Near failure, the strain on stirrups-3 and stirrups-4 was still lower, with a corresponding stress of approximately 200 and 50 MPa (29.01 and 7.25 ksi) (the yield stress of the stirrups is 471 MPa [68.31 ksi]), showing that the longitudinal bars and the horizontal stirrups within the upper half of the section depth carried the majority of the load. Compared to CY54-S0.80, the change rate of the strain on the longitudinal bars of non-yielding specimen CY54-S0.80* is slightly lower with load growth, as shown in Fig. 7(b). Due to the lack of constraint from the horizontal stirrups, the concrete strut underwent premature splitting-tension damage, resulting in insufficient development of stress in the longitudinal bars.

Table 6—Comparison of design and measured capacities

ID	V_t, kN (kip)	$F_{de,A}$, kN (kip)	$V_t/F_{de,A}$
CY24-S0.57	492 (110.6)	404 (90.8)	1.22
CY54-S0.67	730 (164.1)	416 (93.5)	1.75
CY44-S0.73	754 (169.5)	414 (93.1)	1.82
CY54-S0.33	824 (185.2)	467 (105.0)	1.76
CY54-S0.80	662 (148.8)	475 (106.8)	1.39
CY54-S0.33*	658 (147.9)	467 (105.0)	1.41
CY54-S0.67*	611 (137.4)	415 (93.3)	1.47
CY54-S0.80*	445 (100.0)	475 (106.8)	0.94

Note: V_t is actual bearing capacity; $F_{de,A}$ is actual design load capacity.

CODE FORMULAS EVALUATION

A safety factor α_t is defined to evaluate the accuracy and safety of the STM under each variable—that is, the ratio of the actual bearing capacity to the design load capacity. The factor is expressed in Eq. (11). The larger the factor values, the higher the level of conservatism of the STM. The factor values for each specimen are listed in Table 6.

$$\alpha_t = \frac{V_t}{F_{de,A}} \tag{11}$$

Influence of concrete compressive strength

Figure 8(a) shows that when the concrete compressive strength increases from 23.8 to 54.2 MPa (3.45 to 7.86 ksi), the safety factor increases from 1.22 to 1.75. The actual bearing capacity of the corbels designed by the STM will be

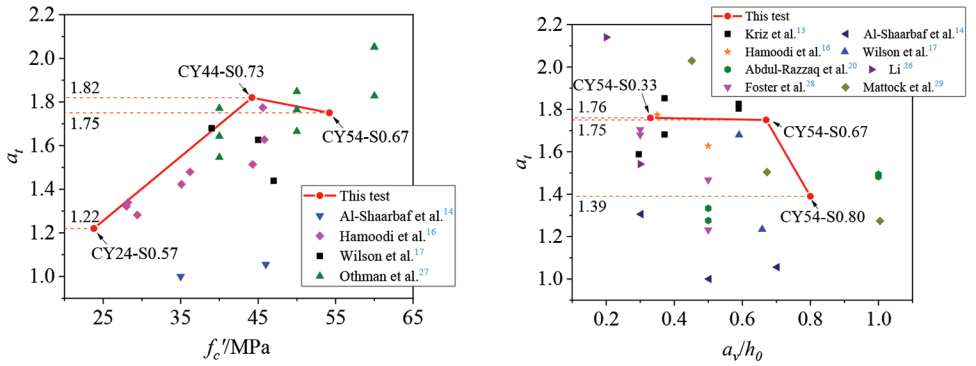

(a) Concrete strength

(b) Shear span-depth ratio

Fig. 8—Influence of variables on safety factor: (a) concrete strength; and (b) shear span-depth ratio. (Note: 1 MPa = 0.145 ksi.)

enhanced by increasing the concrete compressive strength while keeping the design load and shear span constant. It also indicates that when using the STM to design corbels, the increase in the concrete strength and the increase in the area of the longitudinal bars, together, have a more significant effect on the enhancement of load-bearing capacity than the reduction effect caused by the decrease in section depth.

Influence of shear span-depth ratio

Figure 8(b) shows that when the shear span-depth ratio increases from 0.33 to 0.80, the safety factor decreases from 1.76 to 1.39. The actual bearing capacity of the corbels designed by the STM will be reduced by increasing the shear span-depth ratio while keeping the design load and concrete strength constant. It also indicates that when using the STM to design corbels, the increase in the area of longitudinal bars has a lower effect on the enhancement of load-bearing capacity than the reduction effect caused by the increase in the shear span-depth ratio.

Influence of horizontal stirrups

The nominal design capacity of the STM does not consider the presence of horizontal stirrups but only takes into account the influence of the stirrup reinforcement ratio on the strength coefficient (β_s) of the concrete compression strut. For specimens with horizontal stirrups ratios greater than $0.0025/(\sin^2\theta)$ (where θ is the angle between the tie and the strut), β_s was assumed to be 0.75; otherwise, it was taken as 0.40.[9] In this test, all hooped corbels had a β_s of 0.75. Based on the same design parameters, the actual bearing capacity of non-stirrup specimens was significantly lower than that of hooped specimens. As the shear span-depth ratio increased from 0.33 to 0.80, the ratio of load-bearing capacity between the non-stirrup corbels and the hooped corbels generally tended to decrease from 84 to 67%, as shown in Fig. 9. This indicates that the strengthening effect of the horizontal stirrups on the load-bearing capacity became more significant as the shear span-depth ratio increased.

Moreover, the horizontal stirrups restricted the cracks in the compression strut and reduced the crack width, as depicted in Fig. 6(b). The cracks were more prominent in non-stirrup specimens, such as CY54-S0.80*, which failed due to DS failure, while hooped specimens, like CY54-S0.80, failed due to TT&CS failure. The actual load-bearing capacity of

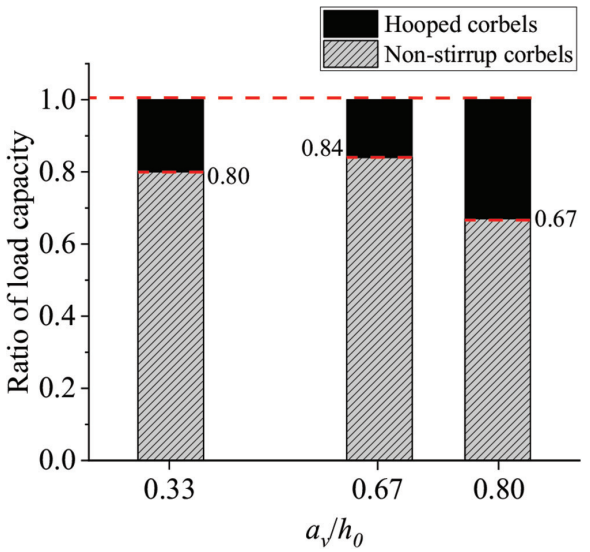

Fig. 9—Ratio of load-bearing capacity between corbels with and without stirrups under various shear span-depth ratios.

CY54-S0.80* was 94% of its designed load capacity. Therefore, to enhance the load-bearing capacity and improve the visibility of corbel failure, horizontal stirrups should be used to improve the strength of the compression strut, and the β_s should be increased to 0.7.

Comparison with previous studies

To verify the reliability of the test results in this paper, a comparison was made with previous studies[13,14,16,17,20,26-29] involving 44 corbels. The compressive strength or shear span-depth ratio of the 44 corbels was close to that of the specimens in this paper, ensuring comparability among test data. Table 7 lists the corbels' details and calculated safety factors. The comparison was made by keeping one of the two variables constant while comparing the safety factor at the concrete compressive strength or the shear span-depth ratio.

Figure 8(a) indicates that the safety factor generally increased with an increase in the compressive strength of the concrete in most of the tests conducted by Al-Shaarbaf et al.,[14] Hamoodi et al.,[16] and Othman and Aziz.[27] Figure 8(b) shows that the safety factor generally decreased with an increase in the shear span-depth ratio in most of the tests

Table 7—Corbels' details in previous studies and calculated safety factor

Sources	Label	h_0, mm	b, mm	a_v, mm	a_v/h_0	f_c', MPa	f_y, MPa	A_s, mm^2	V_t, kN	V_{STM}, kN	α_t
Kriz and Raths[13]	2S	409	203	241	0.59	32	304	773	484	265	1.83
	3S	409	203	241	0.59	31	311	773	487	270	1.80
	5S	409	203	152	0.37	30	305	773	602	358	1.68
	6S	409	203	152	0.37	31	305	773	665	359	1.85
	10S	409	203	121	0.30	29	328	773	694	437	1.59
Al-Shaarbaf et al.[14]	HSCC1	215	150	108	0.50	48	532	339	229	229	1.00
	LNC5	215	150	151	0.70	35	532	339	175	175	1.00
	HNC5	215	150	151	0.70	46	532	339	190	180	1.06
	HNC6	215	150	65	0.30	46	532	339	410	314	1.31
Hamoodi et al.[16]	C1	275	200	138	0.50	28	440	339	345	257	1.34
	C2	275	200	138	0.50	28	440	339	340	257	1.32
	C3	275	200	138	0.50	36	440	339	389	263	1.48
	C4	275	200	138	0.50	35	440	339	375	263	1.42
	C5	275	200	138	0.50	46	440	339	433	266	1.63
	C6	275	200	138	0.50	44	440	339	403	266	1.51
	C7	275	200	96	0.35	29	440	339	363	283	1.28
	C8	275	200	96	0.35	46	440	339	520	293	1.77
Wilson et al.[17]	C0	559	356	368	0.66	37	506	2039	1427	1156	1.23
	C1	559	356	330	0.59	45	487	2039	1678	1032	1.63
	C2	559	356	330	0.59	47	487	2039	1785	1241	1.44
	C3	559	356	330	0.59	39	487	2039	1545	920	1.68
Abdul-Razzaq and Dawood[20]	RI0.5	360	120	180	0.50	32	440	452	596	447	1.33
	RI1	360	120	360	1.00	31	440	452	473	319	1.48
	RE0.5	360	120	180	0.50	31	440	452	560	439	1.28
	RE1	360	120	360	1.00	30	440	452	466	312	1.49
Li[26]	N02	410	200	41	0.10	20	378	452	500	212	2.36
	N03	410	200	82	0.20	20	378	452	460	215	2.14
	N04	410	200	123	0.30	20	378	452	330	214	1.54
Othman and Aziz[27]	C11	239	180	135	0.56	40	415	452	351	227	1.55
	C12	239	180	135	0.56	50	415	452	383	230	1.67
	C13	239	180	135	0.56	60	415	452	424	232	1.83
	C21	239	180	135	0.56	40	415	452	373	227	1.64
	C22	239	180	135	0.56	50	415	452	406	230	1.77
	C23	239	180	135	0.56	60	415	452	476	232	2.05
	C31	239	180	135	0.56	40	415	452	402	227	1.77
	C32	239	180	135	0.56	50	415	452	425	230	1.85
	C33	239	180	135	0.56	60	415	452	476	232	2.05
Foster et al.[28]	SC1–3	600	125	300	0.50	90	430	762	700	477	1.47
	SC2–3	600	125	300	0.50	62	430	762	580	471	1.23
	PC2	500	150	150	0.30	53	420	762	1040	610	1.70
	PF2	500	150	150	0.30	105	420	762	1050	625	1.68
Mattock et al.[29]	B1	226	152	102	0.45	25	335	258	209	103	2.03
	B2	226	152	152	0.67	24	321	400	173	115	1.50
	G4	228	127	229	1.00	26	442	426	107	84	1.27

Note: V_{STM} is calculated load-bearing capacity according to STM; α_t is safety factor, calculated by dividing V_{STM} into V_t; 1 mm = 0.039 in.; 1 MPa = 0.145 ksi; 1 kN = 0.225 kip.

conducted by Al-Shaarbaf et al.,[14] Hamoodi et al.,[16] Wilson et al.,[17] Li,[26] Foster et al.,[28] and Mattock et al.[29] The trend of the safety factor in this paper was similar to that of most of the cited studies. The change rate of the safety factor under the two variables was also within the range of the change of the cited studies. However, the change rate varied in these studies due to different settings of the design parameters and some experimental errors. The difference in the change rate may also be due to the fact that the design bearing capacity of the corbels in this paper was the same, while the design bearing capacity (or the calculated bearing capacity by the STM) in other tests under a variable was different.

CONCLUSIONS

This paper designed eight double-corbel specimens according to the strut-and-tie method (STM) in ACI 318-19. The accuracy and safety of the STM were evaluated under the given variables. In addition, under the different shear span-depth ratios, the strengthening effect of the horizontal stirrups on the load-bearing capacity was also investigated. Conclusions can be drawn as follows:

1. Keeping the design load constant and improving the compressive strength of the concrete results in a higher level of safety in the STM. For example, the safety factor increased from 1.22 to 1.75 once the compressive strength of the concrete increased from 23.8 to 54.2 MPa (3.45 to 7.86 ksi).

2. Keeping the design load constant and increasing the shear span of the corbels results in a lower level of safety in the STM. For example, the safety factor decreased from 1.76 to 1.39 once the shear span-depth ratio increased from 0.33 to 0.80.

3. The horizontal stirrups' strengthening effect on the load-bearing capacity becomes more significant as the shear span-depth ratio increases. The setting of horizontal stirrups (ensuring β_s of 0.7) helps to avoid premature failure of the corbels with large shear span-depth ratios (such as 0.80 in this test).

4. At the design stage, choosing a higher concrete strength or a lower shear span can help mitigate the crack width under the serviceability limit state for the corbels. In addition, the larger the shear span-depth ratio of a corbel, the more effective the mitigation for the crack width by the horizontal stirrups under the serviceability limit state.

5. The horizontal stirrups within the upper half of the corbels' section depth can fully develop the tensile stress. The farther away the stirrups are from the longitudinal bars, the lower the degree of stress development.

AUTHOR BIOS

Bing Han *is a Postdoctoral Fellow in the College of Civil Engineering at Hunan University, Changsha, Hunan, China, where he received his PhD in 2023. His research interests include the strut-and-tie method of deep members and design of reinforced concrete structures.*

Yuan Huang *is a Professor in the Department of Civil Engineering at Hunan University. He received his PhD in 2009 from the School of Civil Engineering at Tsinghua University, Beijing, China. His research interests include the behavior of concrete and precast concrete structures, the behavior of steel-concrete composite structures, and seismic design and analysis of structures.*

ACKNOWLEDGMENTS

This research was funded by the National Natural Science Foundation of China (No. 51890901), and the Natural Science Foundation of Hunan Province, China (No. 2020JJ2003, 2020RC5005).

REFERENCES

1. Yong, Y.-K., and Balaguru, P., "Behavior of Reinforced High-Strength-Concrete Corbels," *Journal of Structural Engineering*, ASCE, V. 120, No. 4, Apr. 1994, pp. 1182-1201. doi: 10.1061/(ASCE)0733-9445(1994)120:4(1182)

2. Schlaich, J., and Schäfer, K., "Design and Detailing of Structural Concrete Using Strut-and-Tie Models," *The Structural Engineer*, V. 69, No. 6, Mar. 1991, pp. 113-125.

3. Wang, T.; Su, X.; and Fang, J., "Application of STMs for Calculation of Reinforced Concrete Frame Joints," *China Civil Engineering Journal*, V. 40, No. 11, 2007, pp. 36-40.

4. Hsu, T. T. C., *Unified Theory of Reinforced Concrete*, Routledge, New York, 2017, 329 pp.

5. Schlaich, J.; Schäfer, K.; and Jennewein, M., "Toward a Consistent Design of Structural Concrete," *PCI Journal*, V. 32, No. 3, May-June 1987, pp. 74-150. doi: 10.15554/pcij.05011987.74.150

6. Hwang, S.-J., and Lee, H.-J., "Strength Prediction for Discontinuity Regions by Softened Strut-and-Tie Model," *Journal of Structural Engineering*, ASCE, V. 128, No. 12, Dec. 2002, pp. 1519-1526. doi: 10.1061/(ASCE)0733-9445(2002)128:12(1519)

7. Hwang, S.-J.; Tsai, R.-J.; Lam, W.-K.; and Moehle, J. P., "Simplification of Softened Strut-and-Tie Model for Strength Prediction of Discontinuity Regions," *ACI Structural Journal*, V. 114, No. 5, Sept.-Oct. 2017, pp. 1239-1248. doi: 10.14359/51689787

8. Ritter, W., "Die Bauweise Hennebique [Hennebiques Construction Method]," *Schweizerische Bauzeitung*, V. 33, No. 5, Feb. 1899, pp. 41-43. (in German)

9. ACI Committee 318, "Building Code Requirements for Structural Concrete (ACI 318-19) and Commentary (ACI 318R-19) (Reapproved 2022)," American Concrete Institute, Farmington Hills, MI, 2019, 624 pp.

10. Khosravikia, F.; Kim, H.; Yi, Y.; Wilson, H.; Yousefpour, H.; Hrynyk, T.; and Bayrak, O., "Experimental and Numerical Assessment of Corbels Designed Based on Strut-and-Tie Provisions," *Journal of Structural Engineering*, ASCE, V. 144, No. 9, Sept. 2018, p. 04018138. doi: 10.1061/(ASCE)ST.1943-541X.0002137

11. *fib*, "*fib* Model Code for Concrete Structures 2010," International Federation for Structural Concrete, Lausanne, Switzerland, 2013, 434 pp.

12. Tuchscherer, R.; Birrcher, D.; Huizinga, M.; and Bayrak, O., "Confinement of Deep Beam Nodal Regions," *ACI Structural Journal*, V. 107, No. 6, Nov.-Dec. 2010, pp. 709-717.

13. Kriz, L. B., and Raths, C. H., "Connections in Precast Concrete Structures—Strength of Corbels," *PCI Journal*, V. 10, No. 1, Feb. 1965, pp. 16-61. doi: 10.15554/pcij.02011965.16.61

14. Al-Shaarbaf, I. A.; Al-Azzawi, A. A.; and Farahan, R. S., "Experimental Investigation on the Behavior of Reinforced Concrete Corbels under Repeated Loadings," *Journal of Engineering and Sustainable Development*, V. 19, No. 4, 2015, pp. 126-147.

15. Abdul-Razzaq, K. S.; Dawood, A. A.; and Mohammed, A. H., "A Review of Previous Studies on the Reinforced Concrete Corbels," *IOP Conference Series: Materials Science and Engineering*, V. 518, No. 2, 2019, Article No. 022057. doi: 10.1088/1757-899X/518/2/022057

16. Hamoodi, A. Z.; Chkheiwer, A. H.; and Kadim, J. A., "Shear Strength of Reinforced Recycled Aggregate Concrete Corbels," *Journal of Engineering*, V. 2021, 2021, Article No. 6652647. doi: 10.1155/2021/6652647

17. Wilson, H. R.; Yousefpour, H.; Brown, M. D.; and Bayrak, O., "Investigation of Corbels Designed According to Strut-and-Tie and Empirical Methods," *ACI Structural Journal*, V. 115, No. 3, May 2018, pp. 813-824.

18. AASHTO, "AASHTO LRFD Bridge Design Specifications," eighth edition, American Association of State Highway and Transportation Officials, Washington, DC, 2017, 1780 pp.

19. Abdul-Razzaq, K. S., and Dawood, A. A., "Corbel Strut and Tie Modeling – Experimental Verification," *Structures*, V. 26, Aug. 2020, pp. 327-339. doi: 10.1016/j.istruc.2020.04.021

20. Abdul-Razzaq, K. S., and Dawood, A. A., "Reinforcing Struts and Ties in Concrete Corbels," *ACI Structural Journal*, V. 118, No. 4, July 2021, pp. 153-162.

21. Hwang, S.-J.; Lu, W.-Y.; and Lee, H.-J., "Shear Strength Prediction for Reinforced Concrete Corbels," *ACI Structural Journal*, V. 97, No. 4, July-Aug. 2000, pp. 543-552.

22. Shen, P. S., *Design of Concrete Structures*, third edition, Higher Education Press, Beijing, China, 2007, 365 pp.

23. Yao, J.; Gu, H.; Li, Q.; and Huang, B., "Research on Bearing Capacity Design Reliability of RC Crane Beams," *Journal of Hunan University (Natural Sciences)*, V. 46, No. 9, Sept. 2019, pp. 21-30.

24. ASTM C39/C39M-17, "Standard Test Method for Compressive Strength of Cylindrical Concrete Specimens," ASTM International, West Conshohocken, PA, 2017, 8 pp.

25. ASTM A370-17, "Standard Test Methods and Definitions for Mechanical Testing of Steel Products," ASTM International, West Conshohocken, PA, 2017, 49 pp.

26. Li, G., "Experimental Study on Design Method of Reinforced Concrete Corbel with Small Shear Span Ratio," master's thesis, Hohai University, Nanjing, Jiangsu, China, 2008.

27. Othman, Z. S., and Aziz, O. Q., "Ultimate Shear Strength of Reinforced High Strength Concrete Corbels Subjected to Vertical Load," *Al-Rafidain Engineering Journal (AREJ)*, V. 18, No. 1, Feb. 2010, pp. 1-12.

28. Foster, S. J.; Powell, R. E.; and Selim, H. S., "Performance of High-Strength Concrete Corbels," *ACI Structural Journal*, V. 93, No. 5, Sept.-Oct. 1996, pp. 555-563.

29. Mattock, A. H.; Chen, K. C.; and Soongswang, K., "The Behavior of Reinforced Concrete Corbels," *PCI Journal*, V. 21, No. 2, Mar.-Apr. 1976, pp. 52-77. doi: 10.15554/pcij.03011976.52.77

ACI STRUCTURAL JOURNAL TECHNICAL PAPER

Title No. 121-S29

Early-Age Cracking Resistance of Reinforced High-Strength Concrete

by Chuyuan Wen, Dejian Shen, Yang Jiao, Ci Liu, and Ming Li

*High-strength concrete (HSC) with a low water-cement ratio (*w/c*) may experience large autogenous shrinkage (AS). When shrinkage of concrete is restrained by the subgrade, foundation, or other part of the structure, HSC is more prone to crack. However, studies devoted to the early-age cracking resistance of reinforced HSC under uniaxial restrained conditions and adiabatic conditions are still lacking. In the current research, the effect of reinforcement percentage and reinforcement configuration on the temperature history, shrinkage, stress, and creep behavior of reinforced HSC at early age was analyzed using the temperature-stress test machine. Test results showed that reinforcement could effectively restrain the development of concrete shrinkage and creep. The cracking resistance of HSC increased with increasing reinforcement percentage, evaluated by the integrated criterion. With the same reinforcement percentage, reinforced HSC with distributed reinforcement along with a proper thickness of concrete cover exhibited higher cracking resistance compared with that of central reinforcement.*

Keywords: cracking resistance; early age; high-strength concrete (HSC); reinforcement; temperature-stress test machine (TSTM).

INTRODUCTION

Nowadays, high-strength concrete (HSC) is widely used in practical engineering. However, the low water-cement ratio (*w*/*c*) of HSC brings about serious self-desiccation and large autogenous shrinkage (AS) of concrete.[1] Due to the time-dependent behavior of concrete, such as the tensile strength, shrinkage, creep, and thermal deformation, the tensile stress of concrete is generated when the temperature of concrete gradually decreases. Cracks occur when the tensile stress of concrete reaches its tensile strength.[2] Cracks can penetrate deeply into the structure and shorten its service life due to the penetration of chemical components.[3] In engineering practices, reinforced concrete structures are the most common structural form.[4] The role of reinforcement is to serve as a kind of restraint source and limit the crack width of reinforced concrete members.[5] When various constraints restrict concrete shrinkage, reinforcing bars can not only contribute to the evolution of shrinkage stress, but also serve a significant function in resisting the shrinkage stress arising from other constraints.[6] Many studies have indicated that reinforced concrete buildings have a higher failure probability during construction than during the service period.[7] Therefore, the effect of reinforcement on the cracking resistance of HSC at early age needs to be studied.

Investigation on AS of concrete is critical for estimating the cracking resistance. Several studies have reported the influence of reinforcement on concrete shrinkage. Huang et al.[6] found that the restraining effect of reinforcement on the shrinkage of concrete declined with increasing distance to the reinforcing bar. Yoo et al.[8] revealed that reinforcing bars with a relatively lower stiffness cause a decline in the AS stress, the degree of restraint, and the cracking potential of concrete. Many classical models have been established for the prediction of the AS of concrete. However, the influence of reinforcement on the time-dependent AS of concrete is not considered. Therefore, in-depth investigations are necessary to predict the AS of reinforced HSC.

Cracking highly depends on creep denoting the viscoelastic response of concrete under a constant load.[9,10] Early-age tensile creep (TC) is the time-dependent deformation caused by the sustained shrinkage stress in restrained concrete, which plays an important role in relaxing shrinkage-induced tensile stresses and delaying the time to cracking.[11] Investigations of early-age TC are crucial for the in-depth analysis of the cracking resistance of concrete. The effect of reinforcement on concrete creep behavior under long-term loading has been investigated.[12] However, relevant research concerning early-age TC is limited due to measurement difficulties.[13] Thus, investigations on early-age TC of reinforced HSC are necessary for further estimating the cracking resistance.

Many factors, such as restraint degree, temperature variations, and shrinkage deformation, can lead to the cracking of structures at early age. Test methods such as the ring and doubly restrained plate have been adopted to investigate the cracking resistance of reinforced concrete.[14,15] Briffaut et al.[16] indicated that reinforcing bars can postpone cracking through the thermal active restrained shrinkage ring test. However, some limitations of the aforementioned methods exist, such as uncontrolled temperature history and restraint degree. To overcome these limitations, a temperature-stress test machine (TSTM) is developed to investigate the early-age behavior and cracking resistance of concrete. Recent findings are reported on the cracking resistance of concrete by using the TSTM.[17,18] The adiabatic condition is required in the test so that the actual thermal behavior in concrete can be reflected because the interior of real mass concrete is close to the state of adiabatic temperature rise.[19] The creep behavior in real concrete structures varies under different restrained conditions, and the controllable restraint degree is necessary for precise investigation.[20] Experimental studies on early-age cracking resistance of reinforced normal-strength concrete have been investigated

ACI Structural Journal, V. 121, No. 3, May 2024.
MS No. S-2022-276.R2, doi: 10.14359/51740456, received August 5, 2023, and reviewed under Institute publication policies.

using the TSTM.[5,21] However, the strength development of HSC is different from that of normal-strength concrete, and the bond behavior between concrete and reinforcing bars is different. Therefore, investigations on the influence of reinforcement on the early-age cracking resistance of HSC under adiabatic conditions and uniaxial restraint using the TSTM are imperative. For a better judgment of the cracking resistance of concrete structures, single evaluation indexes and comprehensive evaluation indexes should be analyzed under different reinforcement conditions.

Previously, researchers have conducted studies on the properties of reinforced HSC, such as the pore structure,[22] bond behavior,[23] and shrinkage of reinforced concrete.[24] However, investigations on the early-age cracking resistance of reinforced HSC considering the influence of reinforcement based on the comprehensive analyses of temperature, shrinkage, stress, and creep behavior remain lacking. Therefore, the early-age behavior of real concrete was analyzed under adiabatic conditions and uniaxial constant restraint degree by using the TSTM.

RESEARCH SIGNIFICANCE

Reinforced concrete structures are common in engineering practices. Studies on the early-age cracking resistance of reinforced HSC under uniaxial restrained conditions and adiabatic conditions are lacking. The influence of four kinds of reinforcement percentage and three kinds of reinforcement configuration on the early-age cracking resistance of reinforced HSC was comprehensively studied using the TSTM. The specific objectives of the current research were to provide guidance and reference for the application of reinforced HSC in practical engineering.

EXPERIMENTAL PROCEDURE

Materials and sample preparation

As per Chinese standard GB 175-2007/XG3-2018,[25] portland cement (P.II 52.5R) was used. Fine aggregate of traditional river sand had a fineness modulus of 2.3. Coarse aggregate of crushed limestone was evenly distributed in the range of 4.75 to 25.0 mm (0.19 to 0.98 in.). The liquid high-range water-reducing admixture (HRWRA) was polycarboxylate-based, and the mixing water was tap. Mixture proportions by weight were given as follows. Water:cement:coarse aggregate:fine aggregate:HRWRA = 158.4:480:1131:636:3.84.

The specimens were reinforced with HRB 400 reinforcing bars, with four different percentages of longitudinal reinforcement (0, 0.50, 0.89, and 1.40%). Figure 1 depicts that 0.50% reinforcement is realized with different configurations of reinforcing bars—that is, four reinforcing bars in

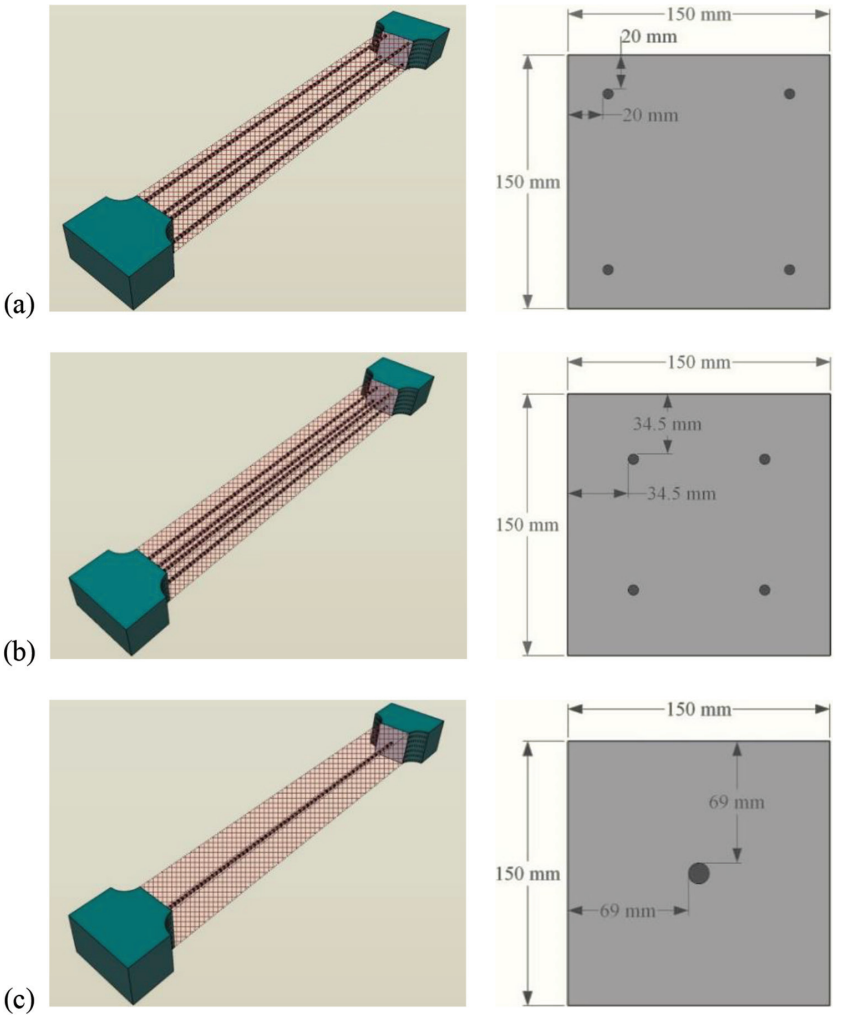

Fig. 1—Three different configurations of reinforcing bars.

the corners of the specimen with a concrete cover of 20 mm (0.79 in.), four reinforcing bars in the corners of the specimen with a concrete cover of 34.5 mm (1.36 in.), and one reinforcing bar at the center. Specimen labels and parameters are shown in Table 1.

TSTM test

The TSTM system is developed to measure the uniaxial restrained shrinkage for sealed specimens, as well as to evaluate the cracking resistance of concrete quantitatively, which often assumes simplified boundary conditions.[26,27] The TSTM test is controlled by a closed-loop system with high accuracy and smooth loading. The reliability of the system and reproducibility of test results were extensively examined in references by repeating the test or by simulation, and satisfactory results were obtained.[28] To substantiate the lab tests, further study needs to consider field and large-scale specimen validations. The actual photo and schematic diagram of the TSTM is shown in Fig. 2. The horizontal steel frame is designed as the TSTM mold, which consisted of a fixed steelhead, a moving end, as well as a central straight part. Restrained and free specimens possessed the same dog-bone mold, which was characterized by a cross section measuring 150 x 150 mm (5.9 x 5.9 in.) in the central part and measuring 150 x 280 mm (5.9 x 11.0 in.) at the heads. The length of the central part was 1500 mm (59 in.). Uniform stress distribution in the central part of the specimen could be assumed owing to the design of enlarged ends. Concrete was directly placed into the TSTM molds after mixing. The specimen was sealed with a plastic sheet to maintain a constant humidity. Measurements started after concrete placement and stopped when the concrete cracked.

Temperature control—The temperature in restrained samples was monitored in real time, transformed into data, and fed back to the computer-control system. Then, the temperature of the circulating liquid in the outer part of the mold was adjusted by a heating-cooling system to ensure that the temperature in the free sample was consistent with that in the restrained sample. The tested specimen went through three temperature phases: an adiabatic temperature phase, an isothermal temperature phase, and a cooling temperature phase. The temperature of the specimen increased to peak value, and kept isothermal for 36 hours. Then, the concrete sample cooled down at the cooling rate of 0.75°C/h (1.35°F/h) until the restrained specimen cracked.[29] With this specific cooling rate, the thermal gradient would

Table 1—Specimen labels and parameters

Label	Reinforcement percentage	Reinforcement configuration
HP-00	0	—
HRB-A-06	0.50%	4 ⌀ 6 (Fig. 1(a))
HRB-A-08	0.89%	4 ⌀ 8 (Fig. 1(a))
HRB-A-10	1.40%	4 ⌀ 10 (Fig. 1(a))
HRB-B-06	0.50%	4 ⌀ 6 (Fig. 1(b))
HRB-C-12	0.50%	1 ⌀ 12 (Fig. 1(c))

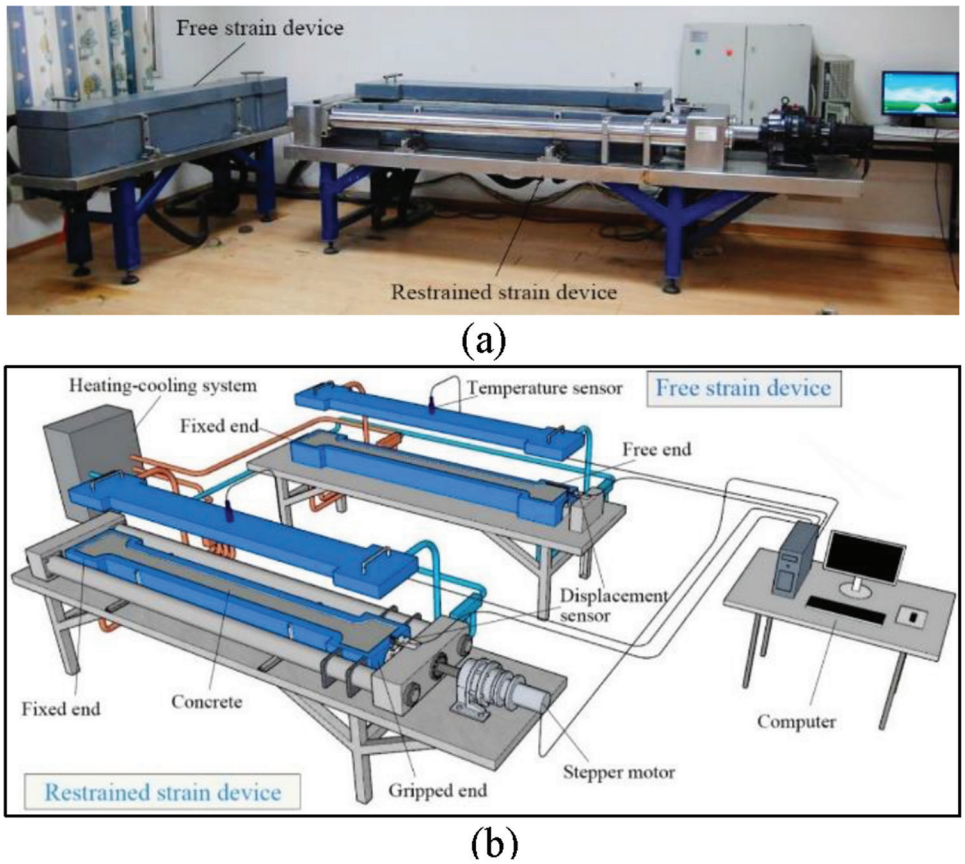

Fig. 2—TSTM used in experiment: (a) actual photo; and (b) schematic diagram.

not generate in the cross section of specimens due to excessively rapid cooling.[15]

Free strain measurement—One end of the free sample is free to move, and the other end is restrained by a fixed steelhead. The total strain of free specimens was calculated with Eq. (1)

$$\varepsilon_{total} = \frac{\Delta l}{L} \quad (1)$$

where Δl is recorded in real time by the linear variable deformation transducer (LVDT) fixed on the free end of the specimen; and L is the effective length of free specimen.

Restrained strain measurement—The restrained specimen was loaded by the computer-controlled stepper motor connected to the moving end, and the load was applied automatically to control the specimen at the initial length. The restrained sample was free to move until the strain reached a predetermined limit after time-zero. Once the strain reached this threshold, the deformation was set back to zero, resulting in an increase in the restrained stress of the restrained sample. The stepper motor maintained a constant load, and the restrained sample kept deforming until the strain reached the threshold value again and started a new compensation cycle. This procedure facilitated the accumulation of stress, elastic strain, and creep in the restrained sample, as shown in Fig. 3.

Restrained stress measurement—The specimen could achieve 100% restraint degree because the allowed deformation was very small. There was a load cell connected between the tested restrained specimen and the stepper motor, which could measure the stress of the specimen under the fully restraint degree, so that the stress development process of the restrained specimen under the corresponding temperature history could be recorded.

Calculation of test results

Early-age AS—Early-age AS was analyzed from time-zero, which was set as the starting time of restrained stress development.[30] The prediction of the coefficient of thermal expansion (CTE) could be calculated with Eq. (2)[31]

$$\alpha_T(t) = \alpha_k \times (1 + 41 \times t^{-m}) \quad (2)$$

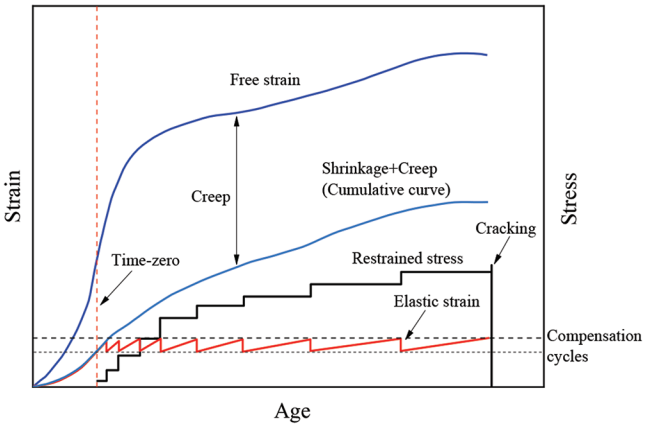

Fig. 3—Schematic diagram of strain and stress in TSTM test.[26]

where $\alpha_T(t)$ is the CTE of HSC, in με/°C; α_k is the 28-day CTE of HSC, in με/°C; t is the age, in days; and m is the parameter that depends on the concrete sample, taken as 2.0.

The total deformation of tested HSC specimens during the cooling stage was composed of thermal deformation and AS. However, the AS mainly occurred in the initial 24 hours after casting, and the duration of the forced cooling stage was short. Therefore, the AS of concrete was minimal at this stage. The CTE of HSC specimens was obtained by regression analysis of the deformation versus temperature curve in the forced cooling stage. The CTE of HSC increases initially and tends to be stable within 1 day. Thus, the CTE during the forced cooling stage was taken as the 28-day CTE.

Thermal deformation was non-constant due to the temperature variations over time. The AS was obtained by subtracting the thermal deformation from the total strain in the free specimens, as given in Eq. (3).[32]

$$\varepsilon_{as}(t) = \varepsilon_{total} - \alpha_T(t) \times [T(t) - T_{time-zero}] \quad (3)$$

where $\varepsilon_{as}(t)$ is the AS at time t, in με; ε_{total} is the total strain of free specimens, in με; $T(t)$ is the temperature of HSC, in °C; and $T_{time-zero}$ is the temperature of HSC at time-zero, in °C.

Equivalent age—The equivalent age of concrete was determined based on the maturity of the concrete, as given in Eq. (4).[33]

$$t_e = \int_0^t \exp\left[\frac{E_a(T)}{R}\left(\frac{1}{T_{ref}+273} - \frac{1}{T(t)+273}\right)\right] dt \quad (4)$$

where $E_a(T)$ is the activation energy and can be calculated by the method reported in Xin et al.,[2] in kJ·mol^{-1}; R is the ideal gas constant (8.315 J/(mol·K)); T_{ref} is the reference temperature, in °C; and $T(t)$ is the real temperature, in °C.

Early-age creep—The total strain for the 100% restrained specimen included free deformation, elastic strain, and basic creep. Because the specimen was tightly sealed with the plastic films and covered with the mold lid to prevent water evaporation, drying creep could be ignored. The incremental load during the compensation cycle was applied to keep the zero total strain. As shown in Fig. 3, subtracting the strain of free specimens and the elastic strain from the total strain of restrained specimens gives the creep strain.[26] Equation (5) was used to calculate the basic creep of the restrained specimen.[27]

$$\varepsilon_{cr} = -\varepsilon_e - \varepsilon_{sh} \quad (5)$$

where ε_{cr} is the basic creep, in με; ε_e is the accumulation of elastic strain increments during each compensation cycle, in με; and ε_{sh} is determined from the free specimen, in με.

EXPERIMENTAL RESULTS AND DISCUSSION

Temperature history and deformation

The primary factor affecting the thermal deformation and thermal stress of HSC is the heat released by cement hydration. In the case of mass concrete, the cement hydration heat is hard to dissipate, leading to a rapid rise in internal temperature. Figure 4 shows the temperature history of reinforced HSC specimens. The internal temperature of the

tested HSC specimens increased rapidly due to the intense cement hydration. The highest temperature kept constant for 36 hours and was then forced to cool down. The casting temperature was 19.27, 20.30, 16.30, 15.21, 19.52, and 20.91°C (66.69, 68.54, 61.34, 59.38, 67.14, and 69.64°F) for samples HP-00, HRB-A-06, HRB-A-08, HRB-A-10, HRB-B-06, and HRB-C-12, respectively. The current research did not consider the effect of casting temperature on the cracking resistance of HSC. The adiabatic temperature rise was obtained by subtracting the casting temperature from the peak temperature of HSC specimens.[34] The adiabatic temperature rise of samples HP-00, HRB-A-06, HRB-A-08, HRB-A-10, HRB-B-06, and HRB-C-12 was 37.26, 35.20, 35.20, 34.57, 33.85, and 36.28°C (99.07, 95.36, 95.36, 94.23, 92.93, and 97.30°F), respectively.

During the forced cooling stage, the concrete underwent contraction, and stress developed when HSC was restrained. The temperature drop could reflect the ability of concrete to resist cracking in the forced cooling stage. The higher temperature drop corresponded to the stronger ability of concrete to resist cracking caused by temperature change. The temperature drop could be calculated by subtracting the cracking temperature from the peak temperature of HSC specimens.[20] The cracking temperature and the temperature drop of samples are shown in Table 2. When the reinforcement percentage increased from 0 to 0.50%, 0.89%, and 1.40%, the cracking temperature of HSC specimens decreased by 21.1%, 80.5%, and 133.0%, while the temperature drop increased by 1.9%, 4.9%, and 11.4%, respectively. For samples HRB-A-06, HRB-B-06, and HRB-C-12, the maximum temperature drop was obtained in sample HRB-B-06. Results of temperature drop indicated that the early-age cracking resistance of the tested HSC specimens strengthened with increasing reinforcement percentage and a more appropriate reinforcement configuration. The reason was that reinforcement helped to alter the temperature distribution within the concrete.

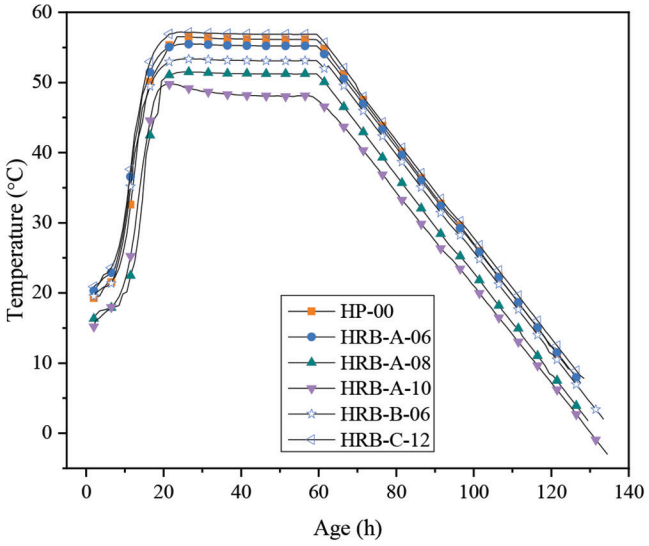

Fig. 4—Temperature history of reinforced HSC. (Note: $t_F = 1.8t_C + 32$.*)*

The total strain of restrained specimens is shown in Fig. 5. Negative values indicated contraction, while the positive ones indicated expansion. The total strain of restrained specimens increased during the temperature rising stage since time-zero. After entering the constant temperature stage, almost no thermal strain occurred. When the concrete cooled down, the total strain of restrained specimens decreased continuously, and finally changed from expansion to contraction. The total strain of restrained specimens at the age when sample HP-00 cracked was −106, −52, −73, −31, −47, and −74 με for samples HP-00, HRB-A-06, HRB-A-08, HRB-A-10, HRB-B-06, and HRB-C-12, respectively. Reinforcement effectively restrained the total strain of the restrained specimens. For samples HRB-A-06, HRB-B-06, and HRB-C-12, the minimum absolute value of the total strain of restrained specimens is obtained in sample HRB-B-06. The inhibition effect of four reinforcing bars on the total strain of restrained specimens was greater than that of one reinforcing bar. The total strain of free specimens is depicted in Fig. 6. The total strain of free specimens increased continuously with the elapse of age. The maximum free total strain was 216, 250, 270, 297, 263, and 225 με for samples HP-00, HRB-A-06, HRB-A-08, and HRB-A-10, respectively.

Analysis and modeling of early-age AS

Influence of reinforcement percentage—Figure 7 depicts the AS of the tested HSC specimens. The AS of reinforced HSC

Table 2—Main parameters for evaluating cracking resistance of concrete

Label	HP-00	HRB-A-06	HRB-A-08	HRB-A-10	HRB-B-06	HRB-C-12
Peak temperature, °C	56.53	55.50	51.50	49.78	53.37	57.19
Cracking temperature, °C	9.14	7.21	1.78	−3.02	2.00	7.82
Temperature drop, °C	47.39	48.29	49.72	52.80	51.37	49.37
Maximum compressive stress, MPa	1.77	2.29	2.41	2.64	2.35	1.87
Second-zero-stress temperature, °C	46.02	45.92	44.37	42.33	43.75	45.75
Restrained tensile stress rate, MPa/days	1.22	1.16	1.14	1.11	1.14	1.17
Cracking stress, MPa	2.54	2.66	2.80	3.02	2.75	2.58
Cracking age, hours	124.5	127.5	129.5	134.5	133.5	128.5
Net time of cracking, days	2.08	2.29	2.46	2.71	2.42	2.21
Integrated criterion of cracking resistance, MPa/days^2	0.587	0.507	0.463	0.410	0.471	0.529

Note: $t_F = 1.8t_C + 32$; 1 MPa = 145 psi.

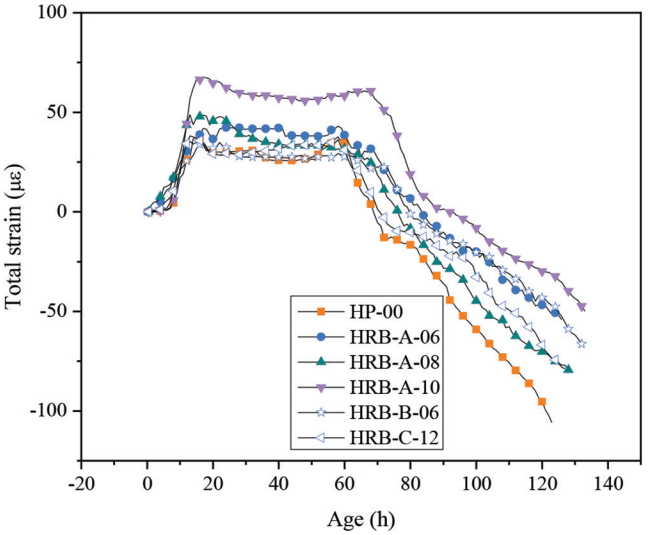

Fig. 5—Total strain of restrained specimens.

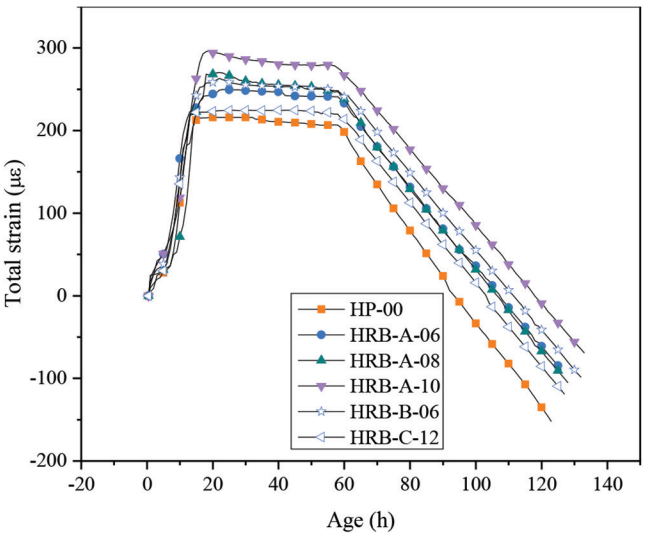

Fig. 6—Total strain of free specimens.

specimens developed significantly in the very early stage (<20 hours). With the increase of age, the development rate of AS of specimens slowed down gradually. Sample HP-00 cracked first at 124.5 hours. The AS for samples at the cracking age of sample HP-00 was −174, −109, −92, and −58με, respectively, the absolute value of which decreased by 37.4%, 47.1%, and 66.7% when the reinforcement percentage increased from 0% to 0.50%, 0.89%, and 1.40%, respectively. Reinforcement had a certain inhibition effect on the AS of HSC specimens, and the AS decreased with the increase in reinforcement percentage. Similar results reported by Gao et al.[35] indicate that the higher the reinforcement ratio, the greater the restraint against the shrinkage of concrete. Huang et al.[36] reported the shrinkage mitigation effect of the reinforcing bar on concrete. The decrease in AS with increasing reinforcement percentage can be attributed to the reason that a higher reinforcement percentage leads to a greater restraint against shrinkage of concrete near the reinforcing bar.[37]

Influence of reinforcement configuration—The AS of the tested HSC specimens with different reinforcement configurations is given in Fig. 7. For samples HRB-A-06, HRB-B-06, and HRB-C-12, the AS at the cracking age of sample HP-00 (124.5 hours) is −109, −82, and −131 με, respectively. The absolute value of the AS of HRB-B-06 (four reinforcing bars in the corners with 34.5 mm [1.36 in.] concrete cover) at 124.5 hours was smaller than that of Specimen HRB-A-06 (four reinforcing bars in the corners with 20 mm [0.79 in.] concrete cover) and HRB-C-12 (one reinforcing bar at the center) by 27 and 49 με, respectively. Similar results reported by Huang et al.[6] suggest that with the same reinforcement percentage, four reinforcing bars placed at the corners of a concrete member can restrain the shrinkage better than a single central reinforcing bar. Four reinforcing bars restrained AS more than one reinforcing bar. The reason is that four reinforcing bars placed in the corners provide a more uniform restraining effect than one reinforcing bar placed at the center.[6] Besides, four reinforcing bars had a bigger specific surface than one reinforcing bar with the same reinforcement percentage, which meant higher interaction between concrete and the reinforcing bar, thus generating more restraint, as reported by Sule and van Breugel.[38]

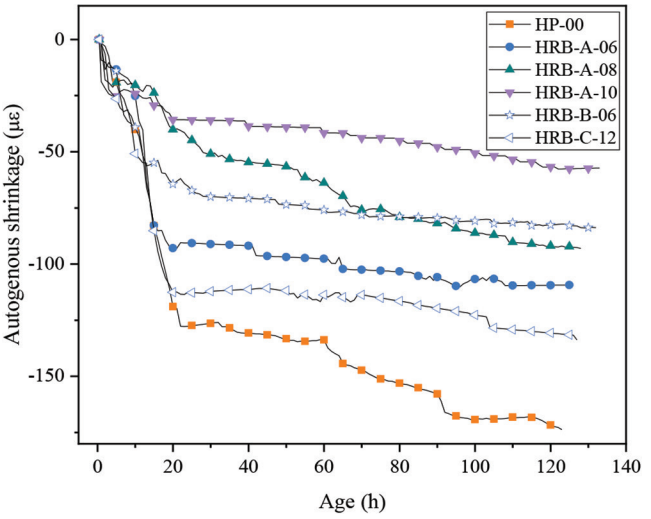

Fig. 7—AS of reinforced HSC specimens.

Modeling of early-age AS considering reinforcement percentage—To predict the AS of reinforced HSC, the actual age of the tested HSC specimens was transformed to the equivalent age at 20°C (68°F). Figure 8 shows the development of AS with the equivalent age. The AS at the equivalent cracking age of sample HRB-A-10 was −147, −103, −84, and −57 με for samples HP-00, HRB-A-06, HRB-A-08, and HRB-A-10, respectively. The predictive model for AS of reinforced HSC with different reinforcement percentages was established based on classical models, as shown in Eq. (6) through (9).[39-41]

$$\varepsilon_{sh}^{s}(t_e) = \frac{\varepsilon_{sh}^{c}(t_e)}{1 + K' \cdot \theta} \tag{6}$$

$$\varepsilon_{sh}^{c}(t_e) = \varepsilon_{sh}^{c}(0) \cdot \beta_a(t_e) \tag{7}$$

$$\beta_a(t_e) = 1 - \exp(-a \cdot t_e^{\,b}) \tag{8}$$

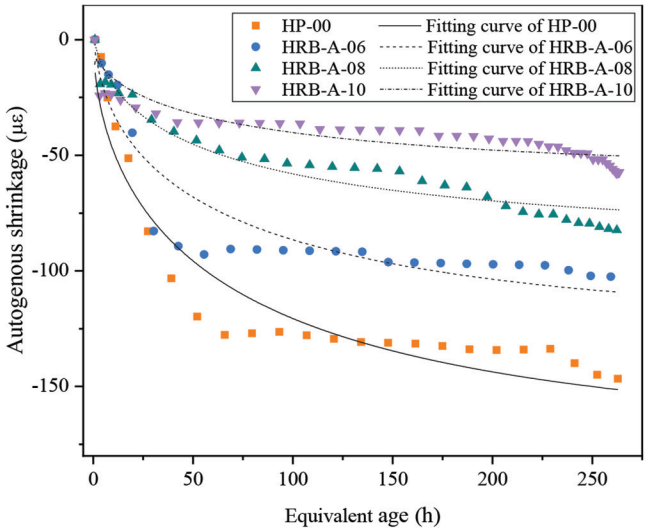

Fig. 8—Test results and predicted values of AS of reinforced HSC specimens.

$$K' = m \cdot \frac{1}{t_e} + n \tag{9}$$

where $\varepsilon_{sh}^{s}(t_e)$ is the AS of reinforced concrete, in με; $\varepsilon_{sh}^{c}(t_e)$ is the AS of unreinforced concrete, in με; t_e is the equivalent age, in days; K' is the correction factor; θ is the reinforcement percentage, in %; $\varepsilon_{sh}^{c}(0)$ is the AS of sample HP-00 at equivalent cracking age, taken as −174 με; $\beta_a(t_e)$ is the development coefficient of AS; a and b are fitting parameters; and m and n are parameters related to the reinforcement percentage.

The fitting results of a and b were 0.088 and −0.565, respectively. The average values of m and n were 2.016 and 1.128, respectively. Equation (10) present the model for predicting AS of reinforced HSC considering the reinforcement percentage.

$$\varepsilon_{sh}^{s}(t_e) = \frac{\varepsilon_{sh}^{c}(0) \cdot (1 - \exp(-0.088 \cdot t_e^{-0.565}))}{1 + (2.016 \cdot \frac{1}{t_e} + 1.128) \cdot \theta} \tag{10}$$

The predicted AS at the equivalent cracking age of sample HRB-A-10 was −151, −109, −74, and −50 με when the reinforcement percentage increased from 0 to 0.50%, 0.89%, and 1.40%, respectively. The deviation between the fitting results and test results was 2.7%, 5.8%, −11.9%, and −12.3% for samples HP-00, HRB-A-06, HRB-A-08, and HRB-A-10, respectively, which were in the applicable range. Thus, the proposed model could be used to predict the AS of reinforced HSC considering the reinforcement percentage. Notably, further investigation is necessary to reveal the influence mechanism of the reinforcing bars on concrete and consider the influence of reinforcement configuration in the model.

Analysis of restrained stress

Figure 9 exhibits the evolution of restrained stress of restrained specimens. The abrupt stress drop indicated the cracking of specimens. Table 2 shows that the maximum compressive stress of reinforced HSC specimens increased with increasing reinforcement percentage from 0 to 1.4%. For samples HRB-A-06, HRB-B-06, and HRB-C-12, the highest maximum compressive stress was obtained in sample HRB-B-06. The compressive stress increased due to thermal expansion caused by cement hydration, and this stress decreased after the temperature peak.[42] The rise in compressive stress was highly beneficial in postponing the onset of tensile stress triggered by thermal strain during the subsequent cooling stage under the restrained condition.

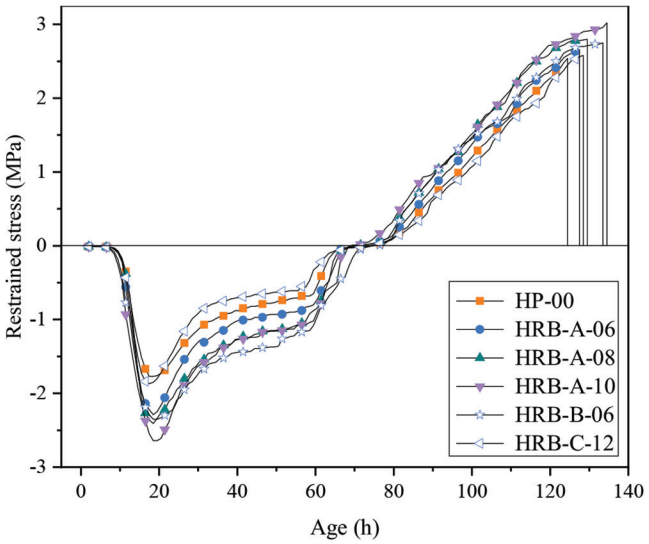

Fig. 9—Development of restrained stress of restrained specimens. (Note: 1 MPa = 145 psi.)

The critical moment when the tensile stress generated is defined as the point of second-zero-stress age.[43,44] The corresponding temperature at this critical moment was defined as $T_{second\text{-}zero\text{-}stress}$. The second-zero-stress temperature is given in Table 2. Compared with sample HP-00, the second-zero-stress temperature decreased by 0.2%, 3.6%, 8.0%, 4.9%, and 0.6% for samples HRB-A-06, HRB-A-08, HRB-A-10, HRB-B-06, and HRB-C-12, respectively. Concrete with a higher tensile stress rate is more susceptible to cracking. The result of the restrained tensile stress rate declined with increasing reinforcement percentage, as given in Table 2. For samples HRB-A-06, HRB-B-06, and HRB-C-12, the lowest restrained tensile stress rate was obtained in sample HRB-B-06. Similar results reported by Sule and van Breugel[38] indicate that concrete with higher reinforcement percentages demonstrate lower stress rates.

The cracking stress of the restrained specimens increased by 4.7%, 10.2%, and 18.9% when the reinforcement percentage increased from 0% to 0.50%, 0.89%, and 1.40%, respectively. With the same reinforcement ratio, sample HRB-B-06 showed the highest cracking stress. The reason was that placing reinforcing bars at four corners of the concrete exhibited a more uniform restraining effect throughout the cross section than that of one bar placed at the center.[6] The cracking age of samples is listed in Table 2. An increase of 2.4%, 4.0%, and 8.0% in the cracking age was observed with increasing reinforcement percentages from 0 to 0.50%, 0.89%, and 1.40%. For samples HRB-A-06, HRB-B-06, and HRB-C-12, the longest cracking age is obtained in sample HRB-B-06. Similar results reported by Sdiri et al.[45] suggest that the presence of the reinforcing bars delays the cracking time. Sule and van Breugel[38] reported

that four reinforcing bars in the corners of the tested specimens postpone the moment of through-cracking, whereas specimens with one centrally placed reinforcing bar cracked nearly as suddenly as plain specimens.

Analysis of early-age creep behavior

Figure 10 illustrates the basic TC of reinforced HSC specimens. The basic TC at the cracking age of sample HP-00 was 182, 177, 174, 171, 169, and 180 με for samples HP-00, HRB-A-06, HRB-A-08, HRB-A-10, HRB-B-06, and HRB-C-12, respectively. However, the creep of concrete was affected by the applied stress level. Therefore, for normalizing the creep of concrete with different stresses, the specific basic TC (that is, the cumulative basic TC per unit tensile stress) was analyzed. The development of specific basic TC of reinforced HSC specimens is depicted in Fig. 11. The specific basic TC increased first and then dropped to stable values. The specific basic TC at the cracking age of sample HP-00 was 71.7, 68.8, 63.3, 61.1, 64.0, and 73.5 με for samples HP-00, HRB-A-06, HRB-A-08, HRB-A-10, HRB-B-06, and HRB-C-12, respectively. When the reinforcement percentage increased from 0% to 0.50%, 0.89%, and 1.40%, the specific basic TC decreased by 4.0%, 11.7%, and 14.8%, respectively. The reinforcing bar effectively restrained the specific basic TC of concrete, and the effect is more obvious with a higher reinforcement percentage, which was in line with the results reported by Gosaye et al.[46] Similar results reported by Sun et al.[47] suggest that the creep and shrinkage strain of concrete with a high reinforcement ratio are lower than those in plain concrete. For samples HRB-A-06, HRB-B-06, and HRB-C-12, the minimum specific TC is obtained in sample HRB-B-06. The results demonstrated that with the same reinforcement ratio, four reinforcing bars placed at the corners of HSC restrained the specific basic TC better than a single reinforcing bar placed at the center.

Estimation of cracking potential

Single criteria, such as cracking age,[48] stress rate at cracking,[49] cracking temperature drop,[50] and cracking stress/axial tensile strength,[51] have been used to assess the cracking resistance of concrete. The integrated criterion of cracking resistance could also be used to evaluate the cracking resistance of HSC. The integrated criterion of cracking resistance is obtained with Eq. (11) by dividing the restrained tensile stress rate by the net time of cracking, which was also adopted by many researchers.[2,52]

$$\varphi_N = \frac{S}{t_{tcr}} \tag{11}$$

where φ_N is the integrated criterion of cracking resistance, in MPa/days^2; S is the restrained tensile stress rate, in MPa/days; and t_{tcr} is the net time of cracking, which is calculated from the time at which the tensile stress occurs, in days.

The age when the restrained specimens converted from the compression state to the tension state was 74.5, 72.5, 70.5, 69.5, 75.5, and 75.5 hours for samples HP-00, HRB-A-06, HRB-A-08, HRB-A-10, HRB-B-06, and HRB-C-12, respectively. Thus, the results of the net time of cracking and the calculated integrated criterion of cracking resistance could be obtained and are depicted in Table 2. When the reinforcement percentage increased from 0 to 0.50%, 0.89%, and 1.40%, the integrated criterion of cracking resistance decreased by 13.6%, 21.1%, and 30.2%, respectively. For samples HRB-A-06, HRB-B-06, and HRB-C-12, the lowest integrated criterion of cracking resistance was obtained in sample HRB-B-06. The lower integrated criterion indicated a higher cracking resistance of concrete. Similar results reported by Shi et al.[5] suggest that reinforcement can improve the cracking resistance of concrete by nearly 20%. The results reported by Huang et al.[6] suggest that placing reinforcing bars at the four corners can decrease the cracking potential of concrete with the same reinforcement ratio. The following aspects could be used to explain the mechanism that the reinforcement increased the cracking resistance of concrete. On one hand, with the reinforcement of finer and denser bars, microcracks appear before the initiation of the primary crack, which results in a delay before the major

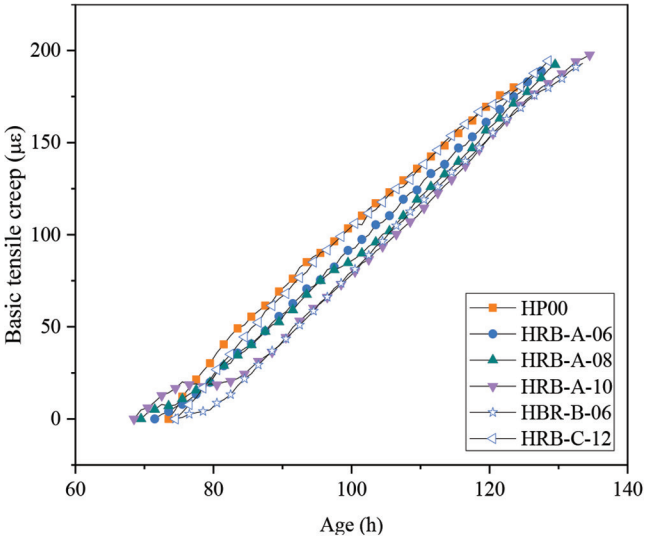

Fig. 10—Development of TC of reinforced HSC specimens.

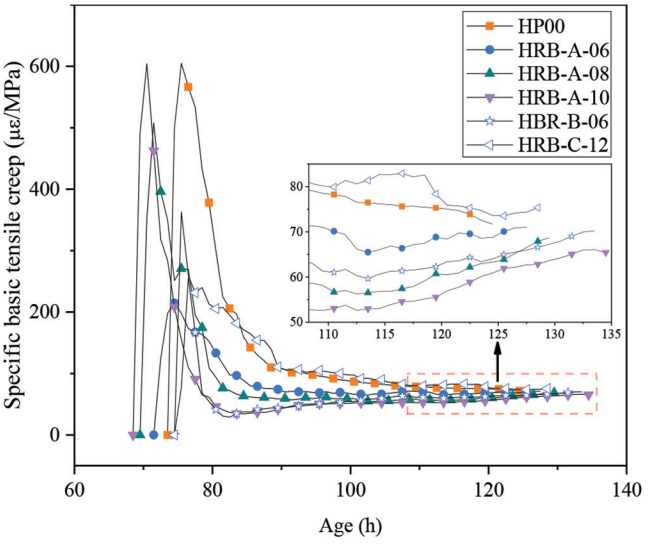

Fig. 11—Development of specific basic TC of reinforced HSC specimens. (Note: 1 MPa = 145 psi.)

crack formation, during which the tensile strength of the concrete further develops.[53] On the other hand, when the reinforcement percentage was in the range of 0 to 1.4%, the use of finer and denser reinforcing bars increased the contact area between the reinforcing bar and concrete, leading to a more evenly distributed stress in reinforced HSC. Consequently, the improvement in stress distribution enhances the cracking resistance of the HSC.

CONCLUSIONS

The current research presented findings on the effects of reinforcement percentage and configuration on the early-age behavior and cracking resistance of reinforced high-strength concrete (HSC). Analyses of the temperature history, shrinkage, stress, and creep behavior were conducted by the temperature-stress test machine (TSTM) test on reinforced HSC. The following conclusions were drawn.

1. Reinforcement significantly affects the early-age behavior of HSC. The temperature drop, cracking age, and cracking stress increased when the reinforcement percentage increased from 0 to 0.50%, 0.89%, and 1.40%. Among different reinforcement configurations with the same reinforcement percentage, reinforced HSC with distributed reinforcement along with a proper thickness of concrete cover exhibited higher temperature drop, longer cracking age, and higher cracking stress compared with that of central reinforcement.

2. Reinforcement decreased the autogenous shrinkage (AS) of HSC when the reinforcement percentage is in the range of 0 to 1.4%. With the same reinforcement percentage, four reinforcing bars with a proper thickness of concrete cover restrained AS more than one reinforcing bar. A prediction model of early-age AS of HSC with different reinforcement percentages was proposed.

3. The specific basic tensile creep (TC) of reinforced HSC decreased with the increase of reinforcement percentage. When the reinforcement percentage was the same, reinforced HSC with distributed reinforcement along with a proper thickness of concrete cover exhibited a lower early-age TC when compared with that of central reinforcement.

4. When the reinforcement percentage is in the range of 0 to 1.4%, finer and denser reinforcing bars could improve the cracking resistance of the reinforced HSC. The integrated criterion of cracking resistance decreased with increasing reinforcement percentage. With the same reinforcement percentage, reinforced HSC with distributed reinforcement along with a proper thickness of concrete cover exhibited higher cracking resistance compared with that of central reinforcement.

Notably, the comparison between early-age cracking resistance of normal-strength concrete and HSC needs to be further studied in follow-up research. Recognizing the limitations of the TSTM setup, it is essential to conduct further research to consider the scale effect, volume of concrete effect, mass enthalpy effect, and real-life two- or three-dimensional restrained effect in the TSTM test.

AUTHOR BIOS

Chuyuan Wen *is a PhD Student at Hohai University, Nanjing, China, where she received her BS. Her research interests include early-age properties and cracking control of concrete.*

Dejian Shen *is a Professor at Hohai University, where he received his BS and MS. He received his PhD from Tongji University, Shanghai, China. His research interests include the assessment, control, and repair of cracking of early-age concrete; seismic performance and design method of industrial buildings; and fiber-reinforced polymer (FRP) technology for repairing reinforced concrete structures.*

Yang Jiao *is a PhD Student at Southeast University, Nanjing, China. He received his BS and MS from Hohai University. His research interests include early-age creep and shrinkage of concrete.*

Ci Liu *is a PhD Student at Hohai University. He received his BS from Yanbian University, Yanji, China. His research interests include the early-age behavior of concrete.*

Ming Li *is a PhD student at Hohai University, where he received his MS. He received his BS from Nantong University, Nantong, China. His research interests include early-age cracking of concrete.*

ACKNOWLEDGMENTS

The financial support of the Fundamental Research Funds for the Central Universities (Grant No. B230201060) is gratefully acknowledged.

REFERENCES

1. Liu, J. H.; Shi, C. J.; Ma, X. W.; Khayat, K. H.; Zhang, J.; and Wang, D. H., "An Overview on the Effect of Internal Curing on Shrinkage of High Performance Cement-Based Materials," *Construction and Building Materials*, V. 146, 2017, pp. 702-712. doi: 10.1016/j.conbuildmat.2017.04.154

2. Xin, J. D.; Zhang, G. X.; Liu, Y.; Wang, Z. H.; and Wu, Z., "Effect of Temperature History and Restraint Degree on Cracking Behavior of Early-Age Concrete," *Construction and Building Materials*, V. 192, 2018, pp. 381-390. doi: 10.1016/j.conbuildmat.2018.10.066

3. Klemczak, B., and Knoppik-Wróbel, A., "Analysis of Early-Age Thermal and Shrinkage Stresses in Reinforced Concrete Walls," *ACI Structural Journal*, V. 111, No. 2, Mar.-Apr. 2014, pp. 313-322. doi: 10.14359/51686523

4. Shariff, M. N.; and Menon, D., "Experimental Studies on Creep and Shrinkage Behavior of Reinforced Concrete Walls," *ACI Structural Journal*, V. 117, No. 3, May 2020, pp. 249-260. doi: 10.14359/5172350210.14359

5. Shi, N. N.; Ouyang, J. S.; Zhang, R. X.; and Huang, D. H., "Experimental Study on Early-Age Crack of Mass Concrete under the Controlled Temperature History," *Advances in Materials Science and Engineering*, 2014, pp. 1-10. doi: 10.1155/2014/671795

6. Huang, L. P.; Hua, J. M.; Kang, M.; and Zhang, A. L., "Influence of Reinforcement Configuration on the Shrinkage and Cracking Potential of High-Performance Concrete," *Construction and Building Materials*, V. 140, 2017, pp. 20-30. doi: 10.1016/j.conbuildmat.2017.02.074

7. Fang, D. P.; Xi, H. F.; Wang, X. M.; and Zhang, C. M., "Influences of Shrinkage, Creep, and Temperature on the Load Distributions in Reinforced Concrete Buildings During Construction," *Tsinghua Science and Technology*, V. 14, No. 6, 2009, pp. 756-764. doi: 10.1016/S1007-0214(09)70146-4

8. Yoo, D.-Y.; Park, J.-J.; Kim, S.-W.; and Yoon, Y.-S., "Influence of Reinforcing Bar Type on Autogenous Shrinkage Stress and Bond Behavior of Ultra High Performance Fiber Reinforced Concrete," *Cement and Concrete Composites*, V. 48, 2014, pp. 150-161. doi: 10.1016/j.cemconcomp.2013.11.014

9. Gu, C. P.; Wang, Y. C.; Gao, F.; Yang, Y.; Ni, T. Y.; Liu, J. T.; Lou, X.; and Chen, J., "Early Age Tensile Creep of High Performance Concrete Containing Mineral Admixtures: Experiments and Modeling," *Construction and Building Materials*, V. 197, 2019, pp. 766-777. doi: 10.1016/j.conbuildmat.2018.11.218

10. Klausen, A. E.; Kanstad, T.; Bjøntegaard, Ø.; and Sellevold, E., "Comparison of Tensile and Compressive Creep of Fly Ash Concretes in the Hardening Phase," *Cement and Concrete Research*, V. 95, 2017, pp. 188-194. doi: 10.1016/j.cemconres.2017.02.018

11. Garas, V. Y.; Kahn, L. F.; and Kurtis, K. E., "Short-Term Tensile Creep and Shrinkage of Ultra-High Performance Concrete," *Cement and Concrete Composites*, V. 31, No. 3, 2009, pp. 147-152. doi: 10.1016/j.cemconcomp.2009.01.002

12. Xin, J. D.; Li, J. H.; and Huang, D. H., "Analysis of Effect of Reinforcement on Concrete Creep Behavior," *Proceedings of the International Conference on Advances in Mechanical Engineering and Industrial Informatics*, Henan, China, 2015, pp. 1307-1312.

13. Altoubat, S. A., and Lange, D. A., "Creep, Shrinkage, and Cracking of Restrained Concrete at Early Age," *ACI Materials Journal*, V. 98, No. 4, July-Aug. 2001, pp. 323-331. doi: 10.14359/10401

14. Altoubat, S. A., and Lange, D. A., "Tensile Basic Creep: Measurements and Behavior at Early Age," *ACI Materials Journal*, V. 98, No. 5, Sept.-Oct. 2001, pp. 386-393. doi: 10.14359/10728

15. Schlitter, J. L.; Bentz, D. P.; and Weiss, W. J., "Quantifying Stress Development and Remaining Stress Capacity in Restrained, Internally

Cured Mortars," *ACI Materials Journal*, V. 110, No. 1, Jan. 2013, pp. 3-11. doi: 10.14359/51684361

16. Briffaut, M.; Benboudjema, F.; Torrenti, J. M.; and Nahas, G., "A Thermal Active Restrained Shrinkage Ring Test to Study the Early Age Concrete Behaviour of Massive Structures," *Cement and Concrete Research*, V. 41, No. 1, 2011, pp. 56-63. doi: 10.1016/j.cemconres.2010.09.006

17. Wen, C. Y.; Shen, D. J.; Luo, Y. Y.; Wang, W. T.; Liu, C.; and Li, M., "Early-Age Autogenous Shrinkage and Tensile Creep of Concrete Reinforced with Polypropylene Macro Fiber," *Journal of Sustainable Cement-Based Materials*, V. 12, No. 10, 2023, pp. 1-15. doi: 10.1080/21650373.2023.2214135

18. Liu, C.; Shen, D. J.; Yang, X.; Shao, H. Z.; Tang, H. W.; and Cai, L. L., "Early-Age Properties and Shrinkage Induced Stress of Ultra-High-Performance Concrete under Variable Temperature and Uniaxial Restrained Condition," *Construction and Building Materials*, V. 384, 2023, p. 131382. doi: 10.1016/j.conbuildmat.2023.131382

19. Barrett, T. J.; De la Varga, I.; and Weiss, W. J., "Reducing Cracking in Concrete Structures by Using Internal Curing with High Volumes of Fly Ash," *Structures Congress 2012,* J. Carrato and J. Burns, eds., Chicago, IL, 2012, pp. 699-707.

20. Raoufi, K.; Schlitter, J.; Bentz, D.; and Weiss, J., "Parametric Assessment of Stress Development and Cracking in Internally Cured Restrained Mortars Experiencing Autogenous Deformations and Thermal Loading," *Advances in Civil Engineering*, V. 2011, 2011, pp. 1-16. doi: 10.1155/2011/870128

21. Sule, M. S., and van Breugel, K., "The Effect of Reinforcement on Early-Age Cracking Due to Autogenous Shrinkage and Thermal Effects," *Cement and Concrete Composites*, V. 26, No. 5, 2004, pp. 581-587. doi: 10.1016/S0958-9465(03)00078-7

22. Hua, J. M.; Zhou, F. B.; Huang, L. P.; Chen, Z. S.; Xu, Y. M.; and Xie, Z. L., "Influence of Reinforcement Bars on Concrete Pore Structure and Compressive Strength," *Materials (Basel)*, V. 13, No. 3, 2020, p. 658. doi: 10.3390/ma13030658

23. Balevičius, R., and Augonis, M., "The Effects of Bond, Shrinkage and Creep on Cracking Resistance of Steel and GFRP RC Members," *Composite Structures*, V. 187, 2018, pp. 85-101. doi: 10.1016/j.compstruct.2017.12.025

24. Gribniak, V.; Kaklauskas, G.; and Bacinskas, D., "Shrinkage in Reinforced Concrete Structures: A Computational Aspect," *Journal of Civil Engineering and Management*, V. 14, No. 1, 2008, pp. 49-60. doi: 10.3846/1392-3730.2008.14.49-60

25. GB 175-2007/XG3-2018, "Common Portland Cement," General Administration of Quality Supervision, Inspection and Quarantine of the People's Republic of China and Standardization Administration of the People's Republic China, Beijing, China, 2018.

26. Kovler, K., "Testing System for Determining the Mechanical Behaviour of Early Age Concrete Under Restrained and Free Uniaxial Shrinkage," *Materials and Structures*, V. 27, No. 6, 1994, pp. 324-330. doi: 10.1007/BF02473424

27. Kolver, K.; Igarashi, S.; and Bentur, A., "Tensile Creep Behavior of High Strength Concretes at Early Ages," *Materials and Structures*, V. 32, No. 5, 1999, pp. 383-387. doi: 10.1007/BF02479631

28. Shen, D. J.; Jiang, J. L.; Wang, W. T.; Shen, J. X.; and Jiang, G. Q., "Tensile Creep and Cracking Resistance of Concrete with Different Water-to-Cement Ratios at Early Age," *Construction and Building Materials*, V. 146, 2017, pp. 410-418. doi: 10.1016/j.conbuildmat.2017.04.056

29. Shen, D. J.; Liu, C.; Li, C. C.; Zhao, X. G.; and Jiang, G. Q., "Influence of Barchip Fiber Length on Early-Age Behavior and Cracking Resistance of Concrete Internally Cured with Super Absorbent Polymers," *Construction and Building Materials*, V. 214, 2019, pp. 219-231. doi: 10.1016/j.conbuildmat.2019.03.209

30. Lura, P.; van Breugel, K.; and Maruyama, I., "Effect of Curing Temperature and Type of Cement on Early-Age Shrinkage of High-Performance Concrete," *Cement and Concrete Research*, V. 31, No. 12, 2001, pp. 1867-1872. doi: 10.1016/S0008-8846(01)00601-9

31. Zhang, J.; Hou, D. W.; and Sun, W., "Experimental Study on the Relationship Between Shrinkage and Interior Humidity of Concrete at Early Age," *Magazine of Concrete Research*, V. 62, No. 3, 2010, pp. 191-199. doi: 10.1680/macr.2010.62.3.191

32. Chu, I.; Kwon, S. H.; Amin, M. N.; and Kim, J.-K., "Estimation of Temperature Effects on Autogenous Shrinkage of Concrete by a New Prediction Model," *Construction and Building Materials*, V. 35, 2012, pp. 171-182. doi: 10.1016/j.conbuildmat.2012.03.005

33. Hansen, P., and Pedersen, J., "Maturity Computer for Controlled Curing and Hardening of Concrete," *Nordisk Betong*, V. 1, 1977, pp. 19-34.

34. Shen, D. J.; Liu, K. Q.; Wen, C. Y.; Shen, Y. Q.; and Jiang, G. Q., "Early-Age Cracking Resistance of Ground Granulated Blast Furnace Slag Concrete," *Construction and Building Materials*, V. 222, 2019, pp. 278-287. doi: 10.1016/j.conbuildmat.2019.06.028

35. Gao, X. J.; Qu, G. B.; and Zhang, A. L., "Influences of Reinforcement on Differential Drying Shrinkage of Concrete," *Journal of Wuhan University of Technology. Materials Science Edition*, V. 27, No. 3, 2012, pp. 576-580. doi: 10.1007/s11595-012-0508-1

36. Huang, L. P.; Hua, J. M.; Kang, M.; Zhou, F. B.; and Luo, Q. M., "Capillary Tension Theory for Predicting Shrinkage of Concrete Restrained by Reinforcement Bar in Early Age," *Construction and Building Materials*, V. 210, 2019, pp. 63-70. doi: 10.1016/j.conbuildmat.2019.03.154

37. Li, W. G.; Zhengyu, H.; Hu, G. Q.; Duan, W. H.; and Shah, S. P., "Early-Age Shrinkage Development of Ultra-High-Performance Concrete under Heat Curing Treatment," *Construction and Building Materials*, V. 131, 2017, pp. 767-774. doi: 10.1016/j.conbuildmat.2016.11.024

38. Sule, M. S., and van Breugel, K., "Effect of Reinforcement on Early-Age Cracking in High Strength Concrete," *Heron*, V. 49, No. 2, 2004, pp. 273-292.

39. BS 8110-2:1985, "Structural Use of Concrete—Part 2: Code of Practice for Special Circumstances," British Standards Institution, London, UK, 1985.

40. Kang, M., "Research on Restrained Deformation Properties of Reinforced Concrete Members due to Early Shrinkage during Construction," PhD thesis, Chongqing University, School of Civil Engineering, 2010. (in Chinese)

41. Miyazawa, S., and Tazawa, E., "Prediction Model for Shrinkage of Concrete Including Autogenous Shrinkage," *Autogenous Shrinkage of Concrete: Proceedings of the International Workshop, Organized by JCI (Japan Concrete Institute)*, E.-I. Tazawa, ed., Hiroshima, Japan, 1998, pp. 735-740.

42. Xin, J. D.; Lin, S. Q.; Shi, N. N.; Ouyang, J. S.; and Huang, D. H., "Effect of Reinforcement on Early-Age Concrete Temperature Stress: Preliminary Experimental Investigation and Analytical Simulation," *Advances in Materials Science and Engineering*, V. 2015, 2015, pp. 1-9. doi: 10.1155/2015/231973

43. Wei, Y., and Hansen, W., "Tensile Creep Behavior of Concrete Subject to Constant Restraint at Very Early Ages," *Journal of Materials in Civil Engineering*, ASCE, V. 25, No. 9, 2013, pp. 1277-1284. doi: 10.1061/(ASCE)MT.1943-5533.0000671

44. Yeon, J. H.; Choi, S.; and Won, M. C., "Evaluation of Zero-Stress Temperature Prediction Model for Portland Cement Concrete Pavements," *Construction and Building Materials*, V. 40, 2013, pp. 492-500. doi: 10.1016/j.conbuildmat.2012.10.013

45. Sdiri, A.; Kammoun, S.; and Daoud, A., "Numerical Modeling of the Interaction Between Reinforcement and Concrete at Early Age—A Comparison Between Glass Fiber Reinforced Polymer and Steel Rebars," *Structural Concrete*, V. 22, No. 1, 2020, pp. 168-182. doi: 10.1002/suco.201900314

46. Gosaye, J.; Gardner, L.; Ahmer Wadee, M.; and Ellen, M. E., "Tensile Performance of Prestressed Steel Elements," *Engineering Structures*, V. 79, 2014, pp. 234-243. doi: 10.1016/j.engstruct.2014.08.009

47. Sun, G. J.; Xue, S. D.; Qu, X. S.; and Zhao, Y. F., "Experimental Investigation of Creep and Shrinkage of Reinforced Concrete with Influence of Reinforcement Ratio," *Advanced Concrete Construction*, V. 7, No. 4, Jun. 2019, pp. 211-218. doi: 10.12989/acc.2019.7.4.211

48. Tongaroonsri, S., and Tangtermsirikul, S., "Effect of Mineral Admixtures and Curing Periods on Shrinkage and Cracking Age under Restrained Condition," *Construction and Building Materials*, V. 23, No. 2, 2009, pp. 1050-1056. doi: 10.1016/j.conbuildmat.2008.05.023

49. ASTM C1581/C1581M-18a, "Standard Test Method for Determining Age at Cracking and Induced Tensile Stress Characteristics of Mortar and Concrete Under Restrained Shrinkage," ASTM International, West Conshohocken, PA, 2018.

50. Shen, D. J.; Liu, C.; Feng, Z. Z.; Zhu, S. S.; and Liang, C., "Influence of Ground Granulated Blast Furnace Slag on the Early-Age Anti-Cracking Property of Internally Cured Concrete," *Construction and Building Materials*, V. 223, 2019, pp. 233-243. doi: 10.1016/j.conbuildmat.2019.06.149

51. Passuello, A.; Moriconi, G.; and Shah, S. P., "Cracking Behavior of Concrete with Shrinkage Reducing Admixtures and PVA Fibers," *Cement and Concrete Composites*, V. 31, No. 10, 2009, pp. 699-704. doi: 10.1016/j.cemconcomp.2009.08.004

52. Shen, D. J.; Jiang, J. L.; Shen, J. X.; Yao, P. P.; and Jiang, G. Q., "Influence of Prewetted Lightweight Aggregates on the Behavior and Cracking Potential of Internally Cured Concrete at an Early Age," *Construction and Building Materials*, V. 99, 2015, pp. 260-271. doi: 10.1016/j.conbuildmat.2015.08.093

53. Sule, M. S., and van Breugel, K., "Cracking Behaviour of Reinforced Concrete Subjected to Early-Age Shrinkage," *Materials and Structures*, V. 34, No. 5, 2001, pp. 284-292. doi: 10.1007/BF02482208

ACI STRUCTURAL JOURNAL TECHNICAL PAPER

Title No. 121-S30

Punching Shear Strength of Isolated Concrete Column Footings with Low Shear Span-Depth Ratios

by Ngoc Hieu Dinh, Juok Noh, Kyoung-Kyu Choi, and Hong-Gun Park

*In the present research, an experimental study was performed to investigate the punching shear strength of isolated concrete column footings having low shear span-depth ratios (*a/d*). The primary test parameters included the* a/d*, concrete compressive strength, and soil-bearing stiffness. Twelve column footings were tested for* a/d *ranging from 1.0 to 2.5. A support system using rubber-wood composite blocks was designed to simulate the equivalent soil-bearing stiffness. The test results showed that as the* a/d *decreased, the punching shear strength of the footings significantly increased with a change in the angle of the punching failure surface. Contrarily, the soil-bearing stiffness did not significantly affect the punching shear strength, although it did affect the stiffness and deflection of the footings, as well as the contact pressure distribution beneath the footings. Furthermore, to evaluate the punching shear strength of footings with low* a/d*, an analytical model was proposed based on the web-shear cracking mechanism.*

Keywords: analytical model; design codes; punching shear; reinforced concrete (RC) footings; soil-bearing stiffness.

INTRODUCTION

Reinforced concrete (RC) footings are an essential component of concrete structures, which support columns and walls that transfer the load from the upper structure to the ground beneath. The number and dimensions of footings are relatively large, leading to a heavy workload for excavation and construction work. Therefore, column footings should be appropriately designed to achieve structural safety and economic efficiency in construction.

Figure 1 illustrates the distribution of the footing number according to the shear aspect ratio based on a statistical investigation of typical RC office buildings in South Korea.[1] The dimensions of the footing slabs vary from 1.5 to 5 m (59 to 196.9 in.), with the thickness varying from 0.5 to 2 m (19.7 to 78.7 in.). The results implied that approximately 90% of the investigated footings have shear span-depth ratios (*a*/*d*) lower than 2.5. Therefore, it is necessary to pay more attention to footings with a low *a*/*d*.

According to previous studies, punching shear failure is the governing failure mechanism considered in the shear design of RC column footings. Currently, in existing design codes such as ACI 318-19,[2] Eurocode 2 (EC2),[3] or KDS 14 20 22,[4] the punching shear strength models of column footings are mainly based on previous empirical and theoretical investigations[5,6] on slab-column connections with high *a*/*d* ranging from 5 to 10. Notably, in EC2,[3] in the punching shear strength evaluation of the column footings, an iterative calculation method is used to determine the control perimeter within a distance of 2*d* from the column face. For this

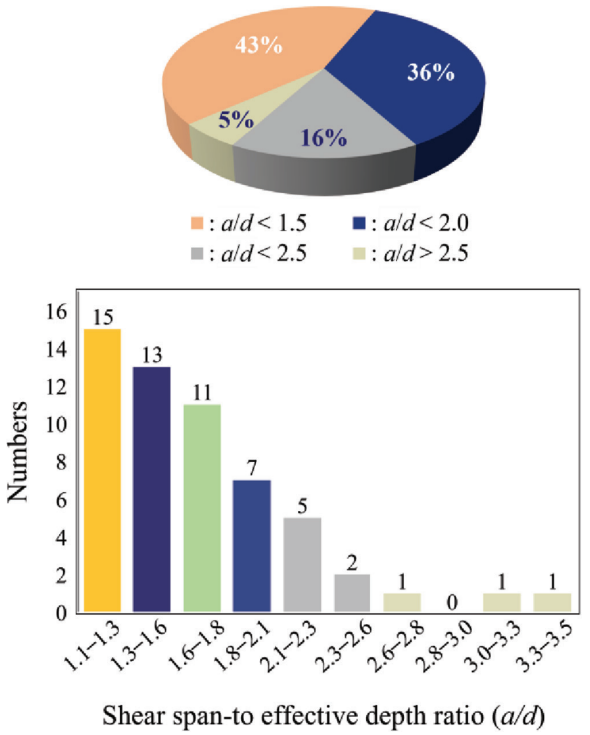

Fig. 1—Distribution of number of investigated footings according to a/d *in Korea.*[1]

reason, for footings with low $a/d \leq 2.0$, the applicability of the current design equations must be evaluated.

Figure 2 shows a comparison of the punching failure modes between column footings and flat slabs.[7] This difference is caused by two main aspects. First, in slender slabs with high *a*/*d* (Fig. 2(b)), punching shear failure occurred after the slab-column connections suffered severe damage induced by flexural cracking or yielding. Thus, punching shear strength is affected by the contributions of the intact compression zone depth, flexural reinforcement ratio, and concrete compressive strength.[8,9] In contrast, in column footings with low *a*/*d* (Fig. 2(a)), prior to flexural yielding, sudden punching shear failure is caused by major critical shear cracks in the web part of the footings without severe flexural cracking. Thus, the effect of flexural damage on the punching shear strength is insignificant. Second, the load

ACI Structural Journal, V. 121, No. 3, May 2024.
MS No. S-2022-336.R3, doi: 10.14359/51740457, received September 21, 2023, and reviewed under Institute publication policies.

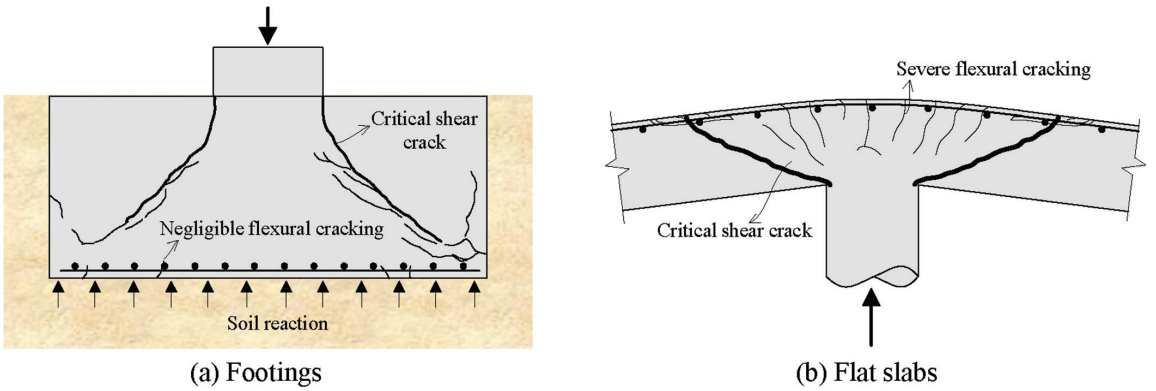

Fig. 2—Comparison of punching shear failure modes of footings with low a/d *and flat slabs with high* a/d.

distributions at the critical section were different. In slab-column connections, the magnitude of the punching shear force is determined by the gravitational load applied to the slab. However, the magnitude of the punching shear force in column footings depends on the soil-bearing pressure distribution.[10-12] Moreover, in short foundation slabs, a portion of the column load is directly transferred to the soil underneath the column by direct bearing.

Thus far, numerous studies have been conducted to investigate the punching shear behavior of RC column footings. Hegger et al.[13,14] investigated influencing parameters such as soil pressure distribution, concrete compressive strength, the area of shear reinforcement, footing dimensions, *a*/*d*, and effective depth of the footings. The results revealed that the punching shear strength of the footings increased as the *a*/*d* decreased and was significantly influenced by the soil stiffness and the distribution of the soil pressure underneath. Punching failure loads of footings with a wide range of design parameters (concrete compressive strengths of 15.4 to 38.1 MPa [2.23 to 5.53 ksi], *a*/*d* of 1.27 to 2.70, and effective depths of the footings of 100 to 470 mm [3.9 to 18.5 in.]) were evaluated and compared with the predictions of current design codes by Abdrabbo et al.[15] Additionally, the detailed contributions of concrete and shear reinforcement to the overall punching shear resistance of column footings were comprehensively investigated by Schmidt et al.[16] To simulate a more realistic support condition, Bonić et al.[17] investigated column footings resting on the subgrade cohesionless soil and compared their punching shear capacity with evaluation by existing design codes.

In recent publications,[18,19] the effects of eccentric loads on the punching shear behavior of RC footings have been investigated. The studies revealed a substantial influence of load eccentricity on the punching shear capacity of the footings, with up to a 60% decrease in the punching shear capacity induced by the tested eccentricity. Furthermore, it was experimentally observed that the eccentric load effect considered in the current design codes was underestimated in EC2, *fib* Model Code 2010,[20] and the forthcoming updated version of EC2. Despite previous endeavors, the investigations of footings with low *a*/*d* are limited.

Although a large portion of the column footings of concrete buildings are designed with low *a*/*d*, the punching shear strength used in the current design codes is based on the test results for slender slabs. Therefore, the current study investigated the punching shear strength of footings with low *a*/*d*. Twelve column footings were tested considering *a*/*d* ranging from 1.0 to 2.5 and various soil-bearing stiffnesses. Furthermore, to evaluate the punching shear strength of footings with low *a*/*d*, an analytical model based on the web shear cracking mechanism was developed considering the effective web area.

RESEARCH SIGNIFICANCE

The punching shear failure mechanism of column footings with low *a*/*d* is different from that of slender slabs, which is the basis of the current punching shear design methods. Thus, an experimental study was performed to investigate a rational punching shear design method for column footings with low *a*/*d*. Based on the test results, an analytical model was developed to evaluate the punching shear strength of footings. The proposed model is expected to be beneficial for the safe and economical design of column footings with low *a*/*d*, which are susceptible to punching shear.

EXPERIMENTAL PLAN

Materials properties

Footing specimens were fabricated using ready mixed normalweight concrete with a maximum coarse aggregate size of 25 mm (0.98 in.). Two types of concrete mixtures with compressive strengths of 24 and 32 MPa (3.48 and 4.64 ksi) were used according to KS F 2405.[21] The details of the mixture proportions are listed in Table A1 in Appendix A.*

Grade 600 deformed bars D25 were used for the longitudinal reinforcement of the footing slabs. Grade 500 deformed bars D19 and Grade 400 deformed bars D10 were used for the longitudinal and transverse reinforcements of the column stubs, respectively. The actual tensile strengths of the steel reinforcing bars were obtained based on KS B 0802[22] and are summarized in Table A2 in Appendix A.

Specimen details

Twelve half-scale square footing specimens were designed and fabricated for punching shear tests. Figure 3 and Table 1

*The Appendix is available at **www.concrete.org/publications** in PDF format, appended to the online version of the published paper. It is also available in hard copy from ACI headquarters for a fee equal to the cost of reproduction plus handling at the time of the request.

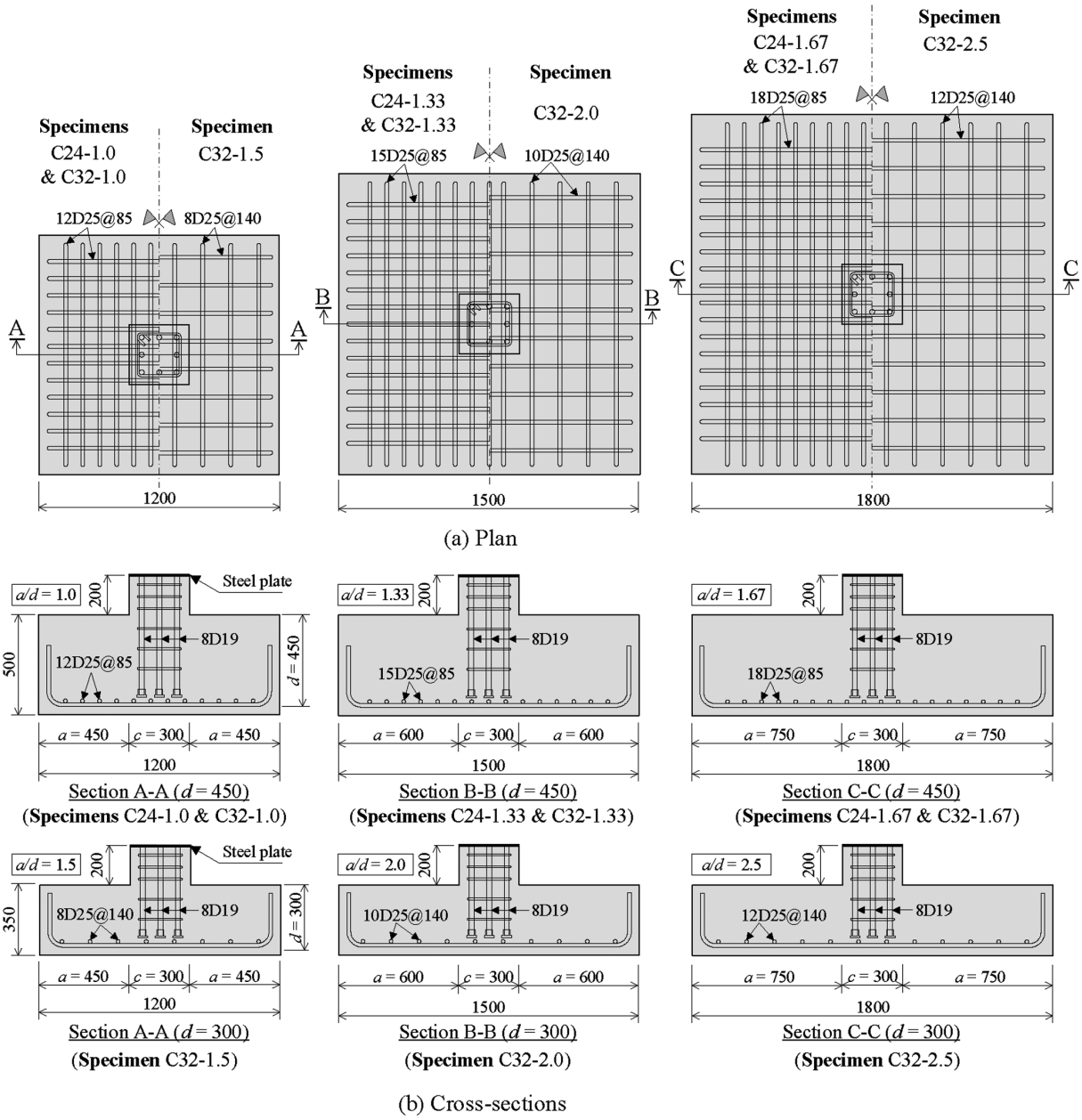

Fig. 3—Geometric characteristics and reinforcement layout of test specimens. (Note: Units in mm; 1 mm = 0.039 in.)

show the geometrical characteristics and reinforcement configurations of the test specimens, respectively. Each column footing specimen consisted of a footing slab with a longitudinal reinforcement ratio of 0.64% and a square column stub with cross-sectional dimensions of 300 x 300 mm (11.81 x 11.81 in.).

As indicated in Table 1, the primary test parameters included the concrete compressive strength (f_c'), a/d, and soil stiffness. The test specimens were named in "CX-Y" format, where X indicates the concrete compressive strength and Y indicates the value of the a/d. For the first group (C24-1.0, C24-1.33, and C24-1.67), the footings were fabricated with a concrete compressive strength of 24 MPa (3.48 ksi) and footing depth of 500 mm (19.7 in.). In this group, the effects of different a/d (1.0 to 1.67) were investigated. In addition, each specimen was tested with two different soil-bearing stiffnesses of $0.25k_0$ and $0.56k_0$. The calculation of k_0 is detailed in the following subsections. For the second group (C32-1.0, C32-1.33, and C32-1.67), the footings were fabricated with a higher concrete strength of 32 MPa (4.64 ksi) and the same footing depth of 500 mm (19.7 in.) as that of the first group. In this group, the effect of a/d of 1.0 to 1.67 was investigated using a uniform soil-bearing stiffness of k_0. For the third group (C32-1.5, C32-2.0, and C32-2.5), to investigate the influence of the size effect, all specimens were fabricated with a smaller footing depth of 300 mm (11.81 in.) with a/d widely ranging from 1.5 to 2.5.

Test setup and support condition

Figure 4 shows the test setup for the footing specimens. The vertical loading system comprises a hinge support, hydraulic actuator, and load cell. The punching shear was induced by the vertical load applied to the column stub using a hydraulic actuator with a capacity of 5000 kN (1124 kip)

Table 1—Test specimens and parameters

Specimens	h, mm	d, mm	c, mm	L, m	D, mm	a/d	f_c', MPa	ρ_l, %	Soil stiffness
C24-1.0	500	450	300	1.2	25	1.00	24	0.64	$0.25k_0$ or $0.56k_0$
C24-1.33	500	450	300	1.5	25	1.33	24	0.64	$0.25k_0$ or $0.56k_0$
C24-1.67	500	450	300	1.8	25	1.67	24	0.64	$0.25k_0$ or $0.56k_0$
C32-1.0	500	450	300	1.2	25	1.00	32	0.64	k_0
C32-1.33	500	450	300	1.5	25	1.33	32	0.64	k_0
C32-1.67	500	450	300	1.8	25	1.67	32	0.64	k_0
C32-1.5	350	300	300	1.2	25	1.50	32	0.64	k_0
C32-2.0	350	300	300	1.5	25	2.00	32	0.64	k_0
C32-2.5	350	300	300	1.8	25	2.50	32	0.64	k_0

Note: h is footing height; d is effective depth; c is square column dimensions; L is square footing dimensions; D is diameter of flexural reinforcement; ρ_l is flexural reinforcement ratio of footings; k_0 is soil-bearing stiffness corresponding to well-compacted soil (= 0.051 N/mm^3 [0.184 kip/in.^{3}]). 1 kN = 0.225 kip; 1 mm = 0.039 in.; 1 MPa = 0.145 ksi.

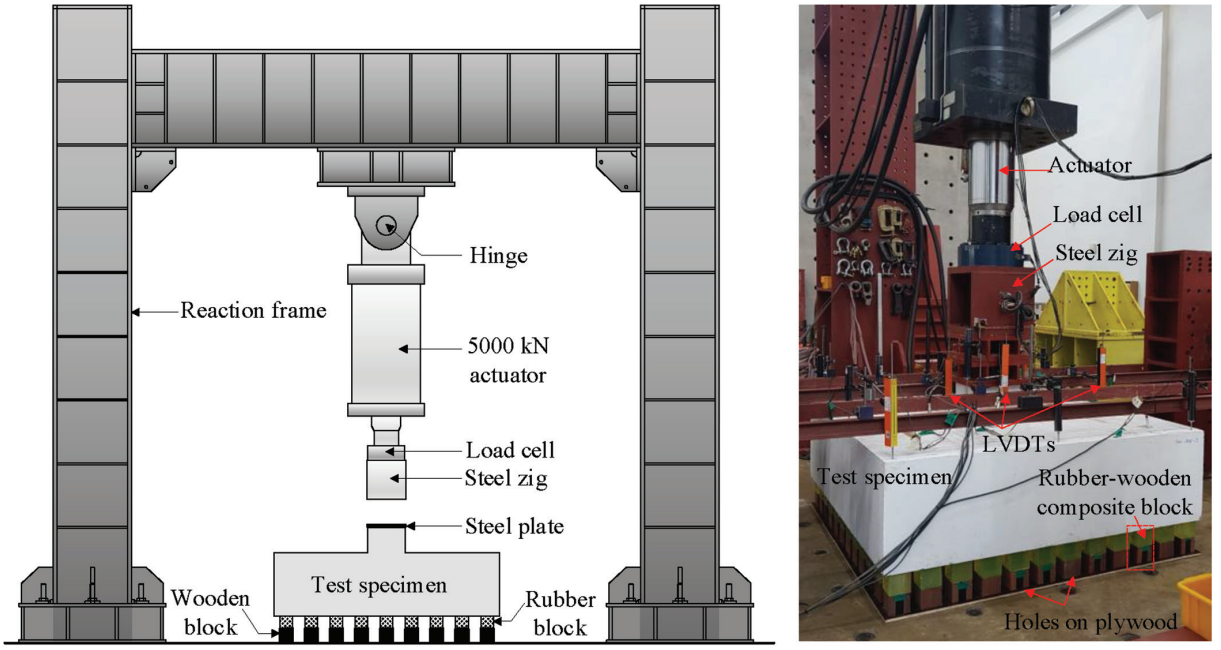

(a) Schematic of the test setup

(b) Photograph of the test setup

Fig. 4—Test setup.

and mounted into a strong reaction steel frame. A load was applied at a rate of 0.05 mm/s (0.039 in./s) using a displacement-controlled method.

To simulate soil-bearing condition of the footings, the rubber-wood composite block system proposed by Zhang et al.[23] was employed. The characteristics of the block system are presented in Fig. A1 in Appendix A. The rubber blocks simulate the bearing stiffness of the soil and control the deformation of the footing slabs, while the wooden blocks support the reaction forces. Figures A1(b) and (c) present the global load-displacement relationships of the composite blocks and the stress-strain relationships of the wood in the composite blocks, respectively. To simulate the confinement of real soil and to restrain the lateral movement of test specimens, the composite blocks were placed into preformed holes on the plywood base plate (Fig. 4(b)). The equivalent elastic stiffness,[24] k, of the soil beneath the footings was defined based on the stiffness coefficient, K_b, of the composite blocks. Considering different layouts of distributed blocks (Fig. 5), this study investigated three typical soil stiffnesses in foundation design, simulating humus soil or peat, fine or slightly compacted soil, and well-compacted sand. The detailed calculations are presented in Appendix B.

Measuring apparatus

Figure 6 shows the representative measuring apparatus layout of specimen C24-1.0. During testing, the radial concrete compression strain was measured at several locations on the slab surface using four to six concrete strain gauges (Fig. 6(a)), and the flexural reinforcement strain was measured in the radial directions (XR and YR) and tangential directions (XT and YT) at several locations parallel to the footing edges (Fig. 6(b)). In addition, as shown in Fig. 6(c), the vertical displacement of the footing specimens was measured at 11 locations using linear variable differential transformers (LVDTs): the periphery of the column stubs

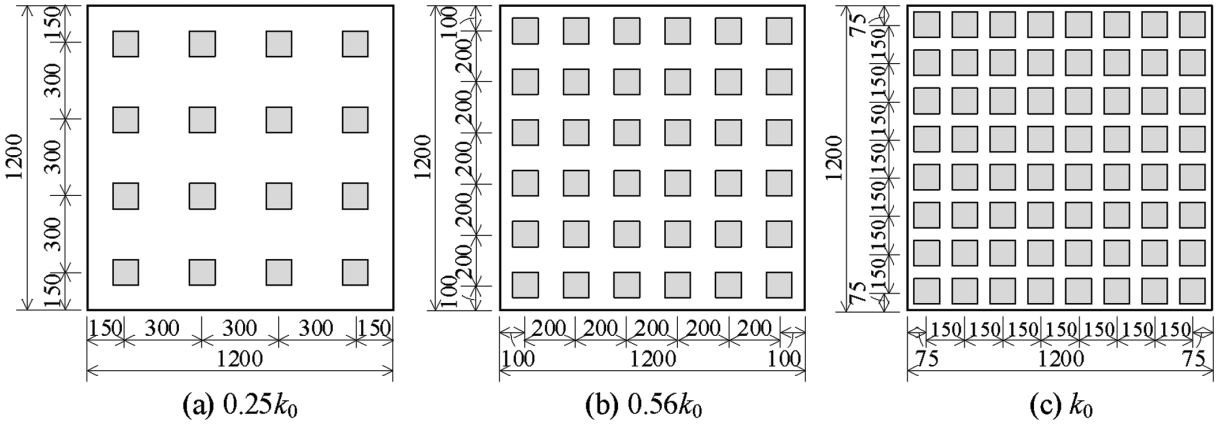

Fig. 5—Layout of rubber-wood composite blocks simulating different soil stiffnesses (footing dimensions of 1200 x 1200 mm). (Note: Units in mm; 1 mm = 0.039 in.)

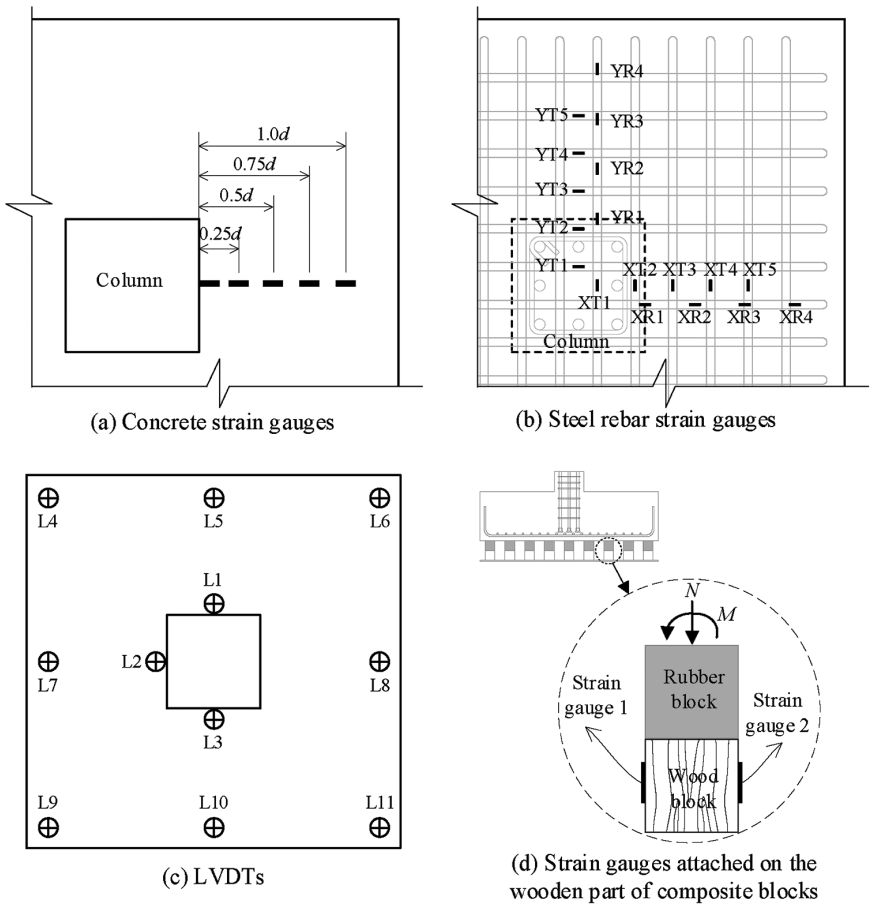

Fig. 6—Layout of measuring apparatus.

(L1 to L3) and footing edges and corners (L4 to L11). The number of strain gauges was different for the test specimens depending on the footing slab dimensions. In addition, two strain gauges were attached to both sides of composite blocks to evaluate the distribution of reaction pressure beneath the footings (Fig. 6(d)). The detailed calculations are presented in Appendix C.

EXPERIMENTAL RESULTS AND DISCUSSION

Crack patterns and failure modes

Figure 7 shows the crack patterns and failure surfaces of the representative footing specimens at the end of the test. After saw cuts at the column edges, crack patterns were observed at the bottom faces of the footings and inside the specimens, and punching failure angles were measured. In general, the crack patterns indicated that the slope angle of the main punching cone with respect to the horizontal plane decreased as the a/d increased. Specifically, for C24-1.0, C24-1.33, and C24-1.67, with soil stiffness of 0.56k_0 (Fig. 7(a), (b), and (c), respectively), the average crack angles in the web part of the left and right sides were 44, 37.5, and 36 degrees, respectively. The crack angles of C32-1.0, C32-1.33, and C32-1.67, with a soil stiffness of 1.0k_0 (Fig. 7(d), (e), and (f), respectively) were 49, 48.5, and 42.5 degrees, respectively;

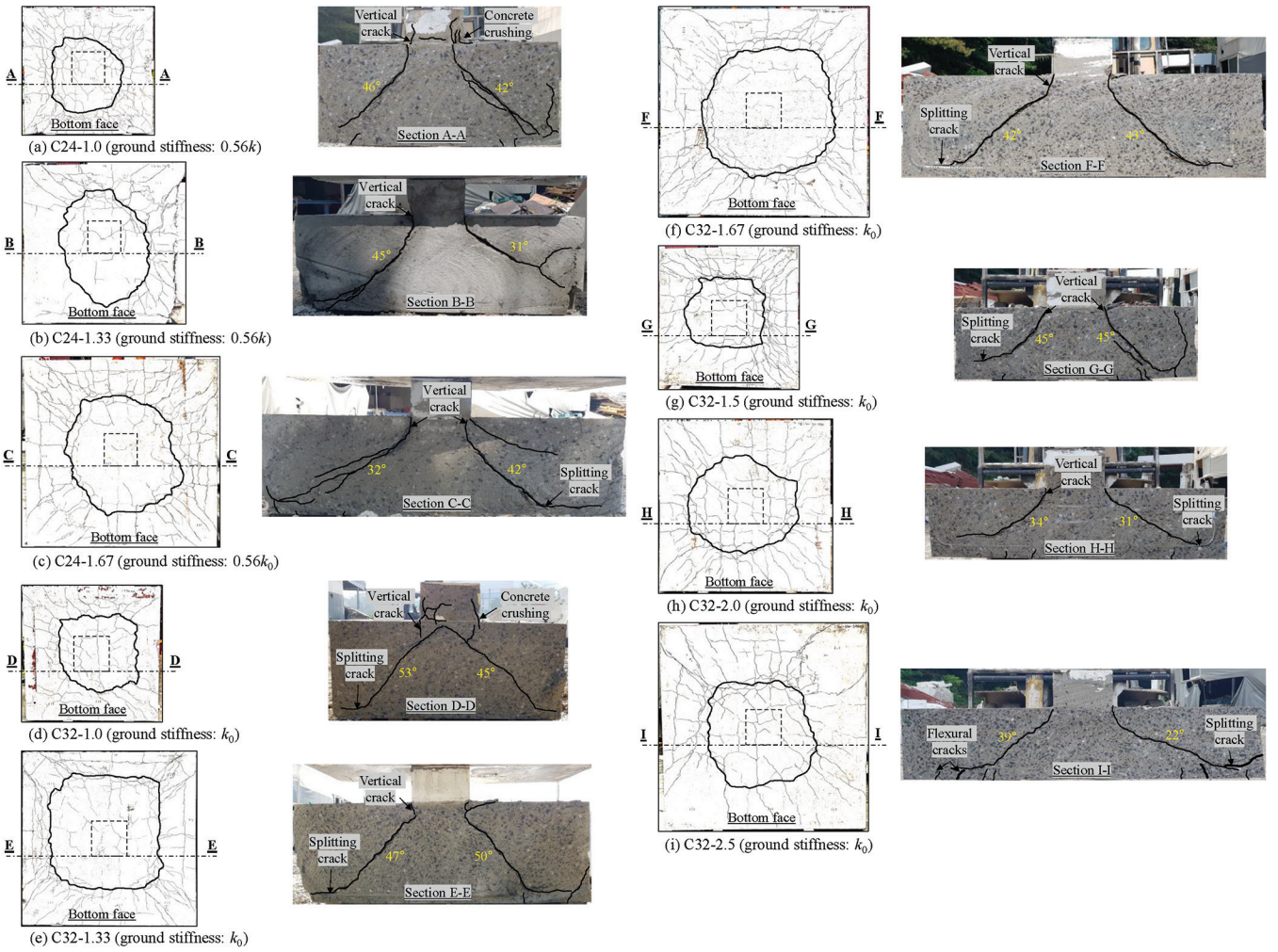

Fig. 7—Crack patterns of footing specimens at end of testing.

and the crack angles of C32-1.5, C32-2.0, and C32-2.5, with soil stiffness of $1.0k_0$ (Fig. 7(g), (h), and (i), respectively) were 45, 32.5, and 30.5 degrees, respectively.

For all the specimens, immediately after the peak load, punching shear failure was caused by inclined web-shear cracking, as shown from the crack patterns in Fig. 7. Such web-shear cracking is mainly caused by splitting of the concrete in the web of the footing slabs.[25,26] Furthermore, for most footings with low *a*/*d*, vertical penetration cracking and/or concrete crushing occurred at the upper part of the footing slabs (Fig. 7(a) to (c)). As the diagonal web cracking propagated to the column face, causing vertical cracking under a high level of punching load,[10,26] the column partially penetrated the footing slab. As the *a*/*d* decreased, the vertical cracking penetration in the upper part of the footing slabs became more severe. At the lower part of the footing slabs, diagonal web cracking propagated to horizontal splitting cracks along the longitudinal reinforcing bar. Flexural cracking was insignificant because of the low *a*/*d* of the footing specimens.

Furthermore, the bottom surfaces of the test specimens exhibited numerous radial cracks that propagated toward the footing slab edges; however, the crack width was not large. The bold solid lines represent the critical perimeter of the punching cone observed at the ultimate punching failure of the specimens. Generally, footing specimens with higher *a*/*d* showed larger critical perimeters than specimens with lower *a*/*d*, which is attributed to the low slope angle of web cracking.

Strain in concrete and flexural reinforcement

Figure 8 shows the representative radial concrete compression strain measured at the top surfaces of the footings. In general, the strain at the top surfaces reached maximum near the column face and gradually decreased toward the slab edges. In specimens C32-2.0 and C32-2.5 (Fig. 8(a) and (b), respectively), the compressive strain of the concrete near the column face exceeded 300 με. However, different behaviors were observed in specimens C32-1.0 and C32-1.33, with lower *a*/*d* (Fig. 8(c) and (d), respectively), wherein tension strain was measured at the top of the footing slabs. In footing slabs with low *a*/*d*, the effect of flexural action decreases while that of shear action increases. Thus, at the top surface of the slabs, the flexural compression strain decreased, and the tension strain caused by the diagonal tension increased. Vacev et al.[26] indicated an analogous phenomenon using a finite element analysis (FEA) of three-dimensional (3-D) footing models.

Figure 9 shows the strain profiles of the longitudinal reinforcing bars arranged in the directions orthogonal (XR) and

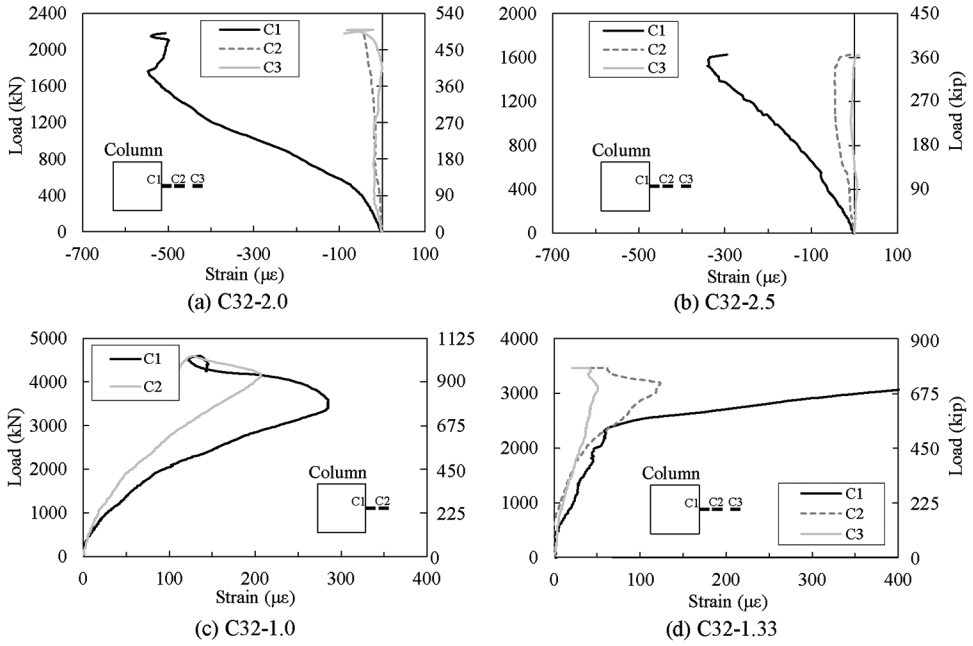

Fig. 8—Concrete strains at top surfaces of footings.

parallel (YT) to the column face for representative test specimens at different loading levels. The strain of the flexural reinforcing bars closer to the columns was greater than those far from the columns. For most specimens, at the peak load, the strain in the flexural reinforcing bars did not reach the yield strain, confirming that punching shear failure occurred before flexural yielding. The reinforcing bar strain in the YT direction is slightly higher than that in the XR direction.

Influence of *a*/*d*

The peak load (P_{test}) and corresponding displacement of the test specimens are summarized in Table 2. Figure 10 shows the effect of the *a*/*d* on the load-displacement relationships of the specimens. The displacement indicates the average vertical deflection measured at the column faces of the footing slabs (Fig. 6). Each figure shows the test results for uniform soil stiffness. As the *a*/*d* decreased, the peak strength increased, and the stiffness decreased. The observed behavior slightly differs from previous literature using the support condition as uniform loading points.[12,18,27] This is because of the same soil stiffness per unit area of the footings; the area of the footing increases as the *a*/*d* increases, accompanied by the increase of installed block numbers. Consequently, global stiffness increases over the entire footing area. However, the column load is transferred by a diagonal strut (that is, direct bearing) rather than flexural action. Thus, the peak strength increased as flexural damage decreased. For specimen C32-1.0, which was subjected to soil bearing stiffness k_0 (Fig. 10(c)), the test was intentionally terminated before punching failure, as the maximum load reached the actuator capacity.

Figure 11 illustrates the effect of the *a*/*d* on the punching failure load and stiffness of footings with different soil stiffnesses. The stiffness (K_{30}) of the test specimens was evaluated from the load-displacement relationships as follows

$$K_{30} = \frac{P_{30} - P_{10}}{\delta_{30} - \delta_{10}} \quad (1)$$

where P_{30} and P_{10} are the applied load values with respect to 10% and 30% of the peak load, respectively; and δ_{30} and δ_{10} are the corresponding displacements. In addition, to investigate the effect of the *a*/*d* on the punching failure load, the peak loads (P_{test}) in Fig. 11(a) were normalized by $\sqrt{f_c'}b_0d$, where b_0 [$= 2c_1 + 2c_2 + 4d$] is the critical perimeter according to ACI 318-19,[2] where c_1 and c_2 are the column dimensions and *d* is the effective depth of the footing slabs.

In Fig. 11(a), regardless of soil stiffness, footings with an *a*/*d* of 1.0 showed the highest normalized punching failure load of 0.6 to 0.7. As the *a*/*d* increased from 1.0 to 1.33, the normalized punching failure load decreased by approximately 25%. However, the decrease in the normalized punching load was insignificant when the *a*/*d* increased from 1.33 to 1.67. In Fig. 11(b), footings having higher *a*/*d* showed higher stiffness, and this trend was more pronounced for the footing groups with higher soil stiffness of $0.56k_0$ and $1.0k_0$. This is attributed to the high settlement of the rubber part of the composite block and the large deformation of the slab under high vertical axial stress when the *a*/*d* decreased. Generally, the stiffness K_{30} increased proportionally with the soil stiffness *k*.

Figure 12 shows the representative reaction pressure distribution beneath footing specimens measured in section A-A of specimens C32-1.0, C32-1.33, C32-1.67, and C32-2.5, subjected to soil bearing stiffness k_0. Overall, the lower the *a*/*d*, the higher the reaction pressure due to the peak strength increase. In addition, the non-uniformly distributed contact pressure was observed. As the applied load increased, the contact pressure concentration was recorded beneath the column at the central part of the footings, which conforms to the theoretical background of previous literature.[10,11]

Furthermore, Fig. 12 indicated that the degree of pressure concentration is significantly affected by the *a*/*d*. For

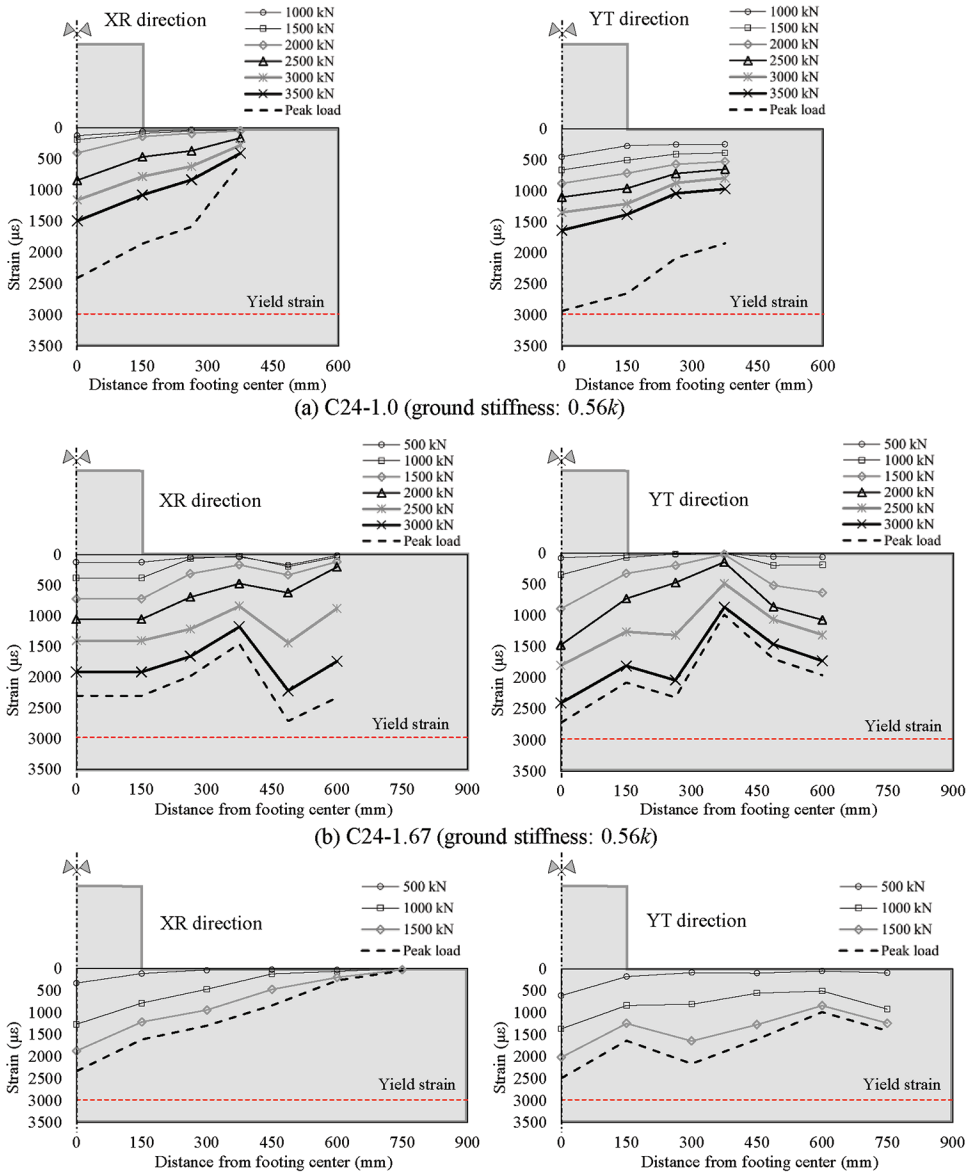

Fig. 9—Distribution of strains in flexural reinforcing bars. (Note: 1 mm = 0.039 in.; 1 kN = 0.225 kip.)

the footing specimens with low *a*/*d* of 1.0 and 1.33 (refer to Fig. 12(a) and (b)), the contact pressure concentration was insignificant at the peak load; the ratios between the maximum pressure measured beneath the central part and the minimum pressure measured at the footing edges were approximately 1.42 and 1.36, respectively. For the footing specimens with higher *a*/*d* of 1.67 and 2.5 (refer to Fig. 12(c) and (d), respectively), such values were 3.65 and 8.62, respectively, indicating a significant contact pressure concentration under the punching body. This is because as the *a*/*d* increased, the effect of flexural cracking was more pronounced, decreasing the rigidity of the footings in the region outside the critical perimeter, leading to the contact pressure concentration toward the central part of the footings under the punching cone. Analogous observations were observed by Fouda et al.[28]

Influence of soil stiffness

Figure 13 indicates the effect of soil stiffness on the load-displacement relationships of the footing specimens under each uniform value of the *a*/*d*. In Fig. 13, the soil stiffness affected the stiffness and deflection of the footings rather than the punching failure load, except for C24-1.0-0.25k_0. Figure 14 shows the specific effect of the soil stiffness on the normalized peak loads and stiffness for each footing group with uniform *a*/*d* of 1.0, 1.33, or 1.67.

In Fig. 14(a), for footing groups with *a*/*d* of 1.33 and 1.67, the effect of soil stiffness on the normalized punching failure load was insignificant. Meanwhile, for the footing group with *a*/*d* of 1.0, the normalized punching failure load increased as the soil stiffness increased from 0.25k_0 to 0.56k_0 and 1.0k_0. Further research is required for higher soil stiffness, as the test of Specimen C32-1.0-1.0k_0 was intentionally terminated owing to the limited capacity of the actuator.

As shown in Fig. 14(b), the stiffness K_{30} of the footings increased proportionally with soil stiffness. As soil

Table 2—Test results for column footings

Specimens	Soil stiffness	P_{test}, kN	δ, mm	Mean of x_c, mm	Mean of θ, degrees	P_{pred}, kN	P_{test}/P_{pred}
C24-1.0	$0.25k_0$	3347.0	76.7	144.0	45.0	3243.5	1.03
C24-1.33	$0.25k_0$	3340.0	61.6	217.5	42.0	3335.9	1.00
C24-1.67	$0.25k_0$	2862.5	53	360.0	39.0	3263.4	0.88
C24-1.0	$0.56k_0$	4537.5	64.9	132.0	44.0	3243.5	1.40
C24-1.33	$0.56k_0$	3393.5	49.7	262.5	38.0	3335.9	1.02
C24-1.67	$0.56k_0$	3219.9	36.4	333.0	37.0	3263.4	0.99
C32-1.0	k_0	4595.9	51.2	126.0	49.0	3745.2	1.23
C32-1.33	k_0	3470.0	29.5	202.5	48.5	3852.0	0.90
C32-1.67	k_0	3458.3	19.5	333.0	42.5	3768.3	0.92
C32-1.5	k_0	2373.3	31.3	192.0	45.0	2084.7	1.16
C32-2.0	k_0	2220.6	20.4	292.5	32.5	1851.8	1.25
C32-2.5	k_0	1628.2	15.6	495.0	30.5	1465.7	0.93
						Average	1.06
						COV	0.155

Note: x_c is distance from the footing edge to the end of the inclined web-shear cracking; k_0 = 0.051 N/mm^3 (0.184 kip/in.^{3}). 1 kN = 0.225 kip; 1 mm = 0.039 in.

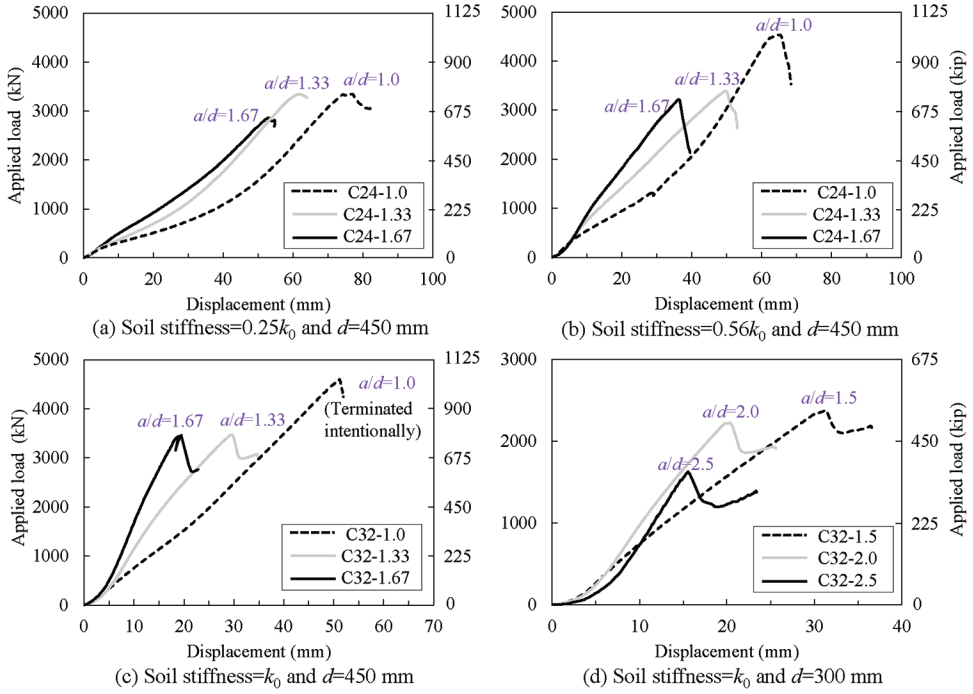

Fig. 10—Effect of a/d *on load-displacement relationships of footing specimens.*

stiffness increased, the stiffness exhibited an increasing trend. Analogous observations were made by Bonić et al.[29] for column footings tested on a cohesionless soil layer. For all test groups, compared to the footing specimens with soil stiffness of $0.25k_0$, K_{30} of footing specimens with soil stiffness of $0.56k_0$ and $1.0k_0$ increased by approximately two and four times, respectively.

Figure 15 shows the effect of soil-bearing stiffness on reaction pressure distribution beneath the footing measured in section A-A of Specimen C24-1.33. The results showed that the stiffness of the soil significantly affected contact pressure distribution beneath the footings. As shown in Fig. 15(a), for footings resting on the ground with low bearing stiffness of $0.25k_0$, uniform distribution of contact pressure was observed at the low level of the applied load. As the applied load increased, the contact pressure was developed and more concentrated at the central part of the footings than the region toward the edges, in particular at high loading levels (2500 kN [562.5 kip] and peak load).

Meanwhile, as shown in Fig. 15(b) and (c), when the soil stiffness increased with the higher density of composite blocks, the contact pressure decreased and was more uniformly redistributed with insignificant pressure concentration beneath the central part of the footing. Analogous

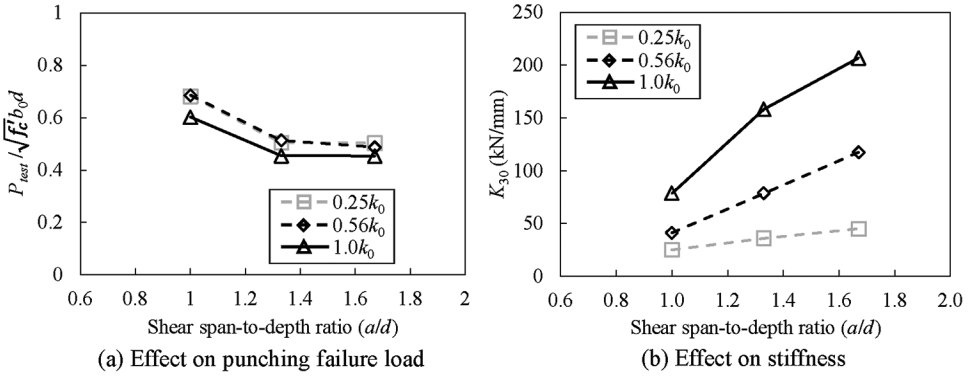

(a) Effect on punching failure load (b) Effect on stiffness

Fig. 11—Effect of a/d *on punching failure load and stiffness* K_{30}. *(Note: 1 mm = 0.039 in.; 1 kN = 0.225 kip.)*

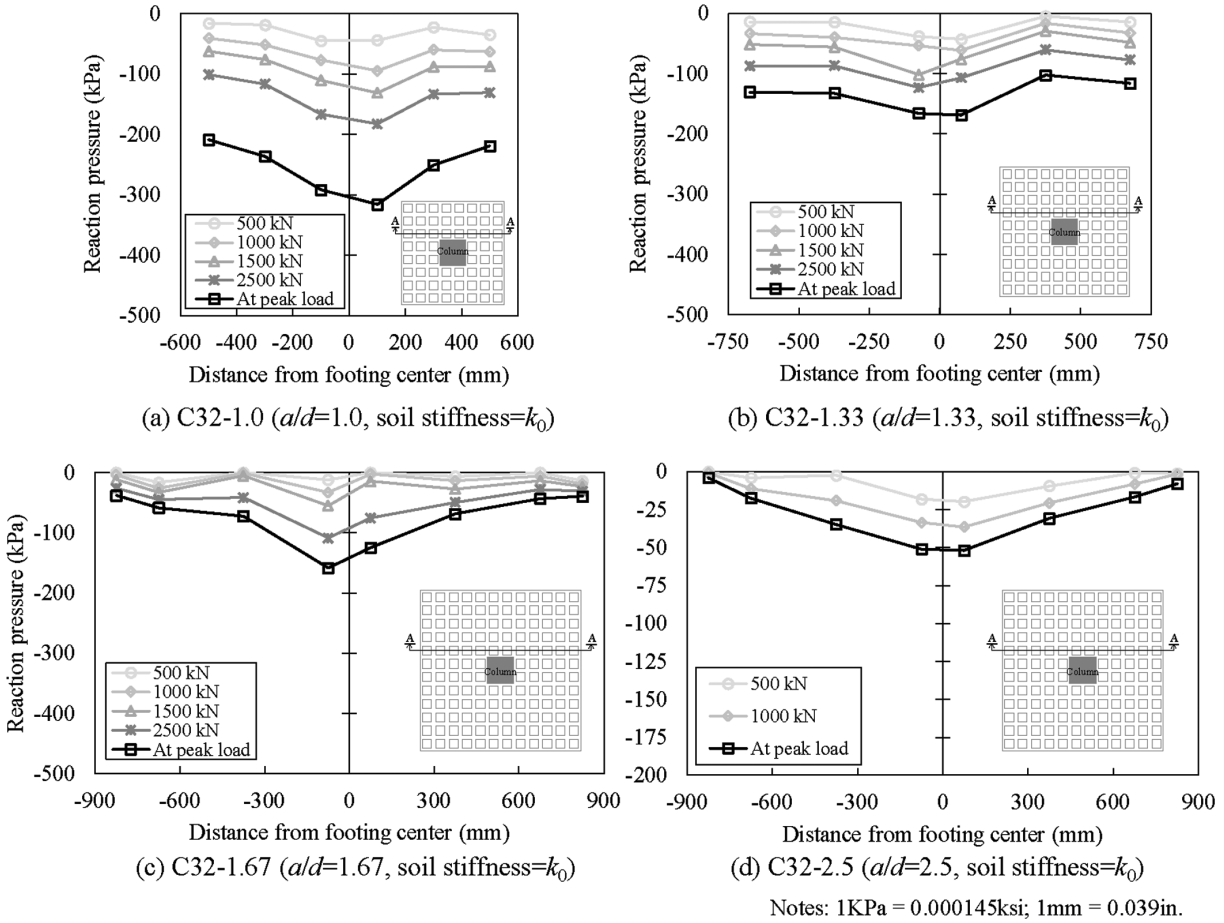

(a) C32-1.0 (a/d=1.0, soil stiffness=k_0)

(b) C32-1.33 (a/d=1.33, soil stiffness=k_0)

(c) C32-1.67 (a/d=1.67, soil stiffness=k_0)

(d) C32-2.5 (a/d=2.5, soil stiffness=k_0)

Notes: 1KPa = 0.000145ksi; 1mm = 0.039in.

Fig. 12—Effect of a/d *on reaction pressure distribution beneath footing specimens (section A-A). (Note: 1 mm = 0.039 in.; 1 kPa = 0.000145 ksi.)*

observations were observed by Bonić et al.[11,17] for column footings tested on the natural ground with different compaction degrees of soil layers.

ANALYTICAL MODEL FOR PUNCHING SHEAR STRENGTH OF FOOTINGS WITH LOW *A/D*

In the existing design codes, various approaches are used to evaluate the punching shear strength of column footings. In ACI 318-19,[2] EC2,[3] and *fib* Model Code 2010,[20] empirical methods considering average shear stress around a critical perimeter are used, whereas the method used in KDS 14 20 22[4] is based on the theory of compression zone failure mechanism originally developed by Park et al.[30] and Choi et al.[31] Furthermore, the critical perimeters (b_0) are defined differently in the existing design codes, as presented in Fig. 16. In ACI 318-19,[2] *fib* Model Code 2010,[20] and KDS 14 20 22,[4] b_0 is considered located at a distance of 0.5d from the column face. On the other hand, in BS 8110-1:1997,[32] a greater distance of 1.5d is considered, and in EC2,[3] the control perimeter is determined by an iterative process in a range of 2.0d from the column face. As previously mentioned, regardless of the a/d and soil stiffness, the punching shear strength models of existing design codes such as ACI 318-19,[2] EC2,[3] or KDS 14 20 22[4] are mainly based on the previous empirical and theoretical investigations[5,6] on slab-column connections with high a/d.

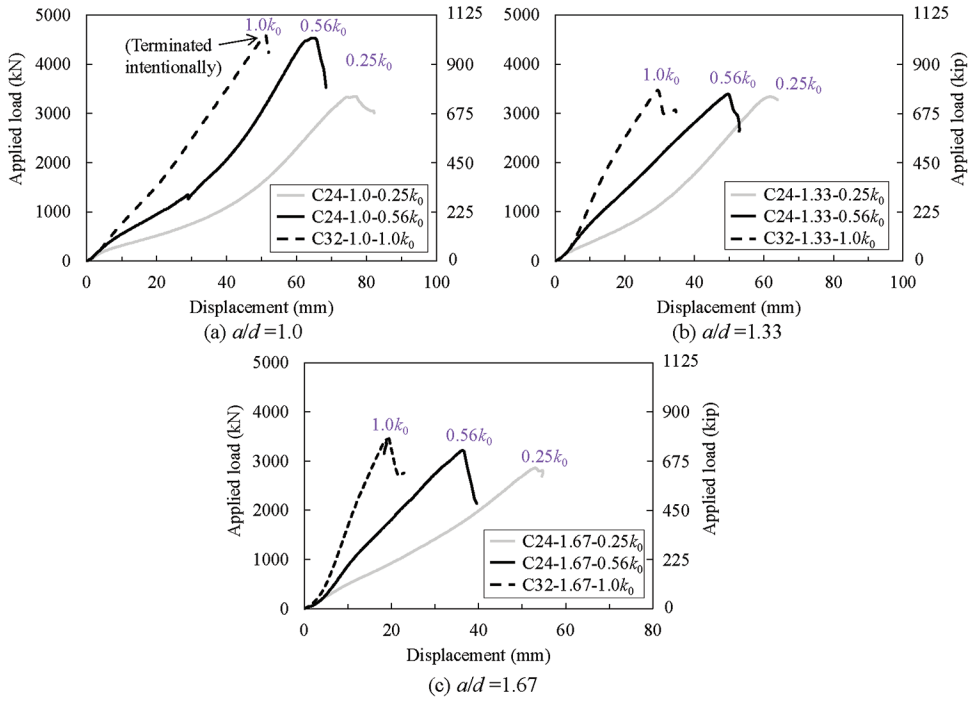

Fig. 13—Effect of soil stiffness on load-displacement relationships of footing specimens. (Note: 1 mm = 0.039 in.)

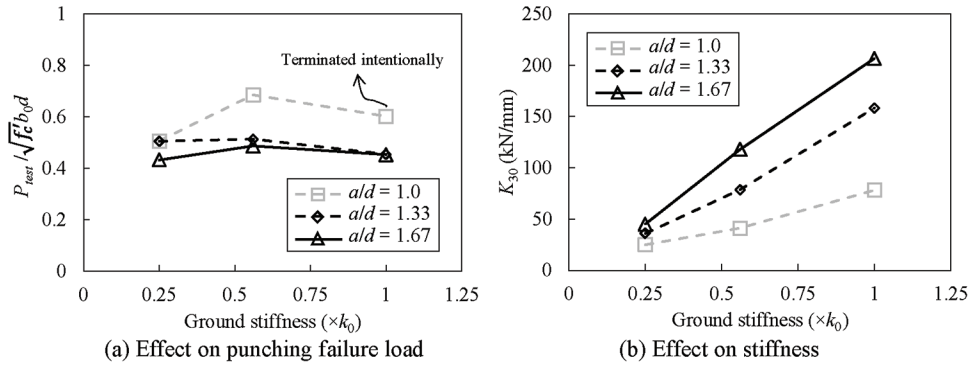

Fig. 14—Effect of soil stiffness on punching failure load and stiffness K_{30}. *(Note: 1 mm = 0.039 in.; 1 kN = 0.225 kip.)*

However, the current test results showed that the punching load of column footings with low a/d was greater than that of specimens with higher a/d.

Further, the column footing specimens with low a/d failed due to the inclined web-shear cracking caused by the splitting of the concrete[25,26] and vertical penetration cracking due to high stress concentration at the upper part of the footing slabs.[25] This failure mechanism differs from that of slender flat slabs or foundations with high a/d. Thus, an analytical model for footing slabs with low a/d was developed based on the web-shear cracking mechanism owing to concrete splitting.

Model development

Figure 17 shows the proposed punching shear model based on the web-shear cracking mechanism for column footings with low a/d subjected to axial vertical loads from the column stub P. The inclined failure surface of the footing web is defined by the slope θ_i originating from the column center, based on the observations of the present tests (refer to Fig. 7). The depth of the vertical penetration cracking is denoted as d_{0i}, and the effective web depth contributing to the punching shear resistance is denoted as d_{ei}. Accordingly, the punching shear strength V_c contributed by the concrete splitting within the effective web depth can be determined as follows

$$V_c = \sum_{i=1}^{2} f_{tc}' A_{0i} \cos\theta_i \tag{2}$$

where f_{tc}' [= $0.292\sqrt{f_c'}$ MPa (= $3.5\sqrt{f_c'}$ psi)] denotes the splitting tensile strength of the concrete[33]; A_{0i} denotes the area of the effective web in two orthogonal directions; and θ_i denotes the inclination angle of the failure surface with respect to the horizontal axis.

From Fig. 17, the effective web area in the form of a truncated cone in two orthogonal directions (area AA′C′C or A′B′D′C′) is evaluated as follows

$$A_{0i} = (2c_i + 2d_{ei} \cdot \cot\theta_i)\frac{d_{ei}}{\sin\theta_i} \tag{3}$$

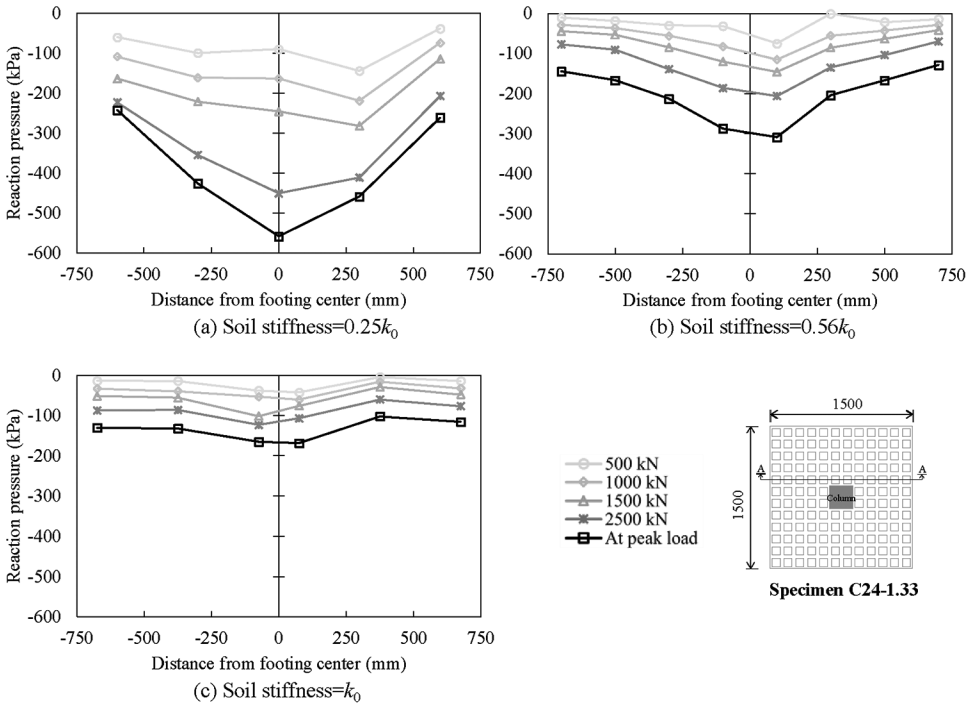

Fig. 15—Effect of soil stiffness on reaction pressure distribution beneath specimen C24-1.33 (section A-A). (Note: 1 mm = 0.039 in.; 1 kPa = 0.000145 ksi.)

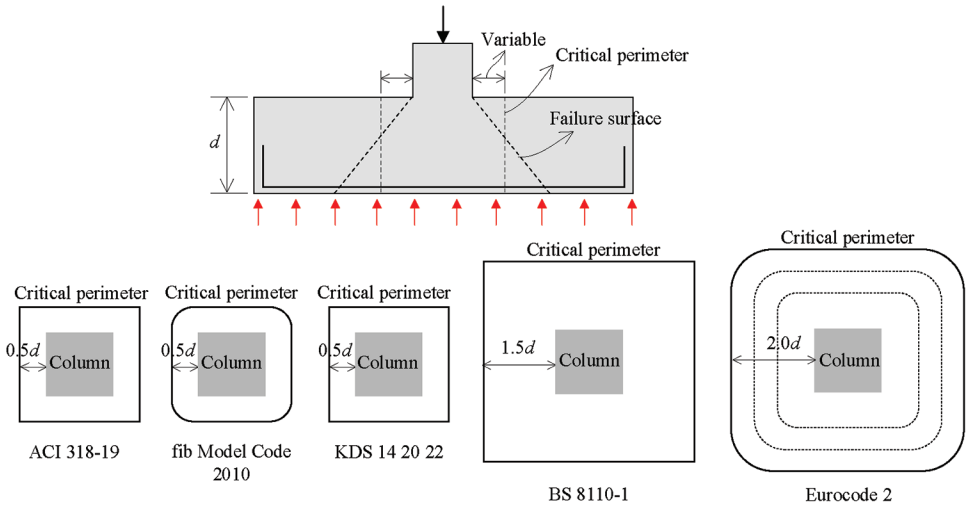

Fig. 16—Different critical perimeters considered in existing design codes.

where c_i (i = 1 or 2) is the column dimension. Inserting Eq. (3) into Eq. (2), the punching shear strength of the footings can be defined as follows

$$V_c = \sum 2 f_{tc}'(c_i + d_{ei} \cdot \cot\theta_i) d_{ei} \cot\theta_i \quad (4)$$

Equation (4) is redefined to consider the size effect factor, k_s, as follows

$$V_c = \sum_{i=1}^{2} 2 k_s f_{tc}'(c_i + d_{ei} \cdot \cot\theta_i) d_{ei} \cot\theta_i \quad (5)$$

where k_s ($=\sqrt[4]{300/d} \le 1.1$, d is in mm [$=\sqrt[4]{11.7/d} \le 1.1$, d is in in.]) is defined according to KDS 14 20 22.[4]

In Fig. 17, the applied column load P at punching failure is evaluated by considering the influence of the reaction pressure p_0 in the effective bearing area enclosed by the critical perimeter. Assuming that p_0 is uniformly distributed beneath the footings (that is, $P/A_{foot}=V_c/(A_{foot} - A_{c0})$), P can be computed as follows

$$P = \frac{V_c}{1 - \frac{A_{c0}}{A_{foot}}} = \frac{\sum_{i=1}^{2} 2 k_s f_{tc}'(c_i + d_{ei} \cdot \cot\theta_i) d_{ei} \cot\theta_i}{1 - \frac{(c_1 + 2d_{e1}\cot\theta_1)(c_2 + 2d_{e2}\cot\theta_2)}{L_1 L_2}} \quad (6)$$

where A_{c0} [$= (c_1 + 2d_{e1}\cot\theta_1)(c_2 + 2d_{e2}\cot\theta_2)$] is the area within the considered critical perimeter (area CDD′C′); L_1 and L_2 are the footing dimensions; and A_{foot} [$= L_1 L_2$] is the area of the footing slabs. In this study, the proposed model

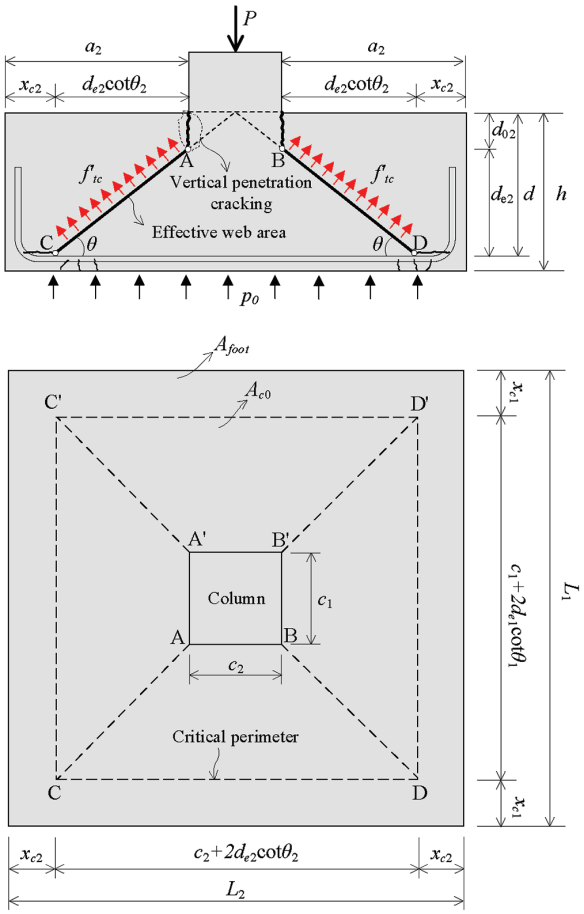

Fig. 17—Web-shear cracking-based punching shear model for column footings with low a/d.

was applied to square footing slabs and columns; thus, c [= $c_1 = c_2$] and L [= $L_1 = L_2$] were used in the calculation.

Figure 18 shows the failure surfaces of the representative specimens observed by saw cuts at the end of the testing. The current test results, as well as previous literature,[25,34,35] showed that the inclination angle θ of the failure surface significantly varied and was affected by the a/d of the footings. Thus, the distance x_c [= $a - d_e\cot\theta$] from the footing edge to the end of the inclined web-shear cracking caused by concrete splitting in the web of footings was affected by the a/d. Campione et al.[35] reported that x_c is affected by many parameters, including the distribution of the reaction stress of the ground, and thus is very complicated to theoretically evaluate. Thus, in this study, x_c was determined based on the test results.

The average results of x_c on the left and right sides of the footings measured from the cross sections of the specimens are summarized in Table 2. Based on the test results, Fig. 19 shows the relationship between the parameters x_c and a/d. The results imply a strong relationship between the parameters x_c and a/d, which can be expressed by the following best-fitted equation

$$x_c = 0.11(a/d)L \le 0.275L \tag{7}$$

By using x_c in Eq. (11), inclination angle θ can be estimated as follows

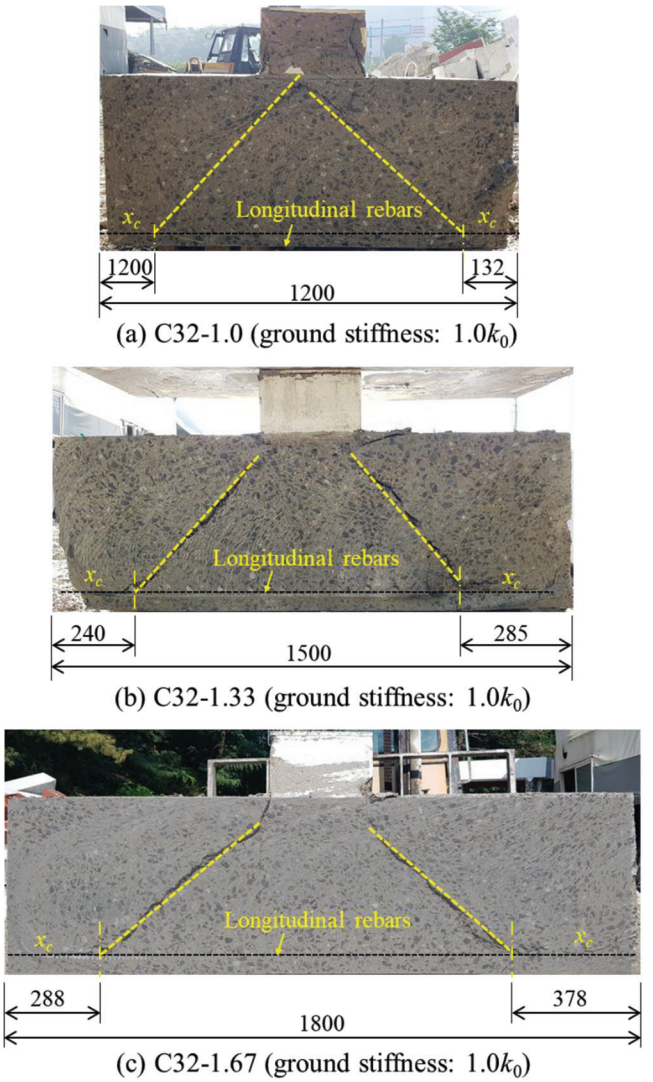

Fig. 18—Failure surfaces of representative footing specimens. (Note: Units in mm; 1 mm = 0.039 in.)

$$\theta = a\tan\left(\frac{2d}{L-2x_c}\right) \tag{8}$$

Figure 20 compares the predicted inclination angle θ of the failure surface and the test results from the present study (refer to Table 2) and previous studies.[14,36] Overall, the predicted θ varied from 25 to 45 degrees with increasing a/d, showing a reasonable correlation with the test results. The decreasing trend of θ with increasing a/d was also reported in previous literature.[25,34,35]

From Fig. 17, by inserting $d_e\cot\theta$[= $(L - c)/2 - x_c$] into Eq. (3) and (5), the punching shear strength, V_c, and punching failure load, P, were redefined by considering the variable x_c as follows

$$V_c = k_s f'_{tc}(L - 2x_c + c)(L - 2x_c - c) \tag{9}$$

$$P = \frac{k_s f'_{tc}(L - 2x_c + c)(L - 2x_c - c)}{1 - \dfrac{(L - 2x_c)^2}{L^2}} \tag{10}$$

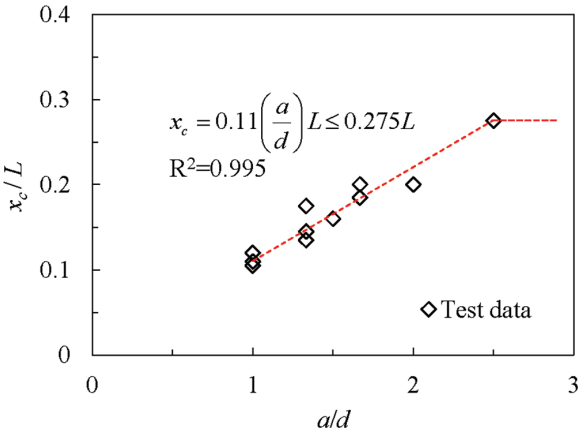

Fig. 19—Relationship between x_c/L *and* a/d *derived from test results.*

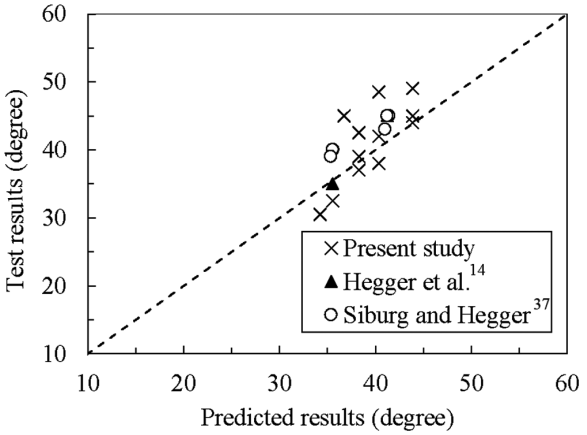

Fig. 20—Comparison of inclination angles predicted by proposed model and obtained from test results.

Verification of proposed model and discussion

The proposed analytical model was applied to the test specimens. Table 2 compares the predicted punching failure load and the tested peak strength. Overall, the predicted results agreed with the test results, showing a mean ratio (P_{test}/P_{pred}) of 1.06 and a coefficient of variation (COV) of 0.155.

To evaluate the reliability, the proposed analytical model was applied to a database collected from previous tests of concrete column footings without shear reinforcement, as summarized in Table D1 in Appendix D. For comparison, the existing design codes KDS 14 20 22[4] and ACI 318-19[2] were also applied to the test specimens. The details of the design equations for KDS 14 20 22[4] and ACI 318-19[2] are summarized in Appendix E. To predict the design codes, the punching failure load P was evaluated considering the effect of the reaction pressure within the area A_{pr} inside the considered perimeter, as follows

$$P = \frac{V_c}{1 - \frac{A_{pr}}{A_{foot}}} \tag{11}$$

where A_{pr} is taken at a distance of $0.5d$ from the column face in ACI 318-19,[2] and at a distance of $0.75d$ in KDS 14 20 22.[4] It should be noted that in the case of the KDS 14 code, the punching shear strength is calculated at the critical section located at a distance of $0.5d$, whereas the punching failure load (demand) is calculated at a distance of $0.75d$ considering the inclined failure surface (that is, the soil pressure within the perimeter at $0.75d$ from the column face is neglected when evaluating the applied punching shear demand).

Figure 21 shows the punching failure load ratio P_{test}/P_{pred} between the test and predicted results according to the a/d for various support types: spring, soil, and block (the present study). In Fig. 21, statistical analysis was performed separately for the groups with low $a/d \le 2.0$ and higher $a/d \ge 2.0$. For each group, the minimum, maximum, and average values and COV of P_{test}/P_{pred} are presented in detail. In addition, the 5% fractile ($P_{0.05}$), which is generally accepted as a nominal value of the resistance in the theory of limit states (EN 1990:2002[36]), was assessed for safety design with an assumption of normal distribution of the P_{test}/P_{pred}. A value of the 5% fractile than 1.0 implies an unsafe design.

In Fig. 21(a), for low $a/d \le 2.0$, the proposed method showed better accuracy in strength predictions than the current design codes. For this group, the mean value of P_{test}/P_{pred} was 1.25, with a COV of 0.140 and an acceptable value of a 5% fractile of 0.88, which is close to the target value of 1.0. For the group with $a/d \ge 2.0$, the analytical method also showed accurate predictions with more scattering, a COV of 0.151, and a lower 5% fractile value of 0.92. However, as the a/d increased, the strength ratio tended to decrease below 1.0, which was in the unsafe zone. In the case of KDS 14 20 22[4] (Fig. 21(b)), the predictions generally agreed with the test results. However, at the low a/d of 1.0, the strength ratio was very low. Compared with the proposed model, for low $a/d \le 2.0$, the mean value of P_{test}/P_{pred} is 1.04, with a larger scattering (COV of 0.194) and a lower value of 5% fractile of 0.71. Meanwhile, for high $a/d \ge 2.0$, the KDS 14 code showed more reasonable and conservative predicted results, with a 5% fractile of 1.11, an average value of 1.36, and a smaller COV of 0.110. This is because the KDS 14 code was developed based on the compression zone failure mechanism considering severe flexural damage, which is appropriate for footings with a high shear slenderness. In the case of ACI 318-19[2] (Fig. 21(c)), the prediction showed high safety for both $a/d \le 2.0$ and $a/d \ge 2.0$, a mean value of 1.48 and COV of 0.138 for $a/d \le 2.0$, and a mean value of 1.40 and COV of 0.186 for $a/d \ge 2.0$. As the a/d increased, the strength ratio also increased.

Parametric study and design consideration

Figure 22 shows the results of a parametric study using the proposed model to understand the influence of the design parameters on the punching failure load of column footings with low a/d. In Fig. 22(a), the main variable was the a/d of 1.26 to 2.0, and the other parameters were kept constant, similar to the specimens tested by Hegger et al.[14] In Fig. 22(b), the main variable was the concrete compressive strength of 19.0 to 52.0 MPa (2.76 to 7.54 ksi), and the other parameters were kept constant, similar to specimens tested by Siburg and Hegger.[37] As shown in Fig. 22(a), the predicted

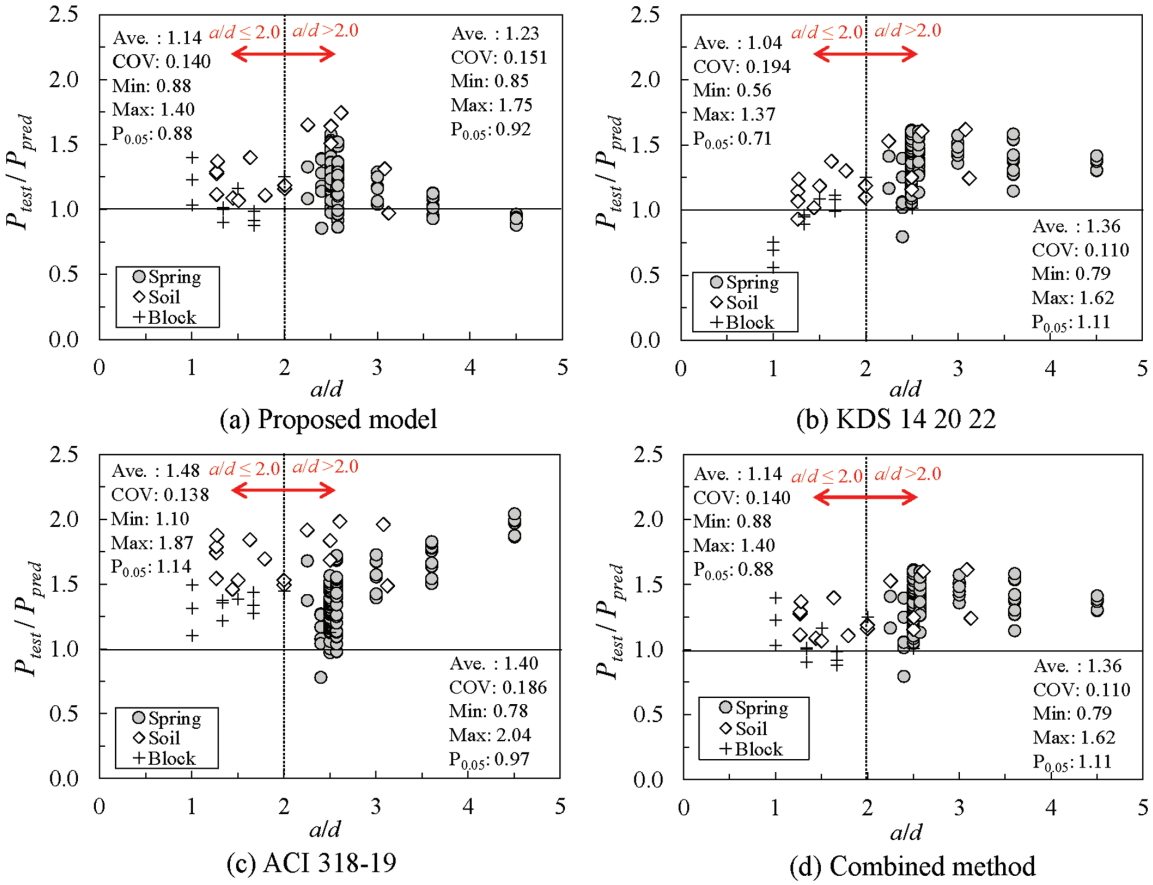

Fig. 21—Verification of proposed model and comparison with existing design codes.

punching failure load decreased as the a/d increased, which coincides with the test results. In Fig. 22(b), the punching failure load increased as the compressive strength increased owing to the increase in the tensile strength of the concrete.

Figure 23 presents a parametric study of the punching shear strength (V_c) predicted by the proposed model and KDS 14[4] model. The main variable was the a/d of the footings. The analytical footing models have identical column dimensions of 200 x 200 mm (7.87 x 7.87 in.), effective depth (d) of 400 mm (15.7 in.), concrete compressive strength (f_c') of 27 MPa (3.92 ksi), and longitudinal reinforcing bar ratio (ρ) of 0.01. The results in Fig. 23 indicate that as the a/d increased, the proposed model showed an increasing trend of the punching shear strength. This is because, as the a/d increases, the depth of the effective region of the footing web contributing to the punching shear resistance (d_e) increases along with the decrease in the inclination angle (θ) of the failure surface (refer to Eq. (8)). Conversely, the punching shear strength predicted by the KDS 14 model exhibited a uniform value because the model did not consider the effect of inclination angle θ according to the a/d.

As shown in Fig. 23, the accuracy and safety of the predictions differed according to the range of the a/d because the failure mechanisms considered in the methods were different. Thus, for safe and economical design, the use of a combined method using multiple design methods could be better. Figure 21(d) presents the prediction of the punching failure loads of the column footings using the proposed method for $a/d \le 2.0$ and the KDS 14 code for $a/d > 2.0$. When the combined method is used, the prediction is reasonable for a wide range of a/d showing low scattering (COV values of 0.133 and 0.139 corresponding to the footing groups with $a/d \le 2.0$ and $a/d > 2.0$, respectively). Further, the combined method provides safe design, showing 5% fractile values of 0.90 and 1.21 for the footing groups with $a/d \le 2.0$ and $a/d > 2.0$, respectively.

SUMMARY AND CONCLUSIONS

In this study, experimental investigations were conducted to understand the punching shear behavior of isolated concrete column footings with low shear span-depth ratios (a/d). The influencing parameters, including the a/d, concrete compressive strength, and soil stiffness, were investigated and analyzed. The primary conclusions drawn from this study are as follows.

1. For footings with low a/d, punching shear failure occurred immediately after the peak load, with a limited occurrence of flexural cracks. Such a failure mode was characterized by inclined web-shear cracking mainly caused by the splitting of the concrete in the web of the footings. The inclined cracks of the punching cone exhibited a decreased slope angle as the a/d increased. In addition, vertical penetration cracking originating from the column face occurred in the upper part of the footing slabs because of the high stress concentration.

2. The punching shear load of the footings decreased as the a/d increased. The test results showed a pronounced reduction in the punching shear load when the a/d increased

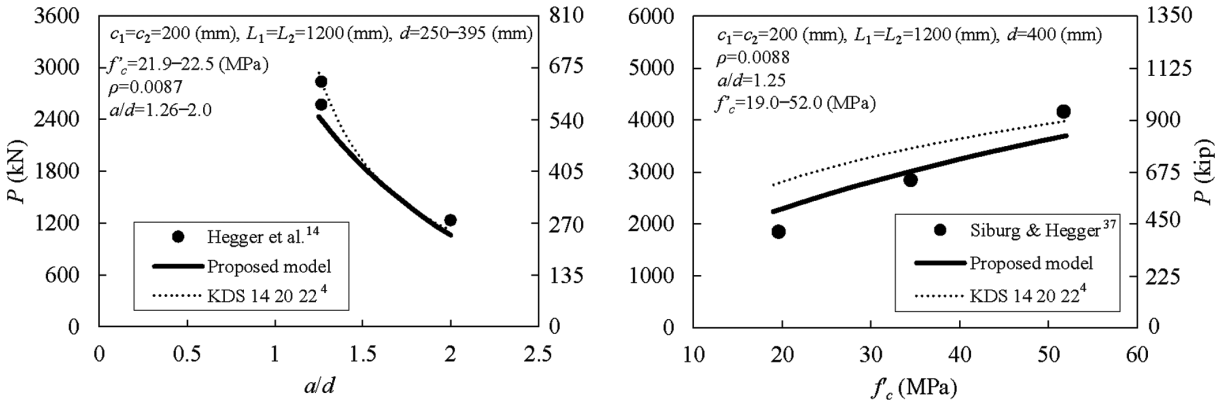

(a) Punching shear load according to a/d ratio

(b) Punching shear load according to f'_c

Fig. 22—Parametric study of proposed model and comparison with test results. (Note: 1 mm = 0.039 in.; 1 MPa = 0.145 ksi.)

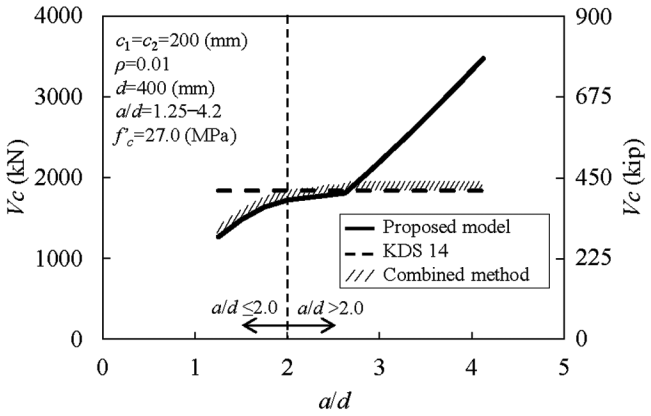

Fig. 23—Variation in punching shear strength according to a/d*. (Note: 1 mm = 0.039 in.; 1 MPa = 0.145 ksi.)*

from 1.0 to 1.33, while showing an insignificant reduction when the a/d increased from 1.33 to 2.0. However, specimens with higher a/d showed higher stiffness of the load-displacement relationship when compared to those with lower a/d, which can be attributed to the high settlement of the composite block caused by high bearing stress occurring beneath the footings. Additionally, the test results revealed a high concentration of contact pressure beneath the central part of the footings for the cases of high a/d of 1.67 and 2.5. This phenomenon could be the result of pronounced flexural cracking decreasing the rigidity of the footing body, especially in the region outside the critical perimeter.

3. Soil stiffness did not significantly affect the punching shear strength of the footings, although the higher soil stiffness decreased the deflection of the foundation. Additionally, the test results showed that the stiffness of the soil significantly affected contact pressure distribution beneath the footings. As the soil stiffness increased with the higher density of composite blocks, the contact pressure decreased gradually and was more uniformly redistributed with insignificant pressure concentration beneath the central part of the footings.

4. An analytical model based on the web-shear cracking mechanism was developed to evaluate the punching shear strength of footings with low a/d considering an effective web area. The prediction showed reasonable agreement with the test results of existing studies as well as the present study and showed better accuracy than current design codes for footings with low $a/d \leq 2.0$.

AUTHOR BIOS

Ngoc Hieu Dinh *is a Lecturer in the Faculty of Civil Engineering at the University of Da Nang – University of Science and Technology, Da Nang, Vietnam. He is also a Postdoctoral Fellow at Soongsil University, Seoul, South Korea, where he received his MS and PhD in architectural engineering. His research interests include seismic design of reinforced concrete (RC) structures and application of fiber- and textile-reinforced concrete.*

Juok Noh *is a Research Assistant at Seoul National University, Seoul, South Korea, where she received her MS and PhD in architectural engineering. Her research interests include shear design of RC members.*

Kyoung-Kyu Choi *is a Professor of Architectural Engineering at Soongsil University. He received his BE, MS, and PhD in architectural engineering from Seoul National University. He received the ACI Chester Paul Siess Award for Excellence in Structural Research in 2009 and 2012. His research interests include the shear and seismic design of RC structures and application of fiber-reinforced concrete.*

Hong-Gun Park, *FACI, is a Professor in the Department of Architecture and Architectural Engineering at Seoul National University, where he received his BE and MS in architectural engineering. He received his PhD in civil engineering from The University of Texas at Austin, Austin, TX. His research interests include inelastic analysis and seismic design of RC structures.*

ACKNOWLEDGMENTS

This research was financially supported by Institute of Construction and Environmental Engineering at Seoul National University and the National Research Foundation of Korea (Grant No. NRF-2022R1A2C2004351) funded by the Korean government. The authors wish to express their gratitude for the support.

REFERENCES

1. Noh, J. O., "Punching Shear Strength of Column-Footings with Short Shear Span," doctoral dissertation, Seoul National University, Seoul, South Korea, 2021.

2. ACI Committee 318, "Building Code Requirements for Structural Concrete (ACI 318-19) and Commentary (ACI 318R-19) (Reapproved 2022)," American Concrete Institute, Farmington Hills, MI, 2019, 624 pp.

3. EN 1992-1-1:2004, "Eurocode 2: Design of Concrete Structures - Part 1-1: General Rules and Rules for Buildings," European Committee for Standardization, Brussels, Belgium, 2004.

4. KDS 14 20 22, "Design Code for Shear and Torsion of Concrete Structures," Korea Concrete Institute, Seoul, South Korea, 2021. (in Korean)

5. Lips, S.; Fernández Ruiz, M.; and Muttoni, A., "Experimental Investigation on Punching Strength and Deformation Capacity of Shear-Reinforced Slabs," *ACI Structural Journal*, V. 109, No. 6, Nov.-Dec. 2012, pp. 889-900.

6. Schmidt, P.; Kueres, D.; and Hegger, J., "Punching Shear Behavior of Reinforced Concrete Flat Slabs with a Varying Amount of Shear

Reinforcement," *Structural Concrete*, V. 21, No. 1, 2020, pp. 235-246. doi: 10.1002/suco.201900017

7. Fernández Ruiz, M., and Muttoni, A., "Performance and Design of Punching-Shear Reinforcing Systems," *3rd* fib *International Congress*, Washington, DC, 2010.

8. Farhey, D. N.; Yankelevsky, D. Z.; and Adin, M. A., "Resistance Mechanism Model for Reinforced Concrete Flat Slab-Column Frame Connections," *ACI Structural Journal*, V. 94, No. 6, Nov.-Dec. 1997, pp. 653-662.

9. Elstner, R. C., and Hognestad, E., "Investigation of Reinforced Concrete Slabs Failing in Shear," Department of Theoretical and Applied Mechanics, College of Engineering, University of Illinois Urbana-Champaign, Urbana, IL, 1953.

10. Hegger, J.; Ricker, M.; Ulke, B.; and Ziegler, M., "Investigations on the Punching Behaviour of Reinforced Concrete Footings," *Engineering Structures*, V. 29, No. 9, 2007, pp. 2233-2241. doi: 10.1016/j.engstruct.2006.11.012

11. Bonić, Z.; Zlatanović, E.; Romić, N.; Lukić, D. Č.; and Cvetković, D., "Punching Shear Capacity of Reinforced Concrete Column Footings Accounting for the Soil–Structure Interaction Effect," *Journal of Building Engineering*, V. 46, 2022, p. 103706. doi: 10.1016/j.jobe.2021.103706

12. Simões, J. T.; Bujnak, J.; Ruiz, M. F.; and Muttoni, A., "Punching Shear Tests on Compact Footings with Uniform Soil Pressure," *Structural Concrete*, V. 17, No. 4, 2016, pp. 603-617. doi: 10.1002/suco.201500175

13. Hegger, J.; Sherif, A. G.; and Ricker, M., "Experimental Investigations on Punching Behavior of Reinforced Concrete Footings," *ACI Structural Journal*, V. 103, No. 4, July-Aug. 2006, pp. 604-613.

14. Hegger, J.; Ricker, M.; and Sherif, A. G., "Punching Strength of Reinforced Concrete Footings," *ACI Structural Journal*, V. 106, No. 4, July-Aug. 2009, pp. 706-716.

15. Abdrabbo, F.; Mahmoud, Z. I.; and Ebrahim, M., "Structural Design of Isolated Column Footings," *Alexandria Engineering Journal*, V. 55, No. 3, 2016, pp. 2665-2678. doi: 10.1016/j.aej.2016.06.016

16. Schmidt, P.; Ungermann, J.; and Hegger, J., "Contribution of Concrete and Shear Reinforcement to the Punching Shear Resistance of Column Bases," *Engineering Structures*, V. 245, 2021, p. 112901. doi: 10.1016/j.engstruct.2021.112901

17. Bonić, Z.; Zlatanović, E.; Brčić, S.; Blagojević, P.; Romić, N.; and Cvetković, D., "Theoretical and Experimental Research on the Punching Shear Capacity of Reinforced Concrete Column Footings Rested on the Ground," *Engineering Structures*, V. 249, 2021, p. 113154. doi: 10.1016/j.engstruct.2021.113154

18. Ungermann, J.; Schmidt, P.; Classen, M.; and Hegger, J., "Eccentric Punching Tests on Column Bases–New Insights into the Inner Concrete Strain Development," *Engineering Structures*, V. 262, 2022, p. 114273. doi: 10.1016/j.engstruct.2022.114273

19. Ungermann, J.; Schmidt, P.; Christou, G.; and Hegger, J., "Eccentric Punching Tests on Column Bases-Influence of Column Geometry," *Structural Concrete*, V. 23, No. 3, 2022, pp. 1316-1332. doi: 10.1002/suco.202100744

20. *fib*, "*fib* Model Code for Concrete Structures 2010," Fédération Internationale du Béton, Lausanne, Switzerland, 2013.

21. KS F 2405, "Standard Test Method for Compressive Strength of Concrete," Korean Standards Association, Seoul, South Korea, 2017.

22. KS B 0802, "Method of Tensile Test for Metallic Materials," Korean Standards Association, Seoul, South Korea, 2018.

23. Zhang, W. X.; Li, B.; Hwang, H. J.; Zhang, J. Y.; Xiao, L. J.; Yi, W. J.; and Park, H. G., "Punching Shear Strength of Reinforced Concrete Column Footings under Eccentric Compression: Experiment and Analysis," *Engineering Structures*, V. 198, 2019, p. 109509. doi: 10.1016/j.engstruct.2019.109509

24. Aron, C., and Jonas, E., "Structural Element Approaches for Soil-Structure Interaction," master's thesis, Chalmers University of Technology, Gothenburg, Sweden, 2012.

25. *fib* Bulletin No. 12, "Punching of Structural Concrete Slabs: Technical Report," Fédération Internationale du Béton, Lausanne, Switzerland, 2001.

26. Vacev, T.; Bonić, Z.; Prolović, V.; Davidović, N.; and Lukić, D., "Testing and Finite Element Analysis of Reinforced Concrete Column Footings Failing by Punching Shear," *Engineering Structures*, V. 92, 2015, pp. 1-14. doi: 10.1016/j.engstruct.2015.02.027

27. Kueres, D.; Schmidt, P.; and Hegger, J., "Punching Shear Behavior of Reinforced Concrete Footings with a Varying Amount of Shear Reinforcement," *Structural Concrete*, V. 20, No. 2, 2019, pp. 552-563. doi: 10.1002/suco.201800257

28. Fouda, M. A.; Elkateb, M.; Elkateb, T.; and Khalil, A., "Experimental Investigation of RC Footings Resting on Sand Strengthened with Concrete Jacketing," *Advances in Science, Technology and Engineering Systems Journal*, V. 5, No. 6, 2020, pp. 133-142. doi: 10.25046/aj050615

29. Bonić, Z.; Davidović, N.; Vacev, T.; Romić, N.; Zlatanović, E.; and Savić, J., "Punching Behaviour of Reinforced Concrete Footings at Testing and According to Eurocode 2 and *fib* Model Code 2010," *International Journal of Concrete Structures and Materials*, V. 11, No. 4, 2017, pp. 657-676. doi: 10.1007/s40069-017-0213-8

30. Park, H. G.; Choi, K. K.; and Wight, J. K., "Strain-Based Shear Strength Model for Slender Beams without Web Reinforcement," *ACI Structural Journal*, V. 103, No. 6, Nov.-Dec. 2006, pp. 783-793.

31. Choi, K. K.; Hong-Gun, P.; and Wight, J. K., "Unified Shear Strength Model for Reinforced Concrete Beams-Part I: Development," *ACI Structural Journal*, V. 104, No. 2, Mar.-Apr. 2007, pp. 142-152.

32. BS 8110-1:1997, "Structural Use of Concrete – Part 1: Code of Practice for Design and Construction," British Standards Institution, London, UK, 1997.

33. Neville, A. M., *Properties of Concrete*, fourth edition, Prentice Hall, Upper Saddle River, NJ, 1995.

34. Rizk, E.; Marzouk, H.; and Tiller, R., "Design of Thick Concrete Plates Using Strut-and-Tie Model," *ACI Structural Journal*, V. 109, No. 5, Sept.-Oct. 2012, pp. 677-686.

35. Campione, G.; Cannella, F.; and Cucchiara, C., "Simplified Model for Compressive Response of RC Column Footing with Square Cross-Section," *Engineering Structures*, V. 148, 2017, pp. 936-948. doi: 10.1016/j.engstruct.2017.06.054

36. EN 1990:2002, "Eurocode – Basis of Structural Design," European Committee for Standardization, Brussels, Belgium, 2002.

37. Siburg, C., and Hegger, J., "Experimental Investigations on the Punching Behaviour of Reinforced Concrete Footings with Structural Dimensions," *Structural Concrete*, V. 15, No. 3, 2014, pp. 331-339. doi: 10.1002/suco.201300083

JOIN AN ACI Chapter!

The American Concrete Institute has Chapters and Student Chapters located throughout the world. Participation in a local chapter can be extremely rewarding in terms of gaining greater technical knowledge and networking with leaders in the concrete community.

Because chapters are distinct and independent legal entities, membership includes both ACI members and non-ACI members and is made up of a diverse blend of architects, engineers, consultants, contractors, educators, material suppliers, equipment suppliers, owners, and students—basically anyone interested in concrete. Many active ACI members initially became involved in ACI through their local chapter. In addition to technical programs and publications, many chapters sponsor ACI Certification programs, ACI educational seminars, project award recognition programs, and social events with the goal of advancing concrete knowledge.

Check out the Chapters Special Section from the November 2020 *Concrete International*: www.concrete.org/publications/concreteinternational.aspx

---

Student Chapters

Join or form an ACI Student Chapter to maximize your influence, knowledge sharing, and camaraderie! ACI has 240+ student chapters located throughout the world, each providing opportunities for students to:

- Connect with their peers and participate in concrete-related activities such as: student competitions, ACI Conventions, ACI Certification Programs, ACI Educational Seminars, local chapter meetings, social events, and community service projects;
- Network with members of local chapters, many of whom have been in the industry for decades and can help to develop professional relationships and offer career advice;
- Win recognition for their universities through the University Award; and
- Learn about the many scholarships and fellowships offered by the ACI Foundation and by ACI's local chapters.

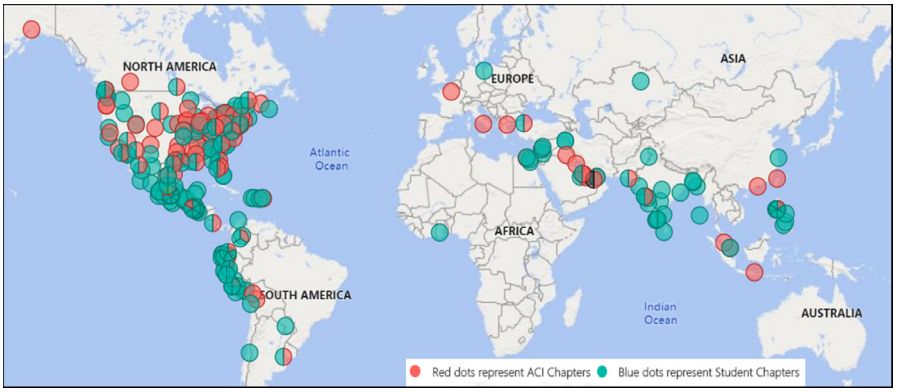

American Concrete Institute

www.concrete.org/chapters

ACI STRUCTURAL JOURNAL TECHNICAL PAPER

Title No. 121-S31

Design Tool for Finding Minimum Heights of Reinforced Concrete Beams and One-Way Slabs

by Marc Sanabra-Loewe, David Garcia, Nikola Tošić, and Albert de la Fuente

Finding the minimum height of reinforced concrete (RC) slabs and beams at the early stages of design is critical for efficient material use. Hence, methods are needed for determining the maximum slenderness, L/h*, that are both easy to use and able to consider as many influencing factors as possible, given that deflection typically controls the design of this kind of structure. One such method is the "long method of Rangan-Scanlon," with recent advances in new closed-form solutions enabling direct calculation. This study builds on those advances, presenting a parametric study for RC beams and one-way slabs to determine the effect of key factors (compressive strength of concrete, reinforcement cover, span, tributary width, load, and boundary conditions) on the effective moment of inertia factor α and slenderness* L/h*. The results provide practical design tools for determining the maximum slenderness of RC one-way slabs by previously finding the α factor and directly determining the maximum slenderness for RC beams.*

Keywords: beam; deflection control; maximum slenderness; one-way solid slab; reinforced concrete (RC); serviceability; stiffness.

INTRODUCTION

Deflection control is an increasingly governing parameter for a wide range of structural reinforced concrete (RC) members, particularly RC beams and one-way slabs.[1] However, deflection calculation, especially in the early stages of design, can be tedious and time-consuming, with available models and the intrinsic scatter of input data still not allowing sufficient precision to justify the effort.[2] Moreover, optimization typically requires an iterative process, making the procedure even more time-consuming. Therefore, indirect deflection control through the establishment of appropriate minimum heights of the elements is currently the most general practice among engineers when designing RC beams and slabs.

The most common form of indirect deflection control in codes is the provision of constant slenderness ratios in the form of L/h and L_n/h. Nonetheless, constant slenderness limits easily lead to either excessively heavy and resource-inefficient solutions or excessively slender and deformable members.[3-8] To overcome this drawback, several authors and codes have been proposing alternatives[3,4,9-12] to integrate different parameters into the proposed slenderness limits to make them variable.

A particularly versatile method for determining slenderness limits was originally proposed by Rangan[13] and subsequently expanded by Scanlon and Choi[14] and Scanlon and Lee,[15] allowing the direct consideration of principal factors such as boundary conditions, span, load, concrete modulus of elasticity, and allowable deflection. The developed method was also adapted to different member types (beams and one- and two-way slabs).

The core of the method is the expression of the effective moment of inertia I_e as a portion of the gross concrete moment of inertia I_g, through multiplication by an effective moment of inertia factor α. When the method was originally proposed, there was no way to easily calculate or estimate α—it was proposed as a constant value,[8,9] even though over time, this was recognized as probably insufficient.[9] The key advantage of the method based on a known value of α is that the minimum height of RC members can be established based exclusively on those parameters that are known at the early stages of design, and in particular, it makes slenderness independent of the reinforcement ratio. Therefore, despite the fact that it has been acknowledged that a constant value of α is not a sufficient solution, it has been proposed that a set of values of α could be found depending on the main parameters governing the deflection control of RC members.[4,5]

Recently, a novel closed-form solution for α was proposed, enabling straightforward and direct calculation of α for RC solid sections and fiber-reinforced concrete (FRC) solid sections.[10] This formulation sets the basis for the systematic study of the value of α depending on the main parameters governing deflection control (span, load, modulus of elasticity of concrete, concrete shrinkage, concrete creep, reinforcement cover, boundary conditions, or deflection limit).

With this in mind, and based on the newly developed formulation, this study presents a parametric study of RC beams and one-way slabs—members for which deflection control is most critical—using the newly proposed formulation for calculating α, and leads to a practical design tool for finding the minimum height of these members in accordance with ACI 318-19.[16] The ultimate goal is to enable easy and fast calculation of minimum height, with flexibility at the early stages of design, while directly considering as many influencing factors as possible. These results may serve as a very precise and expedient tool for engineers already in the early design stages. Because the decisions at these early design stages most influence a structure's economic and environmental impact, the method can lead to more efficient solutions and thus be economically and environmentally advantageous.

ACI Structural Journal, V. 121, No. 3, May 2024.

MS No. S-2022-350.R2, doi: 10.14359/51740458, received August 10, 2023, and reviewed under Institute publication policies.

The paper proceeds as follows: first, an overview of the method (the "long method of Rangan-Scanlon"[8] and the "short method of Rangan-Scanlon"[9]) is presented, and its adaptation to RC beams and one-way slabs is demonstrated (for example, the inclusion of compressive reinforcement and tributary width for RC beams). Then, a parametric study is performed on both types of elements, out of which several design tools (tables, plots, and formulas) are given that lead either to the direct determination of the maximum slenderness (L/h) of the member or to determining the α factor as a step before finding the L/h of the member. Finally, the results and their implications are discussed, and conclusions are drawn.

RESEARCH SIGNIFICANCE

The availability of practical design tools for finding the minimum height of RC beams and one-way slabs is a critical step toward more material-efficient design of concrete structures. The newly developed formulation for calculating the effective moment of inertia factor α within the Rangan-Scanlon method needs to be translated into easy-to-use tools for designers to use in their daily practice. The parametric study performed in this research and the resulting graphs, tables, and formulas for the α factor and the slenderness L/h are comprehensive tools for easy and direct application in practice.

CLOSED-FORM SOLUTION FOR EFFECTIVE MOMENT OF INERTIA FACTOR α

Overview of formulation

Herein, only a brief recapitulation of the Rangan-Scanlon method is given,[13,14] as well as of the novel closed-form solution for the factor α.[17]

The starting point for the Rangan-Scanlon method is the incremental deflection Δ_{inc}, defined by Eq. (1)

$$\Delta_{inc} = \frac{\lambda_\Delta \kappa W_{sus} L^4}{384 E_c I_e} + \frac{\kappa W_{sl} L^4}{384 E_c I_e} \tag{1}$$

The key parameter in the expression is the effective moment of inertia I_e that is calculated as

$$I_e = \begin{cases} I_g & \text{for } M_a \le (2/3)M_{cr} \\ \dfrac{I_{cr}}{1 - \left(\dfrac{(2/3)M_{cr}}{M_a}\right)^2 \left(1 - \dfrac{I_{cr}}{I_g}\right)} & \text{for } M_a > (2/3)M_{cr} \end{cases} \tag{2}$$

For a rectangular cross section, the cracking moment M_{cr} is calculated as

$$M_{cr} = W_g f_r = \frac{bh^2}{6} f_r \tag{3}$$

To obtain an expression in terms of span-depth ratio based on Eq. (1), the following is assumed:

1. Δ_{inc} is equated with the maximum allowable value of the incremental deflection $(\Delta_{inc})_{allow}$;
2. I_g is taken as $bh^3/12$, assuming a rectangular solid cross section; and
3. I_e is taken as αI_g.

Then

$$(\Delta_{inc})_{allow} = \frac{12\lambda_\Delta \kappa W_{sus} L^4}{384 E_c \alpha b h^3} + \frac{12 W_{sl} L^4}{384 E_c \alpha b h^3} = \frac{\kappa}{32} \frac{(\lambda_\Delta W_{sus} + W_{sl})L}{\alpha E_c b} \left(\frac{L}{h}\right)^3 \tag{4}$$

$$\frac{L}{h} = \left[\left(\frac{\Delta_{inc}}{L}\right)_{allow} \frac{32 \alpha E_c b}{\kappa(\lambda_\Delta W_{sus} + W_{sl})} \right]^{\frac{1}{3}} \tag{5}$$

The general or "long method of Rangan-Scanlon" consists of the following steps[9]: 1) initial choice of h to account for self-weight (for example, from current code-recommended L/h ratios); 2) calculation of the required steel area for strength requirements; 3) calculation of I_e to determine α; 4) use of the computed α in Eq. (5) to find h; and 5) check for convergence between the obtained and assumed h and iteration until convergence.

As can be seen, the method is unsuitable for establishing element depths at early design stages as it requires knowing the reinforcement ratio.[4] To overcome this drawback, several researchers proposed the "short method of Rangan-Scanlon," which adopts a preestablished value of α. Scanlon and Choi[14] were the first to suggest a preestablished value of α, taking a constant value of 0.4. However, later, Scanlon and Lee[15] suggested a constant value of 0.52. Even though taking a constant value for α in the "short method of Rangan-Scanlon" already provides better results than other existing methods included in current codes,[4] the accuracy and applicability of this criteria to all cases of RC members (beams and one- and two-way slabs) is questionable.[4,9]

With this in mind, Tošić et al.[17] developed a novel closed-form solution to find α, enabling a fast and easy use of the "long method of Rangan-Scanlon," thereby making feasible parametric studies that may lead to finding a set of values of α to be ultimately used in the "short method of Rangan-Scanlon."

The starting point for the closed-form solution for α was Eq. (2), which can be rewritten in terms of $\mu = M_{cr}/M_a$ and $\delta = I_{cr}/I_g$

$$\frac{I_e}{I_g} = \alpha = \begin{cases} 1 & \text{for } \mu \ge 1.5 \\ \dfrac{\delta}{1 - \left(\dfrac{2}{3}\mu\right)^2 (1 - \delta)} & \text{for } \mu < 1.5 \end{cases} \tag{6}$$

First, the cracking moment can be determined as

$$M_{cr} = \frac{bh^2}{6} f_r = \frac{bh^2}{6}\left(0.62\sqrt{f_c'}\right) = \frac{0.62}{6} bh^2 \sqrt{f_c'} \text{ (N·mm)} \tag{7}$$

It should be noted that Eq. (7) is valid only for SI units; for U.S. customary units, 0.62 should be replaced by 7.5. Considering an assumed value of ρ, the applied moment $M_a = \eta M_n$ can be determined as

$$M_a = \eta M_n = \eta\left(\frac{d}{h}\right)^2 bh^2\rho f_y\left(1-\frac{\rho f_y}{1.7f_c'}\right) \text{ (N·mm)} \quad (8)$$

Then, for SI units, μ is obtained as

$$\mu = \frac{M_{cr}}{M_a} = \frac{0.62\sqrt{f_c'}}{6\eta\left(\frac{d}{h}\right)^2\rho f_y\left(1-\frac{\rho f_y}{1.7f_c'}\right)} \quad (9)$$

whereas, for U.S. customary units, 0.62 should be replaced by 7.5. As for $\delta = I_{cr}/I_g$, it is calculated from $I_g = bh^3/12$.

For an RC cross section under bending moments (without an axial force), the position of the neutral axis is independent of the applied load (hence, of M) and can be expressed through the neutral axis coefficient $\xi = c/d$, where c is the depth of the compressed zone

$$I_{cr} = \frac{bh^3}{12}\left[12\left(\frac{d}{h}\right)^3 n\rho(1-\xi)\left(1-\frac{\xi}{3}\right)\right] \text{ (mm}^4\text{)} \quad (10)$$

Then, δ can be obtained as

$$\delta = \frac{I_{cr}}{I_g} = 12\left(\frac{d}{h}\right)^3 n\rho(1-\xi)\left(1-\frac{\xi}{3}\right) \quad (11)$$

For RC sections under bending with only tensile reinforcement and under service load, the neutral axis coefficient ξ can be directly calculated as

$$\xi = -n\rho + \sqrt{(n\rho)^2 + 2n\rho} = n\rho\left(-1+\sqrt{1+\frac{2}{n\rho}}\right) \quad (12)$$

Therefore, using Eq. (9), (11), and (12), α can be calculated as a function of the specified concrete strength (from which E_c is determined), steel grade (from which f_y and E_s are determined), and an assumed (or calculated) reinforcement ratio ρ.

Adaptation of solution to RC beams and one-way slabs

As stated earlier, the objective of this paper is to provide design tools in the form of a set of graphs and tables based on a parametric study using the "long method of Rangan-Scanlon" and the closed-form solution for α to enable designers to directly determine α for their subsequent use in the "short method of Rangan-Scanlon" for different cases of RC rectangular beams and one-way solid slabs.

For this purpose, several adjustments of the closed-form solution for α are necessary as the original formulation by Tošić et al.[17] only considered the presence of tensile reinforcement in the cross section—that is, $\rho' = 0$. Therefore, the concept of compressive reinforcement necessary for strength requirements needs to be introduced. Furthermore, in the original formulation, one sole value of ρ (tensile reinforcement) was defined. But for low-reinforced cross sections, the required tensile reinforcement (ρ*) may be less than the minimum (ρ_{min}) reinforcement that must be provided to avoid brittle failure under tensile stress. That is why, in the following section, a new version of the formulation that differentiates between required tensile reinforcement (ρ*) and provided tensile reinforcement (ρ_{prov}) is developed, ensuring that the provided reinforcement is never below the minimum amount of reinforcement necessary for avoiding brittle failure

$$\rho_{min} = \max\left(\frac{3\sqrt{f_c'}}{f_y}, \frac{200}{f_y}\right) \text{for U.S. customary units}$$

$$\rho_{min} = \max\left(\frac{0.25\sqrt{f_c'}}{f_y}, \frac{1.38}{f_y}\right) \text{ for SI units} \quad (13)$$

with the provided tensile reinforcement defined as

$$\rho_{prov} = \max(\rho^*, \rho_{min}) \quad (14)$$

It is assumed that if the initial calculation of reinforcement (only tensile) turns a neutral axis depth > 0.45d ($c/d > 0.45$), compressive reinforcement is provided. In case of a section that requires compressive reinforcement, the moment capacity of a section can be decomposed by fixing the neutral axis position at 0.45d. In other words, the bending moment M_n consists of a component $M_{0.45d}$, which corresponds to a section with only tension reinforcement, and a component ΔM, which corresponds to the moment resistance of the needed compressive reinforcement and an equal amount of added tensile reinforcement needed for equilibrium. The position of the compressive reinforcement can be expressed through the d'/h ratio.

To determine the quantity of compressive reinforcement needed, the following procedure is to be followed. First, $M_{0.45d}$ is calculated as

$$M_{0.45d} = C_c(d-0.5c) = 0.85f_c'\beta_1 cb(d-0.5c) \quad (15)$$

where $c = 0.45d$; and β_1 varies linearly between 0.85 and 0.65 for f_c' between 4000 and 8000 psi (27.58 and 55.16 MPa), respectively, according to ACI 318-19.[16] Hence

$$M_{0.45d} = 0.85f_c'\beta_1 0.45db(d-0.5\cdot 0.45d) = 0.2964\left(\frac{d}{h}\right)^2 f_c'\beta_1 bh^2 \quad (16)$$

Then, $\Delta M = M_n - M_{0.45d}$

$$\Delta M = A_s'f_y(d-d') = A_s'f_y h\left(\frac{d}{h}-\frac{d'}{h}\right) = \left(\frac{d}{h}\right)\rho' f_y bh^2\left(\frac{d}{h}-\frac{d'}{h}\right) \quad (17)$$

From these, the compressive reinforcement can be directly determined as

$$\rho' = \frac{M_n - 0.2964\left(\frac{d}{h}\right)^2 f_c'\beta_1 bh^2}{f_y bh^2\left(\frac{d}{h}-\frac{d'}{h}\right)} \quad (18)$$

Then, with respect to the original formulation proposed by Tošić et al.,[17] changes are needed in Eq. (8) to (12).

First, Eq. (8) becomes

$$M_a = \eta M_n = \eta b h^2 \left(\frac{d}{h}\right) f_y \left\{ \left(\frac{d}{h}\right) \rho^* \left(1 - \frac{\rho^* f_y}{1.7 f_c'}\right) + \rho' \left(\frac{d}{h} - \frac{d'}{h}\right) \right\} \quad (19)$$

Herein, ρ* refers to only the originally needed tensile reinforcement A_s (for $M_{0.45d}$)—that is, $\rho^* = A_s/(bd)$ and $\rho' = A_s'/(bd)$. As ρ* may easily be found, because $\rho = (0.85 f_c' \beta_1 c)/(f_y d)$ and $c = 0.45d$, then

$$\rho^* = \frac{0.85 \cdot 0.45 f_c' \beta_1}{f_y} = 0.3825 \frac{f_c' \beta_1}{f_y} \quad (20)$$

Then, Eq. (19) becomes

$$M_a = \eta M_n = \eta b h^2 \left(\frac{d}{h}\right) f_y \left\{ \left(\frac{d}{h}\right) 0.3825 \frac{f_c'}{f_y} [\beta_1 - 0.225(\beta_1)^2] + \rho' \left(\frac{d}{h} - \frac{d'}{h}\right) \right\} \quad (21)$$

Equation (9) can be expressed as

$$\mu = \frac{M_{cr}}{M_a} = \frac{0.625\sqrt{f_c'}}{6\eta \left(\frac{d}{h}\right) f_y \left\{ \left(\frac{d}{h}\right) \rho^* \left(1 - \frac{\rho^* f_y}{1.7 f_c'}\right) + \rho' \left(\frac{d}{h} - \frac{d'}{h}\right) \right\}} \quad (22)$$

for SI units; whereas, for U.S. customary units, 0.625 should be replaced by 7.5. Considering ρ* in Eq. (20)

$$\mu = \frac{0.625\sqrt{f_c'}}{6\eta \left(\frac{d}{h}\right) f_y \left\{ \begin{array}{l} \left(\frac{d}{h}\right) 0.3825 \frac{f_c'}{f_y} [\beta_1 - 0.225(\beta_1)^2] \\ + \rho' \left(\frac{d}{h} - \frac{d'}{h}\right) \end{array} \right\}} \quad (23)$$

for SI units; whereas, for U.S. customary units, 0.625 should be replaced by 7.5.

Equation (10) becomes

$$I_{cr} = \frac{b h^3}{12} \left(\frac{d}{h}\right) \left\{ \begin{array}{l} 5.61 \left(\frac{d}{h}\right)^2 n\rho^* + \\ 12\rho' \left[\begin{array}{l} 0.3025 \left(\frac{d}{h}\right)^2 + \\ \left(0.45 \frac{d}{h} - \frac{d'}{h}\right)^2 \end{array} \right] \end{array} \right\} \quad (24)$$

Considering ρ* in Eq. (20)

$$I_{cr} = b h^3 \left(\frac{d}{h}\right)^3 n\rho^* (1 - \xi) \left(1 - \frac{\xi}{3}\right) + \rho' b h \left(\frac{d}{h}\right) (d - c)^2 + \rho' b h \left(\frac{d}{h}\right) (c - d')^2 \quad (25)$$

Finally, Eq. (11) can be expressed as

$$\delta = \frac{I_{cr}}{I_g} = \left(\frac{d}{h}\right) \left\{ \begin{array}{l} 5.61 \left(\frac{d}{h}\right)^2 n\rho^* + \\ 12\rho' \left[0.3025 \left(\frac{d}{h}\right)^2 + \left(0.45 \frac{d}{h} - \frac{d'}{h}\right)^2 \right] \end{array} \right\} \quad (26)$$

and considering ρ* in Eq. (20)

$$\delta = \left(\frac{d}{h}\right) \left\{ \begin{array}{l} 2.97 \cdot 0.85^2 \left(\frac{d}{h}\right)^2 \frac{n f_c' \beta_1}{f_y} + \\ 12\rho' \left[0.3025 \left(\frac{d}{h}\right)^2 + \left(0.45 \frac{d}{h} - \frac{d'}{h}\right)^2 \right] \end{array} \right\} \quad (27)$$

Additionally, Eq. (12) becomes

$$\xi = n\rho_{prov} \left(1 + \frac{\rho'}{\rho_{prov}}\right) \left[-1 + \sqrt{\frac{2\left(1 + \frac{\rho'}{\rho_{prov}} \frac{d'}{h}\right)}{n\rho_{prov} \left(1 + \frac{\rho'}{\rho_{prov}}\right)^2}} \right] \quad (28)$$

Thereby, Eq. (23), (27), and (28) provide a way of considering cases where compressive reinforcement is necessary for strength requirements within the same framework for determining α.

Finally, for RC solid beams, the factor k_B (unitary tributary width) is used to multiply b (breadth) in each one of the closed-form equations described previously. This factor was first proposed by Sanabra and Scanlon[9] and is defined as $k_B = L_{trib}/b$, where L_{trib} is the tributary with of the beam. Extremely narrow beams have a $k_B = 30$, and very wide beams have a $k_B = 8$.

PARAMETRIC STUDY TO FIND VALUES OF EFFECTIVE MOMENT OF INERTIA FACTOR α AND SLENDERNESS *L/H* FOR RC ONE-WAY SOLID SLABS

First, RC one-way solid slabs were analyzed. The study was conceived with the following parameters and values:

- Rectangular cross section b/h;
- Reinforcing steel with a specified yield strength f_y of 60 ksi (413.7 MPa);
- Three specified concrete strengths f_c' of 3000, 4000, and 5000 psi (20.7, 27.6, and 34.5 MPa);
- Relative cover for tensile reinforcement d/h of 0.75, 0.85, and 0.95, and for compressive reinforcement d'/h of 0.1;
- Spans L of 15, 25, and 35 ft (4.6, 7.6, and 10.7 m);
- Superimposed surface loads Q of 80, 120, and 160 lb/ft^2 (3.8, 5.8, and 7.7 kN/m^2);

- Three boundary conditions—fixed-fixed (both ends continuous), fixed-pinned (one end continuous), and pinned-pinned (simply supported); and
- Two incremental deflection limits for floors or roofs: one for floors or roofs supporting or attached to nonstructural elements that are likely to be damaged by large deflections (deflection limit of $L/480$, a case called "damageable"); and one for floors or roofs not likely to be damaged by large deflections (deflection limit of $L/240$, a case called "non-damageable").

In total, there were six parameters, leading to $3 \times 3 \times 3 \times 3 \times 3 \times 2 = 486$ individual cases. For each case, α was calculated using the following procedure:

1. An initial height h_0 was assumed based on existing L/h in ACI 318-19[16];
2. From the superimposed surface load and self-weight (determined based on h_0), the nominal moment(s) is (are) determined, and reinforcement(s) ρ^* necessary for strength requirements is (are) calculated;
3. If during the calculation of ρ^* it is detected that $c > 0.45d$, then the procedure for determining the compressive reinforcement, outlined in the previous section, is followed (however, no cases required it);
4. The required reinforcement ρ^* is checked against the minimum reinforcement (ρ_{min}) given by Eq. (13);
5. The values of ξ, μ, and δ are calculated based on Eq. (12), (9), and (11) for cross sections without compressive reinforcement and Eq. (28), (23), and (27) for cross sections with compressive reinforcement and considering $M_a = 0.67M_n$, that is, $\eta = 0.67$.
6. The effective moment of inertia factor α is calculated according to Eq. (6) for all representative cross sections of the member (midspan cross section and both support cross sections, depending on the boundary conditions). The overall factor α of the entire member is then calculated by averaging the factors for representative sections considering the bending moment law—that is, the portions of length of hogging and sagging moments, which are 0 and 1 for simply supported elements, 0.25 and 0.75 for one end continuous boundary conditions, and 0.42 and 0.58 for both ends continuous boundary conditions.
7. The height h is found using Eq. (5) considering the span (L), effective moment of inertia factor α, allowable deflection $(\Delta/L)_{allow}$, boundary conditions (expressed through the factor κ, which is 5.0, 2.0, and 1.4 for simply supported elements and elements with one or both ends continuous, respectively), modulus of elasticity of concrete (E_c), and long-term deflection multiplier ($\lambda_\Delta = \xi/(1 + 50\rho')$), with $\xi = 2$ for a nominal time-dependent factor for a 5-year duration of loading.[16]
8. The value of h is checked against the initially assumed value, and the process is repeated until convergence.

The first step after completing the parametric study was the analysis and the determination of the influence of individual parameters. For this purpose, in each case, five of the six parameters were fixed, and one was considered with its extreme values—for example, both ends continuous boundary condition, non-damageable nonstructural elements, $Q = 80$ lb/ft^2 (3.8 kN/m^2), $f_c' = 3000$ psi (20.7 MPa), and $d/h = 0.85$. Then, spans L of 15 and 35 ft (4.6 and 10.7 m) are considered, and the obtained L/h limits and α factors are compared for the two cases.

In this particular case, the L/h value for $L = 15$ ft (4.6 m) is obtained as 38.3, and for $L = 35$ ft (10.7 m) as 30.3. This is observed as a $|38.3/30.3 - 1| = 26.4\%$ difference, which is significant. If the value of α for the two cases is considered, it results in 0.338 and 0.308, respectively. In this case, the difference should be analyzed in terms of $\alpha^{1/3}$ because this is how α influences L/h in Eq. (5). Therefore, the difference is $|(0.338/0.308)^{1/3} - 1| = 3.1\%$, much smaller than when considering L/h.

This process was then repeated for each of the individual parameters. Because six parameters were considered in total, to obtain an easy-to-use graphical tool, it was critical to identify which parameters do not significantly affect the value of L/h or α. Once the less-influential parameters were identified, the values of L/h or α depending on those parameters were averaged in a sole value of L/h or α, respectively.

For that reason, it was considered that when the difference between the two extreme values in a set of values of L/h (or $\alpha^{1/3}$) after a certain parameter is smaller than 5%, such a parameter is considered to be of negligible influence. This criterion was taken based on the following reasoning. When a certain parameter is considered negligible, given a certain set of results (L/h or $\alpha^{1/3}$), it is acceptable to take the average value of that set of results. By doing so, it is assumed that the average value of that set of data is approximately the average between the two extreme values of that set, so that the mentioned average would have up to a 2.5% error with respect to each of the extreme values. A 2.5% error on a slab with a depth of 19.7 in. (500 mm) amounts to an error of 0.5 in. (12.5 mm). Such errors can be considered acceptable errors at an early stage of design.

After studying the sensitivity of L/h and $\alpha^{1/3}$ to each of the parameters, it was consistently found that, in the case of slabs, $\alpha^{1/3}$ was far less sensitive to variations in most of the parameters—that is, it is a more robust variable.

Hence, the practical design tools provided in the following sections have been designed to find values of α rather than values of L/h because α could be expressed in terms of a smaller number of parameters (to which it is sensitive). Therefore, to find the slenderness (L/h) of a certain slab, it may be done by using Eq. (5), with the corresponding value of α provided in the design tools; this is using the "short method of Rangan-Scanlon."

After identifying the parameters to which $\alpha^{1/3}$ is sensitive, it was found that the influence of the studied parameters varies significantly depending on whether slabs are attached to "damageable" or to "non-damageable" nonstructural elements.

Slabs attached to "non-damageable" nonstructural elements

For RC one-way solid slabs attached to "non-damageable" nonstructural elements, the parameters significantly affecting $\alpha^{1/3}$ were found to be d/h, load (Q), and boundary conditions. Span (L) and specified concrete compressive strength (f_c') did not show significant influence.

Table 1—α factor values depending on several factors for RC one-way solid slabs attached to non-damageable nonstructural elements, and maximum deviation of α for factors studied but not included in table

α			Deflection control	Maximum deviation from average	
			Attached to non-damageable elements		
Boundary conditions	d/h	Q, lb/ft^2	—	–	+
Both ends continuous (2C)	0.75	80	0.343*	–1.77%	1.63%
		120	0.332*	–1.09%	0.69%
		160	0.330*	–0.82%	1.12%
	0.85	80	0.325*	–1.84%	2.34%
		120	0.309*	–1.58%	1.24%
		160	0.299*	–1.42%	1.02%
	0.95	80	0.314*	–2.28%	*2.75%*
		120	0.296*	–1.60%	1.68%
		160	0.285*	–1.47%	0.97%
One end continuous (1C)	0.75	80	0.314	–1.24%	*2.55%*
		120	0.325	–2.33%	*3.31%*
		160	0.338	*–2.94%*	*3.92%*
Simply supported (SS)	0.75	80	0.293	–0.68%	1.16%
		120	0.295	–0.89%	1.92%
		160	0.299	–1.54%	*2.51%*
One end continuous and simply supported (1C and SS)	0.85	80	0.269*	*–3.63%*	2.12%
		120	0.260*	*–3.44%*	2.14%
		160	0.256*	*–2.90%*	2.13%
	0.95	80	0.264*	*–3.01%*	*2.66%*
		120	0.255*	*–2.80%*	2.23%
		160	0.248*	*–2.63%*	2.04%

*Minimum positive reinforcement required.

Note: Values above 2.5% are given in italics; 1 lb/ft^2 = 0.0479 kN/m^2.

This is demonstrated in Table 1, where the α factor values are shown for each set of influential parameters but averaged for the non-influential parameters. In other words, for a given set of d/h, Q, and boundary conditions, α was averaged for the different studied spans and compressive strengths. This average was done taking only the extreme values of α after each one of these two non-influential parameters—that is, each value of α in Table 1 is an average of four values, corresponding to the combination of the two extreme spans (15 and 35 ft [4.6 and 10.7 m]) and the two extreme compressive strengths (3000 and 5000 psi [20.7 and 34.5 MPa]). The table also shows the deviation of extreme values of α for the non-influential values with respect to the average value of α. As can be seen, the largest deviation is 3.92%, and the majority of deviations are below 2.5% (values above 2.5% are given in italics). It can also be seen that for the majority of cases (except for one end continuous and simply supported slabs with $d/h = 0.75$), the minimum amount of positive reinforcement was required to prevent brittle failure. Additionally, for d/h equal to 0.85 and 0.95, the values of α were practically identical between one end continuous and simply supported boundary conditions, so the values were averaged among eight cases.

The results in Table 1 are also graphically represented in Fig. 1, which allows rapid determination of the value of α based on the influential parameters (d/h, load [Q], and boundary conditions), keeping in mind that L and f_c' can take on any value.

Finally, it is interesting to point out that the whole set of values of α used to compute the average α values shown in Table 1 range from 0.229 to 0.360, with a global average of 0.298. In other words, the precision provided by design tools could eventually be omitted by adopting $\alpha = 0.3$ for RC one-way solid slabs attached to "non-damageable" nonstructural elements. This simplification would lead to values of L/h with a maximum deviation of 8.6% with respect to the correct value. However, the value of $\alpha = 0.3$ may be useful as a first approximation when using Eq. (5) to find the maximum slenderness for slabs with parameters different from those in the current study, such as cases with different allowable deflections or following other code provisions.

Slabs attached to "damageable" nonstructural elements

As for RC one-way slabs attached to "damageable" nonstructural elements, the parameters significantly influencing $\alpha^{1/3}$ were found to be the span (*L*), load (*Q*), and boundary conditions. But it should be noted that boundary conditions have been found to be only partially influential, as results for one end continuous and simply supported cases were practically equal, so only a distinction is made between these two boundary conditions and the both ends continuous boundary condition. In this case, the parameters not significantly influencing $\alpha^{1/3}$ were *d*/*h* and specified concrete compressive strength (f_c').

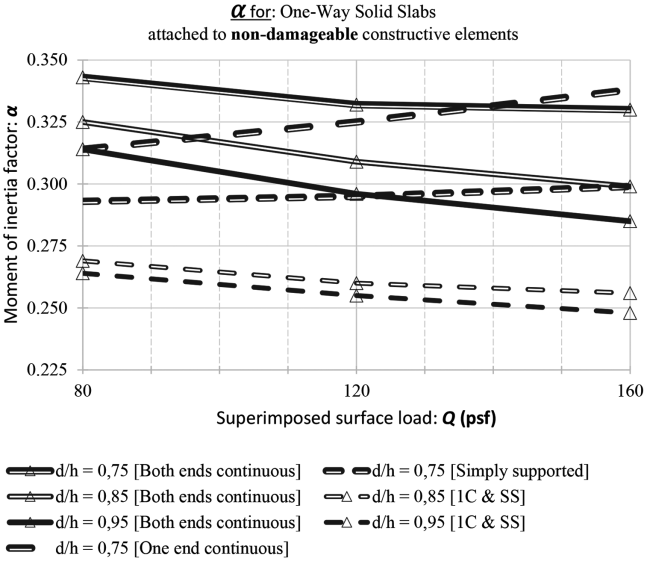

Fig. 1—RC one-way slabs attached to non-damageable nonstructural elements: dependence of factor α on boundary conditions, d/h*, and load* Q*. (Note: Δ indicates cases that require minimum positive reinforcement.)*

The results for RC one-way slabs attached to "damageable" nonstructural elements are shown in Table 2, where each α factor is an average of six or 12 values (averaged by *d*/*h* and f_c' for one or two boundary conditions). The results show that for all cases, the deviation from the average value of α does not exceed 2.04%. Additionally, it can be seen that the majority of cases need both minimum negative and positive moment reinforcements, and only three cases need only positive reinforcement.

Considering the significant parameters in this case, the results in Table 2 are also represented on a graphical design tool (Fig. 2) where only two sets of lines are included: those for the both ends continuous boundary condition and those that jointly represent the one end continuous and simply supported boundary conditions.

Finally, the global range of values of α used to compute the values of α included in Table 1 ranges from 0.293 to 0.563, with an average of 0.389. In this case, for RC one-way solid slabs attached to "damageable" nonstructural elements, a first approximation of α = 0.4 may be considered when high precision is not required, as such an approximation may lead to an error of up to 12.1% with respect to the correct value.

Table 2—α factor values depending on several factors for RC one-way solid slabs attached to damageable nonstructural elements, and maximum deviation of α for factors studied but not included in table

α		Deflection control		
		Attached to damageable elements		
		L, ft		
Boundary conditions	*Q*, lb/ft²	15	25	35
Both ends continuous (2C)	80	0.531†	0.475†	0.431†
	120	0.473†	0.434†	0.403†
	160	0.436†	0.407†	0.383†
One end continuous and simply supported (1C and SS)	80	0.394†	0.351†	0.321*
	120	0.364†	0.333†	0.309*
	160	0.343†	0.319†	0.301*

Maximum deviation from average

L = 15 ft		*L* = 25 ft		*L* = 35 ft	
–	+	–	+	–	+
–2.03%	1.99%	–2.09%	2.04%	–2.12%	2.02%
–1.83%	1.78%	–1.85%	1.87%	–1.96%	1.83%
–1.69%	1.67%	–1.74%	1.73%	–1.85%	1.71%
–1.69%	1.54%	–1.19%	1.14%	–0.88%	1.33%
–1.65%	1.31%	–1.23%	0.77%	–0.85%	1.12%
–1.50%	1.20%	–1.13%	0.67%	–0.91%	1.20%

*Minimum positive reinforcement required.

†Minimum positive and negative reinforcement required.

Note: 1 ft = 0.3 m; 1 lb/ft² = 0.0479 kN/m².

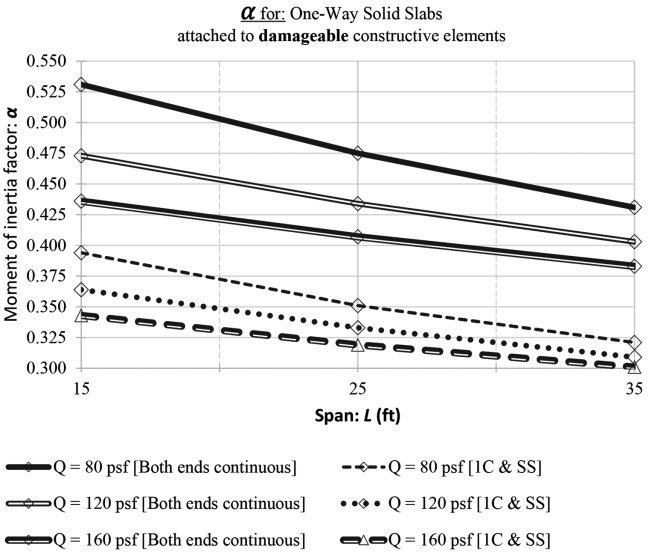

Fig. 2—RC one-way slabs attached to damageable nonstructural elements: dependence of factor α on boundary conditions, span L*, and load* Q*. (Note: Δ indicates cases that require minimum positive reinforcement; ◊ indicates cases that require minimum positive and negative reinforcement.)*

Hence, this lack of precision may only be interesting as a first approximation when dealing with cases different from those included in this study, such as calculations according to other codes.

An example of RC one-way solid slab slenderness calculation is provided in Appendix A.*

PARAMETRIC STUDY TO FIND VALUES OF EFFECTIVE MOMENT OF INERTIA FACTOR α AND SLENDERNESS *L/H* FOR RC RECTANGULAR BEAMS

In the case of RC beams, the study was conceived with the following differences relative to the case of RC one-way solid slabs:

- Relative cover for tensile reinforcement d/h of 0.85 and 0.95, and for compressive reinforcement d'/h of 0.1; and
- Unitary tributary widths k_B of 8, 16, and 24.

In total, there were seven parameters considered, leading to 3 × 2 × 3 × 3 × 3 × 3 × 2 = 972 individual cases. In particular, compared with RC one-way solid slabs, for RC beams, $d/h = 0.75$ was not considered (as it was deemed very uncommon for beams), and the unitary tributary width k_B was introduced. For each case, α was calculated using the same procedure as RC one-way solid slabs.

Once more, the first step after completing the parametric study was the analysis and the determination of the influence of individual parameters. For this purpose, the same approach as for RC one-way solid slabs was followed.

After studying the sensitivity of L/h and $\alpha^{1/3}$ to each parameter, the following was found.

In the first place, for beams, it is obvious that the sensitivity of L/h and $\alpha^{1/3}$ to most of the parameters is inversed. This means that as the deviation of $\alpha^{1/3}$ from the average grows for a certain set of data, the deviation of L/h from the average diminishes for the same set of data. This can be seen by comparing the data in Tables 5 and 6.

Table 3 shows the values of the α factor for the identified significant parameters: d/h, Q, k_B, and boundary conditions, with the values of α for non-influential parameters (that is, L and f_c') averaged over the provided values. Looking at the results in Table 3, it can be seen that they are not acceptable for RC beams attached to "non-damageable" nonstructural elements as the majority of deviations of α from the average are above 2.5%, and some are even above 5% (in boldface in Table 3). Therefore, an analysis was performed on the sensitivity of the slenderness L/h to the same parameters. The results are shown in Table 4, showing a situation inverse to that in Table 3: the deviation of extreme values of L/h from the average is higher for RC beams attached to "damageable" nonstructural elements than the deviation of extreme values of α from the average. It can also be seen how, in Table 3, the deviation of extreme values of α from the average grows from left to right, whereas in Table 4, the deviation of extreme values of L/h from the average decreases from left to right. This is more pronounced the narrower the beam, that is, the higher the k_B, and it becomes more appropriate to directly find the slenderness L/h instead of searching for it using α and the Rangan-Scanlon method.

As a result, a crucial difference between RC beams attached to "non-damageable" nonstructural elements and RC slabs becomes obvious. Whereas, for RC slabs, $\alpha^{1/3}$ is the factor showing the smallest deviation from averages, for RC beams attached to "non-damageable" nonstructural elements, it is clear that L/h shows much less deviation from averages than $\alpha^{1/3}$. However, RC beams attached to "non-damageable" nonstructural elements are in a transition zone between slabs and beams attached to "damageable" elements. So, for these kinds of beams, both $\alpha^{1/3}$ and L/h show acceptable deviations from averages (<5%); thus, any of the two factors may be used to find L/h. Given that, it is more effective to directly find L/h and omit searching using α.

There is an additional reason to avoid using the method of Rangan-Scanlon for beams: these often have significant amounts of compressive reinforcement (particularly those supporting "non-damageable" elements), which leads to a reduced value of the long-term deflection multiplier (λ_Δ). This reduced value of the long-term deflection multiplier is already included in the parametric study to find both L/h and α, but knowing its value would be required to find L/h through Eq. (5), whereas it is not required when searching for L/h directly. Thus, design tools are provided here to directly find L/h for all the studied beams, depending on whether they are attached to "damageable" or "non-damageable" elements. This set of design tools may be referred to as the "variable L/h method," as opposed to the "constant L/h method" currently available in the codes.

To find L/h, up to three design tools are provided. For maximum precision, the L/h values given in Table 4 may be used, and linear interpolation may be done between the

*The Appendix is available at **www.concrete.org/publications** in PDF format, appended to the online version of the published paper. It is also available in hard copy from ACI headquarters for a fee equal to the cost of reproduction plus handling at the time of the request.

Table 3—α factor values depending on several factors for RC beams, and maximum deviation of α for factors studied but not included in table

α			Deflection control			Deflection control		
			Attached to damageable elements			Attached to non-damageable elements		
			k_B			k_B		
Boundary conditions	d/h	Q, lb/ft^2	8	16	24	8	16	24
Both ends continuous (2C)	0.85	80	0.309*	0.287*	0.284*	0.305	0.401†	0.459†
		120	0.294*	0.284*	0.307	0.352	0.459†	0.535†
		160	0.287*	0.296	0.341	0.401†	0.510†	0.595†
	0.95	80	0.296*	0.269*	0.261*	0.260*	0.277	0.331
		120	0.278*	0.261*	0.260*	0.264*	0.331	0.407†
		160	0.269*	0.260*	0.263*	0.277	0.385	0.451†
One end continuous (1C)	0.85	80	0.266*	0.270	0.302	0.353	0.465†	0.559†
		120	0.260*	0.302	0.355	0.416†	0.559†	0.629‡
		160	0.270	0.337	0.404†	0.465†	0.613‡	0.674‡
	0.95	80	0.256*	0.242*	0.238*	0.251	0.330	0.403†
		120	0.247*	0.238*	0.250	0.290	0.403†	0.480†
		160	0.242*	0.241	0.279	0.330	0.455†	0.555†
Simply supported (SS)	0.85	80	0.262*	0.241*	0.249	0.276	0.350	0.425
		120	0.247*	0.249	0.272	0.313	0.425	0.533§
		160	0.241*	0.264	0.299	0.350	0.501	0.576§
	0.95	80	0.262*	0.238*	0.227*	0.217*	0.247	0.289
		120	0.247*	0.227*	0.217*	0.227	0.289	0.351
		160	0.238*	0.220*	0.219	0.247	0.330	0.411
—		Maximum deviation from average						
		—	–0.80%	–1.16%	–1.54%	*–2.64%*	*–4.42%*	*–2.81%*
		—	–1.01%	–1.54%	–2.40%	*–3.70%*	*–2.81%*	–0.72%
		—	–1.16%	–2.05%	*–3.13%*	*–4.42%*	–1.33%	–0.72%
		—	–0.64%	–1.00%	–1.27%	–1.71%	*–2.95%*	*–3.88%*
		—	–0.81%	–1.27%	–1.70%	–2.13%	*–3.88%*	*–4.44%*
		—	–1.00%	–1.62%	–2.05%	*–2.95%*	*–4.53%*	*–2.88%*
		—	–1.49%	–1.80%	*–2.76%*	*–4.17%*	*–3.48%*	–2.49%
		—	–1.34%	*–2.76%*	*–3.69%*	*–4.25%*	–2.49%	–0.45%
		—	–1.80%	*–3.41%*	*–3.97%*	*–3.48%*	–1.07%	–1.69%
		—	–1.38%	–1.65%	–1.82%	*–2.99%*	*–4.14%*	*–4.43%*
		—	–1.57%	–1.82%	–2.44%	*–3.67%*	*–4.43%*	*–3.11%*
		—	–1.65%	–2.23%	*–3.02%*	*–4.14%*	*–3.48%*	–2.46%
		—	–1.66%	–0.97%	–1.43%	*–2.86%*	*–4.04%*	*–4.75%*
		—	–1.60%	–1.43%	–2.21%	*–3.63%*	*–4.75%*	**–5.55%**
		—	–0.97%	–2.01%	*–2.83%*	*–4.04%*	**–5.51%**	*–3.05%*
		—	–1.65%	–1.63%	–1.75%	–1.84%	*–3.01%*	*–3.65%*
		—	–1.58%	–1.75%	–1.78%	*–2.52%*	*–3.65%*	*–4.21%*
		—	–1.63%	–1.28%	–1.84%	*–3.01%*	*–3.99%*	*–4.65%*

*Minimum positive reinforcement required.

†Compressive reinforcement is required for negative moments.

‡Compressive reinforcement is required for positive and negative moments.

§Compressive reinforcement is required for positive moments.

Note: 1 lb/ft^2 = 0.0479 kN/m^2.

Table 4—Slenderness *L/h* values depending on several factors for RC beams, and maximum deviation of *L/h* for factors studied but not included in table

L/h			Deflection control			Deflection control		
			Attached to damageable elements			Attached to non-damageable elements		
			k_B			k_B		
Boundary conditions	*d/h*	*Q*, lb/ft²	8	16	24	8	16	24
Both ends continuous (2C)	0.85	80	16.9*	13.5*	12.0*	21.6	19.4†	18.0†
		120	14.8*	12.0*	10.8	20.2	18.0†	16.8†
		160	13.5*	11.1	10.3	19.4†	17.1†	16.0†
	0.95	80	16.6*	13.2*	11.6*	20.3*	17.0	16.0
		120	14.5*	11.6*	10.2*	18.2*	16.0	15.2†
		160	13.2*	10.6*	9.4*	17.0	15.4	14.4†
One end continuous (1C)	0.85	80	14.0*	11.6	10.8	20.0	18.1†	17.1†
		120	12.5*	10.8	10.1	18.9†	17.1†	15.9‡
		160	11.6	10.3	9.64†	18.1†	16.3‡	15.0‡
	0.95	80	13.8*	11.2*	9.90*	17.6	16.0	15.2†
		120	12.2*	9.90*	8.93	16.6	15.2†	14.3†
		160	11.2*	9.14	8.49	16.0	14.5†	13.7†
Simply supported (SS)	0.85	80	9.87*	8.02*	7.26	13.0	11.8	11.2
		120	8.73*	7.26	6.67	12.3	11.2	10.7§
		160	8.02*	6.83	6.32	11.8	10.9	10.2§
	0.95	80	9.87*	7.99*	7.02*	11.9*	10.4	9.79
		120	8.73*	7.02*	6.16*	10.9	9.79	9.28
		160	7.99*	6.40*	5.67	10.4	9.42	8.97
—		Maximum deviation from average						
		—	*–3.11%*	–2.05%	–1.80%	–1.61%	–0.64%	–0.92%
		—	–2.46%	–1.80%	–0.99%	–1.01%	–0.92%	–1. 28%
		—	–2.05%	–1.24%	–0.84%	–0.64%	–1.11%	–1.40%
		—	*–3.17%*	–2.23%	–1.82%	–2.01%	–1.04%	–0.63%
		—	*–2.58%*	–1.82%	–1.33%	–1.58%	–0.63%	–0.49%
		—	–2.23%	–1.52%	–1.23%	–1.04%	–0.26%	–0.69%
		—	*–2.96%*	–1.66%	–1. 35%	–1.15%	–0.95%	–0.83%
		—	–2.49%	–1. 35%	–0.84%	–0.96%	–0.83%	–1.41%
		—	–1.66%	–1.03%	–0.59%	–0.95%	–1.26%	–1.88%
		—	*–3.03%*	–2.16%	–1.73%	–1.56%	–0.84%	–0.68%
		—	–2.44%	–1.73%	–1.21%	–1.11%	–0.68%	–0.75%
		—	–2.16%	–1.37%	–0.89%	–0.84%	–0.63%	–0.59%
		—	*–3.80%*	*–2.81%*	–2.02%	–1.88%	–1.08%	–0.52%
		—	*–3.15%*	–2.02%	–1.47%	–1.50%	–0.52%	–0.44%
		—	*–2.81%*	–1.63%	–1.11%	–1.08%	–0.58%	–0.90%
		—	*–3.78%*	*–2.77%*	–2.29%	*–2.89%*	–1.48%	–1.02%
		—	*–3.13%*	–2.29%	–1.92%	–1.85%	–1.02%	–0.62%
		—	*–2.77%*	–2.02%	–1.52%	–1.48%	–0.73%	–0.34%

*Minimum positive reinforcement required.

†Compressive reinforcement is required for negative moments.

‡Compressive reinforcement is required for positive and negative moments.

§Compressive reinforcement is required for positive moments.

Note: 1 lb/ft² = 0.0479 kN/m².

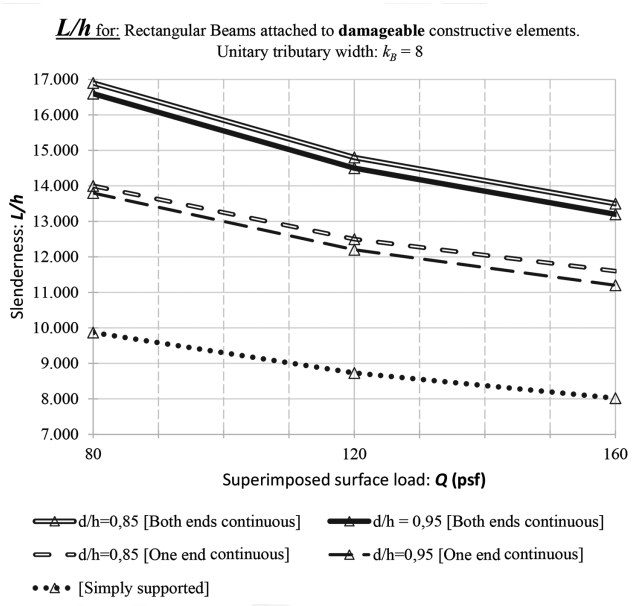

Fig. 3—RC beams with k_B *= 8 attached to damageable nonstructural elements: dependence of slenderness* L/h *on boundary conditions,* d/h*, and load* Q.

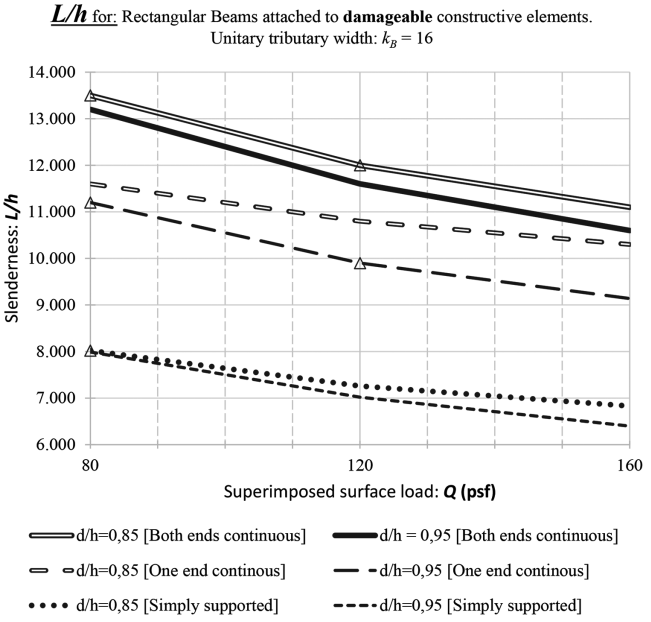

Fig. 4—RC beams with k_B *= 16 attached to damageable nonstructural elements: dependence of slenderness* L/h *on boundary conditions,* d/h*, and load* Q.

values of the tables. For less precision, but still reasonably good results, the graphs provided in Fig. 3 to 8 may be used.

By observing these graphs, it is relatively clear that L/h diminishes almost linearly as the load (Q) grows.

Therefore, linear regressions were performed to find equations that may serve as a design tool to find L/h. The regression was performed separately for each boundary condition, d/h, and k_B value, with the criterion variable being L/h and the predictor variable being Q. The obtained expressions are Eq. (29) for beams attached to "damageable" nonstructural elements and Eq. (30) for beams attached to "non-damageable" nonstructural elements

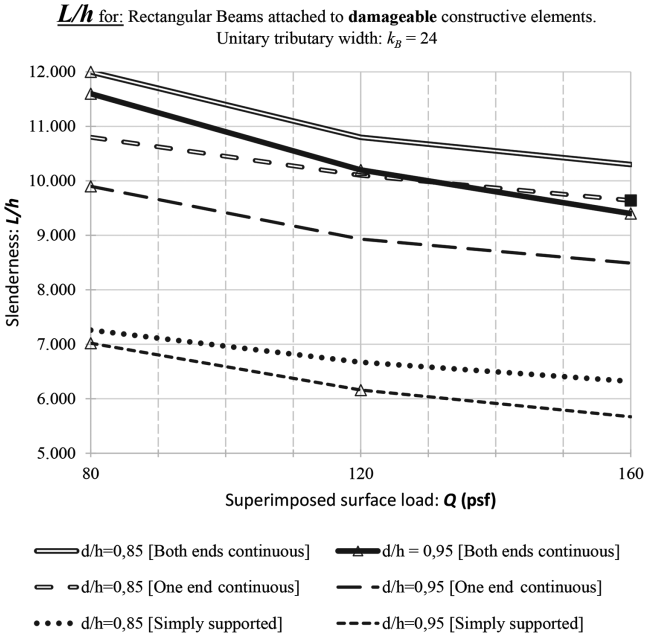

Fig. 5—RC beams with k_B *= 24 attached to damageable nonstructural elements: dependence of slenderness* L/h *on boundary conditions,* d/h*, and load* Q.

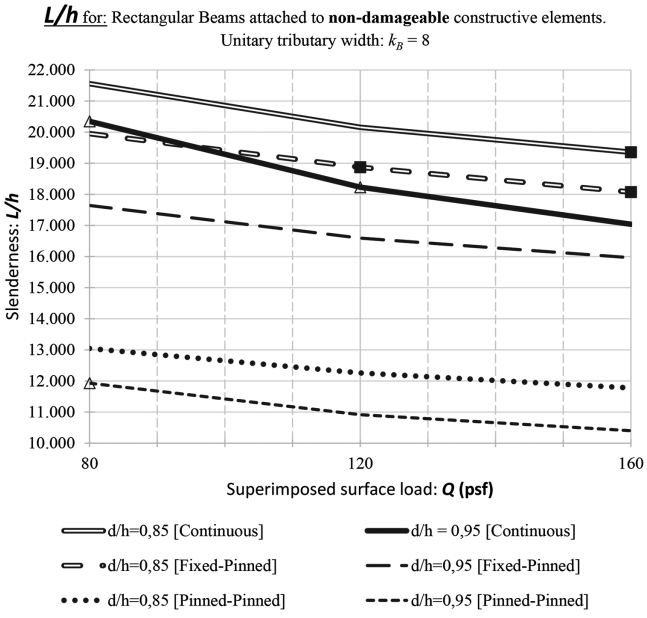

Fig. 6—RC beams with k_B *= 8 attached to non-damageable nonstructural elements: dependence of slenderness* L/h *on boundary conditions,* d/h*, and load* Q.

$$\frac{L}{h} = \left(\frac{L}{h}\right)_0 - k \cdot \left(1.25 - \frac{k_B}{32}\right) \cdot \frac{Q - 80}{100};\ Q \text{ in lb/ft}^2 \quad (29)$$

$$\frac{L}{h} = \left(\frac{L}{h}\right)_0 - k \cdot \frac{Q - 80}{100};\ Q \text{ in lb/ft}^2 \quad (30)$$

where $(L/h)_0$ is called the "basic slenderness" and corresponds to a surface load Q = 80 lb/ft^2 (3.8 kN/m^2); k is the adjustment factor; and k_B is the unitary tributary width.

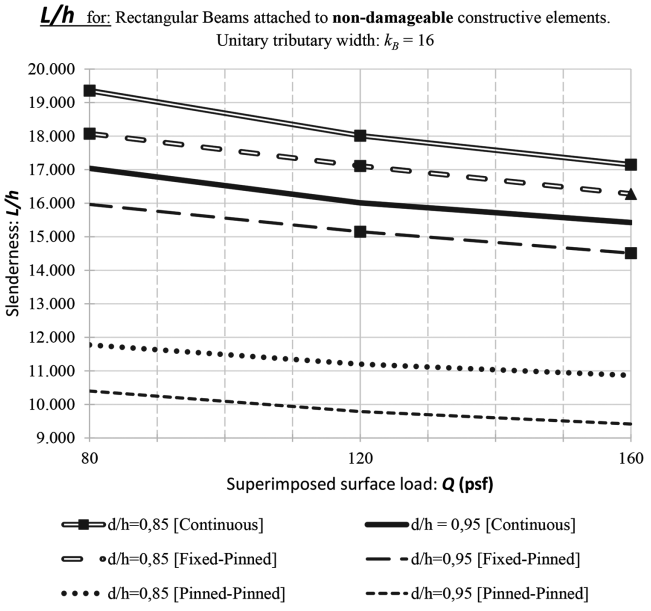

Fig. 7—RC beams with k_B *= 16 attached to non-damageable nonstructural elements: dependence of slenderness* L/h *on boundary conditions,* d/h*, and load* Q*.*

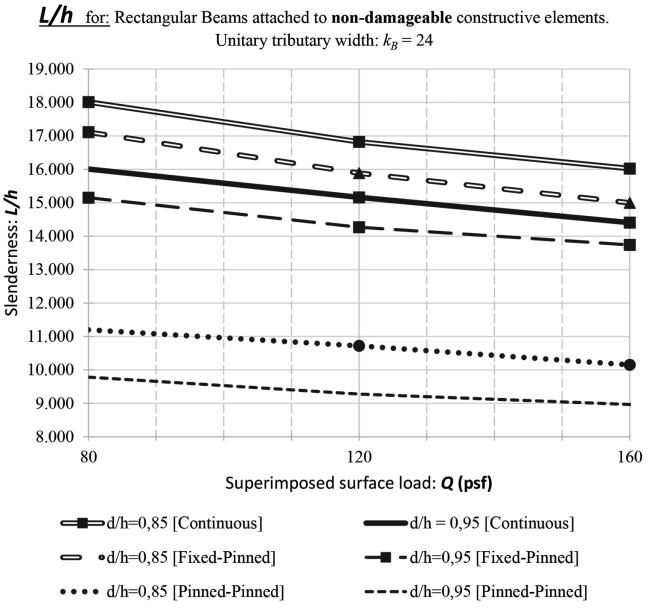

Fig. 8—RC beams with k_B *= 24 attached to non-damageable nonstructural elements: dependence of slenderness* L/h *on boundary conditions,* d/h*, and load* Q*.*

Table 5—Basic $(L/h)_0$ values for use in Eq. (29) and (30)

Basic $(L/h)_0$		Deflection control					
		k_B					
		Attached to damageable elements			Attached to non-damageable elements		
Boundary conditions	d/h	8	16	24	8	16	24
Both ends continuous (2C)	0.85	16.9*	13.5*	12.0	21.6	19.4†	18.0†
	0.95	16.6*	13.2*	11.6*	20.3	17.0	16.0†
One end continuous (1C)	0.85	14.0*	11.6	10.8	20.0†	18.1†	17.1‡
	0.95	13.8*	11.2*	9.90	17.6	16.0†	15.2†
Simply supported (SS)	0.85	9.87*	8.02	7.26	13.0	11.8	11.2§
	0.95	9.87*	7.99*	7.02*	11.9	10.4	9.79

*Minimum positive reinforcement required.

†Compressive reinforcement is required for negative moments.

‡Compressive reinforcement is required for positive and negative moments.

§Compressive reinforcement is required for positive moments.

For beams attached to "damageable" nonstructural elements, the basic slenderness $(L/h)_0$ values are provided in Table 5, and the adjustment factor (k) values are provided in Table 6. The values of Table 6 are summarized as follows: 4.5 for beams with both ends continuous, 3.1 for beams with one end continuous, and 2.5 for simply supported beams, with only one exception: for simply supported beams with $k_B \geq 24$ and $d/h = 0.95$, k is 3.1.

For beams attached to "non-damageable" nonstructural elements, the basic slenderness $(L/h)_0$ values are provided in Table 5, and the adjustment factor (k) values are provided in Table 6. The values in Table 6 can be summarized as follows: $k = 2$ for all cases with only two exceptions: $k = 1.1$ for simply supported beams with $k_B \geq 16$; and $k = 4.5$ for both ends continuous beams with $d/h = 0.95$. For intermediate cases, k may be interpolated.

An example of RC beam slenderness calculation is provided in Appendix B.

CONCLUSIONS

This study presented an in-depth analysis of maximum slenderness calculation for reinforced concrete (RC) one-way slabs and RC beams using the "long method of Rangan-Scanlon." Through a consideration of the effect of different influential parameters, the following conclusions can be drawn:

- For RC one-way slabs attached to either "damageable" or "non-damageable" nonstructural elements, it was found that sensitivity to the large majority of considered parameters is lower for $\alpha^{1/3}$ than for L/h. Therefore, practical design tools for RC one-way slabs are presented in tables and graphs that allow the determination of α, which then needs to be used to calculate L/h.

Table 6—Values of coefficient *k* for use in Eq. (29) and (30)

Coefficient *k*		Deflection control					
		k_B					
		Attached to damageable elements			Attached to non-damageable elements		
Boundary conditions	*d*/*h*	8	16	24	8	16	24
Both ends continuous (2C)	0.85	4.5	4.5	4.5	2.0	2.0	2.0
	0.95	4.5	4.5	4.5	4.5†	2.0	2.0
One end continuous (1C)	0.85	3.1	3.1	3.1	2.0	2.0	2.0
	0.95	3.1	3.1	3.1	2.0	2.0	2.0
Simply supported (SS)	0.85	2.5	2.5	2.5	2.0	1.1†	1.1†
	0.95	2.5	2.5	3.1*	2.0	1.1†	1.1†

*Coefficient *k* different from default value (of 2.5 for SS).
†Coefficient *k* different from default value of 2.0.

- In the case of RC one-way slabs attached to "non-damageable" nonstructural elements, the parameters found to significantly affect $\alpha^{1/3}$ were *d*/*h*, load (*Q*), and boundary conditions. For the range of considered parameters, α varied between 0.229 and 0.360, with an average of 0.298.
- In the case of RC one-way slabs attached to "damageable" nonstructural elements, the parameters found to significantly affect $\alpha^{1/3}$ were span (*L*), load (*Q*), and boundary conditions. For the range of considered parameters, α varied between 0.293 and 0.563, with an average of 0.389.
- For RC beams attached to "non-damageable" nonstructural elements, it was found that sensitivity to the large majority of considered parameters is lower for *L*/*h* than for $\alpha^{1/3}$. Therefore, practical design tools for RC beams attached to "non-damageable" nonstructural elements are presented in tables and graphs that allow the direct determination of *L*/*h*. Additionally, through linear regression, equations for calculating *L*/*h* are provided.
- For RC beams attached to "damageable" nonstructural elements, it was found that sensitivity to the large majority of considered parameters is similar for *L*/*h* and $\alpha^{1/3}$. To facilitate the direct determination of slenderness for RC beams attached to "damageable" nonstructural elements, practical design tools are also presented in tables and graphs that allow the direct determination of *L*/*h*. Additionally, through linear regression, equations for calculating *L*/*h* are provided.
- In the case of RC beams attached to "damageable" nonstructural elements, the parameters found to significantly affect *L*/*h* were span, *d*/*h*, load (*Q*), and boundary conditions. For the range of considered parameters, *L*/*h* varied between 5.7 and 16.9.
- In the case of RC beams attached to "non-damageable" nonstructural elements, the parameters found to significantly affect *L*/*h* were span, *d*/*h*, load (*Q*), and boundary conditions. For the range of considered parameters, *L*/*h* varied between 9.0 and 21.6.

The results of this study can be a practical tool for engineers and architects in the early stages of design to reliably and easily determine the minimum depth of RC rectangular solid beams and one-way solid slabs. Future research in this line may include additional structural members, such as two-way RC flat slabs or hybrid reinforced slabs, including bars and steel fibers.

AUTHOR BIOS

ACI member **Marc Sanabra-Loewe** *is a Lecturer Professor at the Polytechnic University of Catalonia (BarcelonaTech [UPC]), Barcelona, Catalonia, Spain. He received his architect license, MS, and PhD in architecture technology specializing in structures analysis and design from BarcelonaTech in 2005, 2011, and 2014, respectively. He was a founding member of DiCEA, a research group at UPC devoted to the design and analysis of architectural structures. From 2018 to 2019, he was a full-time Lecturer Professor at the University of Illinois Urbana-Champaign, Champaign, IL, as a Hilfinger Faculty Fellow. His research interests include the optimization of reinforced, precast, and prestressed concrete floors.*

ACI member **David Garcia** *is a Lecturer Professor and Serra Húnter Fellow at BarcelonaTech. He received his PhD in architecture, building, and urban planning technology. He is a founding member of DiCEA and the author of numerous articles and publications specializing in concrete structures and foundations. He has designed and surveyed the erection of more than 40 million ft² of concrete structures, including reinforced and post-tensioned concrete floors.*

Nikola Tošić *is a Lecturer Professor at BarcelonaTech. He received his BS, MS, and PhD in civil engineering from the University of Belgrade, Belgrade, Serbia, in 2010, 2011, and 2018, respectively. He is a former Fulbright Visiting Scholar and Marie Skłodowska-Curie Individual Fellow. His research interests include concretes with recycled and waste materials, the serviceability of concrete structures, and fiber-reinforced concrete.*

Albert de la Fuente *has been a Full Professor in the Department of Civil and Environmental Engineering at BarcelonaTech since 2015. His research interests include the design and optimization of concrete structures, fiber-reinforced concrete technology, and sustainability assessment by means of multi-criteria decision-making approaches.*

ACKNOWLEDGMENTS

The authors would like to thank Professor Emeritus A. Scanlon for his continued interest in and support of their work.

NOTATION

A_s	=	area of nonprestressed longitudinal tension reinforcement
b	=	cross-section width
d	=	distance from extreme compression fiber to centroid of longitudinal tension reinforcement
E_c	=	modulus of elasticity of concrete
f_c'	=	specified compressive strength of concrete
f_r	=	modulus of rupture
f_y	=	specified yield strength of reinforcement
h	=	cross-section height
I_{cr}	=	moment of inertia of fully cracked cross section
I_e	=	effective moment of inertia
I_g	=	moment of inertia of gross concrete cross section

L = span length
L_{trib} = tributary width for surface load (for slabs, should be equal to b)
M_a = maximum moment in member due to service loads at stage deflection is calculated[11]
M_{cr} = cracking moment
M_n = nominal flexural strength
n = ratio of steel-to-concrete moduli of elasticity (E_s/E_c)
W_g = gross-section modulus
W_{sl} = additional live load (live load minus sustained fraction of live load)
W_{sus} = all sustained loads (self-weight + superimposed dead loads + sustained fraction of live load)
α = effective moment of inertia factor (I_e/I_g)
Δ_{inc} = incremental deflection
δ = ratio of cracked to gross moment of inertia (I_{cr}/I_g)
η = ratio of maximum moment in member due to service loads (M_a) to nominal flexural strength (M_n)
κ = deflection coefficient depending on support conditions (5, 1.4, 2, and 48 for simply supported, both ends continuous, one end continuous, and fixed-end cantilever conditions, respectively)
λ_Δ = long-term deflection multiplier for sustained loads
μ = ratio of cracking moment to maximum moment in member due to service loads (M_{cr}/M_a)
ρ = tensile reinforcement ratio (at midspan for simply supported and continuous members and at support for cantilevers)
ρ' = compressive reinforcement ratio (at midspan for simply supported and continuous members and at support for cantilevers)
ξ = time-dependent factor (1.0, 1.2, 1.4, and 2.0 for 3, 6, 12, and >60 months, respectively)

REFERENCES

1. Beeby, A. W., and Narayanan, R. S., *Designers' Guide to EN 1992-1-1 and EN 1992-1-2: Eurocode 2: Design of Concrete Structures. General Rules and Rules for Buildings and Structural Fire Design*, H. Gulvanessian, ed., Thomas Telford Limited, London, UK, 2005.

2. *fib* Bulletin No. 52, "Structural Concrete: Textbook on Behaviour, Design and Performance," second edition, Volume 2, *fib* Bulletin No. 52, International Federation for Structural Concrete, Lausanne, Switzerland, 2010, 350 pp.

3. Bondy, K. B., "ACI Code Deflection Requirements—Time for a Change?" *Serviceability of Concrete: A Symposium Honoring Dr. Edward G. Nawy*, SP-225, F. Barth, R. Frosch, H. Nassif, and A. Scanlon, eds., American Concrete Institute, Farmington Hills, MI, 2005, pp. 133-145.

4. Sanabra-Loewe, M.; Capellà-Llovera, J.; Ramírez-Anaya, S.; and Pujadas-Gispert, E., "A Path to More Versatile Code Provisions for Slab Deflection Control," *Proceedings of the Institution of Civil Engineers - Structures and Buildings*, V. 176, No. 4, Apr. 2023, pp. 272-286. doi: 10.1680/jstbu.20.00205

5. Beal, A. N., "Eurocode 2: Span/Depth Ratios for RC Slabs and Beams," *The Structural Engineer*, V. 87, No. 20, Oct. 2009, pp. 35-40.

6. Eren, T., and Dancygier, A. N., "Evaluation of Span-to-Depth Ratio Provisions for Deflection Control of One-Way RC Construction," *Structures*, V. 25, June 2020, pp. 696-707. doi: 10.1016/j.istruc.2020.03.035

7. Pecić, N., and Marinković, S., "Design Aspects of Eurocode 2 Methods for Deflection Control," *Proceedings*, *fib* Symposium: Prague 2011: Concrete Engineering for Excellence and Efficiency, V. 1, V. Šrůma, ed., Prague, Czech Republic, June 2011, pp. 195-198.

8. Vollum, R. L., and Afshar, N., "Influence of Construction Loading on Deflections in Reinforced Concrete Slabs," *Magazine of Concrete Research*, V. 61, No. 1, Feb. 2009, pp. 3-14. doi: 10.1680/macr.2009.61.1.3

9. Sanabra, M., and Scanlon, A., "Reinforced Concrete Predimensioning to Enhance Optimization," *Proceedings of the IABSE Symposium: Engineering for Progress, Nature and People*, Madrid, Spain, Sept. 2014, pp. 1626-1633.

10. Pérez Caldentey, A., and Corres Peiretti, H., "EN 1992. Problems in Its Application and Suggestions for Improvement," *Hormigón y Acero*, V. 65, No. 272, Apr.-June 2014, pp. 113-122. doi: 10.1016/S0439-5689(14)70003-8

11. Pérez Caldentey, A.; Mendoza Cembranos, J.; and Corres Peiretti, H., "Slenderness Limits for Deflection Control: A New Formulation for Flexural Reinforced Concrete Elements," *Structural Concrete*, V. 18, No. 1, Feb. 2017, pp. 118-127. doi: 10.1002/suco.201600062

12. AS 3600-2001, "Concrete Structures," Standards Australia, Sydney, NSW, Australia, 2001.

13. Rangan, B. V., "Control of Beam Deflections by Allowable Span-Depth Ratios," *ACI Journal Proceedings*, V. 79, No. 5, Sept.-Oct. 1982, pp. 372-377. doi: 10.14359/10914

14. Scanlon, A., and Choi, B.-S., "Evaluation of ACI 318 Minimum Thickness Requirements for One-Way Slabs," *ACI Structural Journal*, V. 96, No. 4, July-Aug. 1999, pp. 616-622. doi: 10.14359/699

15. Scanlon, A., and Lee, Y. H., "Unified Span-to-Depth Ratio Equation for Nonprestressed Concrete Beams and Slabs," *ACI Structural Journal*, V. 103, No. 1, Jan.-Feb. 2006, pp. 142-148. doi: 10.14359/15095

16. ACI Committee 318, "Building Code Requirements for Structural Concrete (ACI 318-19) and Commentary (ACI 318R-19) (Reapproved 2022)," American Concrete Institute, Farmington Hills, MI, 2019, 624 pp.

17. Tošić, N.; Sanabra-Loewe, M.; Nogales, A.; and de la Fuente, A., "Effective Moment of Inertia and Slenderness Limits of Reinforced Concrete and Fiber-Reinforced Concrete Slabs," *ACI Structural Journal*, V. 119, No. 5, Sept. 2022, pp. 227-240.

ACI STRUCTURAL JOURNAL TECHNICAL PAPER

Title No. 121-S32

Impact of Confinement on Bar Anchorage in Relocated Plastic Hinges

by Taylor J. Brodbeck, Zachary A. Shurow, Rudolf Seracino, and Mervyn J. Kowalsky

Bridges subjected to extreme damage from earthquakes are usually considered unrepairable, and therefore must be replaced. One location where damage is concentrated in reinforced concrete bridges is in the plastic hinges that form at the ends of columns where the moment demand is the largest, causing buckling or fracture of the reinforcement. Recent studies have shown that plastic hinge relocation can restore reinforced concrete columns to their original force and displacement capacities. In this repair, a plastic hinge damaged by a seismic event is strengthened so that in subsequent seismic events, damage will form in an undamaged section, ensuring a ductile response. The aim of this research is to improve the constructability and performance of the repair using a steel jacket. Tests were conducted on columns subjected to reversed cyclic loading, repaired, and retested. A bolted connection simplified construction. Research has shown that the repair's response is weakened when fractured bars in the original plastic hinge debond. In these tests, anchorage and bond conditions were improved by increasing the confining stresses by using a larger jacket thickness. This enhanced the seismic resilience, evident by an increase in dissipation of energy and reduction in strength degradation.

Keywords: performance-based design; reinforced concrete (RC); repair and strengthening; seismic design.

INTRODUCTION

In recent decades, the seismic resistance of reinforced concrete (RC) bridges has been notably improved through the development of performance-based design procedures whereby structures are designed to achieve prescribed damage levels under defined seismic hazards. For bridge structures, damage is usually chosen to occur in column plastic hinges, while other members (that is, cap beams, joints, and footings) remain elastic through application of capacity design principles (Priestley et al. 1996). The bridge substructure may consist of single cantilever column bents where the plastic hinge would develop at the bottom near the footing, or multicolumn bents where the columns experience double bending, where plastic hinges would likely develop at both the bottom and top of the columns near the cap beam.

While remaining damage-free under a seismic event would certainly be preferred for a bridge system, under very large earthquakes, such criteria are impractical. The sizing of the members would need to be very large, which would not only increase construction costs, but also increase inertia forces that the entire system experience. Even if structures were designed to remain elastic, it is always possible that ground motions will exceed the predicted level for a given site. Alternative options such as rocking columns are possible, but have not been widely deployed. Consequently, ductile design is important, and the concept of performance-based design provides engineers with the tools needed to achieve the desired ductile response while prescribing the damage level.

While there has been extensive research in the repair of structures with mild damage, more extreme damage, such as buckling or rupture of reinforcing bars, was historically considered unrepairable and required complete replacement of the bridge, or at the minimum replacement of the component (Rutledge et al. 2014).

Plastic hinge relocation, originally considered for new design by Hose et al. (1997), was identified as a potential method that could be modified for column repairs. Plastic hinge relocation is achieved by providing an increased moment capacity at the original plastic hinge such that the moment demand exceeds the moment capacity at the desired location of the new plastic hinge, illustrated in Fig. 1.

The concept was first adopted for repair of structures by Lehman et al. (2001), in which an RC jacket was constructed around the plastic hinge of a damaged column. This study was successful in relocating the plastic hinge and restoring the column's flexural capacity. This was followed by Rutledge et al. (2014), who aimed to relocate the plastic hinge using carbon fiber-reinforced polymer (CFRP) as both confinement (transverse wrap) and flexural (longitudinal) reinforcement; however, the large-diameter CFRP anchors used in the repair were not able to provide the necessary force transfer, and the confinement also inadvertently introduced additional forces, which resulted in column yielding at the base. Another experimental

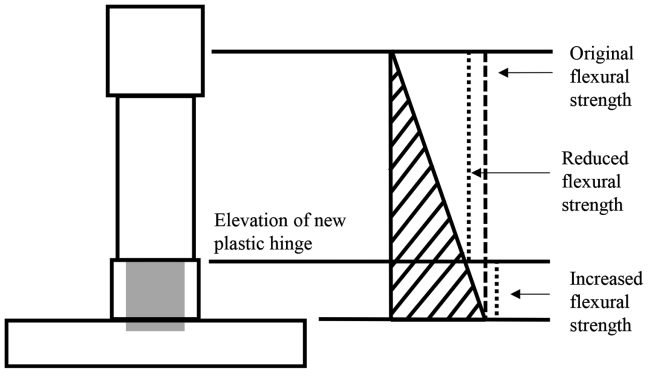

Fig. 1—Repair concept of plastic hinge relocation (after Lehman et al. [2001]).

ACI Structural Journal, V. 121, No. 3, May 2024.
MS No. S-2022-366.R2, doi: 10.14359/51740459, received November 30, 2023, and reviewed under Institute publication policies.

investigation used a CFRP shell for confinement and headed steel anchors for the additional longitudinal reinforcement, and the tests were able to restore the displacement and load-carrying capacities (Parks et al. 2016). Four hexagonal columns with grouted splice sleeve (GSS) connections were repaired. Three of the original columns tested had one fractured longitudinal bar, and the fourth had multiple bars pulling out from the GSS. Two of the repaired columns used concrete to fill the annular ring between the CFRP shell and concrete column, and the force and displacement capacities were restored. In the other two repaired columns, expansive grout was used, and the plastic hinge was not relocated due to failure of the CFRP shell. The authors concluded that while expansive grout provides active confinement, which reduces the demand to the repair, too much expansion also reduces the available capacity of the CFRP shell. A later study by Wu and Pantelides (2017) highlighted the importance of bond conditions, which led to softening and pinching of the global response. In their original column tests, two of the six longitudinal bars fractured. While the repairs restored both the load and displacement capacity, the global response exhibited pinching and softening, and the failure mode was concrete crushing rather than bar fracture. The inability to anchor the bars until fracture was attributed to weak bond, and a gap was noticed between the column and repair. Krish et al. (2021) used a welded steel sleeve for the repair and was successful in relocating the plastic hinge; however, the fractured bars from the original tests debonded during the repair test. The study included, six RC columns with damage ranging from all 16 longitudinal bars being buckled to six out of 16 longitudinal bars being fractured. The emphasis was to develop a rapid repair for modern, well-designed bridge columns with severe seismic damage. The repair design and construction process serves as the foundation for the repairs in this paper, and the relevant design considerations are discussed in the section "Repair Implementation."

As a consequence of the previous summary of current research, two research objectives that aim to improve the plastic hinge relocation repair's constructability and performance are presented in this paper. First, the use of a steel jacket with a mechanically bolted connection was developed as an alternative jacket option to the CFRP shell or welded steel jacket. A bolted steel jacket is simpler to construct and can be used when environmental conditions such as low temperature or accessibility could hinder the installation of the other jacketing techniques that require welding or epoxy curing. Second, the behavior of longitudinal reinforcing bars that fractured during the initial seismic event is studied. It has been shown that the anchorage of these bars within the repair tends to degrade at larger displacements (Wu and Pantelides 2017; Krish et al. 2021), which rapidly leads to a complete loss in load-carrying capacity of those bars and a weakened column response. The results presented in this paper show that this can be prevented by improving the bond conditions and confining stresses to those bars, allowing for those bars to achieve their ultimate strength in the relocated plastic hinge.

RESEARCH SIGNIFICANCE

This paper presents a simple and effective repair method, which restores damaged RC columns to their original load-carrying capacities. Building on a previously developed repair method, plastic hinge relocation, this repair uses a bolted steel jacket, which eases installation. The repair performance is also improved by anchoring the bars that fractured in an initial seismic event such that the bars can fully develop during subsequent seismic events. The method described in this paper allows for bridges that would typically be considered unrepairable to remain in service and perform favorably in subsequent seismic events.

RESEARCH METHODS

As part of the research program, four RC columns that were tested as a part of a separate research study on the use of high-strength steel for seismic design of bridge columns (Manhard 2019) were repaired using the plastic hinge relocation method and subsequently retested. This method could also be applicable to columns in buildings; however, the columns available for repair were designed as, and therefore representative of, bridge columns. Each circular column was constructed with a diameter of 610 mm (24 in.), a height of 2.44 m (8 ft), and longitudinal steel consisting of 16 No. 6 (19 mm [3/4 in.]) ASTM A706 (2016) Grade 80 reinforcing bars. Typical RC columns in seismic regions like Alaska vary in diameter from 1.2 to 2.44 m (4 to 8 ft), so the columns were designed to be half-/quarter-scale. The parameters that varied for these tests were the axial load ratio (ALR) and the transverse spiral spacing. Material properties and reinforcement detailing are shown in Table 1.

Table 1—Reinforcement detailing and properties

Repair No.	ALR, %		Longitudinal steel		Transverse steel		Bolts	Compressive strength		Removal of loose concrete
	Original column	Repaired column	Original column	Repaired column dowel bars	No. 3 column spiral pitch, mm (in.)	Repair jacket thickness, mm (in.)		Concrete, MPa (ksi)	Repair grout, MPa (ksi)	
1	10	5	16 No. 6	11 No. 8	51 (2)	3.4 (0.135)	18 ASTM A325 12.7 mm (1/2 in.)	44.9 (6.5)	54.7 (7.9)	No
2	10	5	16 No. 6	10 No. 8	51 (2)	3.4 (0.135)	18 ASTM A490 15.9 mm (5/8 in.)	47.3 (6.9)	60.8 (8.8)	No
3	5	5	16 No. 6	10 No. 8	38 (1.5)	6.4 (0.25)	24 ASTM A490 15.9 mm (5/8 in.)	38.7 (5.6)	64.3 (9.3)	North side only
4	5	5	16 No. 6	10 No. 8	38 (1.5)	6.4 (0.25)	24 ASTM A490 15.9 mm (5/8 in.)	38.7 (5.6)	54.7 (7.9)	Both sides

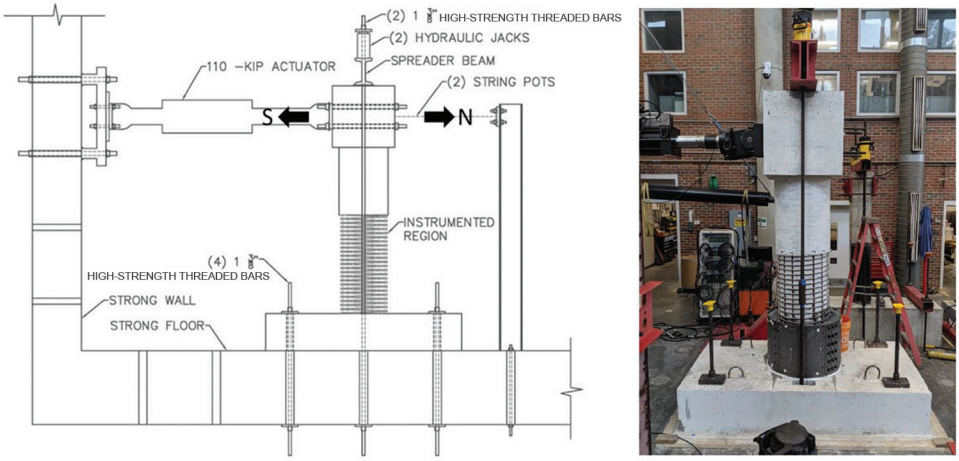

Fig. 2—Laboratory setup (Manhard 2019).

A schematic of the laboratory setup for the original column tests is shown in Fig. 2. The lateral loading of these specimens was applied using a 490 kN (110 kip) actuator, and each column was subjected to the loading protocol shown in Fig. 3. To compare performance between the original column and the repaired column, the repaired column was subjected to the same displacement cycles as the original. For the initial test cycles of the original column, loading was based upon the analytical first yield force (F_y'), where the column was subjected to one cycle of positive and negative forces at $1/4F_y'$, $1/2F_y'$, $3/4F_y'$, and F_y'. The average of the absolute displacements at F_y' was the first yield displacement (Δ_y'). The equivalent yield displacement was then obtained by $\Delta_y = M_n \times \Delta_y'/M_y'$, where M_n is the analytical nominal moment capacity. The calculation of the equivalent yield displacement comes from the moment-area method and allows for the definition of ductility levels as multiples of the equivalent yield displacement. Following the first yield cycle, the column was subjected to three cycles of increasing ductility level until failure. For the repair tests, the lateral loading of the original column was repeated, aside from Repair No. 2, which followed the loading history of Repair No. 1 to aid in evaluating the bolted jacket's performance.

For the axial loading of the original column tests, two columns were subjected to an ALR of 5%, while the other two were subjected to 10% ALR. These ratios were chosen to represent a range of realistic axial loads a bridge column may experience. For the repair tests, an ALR of 5% was used to allow for comparison between all repaired specimens.

The force was measured using the actuator's internal load cell, and the displacement was measured using a horizontal string potentiometer attached at the height of the applied load. Strain measurements were taken from light-emitting diode (LED) markers spaced 50 mm (2 in.) apart along the longitudinal steel and tracked three-dimensional (3-D) positions throughout loading. To facilitate measurement of steel strains, the columns were cast without cover concrete in the instrumented region and the LED markers were placed directly on the steel, and for the extent of damage seen in these column tests, the cover concrete would have likely spalled off at larger displacements. The strains were then calculated using the relative change in the 3-D positions of two adjacent LED markers compared to the initial gauge length.

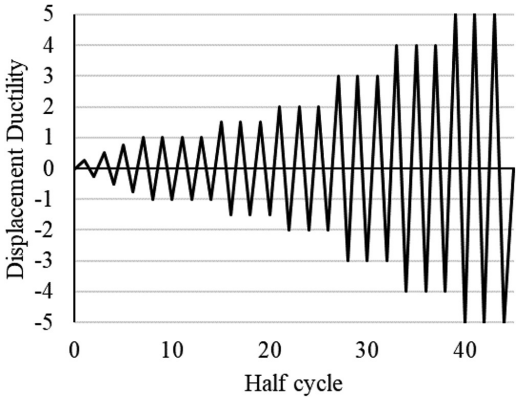

Fig. 3—Lateral loading protocol.

Column condition prior to repair

The original column tests aimed to evaluate the use of Grade 80 reinforcing bars for seismic design, and it required the columns to be subjected to large cyclic deformations, causing extreme damage to the plastic hinges, such as crushing of core concrete, buckling of longitudinal bars, and fracture of bars. These damage levels made these columns ideal specimens for this research into the plastic hinge relocation repair as they represented damage levels that traditionally would result in replacement, rather than repair, of the system.

Repair implementation

Plastic hinge relocation is intended for severely damaged concrete columns with buckled or fractured longitudinal bars and spalling of the cover and core concrete. To improve the bond of the repair to the damaged column, all concrete that was loose enough to remove by hand was removed from the column. For Repairs No. 3 and 4, approximately 20 mm (3/4 in.) of concrete around select longitudinal bars, described in the section on anchoring fractured bars, was removed by drilling beside the bars within the repair height to improve their anchorage inside the repair. Holes were then drilled into the footing 380 mm (15 in.) to the bottom mat

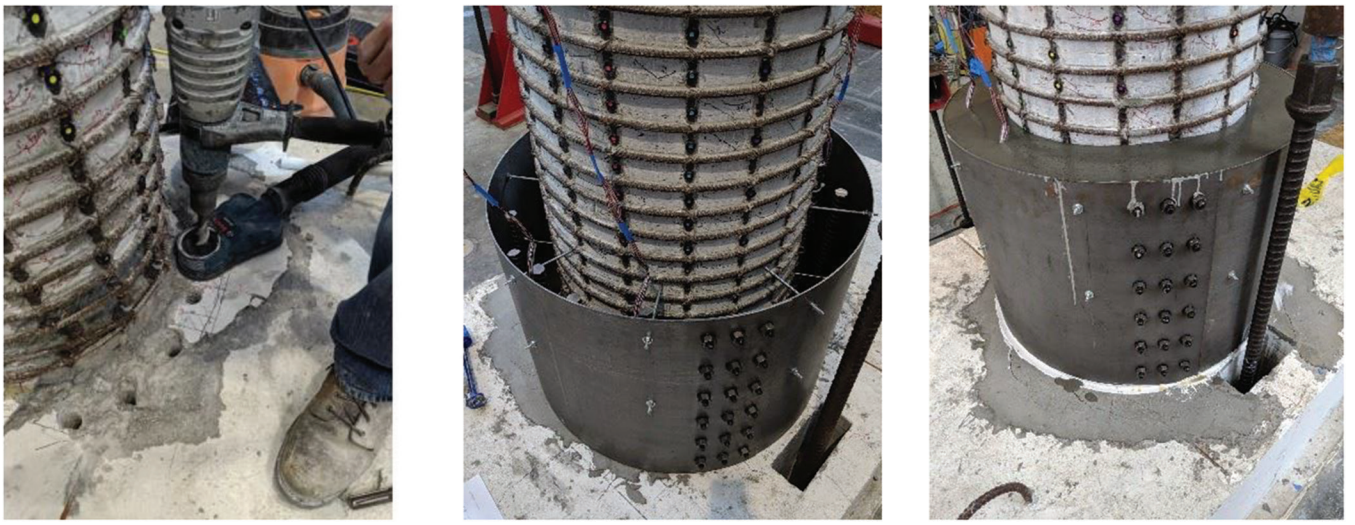

Fig. 4—Repair construction: (a) drilling holes; (b) assembling jacket; and (c) placing grout.

of footing steel using an electro-pneumatic hammer drill to anchor new longitudinal bars into the foundation with an injectable epoxy, as shown in Fig. 4(a). The size and spacing of the longitudinal repair bars was determined such that the capacity of the section at the base exceeds the increased demand from relocating the hinge, as described by Krish et al. (2021). To provide a level surface for the bottom of the steel jacket, a nonshrink grout was used to patch any spalled footing concrete.

To fabricate the steel jacket, two steel plates with pre-drilled bolt holes were cut and cold-rolled to an overlapping semicircle with an 813 mm (32 in.) diameter. The two rolled plates were then placed around the column and bolted together at the overlaps on each side of the column, as shown in Fig. 4(b). The height of the jacket was 559 mm (22 in.) for each repair. This height was determined following the procedure presented in Krish et al. (2021) with the requirements that the column longitudinal bars have not surpassed a strain limit that would reduce their capacity in the relocated hinge, and that the fractured bars have sufficient length within the repair to develop their yield stress. The thickness of the plates for Repairs No. 1 and 2 was 3.4 mm (0.135 in.) and was increased to 6.35 mm (0.25 in.) for Repairs No. 3 and 4. In Repair No. 1, the bolts were tightened to a snug-tight condition using a wrench, but for the remaining repairs, a calibrated torque wrench was used to pretension the bolts and prevent slip in the plates.

With the jacket assembled, it was then centered around the column and sealed with silicone at the base. Repairing a plastic hinge at the column-to-footing interface, such as the repairs discussed herein, allows for the jacket to be placed directly on the footing, while a repair at the top of a column may require additional formwork to hold the jacket at the correct location. Jacket placement is followed by the placement of a nonshrink grout into the annular space between the column and jacket, as shown in Fig. 4(c). Compressive strengths of the nonshrink grout, conducted per ASTM C39/C39M (2018), are shown in Table 1. The measured yield strength of the embedded repair bars was 580 MPa (84 ksi). Designs for the bolts and jackets are described in the following sections.

DETAILS OF REPAIR DESIGNS

A detailed description of the design for the geometry and cross section of this plastic hinge relocation repair has been proposed by others (Krish et al. 2021; Parks et al. 2016); however, new designs for the repair jacket were developed in this research. To begin, designs for the bolted connection in the steel jacket were needed. In typical bolted connection designs, the demand is determined based on the loads applied to the connecting members; however, in this application, the stresses imposed on the jacket result from confining forces that develop from the strain penetration of the original column's longitudinal bars into the repair. This transfer of forces is complex and would be difficult to design. Instead, capacity design principles were used to develop a conservative design for the bolted connection to ensure that the jacket steel would yield before failure of the bolts.

Bolted connection design

Initial designs for the bolted jacket assumed that the jacket would yield along the entire height of the repair. This would mean that the demand for the jacket would simply be the yield stress times the gross area of the jacket at the bolted connection. However, after the first two repair tests, the strains measured with LEDs on the jacket remained below yield and were nearly zero at the base of the sleeve. Using the jacket design proposed later in this section, the design assumptions can be refined to a lower demand.

In combination with the jacket design in the following section, a triangular stress profile was used to design the bolted connection. This stress distribution assumes that the jacket is at its expected yield stress at the top of the repair and has no stress at the base. While this would imply an eccentrically loaded connection, effects of eccentricity were ignored given that the jacket should not actually yield, and that the bolt geometry is relatively square, which would reduce the effects of eccentricity. These assumptions provide a simple design procedure for the bolted connection, which

includes checking bolt bearing, bolt shear, and the base yield/rupture per the requirements of a steel design manual. The connections were designed following the ANSI/AISC 360-16 (2016) specifications to ensure that jacket yielding will precede any bolt failures.

Bolt slip design

Through the experimental tests performed in this research, it will be shown that minimizing slip at the bolted connection improves the repair response. Bolt pretension was applied using a calibrated torque wrench clamping the two plates together, which acts to prevent slip though friction between the plates. The design for this connection followed the slip-critical connection design in ANSI/AISC 360-16; however, no surface preparation was performed on the steel jackets in the tests. While ANSI/AISC 360-16 requires some level of surface preparation to use the slip-critical connection design, the method simply solves static equilibrium using an assumed coefficient of friction, μ, which would be the only variable affected by surface preparation. A value of $\mu = 0.3$ was used for the repairs in this project in the absence of any other recommended values, which is the lowest value in ANSI/AISC 360-16.

Using the ANSI/AISC 360-16 slip-critical design and assumed jacket stress profile presented in the previous section, Eq. (1) was developed where the frictional force between the plates is expected to be greater than the total force applied to the jacket. For the bolts in this project, the normal force, T_b, for the bolt pretension was the minimum bolt pretension using Table J3.1 in ANSI/AISC 360-16.

$$\mu \cdot T_b \cdot n_{bolts} \geq 1/2 \cdot f_y \cdot H_{Repair} \cdot t_j \quad (1)$$

It should be noted that in ANSI/AISC 360-16, T_b is usually increased by a factor of 1.13, which is based on statistical analysis of the ratio of mean installed pretension to the table minimums. Because a calibrated torque wrench was used to apply pretension, the 1.13 factor was not used. In actual construction, the use of direct tension indicators (DTIs) is suggested, as this would provide a more reliable measure of pretension for T_b in Eq. (1). For the 16 mm (5/8 in.) diameter pretensioned bolts used in this research program, a torque of 339 N·m (250 ft·lb) was used to apply an estimated 107 kN (24 kip) of pretension.

Jacket thickness design

In previous studies, jackets were designed to provide shear strength for the repair and strengthen the concrete through confinement. While those designs have provided repairs that relocate the plastic hinge and can restore strength and ductility capacities, if column longitudinal bars are fractured, they tend to debond in repair tests. This has been shown to degrade and soften the repair at larger ductilities, which could lower their seismic resistance.

It was hypothesized that increasing the confining forces of the jacket to the repair may prevent the debonding behavior of the fractured bars by improving their bond inside the repair. To fully anchor the fractured bars, the model developed by Priestley et al. (1996) was adapted to the plastic hinge relocation repair.

The model of Priestley et al. (1996) was intended for columns that were constructed using starter bars that extend from the footing and are lapped with column longitudinal bars in the plastic hinge. These columns had insufficient confinement, and lap splice failures were shown to severely limit the column's ductility. The model for these columns assumes that a crack will form around the longitudinal bars along the length of a lap splice, and confinement will apply stresses normal to this crack. A static friction relationship is then used to predict lap splice failure. If confining forces are inadequate, the two sides of the crack will slide when the force in the bar is greater than the resistance from friction along this assumed crack.

To adapt the model to the plastic hinge relocation repair, a new assumption for the crack location was needed. Based on previous experimental tests, the splitting crack surface was assumed to be along the radius of the column's fractured longitudinal bars, as is shown in Fig. 5. The length of the crack can then be calculated for each bar using Eq. (2) from Priestley et al. (1996), where D' is the diameter of the column core and n is the total number of longitudinal bars. Using the required volumetric ratio shown in Eq. (3) and the provided volumetric ratio shown in Eq. (4), from Priestley et al. (1996), an equation for the required jacket thickness to fully anchor fractured bars in the plastic hinge relocation repair was proposed and is shown in Eq. (5). The volumetric ratios presented here are for circular columns but can generically be taken as the ratio of the volume of steel to the volume of concrete. The lap length, l_s, is taken as the jacket height, which was determined earlier based on the development length of the fractured bars. In this repair, the thickness of the jacket provides confinement, which improves development conditions for the fractured bars, and a jacket with a height less than the development length of the fractured bar in plain concrete may be used if the thickness is designed following Eq. (5). For the columns in this research, Eq. (5) gives a required jacket thickness of 5 mm (0.20 in.), so a thickness of 6.35 mm (0.25 in.) was used for Repairs No. 3 and 4 based on available plate thicknesses.

$$p = \frac{\pi D'}{n} \quad (2)$$

$$\rho_{sj} = \frac{2.42 A_b f_{yl}}{p l_s (0.0015 E_{sj})} \leq \frac{2.42 A_b f_{yl}}{p l_s f_{yj}} \quad (3)$$

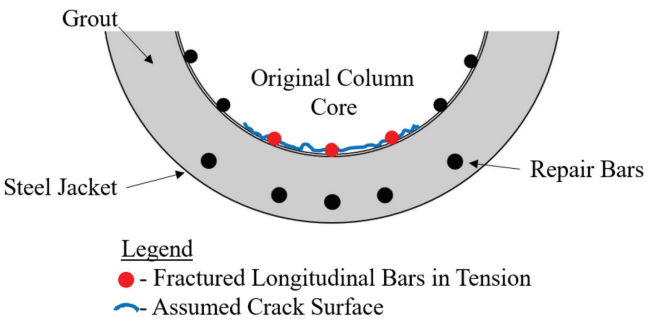

Fig. 5—Assumed crack shape for lap splice failure.

$$\rho_{sj} = \frac{4t_j}{D_j} \tag{4}$$

$$t_j = \frac{0.605 \cdot D_j n A_b f_{yl}}{D' \pi l_s (0.0015 E_{sj})} \leq \frac{0.605 \cdot D_j n A_b f_{yl}}{D' \pi l_s f_{yj}} \tag{5}$$

Fig. 6—Bolted connection.

Development of mechanically bolted steel jacket

As previously mentioned, Repairs No. 1 and 2 were designed to demonstrate the feasibility of using a bolted, as opposed to welded, steel jacket for the column repair. Repair No. 1 was a baseline where a bolted connection was used instead of a welded connection. By assuming the jacket would yield along the entire height of the repair, a connection was designed that should prevent failure from occurring at the connection. This led to the design of eighteen 12.7 mm (1/2 in.) diameter ASTM A325 bolts, arranged as shown in Fig. 6, spaced 76 mm (3 in.) vertically and 38 mm (1.5 in.) horizontally, with an edge distance of 38 mm (1.5 in.). The bolts in Repair No. 1 were tightened to a snug-tight condition using a wrench, typical for most bolted connections.

Repair No. 2 furthered the study of a bolted steel jacket by using pretensioned bolts to prevent slip from occurring at the connection. For a typical bearing connection, small levels of slip must occur before the bolts begin to bear on the plate and carry load. It is believed that this slip may result in cracking within the repair, weakening the bond of the repair to the column. Hence, the bolt pretension was designed to prevent slip from occurring so that the repair would behave more like a steel jacket with a welded connection. This resulted in eighteen 16 mm (5/8 in.) diameter ASTM A490 bolts with 339 N·m (250 ft·lb) of torque applied using a calibrated torque wrench.

The damage states and repair configurations for Repairs No. 1 and 2 are shown in Fig. 7, as well as a photo of the damage prior to Repair No. 1. While Repair No. 2 had less damage than Repair No. 1, the south sides of each column had similar damage levels and were therefore repaired similarly. This was determined to be the optimal location to

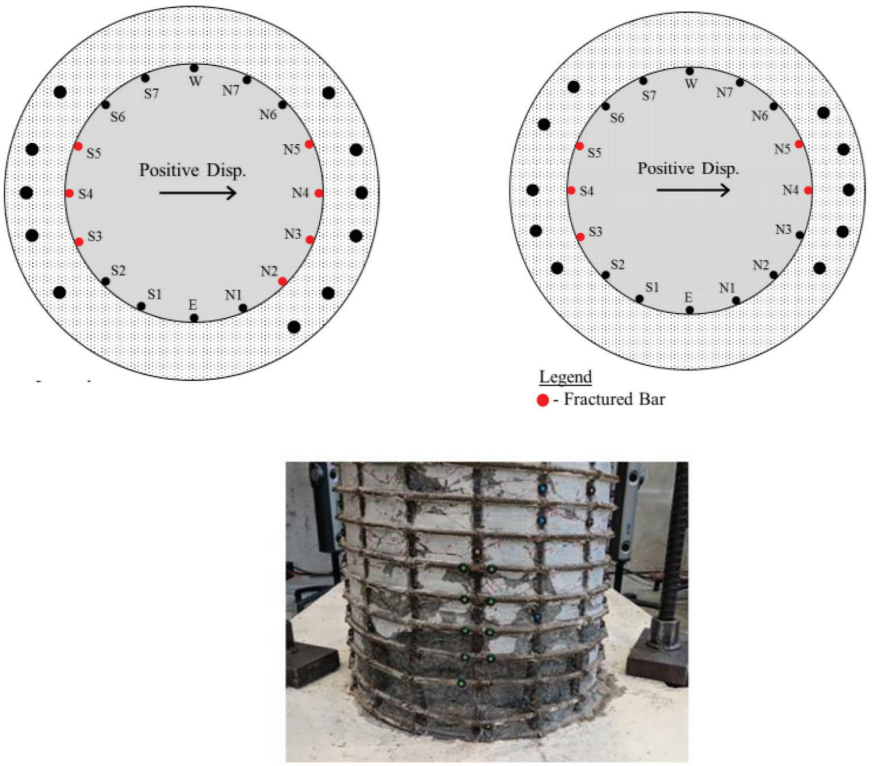

Fig. 7—Damage conditions of: (a) Repair No. 1; (b) Repair No. 2; and (c) original plastic hinge of Repair No. 1 prior to repair.

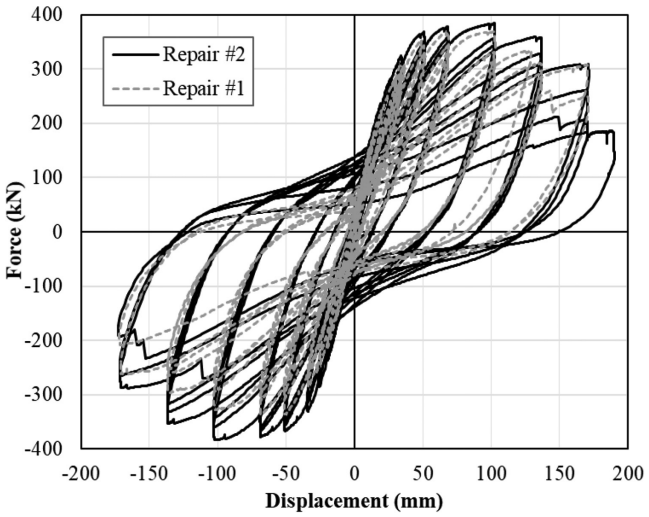

Fig. 8—Force-versus-displacement response of Repairs No. 1 and 2.

compare results between the two repairs and evaluate the effectiveness of the pretensioned bolts.

The global force-displacement response of the two repaired columns is shown in Fig. 8. An important difference between the two repairs is the pinching behavior. Pinching in the global response of an RC column is indicative of a reduction in the dissipation of energy for the structure. This behavior has been observed in past studies using this repair technique and has been attributed to the loss of anchorage for fractured bars within the repair.

During the Repair No. 1 test, slip at the bolted connection was observed where a bead of silicone used to seal the base of the jacket ruptured during the repair test (refer to Fig. 9). It is believed that in cases where bolt slip occurs, the confining stress from the jacket would be small until bolt bearing with the bolt holes occurs. This lack of confinement would not only limit the strength of the concrete inside the repair, but also the bond conditions for the reinforcement, and likely explains why Repair No. 1 was more degraded than Repair No. 2, where the pretensioned bolts prevented slip from occurring. This behavior will be further analyzed in the next section where the anchorage of fractured bars is discussed.

While Repair No. 2 still exhibited some levels of strength degradation, it appears to be consistent with the levels seen in previous studies, and it is logical that a pretensioned bolted connection that prevents slip would behave more like a welded steel jacket connection. From this, Repair No. 2 shows that the pretensioned bolted connection is a viable alternative for the repair jacket as long as slip at the connection is prevented. The use of pretensioned bolts was continued in the final two repairs using the lower design load assumptions previously described. There was no evidence of slip in the remaining tests, and they act as further evidence of the acceptable use of the pretensioned bolted jacket.

Anchoring of fractured bars within repair

With the pretensioned bolted connection considered to be an acceptable jacket alternative, attention was then directed toward understanding and improving the anchorage of

Fig. 9—Ruptured silicone seal of Repair No. 1.

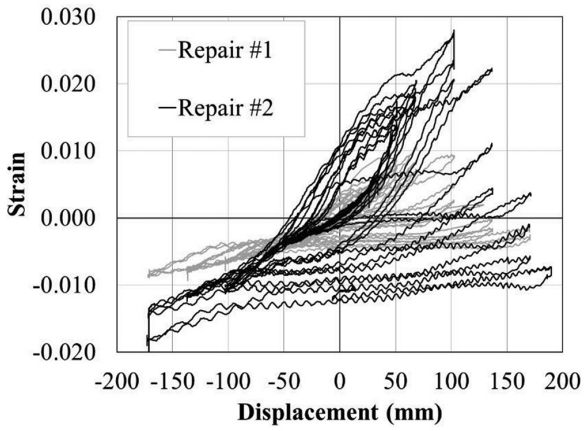

Fig. 10—Comparison of strain history of S4 in Repairs No. 1 and 2.

fractured bars within the repair. In the previous section, it was hypothesized that the connection slip in Repair No. 1 would limit the confining stress provided by the jacket, reducing both the strength and bond of concrete within the repair. To evaluate this hypothesis, the strains in the extreme south longitudinal bar (S4) of both repairs are compared in Fig. 10. Each of these bars fractured during the original column tests and due to debonding, evidenced by the inability to develop strains beyond a certain displacement, did not refracture during the repair test.

Typically, the strains in the bar will increase with positive displacements and decrease with negative displacements until bar buckling occurs. Due to insufficient anchorage inside the repair, both bars debonded, which rapidly leads to a complete loss in load-carrying capacity of the bar. From Fig. 10, it can be seen that the S4 bar of Repair No. 1 reached

a peak strain of approximately 0.01 at a column displacement of 68 mm (2.68 in.), while in Repair No. 2, the S4 bar reached a peak strain of 0.028 with a column displacement of 102 mm (4.02 in.). Considering that the south side of both columns were similarly damaged and repaired, this difference is largely attributed to the use of pretensioned bolts to prevent slip at the connection. By eliminating slip in Repair No. 2, it is believed that larger confining forces and better bond conditions were provided by the jacket, which would explain the improvement in anchorage of the fractured bars. Both repairs were able to develop the yield strain of the bar (0.0038 for the Grade 80 longitudinal reinforcement), but the strain developed prior to debonding was far below the ultimate strain capacity for these bars (0.10) in both cases.

As a result of the observed behavior of the first two repair tests, it was decided to use a thicker steel jacket for the remaining two repairs. Because a thicker jacket increases the rigidity of the hoop direction and provides even greater confining stress, it is possible to fully anchor the fractured bars inside the repair. For Repairs No. 3 and 4, a jacket thickness of 6.35 mm (0.25 in.) was used, nearly twice as thick as the 3.4 mm (0.135 in.) jacket used in the first two repairs. The 6.35 mm (0.25 in.) thickness is slightly larger than the required thickness of 5 mm (0.20 in.) using the jacket design described previously.

The third column repaired in this project was the first to be symmetrically damaged, having three fractured bars on each side, which provided an opportunity to investigate an additional method of improving the anchorage of fractured bars. While both sides would of course be affected by the larger jacket thickness, on the north side of the column the concrete around the perimeter of the fractured bars was removed, as shown in Fig. 11. This method was investigated previously by Krish et al. (2021) using a welded steel jacket with a thickness of 3 mm (0.120 in.); while it was shown to improve the anchorage of the bars, it was not sufficient to completely anchor the fractured bars. Using the larger jacket thickness in Repair No. 3, this technique could be re-evaluated by comparing the results of the north and south sides.

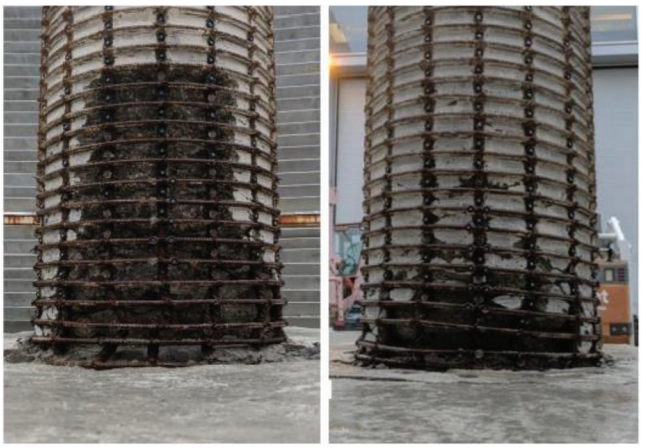

Fig. 11—Repair conditions for: (left) north; and (right) south sides of Repair No. 3.

The final damage states of both sides of Repair No. 3 are shown in Fig. 12. The test concluded with the south side behaving similarly to Repair No. 2. The three extreme bars, S3, S4, and S5, which fractured in the original test debonded, and the next most extreme bars, S2 and S6, exhibited the highest strains and fractured during the repair test. The north side, however, performed differently due to the removal of concrete around the fractured bars. On the north side, the three originally fractured bars were sufficiently anchored, permitting the bars to reach their ultimate capacity and fracture at the location of the relocated plastic hinge, with little damage to the repair grout in comparison with the south side.

The global force-displacement response of Repair No. 3 and the original column test is shown in Fig. 13. The pinching behavior in the previous repairs was essentially eliminated, indicating a higher energy dissipation for this repair. While softening is still observed, it appears to have been improved, particularly for the negative displacements when the north side with fully anchored bars is in tension.

Figure 14 presents the strains recorded in the S4 and N4 bars and confirms the visual observations. While S4 reached a higher peak strain than the previous tests, at a displacement of 98 mm (3.87 in.), the bar debonded and rapidly lost all load-carrying capacity. In contrast, the N4 bar did not debond and instead performed as typical for a longitudinal bar in a plastic hinge, with strains increasing with larger displacements until bar buckling and eventual fracture.

Having shown that the combination of a thicker jacket and chipping the perimeter concrete is sufficient to fully anchor fractured bars, Repair No. 4 aimed to replicate this on both sides of the column to further evaluate the design approach. The damaged column originally had five fractured bars;

Fig. 12—Damage comparison of: (left) north; and (right) south sides after Repair No. 3 test with loose grout removed.

however, to facilitate comparison, the next extreme bar was cut at the base of the column to provide the same symmetrical damage state as Repair No. 3.

To take the technique one step further, concrete around all the bars on the north side was removed, not just the fractured ones. This theoretically provides the best possible bond between the damaged column and the repair, which should improve the repaired column's response and may help understand the behavior of the repair. Improved bond should theoretically make the response of the repaired column similar to a nominally identical but shorter column.

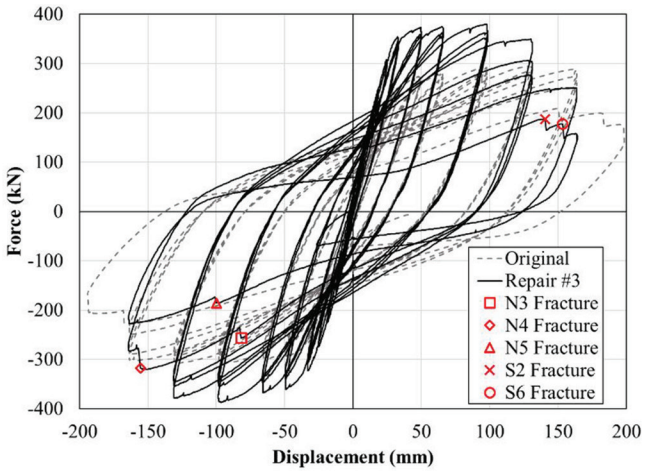

Fig. 13—Force-versus-displacement response of Repair No. 3 and comparison column.

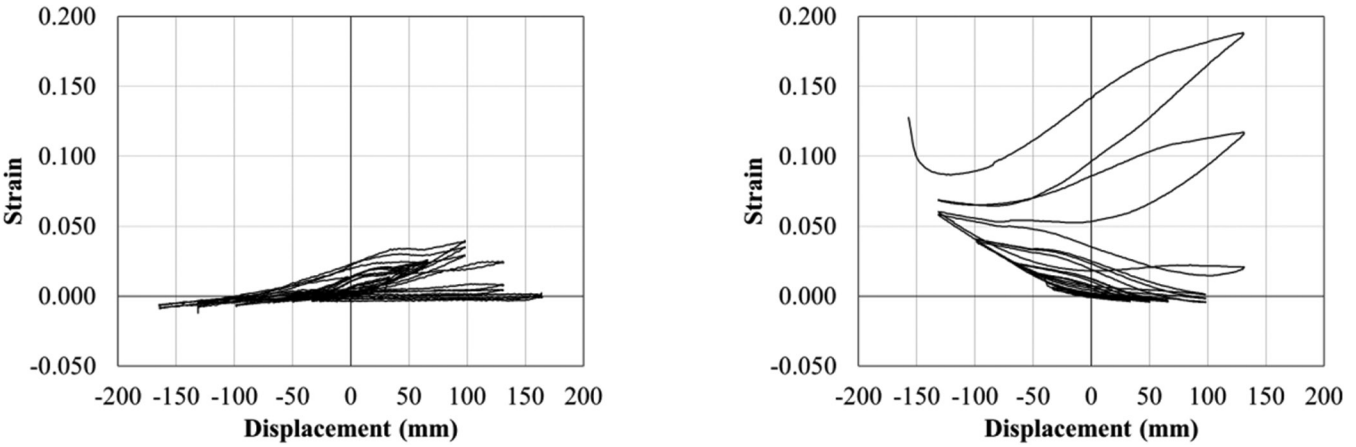

Fig. 14—Strain history of: (a) S4; and (b) N4 in Repair No. 3.

Fig. 15—Damage comparison after Repair No. 4 test with loose grout removed on: (left) north; and (right) south sides.

Verification of this would greatly simplify the design and modeling of the repair.

The final damage states of both sides of the repair are shown in Fig. 15. For both sides of the column, all six previously fractured bars were fully anchored and refractured in the repair test, and the S6 bar fractured as well. The hinge was relocated to above the repair grout, which remained mostly intact.

Figure 16 shows the global force-displacement response of Repair No. 4 compared to Repair No. 1. As with Repair No. 3, the pinching behavior was eliminated and the softening was minimal. Comparatively, the north and south sides responded similarly, indicating that removing the loose concrete around unfractured bars does not provide substantial benefits.

The results of Repair No. 4 confirm the need for the combination of the thicker jacket and removal of perimeter concrete to anchor previously fractured bars.

COMPARISON OF REPAIR PERFORMANCE

In Table 2, the performance of the repaired column is compared with the comparison column. For the maximum displacement (Δ_{max}) and corresponding ductility (μ), the smaller of the displacement prior to first bar fracture or the displacement at a 20% loss in load capacity was used. Of note, for Repairs No. 3 and 4, the positive and negative forces are both given to compare the behavior of the improved bond conditions on the north side of the column. For all four repairs, the repaired column had a larger maximum load but

a lower ductility capacity. This is explained by the repaired column having a shorter effective height, which increases the stiffness of the column, but at the cost of increasing the demand to the plastic hinge.

Also included in Table 2 is the lateral force at Δ_{max}, which serves to compare the softening in the global response described earlier. In the comparison columns, there is only a minor drop in the forces, which is typical for modern, well-designed RC columns. In contrast, the first two repairs show a reduction in load capacity of nearly 20%. This softening has been attributed to debonding of fractured bars within the repair. For Repair No. 3, the bars on the north side did not debond; this explains why, for negative displacements, when these bars are in tension, the softening behavior is similar to the amount observed in the comparison columns. For positive displacements, the softening is in between what was observed in the first two repairs and the comparison columns. This is likely due to the north bars not debonding; however, the thicker steel jacket could have also improved the behavior.

In Repair No. 1, the pinching behavior observed in the global response of the column was concerning because it indicates less energy dissipation which would imply less seismic resistance. It was visually apparent that this was improved in Repair No. 2 through pretensioned bolts, and in Repairs No. 3 and 4, the pinching was essentially eliminated by using the thicker steel jacket along with removal of damaged concrete around the fractured bars.

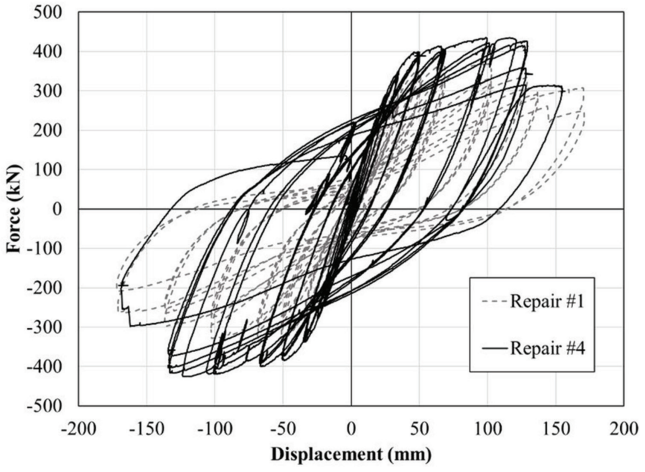

Fig. 16—Force-versus-displacement response of Repair No. 4.

CONCLUSIONS

- The use of a steel jacket with a pretensioned bolted connection is an acceptable repair technique to relocate the plastic hinge. The pretensioned bolts are needed to prevent slip of the plates, which has been shown to weaken the repair.
- It was experimentally shown that the combination of using a thicker steel jacket to increase confinement and replacing the cracked column concrete around fractured bars with fresh repair grout can fully anchor the bars inside the repair. Experimental tests where only one of these methods were used without the other, such as the south side of Repair No. 3, have been incapable of fully anchoring previously fractured bars.
- The repaired column's displacement capacity will inherently be reduced when the bars are fully anchored due to the reduced effective height of the column. When fractured bars debond, the repaired column has more deformation due to strain penetration into the repair and may be capable of maintaining the same displacement capacity as the original column. The trade-off for this additional displacement is a softened and pinched global response.

AUTHOR BIOS

ACI member **Taylor J. Brodbeck** *is a PhD Student in the Department of Civil, Construction, and Environmental Engineering at North Carolina State University, Raleigh, NC, where she received her BS. Her research interests include the behavior of concrete structures.*

ACI member **Zachary A. Shurow** *is a Structural Engineer with Ehlert Bryan. He received his BS and MS from North Carolina State University. His research interests include seismic repair of bridge structures.*

Rudolf Seracino, *FACI, is a Professor in the Department of Civil, Construction, and Environmental Engineering at North Carolina State University. He received his BASc and MASc from the University of Toronto, Toronto, ON, Canada, and his PhD from The University of Adelaide, Adelaide, Australia. He is a member of ACI Committee 440, Fiber-Reinforced Polymer Reinforcement. His research interests include the repair and strengthening of concrete infrastructure using fiber-reinforced polymers.*

ACI member **Mervyn J. Kowalsky** *is a Professor in the Department of Civil, Construction, and Environmental Engineering at North Carolina State University. He received his BS, MS, and PhD from the University of California San Diego, La Jolla, CA. He is Chair of ACI Committee 341, Perfor-*

Table 2—Comparison of repair performance

	Repair No. 1		Repair No. 2		Repair No. 3		Repair No. 4	
	Comparison column	Repaired column	Comparison column	Repaired column	Comparison column	Repaired column	Comparison column	Repaired column
F_{max}, kN (kip)	330 (74)	370 (83)	330 (74)	385 (87)	308 (69)	379/–387 (85/–87)	308 (69)	435/–425 (98/–96)
Δ_{max}, mm (in.)	160 (6.3)	171 (6.7)	160 (6.3)	171 (6.7)	164 (6.5)	131 (5.2)	164 (6.5)	131 (5.2)
μ	6	5	6	5	5	4	5	4
F @ Δ_{max}, kN (kip)	326 (73)	308 (69)	326 (73)	309 (70)	303 (68)	350/–378 (79/–85)	303 (68)	425/–414 (96/–93)
Fractured bars	N2, N3, N4, N5, S3, S4, and S5	S6	N4, N5, S3, S4, and S5	N2, N3, N6, S2, and S6	N3, N4, N5, S3, S4, and S5	N3*, N4*, N5*, S2, and S6	N3, N4, N5, S3, S4, and S5	N4*, S3*, S4*, and S5*

*Indicates refractured bar.

mance-Based Seismic Design of Concrete Bridges. His research interests include earthquake engineering and seismic design of concrete structures.

ACKNOWLEDGMENTS

The authors gratefully acknowledge the support of the Alaska Department of Transportation and Public Facilities. They also wish to thank the technical staff of the Constructed Facilities Laboratory at North Carolina State University for all their guidance and assistance with experiments, as well as the staff of the Department of Biological and Agricultural Engineering Research Shop at North Carolina State University for fabrication of the steel jackets.

NOTATION

A_b	=	area of longitudinal bar
D'	=	core diameter of circular column
D_j	=	diameter of steel jacket
E_{sj}	=	elastic modulus of jacket steel
F	=	force
F_{max}	=	maximum force
F_y'	=	analytical first yield force
f_y	=	specified yield strength
f_{yj}	=	yield stress of jacket steel
f_{yl}	=	yield stress of longitudinal reinforcement
H_{repair}	=	height of repair
l_s	=	length of splice or sleeve
M_n	=	nominal moment capacity
M_y'	=	first yield moment
n	=	number of longitudinal bars
n_{bolts}	=	number of bolts
p	=	perimeter of crack surfaces around bar in lap splice failure
T_b	=	minimum bolt pretension
t_j	=	jacket thickness
Δ_{max}	=	maximum displacement
Δ_y	=	equivalent yield displacement
Δ_y'	=	first yield displacement
μ	=	coefficient of friction
μ	=	ductility level
ρ_{sj}	=	volumetric ratio of confining steel

REFERENCES

ANSI/AISC 360-16, 2016, "Specification for Structural Steel Buildings," American Institute of Steel Construction, Chicago, IL, 676 pp.

ASTM A706/A706M-16, 2016, "Standard Specification for Deformed and Plain Low-Alloy Steel Bars for Concrete Reinforcement," ASTM International, West Conshohocken, PA.

ASTM C39/C39M-18, 2018, "Standard Test Method for Compressive Strength of Cylindrical Concrete Specimens," ASTM International, West Conshohocken, PA.

Hose, Y. D.; Priestley, M. J. N.; and Seible, F., 1997, "Strategic Relocation of Plastic Hinges in Bridge Columns," Caltrans Report No. SSRP-97/05, Division of Structural Engineering, University of California San Diego, La Jolla, CA.

Krish, Z. F.; Kowalsky, M. J.; and Nau, J. M., 2021, "Seismic Repair of Circular Reinforced Concrete Bridge Columns by Plastic Hinge Relocation with Grouted Annular Ring," *Journal of Earthquake Engineering*, V. 25, No. 12, pp. 2371-2405. doi: 10.1080/13632469.2019.1688205

Lehman, D. E.; Gookin, S. E.; Nacamull, A. M.; and Moehle, J. P., 2001, "Repair of Earthquake-Damaged Bridge Columns," *ACI Structural Journal*, V. 98, No. 2, Mar.-Apr., pp. 233-242.

Manhard, R., 2019, "Impact of Grade 80 Reinforcing Steel Production Process on the Seismic Behavior of Bridge Columns," master's thesis, Department of Civil, Construction, and Environmental Engineering, North Carolina State University, Raleigh, NC.

Parks, J. E.; Brown, D. N.; Ameli, M. J.; and Pantelides, C. P., 2016, "Seismic Repair of Severely Damaged Precast Reinforced Concrete Bridge Columns Connected with Grouted Splice Sleeves," *ACI Structural Journal*, V. 113, No. 3, May-June, pp. 615-626. doi: 10.14359/51688756

Priestley, M. J. N.; Seible, F.; and Calvi, G. M., 1996, *Seismic Design and Retrofit of Bridges*, John Wiley & Sons, Inc., New York, NY.

Rutledge, S. T.; Kowalsky, M. J.; Seracino, R.; and Nau, J. M., 2014, "Repair of Reinforced Concrete Bridge Columns Containing Buckled and Fractured Reinforcement by Plastic Hinge Relocation," *Journal of Bridge Engineering*, ASCE, V. 19, No. 8, p. A4013001. doi: 10.1061/(ASCE)BE.1943-5592.0000492

Wu, R. Y., and Pantelides, C. P., 2017, "Rapid Seismic Repair of Reinforced Concrete Bridge Columns," *ACI Structural Journal*, V. 114, No. 5, Sept.-Oct., pp. 1339-1350. doi: 10.14359/51700789

REGISTER TODAY

TECHNOLOGY FORUM

MAY 14-16, 2024, SANTA FE, NM, USA

Hilton Santa Fe - Historic Plaza, 100 Sandoval Street

The **Technology Forum** is an innovation-focused educational and networking event for concrete professionals **powered by the ACI Foundation's Concrete Innovation Council**.

Whether you are an emerging professional or a seasoned veteran, the ACI Foundation Technology Forum is the place to learn about **current trends, emerging technologies, and discoveries within the concrete industry**.

Join us for an exciting and insightful event featuring thought leaders and technology innovators to discuss the future of the concrete industry.

aci Foundation
Building the Future

acifoundation.org

ACI STRUCTURAL JOURNAL TECHNICAL PAPER

Title No. 121-S33

Experimental Study of Concrete Columns Reinforced with Lap-Spliced Glass Fiber-Reinforced Polymer Bars under Seismic Load

by Bahareh Nader Tehrani, Ahmed Sabry Farghaly, and Brahim Benmokrane

While reinforcing bar lap splicing is inevitable in reinforced concrete (RC) structures, it critically affects structural behavior, especially in structures subjected to seismic load. That notwithstanding, current North American design standards do not provide any recommendations or equations for lap-spliced glass fiber-reinforced polymer (GFRP) reinforcing bars under seismic load. This study tested six full-scale RC columns measuring 1850 mm (73 in.) in height and 400 x 400 mm (16 x 16 in.) in cross section under constant axial load and incremental reversed cyclic lateral loading. Four columns were reinforced with GFRP bars, and two were reinforced with steel bars for comparison. The test parameters included lap-splice length and type of reinforcement. The structural performance of the specimens was evaluated based on the cracking behavior, failure mechanism, hysteretic response, load-carrying capacity, dissipated energy, stiffness degradation, and strain behavior. Afterward, available models in North American design standards for the splice length of GFRP reinforcing bars under monotonic loading were evaluated based on the experimental results. According to the results, providing adequate splice length can secure satisfactory structural performance in spliced GFRP-RC columns. The splice length determined based on the North American design standards for monotonic loading cannot, however, be directly used to achieve the required drift capacity in GFRP-RC columns under reversed cyclic lateral loading.

Keywords: concrete columns; design codes; design recommendations; glass fiber-reinforced polymer (GFRP) bars; hysteresis response; lap splice; reversed cyclic loading; seismic performance.

INTRODUCTION

The corrosion of steel reinforcement is a serious problem associated with steel-reinforced concrete (RC) structures. Corrosion eventually leads to the degradation of bond strength and loss of serviceability in RC structures. This problem can be exacerbated in structures exposed to aggressive environments such as deicing salts, moisture, temperature, and freezing-and-thawing cycles. A viable solution is to replace conventional steel reinforcing bars with fiber-reinforced polymer (FRP) reinforcing bars (Laoubi et al. 2006; Robert et al. 2009; Manalo et al. 2020). However, FRP and steel reinforcing bars have different material properties, which should be considered in design approaches. While steel exhibits plastic behavior, FRP composites have linear elastic behavior up to failure. Consequently, FRP-RC structures are not expected to be as ductile as steel-RC structures, which raises concerns in structures prone to seismic loads. Nevertheless, the studies available on concrete columns reinforced with FRP reinforcing bars under seismic load have shown high levels of deformability for these columns in seismic regions (Tavassoli 2013, 2015; Naqvi 2016; Deng et al. 2018; Elshamandy et al. 2018; Kharal 2019; Abdallah and El-Salakawy 2022a,b; Prajapati et al. 2022a,b, 2023).

Furthermore, the bond behavior of FRP reinforcement is different than that of steel reinforcing bars (Chaallal and Benmokrane 1993; Aly et al. 2006; Baena et al. 2009; Asadian et al. 2019). Reinforcing bar lap splicing is unavoidable in field applications. The ductility, energy dissipation, and flexural capacity of RC columns can be affected when lap-spliced reinforcing bars are in the plastic-hinge zone. However, the lap splicing of longitudinal reinforcing bars at the bottom of columns is more convenient. Adequate splice length should be provided to develop the elastic strains required in areas of severe seismic activity to avoid slippage and bond failure (Lukose et al. 1982; Kim et al. 2018, 2019).

Based on ACI 440.1R-15, the splice length of FRP reinforcing bars depends on reinforcing bar tensile stress, concrete compressive strength, concrete cover, bar spacing, bar location, and bar diameter. In addition to the mentioned parameters, CAN/CSA S806-12 (R2021) considers concrete density, type of fiber, and reinforcing bar surface condition. Nonetheless, there are no seismic provisions for concrete elements reinforced with lap-spliced FRP reinforcing bars. This is while the splice strength of reinforcing bars deteriorates to a greater degree under reversed cyclic loading than monotonic loading (Lukose et al. 1982). It is worth noting that several studies (Mosley et al. 2008; Pay et al. 2014; Basaran and Kalkan 2020) have highlighted the significant influence of the reinforcement's modulus of elasticity on bond strength. Specifically, increasing the reinforcement's modulus of elasticity is known to increase bond strength. ACI 440.1R-15, however, does not take into account the type of fiber in its equation. In addition, ACI 440.1R-15 disregards the effect of surface properties on splice length. Nonetheless, the splice length of FRP reinforcing bars can be considerably affected by various surface properties such as sand coating, grooved, helically wrapped, and ribbed (Esfahani et al. 2013; Basaran and Kalkan 2020; CAN/CSA S806-12).

ACI Structural Journal, V. 121, No. 3, May 2024.

MS No. S-2022-429.R1, doi: 10.14359/51740460, received August 13, 2023, and reviewed under Institute publication policies.

Another important issue affecting lap-splice performance is stress distribution as a result of the flexural moment and shear force along the length of the structural element (Kim et al. 2018, 2019). The lap-splice length in current design standards was developed based on the uniform distribution of bond stress along beams. Unlike in beams, which have uniform moments, the moment gradient occurs in columns subjected to lateral loading. Thus, the bond demand changes along the splice length in columns. In addition, the presence of shear force in columns is not considered in current standards, which can exacerbate bond-splitting cracks in the lap-splice region.

Extensive research projects have been conducted on the tensile splicing of FRP reinforcing bars in beams (Mosley et al. 2008; Esfahani et al. 2013; Pay et al. 2014; Zemour et al. 2019; Basaran and Kalkan 2020). However, limited work has been done on investigating lap-spliced GFRP reinforcing bars in RC columns (Naqvi 2016; Tabatabaei Kashani 2019). Tabatabaei Kashani (2019) conducted a study on the compression splicing of glass FRP (GFRP) bars in circular concrete columns subjected to monotonically increasing concentric loading. The research aimed to assess the impact of various factors, including splice length, confinement, concrete compressive strength, bar diameter, and reinforcement type (steel and GFRP), on the strength of spliced GFRP bars. The investigation involved testing 30 large-scale RC columns. Their findings revealed that the GFRP bars required a shorter splice length than the steel bars. Moreover, increasing the level of confinement and concrete compressive strength improved the bond strength of the GFRP bars. Additionally, longitudinal bars with larger bar diameters required longer splice lengths. Naqvi (2016) investigated GFRP-RC columns with lap splices subjected to combined axial and reversed cyclic loading. The research involved the construction of 10 full-scale specimens to investigate various parameters, including reinforcement type, splice length, confinement, axial load level, and the use of steel fiber-reinforced concrete (SFRC). The study found that splice lengths of 40 and 50d_b were inadequate for transferring the full bond forces, resulting in splitting cracks and bond slippage. This bond slippage led to a decrease in the lateral strength of the columns. A splice length of 60d_b, however, effectively transferred the full bond stress along the splice length. As the axial loads increased, column deterioration became more pronounced. Despite the significant damage incurred, the columns maintained their load-carrying capacity at large drift ratios. The incorporation of SFRC in specimens with inadequate splice length improved energy dissipation and maximum lateral strength. The spacing of transverse reinforcement was found to have no significant effect on bond transfer between spliced bars.

RESEARCH SIGNIFICANCE

The literature has not thoroughly investigated the seismic response of lap splices in GFRP-RC elements. Due to insufficient research data and relevant discussion, current standards contain no specific recommendations for lap splicing GFRP reinforcing bars in structural elements subjected to seismic load. Therefore, a significant demand exists for a study investigating the performance of lap-spliced GFRP reinforcing bars in columns subjected to seismic load. This study attempted to fill the gap in the literature concerning the seismic performance of lap-spliced GFRP reinforcing bars. The splice length and bar type were investigated to evaluate the response of the tested RC columns under seismic load. The results were compared to the current provisions in ACI 440.1R-15 and CAN/CSA S806-12 for the splice length of GFRP reinforcing bars under monotonic loading. The results reported in this paper represent an important contribution to the literature. They provide engineers and code committees with much-needed data and recommendations to advance the use of GFRP reinforcement in RC concrete columns and to extend the design and code provisions related to GFRP reinforcement for concrete structures subjected to seismic load.

EXPERIMENTAL PROGRAM

Specimen details

Six square RC columns were constructed and tested under constant axial and reversed cyclic lateral loadings. The test matrix consisted of two specimens reinforced with steel reinforcing bars for comparison and four specimens reinforced with GFRP reinforcing bars. The columns measured 400 x 400 mm (16 x 16 in.) in cross section and 1850 mm (73 in.) in length. All specimens were connected to a 1200 x 1200 x 600 mm (47 x 47 x 24 in.) stub. The column specimens represent a column between the maximum moment section and the contraflexure point. Splice length and reinforcing bar type were the variables investigated in this study.

Table 1 lists details of the test specimens. The alphanumeric notations used for specimen designation are as follows: the first letter indicates the reinforcing bar type (G for GFRP and S for steel); Lx denotes the provided lap-splice length (25, 35, or 45d_b); and C is for specimens with continuous reinforcing bars. Figure 1 presents the reinforcement details for the various specimens. The design of the GFRP-RC specimens was based on the relevant clauses in CSA S806-12, where applicable. The columns were designed in flexure such that the failure of specimens was initiated by concrete crushing. The contribution of the GFRP bars in compression was not taken into account. Moreover, the steel-RC specimens were designed according to ACI 318-19 and CSA A23.3-19. The longitudinal reinforcement ratio was 1.6% in all specimens, which is higher than the minimum longitudinal reinforcement ratio of 1.0% specified in ACI 318-19 and CSA A23.3-19 for steel-RC and in CSA S806-12 for GFRP-RC columns. The specimens were designed in such a way that shear failure was prevented during testing to focus specifically on bond performance without the influence of shear failure. A spiral pitch of 100 mm (4 in.) was used for all specimens with No. 4 transverse reinforcement. The spiral pitch was selected based on CSA S806-12 provisions, which specify that the spacing of transverse reinforcement should not exceed the minimum of one-quarter of the minimum column dimension 6d_b or 150 mm (6 in.). A clear concrete cover of 25 mm (1 in.) was considered from the surface of the spiral reinforcing bars. Table 1 presents the specimens'

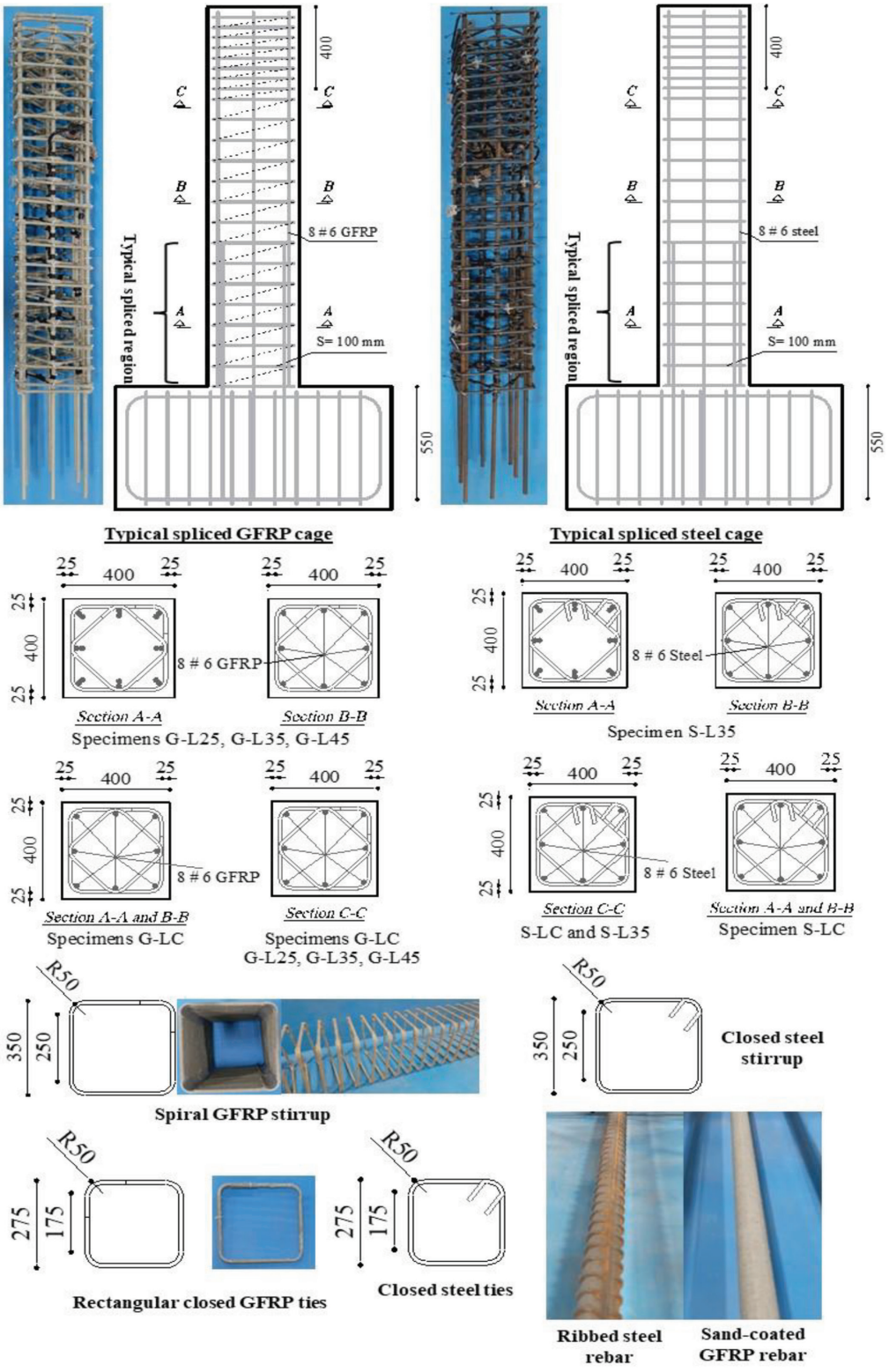

Fig. 1—Reinforcement details of test specimens. (Note: Dimensions in mm; 1 mm = 0.0394 in.)

theoretical flexural and shear capacity based on CAN/CSA S806-12 and ACI 440.1R-15.

Material properties

All GFRP reinforcing bars used in this research program were sand-coated Grade III and high modulus. These GFRP bars were made with boron-free EC-R glass fibers impregnated with vinylester resin in accordance with CAN/CSA S807-19 (Pultrall 2020). Furthermore, the chemical composition of the sand used as the coating of the GFRP bars employed in this study has been presented elsewhere (Mohamed et al. 2020). Straight No. 6 GFRP reinforcing bars were used as longitudinal reinforcement; No. 4 GFRP ties and spirals served as transverse reinforcement. Table 2 presents the material properties as provided by the manufacturer. Note that the manufacturer followed the test methods

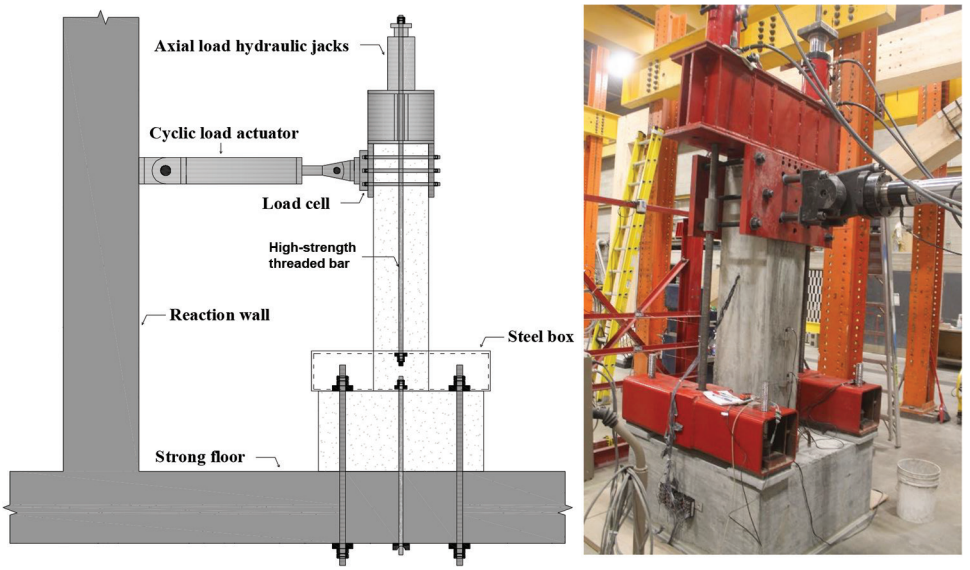

Fig. 2—Schematic illustration of test setup.

Table 1—Details of specimens

Bar type	Specimen designation	Longitudinal reinforcement	Splice length	Stirrup spacing, mm	Axial load, $P/A_g f_c'$	Analytical flexural capacity, kN		Analytical shear capacity, kN	
						CSA S806	ACI 440.1R	CSA S806	ACI 440.1R
GFRP	G-LC	8 No. 6	Continuous	100	20	167	164	277	233
	G-L25	8 No. 6	$25d_b$	100	20	170	166	280	233
	G-L35	8 No. 6	$35d_b$	100	20	170	166	280	233
	G-L45	8 No. 6	$45d_b$	100	20	167	164	277	233
Steel	S-LC	8 No. 6	Continuous	100	20	207	208	507	400
	S-L35	8 No. 6	$35d_b$	100	20	207	208	507	400

Note: 1 mm = 0.0394 in; 1 kN = 0.225 kip.

in ASTM D7205/D7205M-21 and CAN/CSA S807-19. Straight M20 steel reinforcing bars and M10 steel stirrups were used as longitudinal and transverse reinforcement in the column part of the steel-RC specimens. Table 2 lists the properties of the steel reinforcing bars as provided by the manufacturer.

A target 28-day concrete compressive strength of 35 MPa (5.1 ksi) was chosen for the column part of the specimens, but the compressive strength of the concrete for the stub part was designated as 50 MPa (7.3 ksi). To simulate the field conditions, the column part was cast later than the stub. Three 100 x 200 mm (4 x 8 in.) cylinders were tested on the day of testing for each specimen to determine the actual concrete compressive strength of the specimen, as reported in Table 3.

Test setup and loading procedure

The specimens were placed vertically and subjected to constant axial load and quasi-static cyclic lateral load using the testing setup at the structural laboratory of the University of Sherbrooke. An axial load equal to 20% of the column axial capacity $A_g f_c'$ was applied to the specimens using two hydraulic jacks with an individual capacity of 980 kN (220 kip). The load was applied through a rigid steel beam located on top of the column and transferred with two high-strength threaded steel reinforcing bars with a diameter of 66 mm (2.6 in.) placed on both sides of the column. The lateral displacement cycles were applied with an MTS hydraulic actuator with a 500 kN (112 kip) load and 250 mm (10 in.) stroke capacity. The lateral actuator was attached to the strong reaction wall of the laboratory and was connected to the column with two plates and six 40 mm (1.6 in.) high-strength threaded rods. Figure 2 shows the test setup.

The loading procedure followed the provisions in ACI 374.2R-13 (Fig. 3). Each cyclic loading step included two identical excursions up to a drift ratio of 4.0%. After that point, one excursion was applied for each drift ratio until failure. ACI 374.2R-13 recommendations indicate that loading should be continued until an approximate drift ratio of 4.0%. In contrast, the cyclic tests in this study continued beyond this drift ratio until failure occurred.

Instrumentation

A total of 12 linear variable displacement transformers (LVDTs) were used during each test (Fig. 4). The lateral displacement of columns at 100, 400, 700, and 1650 mm (3.9, 15.7, 27.6, and 65.0 in.) from the column-footing interface was measured with four LVDTs mounted horizontally along the length of the columns. Six LVDTs were installed vertically on both sides of the columns to record the columns'

curvature. Two LVDTs were used to monitor the sliding at the column-stub connection and between the stub and rigid floor. Figure 5 gives the locations of strain gauges on all the specimens. The specimens with lap-spliced reinforcing bars had 12 strain gauges installed on the longitudinal reinforcing bars. The specimens with continuous reinforcing bars had only six strain gauges, which were placed on two opposite longitudinal reinforcing bars at the same level as the specimen with a splice length of $35d_b$.

EXPERIMENTAL RESULTS AND DISCUSSION

General behavior and failure mechanism

GFRP-RC columns—Figures 6(a) to (d) show the cracking pattern at a drift ratio of 1.5%, plastic-hinge zone, and failure details of the GFRP-RC specimens. It should be noted that the photographs of the plastic-hinge zone and failure details of the specimens were taken after testing. After the loads had been applied according to the prescribed procedure, the columns took the loads with no sign of cracks up to a drift ratio of 0.5%. At this point, the first flexural crack in the GFRP-RC specimens was observed at a load range of 100 to 120 kN (22 to 27 kip). As the drift ratio increased, further cracks appeared on average at up to 950 mm (37 in.) of the column height. In addition, the cracks developed toward the lateral face of the columns (parallel to load application).

In Specimen G-L25, the splitting crack occurred at a drift ratio of 1.0% near the side reinforcing bar region, demonstrating the bond-slip of the spliced reinforcing bars. None of the other GFRP-RC specimens had signs of a splitting crack. Spalling of the concrete cover was initiated in all the GFRP-RC specimens at a drift ratio of 1.5%. Beyond this drift ratio, more deterioration became evident until concrete crushing failed, followed by the compression failure of longitudinal GFRP reinforcing bars (Fig. 7(a)). It should be noted that G-L25 experienced much greater damage and deterioration than the other GFRP-RC specimens. The lengths of the most damaged zones in G-LC, G-L25, G-L35, and G-L45 were 450, 750, 1050, and 1260 mm (17.7, 29.5, 41.3, and 49.6 in.), respectively. In addition, more cracks with closer spacing were observed in specimens reinforced with spliced reinforcing bars than in specimens without lap-spliced reinforcing bars.

Steel-RC columns—The first flexural crack in the steel-RC specimens occurred at a drift ratio of 0.25% at a load range of 88 to 90 kN (19.8 to 20.2 kip). As the drift ratio increased, more cracks appeared at up to 800 and 1100 mm (31.5 and 43.3 in.) of the column height in S-LC and S-L35, respectively (Fig. 6(e) and (f)). Gradual concrete cover spalling occurred at 1.0% and 1.5% drift ratios in S-LC and S-L35, respectively. In specimen S-LC, longitudinal reinforcing bars began buckling at a drift ratio of 2.5%. The failure of this specimen occurred in subsequent cycles as concrete crushing followed by rupture of longitudinal reinforcing bars in the tension zone (Fig. 6(e)). In S-L35, longitudinal reinforcing bars began buckling at a drift ratio of 6.0%. The fact that buckling occurred later in S-L35 than in S-LC can be attributed to the role of the column reinforcing bar as the dowel reinforcing bar providing side support when the bars are stacked together in the spliced region. This specimen's

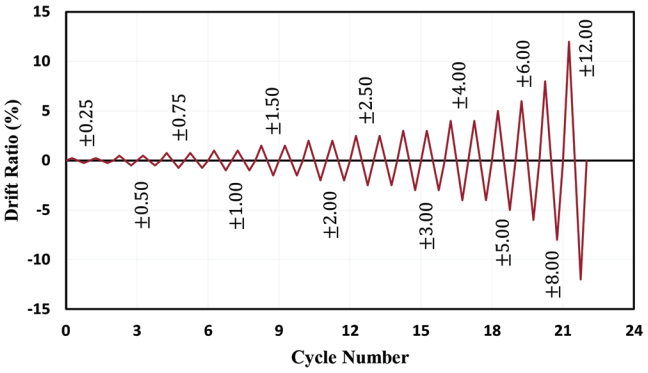

Fig. 3—Loading history.

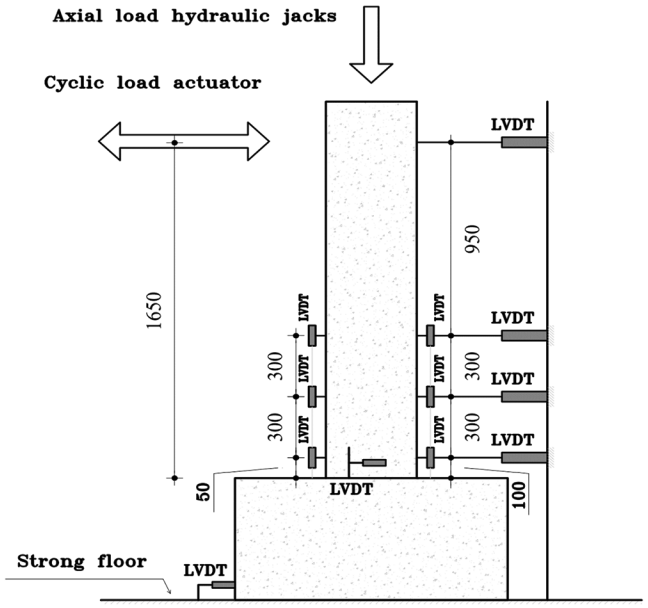

Fig. 4—Location of LVDTs. (Note: Dimensions in mm; 1 mm = 0.0394 in.)

failure was characterized by severe crushing of the concrete cover, followed by rupture of longitudinal reinforcing bars in the tension zone at a drift ratio of 12.0% (Fig. 6(f) and 7(b)). Note that the rupture of the reinforcing bars in the steel-reinforced specimens was visually observed during testing, as shown in Fig. 7. The lengths of the most damaged zone were 350 and 260 mm (13.8 and 10.2 in.) in S-LC and S-L35, respectively. In contrast to the GFRP-RC columns, using a lap splice reduced the length of the most damaged zone in the steel-RC columns.

Hysteretic response and load-carrying capacity

Figure 8 presents the load-displacement hysteretic responses of all the specimens. In addition, the theoretical flexural capacity calculated based on CAN/CSA S806-12 is represented as the horizontal dashed line. The GFRP-RC specimens had nearly linear elastic behavior at the initial drift ratios, followed by inelastic behavior due to concrete deterioration. Specimen G-LC experienced partial strength degradation due to concrete spalling at a drift ratio of 1.5%, followed by a second peak load at a drift ratio of 4.0%. Concrete deterioration and compression failure of

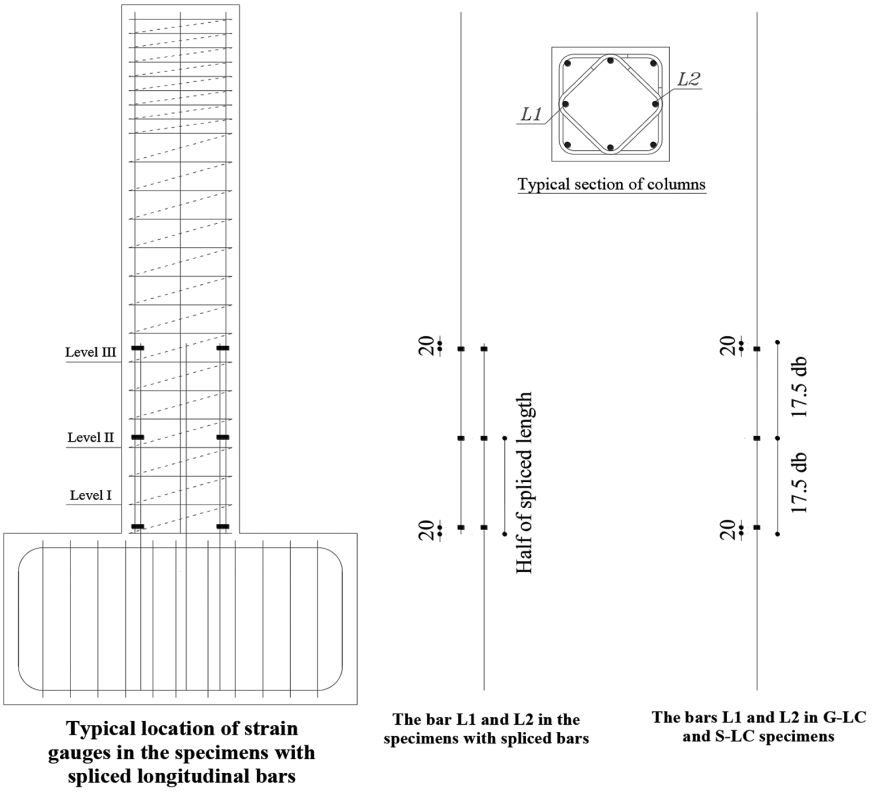

Fig. 5—Location of strain gauges. (Note: Dimensions in mm; 1 mm = 0.0394 in.)

Table 2—Mechanical properties of reinforcement

Reinforcing bar type		Effective diameter, mm	Effective cross-sectional area, mm^2	Nominal cross-sectional area, mm^2	Tensile strength, MPa	Tensile modulus, GPa	Ultimate strain, %
Straight GFRP		19.07	323	285	1399	65	2.2
Bent GFRP	Straight portion	12.7	151	126.7	1570	63	2.5
	Bent portion				801	—	
Straight steel		19.5	300	284	414	200	0.2*
Steel stirrups		11.3	100	100	414	200	0.2*

*Yield strain.

Note: 1 mm = 0.0394 in.; 1 mm^2 = 0.00155 in.^{2}; 1 MPa = 0.145 ksi.

longitudinal reinforcing bars caused strength degradation at the remaining drift ratios.

Concrete spalling in G-L25 caused a load reduction at a drift ratio of 1.5%. Although no further cracking or spalling of the concrete was observed up to a drift ratio of 2.5%, the load could not be recovered due to slippage of the spliced reinforcing bars. Thereafter, the load decreased until failure due to crack propagation and the extended concrete spalling zone.

Spalling of the concrete in specimen G-L35 reduced the load at a drift ratio of 1.5%. The load recovered up to a drift ratio of 4.0%. In subsequent drift ratios, lateral load reduction was observed, attributing to concrete deterioration, buckling of longitudinal reinforcing bars, and splice slippage.

The load reduction due to concrete spalling at a drift ratio of 1.5% was not considerable in G-L45, which reached a peak load at a drift ratio of 4.0%. A gradual load reduction occurred in the subsequent cycles.

Nearly linear behavior was observed in the steel-RC specimens prior to the yielding of longitudinal reinforcement, resulting in nonlinear hysteretic behavior with a gradual load reduction. The load reduction was gradual because the load did not increase much after the reinforcement yielded, so the concrete spalling occurred gradually. As the drift ratio increased, the load decreased until failure.

Figure 9 shows the envelope of the hysteretic response of the tested specimens. According to this figure, the lateral load on G-L25 was lower than on the other GFRP-RC specimens at all drift ratios. Specimens G-L35 and G-LC, however, had almost similar load-drift trends until failure. Specimen G-L45 had greater load-carrying capacity than the other GFRP-reinforced specimens.

Specimen S-L35 recorded a greater lateral load at all drift ratios than S-LC, showing that the provided splice length was adequate. The steel-RC specimens recorded greater load-carrying capacity than the GFRP-RC specimens at a drift ratio of 1.5% due to the steel bars having a higher

Fig. 6—Cracking patterns at drift ratio of 1.5%, most-damaged zone, and failure details of tested columns.

modulus of elasticity than the GFRP reinforcing bars. In contrast to G-LC and G-L35, which recovered the lateral load, S-LC and S-L35 were unable to do so when the drift ratio increased.

Table 3 presents the key results, including lateral load-carrying capacity in two loading directions, the drift ratio corresponding to peak load, load-carrying capacity at failure, the drift ratio corresponding to failure, the load at drift ratios of 1.5 and 4.0%, and lateral load reduction at the drift ratio of 4.0%. In this study, failure was defined as 20% post-peak strength degradation or extensive specimen damage, whichever occurred first. According to Table 3, the GFRP-RC columns with lap splicing (G-L25, G-L35, and G-L45) had load-carrying capacities of 6%, 7%, and 8% higher, respectively, than the control without splicing specimen (G-LC) at a drift ratio of 1.5%. This could be attributed to the greater reinforcement ratio in the spliced zone of the lap-spliced specimens. At a drift ratio of 4.0%, Specimen G-L25 had a 16% lower lateral load than G-LC (based on the average values for pull and push loads). Furthermore, while G-LC did not show strength degradation until a drift ratio of 4.0%, G-L25 experienced a 17% reduction in lateral load-carrying capacity. This implies that the provided splice length in G-L25 was inadequate to develop the required stress after a drift ratio of 1.5%. The lateral load-carrying capacities of G-L35 and G-L45 were 6% and 15% greater than that of G-LC at a drift ratio of 4.0% with minimal strength degradation. This enhancement in flexural strength can be due to a higher reinforcement ratio in the critical zone near the column-beam joint, which is generally undesirable for optimal seismic performance.

In the case of the steel-RC specimens, lap splicing enhanced specimen load-carrying capacity and the drift corresponding to failure by 8% and 50%, respectively. The literature consistently supports that the load-carrying capacity is enhanced when the splice length is sufficient (Bournas and Triantafillou 2011; Kim et al. 2018; Pam and Ho 2010). Note that both S-LC and S-L35 had similar lateral load reductions at a drift ratio of 4.0%.

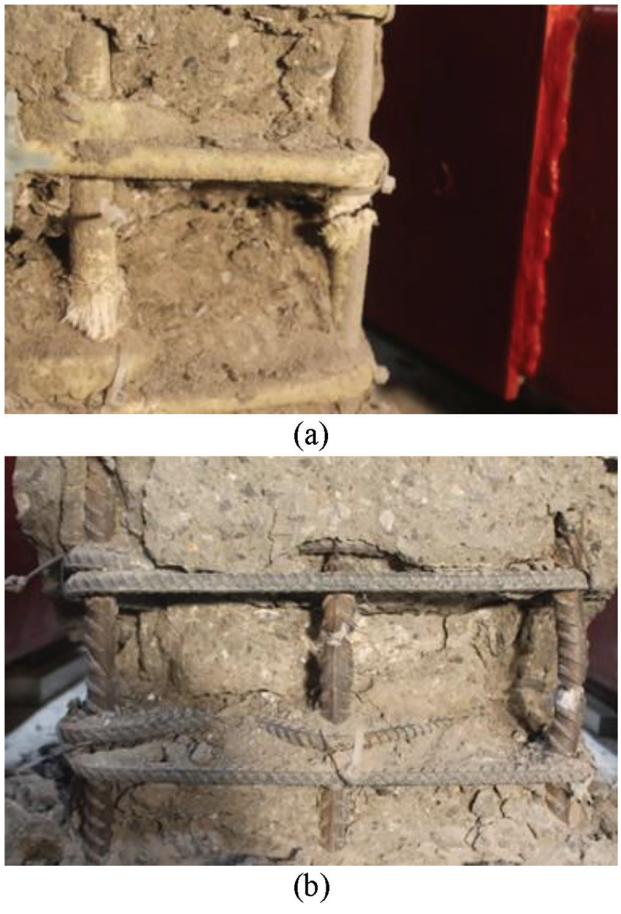

Fig. 7—Typical fracture surface of reinforcing bars: (a) GFRP; and (b) steel.

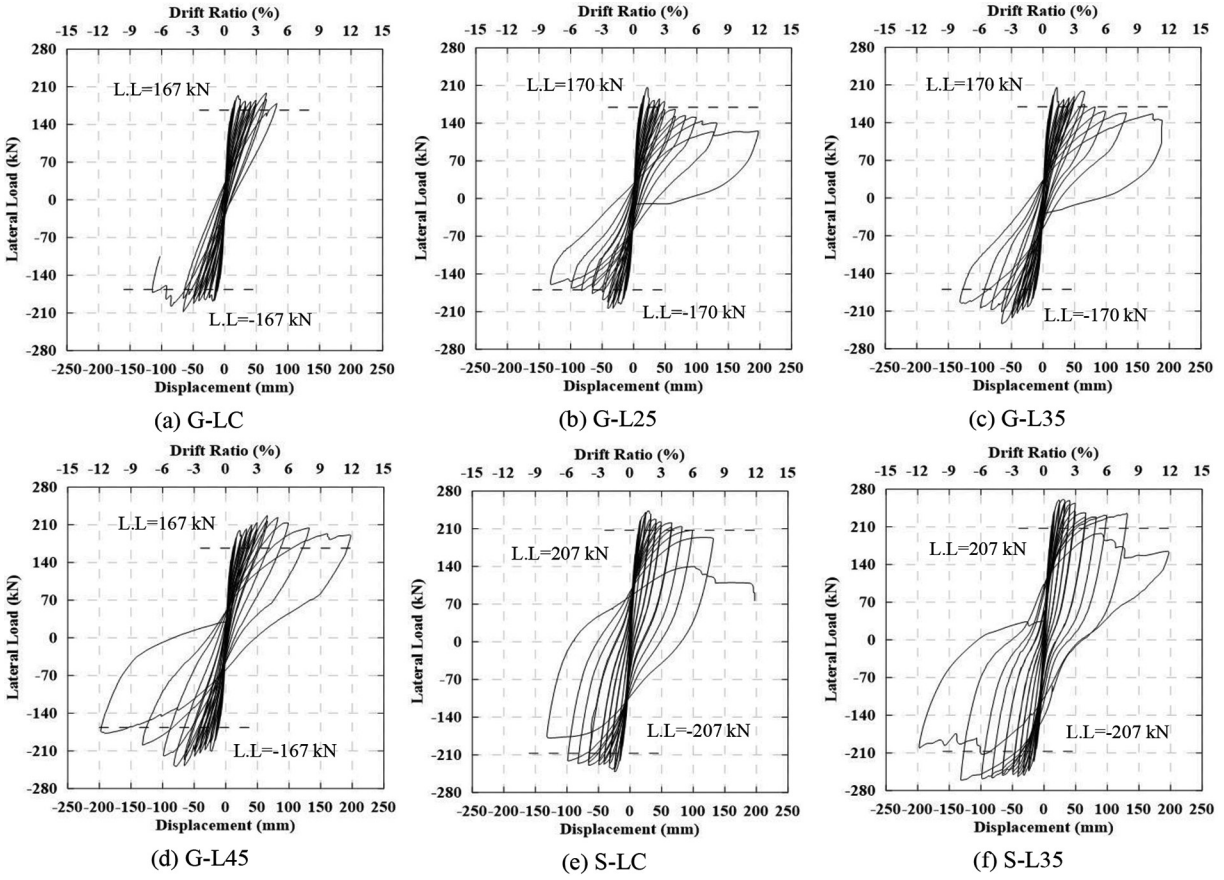

Fig. 8—Hysteretic curves of specimens. (Note: 1 mm = 0.0394 in.; 1 kN = 0.2248 kip.)

Energy dissipation

Energy dissipation is defined as the area under the load-displacement hysteretic loop. Summing the quantities of energy dissipated in consecutive loops throughout the test yields accumulated energy dissipation. Figure 10 shows the accumulative energy dissipation of the tested specimens. All the steel-RC specimens almost had the same energy dissipation before the drift ratio corresponded to the yield of steel reinforcing bars. Energy dissipation in the GFRP-RC columns was generally governed by concrete inelastic deformation (Hassanein et al. 2020). This held true while the yielding of steel reinforcement made the main contribution to energy dissipation in the steel-RC specimens, leading to higher energy dissipation capacity than in the GFRP-RC columns. Dissipated energy in the GFRP-RC specimens followed the same trend until a drift ratio of 6.0%, showing that lap splicing of the GFRP reinforcing bars had minimal effect on the energy-dissipation capacity of the columns at the target drift ratios (the maximum allowable drift ratio of 4.0% for columns subjected to seismic load according to CAN/CSA S806-12). The specimens with longer lap splices dissipated more energy at the following drift ratios, which could be attributed to their greater load-carrying capacity. In addition, while S-LC and S-L35 had almost similar energy dissipation values up to a drift ratio of 6.0%, S-L35 demonstrated greater energy-dissipation capacity at the subsequent drift ratios. This can be attributed to its higher load-carrying capacity at those drift ratios.

Ductility

The ductility level of the steel-reinforced specimens was quantified using the displacement ductility index μ_Δ, as defined by Kharal (2019). The calculation process is outlined as follows

$$\mu_\Delta = \Delta_u/\Delta_y \quad (1)$$

where Δ_u was calculated based on the lateral deflection corresponding to either the post-peak load of $0.8V_{max}$ or column failure, whichever was smaller. The yield deflection Δ_y was determined by the intersection of V_{max} with a line connecting the origin and the pre-peak load of $0.65V_{max}$ in the load-displacement curve.

For the GFRP-reinforced specimens, μ_Δ was calculated as follows

$$\mu_\Delta = \Delta_u/\Delta_e \quad (2)$$

The point at which the secant stiffness at 65% of the maximum load reached the maximum load was defined as the elastic displacement Δ_e (Elshamandy et al. 2018).

Table 4 lists the calculated μ_Δ for the test specimens. The ductility for the GFRP-reinforced specimens was relatively smaller compared to that of the steel-reinforced specimens. As the results show, inadequate splice length can diminish the ductility. In contrast, using a sufficient splice length enhanced the ductility in G-L45.

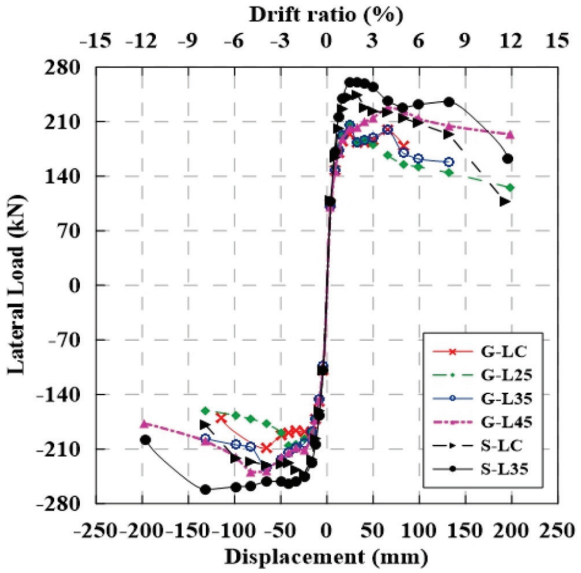

Fig. 9—Envelopes of hysteretic curves. (Note: 1 mm = 0.0394 in.; 1 kN = 0.2248 kip.)

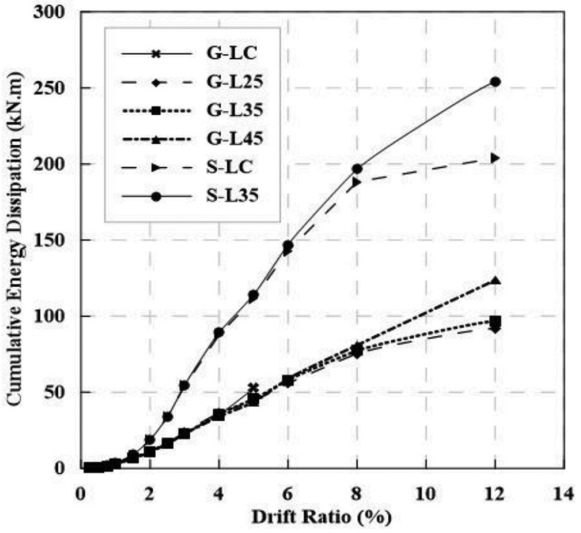

Fig. 10—Cumulative energy dissipation of all columns. (Note: 1 kN.m = 0.7376 kip.ft.)

Stiffness degradation

The slope between the peak points associated with the push and pull direction in each cycle is defined as secant stiffness. Figure 11 presents the stiffness degradation for the tested specimens. As shown in the figure, the rate of stiffness degradation decreased when the drift ratio increased. Rapid stiffness degradation at the initial drift ratios was due to the conversion of the uncracked section of the columns to the cracked section. The GFRP-RC specimens had an almost equal value of stiffness up to a drift ratio of 1.0%. After that, the stiffness degradation was more pronounced in G-L25 but less noticeable in G-L45. This observation indicates that the splice length in G-L45 was adequate, while it was inadequate in Specimen G-L25. Specimen S-L35 generally showed marginally greater stiffness than S-LC, which can be attributed to the stiffness provided by the higher reinforcement ratio in the spliced regions. In addition, the stiffness

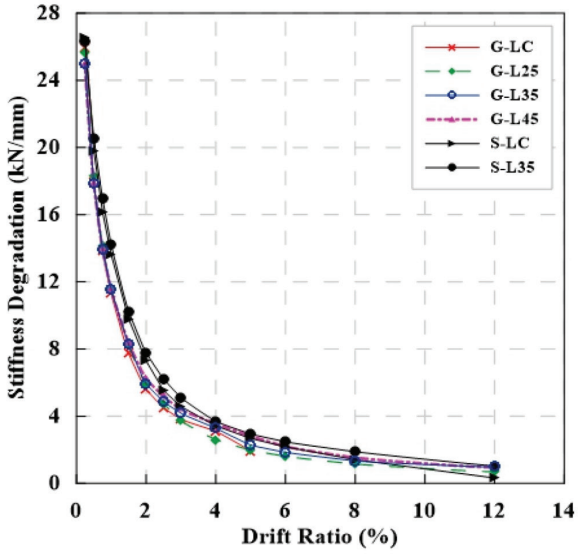

(a)

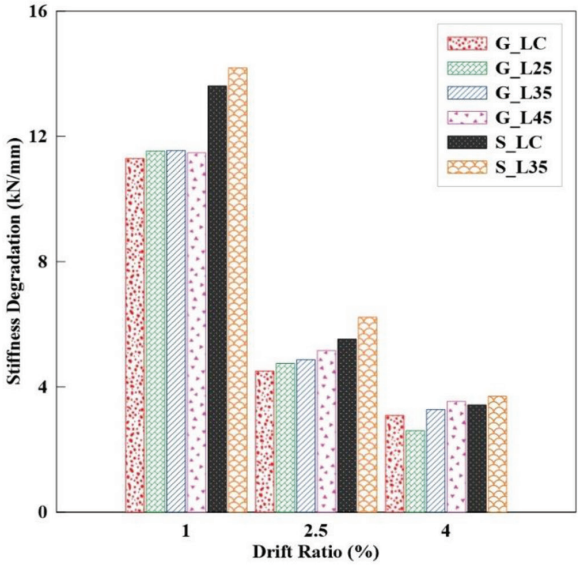

(b)

Fig. 11—Stiffness degradation curves for all test specimens. (Note: 1 kN/mm = 5.7 kip/in.)

degradation rate was higher in S-LC than S-L35. The stiffness of the steel-RC specimens was, on average, 24% higher than their GFRP-RC counterparts. This can be attributed to the higher modulus of elasticity of the steel reinforcing bars compared to the GFRP reinforcing bars. Moreover, the rate of stiffness degradation was higher in the steel-RC specimens than the GFRP-RC ones due to the yielding of the steel reinforcement, which is consistent with the findings of Deng et al. (2018).

Strain analysis

Figure 12 shows the strain distribution along the height of the longitudinal reinforcing bars corresponding to 0.75% to 4.0% drift ratios for the tested specimens. The strains in the column reinforcing bar and dowel reinforcing bar are plotted separately for each specimen with spliced reinforcing bars.

Table 3—Summary of test results

Specimen	Concrete strength, MPa	Maximum lateral load, kN		Failure lateral load, kN	Lateral load at 1.5% drift, kN		Lateral load at 4.0% drift, kN		Lateral load reduction at 4.0% drift, %
		Push	Pull		Push	Pull	Push	Pull	
G-LC	43	199 at 4.0%	–208 at 4.0%	–180 at 5.0%	194	–188	199	–208	0
G-L25	44	207 at 1.5%	–205 at 2.5%	166 at 4.0%	207	–197	166	–177	17
G-L35	44	206 at 1.5%	–234 at 4.0%	165 at 8.0%	206	–203	199	–234	2
G-L45	43	228 at 4.0%	–239 at 5.0%	187 at 12.0%	200	–212	228	–239	0
S-LC	45	244 at 2.0%	–242 at 1.5%	–194 at 8.0%	241	–242	221	–230	7
S-L35	43	261 at 2.0%	–262 at 8.0%	–209 at 8.0%	261	–245	236	–252	7

Note: 1 MPa = 145 psi; 1 kN = 0.225 kip.

Table 4—Displacement ductility index and strain in stirrups and longitudinal bars

Specimen	Δ_u, mm		Δ_e or Δ_y, mm		μ_Δ			Maximum strain at 2% drift		Maximum strain at 4% drift	
	Push	Pull	Push	Pull	Push	Pull	Ave.	Stirrups*	Longitudinal bars†	Stirrups	Longitudinal bars
G-LC	82.4	84.9	9.0	9.2	9.2	9.2	9.2	753	5987	3911	9196
G-L25	66.0	82.5	9.5	9.2	6.9	9.0	8.0	1082	5229	1607	4839
G-L35	88.0	131.9.	10.1	13.0	8.7	10.1	9.4	1220	6372	1608	7128
G-L45	156.7	155.0	12.1	14.2	13.0	10.9	11.9	904	7865	1665	—
S-LC	130.0	121.0	12.0	12.0	10.8	10.1	10.5	436	5201	645	—
S-L35	131.8	131.9	12.5	13.5	10.5	9.8	10.2	389	4661	412	—

*Strain at midheight of lap-spliced region.

†Strain in dowel bar at column-stub interface for lap-spliced specimens.

The strain distribution in Specimens G-LC and S-LC was at the same height level as in G-L35 and S-L35. In addition, the maximum strain recorded in the stirrups and longitudinal bars at drift ratios of 2 and 4% is listed in Table 4 for the tested specimens.

In Specimens G-LC and S-LC, the longitudinal reinforcing bar strain decreased when the height level was increased in a nearly linear trend because of the moment gradient. Something similar occurred in the columns with spliced reinforcing bars: the dowel reinforcing bar strain decreased with increasing height level because of the stress transferring from the dowel reinforcing bar to the column reinforcing bar and the moment gradient. At the intersection of the column and stub, the longitudinal reinforcing bar strain in G-LC and the dowel reinforcing bar strain in G-L45 increased with increasing drift ratio, revealing the sufficiency of the splice length in Specimen G-L45. The strain remained almost constant in G-L35 after a drift ratio of 3.0%. In G-L25, it increased up to a 3.0% drift ratio and then decreased. In addition, Table 4 indicates that increasing the lap-splice length increased the maximum strain in the longitudinal dowel bars, which shows that increasing the length yielded an improvement in the stress-transferring mechanism.

At the midheight of the splice length, the strain kept increasing in G-LC, G-L35, G-L45, S-LC, and S-L35, but decreased in G-L25 after a 3.0% drift ratio. This could be attributed to the splice length $25d_b$ being inadequate to transfer the loads and strains. That would have resulted in a lower load-carrying capacity than that of the control specimen G-LC and more localized concrete spalling over the splice length. On the other hand, Specimen G-L45 was able to transfer the load through its splice length and achieved higher load-carrying capacity than the control specimen (G-LC).

According to Paulay et al. (1981) and Lukose et al. (1982), when the strain at the middle of the spliced length of the column reinforcing bar is sufficiently greater than the developed strain at the bottom and top of that reinforcing bar, the splice length is adequate. The strain distribution along the height of the column reinforcing bar given in Fig. 12 shows increasing strain values with the increase in the height level in G-L25. In the case of G-L35, the maximum strain was observed at the midheight of the splice length of the column reinforcing bar up to a drift ratio of 2.5%. After that, the strain increased when the level height increased. The maximum strain in the column reinforcing bar occurred at midheight of the reinforcing bar in G-L45 and S-L35. Therefore, the provided splice length was adequate in G-L45 and S-L35 but not in G-L25. In the case of G-L35, it can be inferred that the provided length was not adequate to transfer the stress after a drift ratio of 2.5%. Despite S-L35 and G-L35 having identical lap-splice lengths, the results demonstrated the adequacy of the splice length in S-L35. This confirms that the steel reinforcing bars had superior bond strength than the GFRP reinforcing bars due to their higher modulus of elasticity. Numerous studies in the literature have consistently concluded that the higher modulus of elasticity exhibited by steel reinforcing bars is a primary factor contributing to their enhanced bond strength (Mosley et al. 2008; Pay et al. 2014; Basaran and Kalkan 2020).

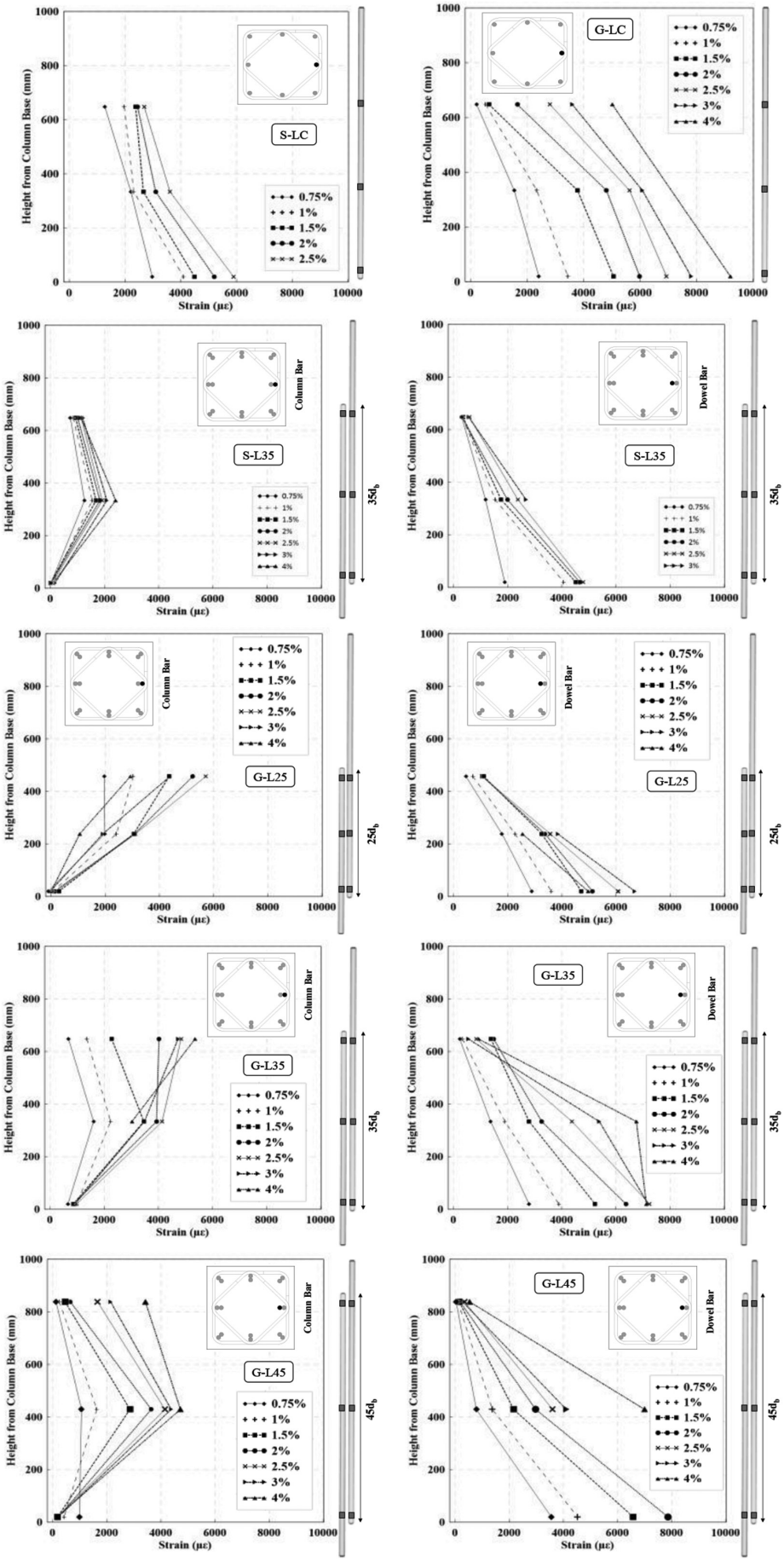

Fig. 12—Strain distribution along longitudinal reinforcing bars at drift ratios of 0.75 to 4.0%. (Note: 1 mm = 0.0394 in.)

Table 4 compares the results of the maximum strain recoded at stirrups in the 2 and 4% drift ratios. According to this table, lap-splice length did not noticeably affect stirrup strain. In addition, the steel-RC specimens had lower recorded stirrup strain than the GFRP-RC specimens. This difference can be attributed to the steel reinforcing bars having a higher modulus of elasticity than the GFRP reinforcing bars, leading to reduced strain levels in the steel-RC specimens.

Comparison to code requirements for splice length

ACI 440.1R-15 proposes the following equation for calculating the tension development length of the FRP reinforcing bar under monotonic loading

$$l_d = \frac{\alpha \dfrac{f_{fr}}{0.083\sqrt{f_c'}} - 340}{13.6 + \dfrac{c}{d_b}} d_b \quad (3)$$

where $c/d_b \le 3.5$ based on ACI 440.1R-15, the classification for lap-splice length is not required because the full tensile strength of the FRP reinforcing bar need not be developed. Accordingly, $1.3l_d$ is proposed for all lap splices in tension.

CAN/CSA S806-12 expresses the development length of the FRP reinforcing bar in monotonic tension as follows

$$l_d = 1.15 \frac{k_1 k_2 k_3 k_4 k_5}{d_{cs}} \frac{f_F}{\sqrt{f_c'}} A_b \quad (4)$$

where $d_{cs} \le 2.5d_b$ and $\sqrt{f_c'} \le 5$ MPa. CAN/CSA S806-12 recommends $1.3l_d$ in calculating the lap-splice length in tension.

The models in Eq. (3) and (4) are related to monotonic loading and cannot be directly applied to seismic load. The following discussion, however, aims to evaluate the effectiveness of these models for use in the case of seismic load. Figure 13 shows the required splice length to reinforcing bar diameter (l_s/d_b) versus FRP reinforcing bar stress (f_F) according to ACI 440.1R-15 and CAN/CSA S806-12. This figure was obtained by considering the specimen details related to this study and the study conducted by Naqvi and El-Salakawy (2017). The figure shows that the slope of the line related to ACI 440.1R-15 is steeper than that calculated according to CAN/CSA S806-12. As a result, ACI 440.1R-15 would require a longer splice length than that required based on CAN/CSA S806-12 in the case of higher reinforcing bar stress.

Table 5 presents the required splice length for the tested specimens in this study and the columns tested by Naqvi and El-Salakawy (2017) according to ACI 440.1R-15 and CAN/CSA S806-12, as well as the adequate splice length based on the experimental results. This table shows that splice lengths of $45d_b$ and $60d_b$ were adequate to develop reinforcing bar stress along the splice length for the columns tested in this study and by Naqvi and El-Salakawy (2017), respectively. In contrast, the calculated splice lengths based on the specified codes were lower than the experimental values. Therefore, the authors concluded that a longer splice length is required to develop reinforcing bar stress in columns subjected to reversed cyclic loading compared to monotonic loading. This position is justified given the areas of disintegrated concrete around the reinforcing bars due to crack propagation in two directions during reversed cyclic loading. In addition, it should be noted that, based on the assumptions in the analytical investigation, the occurrence of concrete spalling was synchronized with the ultimate condition. Based on the experimental results in this study, the concrete spalling occurred at a drift ratio of 1.5%. The maximum allowable drift ratio is 4.0% for columns subjected to seismic load (CSA S806-12 2021), so the maximum reinforcing bar stress in real applications might be greater than the analytical stress. For instance, the reinforcing bar stress at a drift ratio of 4.0% was approximately twice the analytical value for G-LC. Consequently, based on the discussed issues, the bond demand increased in the case of the GFRP-RC columns under reversed cyclic loading.

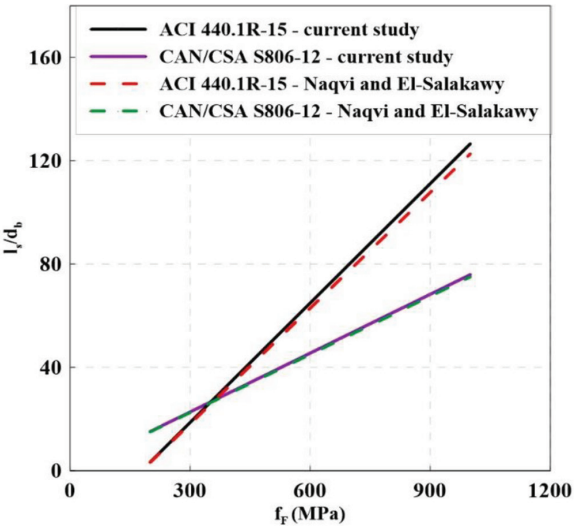

Fig. 13—Prediction of splice length based on ACI 440.1R-15 and CAN/CSA S806-12. (Note: 1 MPa = 0.145 ksi.)

According to the aforementioned discussion and as a result of this work, the splice lengths calculated based on ACI 440.1R-15 and CAN/CSA S806-12 are not adequate in the case of seismic load. Because the data is limited, more experimental work is required with a wider range of parameters (bar size, confinement level, concrete compressive strength, and so on) to recommend a formula for determining an accurate value for the splice length of GFRP reinforcing bars in structural members subjected to seismic loads. In addition, the results and discussion in this study focused on sand-coated GFRP reinforcing bars. More research is required to investigate the seismic behavior of lap-spliced GFRP reinforcing bars with other surface configurations.

SUMMARY AND CONCLUSIONS

The performance of lap-spliced reinforcing bars under reversed cyclic loading was investigated by testing four full-scale glass fiber-reinforced polymer (GFRP)-reinforced concrete (RC) columns and two steel-RC columns

Table 5—Comparison between analytical and experimental results

Reference	Theoretical splice length		Sufficient splice length (experimental)	Ratio of experimental to theoretical	
	ACI 440.1R-15	CAN/CSA S806-12		ACI 440.1R-15	CAN/CSA S806-12
Current study	$23d_b$	$30d_b$	$45d_b$	1.96	1.50
Naqvi and El-Salakawy (2017)	$39d_b$	$38d_b$	$60d_b$	1.54	1.58

for comparison. The test parameters included the splice length and type of reinforcement. After presenting the experimental results, the available models for the prediction of development length in ACI 440.1R-15 and CAN/CSA S806-12(R2021) were evaluated for the tested specimens. The following conclusions may be drawn from the results of this study:

1. A splitting crack was observed in the GFRP-RC column with a splice length of $25d_b$ (G-L25) at a drift ratio of 1.0%, while no signs of splitting cracks were observed in the other specimens.

2. The load continuously decreased after concrete spalling in G-L25. The specimens with longer splice lengths (G-L35 and G-L45) and the G-LC specimen recovered their load after concrete spalling.

3. The lateral loads in G-L35 and G-L45 were 6 and 18% greater than that in G-LC at a drift ratio of 4.0%. However, the lateral load in G-L25 was 18% lower than in G-LC.

4. Lap splicing the GFRP reinforcing bars had a minimal effect on the energy dissipation capacity of columns up to a drift ratio of 6.0%. The stiffness degradation was greater, however, in the GFRP-RC column with an inadequate splice length of $25d_b$. Additionally, inadequate lap-splice length had a negative effect on the ductility of the lap-spliced GFRP-RC columns.

5. Splice lengths of $25d_b$ and $35d_b$ were not enough to transfer the required stress between the spliced reinforcing bars after drift ratios of 1.5% and 2.5%, respectively. The splice length of $45d_b$ was adequate to develop bond stresses. The splice length of $35d_b$ was, however, deemed sufficient for the steel-reinforced column owing to its higher bond strength resulting from the steel reinforcing bars' superior modulus of elasticity compared to the GFRP reinforcing bars.

6. The splice length obtained according to the models proposed in ACI 440.1R and CAN/CSA S806 for lap-splice length under monotonic loading was not adequate for GFRP reinforcing bars under cyclic loading. Therefore, a large experimental study with a wide range of parameters is required to recommend an empirical equation for the splice length of GFRP reinforcing bars required for seismic zones.

7. The results of this study are limited to the lap-spliced sand-coated GFRP bars. Further research is needed to investigate the effect of other surface configurations of GFRP reinforcing bars on their lap-splice behavior under seismic loading.

AUTHOR BIOS

Bahareh Nader Tehrani *is a Doctoral Candidate in the Department of Civil and Building Engineering at the University of Sherbrooke, Sherbrooke, QC, Canada. She received her BSc and MSc from the Department of Civil Engineering, Isfahan University of Technology (IUT), Iran. Her research interests include the internal and external use of fiber-reinforced polymers (FRPs) in reinforced concrete structures.*

Ahmed Sabry Farghaly *is a Research Associate in the Department of Civil and Building Engineering at the University of Sherbrooke, and a Professor in the Department of Civil Engineering at Assiut University, Assiut, Egypt. His research interests include the nonlinear analysis of reinforced concrete structures and the investigation of the applicability and development of design codes and standards.*

Brahim Benmokrane, *FACI, is a Professor in the Department of Civil and Building Engineering at the University of Sherbrooke, Tier-1 Canada Research Chair in Advanced Composite Materials for Civil Structures, NSERC Senior Research Chair in FRP Reinforcement for Concrete Infrastructure, and Director of the University of Sherbrooke Research Center on Structural FRP Composite Materials for Concrete Structures (CRUSMAC). He is a member of ACI Committees 435, Deflection of Concrete Building Structures, and 440, Fiber-Reinforced Polymer Reinforcement, and ACI Subcommittees 440-E, FRP-Professional Education; 440-F, FRP-Repair-Strengthening; 440-H, FRP-Reinforced Concrete; 440-I, FRP-Prestressed Concrete; 440-K, FRP-Material Characteristics; and 440-L, FRP-Durability. He received the ACI Arthur J. Boase Award in 2022. His research interests include the development of FRP reinforcement for concrete structures and their durability, structural performance, and field applications.*

ACKNOWLEDGMENTS

This research study was conducted with funding from the Natural Science and Engineering Research Council of Canada (NSERC) (NSERC-Alliance Program), Fonds de Recherche du Québec Nature et Technologies (FRQNT), and the Tier-1 Canada Research Chair in Advanced Composite Materials for Civil Structures (CRC Research Program). The assistance received from the technical staff of the Canadian Foundation for Innovation (CFI) Structural Laboratory in the Department of Civil & Building Engineering at the University of Sherbrooke is also acknowledged.

NOTATION

A_b	=	area of reinforcing bar
C	=	lesser of cover to center of reinforcing bar being developed or one-half of center-to-center spacing of reinforcing bars being developed
d_b	=	diameter of reinforcing bar
d_{cs}	=	smaller of distance from center of reinforcing bar developed to closest concrete surface or two-thirds center-to-center spacing of reinforcing bars being developed
f_c'	=	concrete compressive strength
f_F	=	design stress in FRP tension reinforcement at ultimate limit state
f_{fr}	=	required reinforcing bar stress in FRP
k_1	=	reinforcing bar location factor
k_2	=	concrete density factor
k_3	=	reinforcing bar size factor
k_4	=	reinforcing bar fiber factor
k_5	=	reinforcing bar surface profile factor
l_d	=	development length in tension of deformed reinforcing bar
l_s	=	tension splice length
α	=	reinforcing bar location factor

REFERENCES

Abdallah, A. E., and El-Salakawy, E. F., 2022a, "Effect of Aspect Ratio on Seismic Behavior of Glass Fiber-Reinforced Polymer-Reinforced Concrete Columns," *ACI Structural Journal*, V. 119, No. 3, May, pp. 205-219.

Abdallah, A. E., and El-Salakawy, E. F., 2022b, "Seismic Performance of GFRP-RC Circular Columns with Different Aspect Ratios and Concrete Strengths," *Engineering Structures*, V. 257, p. 114092. doi: 10.1016/j.engstruct.2022.114092

ACI Committee 318, 2019, "Building Code Requirements for Structural Concrete (ACI 318-19) and Commentary (ACI 318R-19) (Reapproved 2022)," American Concrete Institute, Farmington Hills, MI, 624 pp.

ACI Committee 374, 2013, "Guide for Testing Reinforced Concrete Structural Elements under Slowly Applied Simulated Seismic Loads (ACI 374.2R-13)," American Concrete Institute, Farmington Hills, MI, 18 pp.

ACI Committee 440, 2015, "Guide for the Design and Construction of Structural Concrete Reinforced with Fiber-Reinforced Polymer Bars (ACI 440.1R-15)," American Concrete Institute, Farmington Hills, MI, 88 pp.

Aly, R.; Benmokrane, B.; and Ebead, U., 2006, "Tensile Lap Splicing of Bundled CFRP Reinforcing Bars in Concrete," *Journal of Composites for Construction*, ASCE, V. 10, No. 4, pp. 287-294. doi: 10.1061/(ASCE)1090-0268(2006)10:4(287)

Asadian, A.; Eslami, A.; Farghaly, A. S.; and Benmokrane, B., 2019, "Splice Strength of Staggered and Non-Staggered Bundled Glass Fiber-Reinforced Polymer Reinforcing Bars in Concrete," *ACI Structural Journal*, V. 116, No. 4, July, pp. 129-142. doi: 10.14359/51714482

ASTM D7205/D7205M-21, 2021, "Standard Test Method for Tensile Properties of Fiber Reinforced Polymer Matrix Composite Bars," ASTM International, West Conshohocken, PA, 13 pp.

Baena, M.; Torres, L.; Turon, A.; and Barris, C., 2009, "Experimental Study of Bond Behaviour between Concrete and FRP Bars Using a Pull-Out Test," *Composites Part B: Engineering*, V. 40, No. 8, pp. 784-797. doi: 10.1016/j.compositesb.2009.07.003

Basaran, B., and Kalkan, I., 2020, "Investigation on Variables Affecting Bond Strength between FRP Reinforcing Bar and Concrete by Modified Hinged Beam Tests," *Composite Structures*, V. 242, p. 112185. doi: 10.1016/j.compstruct.2020.112185

Bournas, D. A., and Triantafillou, T. C., 2011, "Bond Strength of Lap-Spliced Bars in Concrete Confined with Composite Jackets," *Journal of Composites for Construction*, ASCE, V. 15, No. 2, pp. 156-167. doi: 10.1061/(ASCE)CC.1943-5614.0000078

CAN/CSA A23.3-19, 2019, "Design of Concrete Structures," CSA Group, Toronto, ON, Canada, 515 pp.

CAN/CSA S806-12, 2021, "Design and Construction of Building Components with Fiber Reinforced Polymers," CSA Group, Toronto, ON, Canada, 187 pp.

CAN/CSA S807-19, 2019, "Specification for Fibre-Reinforced Polymers," CSA Group, Toronto, ON, Canada, 67 pp.

Chaallal, O., and Benmokrane, B., 1993, "Pullout and Bond of Glass-Fibre Rods Embedded in Concrete and Cement Grout," *Materials and Structures*, V. 26, No. 3, pp. 167-175. doi: 10.1007/BF02472934

Deng, Z.; Gao, L.; and Wang, X., 2018, "Glass Fiber-Reinforced Polymer-Reinforced Rectangular Concrete Columns under Simulated Seismic Loads," *Journal of the Brazilian Society of Mechanical Sciences and Engineering*, V. 40, No. 2, p. 111. doi: 10.1007/s40430-018-1041-8

Elshamandy, M. G.; Farghaly, A. S.; and Benmokrane, B., 2018, "Experimental Behavior of Glass Fiber-Reinforced Polymer-Reinforced Concrete Columns under Lateral Cyclic Load," *ACI Structural Journal*, V. 115, No. 2, Mar., pp. 337-349. doi: 10.14359/51700985

Esfahani, M. R.; Rakhshanimehr, M.; and Mousavi, S. R., 2013, "Bond Strength of Lap-Spliced GFRP Bars in Concrete Beams," *Journal of Composites for Construction*, ASCE, V. 17, No. 3, pp. 314-323. doi: 10.1061/(ASCE)CC.1943-5614.0000359

Hassanein, A., and Mohamed, N., Sabry Farghaly, A., and Benmokrane, B., 2020, "Effect of Boundary Element Confinement Configuration on the Performance of GFRP-Reinforced Concrete Shear Walls," *Engineering Structures*, V. 225, p. 111262. doi: 10.1016/j.engstruct.2020.111262

Kharal, Z., 2019, "Towards Understanding the Seismic Behaviour of GFRP Confined Concrete Columns," PhD dissertation, University of Toronto, Toronto, ON, Canada

Kim, C.-G.; Park, H.-G.; and Eom, T.-S., 2018, "Seismic Performance of Reinforced Concrete Columns with Lap Splices in Plastic Hinge Region," *ACI Structural Journal*, V. 115, No. 1, Jan., pp. 235-245. doi: 10.14359/51701109

Kim, C.-G.; Park, H.-G.; and Eom, T.-S., 2019, "Effects of Type of Bar Lap Splice on Reinforced Concrete Columns Subjected to Cyclic Loading," *ACI Structural Journal*, V. 116, No. 2, Mar., pp. 183-194. doi: 10.14359/51711142

Laoubi, K.; El-Salakawy, E.; and Benmokrane, B., 2006, "Creep and Durability of Sand-Coated Glass FRP Bars in Concrete Elements under Freeze/Thaw Cycling and Sustained Loads," *Cement and Concrete Composites*, V. 28, No. 10, pp. 869-878. doi: 10.1016/j.cemconcomp.2006.07.014

Lukose, K.; Gergely, P.; and White, R., 1982, "Behavior of Reinforced Concrete Lapped Splices for Inelastic Cyclic Loading," *ACI Journal Proceedings*, V. 79, No. 5, Sept.-Oct., pp. 355-365.

Manalo, A.; Maranan, G.; Benmokrane, B.; Cousin, P.; Alajarmeh, O.; Ferdous, W.; Liang, R.; and Hota, G., 2020, "Comparative Durability of GFRP Composite Reinforcing Bars in Concrete and in Simulated Concrete Environments," *Cement and Concrete Composites*, V. 109, p. 103564. doi: 10.1016/j.cemconcomp.2020.103564

Mohamed, K.; Benmokrane, B.; and Krall, M., 2020, "Alkali-Silica Reactivity of Sand Used in Sand-Coating Fiber-Reinforced Polymer Bars as Internal Reinforcement for Concrete," *Journal of Composites for Construction*, ASCE, V. 24, No. 6, p. 06020002. doi: 10.1061/(ASCE)CC.1943-5614.0001079

Mosley, C. P.; Tureyen, A. K.; and Frosch, R. J., 2008, "Bond Strength of Nonmetallic Reinforcing Bars," *ACI Structural Journal*, V. 105, No. 5, Sept.-Oct., pp. 634-642

Naqvi, S., 2016, "Lap Splice in Glass Fiber Reinforced Polymer-Reinforced Concrete Rectangular Columns Subjected to Cyclic-Reversed Loads," MSc thesis, Department of Civil Engineering, University of Manitoba, Winnipeg, MB, Canada

Naqvi, S., and El-Salakawy, E., 2017, "Lap Splice in GFRP-RC Rectangular Columns Subjected to Cyclic-Reversed Loads," *Journal of Composites for Construction*, ASCE, V. 21, No. 4, p. 04016117. doi: 10.1061/(ASCE)CC.1943-5614.0000777

Pam, H. J., and Ho, J. C. M., 2010, "Effects of Steel Lap Splice Locations on Strength and Ductility of Reinforced Concrete Columns," *Advances in Structural Engineering*, V. 13, No. 1, pp. 199-214. doi: 10.1260/1369-4332.13.1.199

Paulay, T.; Zanza, T.; and Scarpas, A., 1981, "Lapped Splices in Bridge Piers and in Columns of Earthquake Resisting Reinforced Concrete Frames," Department of Civil Engineering, University of Canterbury, Christchurch, New Zealand.

Pay, A. C.; Canbay, E.; and Frosch, R. J., 2014, "Bond Strength of Spliced Fiber-Reinforced Polymer Reinforcement," *ACI Structural Journal*, V. 111, No. 2, Mar.-Apr., pp. 257-266.

Prajapati, G. N.; Farghaly, A. S.; and Benmokrane, B., 2022a, "Behavior of Reinforced Concrete Columns with Hybrid Reinforcement (Steel/Glass Fiber-Reinforced Polymer) under Reversed Cyclic Load," *ACI Structural Journal*, V. 119, No. 4, July, pp. 141-155.

Prajapati, G. N.; Farghaly, A. S.; and Benmokrane, B., 2022b, "Performance of Concrete Columns Longitudinally Reinforced with Steel and GFRP Bars and Confined with GFRP Spirals and Cross Ties under Reversed Cyclic Loading," *Engineering Structures*, V. 270, p. 114863. doi: 10.1016/j.engstruct.2022.114863

Prajapati, G. N.; Farghaly, A. S.; and Benmokrane, B., 2023, "Behavior of Glass Fiber-Reinforced Polymer- Reinforced Concrete Columns Subjected to Simulated Seismic Load," *ACI Structural Journal*, V. 120, No. 1, Jan., pp. 3-16.

Pultrall, 2020, "Data Sheet – Fiberglass and Carbon Reinforcements," https://fiberglassrebar.com/technical-data-sheets/. (last accessed April 9, 2024)

Robert, M.; Cousin, P.; and Benmokrane, B., 2009, "Durability of GFRP Reinforcing Bars Embedded in Moist Concrete," *Journal of Composites for Construction*, ASCE, V. 13, No. 2, pp. 66-73. doi: 10.1061/(ASCE)1090-0268(2009)13:2(66)

Tabatabaei Kashani, A., 2019, "Compression Lap Splices of GFRP Bars in Reinforced Concrete Columns," PhD thesis, University of Sherbrooke, Sherbrooke, QC, Canada, 171 pp.

Tavassoli, A., 2013, "Behaviour of GFRP Reinforced Concrete Columns under Combined Axial Load and Flexure," MSc thesis, Department of Civil Engineering, University of Toronto, Toronto, ON, Canada, 214 pp.

Tavassoli, A., 2015, "Behaviour of Circular Concrete Columns Internally Reinforced with Steel and GFRP under Simulated Earthquake Load," MSc thesis, Department of Civil Engineering, University of Toronto, Toronto, ON, Canada, 193 pp.

Zemour, N.; Asadian, A.; Ahmed, E. A.; Benmokrane, B.; and Khayat, K. H., 2019, "Experimental Study on Splice Strength of Glass Fiber-Reinforced Polymer Reinforcing Bars in Normal and Self-Consolidating Concrete," *ACI Materials Journal*, V. 116, No. 3, May, pp. 105-118. doi: 10.14359/51714459

ACI STRUCTURAL JOURNAL TECHNICAL PAPER

Title No. 121-S34

Hysteresis Behavior of Glass Fiber-Reinforced Polymer-Reinforced Precast Concrete Tunnel Segments under Cyclic Load

by Basil Ibrahim, Salaheldin Mousa, Hamdy M. Mohamed, and Brahim Benmokrane

The hysteresis response of precast concrete tunnel lining (PCTL) segments reinforced internally with fiber-reinforced polymer (FRP) bars under quasi-static cyclic flexural loading is an area for which no experimental research results are available. This paper reports on an investigation on the hysteresis behavior of PCTL segments reinforced internally with glass fiber-reinforced polymer (GFRP) bars. Full-scale curvilinear GFRP-reinforced PCTL segments were designed, fabricated, and tested under quasi-static cyclic flexural loading. The segments measured 3100 mm (122 in.) in length, 1500 mm (59 in.) in width, and 250 mm (9.8 in.) in thickness. The test parameters were the longitudinal reinforcement ratio, the transverse reinforcement configuration, and the concrete compressive strength. The hysteresis response, cracking pattern, and ductility of the PCTL segments were identified and experimentally evaluated. The experimental results of the current study demonstrate that the hysteresis response of the curvilinear GFRP-reinforced PCTL segments had stable cyclic behavior with no or limited strength degradation until failure. In addition, analytical prediction of the load-carrying capacity, deflection, and unloading stiffness of the test segments was carried out. The segments' analytically predicted responses were validated and compared to the experimental results. The segments' analytically predicted models for the post-cracking loading tangent stiffness and unloading stiffness for the curvilinear GFRP-reinforced PCTL segments are proposed herein. The analytically predicted hysteresis response shows accurate predictions with comparable loading stiffness, unloading stiffness, and residual deformation at the end of each loading cycle.

Keywords: deformability; glass fiber-reinforced polymer (GFRP) bars; high-strength concrete (HSC); hysteresis behavior; normal-strength concrete (NSC); precast concrete tunnel lining (PCTL) segments; quasi-static cyclic flexural loading.

INTRODUCTION

Reinforcement corrosion in precast concrete tunnel lining (PCTL) segments conventionally reinforced with steel causes premature degradation, requiring costly maintenance and repairs. Many concrete tunnels conventionally reinforced with steel are deteriorating as they age (Zhiqiang and Mansoor 2013). Because concrete is not perfectly impermeable, chlorinated groundwater saturating the concrete in tunnel applications conventionally reinforced with steel allows permeation of the concrete cover and initiates an electrolytic reaction with the reinforcement, which accelerates reinforcement corrosion and loss of structural integrity (Rancourt 2016). According to ACI 440.1R-15, corrosion is the most problematic deterioration and cost issue in concrete structures reinforced with conventional steel reinforcement. The corrosion of reinforcement in concrete structures conventionally reinforced with steel costs the United States' economy approximately 1% of the country's gross domestic product (Whitmore and Ball 2004). Likewise, repairing the corrosion damage in concrete structures conventionally reinforced with steel costs Canada more than $10 billion annually (Davis 2000). As they are characterized by corrosion resistance, long life span, and reduced maintenance costs, noncorroding lightweight and high-strength fiber-reinforced polymer (FRP) reinforcement is one effective alternative to conventional steel reinforcement to solve corrosion issues (Mohamed and Benmokrane 2015, 2016; Wang et al. 2017; Mohamed et al. 2017, 2019, 2020; Mousa et al. 2018, 2019, 2020; Solyom and Balázs 2020; Pan and Yan 2021; Benmokrane et al. 2021).

The flexural behavior of PCTL segments reinforced with noncorroding curvilinear glass-FRP (GFRP) reinforcement bars as an alternative to conventional steel reinforcement has been narrowly investigated in the literature (Caratelli et al. 2016, 2017; Spagnuolo et al. 2017; Hosseini et al. 2022). Comparisons to the flexural behavior of steel-reinforced PCTL segments have demonstrated that curvilinear GFRP reinforcement can be an effective alternative to conventional steel reinforcement (Caratelli et al. 2017; Hosseini et al. 2022). Moreover, it has been demonstrated that curvilinear GFRP-reinforced and steel-reinforced PCTL segments have comparable flexural behavior (Spagnuolo et al. 2017). Caratelli et al. (2016) found that curvilinear GFRP-reinforced PCTL segments exhibited adequate ductility compared to PCTL segments conventionally reinforced with steel, despite the brittleness of curvilinear GFRP reinforcement. In addition, the failure warning of the curvilinear GFRP-reinforced PCTL segments was ensured by the wide cracking generated by the high strain that the curvilinear GFRP bars exhibited before failure (Spagnuolo et al. 2017).

According to ACI 544.7R-16, the loads acting on PCTL segments from casting up to erection within a tunnel boring machine (TBM) shield fall into three stages: production and transient stage, construction stage, and service stage. The final service stages are represented by the long-term loads acting on the lining from the ground, groundwater,

ACI Structural Journal, V. 121, No. 3, May 2024.
MS No. S-2023-016.R1, doi: 10.14359/51740480, received August 16, 2023, and reviewed under Institute publication policies.

surcharges, and other loads (such as seismic loads). The literature contains no research results on the hysteresis response of curvilinear GFRP-reinforced PCTL segments under seismic loads. Abbas (2014) studied the flexural cyclic behavior of steel fiber-reinforced concrete (SFRC) and PCTL segments conventionally reinforced with steel under quasi-static cyclic flexural loading. Both the SFRC and PCTL segments conventionally reinforced with steel exhibited reasonable ductility and energy dissipation capacities and stratified the flexural requirements.

Al-Saadi et al. (2019) found that, generally, the hysteresis behavior of the reinforced concrete structures subjected to large cyclic loading exhibited levels of stiffness degradation, which is caused by cracking, loss of bond, or integration with high shear or axial stress. Xiao et al. (2018) found that the level of stiffness degradation depended on the loading history and the characteristics of the reinforced concrete members. In their study, Fahmy et al. (2009) determined that the unloading stiffness was an essential constraint in determining the recoverability and residual deformation of reinforced concrete members under cyclic loading conditions. Ding et al. (2013) considered unloading stiffness degradation advantageous in improving the structural reparability under cyclic loading conditions, as the structural residual deformation was directly associated with the unloading stiffness of the reinforced concrete members. In terms of loading and unloading stiffness, there are no available experimental results on the hysteresis behavior of curvilinear GFRP-reinforced PCTL segments. Accordingly, the authors' study investigated the hysteresis behavior of curvilinear GFRP-reinforced PCTL segments under quasi-static cyclic flexural loading.

This work is part of an ongoing comprehensive research program carried out in the Department of Civil and Building Engineering at the University of Sherbrooke. It aims at improving the existing practices and developing more competent design and construction approaches for the use of curvilinear GFRP bars in PCTL segments. This ongoing research (Hosseini et al. 2022a,b, 2023; Ibrahim et al. 2022, 2023) investigates the behavior of full-scale curvilinear GFRP-reinforced PCTL segments under different loading conditions: static flexural loading; quasi-static cyclic flexural loading; punching shear and settlement. This is the first experimental work to date providing experimental data through laboratory testing on the performance of curvilinear GFRP-reinforced PCTL segments under quasi-static cyclic flexural loading in accordance with the provisions in ACI 374.2R-13. This data could be considered in the forthcoming code provisions for the efficiency of replacing conventional steel reinforcement with noncorroding curvilinear GFRP reinforcement for the cyclic behavior of PCTL segments.

RESEARCH SIGNIFICANCE AND OBJECTIVES

The hysteresis behavior, in terms of loading and unloading stiffness of the curvilinear-GFRP reinforced PCTL segments, is one area for which no experimental research results are available. This study investigated the loading and unloading stiffness of curvilinear GFRP-reinforced PCTL segments under quasi-static cyclic flexural loading. An experimental program to evaluate the hysteresis response was carried out. In addition, the hysteresis behavior of the PCTL segments, in terms of loading and unloading stiffness, was analytically investigated, and compared to the experimental results. Furthermore, to experimentally and analytically examine the recoverability of the curvilinear GFRP-reinforced PCTL segments in this study, a damage index for the PCTL segments was defined and evaluated in accordance with the residual deformation. All the experimental and analytical outcomes and conclusions of this work are implemented to assess and explore the feasibility of the use of the curvilinear GFRP bars as internal reinforcement for the PCTL segments application under seismic loading conditions. Moreover, the outcomes of this study will be useful for design engineers and represent a significant contribution to North American technical committees engaged in developing standards and design provisions for PCTL segments reinforced with GFRP bars.

EXPERIMENTAL PROGRAM

Materials

The mechanical properties of the different sand-coated GFRP bars employed in this study were determined in accordance with ASTM D7205/D7205M (2021), as listed in Table 1. Number 6 and No. 5 (20 and 15 mm) curvilinear GFRP bars were used as the PCTL segments' longitudinal reinforcement. In addition, No. 6 and No. 5 (20 and 15 mm) U-shaped GFRP bars were used as anchorage for the longitudinal reinforcement at both ends of each segment. For the transverse reinforcement, No. 4 (13 mm) closed and double U-shaped ties were used for the PCTL segments. All the PCTL segments were cast at the SYM-TECH precast concrete facility in Saint-Hyacinthe, QC, Canada. The targeted concrete compressive strength was 40 and 80 MPa (5.8 and 11.6 ksi) for the normal-strength concrete (NSC) and high-strength concrete (HSC) segments, respectively. Table 2 lists the actual average concrete compressive strengths based on

Table 1—Mechanical properties of reinforcement bars

Reinforcement type	Bar size	Bar diameter, mm	Cross-sectional area – nominal, mm^2	Cross-sectional area – immersed, mm^2	Modulus of elasticity, GPa	Tensile strength, MPa	Tensile strain, %
Curvilinear GFRP bars	No. 5	15.0	199	222 ± 1.2	55.1	1115	2.0
	No. 6	20.0	284	339 ± 0.5	52.9	1068	2.0
U-shaped GFRP bars	No. 5	15.0	199	222 ± 1.2	53.5	1283	2.4
	No. 6	20.0	284	339 ± 0.5	53.2	1131	2.1
Closed GFRP ties	No. 4	13.0	129	148 ± 1.1	55.6	1248	2.2

Note: 1 mm = 0.0394 in.; 1 MPa = 145 psi; 1 GPa = 145 ksi.

the average test results of ten 100 x 200 mm (3.94 x 7.89 in.) concrete cylinders tested for each PCTL segment on the first day of the start of testing the segments.

Test segments

The experimental program was designed to provide data on the cyclic behavior of curvilinear GFRP-reinforced PCTL segments. Four full-scale curvilinear GFRP-reinforced PCTL segments were designed, fabricated, and tested under quasi-static cyclic flexural loading. The PCTL segments were kept skewed at both ends, and the clear cover was kept constant at 40 mm (1.57 in.) for all test segments. The segments were designed in accordance with ACI 440.1R-15 and CAN/CSA S806-12 (R2017). The test parameters in this experimental program included the longitudinal reinforcement ratio, the transverse reinforcement configuration (closed versus double U-shaped ties), and the concrete compressive strength. Table 2 shows the reinforcement details and the test matrix for the PCTL segments. Each segment is identified with an alphanumeric code. The first number of the code represents the number of the top/bottom longitudinal reinforcement bars. The letter G refers to GFRP reinforcement. The second number represents the curvilinear nominal diameter of the top/bottom longitudinal GFRP reinforcing bars. To differentiate between the segments with different transverse reinforcement configurations, the letter U designates the segments reinforced transversely with double U-shaped ties. The letter H identifies the segment cast with HSC. Segments 7G15 and 7G20 are NSC segments with top and bottom longitudinal reinforcement consisting of seven No. 5 curvilinear GFRP bars and seven No. 6 curvilinear GFRP bars with longitudinal reinforcement ratios of 0.50% and 0.70%, respectively. Both segments were reinforced transversely with closed No. 4 GFPR ties spaced at 200 mm (7.87 in.). Seven No. 5 and No. 6 U-shaped GFRP anchorage bars were installed on each side of segments 7G15 and 7G20, respectively. Segment 7G15-U was also fabricated with NSC and reinforced longitudinally (top and bottom) with seven No. 5 curvilinear GFRP bars. This segment was reinforced transversely with No. 4 double U-shaped GFRP ties spaced at 200 mm (7.87 in.). Similarly, the HSC segment (7G15-U-H) was reinforced longitudinally (top and bottom) with seven No. 5 curvilinear GFRP bars and reinforced transversely with No. 4 double U-shaped GFRP ties spaced at 200 mm (7.87 in.). Moreover, No. 5 U-shaped GFRP anchors were installed on each side of segments 7G15-U and 7G15-U-H. Figure 1 illustrates the reinforcement details for the test segments.

Test setup and instrumentation

The test setup (designed and fabricated at the University of Sherbrooke's CFI structural laboratory) consisted

Table 2—Test matrix and segment details

Segment ID	Reinforcement type	Concrete type	Actual concrete compressive strength f_c', MPa	Longitudinal reinforcement		Transverse reinforcement
				Number of bars	ρ_f, %	
7G15	GFRP	NSC	52 ± 1.1	Seven No. 5 bars	0.50	No. 4 closed GFRP ties spaced at 200 mm
7G20	GFRP	NSC	47 ± 1.4	Seven No. 5 bars	0.70	No. 4 closed GFRP ties spaced at 200 mm
7G15-U	GFRP	NSC	50 ± 0.9	Seven No. 5 bars	0.50	No. 4 double U-shaped GFRP ties spaced at 200 mm
7G15-U-H	GFRP	HSC	81 ± 3.4	Seven No. 5 bars	0.50	No. 4 double U-shaped GFRP ties spaced at 200 mm

Note: 1 MPa = 145 psi; 1 mm = 0.0394 in.

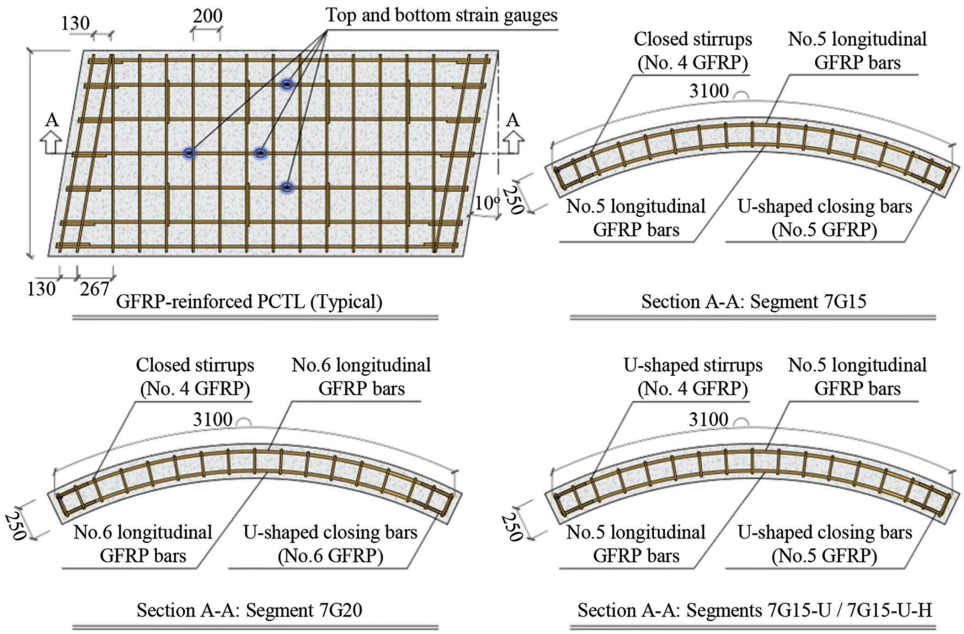

Fig. 1—Reinforcement details for test segments. (Note: All dimensions in mm; 1 mm = 0.0394 in.)

of an 11,000 kN (247.3 kip) capacity MTS universal testing machine attached to a spreader beam, as shown in Fig. 2. Three-point bending load was applied at a displacement-controlled rate of 0.8 mm/min. The test span for the PCTL segments was 2400 mm (94.5 in.). Five different linear potentiometers (LPOTs) were placed to measure the segments' mid- and quarter-span deflections (Fig. 2). In addition, to measure the strain at mid- and quarter-span of the PCTL segments, 10 and 60 mm (0.39 and 2.36 in.) electrical resistance strain gauges were installed on the reinforcing bars and attached to the concrete surface, respectively (Fig. 1). The load was moreover applied in accordance with the tests of structural components under slowly applied quasi-static loading as in ACI 374.2R-13. The quasi-static cyclic flexural loading was applied in terms of percentage of the maximum displacement obtained from the static testing results (Hosseini et al. 2022). Two loading/unloading cycles were conducted at 1.25, 2.5, 5, 10, 25, 50, and 75% of the maximum displacement, followed by one cycle up to failure. In all cycles, the unloading phase was stopped at a minimum load of 5 kN (1.12 kip) to keep the test machine engaged with the segments.

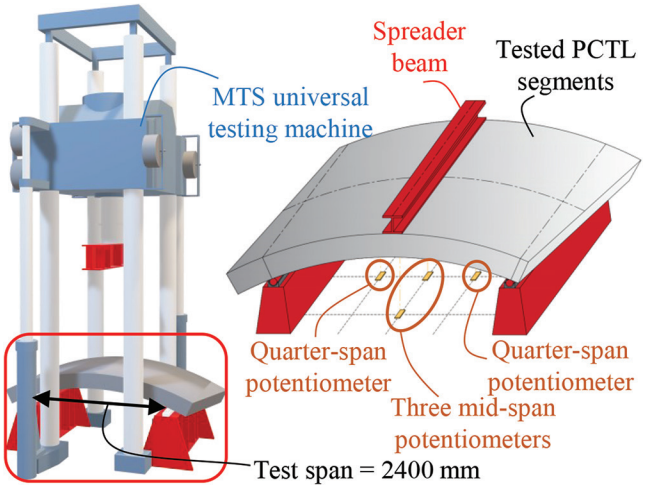

Fig. 2—Test setup. (Note: 1 mm = 0.0394 in.)

TEST RESULTS AND DISCUSSION

This section discusses the experimental hysteresis behavior of the PCTL segments. In addition, ductility index, crack width, and deformability of the PCTL segment are defined, estimated, and evaluated in this section. Table 3 summarizes the experimental test results.

Hysteresis response

Figure 3 shows the hysteresis behavior of the tested segments in the form of load-versus-midspan deflection. At 1.25 and 2.5% of the maximum displacement cycles, all segments exhibited the same linear hysteresis response, corresponding to the condition of uncracked section of the segments. Beyond these loading cycles, the first flexural cracks in the tension zone of the tested segments initiated under the loading point at 5% of the maximum displacement cycle. The cracking load P_{cr} ranged between 59 and 70 kN (13.26 and 15.74 kip) for all tested segments. The stiffness of all tested segments decreased after cracking, with

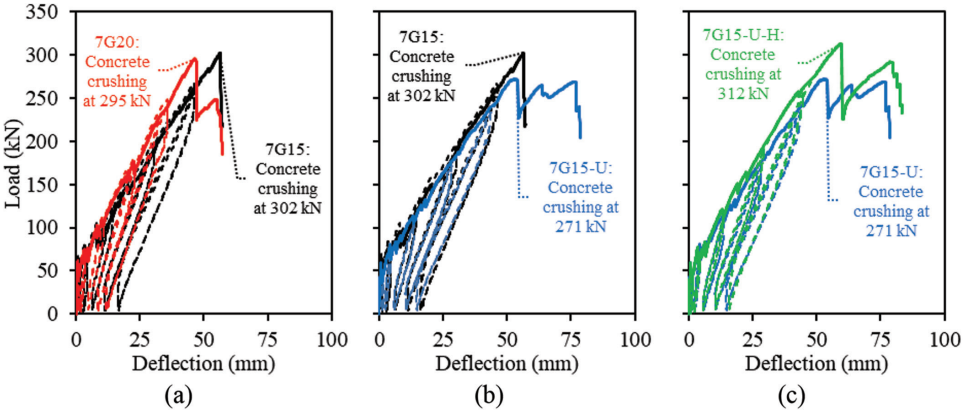

Fig. 3—Hysteresis response for: (a) segments with different reinforcement ratios; (b) segments with different transverse reinforcement configurations; and (c) segments with different concrete compressive strengths.

Table 3—Summary of results

Segment ID	Cracking load, kN	Failure load, kN	Type of failure	Deflection at failure, mm	Ductility index μ_e	J-factor	P_{exp}/P_{pred} at P_n
7G15	70	302	Concrete crushing	56.5	1.49	5.9	0.93
7G20	62	295	Concrete crushing	46.5	1.43	4.7	0.93
7G15-U	59	271	Concrete crushing	52.8	1.51	5.9	0.95
7G15-U-H	60	312	Concrete crushing	59.5	1.78	4.3	0.88
						Average	0.92
						Standard deviation	0.03
						Coefficient of variance (COV), %	3.24

Note: 1 mm = 0.0394 in.; 1 kN = 0.2248.

an almost linear hysteresis response up to the initiation of failure. At 10 and 25% of the maximum displacement cycle, additional flexural cracks initiated within the shear span of the tested segments. At 75% of the maximum displacement cycle, the main flexural cracks became wider and propagated toward the loading point until failure occurred. All the curvilinear GFRP-reinforced PCTL segments failed by concrete crushing in the compression zone of the segments' midspan at load-carrying capacities P_n of 302, 295, 271, and 312 kN (67.89, 66.32, 60.92, and 70.14 kip) for Segments 7G15, 7G20, 7G15-U, and 7G15-U-H, respectively, as illustrated in Fig. 4. Moreover, at 1.25 and 2.5% of the maximum displacement cycle, the unloading stiffness was relatively high in all tested segments. Figure 3 reveals that, beyond 5% of the maximum displacement cycle, the unloading stiffness of the segments rapidly decreased. This drop in unloading stiffness through the loading cycles helped improve segment reparability. In good agreement with the work of Ding et al. (2013), the drop in unloading stiffness decreased the segments' residual deformation. The residual deformation of the tested segments was therefore smaller at 50 and 75% of the maximum displacement cycle than at the lower loading cycles. Furthermore, in all second excursion loading cycles, the hysteresis response for the GFRP-reinforced PCTL segments reflected stable cyclic behavior with no or limited strength degradation until failure.

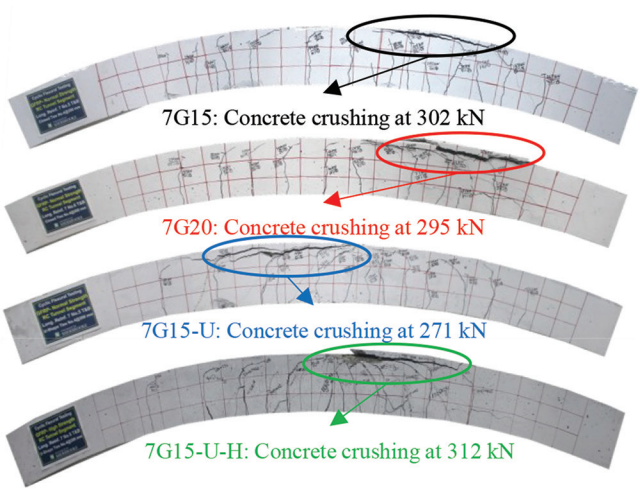

Fig. 4—Failure mode for all test segments. (Note: 1 kN = 0.2248.)

Strain readings

Figure 5 shows the load-strain relationships for the tested segments at midspan, up to failure. Prior to cracking at 1.25 and 2.5% of the maximum displacement cycles, the strain readings at the top concrete fibers in all segments were insignificant (–80 to –200 με), as shown in Fig. 5(a). Beyond the 5% of the maximum displacement cycles, the midspan concrete strain readings at the top concrete fibers of the tested segments increased almost linearly until the failure initiation. The maximum recorded midspan concrete compressive strain readings in Segments 7G15, 7G20, 7G15-U, and 7G15-U-H were –3840, –2683, –2640, and –2950 με, respectively, as shown in Fig. 5(a). In addition, Fig. 5(b) and (c) show that before the 5% of the maximum displacement cycles, there were no significant strain readings neither in the bottom nor the top reinforcement bars. The bottom and top GFRP bars exhibited a gradual strain increase until the failure occurred. The maximum recorded midspan strain for the bottom bars in Segments 7G15, 7G20, 7G15-U, and 7G15-U-H was 17,965, 11,637, 14,326, and 17,890 με, respectively, as shown in Fig. 5(b). Proportionally, Fig. 6 shows that the maximum recorded stress in the bottom GFRP reinforcement bars in Segments 7G15, 7G20, 7G15-U, and 7G15-U-H was 975, 616, 789, and 986 MPa (141, 89, 114, and 143 ksi), respectively (88%, 58%, 72%, and 89% of the ultimate tensile stress of the GFRP bars, respectively). The midspan strains in the bottom longitudinal reinforcement bars demonstrate that the increase of the longitudinal reinforcement ratio in Segment 7G20 resulted in reducing the tensile strains in the longitudinal reinforcement bars compared to its counterpart Segment 7G15. The maximum recorded midspan strains in the bottom longitudinal reinforcement bars in Segments 7G15 and 7G20 represent 88% and 58% of the curvilinear-GFRP bars' ultimate tensile strain, respectively. Moreover, in agreement with the work of Faza and Gangarao (1993), the use of HSC in Segment 7G15-U-H resulted in exploiting higher tensile strain of the reinforcement bars. The maximum recorded midspan strains in the bottom longitudinal reinforcement bars in Segments 7G15-U and 7G15-U-H represent 72%

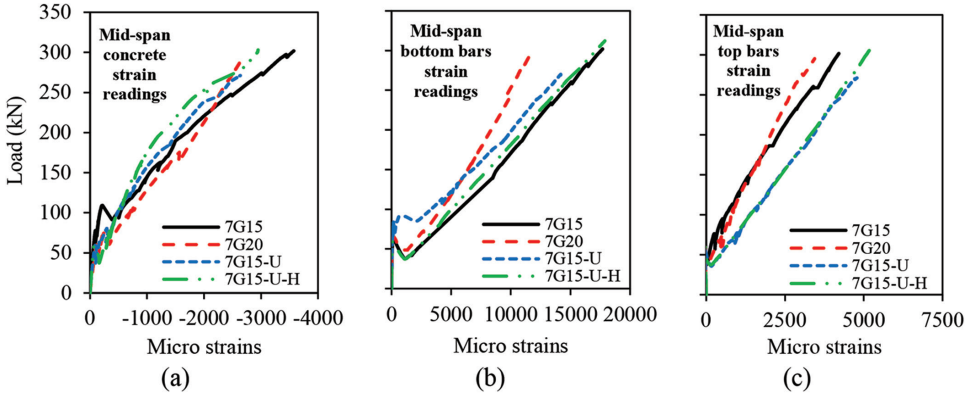

Fig. 5—Envelope load-strain relationship at midspan: (a) at concrete surface; (b) in bottom reinforcement bars; and (c) in top reinforcement bars. (Note: 1 kN = 0.2248.)

and 89% of the curvilinear-GFRP bars' ultimate tensile strain, respectively. Furthermore, the strain gauge readings illustrated that, at failure, the top reinforcement bars, for all tested segments, were under tension, with maximum recorded midspan strains of 4210, 3444, 4787, and 7380 με for Segments 7G15, 7G20, 7G15-U, and 7G15-U-H, respectively (Fig. 5(c)). The test results indicate that the strains in the top concrete fibers, the bottom reinforcement bars, and the top reinforcement bars at quarter-span of all segments was less than that at midspan. The maximum recorded concrete compressive strains at the quarter-span in Segments 7G15, 7G20, 7G15-U, and 7G15-U-H were –1162, –1285, –995, and –617 με, respectively. Similarly, the maximum recorded quarter-span strains in the bottom longitudinal reinforcement bars in Segments 7G15, 7G20, 7G15-U, and 7G15-U-H were 8197, 6676, 7760, and 7380 με, respectively. In contrast, the maximum recorded quarter-span strains in the top longitudinal reinforcement bars in Segments 7G15, 7G20, 7G15-U, and 7G15-U-H were 1168, 783, 1819, and 2105 με, respectively.

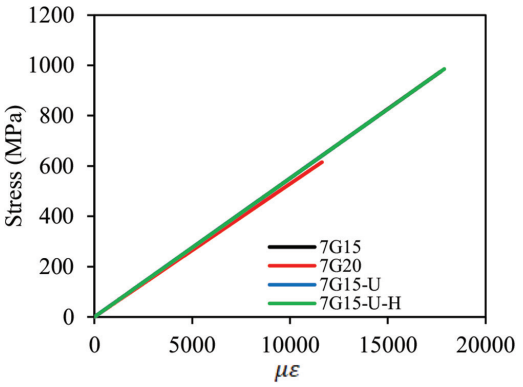

Fig. 6—Stress-strain relationship at midspan for bottom reinforcement bars. (Note: 1 MPa = 145 psi.)

Crack width

Figure 7 shows the cracking pattern of the tested segments. Concrete fractures under cyclic loading are characterized by larger cracks and strains than concrete fractures under static loading (Xiao et al. 2018). The linear behavior of the curvilinear GFRP-reinforced PCTL segments, however, reduced the cyclic effects on the crack width and eliminated the residual cracks at the end of each unloading cycle. The LVDT readings at the end of each unloading cycle indicate that the crack widths were insignificant. Up to 75% of the maximum displacement cycle, the maximum LVDT reading recorded at the end of each unloading cycle in all tested segments ranged between 0.25 and 0.4 mm (0.01 and 0.014 in.). Moreover, as seen in Fig. 7, increasing the longitudinal reinforcement ratio from 0.50% in 7G15 to 0.70% in 7G20 generally enhanced the cracking behavior, where increasing the reinforcement ratio resulted in narrower cracks with narrower cracking spacing in all loading cycles. As

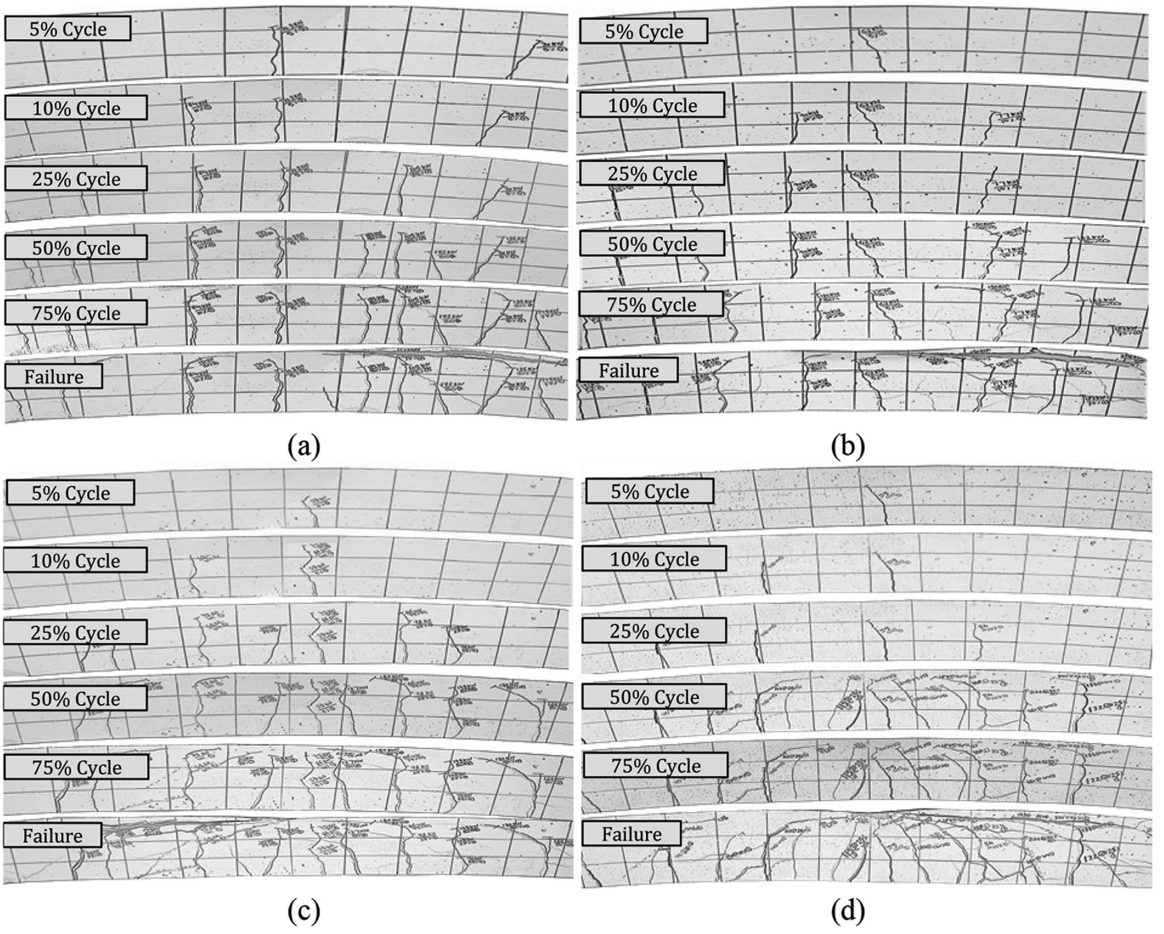

Fig. 7—Cracking pattern in: (a) Segment 7G15; (b) Segment 7G20; (c) Segment 7G15-U; and (d) Segment 7G15-U-H.

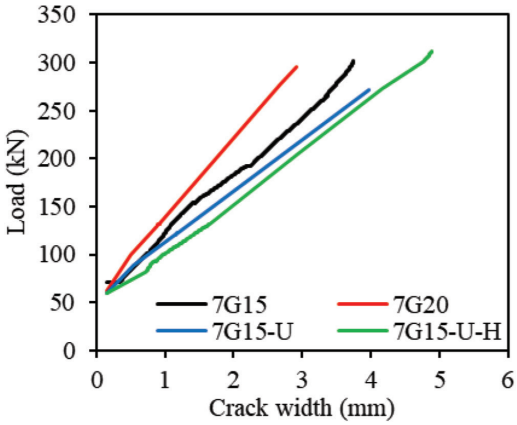

Fig. 8—Load versus crack width for all test segments. (Note: 1 kN = 0.2248; 1 mm = 0.0394 in.)

crack width is mainly controlled by reinforcing bar spacing, and because both 7G15 and 7G20 had the same bar spacing, both segments had almost the same crack width of 0.52 mm (0.02 in.) at service-load levels (2000 με). In contrast, the crack width in 7G15 was approximately 29% greater than that of 7G20 at ultimate load levels (P_n), as shown in Fig. 8. Similarly, Fig. 7 reveals that the closed-tie configuration in 7G15 slightly enhanced the crack width compared to the double U-shaped tie configuration in 7G15-U. At both the service and ultimate load levels, the crack width in 7G15-U was approximately 5% greater than that in 7G15, as shown in Fig. 8. Moreover, Fig. 7 illustrates the concrete compressive strength's effect on the cracking behavior of the curvilinear GFRP-reinforced PCTL segments. Increasing the concrete compressive strength resulted in narrower cracks with closer cracking spacing. The crack width in 7G15-U was approximately twice wider than that of the HSC segment (7G15-U-H) at 2000 με.

Ductility

A member's ductility is its capacity to withstand inelastic deformation without experiencing a reduction in its carrying capacity. Concrete members reinforced with conventional steel reinforcement have ductility expressed directly as the ratio of the ultimate deformation to the deformation at yield. In contrast, FRP-reinforced concrete members have no yield point. Subsequently, the ductility of the concrete members reinforced with FRP reinforcement is computed indirectly in terms of energy deformation or an energy-based ductility index (Grace et al. 1998).

To determine the deformability of the FRP-reinforced concrete members, CAN/CSA S6-19 uses the *J*-factor approach of Jaeger et al. (1997). CAN/CSA S6-19 requires a *J*-factor greater than 4 for rectangular sections: the higher the *J*-factor values, the greater the warning given by the FRP-RC specimen before failure. In this approach, the moment-carrying capacity and the curvature of the FRP-reinforced concrete members—at both the service and ultimate conditions—are considered, as expressed in Eq. (1)

$$J = (M_{ultimate}/M_s) \times (\psi_{ultimate}/\psi_s) \quad (1)$$

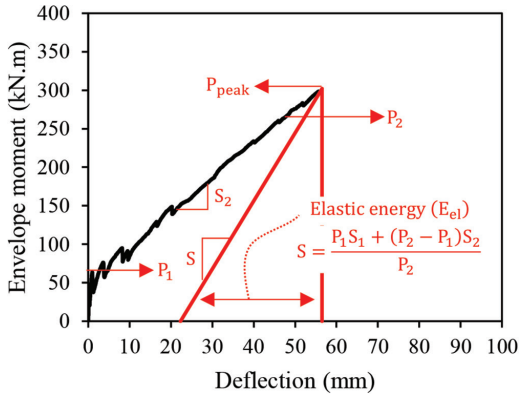

Fig. 9—Energy-based ductility index. (Note: 1 kN·m = 0.7376 kip·ft; 1 mm = 0.0394 in.)

where ψ_s is the curvature at the service condition (strain in the top concrete surface = 1000 με); ψ_u is the ultimate curvature exhibited at failure; M_s is the moment at the service condition; and M_u is the ultimate moment.

In addition to the deformability *J*-factor approach in examining the curvilinear GFRP-reinforced PCTL segments' ductility, the ductility index μ_e was computed based on the energy absorption approach of Naaman and Jeong (1995), as shown in Fig. 9 and expressed in Eq. (2). The ductility index μ_e for the segments was used to evaluate the segments' capacity to withstand inelastic deformation without experiencing a reduction in carrying capacity

$$\mu_e = 0.5[(E_{tot}/E_{el}) + 1] \quad (2)$$

where E_{tot} is the segment's overall energy; and E_{el} is the released elastic energy at failure. The total energy E_{tot} and the elastic energy E_{el} are calculated as the area under the segment's load-deflection envelope curve and the area of the triangle formed at failure load using the weighted average slopes of the two initial stiffness values of the load-deflection curve envelope, respectively.

Table 3 shows that, when compared to the CAN/CSA S6-19 *J*-factor limit of 4 for rectangular GFRP-reinforced concrete sections, all curvilinear GFRP-reinforced PCTL segments demonstrated adequate deformability. The deformability *J*-factor for 7G15, 7G20, 7G15-U, and 7G15-U-H were 5.9, 4.7, 5.9, and 4.3, respectively. Moreover, Table 3 indicates that increasing the reinforcement ratio from 0.50% in 7G15 to 0.70% in 7G20 did not significantly reduce the ductility index of the curvilinear GFRP-reinforced PCTL segments. Both 7G15 and 7G20 exhibited comparable computed μ_e of 1.49 and 1.43, respectively. Likewise, using different types of transverse reinforcement had no consequential effect on the segments' ductility index. As listed in Table 3, 7G15-U had a computed μ_e of 1.51.

Effect of reinforcement type

This section presents the effect of the reinforcement type (GFRP versus conventional steel) on segment behavior. As part of the current comprehensive research program, the hysteresis response of Segment 7G15 was compared to a segment conventionally reinforced with steel (7S15), which the authors tested in a past study (Ibrahim et al. 2023). Both

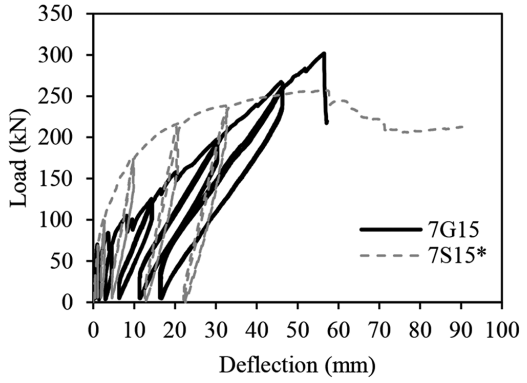

Fig. 10—Effect of reinforcement type on hysteresis response. (Note: Segment 7S15 was investigated by authors in past study; 1 kN = 0.2248; 1 mm = 0.0394 in.)

7G15 and 7S15 had the same flexural longitudinal reinforcement ratio (0.50%). Before cracking occurred, identical linear moment-deflection behavior was observed in both Segments 7G15 and 7S15 (conventionally reinforced with steel), as shown in Fig. 10. After cracking occurred, the response of Segment 7G15 was almost linear up to failure. Figure 10 shows a typical yielding plateau for the segment conventionally reinforced with steel (7S15), followed by concrete crushing in the compression zone. Afterward, a sudden load drop occurred, followed by a total loss of flexural stiffness. Moreover, before Segment 7G15 cracked, its stiffness was similar to that of segment conventionally reinforced with steel (7S15). Segment 7G15 had lower post-cracking flexural stiffness—calculated as the average slope of the curve—than its steel-reinforced counterpart. The ratio between the post-cracking flexural stiffness of Segment 7S15 to Segment 7G15 was approximately 4.28. This ratio is approximately the same as the 4.35 ratio of the axial stiffness (EA) of the steel to that of the GFRP bars. It can be seen, however, that Segment 7G15 had a longer ascending branch with higher stiffness compared to the post-yielding flexural stiffness of Segment 7S15 (Fig. 10). This is mainly because, after the steel bars yielded, their tangent modulus was lower than that of the GFRP bars, which maintained their modulus of elasticity throughout the entire duration of loading. In addition, the comparison indicates that Segment 7G15 had 1.5 times the flexural strength of Segment 7S15 at yielding. The higher strength gain of Segment 7G15 provided sufficient deformability according to the CSA S6-19 code limit of 4 for rectangular sections. Consequently, warning of failure in the form of excessive deflection and cracking would be expected before the GFRP bars reached their rupture tensile strain. The behavior of Segment 7G15 compared to the segment conventionally reinforced with steel (7S15) with the same flexural longitudinal reinforcement ratio demonstrates the feasibility and effectiveness of using GFRP bars instead of steel bars for PCTL segments under quasi-static cyclic flexural loading.

ANALYTICAL STUDY

In this section, the hysteresis response of the curvilinear GFRP-reinforced PCTL segments under quasi-static cyclic flexural loading is analytically investigated. In addition, both the loading and unloading stiffness for the curvilinear GFRP-reinforced PCTL segments were predicted, evaluated, and compared to the experimental results.

Flexural load deflection

Based on the strain compatibility and force equilibrium principles, the flexural capacity of the curvilinear GFRP-reinforced PCTL segments was first computed in the analytical analysis. Based on Bernoulli's hypothesis, the concrete and the curvilinear GFRP bar strains, moreover, were assumed in the analytical analysis to be proportional to the distance from the neutral axis. Furthermore, in accordance with ACI CODE-440.11-22 (ACI Committee 440 2022), the concrete crushing failure was assumed to occur at a concrete compressive strain of 0.003. In addition, the curvilinear GFRP bars' tensile behavior was assumed to be linearly elastic in all loading states until failure, and the bond between the concrete, and the curvilinear GFRP bars was assumed to be perfect.

The parameters α_1 and β_1, presented in the equivalent rectangular stress block in Fig. 11(a), are used to describe the concrete compressive strength distribution according to ACI CODE-440.11-22, as expressed in Eq. (3) and (4).

$$\alpha_1 = 0.85 \tag{3}$$

$$\beta_1 = 0.85 - \frac{0.05(f_c' - 28)}{7} \geq 0.65 \tag{4}$$

To calculate the static load-carrying capacity of the curvilinear GFRP-reinforced PCTL segments, the PCTL section properties and material properties were first defined. The neutral axis depth c was then initially assumed. Thereafter, the concrete compression force C_c was calculated with Eq. (5)

$$C_c = \alpha_1 f_c' A_c \tag{5}$$

where f_c' is the concrete compressive strength of the PCTL segments; and A_c is the cross-sectional area of the PCTL segment.

Subsequently, the strain in the bottom and top curvilinear GFRP bars ε_f and ε_f' was computed using the strain compatibility principle with reference to the ultimate usable concrete strain of 0.003 stated in ACI CODE-440.11-22. The tensile forces in the curvilinear GFRP bars were then calculated with Eq. (6)

$$T = \varepsilon_f E_f A_f + \varepsilon_f' E_f' A_f' \tag{6}$$

where T is the tensile force in the curvilinear GFRP bars; E_f and E_f' are the modulus of elasticity of the bottom and top curvilinear-GFRP bars; and A_f and A_f' are the area of the bottom and top curvilinear GFRP bars.

Once both the concrete and reinforcement forces had been determined, the section equilibrium was checked. The process was repeated with the new assumed neutral-axis depth c until equilibrium was reached. The curvilinear GFRP-reinforced PCTL section's moment-carrying capacity

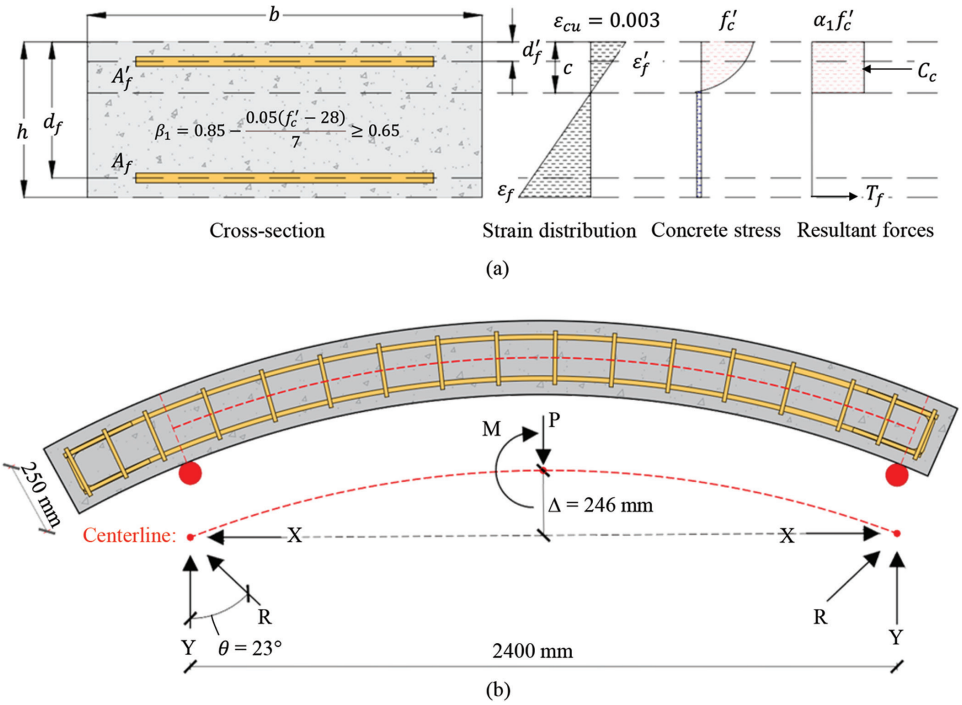

Fig. 11—(a) Idealized cross section and stress-strain distribution; and (b) arch effect on section's load-carrying capacity. (Note: 1 mm = 0.0394 in.)

was obtained by taking the moment of the forces around the centroid of the PCTL section. The curvilinear GFRP-reinforced PCTL segments' arch effect was also considered in calculating the load-carrying capacity from the sections' ultimate moment capacity with Eq. (7) to (10)

$$X = N\sin\theta \tag{7}$$

$$Y = N\cos\theta \tag{8}$$

$$P = 2N\cos\theta \tag{9}$$

$$\text{Moment} = N\cos\theta \times \frac{L}{2} + N\Delta\sin\theta \tag{10}$$

where N is the reactions at the supports; θ is the angle of inclination of the segment's supports from the vertical access; and Δ is the vertical distance between the segment's centerline at midspan and the supports' resistance forces, as shown in Fig. 11(b).

For the curvature predictions, the radius of curvature R to the neutral axis was calculated first. The radius of curvature R, the neutral-axis depth kd, and the concrete strain in the extreme compression fibers ε_c varied along the member, as the concrete between the cracks does carry some tension. Considering only a small element of length dx of the segment, the rotation between the ends of the element was calculated with Eq. (11) and (12).

$$\frac{dx}{R} = \frac{\varepsilon_c dx}{kd} = \frac{\varepsilon_f dx}{d(1-k)} \tag{11}$$

$$\frac{1}{R} = \frac{\varepsilon_c}{kd} = \frac{\varepsilon_f}{d(1-k)} \tag{12}$$

The curvature of the curvilinear GFRP-reinforced PCTL segments ψ was computed as the rotation per segment unit length ($\psi = 1/R$), as expressed in Eq. (13), where the curvature varies along the length of the segment because of the fluctuation in the neutral-axis depth and the strains between the cracks.

$$\psi = \frac{\varepsilon_c}{kd} = \frac{\varepsilon_f}{d(1-k)} = \frac{\varepsilon_c + \varepsilon_f}{d} \tag{13}$$

Hysteresis response prediction

The tensile behavior of the concrete structures reinforced internally with GFRP bars is almost linearly elastic. Moreover, there is no yielding point in GFRP reinforced concrete members. Therefore, the loading stiffness of GFRP-reinforced concrete members can be derived into pre-cracking and post-cracking stages.

Pre-cracking stiffness—In the pre-cracking stage, when cracks have not yet appeared in the concrete section, the effective moment of inertia corresponds to the gross moment of inertial of the transformed uncracked section. Consequently, the tangent stiffness of the curvilinear GFRP-reinforced PCTL at this stage was calculated with the simplified formula, as expressed in Eq. (14) (Dong et al. 2016).

$$K_1 = E_c I_g \tag{14}$$

where E_c is the PCTL segments' initial modulus of elasticity; and I_g is the uncracked PCLT sections' moment of inertia.

Post-cracking stiffness—In the post-cracking stage, cracks started to initiate and kept propagating in the concrete until

failure. Therefore, the effective moment of inertia in this stage decreased until reaching the fully cracked section's moment of inertia at failure. The post-cracking tangent stiffness of the curvilinear GFRP-reinforced PCTL segments was obtained with Eq. (15) and (16)

$$K_{2\_i} = E_c I_e \tag{15}$$

$$I_e = \frac{PL^3}{48 E_c \delta} \tag{16}$$

where K_{2_i} is the post-cracking tangent stiffness at each i cycle; P is the experimentally obtained applied load from the laboratory measures added to the equivalent load due to the self-weight of the PCTL segment; E_c is the initial elastic modulus of concrete; and L is the segment span length.

Unloading stiffness—Unloading stiffness is another important parameter in determining the value of the residual deformation and recoverability of a structure (Fahmy et al. 2009). This is the case when the unloading stiffness degradation is considered advantageous in improving structural reparability under cyclic loading conditions, as the structural residual deformation is directly related to the unloading stiffness. Under cyclic loading conditions, smaller unloading stiffness reduces structural residual deformation (Ding et al. 2013). At the end of each loading cycle of the curvilinear GFRP-reinforced PCTL segments, the unloading stiffness degradation was characterized by the ratio K_{3_i}/K_1, where K_{3_i} is the unloading stiffness at each i cycle, and K_1 is the segment's initial stiffness of the uncracked section at the first 1.25% of the maximum displacement cycle. Using the experimental K_{3_i}/K_1 of the tested segments, the unloading tangent stiffness K_{3_i} was obtained by regression analysis from the load-deflection curves, as shown in Fig. 12, and calculated with Eq. (17)

$$K_{3\_i} = (0.05K_1) \times \left(\frac{\delta}{\delta_{max}}\right)^{-0.7} \tag{17}$$

where δ is the experimentally obtained midspan deflection; and δ_{max} is the experimentally obtained maximum midspan deflection recorded for the segment at failure.

Residual deformation—Figure 13 illustrates the relationship between the unloading stiffness ratio K_{3_i}/K_1, degradation, and the residual deformation ratio $\delta_{residual}/\delta_i$, where $\delta_{residual}$ is the analytically predicted residual deformation, and δ_i is the analytically predicted maximum deformation reached at the end of each i cycle. The residual deformation, $\delta_{residual}$, for the tested segments was calculated at the end of each loading cycle using the analytically predicted unloading stiffness, K_{3_i}, as expressed in Eq. (18)

$$\delta_{residual} = \delta_{max} - \left(\frac{P_{predicted} - P_{unloading}}{K_{3\_i}}\right) \tag{18}$$

where $P_{predicted}$ is the analytically predicted maximum load-carrying capacity at the end of each loading cycle, obtained as described in the flexural-load deflection section; and $P_{unloading}$ is the minimum load-carrying capacity at the end of each unloading cycle, taken as 5 kN (1.12 kip) in line with the experimental load where the unloading stopped to keep the test machine engaged with the segments.

At first, at 1.25% and 2.5% of the maximum displacement cycle, K_{3_i}/K_1 was relatively high in all tested segments. Beyond 5% of the maximum displacement cycle, the K_{3_i}/K_1 rapidly decreased. Figure 13 shows that the residual deformation ratio $\delta_{residual}/\delta_i$ for all tested segments was therefore smaller at 50 and 75% of the maximum displacement cycle than that in the preceding loading cycles. Moreover, Fig. 13 indicates that the degradation of the unloading stiffness ratio K_{3_i}/K_1 and the residual deformation ratio $\delta_{residual}/\delta_i$ for all tested segments was comparable. Therefore, all tested segments had comparable cumulative residual deformation at the end of 75% of the maximum displacement cycle, before failure.

Experimental-to-predicted flexural capacities—Table 3 lists the experimental-to-predicted ratio for the flexural carrying capacities P_{exp}/P_{pred} for all tested segments. The analytical analysis yielded accurate predictions of the ultimate load-carrying capacity. The average P_{exp}/P_{pred} for all tested segments was 0.92, with a standard deviation of 0.03 and coefficient of variance (COV) of 3.24%. In addition, the hysteresis behavior of the curvilinear GFRP-reinforced PCTL segments was compared to the analytically predicted response according to the loading and unloading stiffness predictions, as shown in Fig. 14. The analytically predicted hysteresis response shows accurate predictions

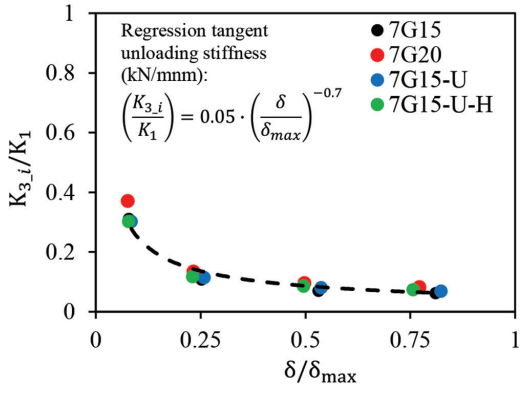

Fig. 12—Regression of post-cracking unloading tangent stiffness for all tested segments.

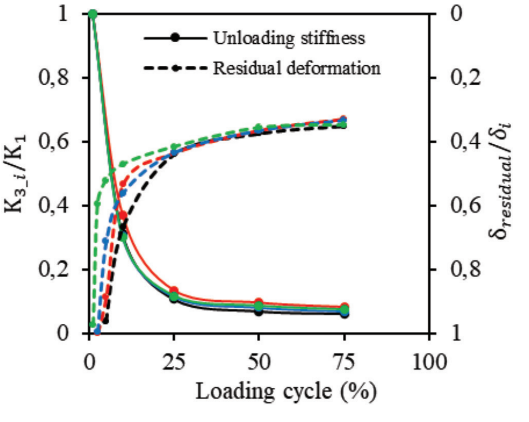

Fig. 13—Unloading stiffness degradation versus residual deformation ratio.

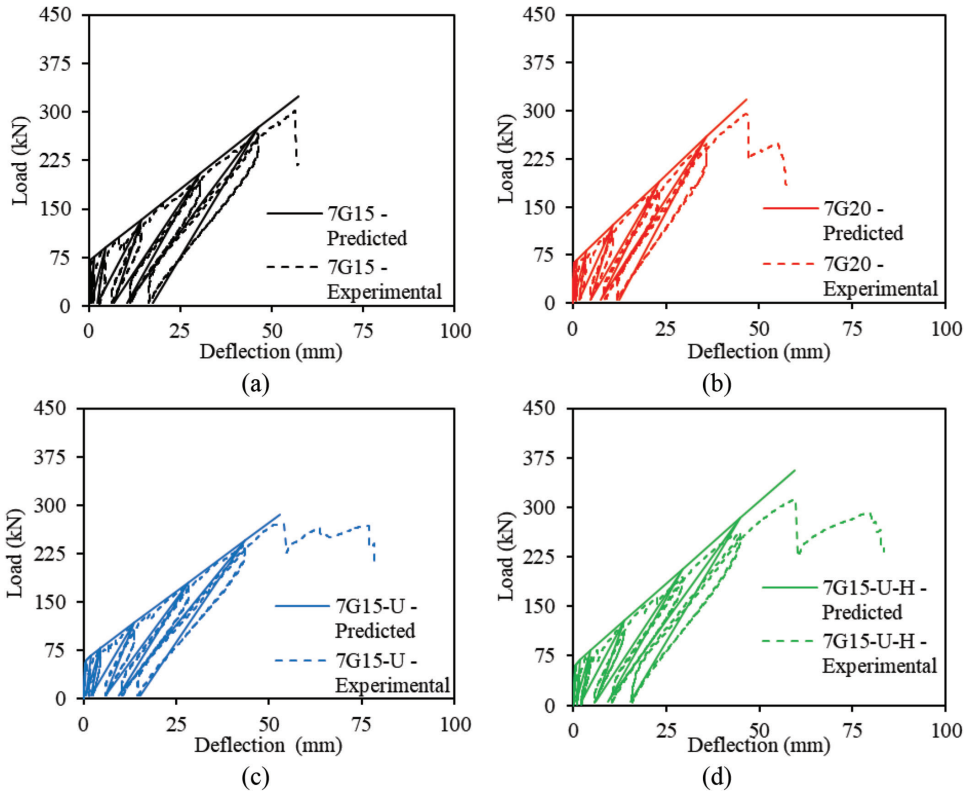

Fig. 14—Experimental versus analytically predicted hysteresis behavior for: (a) Segment 7G15; (b) Segment 7G20; (c) Segment 7G15-U; and (d) Segment 7G15-U-H. (Note: 1 kN = 0.2248; 1 mm = 0.0394 in.)

with comparable loading stiffness, unloading stiffness, and residual deformations at the end of each loading cycle.

CONCLUSIONS

This paper reported on an experimental and analytical investigation of the hysteresis behavior of curvilinear glass fiber-reinforced polymer (GFRP)-reinforced precast concrete tunnel lining (PCTL) segments under quasi-static cyclic flexural loading. Based on the experimental results and analytical findings presented herein, the following conclusions can be drawn.

1. In all second excursion loading cycles, the hysteresis response of all tested segments reflected stable cyclic behavior, with no or limited strength degradation until failure. Moreover, the unloading stiffness degradation under quasi-static cyclic flexural loading helped improve structural reparability and reduced residual deformation at the end of each cycle.

2. Although concrete fractures under cyclic loading is characterized by larger cracks and strains than concrete fractures under static loading, the linear behavior of the curvilinear GFRP-reinforced PCTL segments reduced the cyclic effects on the crack width and eliminated the residual cracks at the end of each unloading cycle.

3. All the curvilinear GFRP-reinforced PCLT segments demonstrated adequate deformability under quasi-static cyclic flexural loading when compared to the CAN/CSA S6-19 limit of 4 for rectangular GFRP-reinforced concrete sections.

4. The analytical analysis showed accurate predictions of the ultimate load-carrying capacity. The average P_{exp}/P_{pred} ratio for all tested segments was 0.92, with a standard deviation of 0.03 and coefficient of variance (COV) of 3.24%.

5. Analytical models for the post-cracking loading tangent stiffness and the unloading stiffness for the curvilinear GFRP-reinforced PCTL segments were proposed. The analytically predicted hysteresis response showed accurate predictions with comparable loading stiffness, unloading stiffness, and residual deformation at the end of each loading cycle.

6. First-of-their-kind experimental results and analytical predictions were presented for the hysteresis behavior of curvilinear GFRP-reinforced PCTL under quasi-static cyclic flexural loading. These experimental results and analytical predictions could be taken into consideration in the forthcoming design code provisions governing the efficiency of using curvilinear GFRP reinforcement for PCTL segment applications under cyclic conditions.

Additional experimental research is recommended based on the findings of the current study to investigate the mechanism-based behavior of GFRP-reinforced PCTL segments and to exploit the maximum performance of GFRP reinforcement in PCTL segment applications. Moreover, to enhance the comprehensiveness and applicability of the proposed equation for predicting the unloading stiffness of GFRP reinforced PCTL segments under quasi-static cyclic flexural loading, future research should extend the analysis beyond the limited test segments. Although the regression analysis provided valuable insights based on the four tested segments, the predictive capabilities of the equation can be significantly improved by incorporating a broader range of segments.

AUTHOR BIOS

Basil Ibrahim *is a Postdoctoral Fellow in the Department of Civil and Building Engineering at the University of Sherbrooke, Sherbrooke, QC, Canada, where he received his PhD. He received his BSc and MSc in civil engineering from the Faculty of Engineering, University of Sharjah, Sharjah, UAE. His research interests include the use of fiber-reinforced polymers (FRPs) in reinforced concrete structures.*

Salaheldin Mousa *is a Postdoctoral Fellow in the Department of Civil and Building Engineering at the University of Sherbrooke, where he received his PhD. He received his BSc and MSc from and is a Lecturer in the Faculty of Engineering at Shoubra, Benha University, Cairo, Egypt. His research interests include the use of FRPs in reinforced concrete structures.*

Hamdy M. Mohamed *is a Research Associate and Lecturer in the Department of Civil and Building Engineering at the University of Sherbrooke. He received his BSc and MSc from the Faculty of Engineering, Helwan University, Cairo, Egypt, and his PhD from the University of Sherbrooke. His research interests include the use and field applications of FRPs in reinforced concrete structures.*

Brahim Benmokrane, *FACI, is a Professor in the Department of Civil and Building Engineering at the University of Sherbrooke, Tier-1 Canada Research Chair in Advanced Composite Materials for Civil Structures, NSERC Senior Research Chair in FRP Reinforcement for Concrete Infrastructure, and Director of the University of Sherbrooke Research Center on Structural FRP Composite Materials for Concrete Structures (CRUSMAC). He is a member of ACI Committees 435, Deflection of Concrete Building Structures, and 440, Fiber-Reinforced Polymer Reinforcement, and ACI Subcommittees 440-E, FRP-Professional Education; 440-F, FRP-Repair-Strengthening; 440-H, FRP-Reinforced Concrete; 440-I, FRP-Prestressed Concrete; 440-K, FRP-Material Characteristics; and 440-L, FRP-Durability. He received the ACI Arthur J. Boase Award in 2022. His research interests include the development of FRP reinforcement for concrete structures and their durability, structural performance, and field applications.*

ACKNOWLEDGMENTS

This research was conducted with funding from the Natural Sciences and Engineering Research Council of Canada (NSERC), the Fonds de recherche du Québec en nature et technologies (FRQ-NT), the Pole de Recherche et d'Innovation en Materiaux Avances au Quebec (PRIMA Quebec), and the Tier-1 Canada Research Chair in Advanced Composite Materials for Civil Structures. The authors are grateful to the precast company (Sym-Tech Béton Préfabriqué, Sainte-Hyacinthe, QC, Canada) and to the GFRP bar manufacturer (Pultrall Inc., Thetford Mines, QC, Canada) for their effective involvement in this project, and to the technical staff of the structural lab in the Department of Civil Engineering at the University of Sherbrooke.

REFERENCES

Abbas, S., 2014, "Structural and Durability Performance of Precast Segmental Tunnel Linings," doctoral dissertation, Western University, London, ON, Canada.

Al-Saadi, N. T. K.; Mohammed, A.; Al-Mahaidi, R.; and Sanjayan, J., 2019, "A State-of-the-Art Review: Near-Surface Mounted FRP Composites for Reinforced Concrete Structures," *Construction and Building Materials*, V. 209, pp. 748-769. doi: 10.1016/j.conbuildmat.2019.03.121

ACI Committee 374, 2013, "Guide for Testing Reinforced Concrete Structural Elements under Slowly Applied Simulated Seismic Loads (ACI 374.2R-13)," American Concrete Institute, Farmington Hills, MI, 18 pp.

ACI Committee 440, 2015, "Guide for the Design and Construction of Structural Concrete Reinforced with Fiber-Reinforced Polymer (FRP) Bars (ACI 440.1R-15)," American Concrete Institute, Farmington Hills, MI.

ACI Committee 440, 2022, "Building Code Requirements for Structural Concrete Reinforced with Glass Fiber-Reinforced Polymer (GFRP) Bars—Code and Commentary (ACI CODE-440.11-22)," American Concrete Institute, Farmington Hills, MI, 260 pp.

ACI Committee 544, 2016, "Report on Design and Construction of Fiber-Reinforced Precast Concrete Tunnel Segments (ACI 544.7R-16)," American Concrete Institute, Farmington Hills, MI, 36 pp.

ASTM D7205/D7205M-21, 2021, "Standard Test Method for Tensile Properties of Fiber Reinforced Polymer Matrix Composite Bars," ASTM International, West Conshohocken, PA.

Benmokrane, B.; Mousa, S.; Mohamed, K.; and Sayed-Ahmed, M., 2021, "Physical, Mechanical, and Durability Characteristics of Newly Developed Thermoplastic GFRP Bars for Reinforcing Concrete Structures," *Construction and Building Materials*, V. 276, p. 122200. doi: 10.1016/j.conbuildmat.2020.122200

Caratelli, A.; Meda, A.; Rinaldi, Z.; and Spagnuolo, S., 2016, "Precast Tunnel Segments with GFRP Reinforcement," *Tunnelling and Underground Space Technology*, V. 60, pp. 10-20. doi: 10.1016/j.tust.2016.07.011

Caratelli, A.; Meda, A.; Rinaldi, Z.; Spagnuolo, S.; and Maddaluno, G., 2017, "Optimization of GFRP Reinforcement in Precast Segments for Metro Tunnel Lining," *Composite Structures*, V. 181, pp. 336-346. doi: 10.1016/j.compstruct.2017.08.083

CAN/CSA-S806-12, 2012, "Design and Construction of Building Components with Fiber-Reinforced Polymers (Reapproved 2017)," CSA Group Toronto, ON, Canada.

CAN/CSA-S6-19, 2019, "Canadian Highway Bridge Design Code," CSA Group, Toronto, ON, Canada.

Davis, J. R., 2000, "Corrosion: Understanding the Basics," ASM International, The Materials Information Society, Materials Park, OH, 571 pp.

Ding, L.; Wu, G.; Yang, S.; and Wu, Z., 2013, "Performance Advancement of RC Columns by Applying Basalt FRP Composites with NSM and Confinement System," *Journal of Earthquake and Tsunami*, V. 7, No. 2, p. 1350007. doi: 10.1142/S1793431113500073

Dong, Z.; Zhang, P.; Zhu, H.; Wu, G.; and Wu, Z., 2016, "Study on Stiffness and Recoverability of Fiber Reinforced Polymers-Reinforced Concrete (FRP-RC) Composite T-Beams with Prefabricated Basalt Fiber-Reinforced Polymers Shell," *Journal of Reinforced Plastics and Composites*, V. 35, No. 6, pp. 516-529. doi: 10.1177/0731684415618019

Fahmy, M. F.; Wu, Z.; and Wu, G., 2009, "Seismic Performance Assessment of Damage-Controlled FRP-Retrofitted RC Bridge Columns Using Residual Deformations," *Journal of Composites for Construction*, ASCE, V. 13, No. 6, pp. 498-513. doi: 10.1061/(ASCE)CC.1943-5614.0000046

Faza, S. S., and Gangarao, H. V., 1993, "Theoretical and Experimental Correlation of Behavior of Concrete Beams Reinforced with Fiber Reinforced Plastic Rebars," *Fiber-Reinforced-Plastic Reinforcement for Concrete Structures—International Symposium*, SP-138, A. Nanni and C. W. Dolan, eds., American Concrete Institute, Farmington Hills, MI, pp. 599-614.

Grace, N. F.; Soliman, A. K.; Abdel-Sayed, G.; and Saleh, K. R., 1998, "Behavior and Ductility of Simple and Continuous FRP Reinforced Beams," *Journal of Composites for Construction*, ASCE, V. 2, No. 4, pp. 186-194. doi: 10.1061/(ASCE)1090-0268(1998)2:4(186)

Hosseini, S. M.; Mousa, S.; Mohamed, H. M.; and Benmokrane, B., 2022, "Structural Behavior of Precast RC Tunnel Segments with GFRP Bars and Ties under Bending Load," *ACI Structural Journal*, V. 119, No. 1, Jan., pp. 1-13.

Hosseini, S. M.; Mousa, S.; Mohamed, H. M.; and Benmokrane, B., 2023a, "Development of Strength Interaction Diagrams for Designing Precast Concrete Tunnel Lining Segments Reinforced with GFRP Bars," *Engineering Structures*, V. 284, p. 115976. doi: 10.1016/j.engstruct.2023.115976

Hosseini, S. M.; Mousa, S.; Mohamed, H. M.; Ferrier, E.; and Benmokrane, B., 2023b, "Experimental and Analytical Investigation of Precast Fiber-Reinforced Concrete (FRC) Tunnel Lining Segments Reinforced with Glass-FRP Bars," *Tunnelling and Underground Space Technology*, V. 139, p. 105230. doi: 10.1016/j.tust.2023.105230

Ibrahim, B.; Mousa, S.; Mohamed, H. M.; and Benmokrane, B., 2022, "GFRP Reinforced Precast Concrete Tunnel Lining Segments under Flexural Cyclic Loading," *8th International Conference on Advanced Composite Materials in Bridges and Structures*, V. 2, pp. 149-156.

Ibrahim, B.; Mousa, S.; Mohamed, H. M.; and Benmokrane, B., 2023a, "Quasi-Static Cyclic Flexural Loading Behavior of Precast Reinforced Concrete Tunnel Segments with Glass Fiber-Reinforced Polymer Bars," *ACI Structural Journal*, V. 120, No. 4, July, pp. 73-87.

Ibrahim, B.; Mousa, S.; Mohamed, H. M.; and Benmokrane, B., 2023b, "Quasi-Static Cyclic Behavior of Precast High-Strength Concrete Tunnel Segments Reinforced with GFRP Bars," *Engineering Structures*, V. 286, p. 116159 doi: 10.1016/j.engstruct.2023.116159

Jaeger, L. G.; Mufti, A. A.; and Tadros, G., 1997, "The Concept of the Overall Performance Factor in Rectangular-Section Reinforced Concrete Members," *Proceedings*, 3rd International Symposium on Non-Metallic (FRP) Reinforcement for Concrete Structures, FRPRCS-3, V. 2, Japan Concrete Institute, Tokyo, Japan, pp. 551-559.

Mohamed, H. M.; Ali, A. H.; and Benmokrane, B., 2017, "Behavior of Circular Concrete Members Reinforced with Carbon-FRP Bars and Spirals Under Shear," *Journal of Composites for Construction*, ASCE, V. 21, No. 2, p. 04016090. doi: 10.1061/(ASCE)CC.1943-5614.0000746

Mohamed, H. M.; Ali, A. H.; and Benmokrane, B., 2019, "Mechanism of Distributed Composite GFRP Bars in Circular Concrete Members with and without Spirals under Shear," *Composites. Part B, Engineering*, V. 162, pp. 62-72. doi: 10.1016/j.compositesb.2018.10.083

Mohamed, H. M.; Ali, A. H.; Hadhood, A.; Mousa, S.; Abdelazim, W.; and Benmokrane, B., 2020, "Testing, Design, and Field Implementation of GFRP RC Soft-Eyes for Tunnel Construction," *Tunnelling and Underground Space Technology*, V. 106, p. 103626. doi: 10.1016/j.tust.2020.103626

Mohamed, H. M., and Benmokrane, B., 2015, "Torsion Behavior of Concrete Beams Reinforced with Glass Fiber-Reinforced Polymer Bars and Stirrups," *ACI Structural Journal*, V. 112, No. 5, Sept.-Oct., pp. 543-552. doi: 10.14359/51687824

Mohamed, H. M., and Benmokrane, B., 2016, "Reinforced Concrete Beams with and without FRP Web Reinforcement under Pure Torsion," *Journal of Bridge Engineering*, ASCE, V. 21, No. 3, p. 04015070. doi: 10.1061/(ASCE)BE.1943-5592.0000839

Mousa, S.; Mohamed, H. M.; and Benmokrane, B., 2018, "Flexural Strength and Design Analysis of Circular Reinforced Concrete Members with Glass Fiber-Reinforced Polymer Bars and Spirals," *ACI Structural Journal*, V. 115, No. 5, Sept.-Oct., pp. 1353-1357. doi: 10.14359/51702282

Mousa, S.; Mohamed, H. M.; and Benmokrane, B., 2019, "Strength and Deformability Aspects of Circular Concrete Members Reinforced with Hybrid Carbon-FRP and Glass-FRP Under Flexure," *Journal of Composites for Construction*, ASCE, V. 23, No. 2, p. 04019005. doi: 10.1061/(ASCE)CC.1943-5614.0000931

Mousa, S.; Mohamed, H. M.; Benmokrane, B.; and Nanni, A., 2020, "Flexural Behavior of Long-Span Square Reinforced Concrete Members with Uniformly Distributed Fiber-Reinforced Polymer Bars," *ACI Structural Journal*, V. 117, No. 4, July, pp. 209-222.

Naaman, A. E., and Jeong, S. M., 1995, "Structural Ductility of Concrete Beams Prestressed with FRP Tendons," *Proceedings of the 2nd International RILEM Symp. on Non-Metallic (FRP) Reinforcement for Concrete Structures*, RILEM, Bagneux, France, pp. 379-386.

Pan, Y., and Yan, D., 2021, "Study on the Durability of GFRP Bars and Carbon/Glass Hybrid Fiber Reinforced Polymer (HFRP) Bars Aged in Alkaline Solution," *Composite Structures*, V. 261, p. 113285. doi: 10.1016/j.compstruct.2020.113285

Rancourt, A., 2016, "Analysis of the Costs of a Tunnel Drilled between Beauport and Lévis," *Report*, Géosys, pp. 35.

Solyom, S., and Balázs, G. L., 2020, "Bond of FRP Bars with Different Surface Characteristics," *Construction and Building Materials*, V. 264, p. 119839. doi: 10.1016/j.conbuildmat.2020.119839

Spagnuolo, S.; Meda, A.; Rinaldi, Z.; and Nanni, A., 2017, "Precast Concrete Tunnel Segments with GFRP Reinforcement," *Journal of Composites for Construction*, ASCE, V. 21, No. 5, p. 04017020. doi: 10.1061/(ASCE)CC.1943-5614.0000803

Wang, Z.; Zhao, X. L.; Xian, G.; Wu, G.; Raman, R. S.; Al-Saadi, S.; and Haque, A., 2017, "Long-Term Durability of Basalt-and Glass-Fibre Reinforced Polymer (BFRP/GFRP) Bars in Seawater and Sea Sand Concrete Environment," *Construction and Building Materials*, V. 139, pp. 467-489. doi: 10.1016/j.conbuildmat.2017.02.038

Whitmore, D. W., and Ball, J. C., 2004, "Corrosion Management," *Concrete International*, V. 26, No. 12, Dec., pp. 82-85.

Xiao, S.; Li, J.; and Mo, Y. L., 2018, "Effect of Loading Rate on Cyclic Behavior of Reinforced Concrete Beams," *Advances in Structural Engineering*, V. 21, No. 7, pp. 990-1001. doi: 10.1177/1369433217737114

Zhiqiang, Z., and Mansoor, Y. A., 2013, "Evaluating the Strength of Corroded Tunnel Lining under Limiting Corrosion Conditions," *Tunnelling and Underground Space Technology*, V. 38, pp. 464-475. doi: 10.1016/j.tust.2013.08.003

aci Foundation

Building the Future

We're Building the Future

OUR MISSION

We make strategic investments in ideas, research, and people to create the future of the concrete industry.

Through its councils and programs, the ACI Foundation helps to keep the concrete industry at the forefront of advances in material composition, design, and construction.

OUR FOCUS

- Identifying technologies and innovations which provide needed solutions for the concrete industry
- Seeking concrete research projects that further the knowledge and sustainability of concrete materials, construction, and structures
- Supporting our future concrete innovators and leaders by administering fellowships and scholarships
- Helping honorably discharged veterans with our Veterans Rebate for ACI Certification program

www.acifoundation.org

ACI STRUCTURAL JOURNAL TECHNICAL PAPER

Title No. 121-S35

Numerical Analysis of Ultimate State of Reinforced Concrete Slabs under Low-Velocity Impact

by Dandan Zheng, Masato Komuro, Norimitsu Kishi, and Tomoki Kawarai

The goal of this study was to establish a numerical analysis method for predicting the ultimate state of rectangular reinforced concrete (RC) slabs simply supported on all four sides under low-velocity impact loading. To meet this goal, three-dimensional (3-D) elasto-plastic dynamic response analyses were conducted, and the applicability of the new method was investigated by comparing predictions with the experimental results. First, a preliminary analysis was conducted to determine an appropriate element size of the concrete component, a constitutive model for the concrete, and the damping factor. Then, the applicability of the method was investigated by comparing predictions with experimental results for concrete slabs with various compressive strengths. The results showed that the proposed method provides safe predictions of the maximum impact energy capacity, which may be equivalent to the load-carrying capacity of RC slabs under impact loading.

Keywords: compressive strength of concrete; low-velocity impact loading; reinforced concrete (RC) slab; three-dimensional (3-D) elasto-plastic numerical analysis; ultimate state.

INTRODUCTION

Reinforced concrete (RC) structures may be subjected to low-velocity impact loading during their service lives; for example, rocks fall on rockfall protection galleries, vehicles and/or ships collide with transportation structures, and objects are dropped during the operation of industrial or nuclear power plants. The response behavior of RC structures under low-velocity impact loading has always attracted wide attention from researchers and engineers. In recent decades, extensive experimental and numerical studies[1-5] have been performed to establish rational impact-resistant design procedures for RC structures under low-velocity impact loading. These have included studies to investigate the impact response behavior of RC slabs, which are one of the main types of structural members.

Batarlar[6] performed a comparative experimental study on the static and dynamic response behavior of RC slabs; three pairs of identical specimens were investigated. The results showed that the impact response behavior of the slabs differed significantly from the static behavior, and the displacement profiles and force distributions were greatly affected by the large inertial forces produced during impact loading. In addition, in recent years, the influence of the reinforcing bar ratio[7,8] and reinforcing bar type[9] on the impact resistance of slabs has often been investigated experimentally. The influences of the support conditions[10,11] and the contact area between the RC slab and the nose of the drop weight[12] have also been investigated experimentally.

Additionally, numerical studies have been conducted; for example, the finite element (FE) method of analysis was validated and verified to investigate the impact response behavior of RC slabs under low-velocity impact loading.[13-18] However, load-carrying capacity is one of the main design indexes for RC slabs. Thus, engineers have been interested in finding a better way of predicting and evaluating the maximum load-carrying capacity of slabs under low-velocity impact loading. Sudarsana Rao et al.[19] estimated the impact energy capacity of slurry-infiltrated fiber concrete (SIFCON) slabs by summarizing the corresponding impact energies of repeated impacts. Based on experimental results, regression models have been proposed to evaluate the impact energy of SIFCON slabs with various fiber volume fractions at the development of the first crack and in the ultimate strength stages.

In Japan, researchers proposed using the maximum reaction force to evaluate the ultimate load-carrying capacity of RC slabs subjected to low-velocity impact loading. At Muroran Institute of Technology, Kishi et al.[20,21] conducted impact load testing by dropping a 300 kg (675 lb) steel hammer on rectangular RC slabs to investigate the influence of various parameters on load-carrying capacity. They studied the effects of the diameter of the nose of the weight, slab thickness, support conditions, and loading method for single and consecutive impacts.

Xiao et al.[22] conducted numerical analyses to study the behavior of RC slabs for various conditions not included in the experimental study. The punching shear failure of RC slabs was estimated numerically from the residual deflection at the midpoint (hereafter referred to as the residual deflection) of the slab when not restored to its original state, together with the surrounding area, when deflected more than 3 mm (0.12 in.). Based on the numerical analysis results, two dimensionless empirical equations were proposed to assess the load-carrying capacities of the slabs under low-velocity impact loading. However, their accuracy has not been verified because of a lack of experimental data. Thus, it is necessary to establish a numerical analysis method for appropriately evaluating the capacity of slabs based on test data.

Thus, in this study, three-dimensional (3-D) elasto-plastic dynamic response analyses on rectangular slabs simply supported on all four sides were conducted to establish a numerical analysis method that appropriately evaluates the ultimate state of RC slabs under low-velocity impact loading.

ACI Structural Journal, V. 121, No. 3, May 2024.
MS No. S-2023-020.R1, doi: 10.14359/51740481, received August 2, 2023, and reviewed under Institute publication policies.

Table 1—Experimental program: material properties of specimens and experimental cases

Specimen	Depth of slab, mm (in.)	Yield strength of reinforcing bar f_y, MPa (ksi)	Compressive strength of concrete f_c', MPa (ksi)	Impact velocity V, m/s (ft/s)
C11	180 (7.2)	390 (56.56)	11 (1.6)	3 (9.84); 3.5 (11.48); 4 (13.12); 4.5 (14.76)
C26			26 (3.77)	4 (13.12); 4.5 (14.76); 5 (16.4); 5.5 (18.04)
C39			39 (5.66)	5.3 (17.38); 5.7 (18.7); 6 (19.68); 6.3 (20.66)

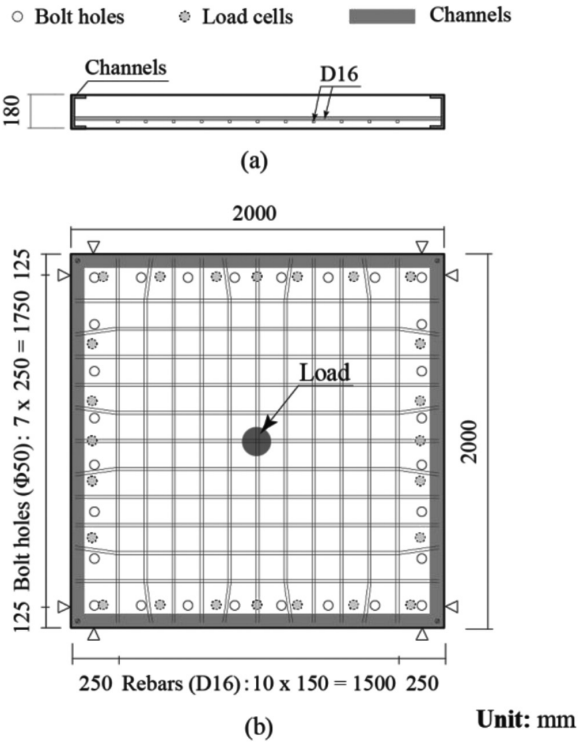

Fig. 1—Dimensions and reinforcing bar arrangement of rectangular RC slab: (a) cross-sectional view; and (b) planar view. (Note: Units in mm; 1 mm = 0.04 in.)

First, a preliminary analysis was conducted to determine an appropriate element size for the concrete model and a constitutive model for concrete together with the damping factor. Then, the numerical results for the dynamic responses of the slabs were inspected, and a numerical analysis method for predicting the ultimate state of the slabs under low-velocity impact loading was proposed. Finally, its applicability was investigated by comparing numerical predictions with experimental results for concrete slabs of various compressive strengths. The LS-DYNA commercial FE program (Version R9.0)[23] was used for the numerical simulations.

RESEARCH SIGNIFICANCE

It is not easy to numerically evaluate the load-carrying capacity of rectangular RC slabs simply supported on four sides under low-velocity impact loading. Precise numerical analysis of the behavior of the formation of the shear cone and separation from the outer area due to punching shear failure under impact loading is not feasible. However, the natural vibration state of the reaction force and deflection of a slab without structural damage can be precisely analyzed. Then, when these dynamic characteristics are completely analyzed, the slabs can be evaluated when they reach the ultimate state.

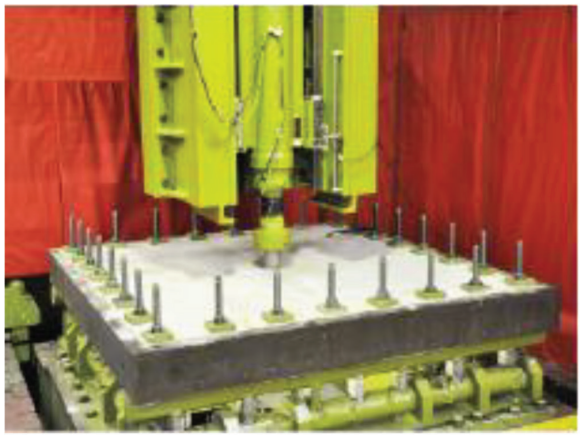

Fig. 2—Experimental setup.

EXPERIMENTAL INVESTIGATION

Experimental cases

The experimental cases chosen for this study are listed in Table 1. Twelve sets of drop-weight impact loading tests of rectangular RC slabs were performed on concretes of various compressive strengths. In this table, the specimens are designated by adding "C" to the compressive strength of the concrete (MPa). The compressive strengths of the concrete used in this study were between 11 and 39 MPa (1.6 and 5.66 ksi), as obtained from compressive strength tests. The tensile strength of the main reinforcing bar (SD345 for all cases) was 390 MPa (56.56 ksi), as obtained from testing small specimens.

Dimensions of RC slabs

Figure 1 shows the dimensions and reinforcing bar arrangement of the rectangular RC slabs simply supported on all four sides that were used in this study. The dimensions (width x length x depth) of all the slabs were 2000 x 2000 x 180 mm (80 x 80 x 7.2 in.), and the clear spans in the two directions were both 1750 mm (70 in.). The slab considered in this study may be applicable for practical design purposes because the shear span-depth ratio of the slab is more than 5. The reinforcing bars were placed only at the lower fiber of the slabs, and the average depth of the concrete cover was 40 mm (1.6 in.) for all slabs. Deformed reinforcing bars φ = 16 mm (0.64 in.) in diameter were placed at intervals of 150 mm (6 in.) in two directions and welded to channel-shaped steel members at both ends of the slabs to save anchorage length. The reinforcing bar ratio was 1.1% in both directions.

Experimental method and measured quantities

Figure 2 shows the experimental setup used in this study. Impact tests were conducted by a single free drop of a 300 kg (675 lb) steel weight from a prescribed height onto the center of the slab. In addition, to confirm the drop height of the weight, the impact velocity was measured in the experiment and converted to the corresponding drop height. The velocities for each specimen are listed in Table 1. The weight was made of a solid steel cylinder 1400 mm (56 in.) in height, the striking part was 90 mm (3.6 in.) in diameter, and its impacting nose was tapered with a height of 2 mm (0.08 in.) to prevent one-sided contact.

The slab was simply supported on all four sides and fixed with bolts and nuts to prevent the ends of the slab from lifting. The boundary conditions of the supporting structure were at least close to a pin support, where only rotation was allowed, and horizontal movement was restrained.

In this experiment, the time histories of the impact force, the total reaction force (hereafter referred to as the reaction force), and the midpoint deflection (hereafter referred to as the deflection) were measured. The impact and reaction forces were measured using load cells that were installed in the steel weight and the supports, respectively, and the deflection was measured by using noncontact laser-type linear variable displacement transducers (LVDTs). Crack patterns on the lower surface and in the central cross section of each slab were sketched after the experiment.

OVERVIEW OF NUMERICAL ANALYSIS

FE model

Figure 3 shows an example of the FE model with element size L = 5 mm (0.2 in.) for the slabs used in this study. Because there were two axes of symmetry, only one-quarter of the slab, the steel weight, and the support were modeled. In this numerical model, eight-node solid elements were used with one integration point, except for the channel-shaped steel members at the ends of the slabs, which were modeled using four-node shell elements. To properly consider the dowel effect of the reinforcing bar due to the punching shear crack of the slab, solid elements were used in this analysis instead of beam elements. Meanwhile, for simplicity of the FE model, the cross section of the main reinforcing bar was modified into a square shape with the same area as the real one. A cubic solid element was used for the concrete part.

Regarding boundary conditions in the FE model for numerical analysis, the displacement in the direction normal to the symmetrical surface was restrained, and the central axes at the lower surfaces of the supports were allowed to rotate freely in accordance with experimental conditions. It was assumed that the concrete was perfectly bonded to the reinforcing bars and the channel-shaped steel members. The contact surface model was introduced to consider the interactions between the impacted surface of concrete and the nose of the steel weight and between the concrete and the supports, including the bolts and nuts. The friction factor at the contact surface was assumed to be 0.2 based on previous studies[14,24] and pre-analysis results.

The impact load was applied by inputting the impact velocity for all elements of the steel weight placed in contact with the upper surface of the slab. Gravity was considered in the numerical analysis.

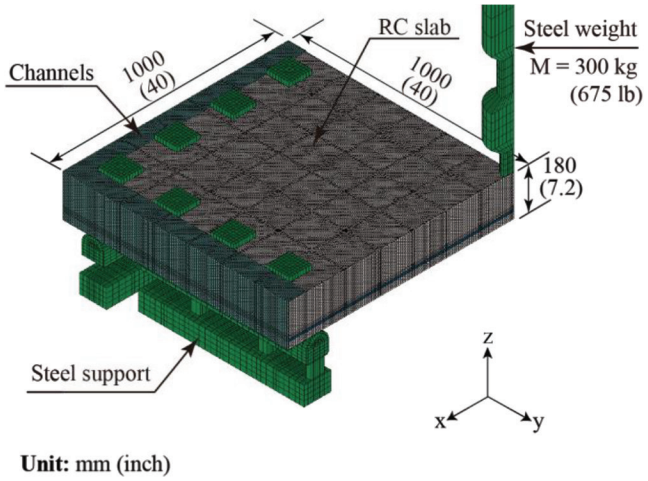

Fig. 3—Example of finite element model with element length L = 5 mm (0.2 in.) for rectangular RC slab.

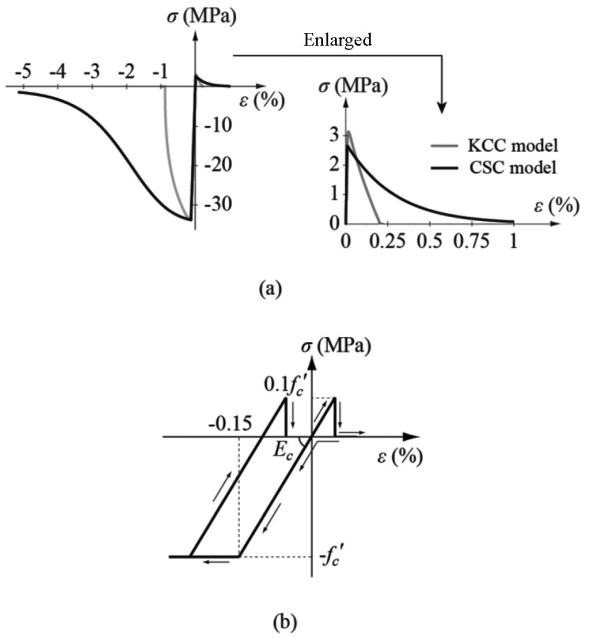

Fig. 4—Constitutive model for concrete: (a) KCC and CSC models; and (b) proposed model. (Note: 1 MPa = 145 psi.)

Material models

Figures 4 and 5 show the stress-strain relationships of the concrete and reinforcing bar used in this study. In the numerical analysis, because the impact velocity was relatively small, the strain-rate effect was not considered for all the materials.

Figure 4 shows the stress-strain relationships of the concrete used in this study. A preliminary analysis was performed to investigate the effect of the constitutive model for the concrete on the dynamic responses of the slabs. Three other constitutive models for concrete were used: the Karagozian and Case concrete (KCC) model,[25] the continuous surface cap (CSC) model,[26] and the proposed model. Figure 4(a) shows the KCC and CSC constitutive models;

both models considered tension and compression softening. Figure 4(b) shows the isotropic elasto-plastic model used in this study, in which a bilinear model was applied in the compression region, and a cutoff model was applied in the tension region having the same elastic modulus as the compression region based on previous studies.[27,28] The strain-rate effects for reinforcing bar and concrete materials were not considered for simplicity because the low-velocity impact load was surcharged to the slab. In this model, it was assumed that: 1) the concrete yielded at 0.15% strain; 2) the yield stress was equal to the compressive strength f_c' listed in Table 1; 3) the yielding of concrete was evaluated using the Drucker-Prager yield criterion; and 4) the tensile stress was interrupted when an applied negative pressure reached the tensile strength of concrete f_{t0}, which was set to one-tenth of the compressive strength f_c'. The internal friction angle for the concrete was set to 30 degrees. For the three different constitutive models of the concrete, the values of the density ρ_c and Poisson's ratio ν_c were assumed to be $\rho_c = 2.35 \times 10^3$ kg/m^3 (146.69 lb/ft^3) and $\nu_c = 0.167$, respectively.

Figure 5 shows the stress-strain relationships for the reinforcing bar. In this study, an isotropic elasto-plastic model was applied, and a plastic hardening modulus H' was not considered. The yielding of the reinforcing bar was determined by means of the von Mises yield criterion. The density ρ_s, Young's modulus E_s, and Poisson's ratio ν_s of the main reinforcing bar were assigned the following nominal values: $\rho_s = 7.85 \times 10^3$ kg/m^3 (490 lb/ft^3), $E_s = 206$ GPa (29.88×10^3 ksi), and $\nu_s = 0.3$, respectively.

The steel weight, the supporting apparatus, and the channel-shaped steel members at the ends of the slabs were assumed to be elastic bodies because no plastic deformation was observed during the experiment. These material properties, except the density of the steel weight, were assumed to be identical to those of the reinforcing bar. The density of the weight was evaluated by dividing the actual mass (300 kg [675 lb]) by the volume of the FE model.

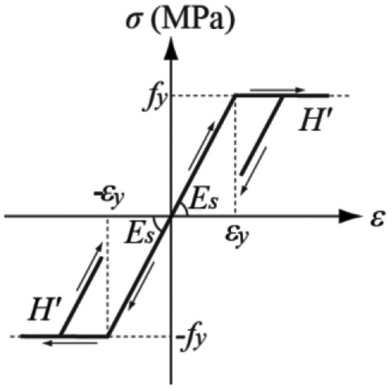

Fig. 5—Constitutive model for reinforcement.

PRELIMINARY ANALYSIS FOR SLAB C26 UNDER IMPACT LOADING

In this study, a preliminary numerical analysis was conducted to determine an appropriate element size for the concrete model, a constitutive model for the concrete, and a damping factor by comparing the numerical and experimental results for the time histories of the impact response waves for Slab C26.

Element size in concrete model

Figure 6 shows the influence of the element size in the concrete model on the time histories of the impact force, reaction force, and deflection for Slab C26. The proposed

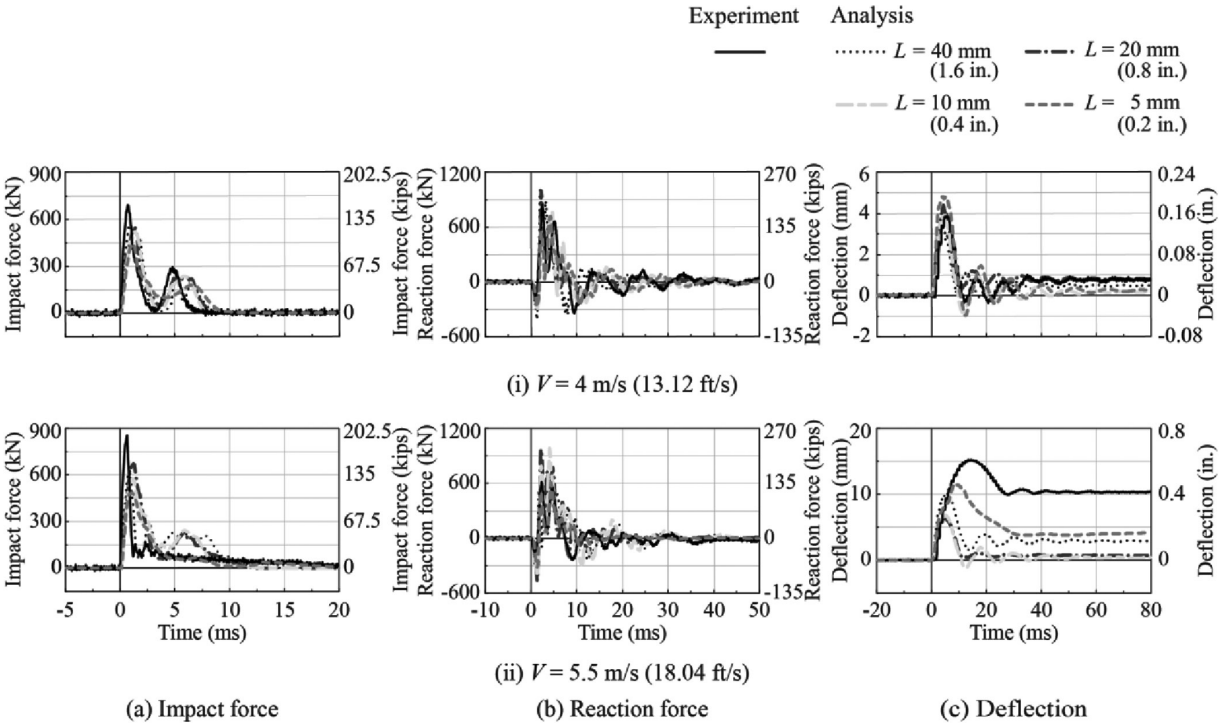

Fig. 6—Comparison of impact response waves with varying element size L *of concrete: (a) impact force; (b) reaction force; and (c) deflection.*

constitutive model of the concrete was used, the damping factor was set to h = 5%, and various values of the cubic element length L were used: 40, 20, 10, and 5 mm (1.6, 0.8, 0.4, and 0.2 in.). Two cases of the impact velocity V were considered, V = 4 and 5.5 m/s (13.12 and 18.04 ft/s). In the case of V = 5.5 m/s (18.04 ft/s), after the experiment, the slab was severely damaged due to punching shear failure.

These comparisons showed that: 1) in the case of impact velocity V = 4 m/s (13.12 ft/s), the numerical impact response waves were similar to those of the experimental results irrespective of the magnitude of the element size; and 2) in the case of impact velocity V = 5.5 m/s (18.04 ft/s), even though the maximum impact force underestimated that given by the experimental results when adopting the element size L = 5 mm (0.2 in.), the reaction force and deflection could be better evaluated than for the other element sizes.

Constitutive model of concrete

Figure 7 shows the influence of the constitutive model of the concrete on the time histories of the dynamic responses for Slab C26 under impact velocities V = 4 and 5.5 m/s (13.12 and 18.04 ft/s), where the element size in the concrete model was L = 5 mm (0.2 in.), and the damping factor was set to h = 5%.

According to the comparisons, when using the KCC model, the analyses of the second wave of the impact force and the natural vibration state of the reaction force after unloading cannot be analyzed numerically. Additionally, the maximum and residual deflections overestimated the experimental results. When using the CSC model at an impact velocity V = 4 m/s (13.12 ft/s), the predicted time histories of the impact and reaction forces were better than those using the KCC model. However, the residual deflection was overestimated, and the natural vibration state of the deflection after unloading cannot be analyzed fully. At impact velocity V = 5.5 m/s (18.04 ft/s), the flattened second wave of the impact force cannot be analyzed accurately, and the maximum reaction force was overestimated. With the proposed constitutive model, even though the maximum impact force was underestimated, the second impact force, the reaction force, and the deflection time histories could be qualitatively well predicted by the three models for both impact velocities, V = 4 and 5.5 m/s (13.12 and 18.04 ft/s).

Therefore, the dynamic response of the slabs under low-velocity impact loading may be qualitatively better analyzed by using the proposed constitutive model for the concrete than the KCC and CSC models.

Damping factor

In this study, the damping factor, depending on the mass effect, was considered for the fundamental vertical natural vibration frequency of the slab. Figure 8 compares the numerical and experimental results for the impact responses of Slab C26 for various values of the damping factor from 0 to 7.5% under the impact velocity V = 4 m/s (13.12 ft/s), where the concrete element size was set as L = 5 mm (0.2 in.), and the proposed constitutive model for concrete was used.

This figure shows that: 1) the time histories of the impact and reaction forces obtained from the numerical results were in good agreement with the experimental results irrespective of the magnitude of the damping factor considered in this study; 2) the deflections tended to decrease with an increase in the damping factor h; and 3) in the case of damping factors h = 5 and 7.5%, the configuration of the time history of the deflection and the maximum deflection obtained from the numerical results were similar and in good agreement with those of the experimental results. Therefore, the damping factor h = 5% was used for subsequent numerical analyses.

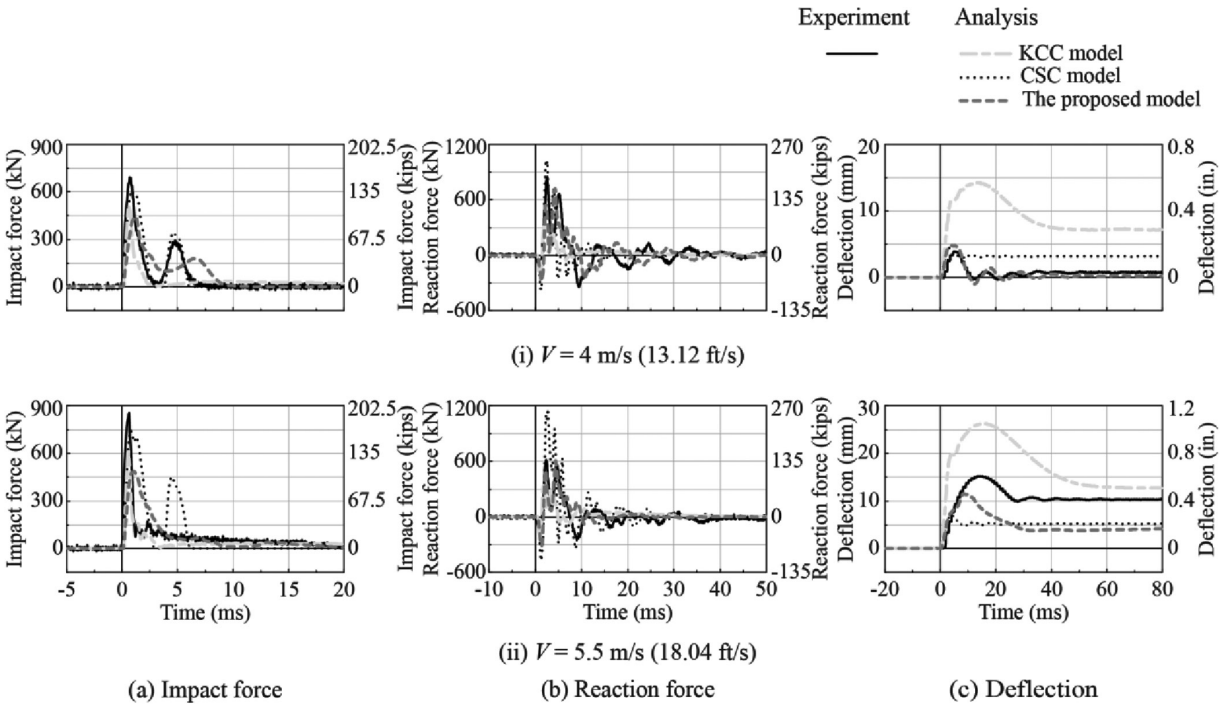

Fig. 7—Comparison of impact response waves for various concrete constitutive models: (a) impact force; (b) reaction force; and (c) deflection.

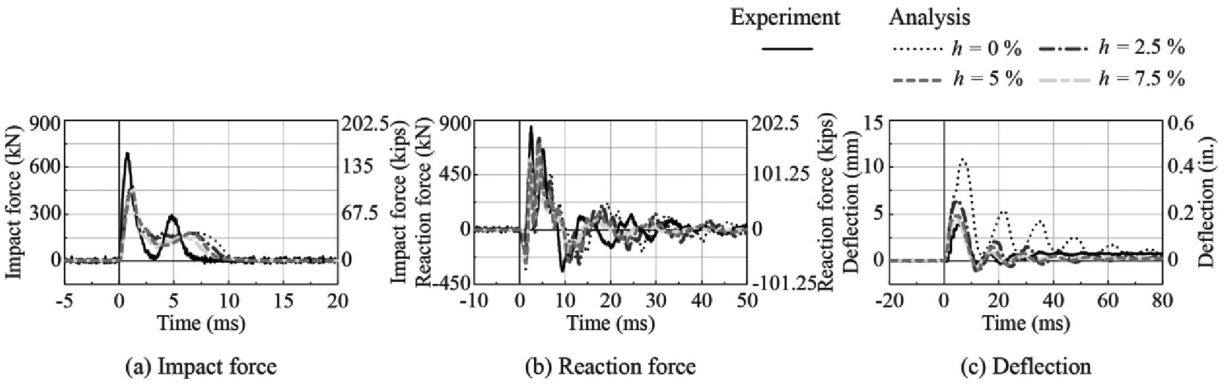

Fig. 8—Comparison of impact response waves for various values of damping factor h *under impact velocity* V = *4 m/s (13.12 ft/s): (a) impact force; (b) reaction force; and (c) deflection.*

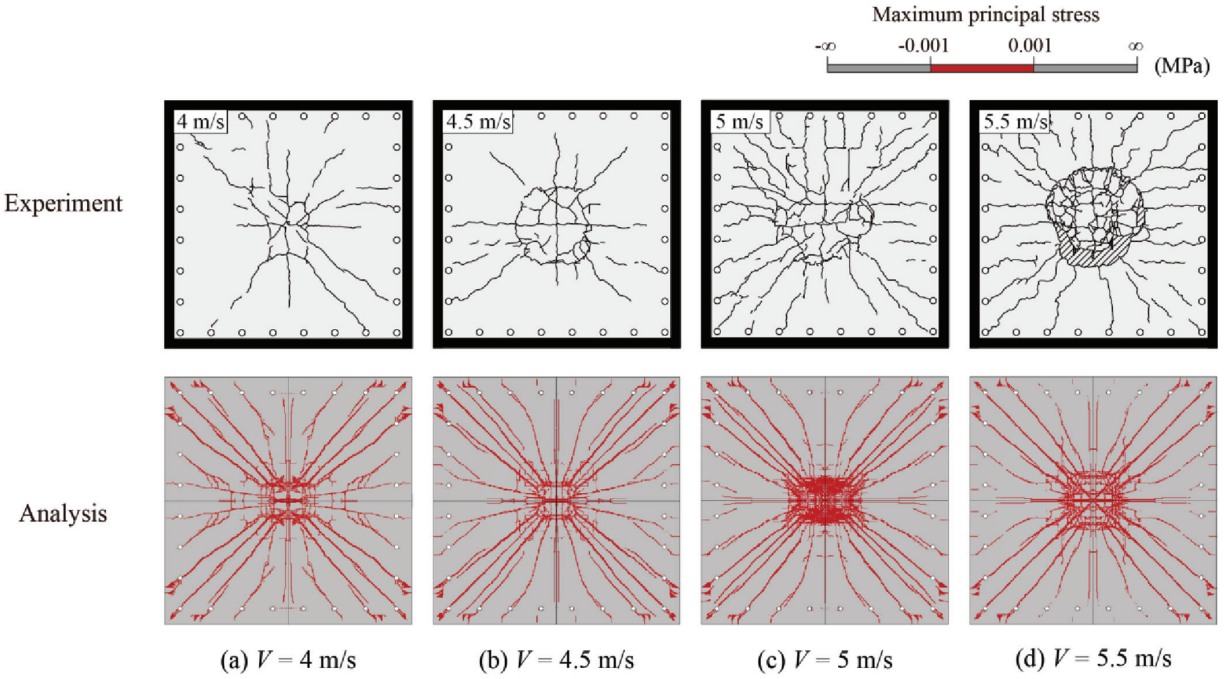

Fig. 9—Comparisons of crack patterns on bottom surface in Slab C26. (Note: 1 m/s = 3.28 ft/s.)

NUMERICAL RESULTS AND DISCUSSION

Comparisons of crack patterns after experiment for Slab C26

Adopting the constitutive law model for concrete, as shown in Fig. 4(b), cracks occurred in the elements when the tensile stress reached the cutoff value and the stress in the element was lost. In this study, applying this idea, the crack occurring in the element will be predicted, in which the concrete element will have a zero-stress contour (–0.001 to 0.001), as shown in Fig. 9 and 10.

Figures 9 and 10 show comparisons between the crack patterns on the bottom and central section surfaces of Slab C26 during the experiment and the maximum principal stress contours when the maximum deflection occurred. In the experimental results, for an impact velocity V = 4 m/s (13.12 ft/s), the crack patterns consisted of circular cracks on the impacted area and cross-diagonal cracks from the center to the corners on the bottom surface, with faint diagonal cracks on the central section surface. With increasing impact velocity, in the cases of impact velocities V = 4.5 and 5 m/s (14.76 and 16.4 ft/s), circular cracks, cross-diagonal cracks, and flexural cracks occurred more extensively on the bottom surface, and punching shear failure-type diagonal cracks clearly developed on the central section surface. However, the slabs were more or less still in an undamaged state. In the case of impact velocity V = 5.5 m/s (18.04 ft/s), spalling along the circular cracks on the bottom surface was observed, and a punching shear cone was generated in the center section surface and separated from the slab. Then, the slab failed due to punching shear.

Comparing the crack patterns between the experimental and numerical results, it is seen that when RC slabs under low-velocity impact loading are in a damaged state before reaching punching shear failure, circular and diagonal cracks on the bottom surface and 45-degree shear cracks on the central section surface can be appropriately evaluated. On the other hand, when the RC slab reached the ultimate state with punching shear failure in the case of V = 5.5 m/s (18.04 ft/s), the damage state of concrete spalling on the bottom surface and separation between the punching shear

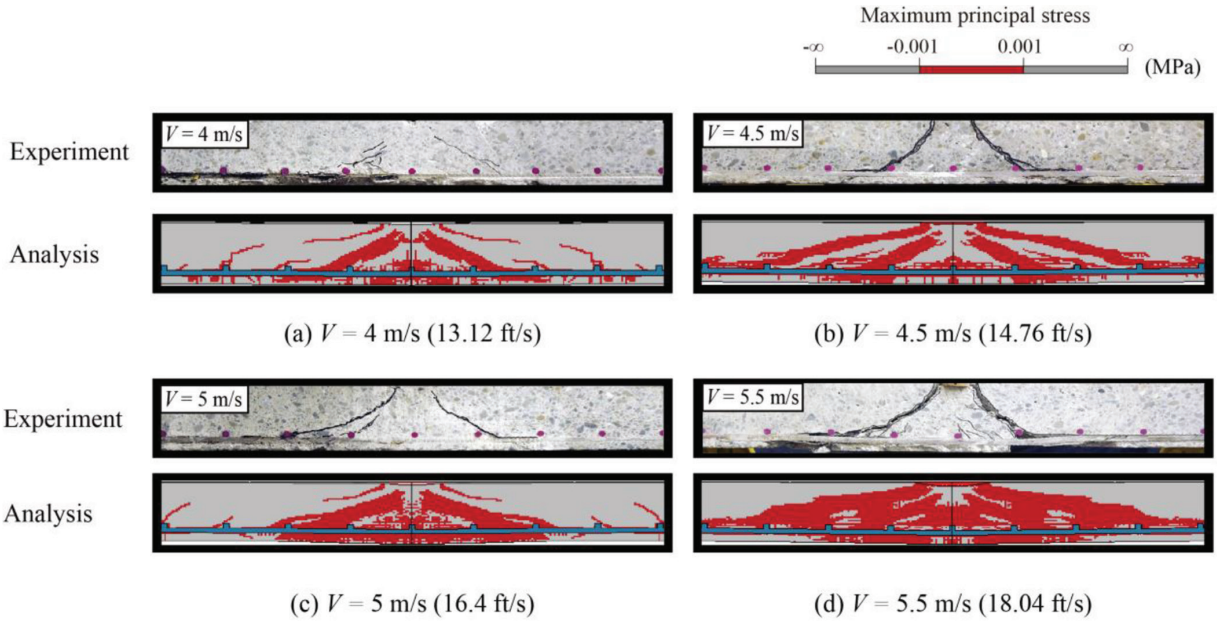

Fig. 10—Comparisons of crack patterns on central section surface in Slab C26.

cone and RC slab on the central section surface that occurred in the experiment cannot be numerically and better reproduced due to the smeared crack model being applied in this numerical analysis.

Comparisons of impact response waves for Slab C26

Figure 11 compares the time histories of the impact force, reaction force, and deflection from the experimental and numerical results for Slab C26 under various impact velocities.

Figure 11(a) shows comparisons of the time histories of the impact force during a 20 ms time interval from the beginning of impact. The experimental results show that: 1) the configurations of the time history of impact forces were composed of two triangular waves, where the first wave had a large amplitude and short duration, and the second wave had a smaller amplitude and longer duration; 2) however, in the case of impact velocity V = 5.5 m/s (18.04 ft/s), in which the slab failed in the punching shear failure mode, the second wave was flattened, and its duration was prolonged; and 3) the maximum impact force tended to increase with increasing impact velocity.

The comparison between the experimental and numerical results showed that although the maximum impact force obtained from the numerical results underestimated the force obtained from the experimental results, configurations of the time history were qualitatively in good agreement with the numerical and experimental results, including a flattened second wave in the case of V = 5.5 m/s (18.04 ft/s).

Figure 11(b) shows comparisons of the time histories of the reaction force during a 50 ms time interval from the beginning of impact. The findings from this figure indicated that: 1) the main wave of the reaction force was composed of a half-sine wave with approximately 10 ms duration and high-frequency components with a period of approximately 2.5 ms; 2) afterward, damped free vibration occurred; 3) in the case of impact velocities V = 4, 4.5, and 5 m/s (13.12, 14.76, and 16.4 ft/s), the configurations of the time history obtained from the numerical results better predicted the experimental results consisting of a loading state and a natural vibration state; 4) however, in the case of the impact velocity V = 5.5 m/s (18.04 ft/s), even though the time histories obtained from the numerical results better described the main response of the experimental results, they did not describe the natural vibration state.

Figure 11(c) shows comparisons of the time histories of the deflection from the experimental and numerical results during an 80 ms time interval from the beginning of impact. From this figure, it follows that: 1) in the cases of impact velocities V = 4, 4.5, and 5 m/s (13.12, 14.76, and 16.4 ft/s), the numerical results were qualitatively in good agreement with the experimental results that were composed of a half-sine wave with the maximum response at the beginning of impact, and afterward, there was a damped free vibration state with some residual deflection; and 2) in the case of V = 5.5 m/s (18.04 ft/s), even though a damped free vibration of small amplitude was excited experimentally, the numerical analysis produced only a residual deflection without vibration.

Based on the numerical results for the slab that underwent punching shear failure, the evaluated second wave of the impact force time history was found to be flattened, and a damped free vibration state of the reaction force, the deflection time histories, and the residual deflection could not be more accurately evaluated; thus, the ultimate state of the slabs may be evaluated for the impact velocity V = 5.5 m/s (18.04 ft/s).

The applicability of the proposed numerical method for predicting the ultimate state of the slabs under low-velocity impact loading is investigated in the cases of Slabs C11 and C39 in the subsequent sections.

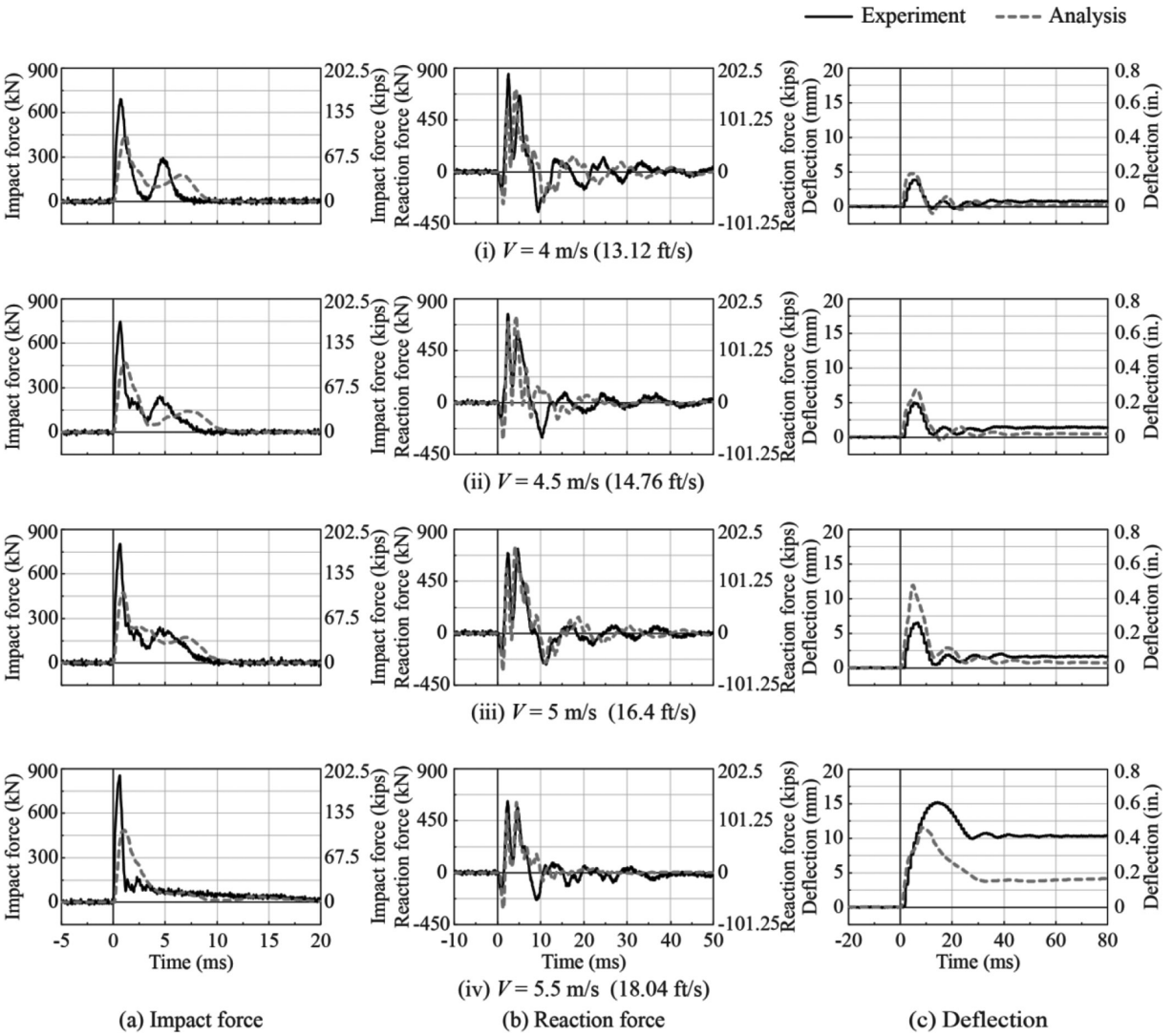

Fig. 11—Comparison of impact response waves for Slab C26: (a) impact force; (b) reaction force; and (c) deflection.

Crack patterns after experiment for Slab C11

Figure 12 shows the crack patterns on the bottom surface and the central section surface of Slab C11 after the experiments. In this figure: 1) in the cases of impact velocities V = 3 and 3.5 m/s (9.84 and 11.48 ft/s), cross-diagonal cracks on the bottom surface and faint diagonal cracks in the central section occurred, but the slab was still in an undamaged state; 2) in the case of V = 4 m/s (13.12 ft/s), even though diagonal cracks occurred in the central section, the slab was not punched out perfectly; and 3) in the case of V = 4.5 m/s (14.76 ft/s), the slab was perfectly punched out near the loading point, and then the slab reached the ultimate state.

Comparisons of impact response waves for Slab C11

Figure 13 shows comparisons of the time histories of the impact force, reaction force, and deflection for the experimental and numerical results of Slab C11. In this figure: 1) the impact force waves for both experimental and numerical results flattened at an impact velocity of V = 4 m/s (13.12 ft/s); 2) the damped free vibration state did not appear for the numerical reaction force time history at V = 4 m/s (13.12 ft/s); and 3) even though the damped free vibration of the deflection did not occur at V = 4.5 m/s (14.76 ft/s) experimentally, the vibration disappeared at V = 3.5 m/s (11.48 ft/s) numerically. Thus, according to the numerical results, the slab reached its ultimate state at V = 4 m/s (13.12 ft/s).

Crack patterns after experiment for Slab C39

Figure 14 shows the crack patterns of Slab C39 after the experiments. In this figure, for impact velocities of V = 5.3, 5.7, and 6 m/s (17.38, 18.7, and 19.68 ft/s), the crack patterns were composed of circular cracks and cross-diagonal cracks on the bottom surface, and punching shear-type diagonal cracks formed on the central section surface; however, the slab was still in an undamaged state. However, in the case of impact velocity V = 6.3 m/s (20.66 ft/s), spalling occurred on the lower surface of the impacted area, and the shear cone was punched out. The slab completely collapsed at this stage.

Comparisons of impact response waves for Slab C39

Figure 15 shows comparisons of the time histories of the impact response waves between the experimental results and the numerical results for Slab C39. This figure indicates the following: 1) the numerical impact force flattened at an

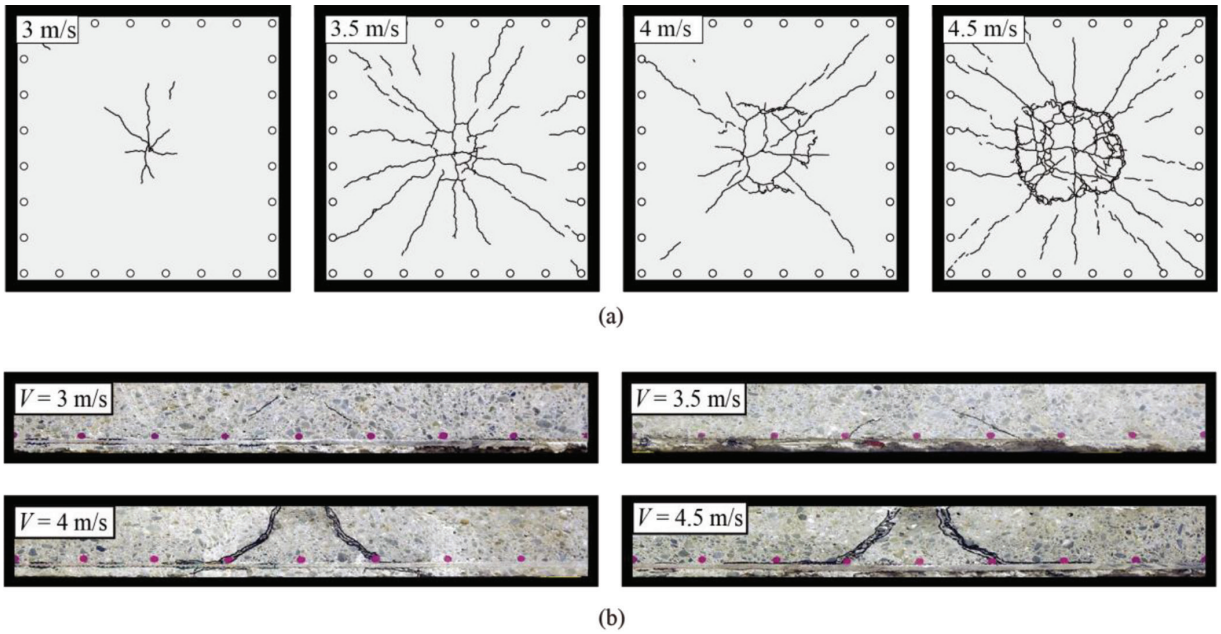

Fig. 12—Crack patterns in Slab C11 after the experiment: (a) bottom surface; and (b) central section surface.

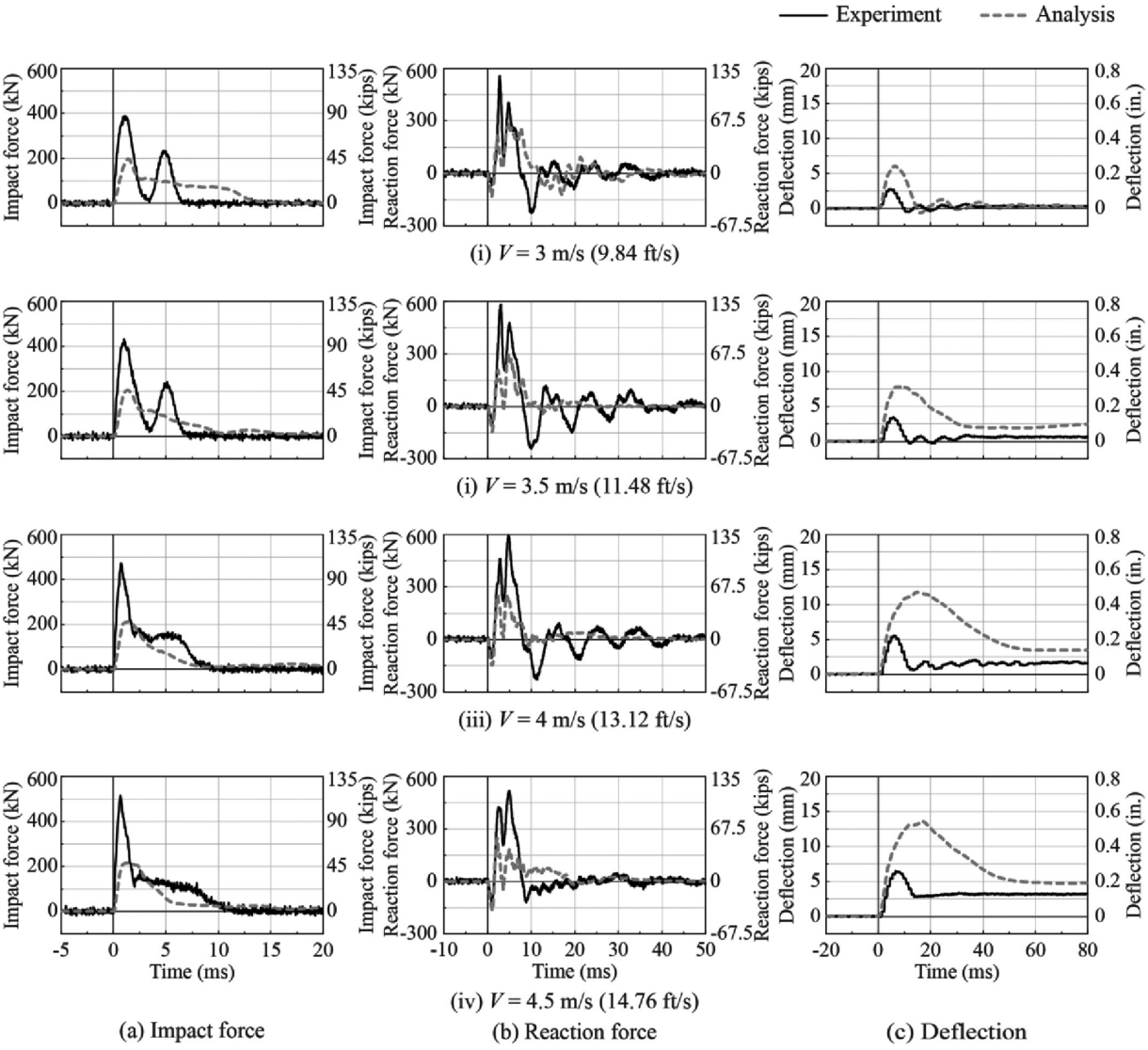

Fig. 13—Comparison of impact response waves for Slab C11: (a) impact force; (b) reaction force; and (c) deflection.

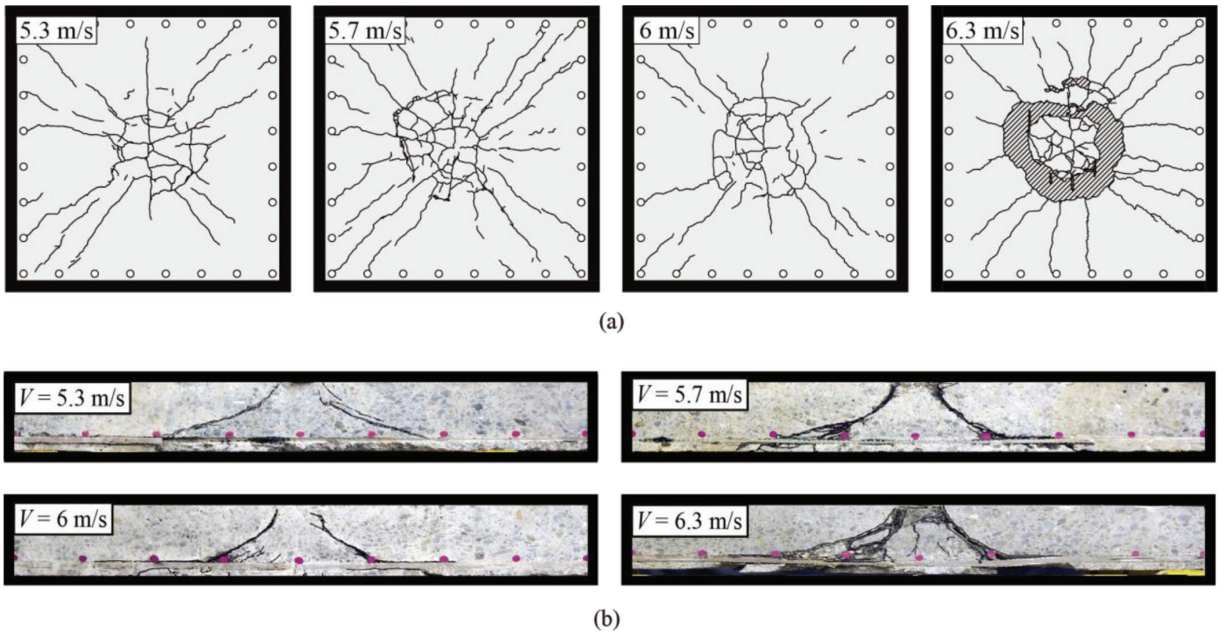

Fig. 14—Crack patterns in Slab C39 after experiment: (a) bottom surface; and (b) central section surface.

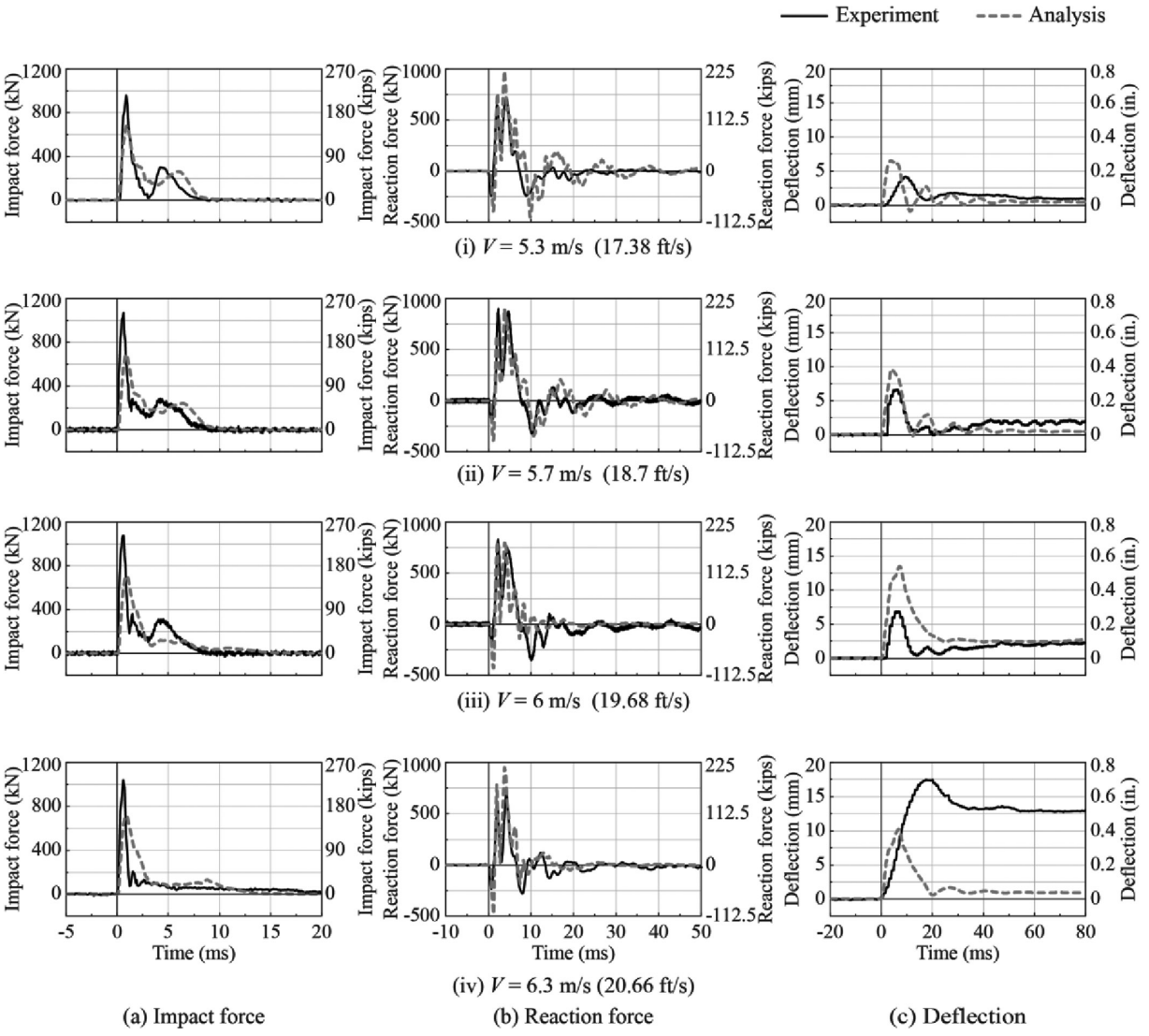

Fig. 15—Comparison of impact response waves for Slab C39: (a) impact force; (b) reaction force; and (c) deflection.

Table 2—Minimum impact velocities for slabs reaching ultimate state

Specimen	Experimental results V_{min}, m/s (ft/s)	Numerical results V_{min}, m/s (ft/s)
C11	4.5 (14.76)	4 (13.12)
C26	5.5 (18.04)	5.5 (18.04)
C39	6.3 (20.66)	6 (19.68)

impact velocity V = 6.3 m/s (20.66 ft/s); 2) the damped free vibration state in the numerical reaction force and deflection waves were missing at V = 6 m/s (19.68 ft/s); and then 3) the ultimate state of the slab was estimated numerically as V = 6 m/s (19.68 ft/s), which was a conservative (safe) value.

Comparisons of impact velocities at slab upon reaching ultimate state

The comparisons of the experimental and numerical results for the impact velocity at the energy capacity of the simply supported rectangular RC slabs are summarized in Table 2.

Defining the smallest impact velocity as the minimum impact velocity V_{min} when the RC slab reaches the ultimate state with punching shear failure, according to the comparisons of the velocity V_{min} between the numerical and experimental results: 1) V_{min} tended to increase with increasing compressive strength of the concrete; and 2) V_{min} obtained from the numerical results was preferably evaluated conservatively (on the safe side) from the engineering perspective.

Therefore, the maximum impact energy capacity of simply supported rectangular RC slabs under low-velocity impact loading may be evaluated conservatively (on the safe side) using the proposed method, in which the energy capacity can be considered equivalent to the load-carrying capacity of the slab under impact loading.

CONCLUSIONS

In this study, a method was proposed for predicting the ultimate state of rectangular slabs simply supported on all four sides under low-velocity impact loading. The proposed method was applied by comparing the numerical dynamic response of the impact force, the reaction force, and the midpoint deflection with the experimental results. Its applicability was investigated by comparing experimental results for various compressive strengths of the concrete. As a result, the following conclusions were obtained:

1. When reinforced concrete (RC) slabs under low-velocity impact loading are in a structurally undamaged state, the impact response waves can be adequately analyzed numerically by using the proposed constitutive model for concrete regardless of the concrete element length considered in this study.

2. The dynamic response waves of the slabs under low-velocity impact loading may be qualitatively better analyzed using the proposed constitutive model for concrete than the Karagozian and Case concrete (KCC) and continuous surface cap (CSC) models.

3. When the RC slabs under low-velocity impact loading are in a structurally undamaged state, the circular and diagonal cracks on the bottom surface and 45-degree shear cracks on the central section surface can be appropriately evaluated by means of the proposed analysis method.

4. When the RC slabs under low-velocity impact loading are in a structurally undamaged state, the second wave of the impact force, the natural vibration state of the reaction force and the deflection, and residual deflection after unloading can be analyzed numerically. Therefore, if these dynamic characteristics cannot be analyzed numerically, then the slab can be evaluated upon reaching the ultimate state.

5. The maximum impact energy capacity, which may be equivalent to the load-carrying capacity of the RC slabs under impact loading, can be better evaluated using the proposed numerical analysis method conservatively (on the safe side) from the engineering perspective.

AUTHOR BIOS

Dandan Zheng *is a Lecturer in the College of Civil and Architectural Engineering at Liaoning University of Technology, Jinzhou, Liaoning, China. She received her PhD from Muroran Institute of Technology, Muroran, Hokkaido, Japan. Her research interests include numerical analysis studies of reinforced concrete structures under impact loading.*

Masato Komuro *is a Professor in the College of Engineering at Muroran Institute of Technology, where he received his PhD. His research interests include experimental and numerical analysis studies of impact problems in rockfall protection structures.*

ACI member **Norimitsu Kishi** *is a Specially Appointed Professor in the College of Engineering at Muroran Institute of Technology. He received his PhD from Hokkaido University, Sapporo, Hokkaido, Japan. His research interests include experimental and numerical analysis studies of impact and strengthening problems in concrete structures using advanced materials.*

Tomoki Kawarai *is an Assistant Professor in the College of Engineering at Muroran Institute of Technology, where he received his PhD. His research interests include experimental and numerical analysis studies of impact and strengthening problems in concrete members.*

REFERENCES

1. Kishi, N.; Khasraghy, S. G.; and Kon-No, H., "Numerical Simulation of Reinforced Concrete Beams under Consecutive Impact Loading," *ACI Structural Journal*, V. 108, No. 4, July-Aug. 2011, pp. 444-452.

2. Kishi, N., and Mikami, H., "Empirical Formulas for Designing Reinforced Concrete Beams under Impact Loading," *ACI Structural Journal*, V. 109, No. 4, July-Aug. 2012, pp. 509-519.

3. Sohel, K. M. A.; Al-Jabri, K.; and Al Abri, A. H. S., "Behavior and Design of Reinforced Concrete Building Columns Subjected to Low-Velocity Car Impact," *Structures*, V. 26, Aug. 2020, pp. 601-616. doi: 10.1016/j.istruc.2020.04.054

4. Asad, M.; Dhanasekar, M.; Zahra, T.; and Thambiratnam, D., "Failure Analysis of Masonry Walls Subjected to Low Velocity Impacts," *Engineering Failure Analysis*, V. 116, Oct. 2020, Article No. 104706. doi: 10.1016/j.engfailanal.2020.104706

5. Zhu, X.; Zhao, P.; Tian, Y.; and Wang, R., "Experimental Study of RC Columns and Composite Columns under Low-Velocity Impact," *Thin-Walled Structures*, V. 160, Mar. 2021, Article No. 107374. doi: 10.1016/j.tws.2020.107374

6. Batarlar, B., "Behavior of Reinforced Concrete Slabs Subjected to Impact Loads," master's thesis, Department of Civil Engineering, İzmir Institute of Technology, Urla, İzmir, Turkey, 2013, 112 pp.

7. Yılmaz, T.; Kıraç, N.; Anil, Ö.; Erdem, R. T.; and Kaçaran, G., "Experimental Investigation of Impact Behaviour of RC Slab with Different Reinforcement Ratios," *KSCE Journal of Civil Engineering*, V. 24, No. 1, Jan. 2020, pp. 241-254. doi: 10.1007/s12205-020-1168-x

8. Said, A. I., and Mabrook Mouwainea, E., "Experimental Investigation on Reinforced Concrete Slabs under High-Mass Low Velocity Repeated Impact Loads," *Structures*, V. 35, Jan. 2022, pp. 314-324. doi: 10.1016/j.istruc.2021.11.016

9. Zineddin, M., and Krauthammer, T., "Dynamic Response and Behavior of Reinforced Concrete Slabs under Impact Loading," *International*

Journal of Impact Engineering, V. 34, No. 9, Sept. 2007, pp. 1517-1534. doi: 10.1016/j.ijimpeng.2006.10.012

10. Anil, Ö.; Kantar, E.; and Yilmaz, M. C., "Low Velocity Impact Behavior of RC Slabs with Different Support Types," *Construction and Building Materials*, V. 93, Sept. 2015, pp. 1078-1088. doi: 10.1016/j.conbuildmat.2015.05.039

11. Yılmaz, T.; Kıraç, N.; Anıl, Ö.; Erdem, R. T.; and Hoşkal, V., "Experimental and Numerical Investigation of Impact Behavior of Reinforced Concrete Slab with Different Support Conditions," *Structural Concrete*, V. 21, No. 6, Dec. 2020, pp. 2689-2707. doi: 10.1002/suco.202000216

12. Şengel, S.; Erol, H.; Yılmaz, T.; and Anıl, Ö., "Investigation of the Effects of Impactor Geometry on Impact Behavior of Reinforced Concrete Slabs," *Engineering Structures*, V. 263, July 2022, Article No. 114429. doi: 10.1016/j.engstruct.2022.114429

13. Kishi, N.; Kurihashi, Y.; Ghadimi Khasraghy, S.; and Mikami, H., "Numerical Simulation of Impact Response Behavior of Rectangular Reinforced Concrete Slabs under Falling-Weight Impact Loading," *Applied Mechanics and Materials*, V. 82, 2011, pp. 266-271. doi: 10.4028/www.scientific.net/AMM.82.266

14. Mokhatar, S. N., and Abdullah, R., "Computational Analysis of Reinforced Concrete Slabs Subjected to Impact Loads," *International Journal of Integrated Engineering*, V. 4, No. 2, 2012, pp. 70-76.

15. Trivedi, N., and Singh, R. K., "Prediction of Impact Induced Failure Modes in Reinforced Concrete Slabs through Nonlinear Transient Dynamic Finite Element Simulation," *Annals of Nuclear Energy*, V. 56, June 2013, pp. 109-121. doi: 10.1016/j.anucene.2013.01.020

16. Kezmane, A.; Chiaia, B.; Kumpyak, O.; Maksimov, V.; and Placidi, L., "3D Modelling of Reinforced Concrete Slab with Yielding Supports Subject to Impact Load," *European Journal of Environmental and Civil Engineering*, V. 21, No. 7-8, 2017, pp. 988-1025. doi: 10.1080/19648189.2016.1194330

17. Anas, S. M.; Alam, M.; and Umair, M., "Effect of Design Strength Parameters of Conventional Two-Way Singly Reinforced Concrete Slab under Concentric Impact Loading," *Materials Today: Proceedings*, V. 62, Part 4, 2022, pp. 2038-2045. doi: 10.1016/j.matpr.2022.02.441

18. Yılmaz, T.; Anil, Ö.; and Erdem, R. T., "Experimental and Numerical Investigation of Impact Behavior of RC Slab with Different Opening Size and Layout," *Structures*, V. 35, Jan. 2022, pp. 818-832. doi: 10.1016/j.istruc.2021.11.057

19. Sudarsana Rao, H.; Ghorpade, V. G.; Ramana, N. V.; and Gnaneswar, K., "Response of SIFCON Two-Way Slabs under Impact Loading," *International Journal of Impact Engineering*, V. 37, No. 4, Apr. 2010, pp. 452-458. doi: 10.1016/j.ijimpeng.2009.06.003

20. Kishi, N.; Mikami, H.; and Kurihashi, Y., "An Impact Resistant Design Procedure for Simply Supported RC Slabs under Low-Velocity Impact Loading," *Journal of Structural Engineering, A*, V. 55A, 2009, pp. 1327-1338. (in Japanese)

21. Kishi, N.; Mikami, H.; and Kurihashi, Y., "Effects of Support Condition and Slab Thickness on Impact Resistant Behavior of Reinforced Concrete Slabs," *Journal of Structural Engineering, A*, V. 58A, 2012, pp. 1000-1009. (in Japanese)

22. Xiao, Y.; Li, B.; and Fujikake, K., "Behavior of Reinforced Concrete Slabs under Low-Velocity Impact," *ACI Structural Journal*, V. 114, No. 3, May-June 2017, pp. 643-658. doi: 10.14359/51689565

23. LSTC, "LS-DYNA Keyword User's Manual," Version R9.0, Livermore Software Technology Corporation, Livermore, CA, 2016.

24. Erdem, R. T., and Gücüyen, E., "Non-Linear Analysis of Reinforced Concrete Slabs under Impact Effect," *Građevinar*, V. 69, No. 6, 2017, pp. 479-487. doi: 10.14256/JCE.1557.2016

25. Malvar, L. J.; Crawford, J. E.; Wesevich, J. W.; and Simons, D., "A Plasticity Concrete Material Model for DYNA3D," *International Journal of Impact Engineering*, V. 19, No. 9-10, Oct.-Nov. 1997, pp. 847-873. doi: 10.1016/S0734-743X(97)00023-7

26. Murray, Y. D., "Users Manual for LS-DYNA Concrete Material Model 159," Report No. FHWA-HRT-05-062, Federal Highway Administration, McLean, VA, 2007, 92 pp.

27. Bhatti, A. Q.; Kishi, N.; Mikami, H.; and Ando, T., "Elasto-Plastic Impact Response Analysis of Shear-Failure-Type RC Beams with Shear Rebars," *Materials & Design*, V. 30, No. 3, Mar. 2009, pp. 502-510. doi: 10.1016/j.matdes.2008.05.068

28. Kishi, N., and Bhatti, A. Q., "An Equivalent Fracture Energy Concept for Nonlinear Dynamic Response Analysis of Prototype RC Girders Subjected to Falling-Weight Impact Loading," *International Journal of Impact Engineering*, V. 37, No. 1, Jan. 2010, pp. 103-113. doi: 10.1016/j.ijimpeng.2009.07.007

ACI STRUCTURAL JOURNAL TECHNICAL PAPER

Title No. 121-S36

Interface Shear Capacity and Flexural Performance of Hybrid Beams

by Ravi Singh, Yukihiro Sato, Hitoshi Sasaki, David Mukai, and Susumu Kono

This paper introduces details of a new hybrid beam system connected to a reinforced concrete (RC) column. The hybrid beam system is a wide-flange steel beam embedded in RC beams on both ends without any shear connectors. The wide-flange steel beam does not penetrate through the beam-column joint, which reduces the fabrication cost compared to the typical steel beam-RC column hybrid system. A total of 10 hybrid beam specimens were designed with a slab-web interface. Four specimens were used to examine the shear sliding capacity at the slab-web interface, and an equivalent coefficient of friction at the interface, together with a method to evaluate the shear sliding capacity, was proposed. The remaining six specimens were used to examine the flexural capacity and plastic deformation capacity of the hybrid beam, and shear-friction reinforcement details required for ductile flexural behavior were proposed.

Keywords: coefficient of friction; concrete-to-concrete interface; concrete-to-steel interface; flexural capacity; hybrid beam; shear-friction capacity; shear-friction reinforcement; slab-web interface.

INTRODUCTION

Singh et al.[1-5] proposed an innovative hybrid system that consists of reinforced concrete (RC) columns and a hybrid beam system, as shown in Fig. 1. The hybrid beam system consists of a composite beam (W-beam with shear connectors) in the midspan and hybrid beams on both ends. The hybrid beam is a W-beam embedded in cantilevered RC beams without any shear connectors. The W-beam stops at the column face and does not penetrate through the beam-column joint, which reduces the fabrication cost and saves labor when compared to the typical steel beam-RC column hybrid system indicated in a previous paper.[1] Confining reinforcement A and B (high-strength bundled bars) act as a lever action and enable smooth force transfer from the W-beam to the surrounding RC beam, as shown in Fig. 2.

In ordinary construction for the proposed hybrid system, concrete is cast for slabs and webs at the same time, and their concrete strengths are the same. However, the required concrete strength for slabs is lower than that of webs from the structural behavior viewpoint. For buildings with a large-scale floor area, casting the slabs and webs with the same concrete strengths (concrete strength of web) would increase the construction cost, resulting in an uneconomical design. Hence, designers prefer different concrete strengths for slabs and webs for an economical and rational design. Previous researchers[1-8] discussed the flexural performance of hybrid beams with monolithic concrete, but no researchers have clarified the shear-slip behavior at the slab-web interface of the hybrid beams when the concrete of the slab and web are cast at different times.

Mast,[9] Birkeland and Birkeland,[10] and other researchers[11-18] conducted experiments on connections in precast concrete members and introduced the shear-friction theory. The shear-friction theory states that the shear force is resisted by the friction at the interface and the dowel action of reinforcement across the interface. Mattock et al.[19-24] and others[25] conducted further studies on the interface of concrete using pushoff and pulloff tests and expanded the application of this equation. Based on their studies, the design method for shear friction at the interface was introduced in ACI 318-19[26] and the Architectural Institute of Japan (AIJ) guidelines.[27] ACI 318 (Table 22.9.4.2)[26] shows the coefficient of friction between the concrete-to-concrete interface as 1.4 to 0.6, according to the surface preparation. The coefficient of friction between the concrete-to-steel interface is considered 0.7 when the steel has headed studs or welded bars. ACI 318[26] refers to ANSI/AISC 360-16[28] for the design method of concrete to steel (composite beam), but ANSI/AISC 360[28] provides no references for this value of 0.7, as mentioned by Lini.[29] Instead, Lini[29] provides references, mostly with shear connectors, from which designers can select the value that matches their detail. This method cannot be considered rational because the values selected vary according to the designer.

The proposed hybrid beam system has a steel W-beam without any shear connectors in the hybrid beam region, as shown in Fig. 1. The web concrete is cast up to the upper surface of the steel W-beam flange first, and the slab concrete is cast afterward. Therefore, the values indicated in ANSI/AISC 360[28] and the design method for shear friction shown in ACI 318[26] cannot be applied because both concrete-to-concrete and concrete-to-steel interfaces exist at the slab-web interface. This paper shows the experiment on 10 hybrid beam specimens, first to clarify the shear capacity at the slab-web interface of the hybrid beam by introducing an equivalent coefficient of friction, and second to examine the flexural performance of the proposed hybrid beams.

RESEARCH SIGNIFICANCE

This paper explains a design method for shear sliding at the slab-web interface of hybrid beams so that the ductile

ACI Structural Journal, V. 121, No. 3, May 2024.
MS No. S-2023-027.R1, doi: 10.14359/51740482, received November 8, 2023, and reviewed under Institute publication policies.

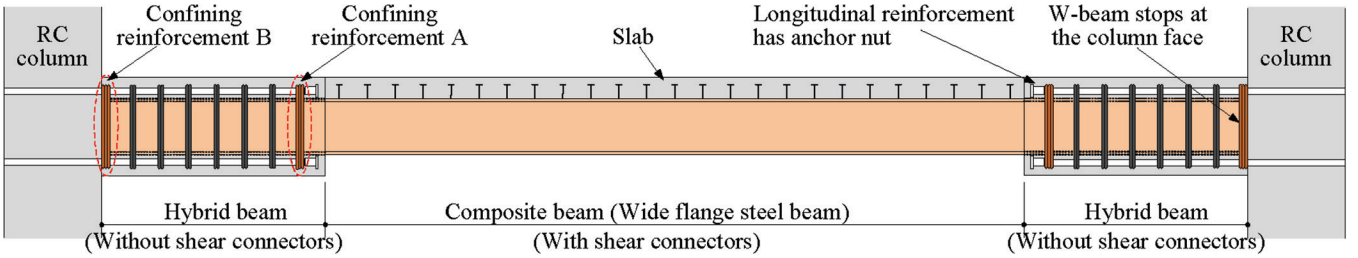

Fig. 1—Proposed hybrid beam system.

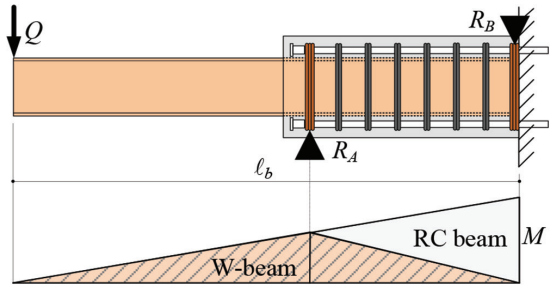

Fig. 2—Lever action and moment distribution of hybrid beam.

flexural behavior is guaranteed under seismic loading. The proposed design method enables engineers and constructors to use different concrete strengths for slabs and webs according to the design requirement because previous studies on the flexural performance of hybrid beams were based on monolithic concrete. This results in a rational and economical design and reduces the construction cost when the proposed hybrid beam system is employed.

EXPERIMENTAL INVESTIGATION

Specimens

A total of 10 half-scale hybrid beam specimens were designed for two series of experiments, as shown in Table 1. Figure 3 shows the dimensions and reinforcement details of No. 1 and No. 2 as examples. Two hybrid beams were anchored to the RC reaction block without interacting with each other during the loading test. The W-beam, which was as-rolled structural steel free of paint and without shear connectors, was placed in the web so that the upper faces of the W-beam and the web of the hybrid beam coincided. The hybrid beam had longitudinal reinforcement with anchor nuts at the end, shear reinforcement, confining reinforcement A (C.R.A), and confining reinforcement B (C.R.B) around the W-beam. C.R.A. is bundled welded square bars placed at the free end of the hybrid beam, and C.R.B is those at the column face. After casting concrete around the W-beam to complete the web of the hybrid beam, the laitance was removed and the concrete surface was roughened to an amplitude of 6 mm. After 1 week of curing, slab concrete was cast on top of the web of the hybrid beam. The hybrid beam had the same width for the slab and web in this experiment.

Four specimens in Series I were designed to fail in shear sliding at the slab-web interface to study the shear sliding capacity. Six specimens in Series II were designed to fail in flexure to study the effect of construction joints on the ductility of the hybrid beams. Series II was designed based on the test results of Series I, and the shear sliding capacity to flexural capacity margin was set to be larger than 1.0.

Series I—The test variable was the amount of shear-friction reinforcement across the slab-web interface, as shown in Table 1. The shear-friction reinforcement included the shear reinforcement, C.R.A, and C.R.B. Specimens No. 1 and 2 were identical but had different shear reinforcement ratios of 0.16% and 0.36%, respectively. Specimens No. 3 and 4 were also identical but had a different amount of C.R.A of 428 and 571 mm^2, respectively. The amount of C.R.A and C.R.B was determined so that the tensile force of C.R.A and C.R.B counterbalanced with the lever reactions R_A and R_B, respectively, shown in Fig. 2, when load Q is applied at the tip of the beam.

Series II—The parameters of this test were concrete design strength of web of 36 and 60 MPa in specimens No. 5 and No. 6, shear reinforcement ratio of 0.33% and 0.50% in specimens No. 7 and No. 8, and amount of C.R.A of 428 and 571 mm^2 in specimens No. 9 and No. 10, while the other variables were identical.

The mechanical properties of the concrete, reinforcement, and steel W-beam are listed in Table 2.

Test procedure

The specimen was set on the reaction floor, as shown in Fig. 4. The cyclic loading was applied simultaneously to the two free ends of the W-beams. The upward loading (slab in compression) was positive. The displacement at the loading point of the W-beam and the free end of the hybrid beam and the slab-web interface slip was measured, as shown in Fig. 5. The drift angle (drift afterward) at the loading point and the drift at the hybrid beam were obtained using the equations in Fig. 5. The loading protocol using drift at the loading point is shown in Table 3. The strain was monitored from strain gauges placed on the reinforcement and W-beam.

EXPERIMENTAL RESULTS

Damage process

Table 4 summarizes the measured shear force for the cracking at the slab-web interface (Q_{jc}): one for the yielding of the shear-friction reinforcement (Q_{fry}), one for the yielding of the longitudinal reinforcement of the hybrid beam (Q_{by}), and one for the maximum capacity ($Q_{b\ max}$). Figure 6 shows crack patterns of the hybrid beam at the maximum capacity. The damage process for Series I and II is presented as follows.

Series I—The discussion focuses on the results under the negative loading because the negative loadings keep the slab

Table 1—Details of specimens

Specimen No.	ℓ_b, mm	ℓ_{RC}, mm	B_c x D_c, mm; t_s, mm	F_{cs}, MPa	F_{cw}, MPa	L.R., mm	Stirrups, mm	p_w, %	C.R.A	C.R.B	D_s x B_s x t_w x t_f, mm
Series I											
No. 1	2200	1150	400 x 480; 90	27	48	6-D22	2-D10@220	0.16	8-D10	6-D10	300 x 200 x 12 x 19
No. 2							2-D10@100	0.36	14-D10	8-D10	
No. 3	2300	920	430 x 480; 90	24	60	4-D22	4-D6@60	0.50	6-K10	6-K10	300 x 120 x 12 x 16
No. 4									8-K10	6-K10	
Series II											
No. 5	2300	920	430 x 480; 90	24	36	4-D22	4-D6@50	0.60	10-K6	6-K10	300 x 120 x 12 x 16
No. 6					60						
No. 7					36	4+2-D19	4-D6@90	0.33	10-K6	6-K10	
No. 8					60		4-D6@60	0.50			
No. 9							4-D6@60	0.50	6-K10	6-K10	
No. 10									8-K10	6-K10	

Note: L.R. is longitudinal reinforcement; C.R.A is confining reinforcement A; C.R.B is confining reinforcement B; D6, D10, D19, and D22 are deformed bars with ordinary strength; K6 and K10 are deformed bars with high strength. Numerals indicate nominal diameter.

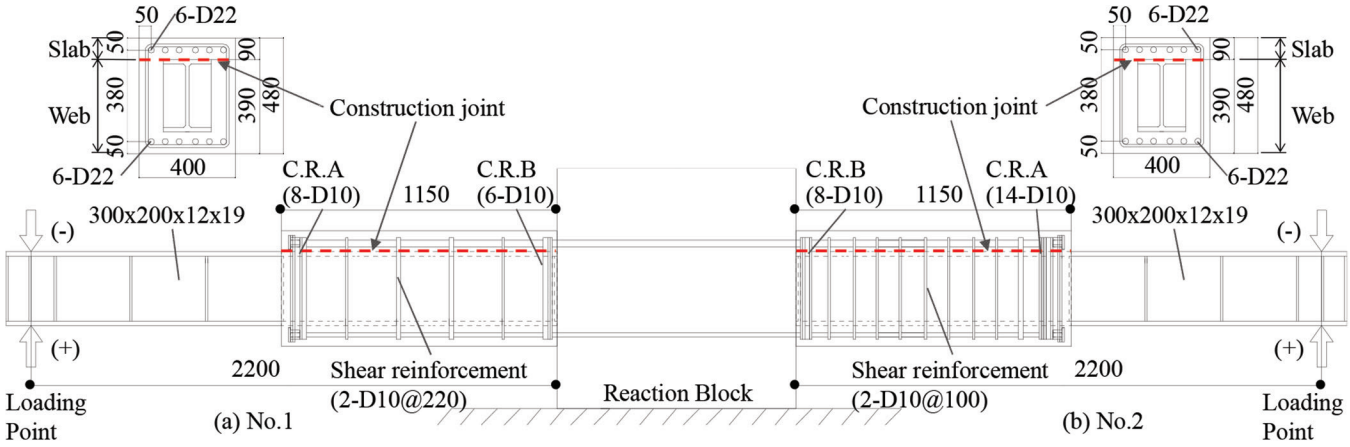

Fig. 3—Reinforcement details.

in tension, and the slip at the interface is more likely to occur. Flexural cracks occurred adjacent to the reaction block, and horizontal cracks occurred at the slab-web interface. Shear-friction reinforcement yielded at R_b = –0.5 to –1.0%, and shear cracks started to occur after R_b = 1.0%. As the drift increased, the horizontal cracks extended along the slab-web interface and reached the flexural cracks but did not reach the reaction block face, as clearly seen in specimens No. 3 and 4. This implies C.R.B does not prevent shear sliding, and this is confirmed when evaluating the shear capacity at the slab-web interface. After the peak, the horizontal cracks at the slab-web interface and flexural cracks grew larger in width, the slip along the interface became several millimeters, and the cover concrete of the slab spalled at the end of the loading. All four hybrid beams failed in shear sliding at the slab-web interface (SL mode) in the negative loading.

Series II—Similarly to specimens in Series I, flexural cracks formed adjacent to the reaction block, horizontal cracks occurred at the slab-web interface, and then the shear cracks occurred in the hybrid beam. As the drift increased, the flexural cracks became remarkable, and the longitudinal reinforcing bars and shear-friction reinforcement across the slab-web interface yielded. At the peak, cover concrete spalled off in specimen No. 7, which had the least shear-friction reinforcement of the six specimens. This implies that the amount of shear-friction reinforcement was not adequate to hold the slab-web interface intact and resist shear sliding. This is discussed later when evaluating the plastic deformation capacity. At the end of the loading, all six hybrid beams failed in flexure (F mode) in the positive loading and failed in shear sliding at the slab-web interface after flexural yielding in the negative loading (FSL mode).

Load-drift relationship

The load-drift relationships are shown in Fig. 7. The dotted lines are the drift at the loading point (R_b), and the solid lines are the drift of the hybrid beam (R_{RC}).

Series I—Similarly to the damage process, the results of the negative loadings are discussed. Specimens No. 1 and 2 showed slip-type load-drift relationships due to slip along the slab-web interface caused by the yielding of the shear-friction reinforcement across the interface. Increasing the shear-friction reinforcement enhanced the shear capacity at the slab-web interface in specimen No. 2. Specimens

Table 2—Mechanical properties of materials

Concrete				
Specimen No.		σ_B, MPa	E_c, GPa	σ_t, MPa
Slab	No. 1, No. 2	30.4	28.1	2.66
	No. 3, No. 4	24.4	25.4	2.42
	No. 5, No. 6	23.1	26.3	2.19
	No. 7, No. 8	23.4	26.0	2.14
	No. 9, No. 10	24.5	25.8	2.29
Web	No. 1, No. 2	53.5	35.3	4.47
	No. 3, No. 4	59.9	34.9	4.42
	No. 5	40.2	31.4	3.27
	No. 6	66.3	37.8	4.47
	No. 7	41.1	30.3	3.13
	No. 8	64.7	36.3	4.83
	No. 9, No. 10	63.3	34.7	4.80

Reinforcement			
Specimen No.	Size, mm	σ_y, MPa	E_s, GPa
No. 3~No. 10	D6	320	152
No. 5~No. 8	K6	833	169
No. 1, No. 2	D10	352	185
No. 3~No. 10	K10	913	168
No. 7~No. 10	D19	505	189
No. 1, No. 2	D22	690	199
No. 3~No. 6	D22	520	191

Steel W-beam			
Specimen No.	Size, mm	σ_y, MPa	E_s, GPa
No. 1, No. 2	t12	382	209
No. 3~No. 10		344	208
	t16	342	209
No. 1, No. 2	t19	412	210

No. 3 and 4 showed a slight load increase after yielding of shear-friction reinforcement until the peak load was reached at a relatively large drift of R_b = 3.5 to 4.0%. The slight load increase is due to the dowel action of shear-friction reinforcement after initial cohesion broke at the interface. However, these two specimens have a negligible difference in the load-drift relationships and do not show the effect of varying C.R.A.

Series II—All six specimens showed stable flexural-type backbone curves up to R_b = 2.0%. Specimens started to show pinched hysteresis loops after the bond deterioration due to yielding of all longitudinal reinforcement at R_b = 2.0%. In the negative loadings, peaks were reached at smaller drifts, and the post-peak load capacities decreased gradually due to the yielding of the shear-friction reinforcement. The damage was little in specimen No. 6 (Fig. 6), which had a higher concrete design strength of the web than No. 5, and a good cohesion between concrete and reinforcement resulted in a slight swelling of the loop. Specimen No. 7, which had the least shear-friction reinforcement, showed a slip-type load-drift relationship, and the load gradually decreased in the negative loading after reaching the peak at R_b = –1.0%. In contrast, specimen No. 8 had a fat hysteresis loop, showing good energy dissipation as a result of a better dowel action. Varying C.R.A showed a negligible difference in the load-drift relationships of specimens No. 9 and 10.

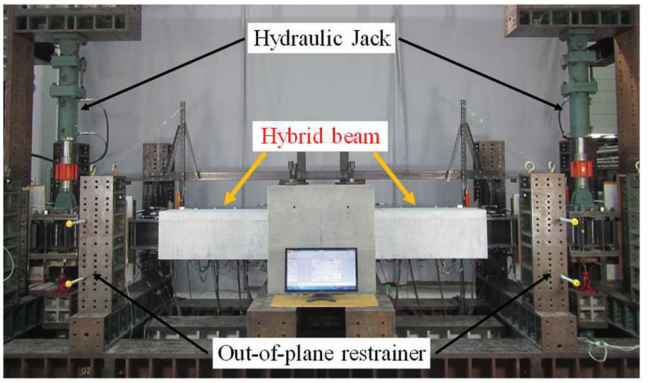

Fig. 4—Loading setup.

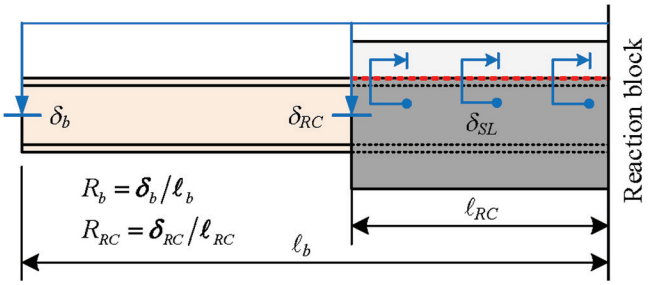

Fig. 5—Measurement of drift angle and interface slip.

Table 3—Loading protocol

R_b, %	0.25	0.5	1.0	1.5	2.0	3.0	4.0	5.0	6.0
No. of cycles	±1		±2				±1		

SHEAR CAPACITY AT SLAB-WEB INTERFACE

The shear capacity at the slab-web interface in hybrid beam was evaluated using Eq. (1) based on the design method in ACI 318.[26] It is assumed that the interface shear capacity is the summation of the interface friction action and dowel action of the shear-friction reinforcement. The interface friction comes from the two kinds of interfaces, as illustrated in Fig. 8: the concrete-to-concrete interface and the concrete-to-W-beam interface. This paper proposes an equivalent coefficient of friction, defined in Eq. (2), to consider frictions from the two kinds of interfaces. It is noted $q_{fr(h)}$ in Eq. (1) is less than the maximum value shown in Table 22.9.4.4 of ACI 318.[26]

$$q_{fr(h)} = \mu_{eq}(a_w \cdot \sigma_{wy} + {}_A a_w \cdot {}_A\sigma_{wy} + {}_B a_w \cdot {}_B\sigma_{wy})\ (\text{N}) \quad (1)$$

$$\mu_{eq} = \frac{\mu_c \cdot b_c + \mu_s \cdot B_s}{B_c} \quad (2)$$

Table 4—Summary of major experimental results

Specimen No.		Q_b, kN				Failure mode
		Q_{jc}	Q_{fry}	Q_{by}	$Q_{b\,max}$	
Series I						
No. 1	+	—	—	—	185	S
	–	–42	–74	—	–83	SL
No. 2	+	—	—	—	239	S
	–	–70	–134	—	–135	SL
No. 3	+	59	—	131	155	F
	–	–110	–98	–108	–119	SL
No. 4	+	101	—	91	156	F
	–	–102	–98	–113	–127	SL
Series II						
No. 5	+	—	—	134	153	F
	–	–32	–112	–132	–142	FSL
No. 6	+	—	—	126	163	F
	–	–28	–126	–129	–153	FSL
No. 7	+	—	120	130	153	F
	–	–113	—	–126	–128	FSL
No. 8	+	—	135	132	165	F
	–	–125	—	–126	–155	F
No. 9	+	—	142	127	159	F
	–	–61	—	–124	–146	FSL
No. 10	+	—	—	130	154	F
	–	–109	–130	–125	–140	FSL

Note: F is flexural failure; SL is shear sliding failure at slab-web interface; FSL is shear sliding after flexural yielding; S is shear failure of hybrid beam.

The coefficient of friction between the concrete-to-concrete interface (μ_c) was based on ACI 318,[26] and μ_c = 1.0 was used in this paper because the laitance was removed and the concrete surface was roughened to an amplitude of 6 mm. The coefficient of friction between the concrete-to-steel interface (μ_s) in ACI 318[26] cannot be applied because the W-beam embedded in the proposed hybrid beam had no shear connectors. Sei[30] and others[31-34] conducted pushoff tests on mortar and steel plate without shear connectors and proposed a coefficient of friction between the concrete-to-steel interface of 0.5. This paper used μ_s = 0.5 based on these tests, as AIJ also uses this value for the interface friction of composite members in their standards and guidelines.[35-37]

Equations (1) and (2) were examined using four specimens (No. 1 through 4), which failed in shear sliding at the interface in negative loadings. The measured peak load in the negative loading ($_{exp}Q_{fr}$) and the computed shear sliding capacity ($Q_{fr(h)}$) are compared in Fig. 9. The computed shear sliding capacity ($Q_{fr(h)}$) is obtained assuming that the tensile force from bending action at the column face is equal to the sliding capacity ($q_{fr(h)}$).

Specimens No. 1 and 2 showed good agreement, but the measured values were smaller than the computed values for

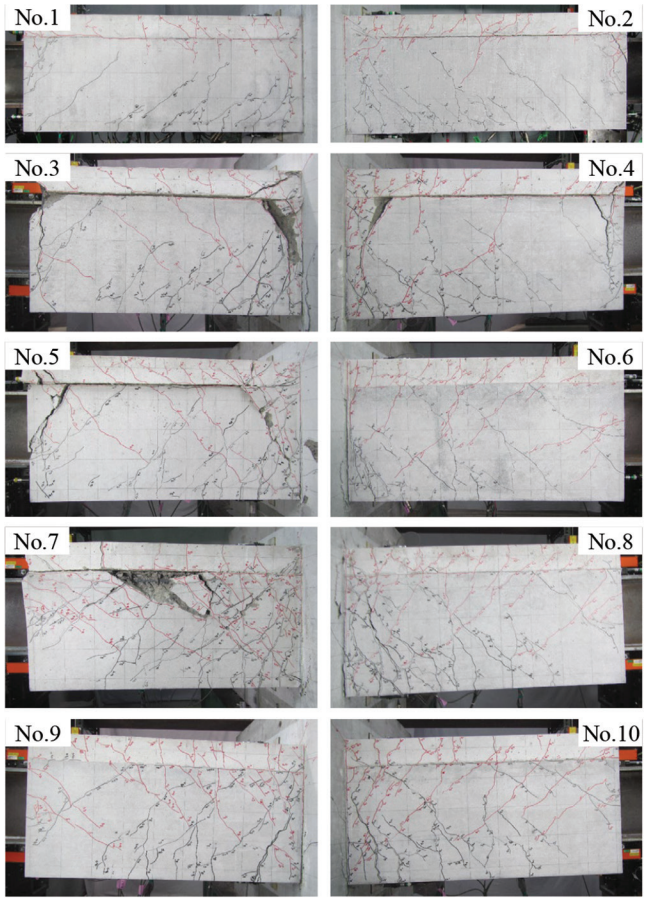

Fig. 6—Crack patterns at maximum capacity.

No. 3 and 4. As mentioned earlier, horizontal cracks along the slab-web interface connected with flexural cracks and did not extend to the reaction block face, and the shear-friction reinforcement near the reaction block does not prevent shear sliding like ordinary shear reinforcement. The confining reinforcement near the reaction block was examined for the shear-friction action.

Figure 10(a) shows the strain-drift (ε_{fr}-R_b) relationships of three types of shear-friction reinforcement, and Fig. 10(b) shows the slip-drift (δ_{SL}-R_b) relationships at three locations for the negative loading. The locations of strain gauges and the slip displacement transducers are shown in Fig. 10(c). Shear reinforcement and C.R.A yielded at R_b = 1.0 to 1.5%, and the slip at the slab-web interface increased rapidly at the same drift. On the other hand, Fig. 10(a) shows that the strain of the C.R.B remained much smaller than the yield strain, as the horizontal interface crack did not reach the reaction block face, as shown in Fig. 6. It is concluded from Fig. 10 that the C.R.B should be neglected for the shear-friction resistance, and Eq. (1) was revised as Eq. (3) by excluding C.R.B. Figure 11 shows the relationship between $_{exp}Q_{fr}$ and Q_{fr}, where Q_{fr} is computed from q_{fr} in Eq. (3). It is seen that the ratio $_{exp}Q_{fr}/Q_{fr}$ is 1.16 and Eq. (3) gives better results than Eq. (1).

$$q_{fr} = \mu_{eq}(a_w \cdot \sigma_{wy} + {}_Aa_w \cdot {}_A\sigma_{wy}) \quad \text{(N)} \tag{3}$$

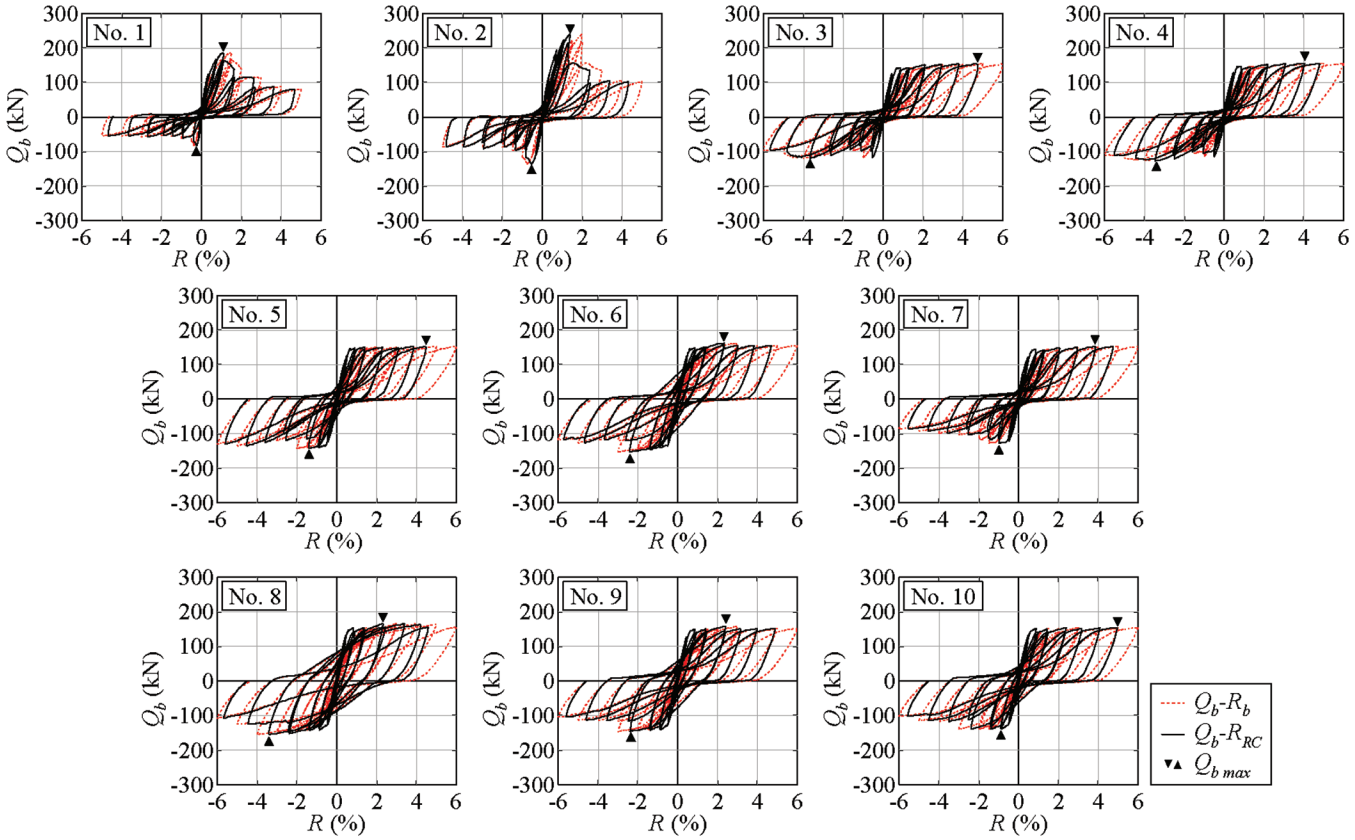

Fig. 7—Load-drift relationships.

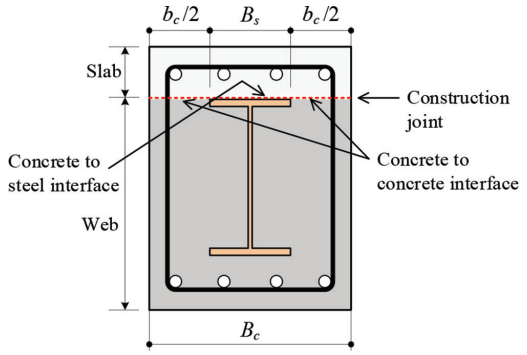

Fig. 8—Interface locations.

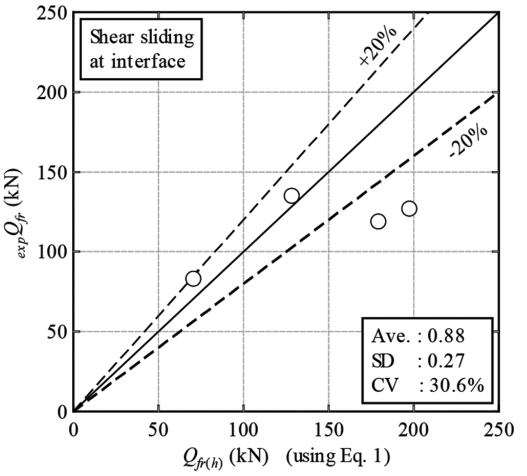

Fig. 9—Experimental and computed values of shear sliding capacity at slab-web interface (Eq. (1)).

FLEXURAL PERFORMANCE OF HYBRID BEAMS

Flexural capacity of hybrid beams

Flexural capacity was examined for the six hybrid beam specimens (No. 5 through 10), which failed in flexural or interface shear sliding after flexural yielding. Previous researchers[1-8] adopted Eq. (4) to estimate flexural capacity of the hybrid beam without construction joints, and Eq. (4) showed good agreement with their test results. It is noted that the effect of the W-beam is neglected in Eq. (4) because the moment of the W-beam becomes zero at the column face, as shown previously in Fig. 2. To examine the effect of the construction joint, this paper also used Eq. (4) to estimate the flexural capacity of the hybrid beam. Figure 12 compares the experimental peak load ($_{exp}Q_{mu}$) and computed flexural capacity (Q_{mu}). The test results of hybrid beams without construction joints discussed previously by Singh et al.[1] are also plotted. The computed capacities of this study agree very well with the experimental results, and the overall average of $_{exp}Q_{mu}/Q_{mu}$ was 1.09. The effect of the construction joint cannot be seen when compared to the previous test results without the construction joints by Singh et al.[1]

$$Q_{mu} = \frac{0.9 \cdot a_t \cdot \sigma_y \cdot d}{\ell_b} \quad \text{(N)} \tag{4}$$

Plastic deformation capacity of hybrid beams

Singh et al.[1] proposed that a ductility factor (μ_{RC}) greater than 3 and a plastic deformation angle (R_{RCp}) greater than 2% is essential to assure a good deformation performance

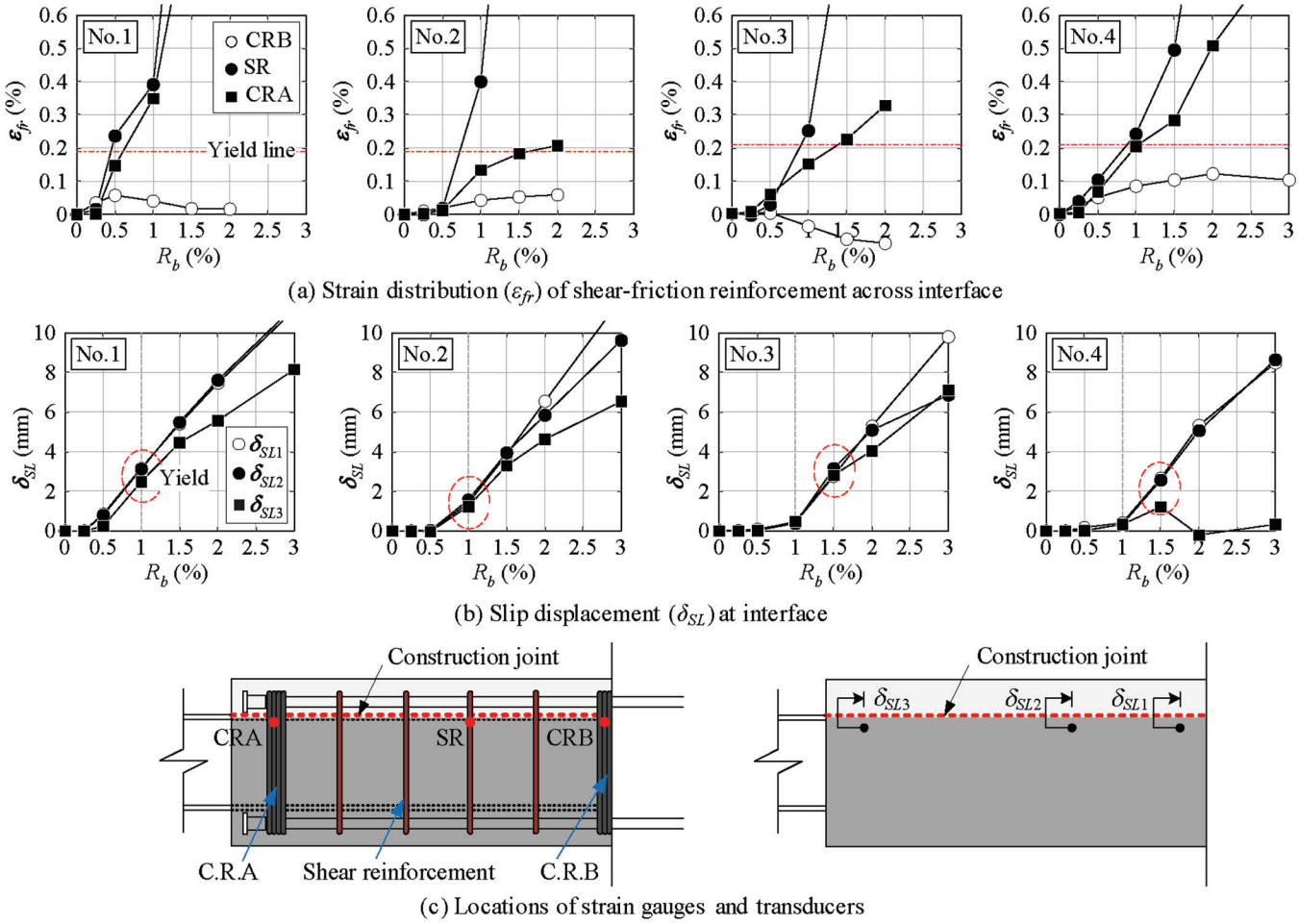

Fig. 10—Strain distribution of shear-friction reinforcement and slip at slab-web interface.

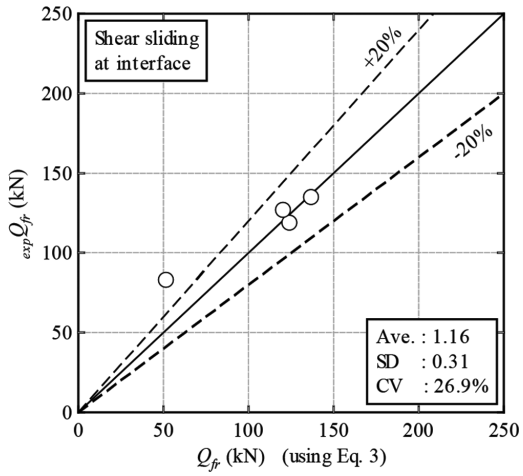

Fig. 11—Experimental and computed values of shear sliding capacity at slab-web interface (Eq. (3)).

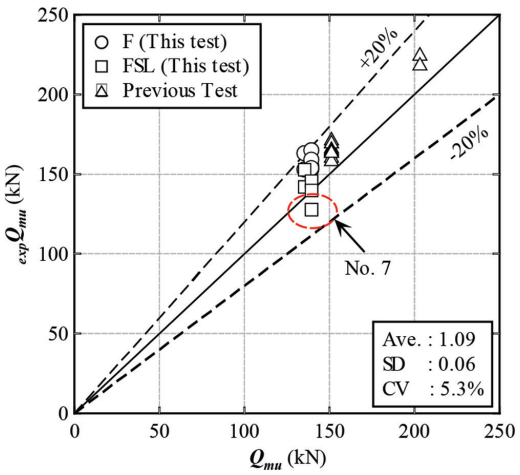

Fig. 12—Experimental and computed values of flexural capacity.

after yielding. Based on the aforementioned proposal, plastic deformation capacity for the six hybrid beam specimens (No. 5 through 10) was examined. Figure 13 shows the μ_{RC} and R_{RCp} of the hybrid beams. The test results of hybrid beams without the construction joint by Singh et al.[1] are also plotted. It is noted that the two triangles circled have more deformation capacity than indicated in the figures because the experimental load did not drop to $0.8Q_{b\,max}$ when the experiment was terminated at $R_b = \pm 6.0\%$. The ductility factor and R_{RCp} were defined as indicated by Singh et al.[1] All six specimens of this study had $\mu_{RC} > 3$ and $R_{RCp} > 2\%$, showing a good plastic deformation performance after flexural yielding. The results of this study showed similar values when compared to the specimens by Singh et al.,[1] and the effect of the construction joint on plastic deformation performance cannot be seen.

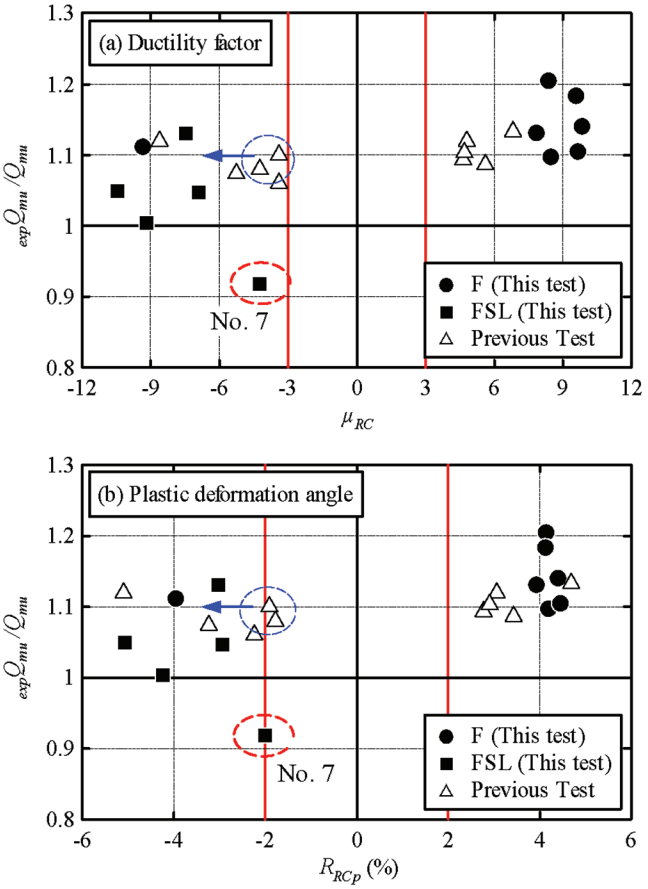

Fig. 13—Flexural capacity versus ductility factor and plastic deformation angle.

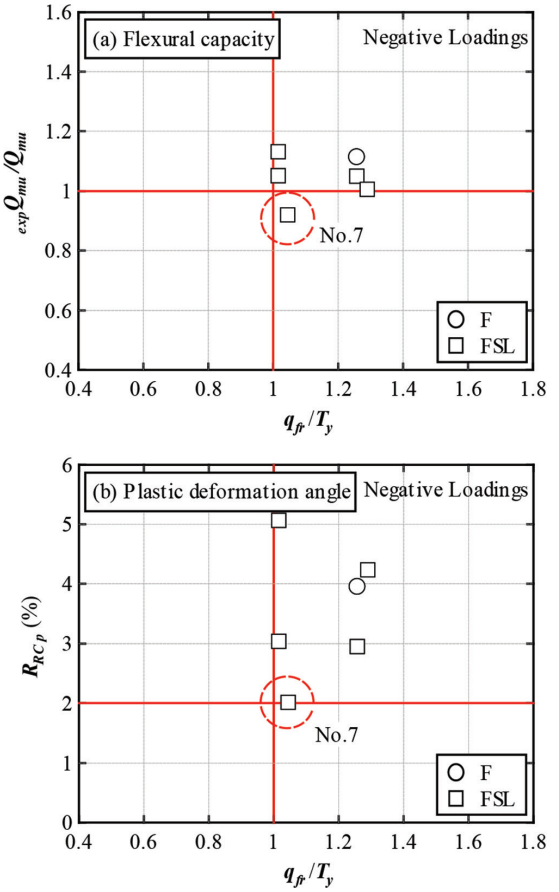

Fig. 14—Flexural capacity and plastic deformation angle versus slip margin (negative loading).

Shear-friction reinforcement across slab-web interface

All the specimens were within the ±20% range in Fig. 12 and had $_{exp}Q_{mu}/Q_{mu} \geq 1.0$, except specimen No. 7, which had the least shear-friction reinforcement of all specimens. As mentioned earlier, the shear sliding capacity to flexural capacity margin was designed to be larger than 1.0. Figure 14 shows the relationship between $_{exp}Q_{mu}/Q_{mu}$-q_{fr}/T_y and R_{RCp}-q_{fr}/T_y for specimens No. 5 through 10 in the negative loading. The computed shear capacity q_{fr} is derived from Eq. (3), and T_y is the yield tensile force of longitudinal reinforcement above the slab-web interface, expressed as $T_y = a_{tfr} \cdot \sigma_{yfr}$. The index q_{fr}/T_y is called a slip margin. Specimen No. 7 did not reach Q_{mu}, although the slip margin is larger than 1.0 and managed to reach $R_{RCp} = 2\%$.

Experimental results showed cover concrete in the central area of specimen No. 7 spalled off and had a slip-type load-drift relationship compared to the other specimens. Despite having a slip margin larger than 1.0, the amount of shear-friction reinforcement in the central area may not be adequate to resist shear sliding. Therefore, the interface shear carried by ordinary shear reinforcement and C.R.A was examined. Figure 15 presents the relationship between $_{exp}Q_{mu}/Q_{mu}$-q_{ws}/q_{fr} and R_{RCp}-q_{ws}/q_{fr}. Variable q_{ws} is the yield shear force carried by ordinary shear reinforcement, and q_{fr} is that carried by both ordinal shear reinforcement and C.R.A. The ratio q_{ws}/q_{fr} is expressed with Eq. (5).

$$\frac{q_{ws}}{q_{fr}} = \frac{a_w \cdot \sigma_{wy}}{a_w \cdot \sigma_{wy} + {}_A a_w \cdot {}_A\sigma_{wy}} \quad (5)$$

Figure 15 shows that $_{exp}Q_{mu}$ became larger than Q_{mu}, and R_{RCp} is almost greater than 3% when $q_{ws}/q_{fr} \geq 55\%$. Specimen No. 7 did not reach Q_{mu} and managed to reach $R_{RCp} = 2\%$, as q_{ws} is smaller than $0.55q_{fr}$. Interface shear capacity in Eq. (3) is a summation of ordinary shear reinforcement and C.R.A. C.R.A. is high-strength bundled bars and accounts for the majority of the shear force, resulting in a smaller amount of ordinary shear reinforcement to satisfy design requirements. This is why specimen No. 7 did not reach Q_{mu}, and R_{RCp} was small. In other words, a sufficient amount of ordinary shear reinforcement has to be provided across the interface to assure good flexural performance.

Only one specimen failed to reach the flexural capacity; however, further study needs to be carried out by varying q_{ws} to see the effect on the flexural capacity and find the minimum shear reinforcement. At this stage, it is preferable that ordinary shear reinforcement has $q_{ws} \geq 0.55q_{fr}$ to achieve a good flexural performance.

CONCLUSIONS

A total of 10 hybrid beam specimens with construction joints were experimentally studied to clarify the shear capacity at the slab-web interface and examine the effect of the construction joint on their flexural performance. The following conclusions are drawn:

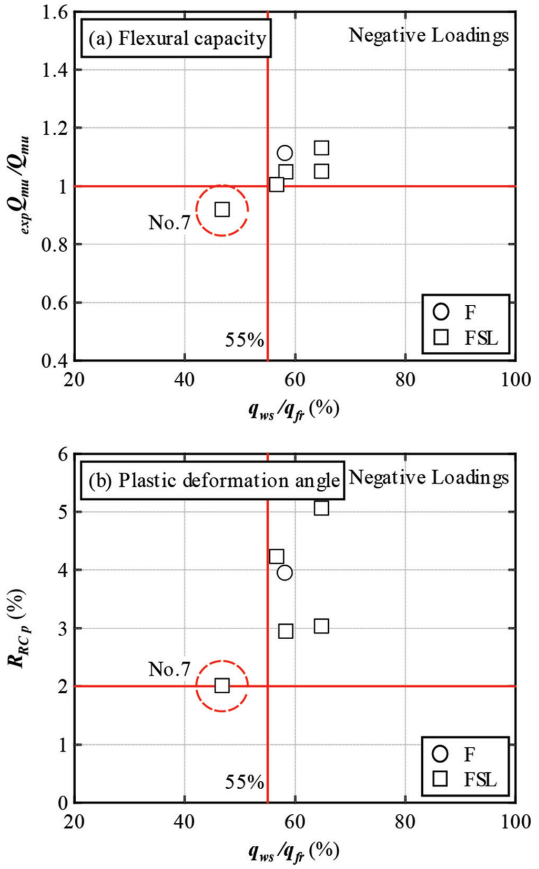

Fig. 15—Flexural capacity and plastic deformation angle versus minimum shear reinforcement ratio.

1. The shear sliding capacity expressed in Eq. (3) properly simulated the observed shear sliding capacities of four specimens (No. 1 through 4). Equation (3) omits confining reinforcement B (C.R.B) because the slab-web interface crack did not reach this reinforcement. Equation (3) employs the concept of equivalent coefficient of friction expressed in Eq. (2). The coefficient of friction at the concrete-to-concrete interface was based on the surface condition provided in ACI 318,[26] and the coefficient of friction at the concrete-to-steel interface was considered as 0.5 based on the Architectural Institute of Japan (AIJ) standards and guidelines.[35-37]

2. The computed flexural capacity showed a good agreement with the experimental values for five specimens (No. 5, 6, 8, 9, and 10), and the same five specimens had a good plastic deformation capacity after yielding. On the other hand, specimen No. 7, which had a lesser amount of ordinary shear reinforcement, did not reach the computed flexural capacity and managed to reach the plastic deformation angle of 2%. From the six specimens (No. 5 through 10), the hybrid beams with construction joints acquired the required flexural performance of monolithic hybrid beams, provided the interface shear force carried by ordinary shear reinforcement was more than 55%.

AUTHOR BIOS

ACI member **Ravi Singh** *is a Senior Researcher in the Technology Development Division, Fujita Corporation, Atsugi, Japan. He received his PhD in urban design and built environment from the Tokyo Institute of Technology, Tokyo, Japan, and his ME in architecture and civil engineering from the Toyohashi University of Technology, Toyohashi, Japan. His research interests include reinforced concrete members and hybrid structures.*

Yukihiro Sato *is a General Manager of the Building Research Department, Fujita Corporation, Atsugi, Japan, and a Technical Advisor for building construction. He received his ME in architecture and building engineering from Tokyo Metropolitan University, Tokyo, Japan. His research interests include precast concrete and hybrid structures.*

Hitoshi Sasaki *is a General Manager of the Central Research Laboratory, Daiwa House Industry Company Limited, Nara, Japan. He received his PhD in engineering from The University of Tokyo, Tokyo, Japan. His research interests include ultra-high-strength concrete, reinforced concrete, precast concrete, and hybrid structures.*

ACI member **David Mukai** *is an Associate Professor at the University of Wyoming, Laramie, WY, and a Visiting Professor at the Tokyo Institute of Technology. He received his PhD in civil engineering from the University of Washington, Seattle, WA. His research interests include theoretical fracture mechanics, reinforced concrete, and structural rehabilitation and monitoring.*

ACI member **Susumu Kono** *is a Professor at the Tokyo Institute of Technology. He received his PhD in civil engineering from the University of Illinois Urbana-Champaign, Urbana, IL. His research interests include performance-based design of reinforced concrete, damage control, and zero-damage design using prestressed/precast concrete structures.*

ACKNOWLEDGMENTS

The authors wish to express their gratitude and sincere appreciation to Fujita Corporation for financing this research work. The authors are also thankful to the WRH Program (International Research Frontiers Initiative) and Collaborative Research Project (MSL) at the Tokyo Institute of Technology.

NOTATION

$_{A}a_w$	=	gross sectional area of confining reinforcement A
$_{A}\sigma_{wy}$	=	yield strength of confining reinforcement A
a_t	=	gross sectional area of longitudinal reinforcement in tension
a_{tfr}	=	gross sectional area of longitudinal reinforcement in tension above slab-web interface
a_w	=	gross sectional area of ordinary shear reinforcement (excluding confining reinforcements)
$_{B}a_w$	=	gross sectional area of confining reinforcement B
B_c	=	width of hybrid beam
B_s	=	width of W-beam
$_{B}\sigma_{wy}$	=	yield strength of confining reinforcement B
b_c	=	width of hybrid beam section excluding width of W-beam (refer to Fig. 9)
D_c	=	depth of hybrid beam
D_s	=	depth of W-beam
d	=	effective depth of hybrid beam
E_c	=	Young's modulus of concrete
E_s	=	Young's modulus of reinforcement and steel
$_{exp}Q_{fr}$	=	experimental peak load in negative loading for specimens No. 1 through 4
$_{exp}Q_{mu}$	=	experimental peak load for specimens No. 5 through 10
F	=	design strength of reinforcement and steel
F_{cs}	=	concrete design strength of slab
F_{cw}	=	concrete design strength of web
ℓ_b	=	length from reaction block to loading point
ℓ_{RC}	=	length of hybrid beam
p_w	=	ratio of shear reinforcement
Q_b	=	shear force at loading point
$Q_{b\,max}$	=	maximum capacity of hybrid beam
Q_{by}	=	yield strength of hybrid beam
Q_{fr}	=	q_{fr} converted to shear force at loading point
$Q_{fr(h)}$	=	$q_{fr(h)}$ converted to shear force at loading point
Q_{fry}	=	yield strength of shear-friction reinforcement
Q_{jc}	=	crack strength at slab-web interface
Q_{mu}	=	ultimate flexural capacity of hybrid beam
q_{fr}	=	shear capacity at slab-web interface using Eq. (3)
$q_{fr(h)}$	=	shear capacity at slab-web interface using Eq. (1)
q_{ws}	=	yield shear force carried by ordinary shear reinforcement
R_b	=	drift at loading point
R_{RC}	=	drift of hybrid beam
R_{RCp}	=	plastic deformation angle of hybrid beam

T_y = yield tensile force of longitudinal reinforcement above slab-web interface
t_f = thickness of W-beam flange
t_s = thickness of slab
t_w = thickness of W-beam web
δ_b = displacement at loading point
δ_{RC} = displacement of hybrid beam
δ_{SL} = slip at slab-web interface
ε_{fr} = strain of shear-friction reinforcement
μ_c = coefficient of friction between concrete-to-concrete interface
μ_{eq} = equivalent coefficient of friction
μ_{RC} = ductility factor of hybrid beam
μ_s = coefficient of friction between concrete-to-steel interface
σ_B = compressive strength of concrete
σ_t = splitting tensile strength of concrete
σ_{wy} = yield strength of ordinary shear reinforcement
σ_y = yield strength of reinforcement and steel (yield strength of longitudinal reinforcing bars in Eq. (4))
σ_{yfr} = yield strength of longitudinal reinforcing bars above slab-web interface

REFERENCES

1. Singh, R.; Sasaki, H.; and Sato, Y., "Ultimate Flexural Strength and Plastic Deformation Performance of Reinforced Concrete Section in Hybrid Beams," *ACI Structural Journal*, V. 118, No. 1, Jan. 2021, pp. 301-310.

2. Singh, R.; Sasaki, H.; Masuda, K.; Sato, Y.; and Arima, Y., "Development of RC Column and Steel Hybrid Beam System (FRASH Method)," *IABSE Conference: Elegance in Structures*, V. 104, No. 16, Nara, Japan, 2015, pp. 1-8.

3. Singh, R., "Development and Construction Example of Hybrid Structure with RC Column and Steel Beam Ends Reinforced by RC," *The Construction Technology*, V. 790, 2015, pp. 54-61. (in Japanese)

4. Singh, U. R.; Sasaki, H.; Sato, Y.; and Arima, Y., "Research Development of Hybrid Structure with Steel Beam Ends Reinforced by RC and Column Being RC—Structural Performance of Hybrid Beams of Interior Beam-Column Sub-Assemblages," *Summaries of Technical Papers of Annual Meeting of AIJ*, 2011, pp. 1271-1272.

5. Singh, U. R.; Sasaki, H.; Masuda, K.; Sato, Y.; and Arima, Y., "Research Development of Hybrid Structure with Steel Beam Ends Reinforced by RC and Column Being RC—Validity of RC Members Plastic Deformation and Coefficient of Shear Reinforcement," *Summaries of Technical Papers of Annual Meeting of AIJ*, 2012, pp. 1393-1394.

6. Suzuki, H., and Nishihara, H., "Shear Strength and Deformation Performance of Hybrid Beam Consisting of H-Shaped Steel and Reinforced Concrete," *Journal of Structural and Construction Engineering (Transactions of AIJ)*, V. 73, No. 631, 2008, pp. 1673-1680. doi: 10.3130/aijs.73.1673

7. Kanemoto, K.; Mase, S.; and Yamanobe, K., "An Estimation of Shear Capacities for Hybrid Steel Beams Jacketed with Reinforced Concrete at Ends Connected to Reinforced Concrete Column," *Journal of Structural and Construction Engineering (Transactions of AIJ)*, V. 76, No. 659, 2011, pp. 205-211. doi: 10.3130/aijs.76.205

8. Kanemoto, K.; Mase, S.; and Yamanobe, K., "Structural Performance of Hybrid Steel Beams with R/C Jacketed Ends Connected to R/C Column," *Proceedings of the Japan Concrete Institute*, V. 31, No. 2, 2009, pp. 1129-1134.

9. Mast, R. F., "Auxiliary Reinforcement in Concrete Connections," *Journal of the Structural Division*, ASCE, V. 94, No. 6, 1968, pp. 1485-1504. doi: 10.1061/JSDEAG.0001977

10. Birkeland, P. W., and Birkeland, H. W., "Connections in Precast Concrete Construction," *ACI Journal Proceedings*, V. 63, No. 3, Mar. 1966, pp. 345-368.

11. Kriz, L. B., and Raths, C. H., "Connections in Precast Concrete Structures—Strength of Corbels," *PCI Journal*, V. 10, No. 1, 1965, pp. 16-61. doi: 10.15554/pcij.02011965.16.61

12. Hofbeck, J. A.; Ibrahim, I. O.; and Mattock, A. H., "Shear Transfer in Reinforced Concrete," *ACI Journal Proceedings*, V. 66, No. 2, Feb. 1969, pp. 119-128.

13. Saemann, J. C., and Washa, G. W., "Horizontal Shear Connections between Precast Beams and Cast-in-place Slabs," *ACI Journal Proceedings*, V. 61, No. 11, Nov. 1964, pp. 1383-1408. Discussion of the paper, June 1965, pp. 1807-1810.

14. Anderson, A. R., "Composite Designs in Precast and Cast-in-Place Concrete," *Progressive Architecture*, V. 41, No. 9, 1960, pp. 172-179.

15. Raths, C. H., "Reader Comments on 'Design Proposals for Reinforced Concrete Corbels' by A. H. Mattock," *PCI Journal*, V. 22, No. 2, Mar.-Apr. 1977, pp. 93-98.

16. Shaikh, A. F., "Proposed Revisions to Shear-Friction Provisions," *PCI Journal*, V. 23, No. 2, Mar.-Apr. 1978, pp. 12-21.

17. Walraven, J.; Frénay, J.; and Pruijssers, A., "Influence of Concrete Strength and Load History on the Shear Friction Capacity of Concrete Members," *PCI Journal*, V. 32, No. 1, 1987, pp. 66-84. doi: 10.15554/pcij.01011987.66.84

18. Mau, S. T., and Hsu, T. T. C., "Reader Comments on 'Influence of Concrete Strength and Load History on the Shear Friction Capacity of Concrete Members' by J. Walraven, J. Frénay, and A. Pruijssers," *PCI Journal*, V. 33, No. 1, Jan.-Feb. 1988, pp. 166-168.

19. Mattock, A. H., and Hawkins, N. M., "Shear Transfer in Reinforced Concrete—Recent Research," *PCI Journal*, V. 17, No. 2, 1972, pp. 55-75. doi: 10.15554/pcij.03011972.55.75

20. Mattock, A. H., "Shear Transfer in Concrete Having Reinforcement at an Angle to the Shear Plane," *Shear in Reinforced Concrete*, SP-42, American Concrete Institute, Farmington Hills, MI, 1974, pp. 17-42.

21. Mattock, A. H.; Johal, L.; and Chow, H. C., "Shear Transfer in Reinforced Concrete with Moment or Tension Acting across the Shear Plane," *PCI Journal*, V. 20, No. 4, 1975, pp. 76-93. doi: 10.15554/pcij.07011975.76.93

22. Mattock, A. H.; Li, W. K.; and Wang, T. C., "Shear Transfer in Lightweight Reinforced Concrete," *PCI Journal*, V. 21, No. 1, 1976, pp. 20-39. doi: 10.15554/pcij.01011976.20.39

23. Mattock, A. H., "Reader Comments on 'Considerations for the Design of Precast Concrete Bearing Wall Buildings to Withstand Abnormal Loads' by PCI Committee on Precast Concrete Bearing Wall Buildings," *PCI Journal*, V. 22, No. 3, May-June 1977, pp. 105-106.

24. Mattock, A. H., "Shear Friction and High-Strength Concrete," *ACI Structural Journal*, V. 98, No. 1, Jan.-Feb. 2001, pp. 50-59.

25. Kahn, L. F., and Mitchell, A. D., "Shear Friction Tests with High-Strength Concrete," *ACI Structural Journal*, V. 99, No. 1, Jan.-Feb. 2002, pp. 98-103.

26. ACI Committee 318, "Building Code Requirements for Structural Concrete (ACI 318-19) and Commentary (ACI 318R-19) (Reapproved 2022)," American Concrete Institute, Farmington Hills, MI, 2019, 624 pp.

27. AIJ, "AIJ Guidelines for Structural Design of Precast Concrete Connection Emulating Cast-in-Place Reinforced Concrete (Draft)," Architectural Institute of Japan, Tokyo, Japan, 2002, 261 pp.

28. ANSI/AISC 360-16, "Specification for Structural Steel Buildings," American Institute of Steel Construction, Chicago, IL, 2016, 677 pp.

29. Lini, C., "Steel Interchange: Steel-on-Concrete Slip Coefficient," *Modern Steel Construction*, May 2015, 1 p.

30. Sei, K., "Coefficient of Friction for Steel Column Base," *Summaries of Technical Papers of Annual Meeting of AIJ*, 1977, pp. 1283-1284.

31. Sei, K., "Coefficient of Friction for Steel Column Base Part 2," *Summaries of Technical Papers of Annual Meeting of AIJ*, 1981, pp. 2039-2040.

32. Washio, K.; Takimoto, G.; Hisatsune, J.; and Suzuki, T., "Research of Fix Effect for Steel Column Base—Slip between Steel Plate and Mortar," *Summaries of Technical Papers of Annual Meeting of AIJ*, 1969, pp. 1177-1178.

33. Nakajima, Y., and Okajima, T., "Research on Bond Resistance between Concrete and Steel," *Summaries of Technical Papers of Annual Meeting of AIJ*, 1972, pp. 981-982.

34. Nagae, T.; Ikenaga, M.; Nakashima, M.; and Suita, K., "Shear Friction between Base Plate and Base Mortar in Exposed Steel Column Base," *Journal of Structural and Construction Engineering (Transactions of AIJ)*, V. 71, No. 606, 2006, pp. 217-223. doi: 10.3130/aijs.71.217

35. AIJ, "AIJ Standard for Structural Calculation of Steel Reinforced Concrete Structures," Architectural Institute of Japan, Tokyo, Japan, 2014, 395 pp.

36. AIJ, "AIJ Recommendations for Design of Connections in Steel Structures," Architectural Institute of Japan, Tokyo, Japan, 2021, 411 pp.

37. AIJ, "Recommendation for Limit State Design of Steel Structures," Architectural Institute of Japan, Tokyo, Japan, 2010, 324 pp.

ACI STRUCTURAL JOURNAL TECHNICAL PAPER

Title No. 121-S37

Post-Cracking Stiffness Model of Solid and Hollow Glass Fiber-Reinforced Polymer-Reinforced Concrete Members under Torsion

by Ibrahim T. Mostafa, Salaheldin Mousa, Hamdy M. Mohamed, and Brahim Benmokrane

Although estimating the post-cracking torsional stiffness is vital for distributing the torsional moment in analyzing statically indeterminate reinforced concrete (RC) structures, none of the North American codes provide an analytical approach for determining the torsional stiffness after cracking. Moreover, the scarcity of experimental work has resulted in the lack of torsion design provisions for concrete box girders reinforced with glass fiber-reinforced polymer (GFRP). Therefore, the purpose of this research was to study the stiffness characteristics of RC box girders reinforced with GFRP reinforcement and to provide a simple analysis technique that can be used to predict post-cracking torsional stiffness. Fourteen concrete box girders were fabricated and tested under a pure torsional moment. In addition, data on 10 solid rectangular RC beams with GFRP reinforcement was collected from the literature. The test results indicate that the concrete strength, as well as the ratio, type, and configuration of the web reinforcement, substantially affected the post-cracking torsional stiffness of the tested specimens. An analytical model was developed for estimating the torsional stiffness after cracking. This model was based on a thin-walled tube and space truss analogy using a concept of post-cracking shear modulus. The proposed model considers the effect of concrete strength, the configuration and ratio of the GFRP web reinforcement, and the ratio of the GFRP longitudinal bars. In addition, an equation to calculate the ultimate twist of the GFRP-RC members was developed. The validity of the proposed model was investigated by analytically regenerating the torque-twist curves of the tested box girders and the other specimens available in the literature.

Keywords: box girders; effective wall thickness; glass fiber-reinforced polymer (GFRP) bars; high-strength concrete (HSC); normal-strength concrete (NSC); post-cracking torsional stiffness; reinforced concrete (RC); spirals; steel reinforcement; ties; twist behavior; ultimate twist.

INTRODUCTION

In designing reinforced concrete (RC) structures subjected to torsion, the torsional moment can be classified into two types (ACI CODE-440.11-22). The first type—equilibrium torsion—occurs in statically determinate structures such as canopy beams and beams supporting cantilever slabs. Thus, the torsional moment can be simply determined using the static condition. This torque cannot be reduced by redistributing internal forces. Torsional reinforcement must be provided to resist the total design torsional moments. The second type—compatibility torsion—occurs in statically indeterminate structures such as spandrel beams supporting an edge strip of a flat slab or transverse beams. Accurate determinations of the torsional moment of such members require that the redistribution of internal forces be considered. Therefore, the torsional stiffness of such members must be taken into account in the structural analysis (Karlsson and Elfagren 1972; Hsu 1968; Lampert 1971; Tavio and Teng 2004). In the case of compatibility torsion, the cracking torque results in a substantial decrease in the torsional stiffness and an increase in the twist of the member, which leads to a reduction in the torsional moment carried by the member (ACI CODE-440.11-22). To consider the reduction in torsional stiffness due to cracking, ACI CODE-440.11-22 specifies an upper limit for the design torsional moment calculated by elastic analysis to a specific value. Acquiring a more accurate redistribution of the torsional moment after cracking in statically indeterminate structures requires more accurate post-cracking torsional stiffness calculations to be considered in the structural analysis. That is the essence of the current study.

Robinson (1966) made the first attempt to derive post-cracking torsional stiffness theoretically. The derivation applied only to circular cross sections, and the torsional stiffness had to be determined by trial and error. On the other hand, the post-cracking torsional stiffness of rectangular RC sections—either solid or hollow—reinforced with steel bars and tie stirrups has been developed in several studies (Karlsson and Elfagren 1972; Hsu 1973; Lampert 1971). Lampert (1971) derived an equation to calculate the post-cracking torsional stiffness based on the thin-walled tube and space truss analogy and kinematic relationships. The derived equation is a function of the ratio of the longitudinal and web reinforcement only and disregards the contribution of the concrete to the post-cracking torsional stiffness. Hsu (1973) used the same concept of the thin-walled tube and space truss analogy to develop his theory for post-cracking torsional stiffness, which is derived with a concept of post-cracking shear modulus. This concept provides the theory generally applicable to arbitrary, circular, and rectangular cross sections. Karlsson and Elfagren (1972) discussed a methodology for assessing the torsional stiffness of RC members at the cracked stage under pure torsional loading. The approach was founded on a truss analogy designed for

ACI Structural Journal, V. 121, No. 3, May 2024.
MS No. S-2023-077.R4, doi: 10.14359/51740483, received October 5, 2023, and reviewed under Institute publication policies.

Table 1—Mechanical properties of GFRP and steel reinforcement

Bar size	Diameter, mm	Nominal area, mm^2	Elastic tensile modulus, GPa	Tensile strength, MPa	Tensile strain, %
No. 3	9.5	71	58.20	f_{ftu} = 1225	2.10
—	—	—	—	$f_{ftu,bent}$ = 671	—
No. 5	15.9	198	62.5	f_{ftu} = 1500	2.4
M10	11.3	100	200	f_y = 480	0.24
M15	16	200	200	f_y = 480	0.24

Note: f_{ftu} is ultimate tensile strength of straight portion of GFRP bent bars (ASTM D7205/D7205M-21); $f_{ftu,bent}$ is ultimate tensile strength at GFRP bent portions (ASTM D7914/D7914M-21); 1 mm = 0.0394 in.; 1 mm^2 = 0.00155 in.^{2}; 1 MPa = 0.145 ksi.

torsional analysis. Theoretical formulations were derived to calculate the torsional stiffness of beams with both arbitrary and rectangular cross sections. These theoretical predictions were then compared to experimental data obtained from rectangular beams. The study briefly explored the practicality of the employed theory and offered a corrective procedure to account for any imperfections in its application. Tavio and Teng (2004) improved upon the post-cracking torsional stiffness equations initially presented by Hsu in 1973 and Lampert in 1971. They achieved this by introducing additional factors that yielded the most accurate alignment with the comprehensive set of experimental data accessible in the literature.

Concrete box girders have been used for significant structures such as curved bridges, cable-supported bridges, pedestrian bridges, and modern elevated structures for light rail transport (Rahal and Collins 1995). Such structures are usually located in harsh environments and might have problems such as cracking due to applied stresses or shrinking and expansion. When this occurs, moisture can enter the structure, corroding the steel reinforcing bars and resulting in a loss of structural integrity. This issue can be overcome by substituting glass fiber-reinforced polymer (GFRP) reinforcement for the steel reinforcement. This eliminates corrosion and its associated deterioration and rehabilitation, thereby extending the service life and reducing maintenance costs. Using GFRP bars as internal reinforcement is gaining popularity as a viable technique for improving the performance of RC structures. In the last two decades, GFRP reinforcing bars have been used in numerous structural applications, such as bridges, piles, parking garages, marine structures, water tanks, and tunnels (Eladawy et al. 2019; El-Salakawy et al. 2004; Mohamed et al. 2020; Mohamed and Benmokrane 2014; Mousa et al. 2018).

This study investigated the effects of concrete strength as well as the web reinforcement ratio, configuration, and type on the torsional stiffness of GFRP-RC box girders. In addition, this paper proposes an analytical model for predicting the post-cracking torsional stiffness and the ultimate twist of RC members reinforced with GFRP bars and ties or spirals. This would constitute the first such attempt in the literature.

RESEARCH SIGNIFICANCE

When analyzing statically indeterminate RC structures, post-cracking torsional stiffness is a crucial factor in calculating an accurate distribution of internal post-cracking forces. It can also be used to calculate the twist of the member. However, the post-cracking torsional stiffness of RC members reinforced with GFRP bars and ties or spirals has not been discussed so far. Besides, all FRP-RC code standards and guidelines (CSA S806-12; AASHTO-18; CSA S6-19; ACI CODE 440.11-22) do not include any provisions or equations to estimate the torsional stiffness after cracking. Accordingly, the authors developed an analytical model for estimating post-cracking torsional stiffness. The developed model considers the effect of the concrete strength, the configuration and ratio of the GFRP web reinforcement, and the ratio of the GFRP longitudinal bars. Thus, this model could be helpful in analyzing GFRP-reinforced RC structures after cracking and up until failure.

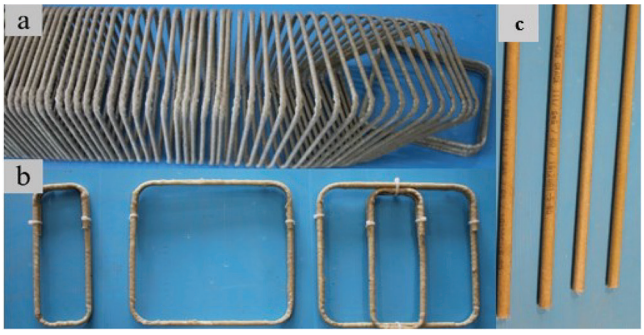

Fig. 1—(a) GFRP continuous square spiral stirrups; (b) GFRP individual square tie stirrups; and (c) GFRP bars.

EXPERIMENTAL PROGRAM

Material properties

Number 5 Grade III sand-coated GFRP longitudinal bars and No. 3 Grade II sand-coated GFRP stirrups (ties and spirals) (CSA S807-19) were used to reinforce all of the GFRP-RC box girders, as shown in Fig. 1. The ultimate tensile strength f_{fu} and modulus of elasticity E_f of the GFRP bars and straight portions of GFRP stirrups were calculated according to ASTM D7205/D7205M-21, as reported by the manufacturer. The ultimate tensile strength of the GFRP stirrups at the bent portions $f_{fu,bent}$ was determined according to ASTM D7914/D7914M-21. Table 1 provides the mechanical properties of the GFRP reinforcement, as reported by the manufacturer. The reinforcement in the steel-reinforced concrete specimens was grade 60 steel bars. Number 5 and 3 (15 and 10M) deformed steel bars were employed as longitudinal and web reinforcement, respectively. Table 1 provides the mechanical properties of the steel bars determined in

Table 2—Details of tested specimens

Specimen identifier	f_c', MPa	Longitudinal bars		Transverse reinforcement				
		No. of bars	ρ_L, %	Conf.	φ, degree	Bar size	S, mm	ρ_T, %
BSNT-120	39.12	12 No. 5	1.66	Tie	90	M10	120	0.47
BSHT-120	71.50	12 No. 5	1.66	Tie	90	M10	120	0.47
BGNT-60	39.12	12 No. 5	1.66	Tie	90	No. 3	60	0.95
BGNT-120	39.12	12 No. 5	1.66	Tie	90	No. 3	120	0.47
BGNT-180	39.12	12 M15	1.66	Tie	90	No. 3	180	0.32
BGNT-240	39.12	12 No. 5	1.66	Tie	90	No. 3	240	0.24
BGNS-60	40.67	12 No. 5	1.66	Spiral	87	No. 3	60	0.95
BGNS-120	40.67	12 No. 5	1.66	Spiral	84	No. 3	120	0.47
BGNS-180	40.67	12 No. 5	1.66	Spiral	81	No. 3	180	0.32
BGNS-240	40.67	12 No. 5	1.66	Spiral	78	No. 3	240	0.24
BGHT-120	71.50	12 No. 5	1.66	Tie	90	No. 3	120	0.47
BGHT-180	71.50	12 No. 5	1.66	Tie	90	No. 3	180	0.32
BGHS-120	71.50	12 No. 5	1.66	Spiral	84	No. 3	120	0.47
BGHS-180	71.50	12 No. 5	1.66	Spiral	81	No. 3	180	0.32

Note: 1 mm = 0.0394 in.; 1 MPa = 0.145 ksi.

accordance with ASTM A615/A615M-20. The specimens were cast from three batches of normal weight, ready mixed concrete: two with normal-strength concrete (NSC) and one with high-strength concrete (HSC). The target 28-day compressive strengths of the NSC and HSC were 35 and 70 MPa, respectively. Table 2 gives the actual concrete compressive strength for all test specimens according to ASTM C39/C39M-21.

Specimens, instrumentation, and testing

Fourteen full-scale RC box girders with a width of 380 mm (15 in.), a depth of 380 mm (15 in.), a total length of 4000 mm (157.48 in.), and a wall thickness of 100 mm (4 in.) were designed, cast, and examined under pure torsional moment until failure over a clear span of 2000 mm (78.74 in.). The test specimens included 12 reinforced entirely with GFRP bars and two with steel reinforcement as reference specimens. The test parameters included the web reinforcement ratio (stirrup spacing) and configuration (ties or spirals), the type of reinforcement (GFRP or steel), and the concrete type (NSC or HSC). All GFRP specimens were reinforced longitudinally with 12 No. 5 GFRP bars and transversely with No. 3 GFRP stirrups. The steel specimens were reinforced longitudinally with twelve 15M steel bars and transversally with 10M steel stirrups. Table 2 summarizes all the details of the tested specimens. Figure 2 illustrates the tested specimens' concrete dimensions and reinforcement details. Each specimen identification consists of letters and a number. The initial pair of letters (BG or BS) refers to GFRP or steel reinforcement, while H and N indicate specimens with HSC or NSC, respectively. The letters T and S represent individual tie stirrups or continuous spiral stirrups, respectively. The number stands for the spiral pitch or stirrup spacing in millimeters.

Four potentiometers were positioned at two different locations within the test region to measure the relative rotation of the specimens. Moreover, one potentiometer was positioned under the applied vertical load, as shown in Fig. 2. A servo-controlled, 1000 kN (224.8 kip) MTS hydraulic actuator connected to a rigid steel arm fastened to the girder was used to apply the torsional moment to the girders. Figure 3 depicts the details of the test setup. Actuator loading procedures were prescribed using the displacement control rate of 0.5 mm/min (0.02 in./min). All specimens were supported by a fixed hinge 2000 mm (78.74 in.) apart.

TEST RESULTS AND DISCUSSION

Torque-twist response

The torque and corresponding twist values were recorded for all specimens throughout testing until failure. Figures 4(a) through (c) give the relationships between the torque versus the corresponding twist from initial loading until the failure of all test specimens in three groups to show the effect of the test parameters on the torsional behavior of RC box girders. Until cracking occurred, the torsional behavior of all specimens was essentially linear, as anticipated. The cracking torsional strength and the corresponding twist of the tested specimens were independent of the configuration, type, and amount of web reinforcement. Interestingly, the similar behavior was reported in the previous studies conducted by Hadhood et al. (2020) and Mohamed and Benmokrane (2015, 2016) for RC beams reinforced by GFRP reinforcement with different web reinforcement configurations, types, and ratios. In contrast, using HSC instead of NSC significantly affected the torsional behavior at the cracking stage. The HSC specimens achieved higher torsional strength and lower twist at cracking than the corresponding NSC specimens by, on average, 26% and 29%, respectively. Interestingly, Rasmussen and Baker (1995) reported similar findings, in which increasing the concrete strength from 41.70 to 76.20 MPa (6.05 to 11.05 ksi) improved the cracking strength by almost 29%. Figure 4 indicates that, immediately

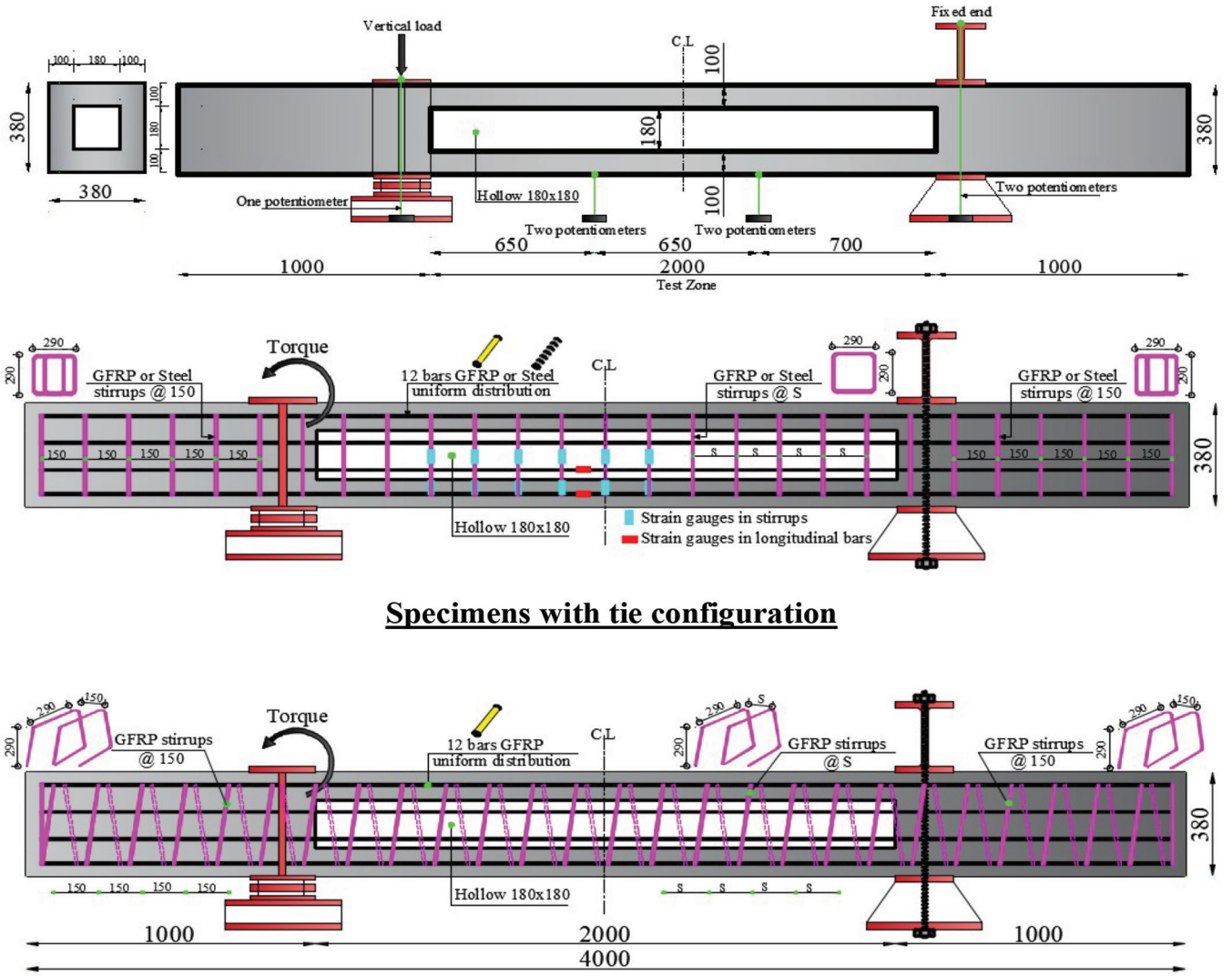

Specimens with tie configuration

Specimens with a spiral configuration

Fig. 2—Dimensions, instrumentation, and reinforcement details of tested box girders. (Note: Dimensions in mm; 1 mm = 0.0394 in.)

after cracking occurred, the GFRP-RC specimens experienced a sudden drop in torsional strength with an increase in twist. The drop's value depended on the ratio of the GFRP reinforcement and concrete strength. In the case of the specimens reinforced with steel, the torsional strength was almost constant immediately after cracking occurred with an increase in twist. This is due to the steel having a higher modulus of elasticity than the GFRP reinforcement. On the other hand, the torsional behavior after cracking was affected by the ratio, type, and configuration of the web reinforcement, regardless of the concrete strength. All GFRP-RC box girders showed a post-cracking response and behaved linearly with increased torsional strength after cracking up to failure. This is due to the linear characteristics of the GFRP reinforcement. Generally, the presence of GFRP web reinforcement in the girders helped to redistribute the internal forces and form the truss shape. The reinforcement acted as tensile links and the concrete as compression struts.

Table 3 summarizes the experimental test results of all specimens. Table 3 points out that, regardless of the stirrup configuration and concrete strength, increasing the web reinforcement ratio increased the specimens' ultimate torsional strength and twist capacity. Specimens BGNT-60 and BGNS-60 had higher torsional strength than their counterparts BGNT-240 and BGNS-240 by 58% and 67%, and higher twist capacity by 15% and 22%, respectively. All specimens reinforced with a continuous spiral experienced higher torsional strength and lower twist capacity than those with individual tie stirrups, regardless of the concrete strength. These findings support the earlier study conducted by Hadhood et al. (2020) for solid NSC beams reinforced with GFRP spirals and tie stirrups, which stated that the RC beams reinforced with continuous spirals produced higher torsional capacity and less twist capacity than those reinforced with individual closed stirrups. Aside from stirrup configurations, the HSC specimens acquired higher ultimate torsional strength and lower twist capacity than their NSC

Table 3—Experimental test results of current study

Specimens ID	Cracking stage			Ultimate stage		
	T_{cr}, kN·m	θ_{cr}, rad/m	k_{un}, kN·m^2/rad	T_u, kN·m	θ_u, rad/m	k_{cr}, kN·m^2/rad
BSNT-120	35.50	0.0011	32,270	56.85	0.0388	1000
BSHT-120	44.95	0.00090	49,900	68.00	0.039	1150
BGNT-60	35.35	0.0013	27,190	68.71	0.0721	564
BGNT-120	35.10	0.0012	29,250	60.11	0.0770	455
BGNT-180	35.39	0.0013	27,220	50.44	0.0671	400
BGNT-240	34.92	0.0014	24,940	43.61	0.0625	340
BGNS-60	35.94	0.0012	29,950	74.10	0.071	635
BGNS-120	35.51	0.0011	32,282	63.70	0.069	525
BGNS-180	35.31	0.0013	27,162	52.20	0.063	430
BGNS-240	34.95	0.0014	24,965	44.45	0.058	390
BGHT-120	44.20	0.00094	47,000	73.20	0.071	500
BGHT-180	44.10	0.00096	45,900	61.10	0.064	410
BGHS-120	44.70	0.00091	49,200	78.30	0.066	580
BGHS-180	44.25	0.00095	46,600	63.90	0.060	450

Note: 1 kN·m = 0.7376 kip·ft; 1 kN·m^2 = 2.42 kip·ft^2; 1 rad/m = 0.305 rad/ft.

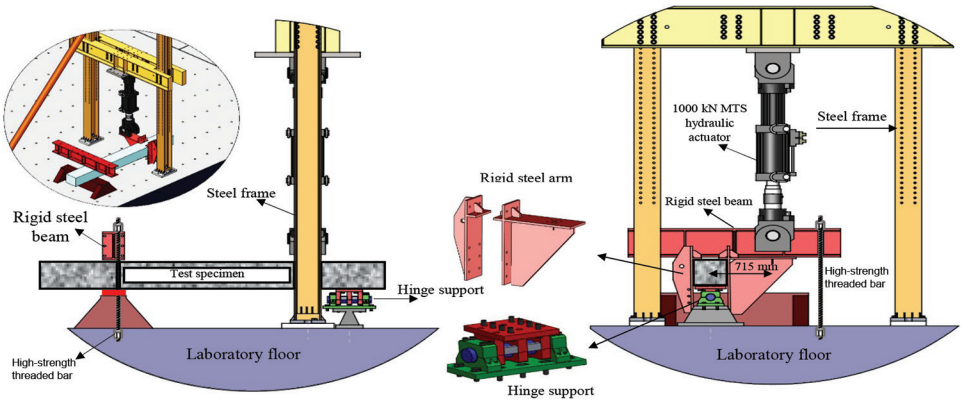

Fig. 3—Test setup schematic.

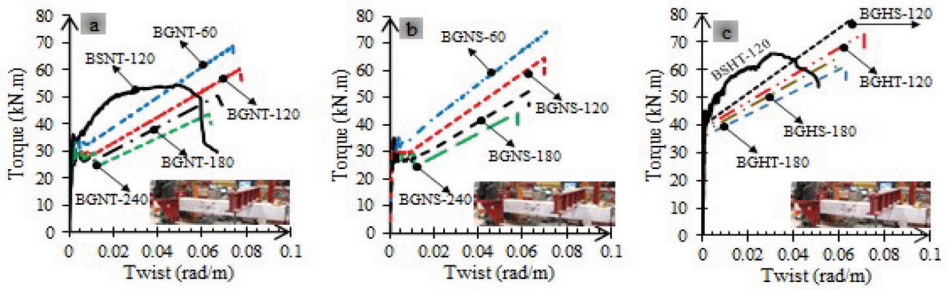

Fig. 4—Torque-twist response. (Note: 1 kN·m = 0.7376 kip·ft; 1 rad/m = 0.305 rad/ft).

counterparts. The ultimate torsional strength of Specimens BGHS-120 and BGHT-120 was higher than that of Specimens BGNS-120 and BGNT-120 by 23% and 22%, respectively. The twist capacity of Specimens BGHS-120 and BGHT-120 was slightly lower than that of their counterparts, BGNS-120 and BGNT-120, by nearly 5% and 7%, respectively. On the other hand, the GFRP specimens exhibited slightly higher ultimate torsional strength than their counterpart steel specimens by 6% and 8% in the case of NSC and HSC, respectively. Interestingly, this behavior agrees with a study conducted by Mohamed and Benmokrane (2016) for solid NSC beams reinforced with GFRP and steel reinforcement.

Effect of test parameters on torsional stiffness

Figure 4 and Table 3 indicate that the pre-cracking torsional stiffness of the tested specimens was independent of the web reinforcement configuration, type, and ratio. This

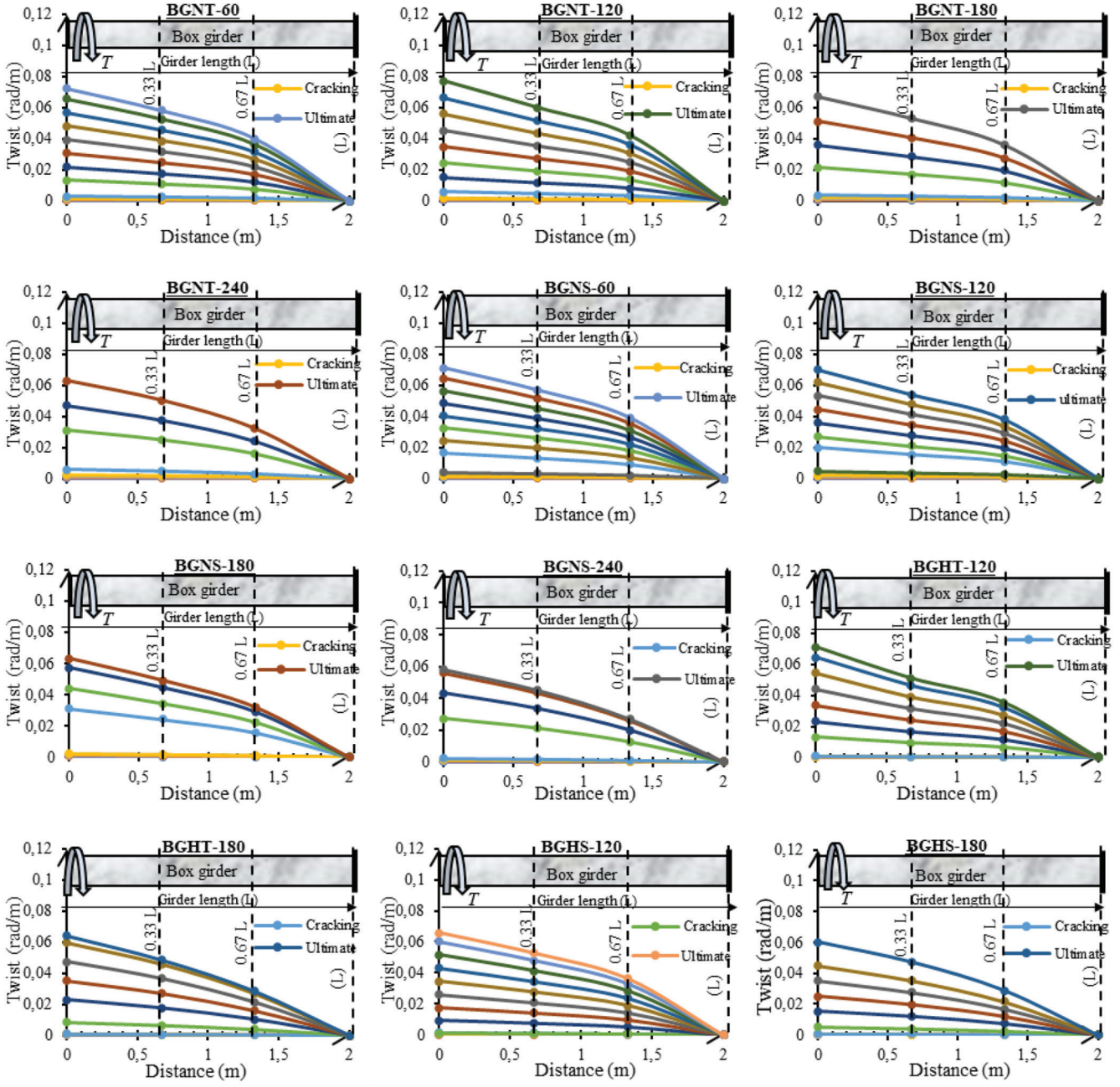

Fig. 5—Twist profile for all GFRP-reinforced box girders. (Note: 1 m = 39.40 in.; 1 rad/m = 0.305 rad/ft.)

is due to the significant contribution of the gross moment of inertia of the concrete cross section in the uncracked phase. In contrast, the concrete strength significantly affected the pre-cracking torsional stiffness of the tested specimens. As anticipated, the specimens constructed with HSC achieved higher pre-cracking torsional stiffness than those with NSC. This was because increasing the concrete strength increased the shear modulus of concrete, thus increasing pre-cracking torsional stiffness. Increasing the concrete strength from 40 to 71 MPa (5.80 to 10.15 ksi) increased the pre-cracking torsional stiffness by, on average, 62%.

On the other hand, the post-cracking torsional stiffness was determined as the slope of the torque-twist curves after cracking. The test results indicate that the post-cracking torsional stiffness of the test specimens was substantially dependent on the test parameters. Regardless of the concrete strength or web reinforcement configuration, increasing the web reinforcement ratio substantially increased the torsional stiffness. Increasing the web reinforcement ratio by almost 300% (from 0.24 to 0.95%) increased the post-cracking torsional stiffness at the ultimate stage by 66% and 63% in the case of the specimens with tie and spiral configurations, respectively. The specimens with a spiral configuration achieved higher post-cracking torsional stiffness than their counterparts reinforced with tie stirrups, regardless of the reinforcement ratio or concrete strength. This might be owing to the spiral branches' inclination being almost perpendicular to the cracking direction and the spirals' continuous nature effectively controlling the width of the major diagonal crack and the distribution of diagonal cracks, thus improving the specimens' post-cracking behavior. On average, the post-cracking torsional stiffness of the HSC specimens at the

ultimate stage was 8% greater than those fabricated with NSC. Regardless of the concrete strength, the post-cracking torsional stiffness of the steel specimens was greater than their counterpart GFRP specimens at any torque level from cracking up to failure. This could be attributed to the fact that the GFRP had a lower modulus of elasticity (58.20 GPa [8440 ksi]) than the steel reinforcement (200 GPa [29,000 ksi]) (almost one-third). The cracked torsional stiffness of the GFRP specimens was almost, on average, 45% of that of the steel specimens at the ultimate stage. The test results indicate that the post-cracking torsional stiffness was a small fraction of the torsional stiffness before cracking, which was, on average, 1.5% and 3% for the GFRP and steel specimens, respectively.

Twist profile

This section discusses the effect of the test parameters on the twist behavior along the specimen's length. Figure 5 shows the twist distribution along the length of the girders at four different locations for all GFRP- RC box girders. These locations were chosen within the test region at 0.00, 0.33, 0.67, and 1.00 of the test region's length (L), where sections 0.00L and 1.00L are located at the applied torque and the fixed end, respectively. Each chart in Fig. 5 involves curves representing different torque levels (a torque step of 5 kN·m [3.70 kip·ft] was chosen). The curves corresponding to the cracking and ultimate levels are highlighted in each chart. Figure 5 displays different phases for different torque levels. Up to the cracking torque level, all the curves are almost horizontal and coincide with the baseline. Moreover, the twist rate was nearly constant throughout the entire length of the girders. This means that the twist behavior along the girders' length until the cracking phase was negligible and was not affected by the configuration or amount of the web reinforcement or concrete strength.

After the cracking level, the successive curves were more separated compared to the successive curves of the pre-cracked stage. Furthermore, regardless of the web reinforcement configuration or concrete strength, decreasing the web reinforcement ratio (increasing the stirrup spacing) resulted in greater separation between the successive curves after cracking. The specimens with continuous spirals achieved lower spacing between the successive curves than those with individual tie stirrups, regardless of concrete strength. The spacing between the successive curves after cracking was almost similar for the HSC and counterpart NSC specimens. Figure 5 indicates that, for the same torque level and reinforcement ratio at locations 0.33L and 0.67L, the HSC specimens with spiral stirrups experienced the lowest twist, thus the higher torsional stiffness along the girder length. For example, at a torque level of 50 kN·m (36.90 kip·ft), Specimen BGHS-120 had 29%, 145%, and 210% less twist, respectively, than Specimens BGHT-120, BGNS-120, and BGNT-120 at location 0.33L. Consequently, it can be concluded that the test parameters discussed herein substantially affected the twist profile of the tested specimens.

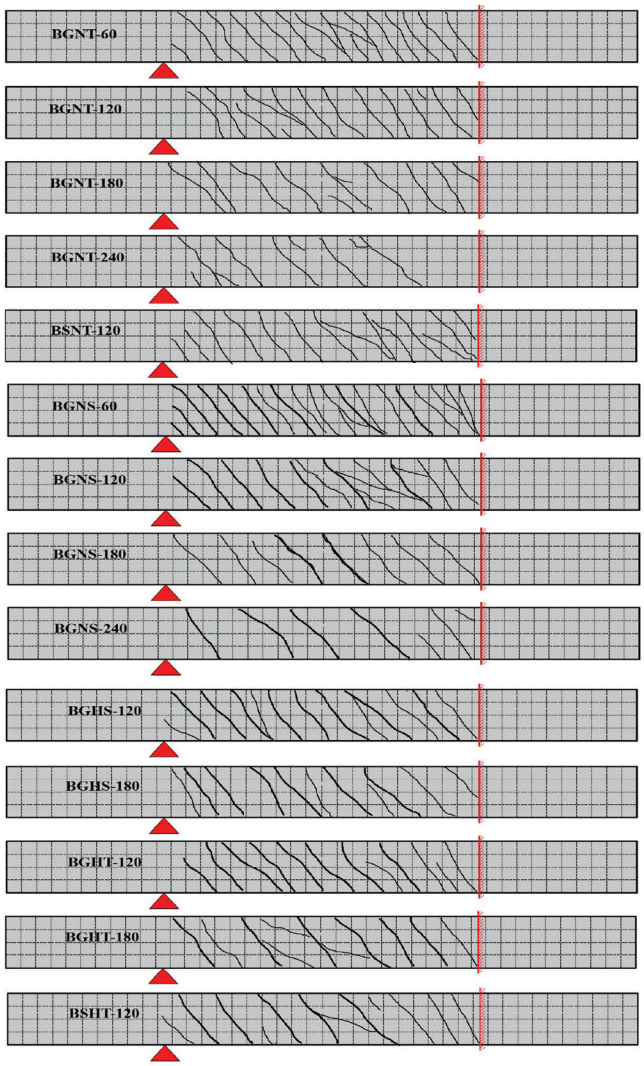

Fig. 6—Cracking pattern of tested specimens at failure.

Crack propagation and failure mechanisms

The growth of cracks at every load step of each girder was observed and recorded during testing until failure. Figure 6 shows the cracks' pattern along with the test specimens' front face at the failure stage. Because the principal stress distribution in a section subjected to pure torsional moment comprises diagonal compression and tension in the concrete, the initial cracks were diagonal (Rasmussen and Baker 1995). When the applied principal tensile stresses reached the tensile capacity of the concrete, the first crack appeared in the middle of the test zone's front face in each specimen, irrespective of whether the specimen was made with NSC or HSC. With a further increase in torque, the first crack spread to the other faces (top, back, and bottom) in a spiral pattern (propagating in opposite directions on opposite sides) along the periphery of the specimen cross section. Subsequently, more spiral cracks parallel to the first one appeared to create the complete crack patterns of the box girders, as shown in Fig. 6.

The final crack patterns of the tested box girders were strongly affected by the ratio and configuration of the web torsional reinforcement. According to observations, there is a positive correlation between the web torsional reinforcement

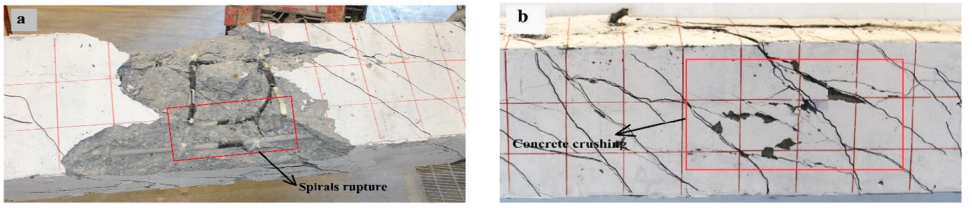

Fig. 7—Typical failure mode: (a) GFRP stirrup rupture; and (b) concrete crushing.

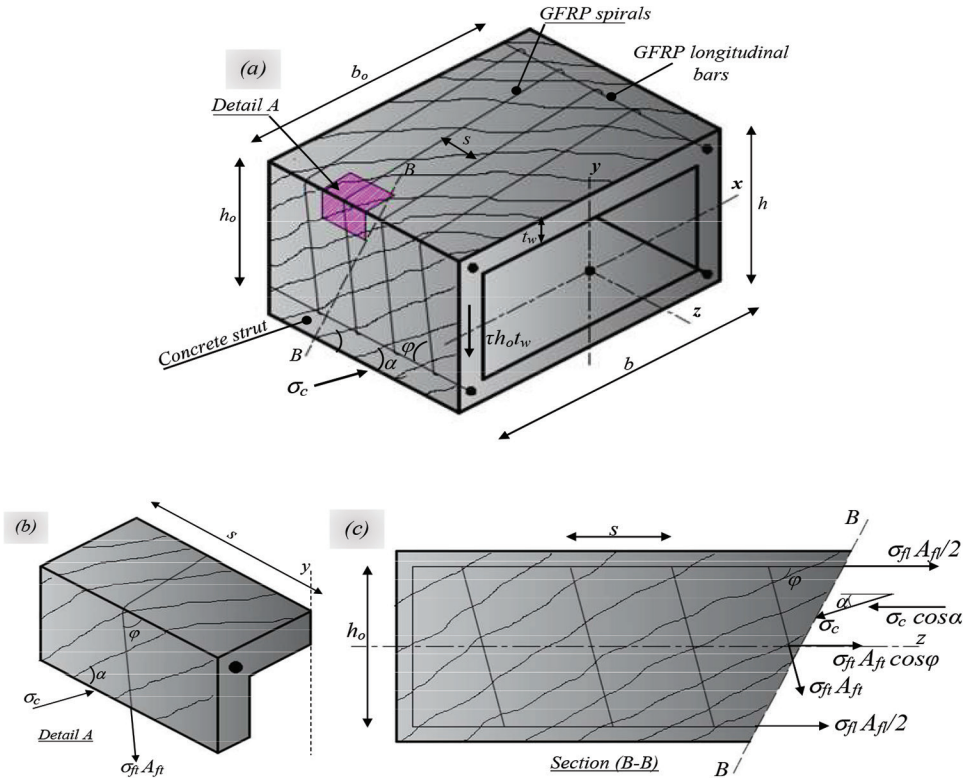

Fig. 8—Equilibrium of space truss model reinforced with GFRP bars and spirals.

ratio, the number of induced torsional cracks, and smaller crack spacing. The specimens reinforced with continuous spiral stirrups had more cracks and narrower crack spacing than the counterparts reinforced with individual tie stirrups, regardless of the concrete strength. In the case of the HSC and NSC specimens with the same reinforcement ratio and configuration, the number of cracks instantly after cracking and up to failure was nearly the same. The cracking behavior of the HSC specimens was substantially different than that of their NSC counterparts. The cracking of the HSC specimens was more brittle than the NSC specimens because the cracks in the HSC traveled through both the matrix and aggregates, resulting in more brittle behavior and straighter diagonal cracks. The crack pattern of the specimens reinforced with steel (BSNT-120 and BSHT-120) was close to that of their counterparts BGNT-120 and BGHT-120.

Figure 7 displays the typical failure mode of the tested box girders. The failure of the GFRP specimens was not affected by concrete strength or web reinforcement configuration. Specimens BGNT-120, BGNT-180, BGNT-240, BGNS-120, BGNS-180, BGNS-240, BGHT-120, BGHT-180, BGHS-120, and BGHS-180 exhibited similar failure mechanisms despite a large difference in the torque at torsional failure. The failure of these specimens was triggered by GFRP spiral or tie rupture at the bent portions at different locations throughout the test zone, as shown in Fig. 7(a). This was accompanied by spalling the concrete cover in the middle of the test region. In contrast, Specimens BGNT-60 and BGNS-60 experienced a failure characterized by the diagonal concrete strut's concrete crushing due to the higher web reinforcement ratio, as shown in Fig. 7(b). Specimens BSNT-120 and BSHT-120—reinforced with steel—failed due to the formation of a main diagonal crack with the web reinforcement yielding, accompanied by concrete crushing in the center of the test region's back face.

DERIVATION OF POST-CRACKING TORSIONAL STIFFNESS

The torsional stiffness after cracking differed between the GFRP-reinforced members and the steel-reinforced members because the two types of reinforcement have different mechanical properties. The post-cracking torsional stiffness is mainly affected by the modulus of elasticity of the reinforcement, reinforcement ratio, and web reinforcement configuration, as shown in the test results of this investigation and that of others (Hadhood et al. 2020; Mohamed

and Benmokrane 2015, 2016). On the other hand, pure torsional moment applied to solid and hollow members with identical cross-sectional dimensions produced no substantial differences in torsional stiffness after cracking (Hsu 1968; Lampert and Thürlimann 1968). Therefore, the derivation of the post-cracking torsional stiffness in this study is based on a hollow section reinforced with GFRP bars and spirals and can be used for solid sections.

Space truss analogy

The space truss model for general cross sections was developed by Rausch in 1929. The truss comprises GFRP longitudinal bars and spirals acting as tension members and the concrete between the cracks acting as diagonal compression struts. The angle of the diagonals with respect to the beam axis depends on the reinforcement and is generally not 45 degrees. For determining stiffness, however, a truss is assumed to have 45-degree diagonals (Hsu 1973). The following assumptions are made in this truss analogy:

1. The GFRP longitudinal bars are considered to support the concrete struts. The spalling of the concrete corner is neglected.
2. The member is subjected to uniform torsion, and the cross section is free to wrap.
3. Diagonal concrete struts resist only compression (no shear resistance). The GFRP reinforcement resists only axial tension (no dowel resistance).
4. The GFRP reinforcement and concrete are assumed to comply with Hooke's law.

Stresses in truss members

The hollow rectangular cross section in Fig. 8 is subjected to a constant external torsional moment T, which is balanced by an internal shear flow q induced in the centerline of the shear flow zone with an effective wall thickness, according to the thin tube theory. The stresses in the truss members due to the shear flow are deduced from the equilibrium conditions of the truss model. Rausch (1929) demonstrated that the stresses in all diagonal compressive struts must be equal. Similarly, the stresses in all web reinforcement and the stresses in all longitudinal bars should be equal. These stresses can be related to the shear stresses τ as follows

$$\tau = \frac{q}{t_w} = \frac{T}{2A t_w} \tag{1}$$

where A is the area enclosed by the centerline of the wall; and t_w is the wall thickness.

The stresses in the concrete strut are determined directly from the equilibrium in the y-direction, shown in Fig. 8(a), as follows

$$\sigma_c t_w h_o \cos\alpha \sin\alpha = \tau t_w h_o \tag{2}$$

The stress in the diagonal compressive strut σ_c is

$$\sigma_c = \frac{2\tau}{\sin 2\alpha} = 2\tau \tag{3}$$

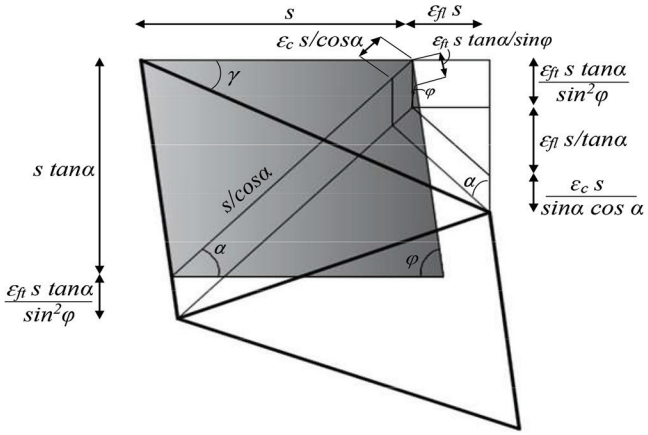

Fig. 9—Shear strain of the concrete, GFRP bars, and GFRP spirals.

where α is the inclination angle of the diagonal strut, and its value is equal to 45 degrees.

The stresses in the GFRP spirals are determined from the equilibrium in the y-direction for Detail A in Fig. 8(b), as follows

$$\sigma_{ft} A_{ft} \sin\varphi = \sigma_c t_w s \sin^2\alpha = \frac{2\tau t_w s \sin^2\alpha}{\sin 2\alpha} = \tau t_w s \tan\alpha \tag{4}$$

The stress in the GFRP spiral σ_{ft} becomes

$$\sigma_{ft} = \frac{\tau t_w s}{A_{ft} \sin\varphi} \tag{5}$$

where s is the GFRP web reinforcement spacing; A_{ft} is the area of one leg of the GFRP web reinforcement; and φ is the inclination angle of the spiral link.

The stresses in the GFRP longitudinal bars are obtained from the equilibrium in the z-direction of Section (B-B) in Fig. 8(c), as follows

$$\sigma_c t_w p_o \cos^2\alpha = \sigma_{fl} A_{fl} + \sigma_{ft} A_{ft} \cos\varphi \tag{6}$$

Substituting σ_{ft} from Eq. (5) into Eq. (6) yields

$$\tau t_w p_o = \sigma_{fl} A_{fl} + \frac{\tau t_w s A_{ft} \cos\varphi}{A_{ft} \sin\varphi} \tag{7}$$

The stress in the GFRP longitudinal bars σ_{fl} is

$$\sigma_{fl} = \frac{\tau t_w p_o}{A_{fl}} - \frac{\tau t_w s \cos\varphi}{A_{fl} \sin\varphi} \tag{8}$$

where p_o is the perimeter of the centerline of the GFRP web reinforcement, and A_{fl} is the total area of the GFRP longitudinal bars. p_o can be calculated from Eq. (9) as follows

$$p_o = 2\left(\frac{h_o}{\sin\varphi} + \frac{b_o}{\sin\varphi}\right) \tag{9}$$

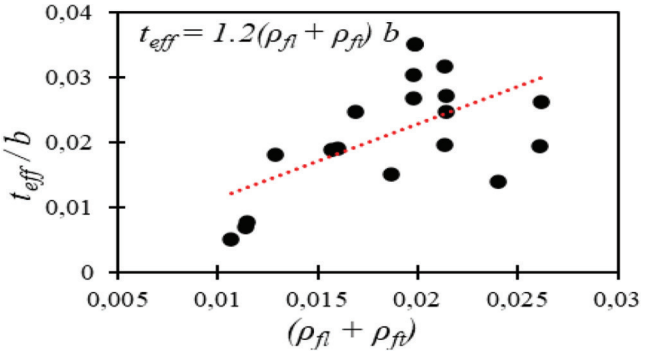

Fig. 10—Total GFRP reinforcement ratio versus effective wall thickness.

where h_o and b_o are the projections of the height and width of the spiral links at the centerlines, respectively.

Strain in truss members

Because the stress-strain relationship for the GFRP reinforcement is linear and assumes the same relation for the concrete, the strains in the concrete and GFRP reinforcement can be determined from Eq. (3), (5), and (8), as follows

Strain in the diagonal concrete struts ε_c is

$$\varepsilon_c = \frac{\sigma_c}{E_c} = \frac{2\tau}{E_c} \tag{10}$$

Strain in the GFRP spirals ε_{ft} is

$$\varepsilon_{ft} = \frac{\sigma_{ft}}{E_{ft}} = \frac{\tau t_w s}{E_{ft} A_{ft} \sin\varphi} \tag{11}$$

Strain in the GFRP longitudinal bars ε_{fl} is

$$\varepsilon_{fl} = \frac{\sigma_{fl}}{E_{fl}} = \frac{\tau t_w p_o}{E_{fl} A_{fl}} - \frac{\tau t_w s \cos\varphi}{E_{fl} A_{fl} \sin\varphi} \tag{12}$$

where E_c, E_{ft}, and E_{fl} are the modulus of elasticity of the concrete, GFRP spirals, and GFRP longitudinal bars, respectively.

Shear strains

The induced strains in the concrete, GFRP spirals, and GFRP longitudinal bars result in shear distortion of the wall. This shear distortion can be determined from the compatibility of deformation, as shown in Fig. 9.

The shear strain of the diagonal concrete strut γ_c is

$$\gamma_c = \frac{\varepsilon_c}{\sin\alpha \cos\alpha} \tag{13}$$

The shear strain of the GFRP spirals γ_{ft} is

$$\gamma_{ft} = \frac{\varepsilon_{ft} \tan\alpha}{\sin^2\varphi} \tag{14}$$

The shear strain of the GFRP longitudinal bars γ_{fl} is

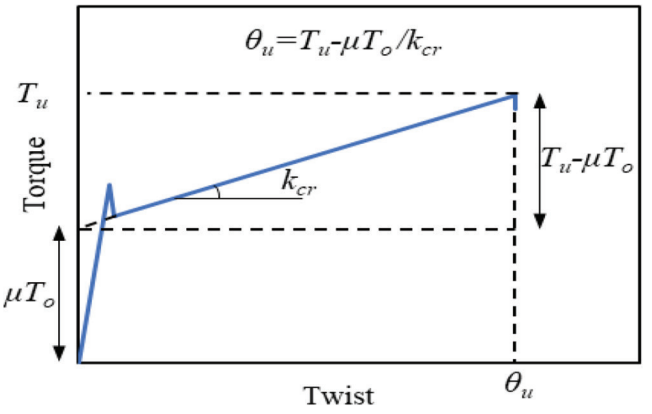

Fig. 11—Typical GFRP torque-twist curve.

$$\gamma_{fl} = \frac{\varepsilon_{fl}}{\tan\alpha} \tag{15}$$

The total shear strain γ of one wall is equal to the summation of the shear strains of the concrete, GFRP spirals, and GFRP bars

$$\gamma = \frac{\varepsilon_c}{\sin\alpha \cos\alpha} + \frac{\varepsilon_{ft} \tan\alpha}{\sin^2\varphi} + \frac{\varepsilon_{fl}}{\tan\alpha} \tag{16}$$

With the assumed inclination angle of diagonal strut $\alpha = 45$ degrees, the total shear strain becomes

$$\gamma = 2\varepsilon_c + \frac{\varepsilon_{ft}}{\sin^2\varphi} + \varepsilon_{fl} \tag{17}$$

By substituting ε_c, ε_{ft}, and ε_{fl} from Eq. (10) through (12) in Eq. (17), the shear strain becomes a function of the shear stress, as follows

$$\gamma = \tau\left(\frac{4}{E_c} + \frac{t_w s \sin\varphi}{E_{ft} A_{ft}} + \frac{t_w p_o}{E_{fl} A_{fl}} - \frac{t_w s \cos\varphi}{E_{fl} A_{fl} \sin\varphi}\right) \tag{18}$$

$A_{ft}/t_w s = \beta_t$ and $A_{fl}/t_w p_o = \beta_l$ are the GFRP spiral and longitudinal reinforcement ratio with respect to the wall area. Therefore, the shear strain can be written as

$$\gamma = \tau\left(\frac{4}{E_c} + \frac{\sin\varphi}{E_{ft}\beta_t} + \frac{1}{E_{fl}\beta_l} - \frac{t_w s \cos\varphi}{E_{fl} A_{fl} \sin\varphi}\right) \tag{19}$$

Determination of torsional shear modulus

The post-cracking shear modulus G_{cr} can be defined as the shear stress divided by shear strain and, therefore, G_{cr} can be written as

$$G_{cr} = \frac{\tau}{\gamma} = \frac{1}{\left(\frac{4}{E_c} + \frac{\sin\varphi}{E_{ft}\beta_t} + \frac{1}{E_{fl}\beta_l} - \frac{t_w s \cos\varphi}{E_{fl} A_{fl} \sin\varphi}\right)} \tag{20}$$

Equation (20) provides the post-cracking shear modulus as mainly a function of the modulus of elasticity of the concrete, GFRP spirals, GFRP longitudinal bars, the GFRP longitudinal and web reinforcement ratios, and the web reinforcement configuration.

Table 4—Test matrix, specimen details, and test results from past studies

Reference	Specimen ID	Transverse reinforcement					Test results	
		Conf.	Size	S, mm	ρ_{ft}, %	T_u, kN·m	θ_u, rad/m	K_{cr}, kN·m^2
Mohamed and Benmokrane (2015, 2016)	BG-60	Tie	No. 3	60	1.07	56.85	0.075	412
	BG-120	Tie	No. 3	120	0.54	52.65	0.084	328
	BG-180	Tie	No. 3	180	0.36	41.75	0.064	300
	BG-240	Tie	No. 3	240	0.27	34.17	0.057	232
	BG-300	Tie	No. 3	300	0.21	29.89	0.051	214
Hadhood et al. (2020)	BG-100	Spiral	No. 3	100	0.85	31.20	0.108	185
	BG-150	Spiral	No. 3	150	0.57	21.20	0.074	160
	BG-200	Spiral	No. 3	200	0.43	16.50	0.065	109
	BG-250	Spiral	No. 3	250	0.35	12.90	0.044	83
	BGST200	Tie	No. 3	200	0.42	14.20	0.081	105

Note: 1 mm = 0.0394 in.; 1 kN·m = 0.7376 kip·ft; 1 rad/m = 0.305 rad/ft; 1 kN·m^2 = 2.42 kip·ft^2.

It is convenient to use the volume of reinforcement percentages with respect to the cross-sectional area in Eq. (20)

$$\rho_{ft} = \frac{A_{ft} p_o}{A_c s} = \beta_t \frac{p_o t_w}{A_c} \tag{21}$$

$$\rho_{fl} = \frac{A_l}{A_c} = \beta_l \frac{p_o t_w}{A_c} \tag{22}$$

where ρ_{ft} and ρ_{fl} are the GFRP web and longitudinal reinforcement ratios, respectively; and A_c is the cross-sectional area enclosed by the perimeter of the concrete. Substituting ρ_{ft} and ρ_{fl} in Eq. (20) gives

$$G_{cr} = \frac{1}{\left(\frac{4}{E_c} + \frac{p_o t_w \sin\varphi}{E_{ft} A_c \rho_{ft}} + \frac{p_o t_w}{E_{fl} A_c \rho_{fl}} - \frac{t_w s \cos\varphi}{E_{fl} A_{fl} \sin\varphi}\right)} \tag{23}$$

Determination of post-cracking torsional stiffness

The post-cracking torsional stiffness k_{cr} is defined as the shear modulus G_{cr} multiplied by the torsional geometric property of the cross section after cracking, which can be called the post-cracking torsional constant C_{cr}. Thin tubes with a uniform wall thickness t_w and constant torque C_{cr} can be determined according to the thin tube theory (Hsu 1973) as follows

$$C_{cr} = \frac{4A^2 t_w}{p_o} \tag{24}$$

The post-cracking torsional stiffness can be written as

$$K_{cr} = G_{cr} C_{cr} = \frac{1}{\left(\frac{4}{E_c} + \frac{p_o t_w \sin\varphi}{E_{ft} A_c \rho_{ft}} + \frac{p_o t_w}{E_{fl} A_c \rho_{fl}} - \frac{t_w s \cos\varphi}{E_{fl} A_{fl} \sin\varphi}\right)} \left(\frac{4A^2 t_w}{p_o}\right) \tag{25}$$

For simplicity, Eq. (25) becomes

$$K_{cr} = \frac{4A^2 A_c}{p_o^2 \left(\frac{4Ac}{E_c p_o t_w} + \frac{\sin\varphi}{E_{ft}\rho_{ft}} + \frac{1}{E_{fl}\rho_{fl}}\left(1 - \frac{s\cot\varphi}{p_o}\right)\right)} \tag{26}$$

This equation calculates the post-cracking torsional stiffness of RC members reinforced with longitudinal bars and spirals or ties. All terms in Eq. (26) are known except t_w, which will be discussed in the following section.

Estimation of effective wall thickness

In Eq. (26), the wall thickness t_w appears only in the first denominator term, which represents the contribution to distortion made by concrete struts. In fact, the entire wall thickness of a hollow section may not be used because only the compressive part of the wall thickness is effective. In addition, the wall thickness is unknown in case of a solid cross section. Hsu (1990) derived an iterative equation to estimate the effective wall thickness. Using this equation results in a complex determination of the post-cracking torsional stiffness. Lampert (1971) neglected the concrete contribution entirely, thus avoiding the calculations pertaining to the effective wall thickness. Karlsson and Elfagren (1972) assumed a constant value for the effective wall thickness as one-fifth of the smaller dimension of the stirrup centerline. Hsu (1973) proposed an empirical equation to estimate the wall thickness based on an analysis of the test results of steel-reinforced RC beams. Because the effective wall thickness appears in only one of three terms in the post-cracking torsional stiffness equation, the theoretical estimation of the effective wall thickness is unnecessary. Therefore, the effective wall thickness estimation in this study followed that used by Hsu (1973).

The effective wall thickness t_{eff} is defined as the depth of the compression zone, similar to the compression zone in the case of bending moment C (Hsu 1990). An increase in the torsional strength due to increasing the GFRP reinforcement results in an increase in the effective wall thickness. In addition, the effective wall thickness is significantly a function of the smaller dimension of the concrete cross section b (Karlsson and Elfagren 1972; Hsu 1973, 1990; Lampert 1971). Therefore, the effective wall thickness can

Table 5—Coefficient μ as function of total GFRP reinforcement

Reference	Specimen ID	$\rho_{fl} + \rho_{ft}$, %	$\mu T_{o(exp)}$, kN·m	T_o, kN·m (Eq. (8))	μ
Current study	BGNT-60	2.61	29	17.70	1.64
	BGNT-120	2.14	25	17.70	1.41
	BGNT-180	1.98	22	17.70	1.24
	BGNT-240	1.90	19	17.70	1.10
	BGNS-60	2.61	30	18.10	1.66
	BGNS-120	2.14	26	18.10	1.44
	BGNS-180	1.98	22	18.10	1.22
	BGNS-240	1.91	19	18.10	1.05
	BGHT-120	2.14	38	23.65	1.60
	BGHT-180	1.98	35	23.65	1.48
	BGHS-120	2.14	40	23.65	1.70
	BGHS-180	1.98	37	23.65	1.56
Mohamed and Benmokrane (2015, 2016)	BG-60	2.40	28	14.90	1.88
	BG-120	1.87	25	15.40	1.63
	BG-180	1.69	22	15.40	1.47
	BG-240	1.60	20	14.95	1.40
	BG-300	1.54	18	15.40	1.24
Hadhood et al. (2020)	BG-100	1.57	11	6.90	1.60
	BG-150	1.29	9.5	6.90	1.37
	BG-200	1.15	9	6.90	1.30
	BG-250	1.07	8.5	6.90	1.27
	BGST-200	1.14	9.2	6.90	1.35

Note: 1 kN·m = 0.7376 kip·ft.

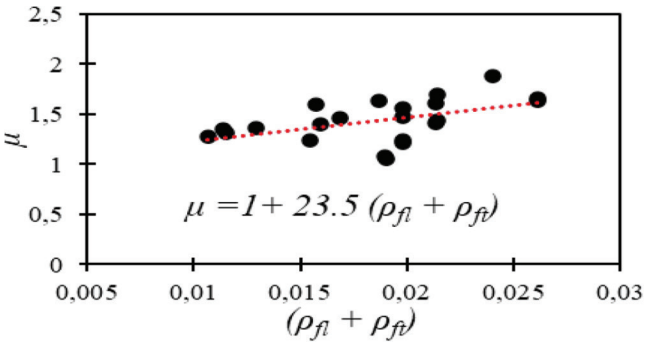

Fig. 12—Coefficient μ versus GFRP reinforcement ratio.

be estimated as a function of the total GFRP reinforcement and the smaller dimension of the cross section. Twenty-two full-scale RC specimens reinforced with GFRP bars and GFRP spirals or ties were collected from the current study and others (Hadhood et al. 2020; Mohamed and Benmokrane 2015, 2016), as shown in Tables 3 and 4. The effective wall thickness t_{eff} was determined from Eq. (26) by using the experimental value of the post-cracking torsional stiffness for all specimens. Figure 10 shows a relationship between t_{eff}/b and the total GFRP reinforcement ($\rho_{fl} + \rho_{ft}$). The effective wall thickness can be written as

$$t_{eff} = 1.2(\rho_{fl} + \rho_{ft})b \quad (27)$$

ULTIMATE TWIST

The torque-twist curve of the GFRP-RC members is essentially linear from cracking until failure. This is due to the linear characteristics of the GFRP materials. Unlike in the case of the steel-RC members, the torque-twist curve initially after cracking is linear and then bends toward horizontal until failure. Therefore, it is simple to derive an equation estimating the ultimate twist of the cross section in the case of the GFRP-RC members, as the inclination of the torque-twist curve after cracking is known, represented by the post-cracking torsional stiffness k_{cr}. Figure 11 shows a typical torque-twist curve of the GFRP-RC members. The figure shows that the extension of the line of the torque twist after cracking intersects the vertical axis. This vertical intersect is called μT_o, where μ is an empirical coefficient and T_o is the contribution of the concrete to torsion strength. Therefore, T_o can be written as (Hsu 1973)

$$T_o = \frac{2.4}{\sqrt{b}} bh\sqrt{f_c'} \quad (28)$$

where b and h are the width and height of the concrete cross section, respectively; and f_c' is the concrete compressive strength. From Fig. 4, the ultimate twist θ_u of the GFRP-RC members is

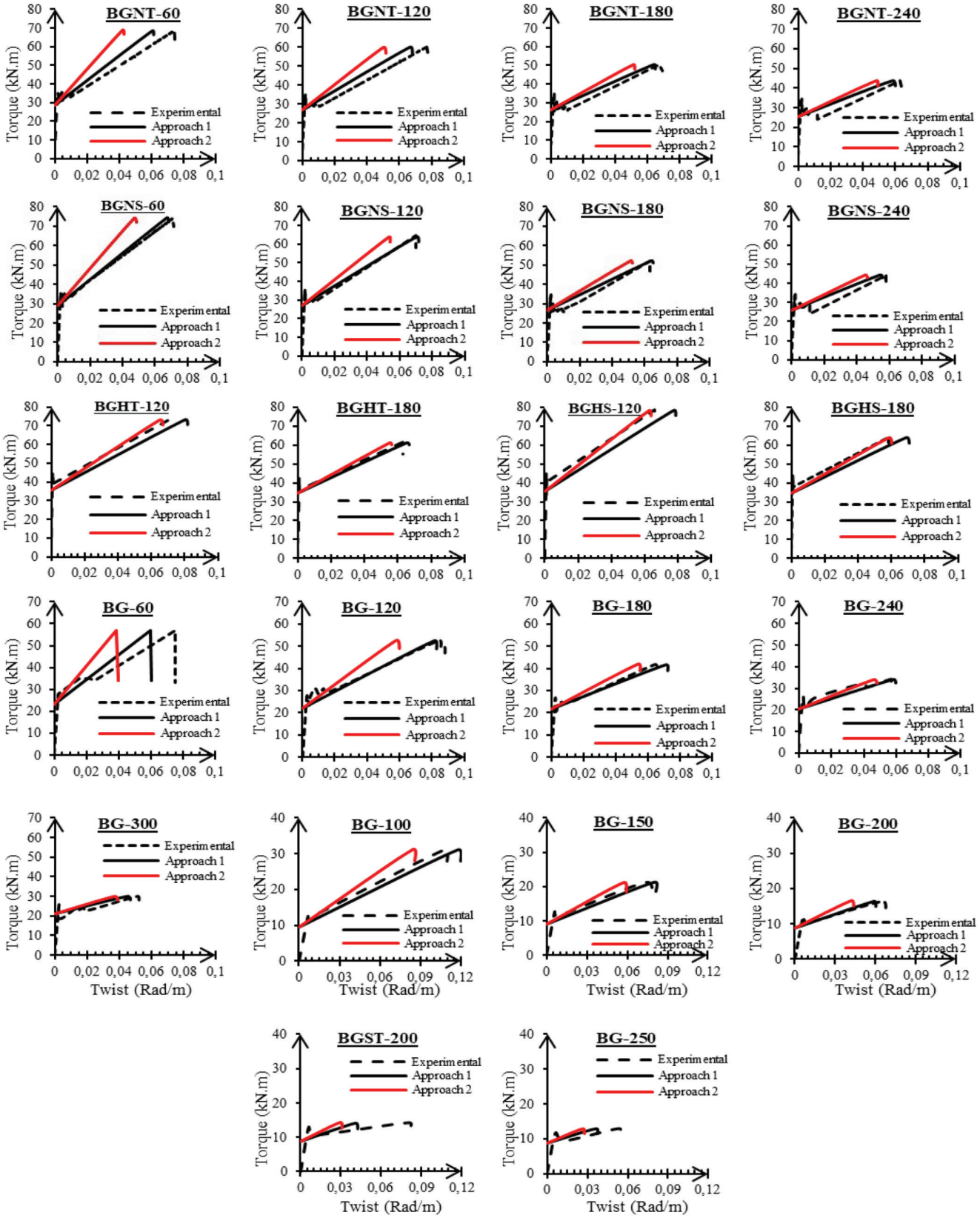

Fig. 13—Experimental to analytical torque-twist curves. (Note: 1 kN.m = 0.7376 kip.ft; 1 rad/m = 0.305 rad/ft.)

$$\theta_u = \frac{T_u - \mu T_o}{k_{cr}} \quad (29)$$

where T_u is the ultimate torsional strength. Equation (29) can be used to estimate the twist of the cross section at any given torque from cracking until failure.

The test results reveal that the vertical intersect μT_o is a function of the total GFRP reinforcement ratio: μT_o increased as the GFRP reinforcement ratio increased. Table 5 provides the experimental values of μT_o for all the specimens.

Table 6—Comparison of analytical to experimental results

Reference	Specimen ID	Approach 1				Approach 2				$\mu T_{o(theo)}$, kN·m	$\mu T_{o(exp)}/\mu T_{o(theo)}$
		$K_{cr(theo)}$, kN·m^2	$K_{cr(exp)}/K_{cr(theo)}$	$\theta_{u(theo)}$, rad/m	$\theta_{u(exp)}/\theta_{u(theo)}$	$K_{cr(theo)}$, kN·m^2/rad	$K_{cr(exp)}/K_{cr(theo)}$	$\theta_{u(theo)}$, rad/m	$\theta_{u(exp)}/\theta_{u(theo)}$		
Current study	BGNT-60	668	0.85	0.060	1.20	955	0.59	0.042	1.71	28.60	1.01
	BGNT-120	504	0.91	0.066	1.15	665	0.68	0.050	1.53	26.60	0.94
	BGNT-180	382	1.04	0.064	1.05	477	0.84	0.052	1.30	25.90	0.85
	BGNT-240	309	1.10	0.058	1.08	372	0.91	0.048	1.30	25.60	0.74
	BGNS-60	671	0.96	0.067	1.06	958	0.66	0.047	1.51	29.13	1.03
	BGNS-120	518	1.13	0.071	0.98	680	0.77	0.054	1.28	27.12	0.96
	BGNS-180	402	1.07	0.064	0.99	502	0.86	0.052	1.23	26.45	0.84
	BGNS-240	338	1.15	0.054	1.07	406	0.96	0.045	1.29	26.12	0.73
	BGHT-120	467	1.07	0.081	0.88	578	0.87	0.065	1.10	35.60	1.07
	BGHT-180	402	1.01	0.066	0.98	477	0.86	0.055	1.16	34.70	1.01
	BGHS-120	549	1.05	0.077	0.85	680	0.85	0.063	1.05	35.60	1.12
	BGHS-180	422	1.06	0.070	0.87	508	0.90	0.058	1.03	34.70	1.06
Mohamed and Benmokrane (2015, 2016)	BG-60	564	0.74	0.060	1.26	867	0.48	0.039	1.94	23.40	1.20
	BG-120	374	0.88	0.082	1.03	528	0.62	0.058	1.46	22.10	1.13
	BG-180	286	1.04	0.071	0.91	380	0.79	0.054	1.20	21.40	1.05
	BG-240	232	1.00	0.059	0.98	297	0.78	0.046	1.24	20.60	1.02
	BG-300	198	1.08	0.045	1.12	243	0.88	0.037	1.38	20.90	0.91
Hadhood et al. (2020)	BG-100	185	1.00	0.12	0.92	258	0.72	0.084	1.28	9.40	1.16
	BG-150	153	1.04	0.080	0.93	215	0.74	0.057	1.30	8.90	1.05
	BG-200	133	0.83	0.059	1.11	185	0.59	0.042	1.55	8.74	1.03
	BG-250	118	0.72	0.037	1.20	161	0.51	0.027	1.64	8.60	1.01
	BGST-200	132	0.80	0.041	1.70	183	0.57	0.030	2.40	8.71	1.06
Average	—	—	0.98	—	1.06	—	0.75	—	1.40	—	1.00
Standard deviation	—	—	0.12	—	0.19	—	0.14	—	0.31	—	0.12
COV, %	—	—	12.95	—	17.70	—	18.77	—	22.40	—	12.48

Note: 1 kN·m^2 = 2.42 kip·ft^2; 1 rad/m = 0.305 rad/ft; 1 kN·m = 0.7376 kip·ft.

Figure 12 depicts the relationship between μ and $(\rho_{fl} + \rho_{ft})$, therefore, μ can be written as

$$\mu = 1 + 23.5(\rho_{fl} + \rho_{ft}) \quad (30)$$

COMPARISON OF ANALYTICAL AND EXPERIMENTAL RESULTS

The accuracy of the proposed equations in estimating the post-cracking torsional stiffness k_{cr}, vertical intersect μT_o, and the ultimate twist θ_u of the cross section was evaluated by comparing their predictions to the experimental results of 22 specimens. The post-cracking torsional stiffness k_{cr} was determined with two approaches: the first considers the effect of the concrete contribution on the torsional stiffness; the second neglect the concrete contribution entirely, thus avoiding the calculations of the effective wall thickness. The torque-twist curves of 22 GFRP specimens were regenerated analytically considering the discussions mentioned previously. Figure 13 compares the experimental and analytical torque-twist curves. The curves labeled Approach 1 and 2

were developed using the experimental value of the ultimate torque. The general applicability of the proposed model is confirmed by the excellent agreement between the experimental and Approach 1 curves for all the specimens. The regeneration of the torque-twist curves using Approach 2 overestimated the corresponding experimental curves for all the specimens. Generally, Fig. 13 indicates that the predicted post-cracking torsional stiffness for the same cross-sectional dimensions increased as the reinforcement ratio increased. Moreover, for the same cross-sectional dimensions and reinforcement ratio, the specimen with spiral configuration exhibited higher post-cracking torsional stiffness. Increasing the concrete strength resulted in an increase in the post-cracking torsional stiffness. Consequently, it can be concluded that the proposed model could estimate the post-cracking torsional stiffness considering many parameters (reinforcement ratio, reinforcement configuration, and concrete strength).

Table 6 gives the average values, standard deviation, and coefficient of variation (COV) for the ratios of experimental to predicted values of $k_{cr(exp)}/k_{cr(theo)}$, $\mu T_{o(exp)}/\mu T_{o(theo)}$, and $\theta_{u(exp)}/\theta_{u(theo)}$. The average value of the ratio $k_{cr(exp)}/k_{cr(theo)}$ was 0.98 and 0.75 with a corresponding COV of 12.95% and 18.77% for Approaches 1 and 2, respectively. Table 6 indicates that the calculated values of the vertical intersect μT_o agree reasonably well with the experimental results. The average value of the ratio $\mu T_{o(exp)}/\mu T_{o(theo)}$ was 1.00 with a COV of 12.48%. Table 6 points out that the calculated values of the ultimate twist θ_u using Approach 1 yielded a good prediction compared to the corresponding experimental results, whereas using Approach 2 resulted in a conservative prediction. The average value of the ratio $\theta_{u(exp)}/\theta_{u(theo)}$ was 1.06 and 1.40 with a corresponding COV of 17.70% and 22.40% for Approach 1 and 2, respectively.

SUMMARY AND CONCLUSIONS

This study investigated the effects of the concrete strength as well as the web reinforcement ratio, configuration, and type on the torsional stiffness of glass-fiber-reinforced polymer-reinforced concrete (GFRP-RC) box girders. Furthermore, it proposed an analytical model for estimating the post-cracking torsional stiffness and the ultimate twist of RC members reinforced with GFRP bars and ties or spirals. To achieve these objectives, 14 concrete box girders were constructed and examined under pure torsional moment. A post-cracking torsional stiffness model was proposed and verified using the experimental results for the tested box girders and the other specimens available in the literature. The main conclusions can be summed up as follows.

1. The test results indicate that the pre-cracking torsional stiffness of the tested specimens was independent of the web reinforcement configuration, type, and ratio. In contrast, the concrete strength significantly affected the pre-cracking torsional stiffness of the tested specimens.

2. The concrete strength and the web reinforcement ratio, configuration, and type significantly affected the post-cracking torsional stiffness. The specimens reinforced with GFRP spirals—whether made with normal- or high-strength concrete—achieved higher torsional stiffness at the cracked stage than their counterparts with GFRP ties.

3. The test results indicate that the post-cracking torsional stiffness was a small fraction of the torsional stiffness before cracking, which was, on average, 1.5% and 3% for the GFRP- and steel-reinforced specimens, respectively.

4. An analytical model was developed for estimating the torsional stiffness after cracking. This model was based on a thin-walled tube and space truss analogy using a concept of post-cracking shear modulus. The proposed model could estimate the post-cracking torsional stiffness of RC members, either solid or hollow, reinforced with GFRP bars and ties or spirals. The applicability of the proposed model was confirmed by regenerating the torque-twist curves of the tested box girders and the other specimens available in the literature.

5. An empirical equation to calculate the thickness of the shear flow zone was presented, which was used to estimate the contribution of the concrete to the post-cracking torsional stiffness. In addition, an analytical equation was derived to determine the twist of the cross section corresponding to any torque level from cracking until failure. The twist values determined using this equation agreed with the experimentally measured ones with an average experimental to calculated twist ratio of 1.06.

6. The calculated post-cracking torsional stiffness using Approach 1—considering the contribution of the concrete to torsional stiffness—provided an excellent prediction, as the average value of the ratio $k_{cr(exp)}/k_{cr(theo)}$ was 0.98. In contrast, using Approach 2—disregarding the contribution of the concrete to torsional stiffness—resulted in an overestimation with an average value of the ratio $k_{cr(exp)}/k_{cr(theo)}$ equal to 0.75.

AUTHOR BIOS

Ibrahim T. Mostafa *is a Doctoral Candidate in the Department of Civil and Building Engineering at the University of Sherbrooke, Sherbrooke, QC, Canada. He received his BSc and MSc in civil engineering from the Faculty of Engineering, Helwan University, Cairo, Egypt. His research interests include the use of fiber-reinforced polymers (FRPs) in reinforced concrete structures.*

Salaheldin Mousa *is a Postdoctoral Fellow in the Department of Civil and Building Engineering at the University of Sherbrooke. He received his BSc and MSc from the Faculty of Engineering at Shoubra, Benha University, Cairo, Egypt, and his PhD from the University of Sherbrooke. His research interests include the use of FRPs in reinforced concrete structures.*

Hamdy M. Mohamed *is a Research Associate and Lecturer in the Department of Civil and Building Engineering at the University of Sherbrooke. He received his BSc and MSc degrees from the Faculty of Engineering, Helwan University, and his PhD from the University of Sherbrooke. His research interests include the use and field applications of FRPs in reinforced concrete structures.*

Brahim Benmokrane, *FACI, is a Professor in the Department of Civil and Building Engineering at the University of Sherbrooke, Tier-1 Canada Research Chair in Advanced Composite Materials for Civil Structures, NSERC Senior Research Chair in FRP Reinforcement for Concrete Infrastructure, and Director of the University of Sherbrooke Research Center on Structural FRP Composite Materials for Concrete Structures (CRUSMAC). He is a member of ACI Committees 435, Deflection of Concrete Building Structures, and 440, Fiber-Reinforced Polymer Reinforcement, and ACI Subcommittees 440-E, FRP-Professional Education; 440-F, FRP-Repair-Strengthening; 440-H, FRP-Reinforced Concrete; 440-I, FRP-Prestressed Concrete; 440-K, FRP-Material Characteristics; and 440-L, FRP-Durability. He received the ACI Arthur J. Boase Award in 2022. His research interests include the development of FRP reinforcement for*

concrete structures and their durability, structural performance, and field applications.

ACKNOWLEDGMENTS

This research was conducted with funding from the Natural Sciences and Engineering Research Council of Canada (NSERC), the Fonds de recherche du Quebec en nature et technologies (FRQ-NT) and the Tier-1 Canada Research Chair in Advanced Composite Materials for Civil Structures. The authors are also grateful to Pultrall Inc. for the donation of FRP materials and to the technical staff of the structural lab in the Department of Civil Engineering at the University of Sherbrooke.

REFERENCES

ACI Committee 440, 2022, "Building Code Requirements for Structural Concrete Reinforced with Glass Fiber-Reinforced Polymer (GFRP) Bars—Code and Commentary (ACI CODE-440.11-22), American Concrete Institute, Farmington Hills, MI, 206 pp.

ASTM A615/A615M-20, 2020, "Standard Specification for Deformed and Plain Carbon-Steel Bars for Concrete Reinforcement," ASTM International, West Conshohocken, PA, 8 pp.

ASTM C39/C39M-21, 2021, "Standard Test Method for Compressive Strength of Cylindrical Concrete Specimens," ASTM International, West Conshohocken, PA, 8 pp.

ASTM D7205/D7205M-21, 2021, "Standard Test Method for Tensile Properties of Fiber Reinforced Polymer Matrix Composite Bars," ASTM International, West Conshohocken, PA, 13 pp.

ASTM D7914/D7914M-21, 2021, Standard Test Method for the Strength of Fiber-Reinforced Polymer Bent Bars in Bend Locations, ASTM International, West Conshohocken, PA, 6 pp.

CSA S807-19, 2019, "Specification for Fibre-Reinforced Polymers," CSA Group, Toronto, ON, Canada.

El-Salakawy, E.; Masmoudi, R.; Benmokrane, B.; Brière, F.; and Desgagné, G., 2004, "Pendulum Impacts into Concrete Bridge Barriers Reinforced with Glass Fibre Reinforced Polymer Composite Bars," *Canadian Journal of Civil Engineering*, V. 31, No. 4, pp. 539-552. doi: 10.1139/l04-006

Eladawy, M.; Hassan, M.; and Benmokrane, B., 2019, "Experimental Study of Interior Glass Fiber-Reinforced Polymer-Reinforced Concrete Slab-Column Connections under Lateral Cyclic Load," *ACI Structural Journal*, V. 116, No. 6, Nov., pp. 165-180. doi: 10.14359/51716803

Hadhood, A.; Gouda, M. G.; Agamy, M. H.; Mohamed, M. H.; and Sherif, A., 2020, "Torsion in Concrete Beams Reinforced with GFRP Spirals," *Engineering Structures*, V. 206, No. 3. 10.1016/j.engstruct.2020.110174

Hsu, T. T. C., 1968, "Torsion of Structural Concrete-Behavior of Reinforced Concrete Rectangular Members," *Torsion of Structural Concrete*, SP-18, American Concrete Institute, Farmington Hills, MI, pp. 261-306.

Hsu, T. T. C., 1973, "Post-Cracking Torsional Rigidity of Reinforced Concrete Sections," *ACI Journal Proceedings*, V. 70, No. 5, Sept.-Oct., pp. 352-360.

Hsu, T. T. C., 1990, "Shear Flow Zone in Torsion of Reinforced Concrete," *Journal of Structural Engineering*, ASCE, V. 116, No. 11. doi: 10.1061/(ASCE)0733-9445(1990)116:11(3206)

Karlsson, I., and Elfagren, L., 1972, "Torsional Stiffness of Reinforced Concrete Members Subjected to Pure Torsion," *Magazine of Concrete Research*, V. 24, No. 80, pp. 149-156. doi: 10.1680/macr.1973.24.80.149

Lampert, P., 1971, "Post-Cracking Stiffness of Reinforced Concrete Beams in Torsion and Bending," Publication No. 71-20, Department of Civil Engineering, University of Toronto, Toronto, ON, Canada.

Lampert, P., and Thürlimann, B., 1968, "Torsionsversuche an Stahlbetonbalken," Institut für Baustatik, ETH Zürich, Zürich, Switzerland. doi:10.3929/ethz-a-000574534.

Mohamed, H. M.; Ali, A. H.; Hadhood, A.; Mousa, S.; Abdelazim, W.; and Benmokrane, B., 2020, "Testing, Design, and Field Implementation of GFRP RC Soft-Eyes for Tunnel Construction," *Tunnelling and Underground Space Technology*, V. 106, Mar., p. 103626. doi: 10.1016/j.tust.2020.103626

Mohamed, H. M., and Benmokrane, B., 2014, "Design and Performance of Reinforced Concrete Water Chlorination Tank Totally Reinforced with GFRP Bars: Case Study," *Journal of Composites for Construction*, ASCE, V. 18, No. 1, p. 05013001. doi: 10.1061/(ASCE)CC.1943-5614.0000429

Mohamed, H. M., and Benmokrane, B., 2015, "Torsion Behavior of Concrete Beams Reinforced with Glass Fiber-Reinforced Polymer Bars and Stirrups," *ACI Structural Journal*, V. 112, No. 5, Sept.-Oct., pp. 543-552. doi: 10.14359/51687824

Mohamed, H. M., and Benmokrane, B., 2016, "Reinforced Concrete Beams with and without FRP Web Reinforcement under Pure Torsion," *Journal of Bridge Engineering*, ASCE, V. 21, No. 3, 14 pp. doi: 10.1061/(ASCE)BE.1943-5592.0000839.

Mousa, S.; Mohamed, H. M.; and Benmokrane, B., 2018, "with Glass Fiber-Reinforced Polymer," *ACI Structural Journal*, V. 115, No. 5, Sept., pp. 1353-1364. doi: 10.14359/51702282

Rahal, K. N., and Collins, M. P., 1995, "Analysis of Sections Subjected to Combined Shear and Torsion—A Theoretical Model," *ACI Structural Journal*, V. 92, No. 4, July-Aug., pp. 459-469. doi: 10.14359/995

Rasmussen, L. J., and Baker, G., 1995, "Torsion in Reinforced Normal and High-Strength Concrete Beams—Part 1: Experimental Test Series," *ACI Structural Journal*, V. 92, No. 1, Jan.-Feb., pp. 56-62.

Rausch, E., 1929, "Design of Reinforced Concrete in Torsion (Berechnung Des Eisenbetons gegen Verdrehung)," PhD thesis, Technische Hochschule, Berlin, Germany, 53 pp.

Robinson, J. R., 1966, "Torsion of Concrete Cylinders of Circular Cross Section, Reinforced with Hoops and Longitudinal Ties," Introductory Report, CEB Sub-Committee on Torsion, Brussels, Belgium, Translated as Foreign Literature Study No. 496, Portland Cement Association, International Association for Bridge and Structural Engineering, Zurich, V. 26, 1966, pp. 399-410. (in French)

Tavio, and Teng, S., 2004, "Effective Torsional Rigidity of Reinforced Concrete Members," *ACI Structural Journal*, V. 101, No. 2, Mar.-Apr., pp. 252-260.

ACI STRUCTURAL JOURNAL TECHNICAL PAPER

Title No. 121-S38

Experimental Investigation of Deep Beams with High-Strength Headed Shear Reinforcement, Part I

by Dhanushka K. Palipana and Giorgio T. Proestos

Using normal-strength (Grade 60) and high-strength (Grade 80) headed bars as shear reinforcement can improve the constructability of reinforced concrete structures. However, the ACI 318-19 Code does not allow the use of headed bars as transverse reinforcement in deep beams. Similarly, ACI 318-19 does not allow engineers to take advantage of the increased yield strength of Grade 80 reinforcement for use as shear reinforcement. Therefore, to investigate the performance of headed and high-strength transverse reinforcement on the shear behavior of deep beams, a series of six large-scale specimens were tested to failure. The member response, including crack widths and strains in transverse reinforcement, were examined. The results show that deep beams containing headed and high-strength transverse reinforcement performed well compared to companion tests using conventional reinforcement.

Keywords: deep beams; high strength; reinforced concrete; reinforcement; shear.

INTRODUCTION

Reinforced concrete deep beams are members that have small shear spans compared to their depth. When the shear span-depth ratio (a/d) of such members becomes less than approximately 2.5, the members are governed by shear deformations, and plane sections do not remain plane. Deep beams are common structural elements that can be found in buildings and bridges, including elements such as footings, transfer girders, corbels, bent caps, and foundations. Deep beams are considered disturbed regions and are typically designed using strut-and-tie procedures or other methods capable of capturing their complex response. It is common for deep beams to be shear-critical. These members are often heavily loaded and contain substantial quantities of longitudinal and transverse reinforcement. Reducing the reinforcement congestion in such members by using high-strength reinforcement can improve the constructability of the members due to more simplified reinforcement cages and better concrete placement. Similarly, using headed bars as shear reinforcement can simplify the construction of such members and reduce the development lengths in comparison to other reinforcement details. Despite these benefits, codes have limits on the yield stress of the shear reinforcing steel that may be used in design and on the use of headed bars as shear reinforcement.

Headed bars use a head or plate attached to the end of reinforcing bars to provide mechanical anchorage between the concrete and the reinforcement. The ACI 318-19 Code[1] allows heads that have a net bearing area of at least four times the bar area. While ACI 318-19 allows the use of headed deformed bars as longitudinal reinforcement, it does not allow headed bars for use as shear reinforcement.

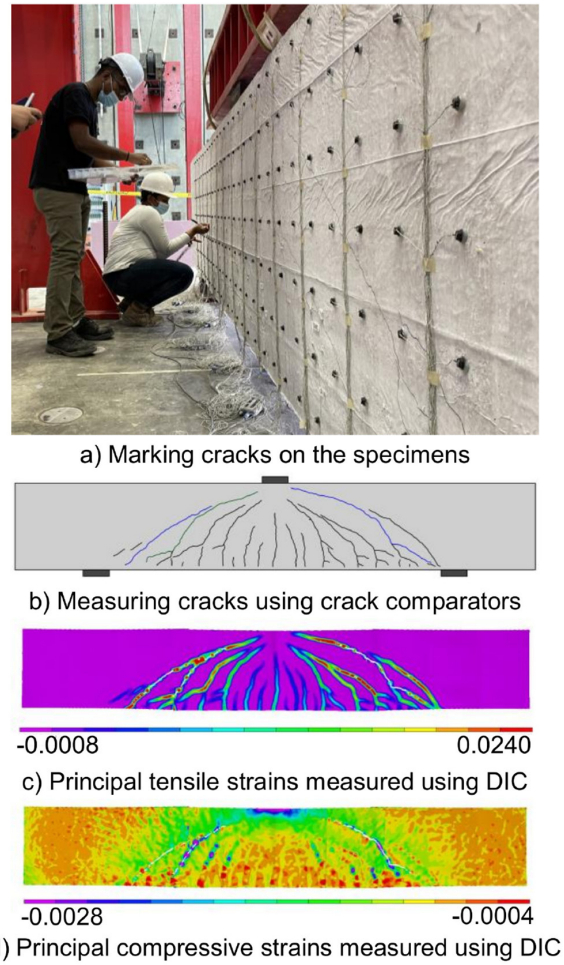

Fig. 1—Experiment of large-scale deep beam, diagram of cracks just prior to failure, and measured strain fields.

In 1962, Joint ACI-ASCE Committee 326, Shear and Diagonal Tension, wrote: "Recent tests at Cornell University included beams which contained stirrups having very high yield points. The test data indicate that the stirrups were not capable of developing their yield strength even though the Krf_y values were moderate. Therefore, a limit of 60,000 psi is proposed on the value of f_y in Eq (6-8)."[2]

This research was based on a small number of beam tests, with some beams that consisted of poor detailing in

ACI Structural Journal, V. 121, No. 3, May 2024.
MS No. S-2023-079.R1, doi: 10.14359/51740486, received September 29, 2023, and reviewed under Institute publication policies.

comparison to modern standards. Based on this limited research, in 1963, the ACI Code placed a limit on the maximum yield stress that could be used for shear reinforcement to 60 ksi (414 MPa).[3] This 60 ksi (414 MPa) limit on the shear reinforcement still exists in the ACI 318-19 Code and can be found in Table 20.2.2.4(a). However, using high-strength shear reinforcement, with yield stresses 80 ksi (552 MPa) and above, could reduce reinforcement congestion and make heavily reinforced structures more constructible. In some design scenarios, designers will increase the depth of a member to avoid using shear reinforcement. Allowing designers to take advantage of the benefits of high-strength steel by liberalizing code provisions would encourage designers to use steel rather than making members deeper and omitting steel. Members with at least minimum shear reinforcement are much more resilient than members without shear reinforcement. Thus, encouraging designers to use high-strength reinforcing steel can encourage engineers to design more resilient structures.

Several studies in literature have shown that high-strength bars perform satisfactorily as shear reinforcement. Proestos et al.[4] conducted a series of 12 reinforced concrete shell elements subjected to combinations of pure shear and biaxial stresses. From the experimental campaign and analytical evaluations, it was concluded that it would be appropriate to increase the ACI 318 limit on the yield stress of shear reinforcement to 80 ksi (552 MPa). Cladera[5] conducted 18 tests on high-strength concrete beams with a/d of 3. These specimens had web reinforcement with yield stresses of 77 and 78 ksi (531 and 538 MPa). The quantity of transverse reinforcement, $\rho_v f_{vy}$, varied between 0 and 197.5 psi (0 and 1.36 MPa). The author observed a general trend of increasing shear strength when the concrete strength increased. The author also observed that adding web reinforcement increases the shear strength of the specimens and the ductility of the members, and that the cracks were more controlled and distributed when shear reinforcement was included. In the study by Munikrishna et al.,[6] 18 tests were conducted on nine 22 ft (6706 mm) long beams, with an a/d of 3. The specimens used No. 3 closed stirrups with a yield stress of 80 ksi (552 MPa), No. 4 closed stirrups with a yield stress of 69 ksi (476 MPa), and No. 4 closed stirrups with a yield stress of 100 ksi (689 MPa). The authors observed that the stirrups yielded before the crushing of the compression zone. They concluded that beams containing smaller amounts of high-strength stirrups can sustain similar loads to members that use larger quantities of lower-strength stirrups. Also refer to Rogowsky et al.[7] and Birrcher et al.[8]

A series of reinforced concrete slender beam experiments containing high-strength headed bars were conducted by Lequesne et al.[9] The beams had a/d of 3. These specimens included No. 4 bars with bearing areas four times the bar area and yield stresses of 66.3 and 84.5 ksi (457 and 583 MPa). The authors concluded that specimens with adequately anchored headed bars can achieve the same shear capacity as specimens that use stirrups for the transverse reinforcement. Their results showed that adequate anchorage to headed bars is provided if one of the following two conditions are met: 1) when the transverse reinforcement was engaged with the longitudinal bars for No. 4 or smaller bars; or 2) when the headed bars are placed inside at least one longitudinal bar and a side cover to the headed bars of at least six bar diameters was provided for No. 6 or smaller bars. When these conditions were met, the headed bars could develop their yield strains. The authors also showed that when high-strength shear reinforcement is used to replace larger quantities of Grade 60 reinforcement, such that the quantity of reinforcement, $\rho_v f_{vy}$, remains unchanged, the specimens achieve the same shear strength, and there is no discernible effect on crack patterns. Forest[10] conducted an experimental program of four specimens to compare the effectiveness of 135-degree hooked stirrups, 90-degree hooked stirrups, and headed bars as single-legged shear reinforcement. The specimen with 135-degree hooked stirrups gave the highest shear strength, while the specimen with headed bars attained 90% of the shear strength compared to the member that contained stirrups. However, the specimens that contained stirrups with 90-degree bends were only able to reach 75% of the peak shear strength of the specimen with 135-degree hooked stirrups, on average. Also refer to Yoshida[11] and Yang et al.[12]

This paper presents a series of six large-scale tests conducted to investigate the response of high-strength headed bars when used as shear reinforcement in reinforced concrete deep beams. Figure 1 shows the marking of cracks and measuring the crack widths on the specimens during the experimental series. Figure 1 also shows the principal strains measured using digital image correlation (DIC). The member response including crack widths and strains in transverse reinforcement are examined and compared for members with lower-strength conventional stirrups, lower-strength headed shear reinforcement, and high-strength headed shear reinforcement.

RESEARCH SIGNIFICANCE

This study examines shear-critical concrete deep beams and the influence of high-strength headed steel reinforcement on member response. The objectives of this research are: 1) to assess the shear behavior of deep beams reinforced with high-strength headed shear reinforcement; 2) to compare the performance of beams with varying quantities of reinforcement; and 3) to compare the performance of beams using varying reinforcement yield stresses. The overall objective of this study is to make recommendations as to the feasibility of allowing the use of headed high-strength reinforcing bars as transverse reinforcement in concrete deep beams and examine if experimental data warrants liberalizing code limits.

EXPERIMENTAL PROGRAM

To investigate the response of deep beams that use headed and high-strength transverse reinforcement, a series of six simply supported large-scale deep beam experiments, the HTS series, was tested to failure. The specimens measured 240 in. (6096 mm) long, 40 in. (1016 mm) deep, and 15 in. (381 mm) wide. The effective depth of the members, d, was 33 in. (838 mm). The effective depth is calculated from the bottom flexural tension reinforcement. All the specimens had an a/d of 2.5. These large members are therefore

representative of full-scale or near-full-scale structures used in practice. These members can also represent strips of wider members; as the literature notes, there is no width effect in shear.[13] All six specimens contained eight No. 10 reinforcing bars for the bottom longitudinal reinforcement, which corresponds to a longitudinal reinforcement ratio (ρ_l) of 2.05%. All six specimens contained horizontally distributed reinforcement consisting of eight Grade 60 No. 4 bars spaced at 6.6 in. (167.6 mm), arranged four on each face of the specimen. This reinforcement satisfies the distributed reinforcement spacing limit of $d/5$ in ACI 318-19.[1] These distributed bars provided a horizontal reinforcement ratio (ρ_h) of 0.40%. The transverse reinforcement was a variable in the experiments and was changed for each specimen. The different transverse reinforcement arrangements investigated included Grade 60 180-degree hooked No. 4 stirrups, Grade 60 No. 4 headed bars, and Grade 80 No. 4 headed bars. The headed bars had a bearing area (A_{brg}) of four times the bar area (A_b) and met the ASTM A970 Class HA standard. Stirrups were anchored around longitudinal bars, as required by ACI 318-19. The headed bars were anchored such that they were engaged with the longitudinal bars; specifically, the headed bars were placed inside of longitudinal bars and the bearing face was in contact with the longitudinal bars (refer to Fig. 2). According to ACI 318-19 the clear cover for headed deformed bars in tension shall be at least two times the bar diameter.[1] Therefore, the minimum clear cover was kept to 2.5 in. (63.5 mm). The detailed arrangement of the transverse reinforcement is explained in the following. The detailed specimen properties are shown in Fig. 2.

HTS1 contained no shear reinforcement and was the control specimen for the experimental series. Specimens HTS2 to HTS6 contained transverse shear reinforcement. The response of these members can therefore be compared to HTS1 to examine the influence of the transverse reinforcement on the shear response. In HTS2 to HTS6, No. 4 bars were used as the shear reinforcement. HTS2 contained Grade 60 stirrups with 180-degree hooks spaced at 10.7 in. (272 mm) along the span. HTS3 contained Grade 60 headed bars spaced at 10.7 in. (272 mm) along the span. HTS2 and HTS3 contained a quantity of reinforcement ρ_v, equal to 0.25%. Therefore, both HTS2 and HTS3 contained the minimum transverse reinforcement stipulated in ACI 318-19[1] for deep beams ($\rho_{v,min}$ of 0.25%). The experiments contained slightly less than the AASHTO LRFD ninth edition[14] minimum requirement for deep beams ($\rho_{v,min}$ of 0.30%). The response of these specimens can be compared to evaluate the performance of nominally identical members where one of the members contains headed transverse reinforcement and one contains traditional stirrups. HTS4 was designed such that the member contained the same $\rho_v f_{vy}$ as HTS3 but replaces the Grade 60 reinforcement with Grade 80 reinforcement in the transverse direction. Therefore, the amount of Grade 80 transverse reinforcement, ρ_v, used in HTS4 was reduced to 0.19%. By comparing HTS3 and HTS4, the response of members that use lower quantities of Grade 80 headed reinforcement with members containing larger quantities of Grade 60 transverse reinforcement can be examined. HTS5 consisted of Grade 60 No. 4 headed

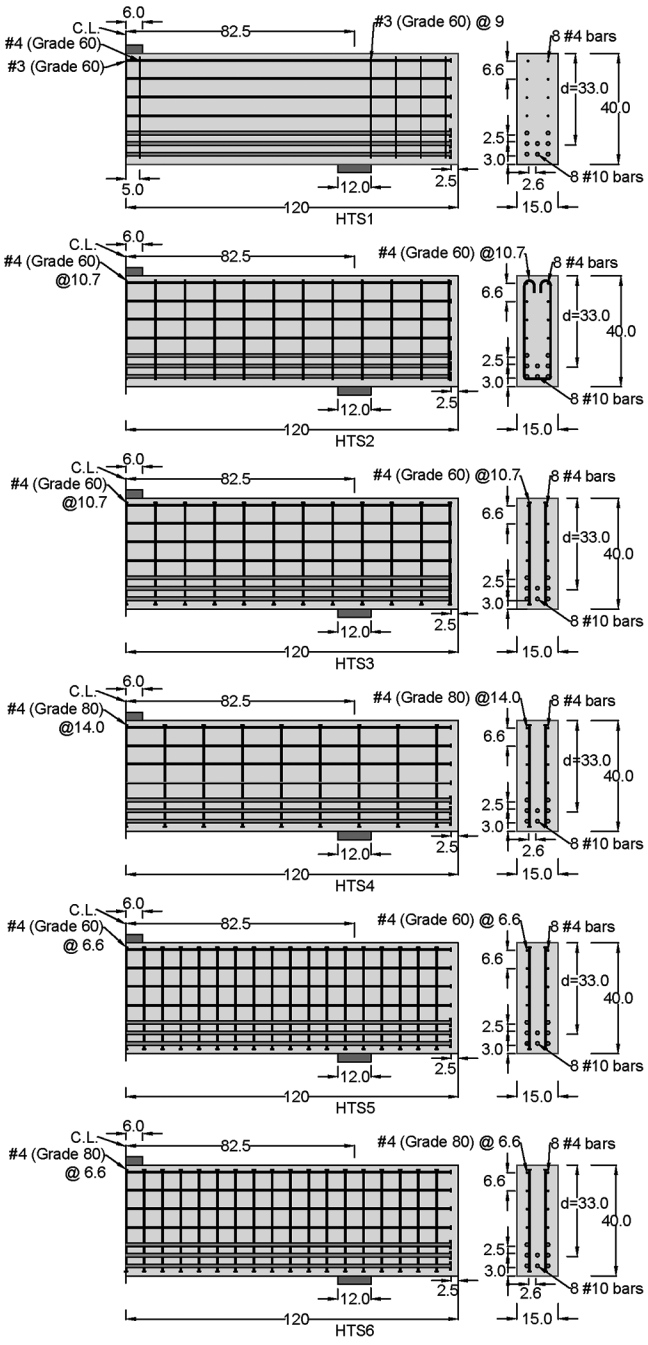

Fig. 2—Specimen geometry and reinforcement details for HTS1 to HTS6. (Note: Dimensions are in inches; 1 in. = 25.4 mm.)

bars for the transverse reinforcement spaced at 6.6 in. (167.6 mm), resulting in a quantity of reinforcement, ρ_v, of 0.40%. HTS6 also contained No. 4 headed bars spaced at 6.6 in. (167.6 mm), resulting in a reinforcement ratio, ρ_v, of 0.40%; however, HTS6 contained Grade 80 bars. Both HTS5 and HTS6 adhere to the minimum shear reinforcement requirements, including the minimum spacing requirement that indicates the reinforcement must not be spaced more than $d/5$ or 12 in. (305 mm).[1] Similarly, both HTS5 and HTS6 adhere to the minimum reinforcement spacing requirements indicated in AASHTO LRFD ninth edition, specifically that the maximum spacing must not exceed $d/4$ or 12 in. (305 mm). Because the transverse reinforcement spacing

used in HTS5 and HTS6 was identical, specimen HTS6 has a larger quantity of transverse reinforcement, $\rho_v f_{vy}$, of 357 psi (2.46 MPa), compared to HTS5 which contained a quantity of reinforcement $\rho_v f_{vy}$, equal to 282 psi (1.94 MPa). Thus, HTS5 and HTS6 can be compared to examine the influence of the quantity of transverse reinforcement and can be used to compare differences in member response when Grade 80 reinforcement directly replaces Grade 60 reinforcement.

Table 1 summarizes the material properties and concrete strength of the test specimens. The concrete cylinder strengths ranged from 3.90 to 5.19 ksi (26.9 to 35.8 MPa). The reinforcement material properties were obtained from steel coupon tests. The yield stress (f_y), yield strain (ε_y), strain-hardening strain (ε_{sh}), ultimate strength (f_u), and strain at ultimate strength (ε_u) are shown in Fig. 3. The yield stress of Grade 60 No. 4 bars and Grade 80 No. 10 bars were obtained using the sharp-kneed method described in ASTM A370-21.[15] The yield stress of Grade 80 No. 4 bars was obtained using the 0.2% offset method as described in ASTM A370-21.[15]

Table 1—Summary of HTS series specimens and material properties

Specimen	f_c', ksi	f_y, ksi	ρ_v, %	f_{vy}, ksi	$\rho_v f_{vy}$, psi	Description of shear reinforcement
HTS1	5.19	87.6	—	—	—	No shear reinforcement
HTS2	4.39	87.6	0.25	69.7	174	Grade 60 180-degree hooked stirrups; resulting ρ_v of 0.25%
HTS3	4.39	87.6	0.25	69.7	174	Grade 60 headed bars; resulting ρ_v of 0.25%
HTS4	3.90	87.6	0.19	88.4	168	Grade 80 headed bars with same $\rho_v f_{vy}$ as HTS3 (ρ_v is 0.19%)
HTS5	4.66	87.6	0.40	69.7	282	Grade 60 headed bars at $d/5$ spacing resulting ρ_v of 0.4%
HTS6	4.67	87.6	0.40	88.4	357	Grade 80 headed bars at $d/5$ spacing; resulting ρ_v of 0.4%

Note: ρ_v is shear reinforcement ratio; f_{vy} is yield stress of transverse reinforcement; 1 in. = 25.4 mm; 1 ksi = 1000 psi = 6.89 MPa.

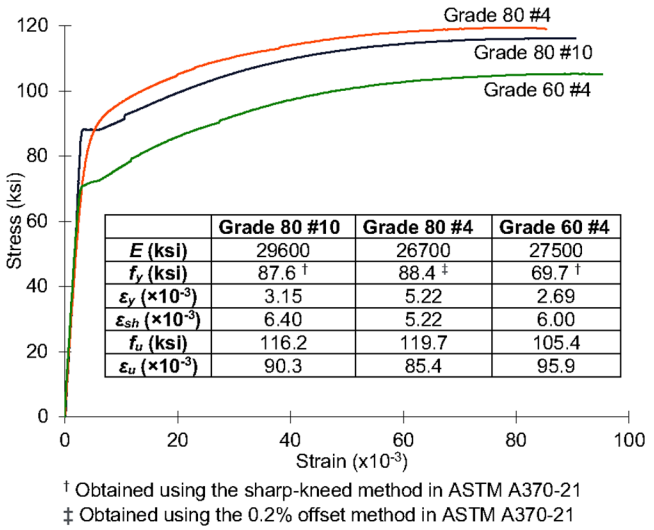

	Grade 80 #10	Grade 80 #4	Grade 60 #4
E (ksi)	29600	26700	27500
f_y (ksi)	87.6 †	88.4 ‡	69.7 †
ε_y (×10^{-3})	3.15	5.22	2.69
ε_{sh} (×10^{-3})	6.40	5.22	6.00
f_u (ksi)	116.2	119.7	105.4
ε_u (×10^{-3})	90.3	85.4	95.9

† Obtained using the sharp-kneed method in ASTM A370-21
‡ Obtained using the 0.2% offset method in ASTM A370-21

Fig. 3—Stress-versus-strain response of steel coupons and reinforcement properties. (Note: 1 ksi = 6.89 MPa.)

The deep beam specimens, measuring 240 in. (6096 mm) long, were supported on two 12 x 15 x 2 in. (305 x 381 x 51 mm) support plates. The support plates rested on roller supports. A loading plate measuring 12 x 15 x 3 in. (305 x 381 x 76 mm) was used in all six experiments in the series. A fiberboard sheathing was used between the loading plate and the beam to ensure the load was evenly distributed on the specimen. A spreader beam was used to distribute the load from the actuator to the loading plate. A spherical bearing was used between the actuator head and the spreader beam to ensure that no moments were transmitted through the actuator. The load was placed in the center of the span of each specimen. A summary of the specimen properties is given in Table 1.

The surface deformations of the specimens were measured throughout loading using DIC equipment on the entire east face of the specimens, infrared light-emitting diode (LED) markers tracked with motion-capture cameras on the west face of the specimens, and a string potentiometer was used at the midspan. In addition to these measurement systems, video was recorded throughout loading. Local high-resolution photographs were also manually obtained to capture local observations and global observations periodically throughout the experiments.

The specimens were loaded monotonically to failure at a rate of approximately 1 kip/s (4.45 kN/s). All experiments were tested to failure. During loading, load stages were conducted where the cracks were measured and marked, on the west face of the specimens using a crack comparator gauge. More details of the experimental program can be found elsewhere.[16]

EXPERIMENTAL OBSERVATIONS AND RESULTS

For all six members in the HTS series, initial loading resulted in flexural cracks near midspan, in the flexural tension region. As the load increased, flexural cracks widened and propagated towards the flexural compression region. Shear cracks formed between the support plate and near the edge of the loading plate. As the load increased the shear cracks grew in width. First shear cracking did not result in failure of the members, however, as the load increased, and cracks widened all specimens ultimately failed in shear. No splitting cracks were observed on the bottom of the specimens up to the last load stage. The peak shear forces for each specimen and the failure span are given in Table 2.

Prior research including Trandafir et al.,[17] Mihaylov et al.,[18] and Kani et al.[19] has demonstrated that the response of nominally identical deep beam specimens can exhibit substantial variability in the peak shear strengths achieved. This variability, which can exceed 15% and, in some cases, has been shown to be as large as 60% for deep beams, can be attributed to the critical crack shape and size of the uncracked region near the loading plate. Trandafir et al.[17] and Palipana et al.[20] have quantified these phenomena and are described elsewhere. This variability should be considered in the context of the experimental results; that is, small differences in peak response may not be significant to the

Table 2—Summary of shear capacities of HTS1 to HTS6

Specimen	f_c', ksi	ρ_v, %	f_{vy}, ksi	Type of shear reinforcement	$\rho_v f_{vy}$, psi	Peak shear force, kip	Failure span
HTS1	5.19	—	—	—	—	101	North
HTS2	4.39	0.25	69.7	Grade 60 stirrups	174	206	South
HTS3	4.39	0.25	69.7	Grade 60 headed	174	197	South
HTS4	3.90	0.19	88.4	Grade 80 headed	168	184	South
HTS5	4.66	0.40	69.7	Grade 60 headed	282	280	South
HTS6	4.67	0.40	88.4	Grade 80 headed	357	288	North

Note: 1 in. = 25.4 mm; 1 kip = 4.45 kN; 1 ksi = 1000 psi = 6.89 MPa.

conclusions as they relate to the use of high-strength headed transverse reinforcement in deep beams.

HTS1, which had no shear reinforcement, achieved the lowest shear capacity of 101 kip (449 kN). With the addition of shear reinforcement, the shear strength of the members increased significantly, regardless of the steel grade or anchorage type used. The shear strengths of HTS2, HTS3, and HTS4, which had approximately the same $\rho_v f_{vy}$ values, were 206, 197, and 184 kip (916, 876, and 818 kN), respectively. HTS2, which contained minimum transverse reinforcement in the form of stirrups, achieved a peak shear force of more than double that of HTS1. HTS3, which contained Grade 60 heads, achieved 96% of the strength of HTS2. HTS4, which contained the minimum $\rho_v f_{vy}$ in the form of headed Grade 80 bars, reached a peak shear 1.8 times that of HTS1, which had no transverse reinforcement. HTS4 reached a shear capacity 89% of that achieved by HTS2, which contained Grade 60 stirrups, and 96% of the strength of HTS3, which contained Grade 60 headed bars with the same $\rho_v f_{vy}$ value of 174 psi (1.20 MPa). It should be emphasized that HTS4 had a concrete cylinder strength of 3.90 ksi (26.9 MPa), which was 89% of the cylinder strength of HTS2 and HTS3 (4.39 ksi [30.3 MPa]). This difference in concrete cylinder strengths contributes to the lower peak capacity of HTS4 compared to HTS2 and HTS3. The average shear strength of HTS2, HTS3, and HTS4 was 196 kip (872 kN) and the peak strength of these three members has a coefficient of variation of 5.65%. This indicates that the variable member strengths for members with the same amount of shear reinforcement is similar regardless of reinforcement yield stress or anchorage type used. HTS5, which contained 0.40% transverse reinforcement, reached a peak load 2.8 times that of HTS1. HTS6 had a peak strength slightly higher than HTS5.

Figure 4 shows the shear force versus the midspan displacement response of the members. The displacement of the specimens was measured on the flexural tension side of the specimens at the midspan using DIC data and was calculated such that the strong floor deformations are neglected. Figure 4 shows that all specimens exhibited a similar uncracked stiffness and indicates that the post-cracking stiffness of the members was slightly lower for specimens using high-strength steel. For example, the stiffness of HTS4 had a slightly lower stiffness than HTS2 and HTS3, which consisted of the same quantity of $\rho_v f_{vy}$ but used Grade 80 reinforcement. Additionally, HTS3 appeared to have a slightly lower post-cracking stiffness than HTS2. These differences

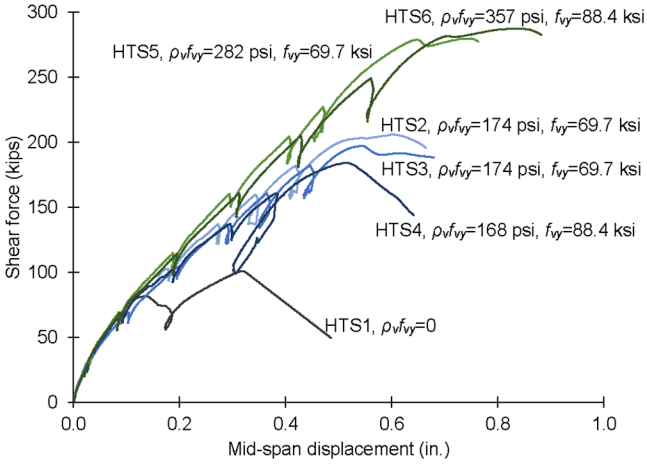

Fig. 4—Load-versus-displacement response for HTS1 to HTS6. (Note: 1 in. = 25.4 mm; 1 kip = 4.45 kN; 1 ksi = 6.89 MPa.)

are expected as a result of the lower stiffness of the shear reinforcement but are relatively small when examining the global member response.

Figure 5 shows the principal tensile strain fields at the peak load for the six experiments. The high strain regions in the principal tensile strains maps indicates the cracked regions. The large critical cracks on the two shear spans that dominated the deformations of HTS1 can be seen from the high-strain regions. In the strain maps, white indicates that there is a loss of correlation in the DIC data; this occurs in regions with large cracks.

Figure 6 shows the principal compressive strain fields at the peak load. At peak load, the large strains under the loading plate shows the concrete reaching strains that exceed the strain at peak concrete cylinder stress. It is also interesting to note that there are strain concentrations near the edges of the plates. For example, refer to HTS4 in Fig. 6. For HTS1, Fig. 6 shows compression struts that extend from the loading plate to the support plates. However, in HTS2 to HTS6, the load paths are distributed within the shear span. These compression fields indicate the effectiveness of the transverse reinforcement in redirecting the compression struts, therefore contributing to the shear strength of the members. Figure 6 also demonstrates that the inclusion of transverse reinforcement results in a larger distributed region of high compressive strains in the shear span.

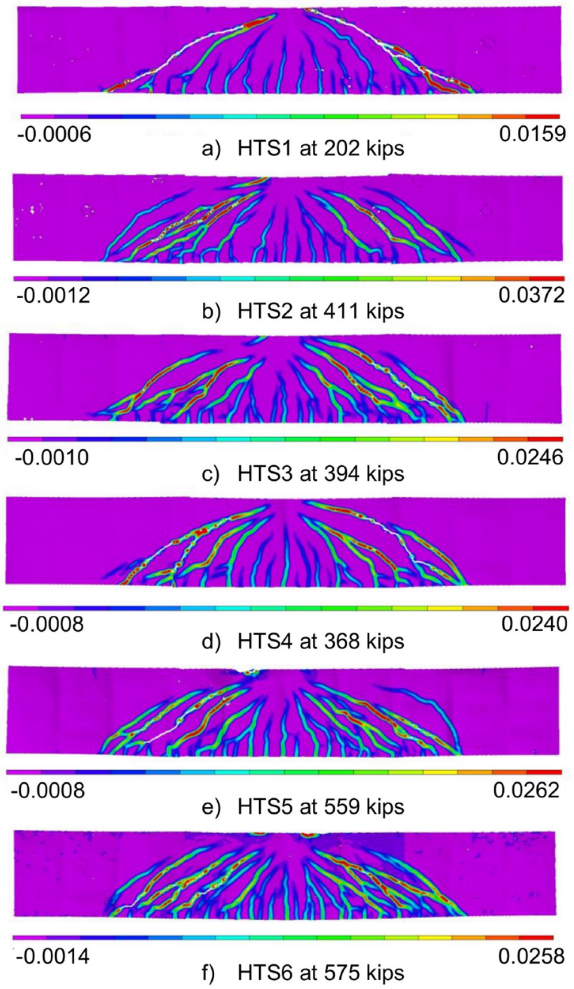

Fig. 5—Principal tensile strain fields on east face of specimens at peak load. (Note: 1 kip = 4.45 kN.)

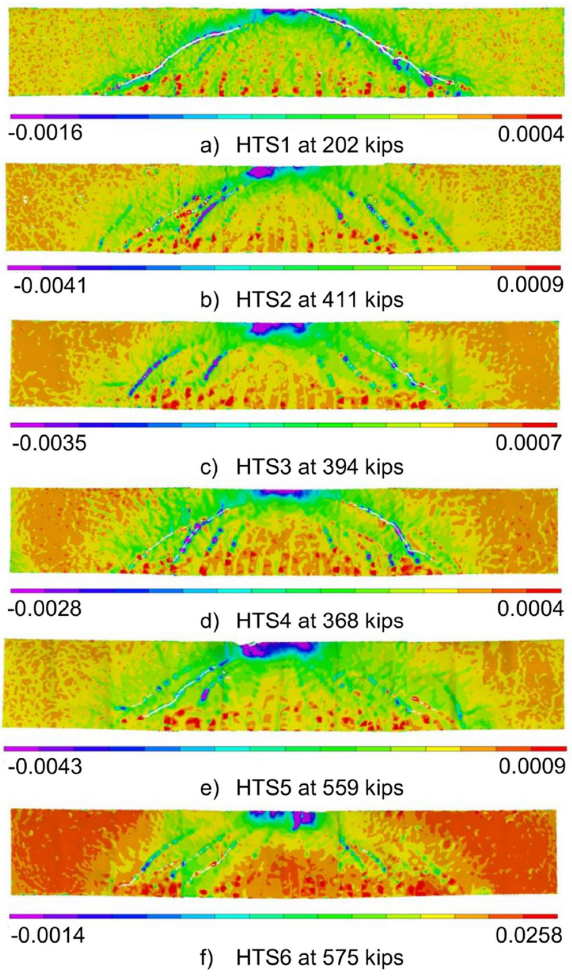

Fig. 6—Principal compressive strain fields on east face of specimens at peak load. (Note: 1 kip = 4.45 kN.)

EXPERIMENTAL OBSERVATIONS OF CRACK WIDTHS

For HTS1, deformations were concentrated along the one critical crack which formed in each shear span. These large shear cracks dominated the response of the member. The crack widths for HTS1 were substantially larger than for members that contained transverse reinforcement. For specimens HTS2 to HTS6, which contained at least minimum shear reinforcement, the members exhibited well-distributed crack patterns, and the crack widths throughout loading were smaller than in HTS1. This can be observed in Fig. 5, which indicates well-distributed crack patterns for the specimens. Well-distributed crack patterns indicate that the inclusion of minimum reinforcement, regardless of whether the reinforcement was Grade 60 or Grade 80 and regardless of the end detail, was able to control the cracks. Additionally, as the spacing of the transverse reinforcement reduced and the quantity of shear reinforcement increased, the crack widths reduced, and the number of the cracks increased.

Crack width measurements were obtained using crack comparator gauges and nominally measured on a uniform grid. The maximum crack width observed at the last load stage on the east face of the specimen, the maximum average crack width of the failure crack at the last load stage, the maximum strain in the shear reinforcement at the peak load using a gauge length of 4 in. (102 mm), and the maximum strain at the peak load calculated using the unbonded length are given in Table 3. The gauge lengths used to calculate the maximum strains are discussed in subsequent sections.

The maximum crack widths observed at the load stages in each specimen are shown in Fig. 7. HTS1, which contained no shear reinforcement, showed the largest maximum crack width. HTS3, which contained Grade 60 headed shear reinforcement, showed larger maximum crack widths compared to specimens HTS2 and HTS4 with the same $\rho_v f_{vy}$. HTS2 and HTS4 exhibited similar crack widths at the peak load, indicating that using headed shear reinforcement or using Grade 80 reinforcement instead of Grade 60 reinforcement while maintaining the same $\rho_v f_{vy}$ has a limited effect on the observed crack widths. HTS5 and HTS6, which included shear reinforcement at $d/5$ spacing, exhibited the smallest maximum crack widths.

Figure 8 shows the average crack widths along the failure crack plotted with the applied shear. The dashed line shows crack widths measuring 0.016 in. (0.41 mm), which is the recommended maximum crack widths at service loads in ACI 224-01.[21] The figure shows that the average crack widths for all the specimens remained below the suggested reasonable limit until high loads were achieved. HTS1,

Table 3—Summary of maximum crack width, average crack width, and maximum strains for HTS1 to HTS6

Specimen	f_{vy}, ksi	$\rho_v f_{vy}$, psi	Maximum crack width, in.	Average crack width of failure crack, in.	Maximum strains, 4 in. gauge length ($\times 10^{-3}$)	Maximum strain using unbonded length ($\times 10^{-3}$)
HTS1	—	—	0.055	0.031	44.8	4.8*
HTS2	69.7	174	0.033	0.019	22.7	24.5
HTS3	69.7	174	0.047	0.013	20.7	18.3
HTS4	88.4	168	0.031	0.014	21.8	32.8
HTS5	69.7	282	0.026	0.011	26.1	23.6
HTS6	88.4	357	0.024	0.016	18.7	30.9

*For HTS1, which does not contain shear reinforcement, a gauge length of 36 in. (914 mm) was used.

Note: 1 in. = 25.4 mm; 1 kip = 4.45 kN; 1 ksi = 1000 psi = 6.89 MPa.

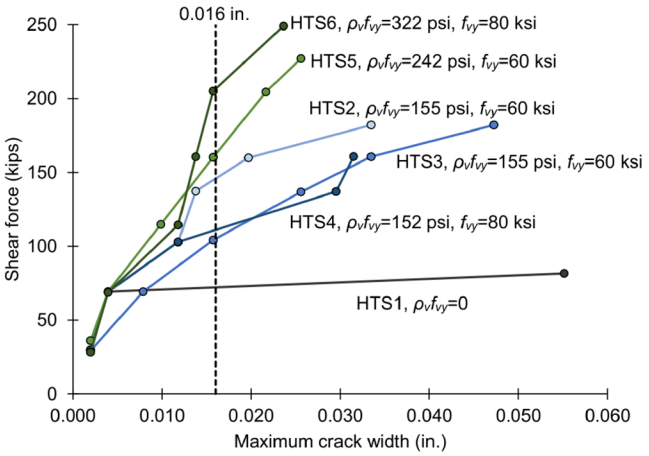

Fig. 7—Maximum crack widths versus shear force for HTS1 to HTS6. (Note: 1 in. = 25.4 mm; 1 ksi = 6.89 MPa; 1 kip = 4.45 kN.)

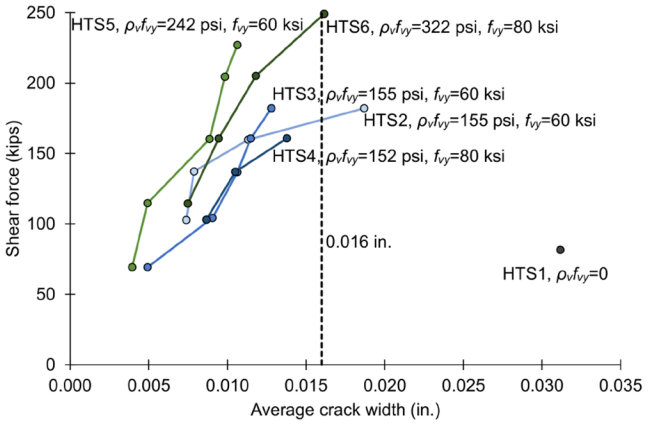

Fig. 8—Average crack width along failure crack versus shear force for HTS1 to HTS6. (Note: 1 in. = 25.4 mm; 1 ksi = 6.89 MPa; 1 kip = 4.45 kN.)

which contained no shear reinforcement, showed the largest average crack widths. HTS2 exhibited larger average crack widths along the failure crack compared to HTS3 and HTS4. HTS6 showed larger average crack widths at the peak load compared to HTS5. These average crack widths indicate a limited observable difference in the response of members that use Grade 80 transverse reinforcement compared to Grade 60 reinforcement for specimens reinforced with similar $\rho_v f_{vy}$ values. It is expected that the crack widths of members with the same $\rho_v f_{vy}$ but higher yield stress reinforcement will have less stiffness in the transverse direction and therefore exhibit larger crack widths. However, given the inherit variability from specimen to specimen arising from specific critical crack shape, size and shape of the uncracked region near the load, and number and location of secondary cracks, the maximum and average crack widths are similar for the members investigated.

Examining the crack widths near service conditions can also be important. The service load can be estimated as approximately 60% of the ultimate load of the members; this approximately corresponds to the ultimate capacity reduced by load factors and strength reduction factors.[6,9] For HTS2 to HTS4, 206 kip (916 kN) corresponds to approximately 60% of the ultimate load of HTS4, which had the lowest strength of the three specimens. At this load level, HTS3 had slightly higher crack widths measuring 0.016 in. (0.40 mm) compared to HTS2 and HTS4, which exhibited a maximum crack width of 0.012 in. (0.30 mm). This shows that neither using headed shear reinforcement nor using high-strength steel reinforcement to replace lower-grade steel with the same $\rho_v f_{vy}$ has a substantial effect on the crack patterns and crack widths of the specimens. That is, no significant difference was observed. For HTS5 and HTS6, 321 kip (1428 kN) corresponds to approximately 60% of the ultimate load of HTS5. The crack widths were well distributed within the shear span. HTS5 showed slightly higher crack widths compared to HTS6. All the specimens with shear reinforcement showed crack widths below the 0.016 in. (0.41 mm) recommended maximum width listed in ACI 224-01 at service loads.[21]

The results indicate that the inclusion of minimum transverse reinforcement is the most important factor in cracking response. Both Grade 60 and Grade 80 reinforcement with headed anchorage or traditional stirrups successfully controlled cracks. The results also suggest that the inclusion of additional transverse reinforcement, beyond the minimum, assists in further distributing cracks and controlling their widths. It should also be noted that in the longitudinal direction, Grade 80 No. 10 headed bars were used, and the flexural cracks were well controlled throughout loading.

CRACK PATTERNS AND REINFORCEMENT STRAINS OBTAINED FROM DIC DATA

The crack patterns on the east face of the specimens were obtained using DIC data. The Automated Crack Detection

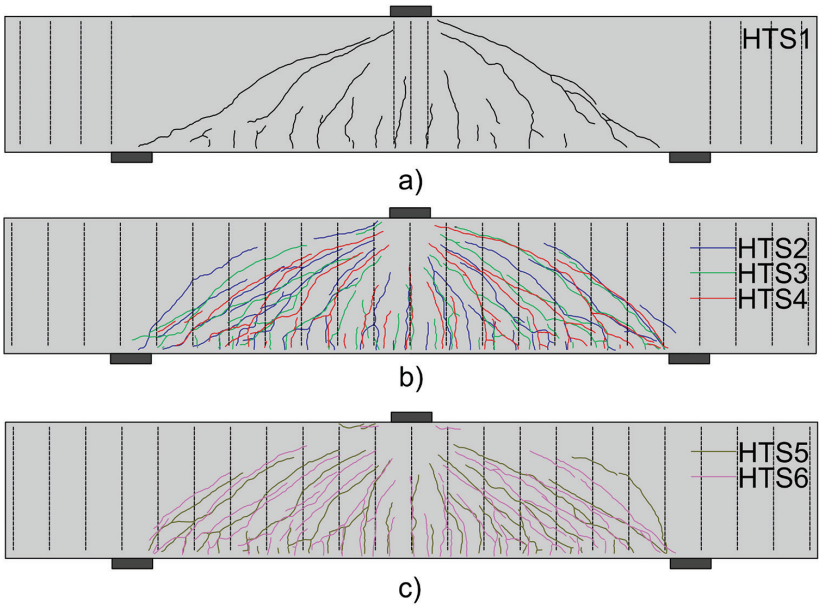

Fig. 9—Comparison of crack patterns on east face of HTS1 to HTS6 at peak load.

and Measurement (ACDM) tool, an open-source tool developed by Gehri et al.,[22] was used in conjunction with the DIC data to obtain crack diagrams. The principal tensile strain fields obtained from the DIC were input to the ACDM tool. The tool then identified the high-tensile-strain regions using two-dimensional image processing. The detected high-strain regions were thinned to obtain crack lines. The crack patterns obtained for the three stereo systems of each specimen were combined to generate the full crack patterns at the peak load on the east face of the specimens.

Figure 9(a) shows the crack pattern determined from the ACDM tool for HTS1. To compare the influence of shear reinforcement on crack patterns, Fig. 9(b) also shows the crack diagrams for HTS2, HTS3, and HTS4. These three specimens contained the same $\rho_v f_{vy}$ reinforcement quantities. As can be seen, the crack patterns, the number of cracks, the crack shapes, and the crack locations were remarkably similar. HTS2 and HTS3 exhibited some additional cracks, shown on the left side of Fig. 9(b) near the support. When comparing the crack patterns of HTS1 to the other crack patterns shown in Fig. 9(b), it is clear that including at least minimum reinforcement improves the crack control characteristics of the specimens. However, no significant difference was evident in the crack patterns or shapes for members reinforced with Grade 60 versus Grade 80 steel or between members reinforced with traditional stirrups compared to headed transverse bars. Figure 9(c) compares the HTS5 and HTS6 crack patterns determined from the ACDM tool. These specimens had same ρ_v. The crack patterns were symmetrical, and the number of cracks in HTS6 was slightly higher than HTS5.

The crack patterns obtained for HTS1 to HTS6 using the ACDM tool are also shown in Fig. 10. Figure 10 highlights, in blue, the critical shear crack in each shear span (full-color PDF can be accessed at www.concrete.org). The critical crack was identified as the crack that extended from the support plate to near the edge of the loading plate and exhibited the largest crack widths at the last load stage. In some cases, particularly those with at least minimum transverse reinforcement and members that have horizontal distributed reinforcement, multiple shear cracks with different widths along the crack may make it difficult to identify the critical crack before failure. For HTS4, the beam failed along a different crack than the crack identified as the critical crack at the last load stage; for HTS4, the failure crack is shown in green in Fig. 10.

An important aspect in the assessment of the performance of transverse reinforcement in deep beams is to develop an understanding of the transverse straining in the member. Strain gauges can give highly localized values. At the cracks, strains in the reinforcement can register 10 to 15 times the strain between the cracks.[23] Unless many strain gauges are applied to the bars embedded in the concrete, the strains from gauges may be difficult to interpret. Additionally, the strains across the critical crack are of importance for commenting on the forces that are transmitted in the transverse reinforcement across the critical shear crack. Because the precise location of the critical shear crack is not known before testing, the use of full-field-of-view displacement field measurements is more amenable to determine the strain in the transverse reinforcement near the critical shear crack. For these reasons, rather than using strain gauges, the DIC system was used to determine the strains in the reinforcement, on average, across the critical shear crack. This approach has been shown to give good results, particularly for use in quantifying the shear transfer mechanisms in deep beams.[20]

Figure 10 shows the strains in each transverse reinforcement calculated across the critical crack. The strains were calculated using a consistent gauge length of 4 in. (102 mm) with 2 in. (51 mm) on either side of the critical crack. This gauge length was selected based on the minimum spacing that was observed between adjacent cracks. The strains calculated in this matter are labeled in blue across the bottom of the specimens in Fig. 10.

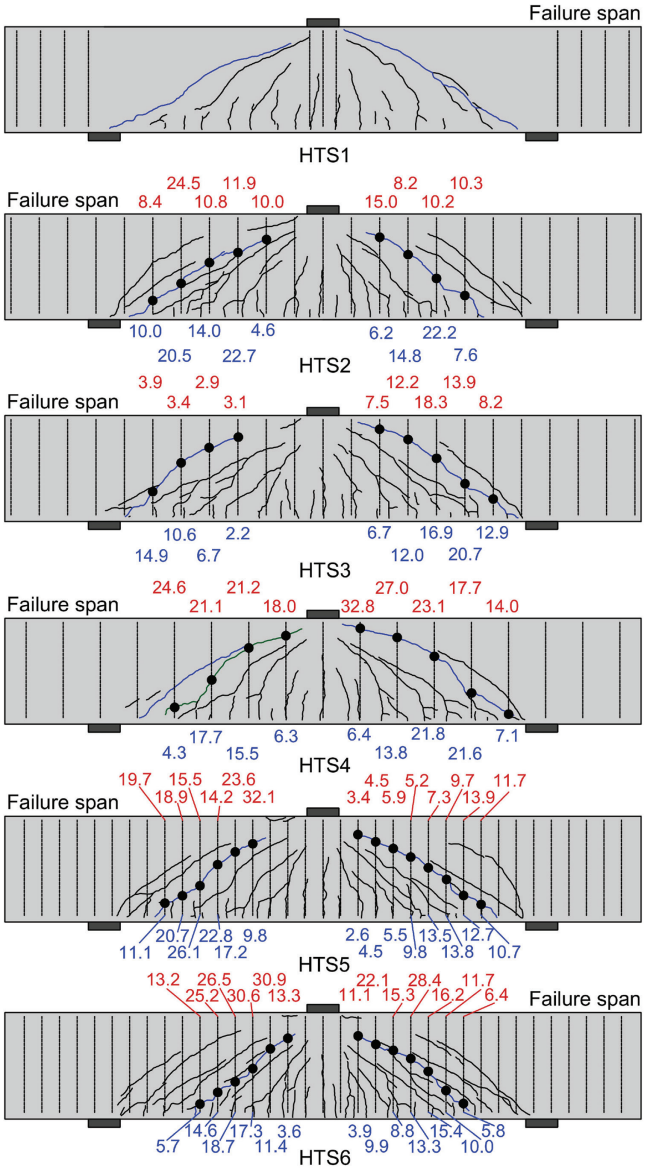

Fig. 10—Crack pattern for HTS1 to HTS6 on east face at peak load and strains in each transverse reinforcement bar at peak load (× 10^{-3}). (Note: Full-color PDF can be accessed at www.concrete.org.)

To further investigate the influence of the gauge length used to determine the strains in the reinforcement across the critical crack, an unbonded length for each transverse bar crossing the critical crack was determined and used to calculate the strain in the reinforcement. In the unbonded zone, the strain in a reinforcement bar (ε_s) is equal to the crack width (w) divided by the unbonded length, L_u[24,25]; refer to Eq. (1)

$$L_u = w/\varepsilon_s \quad (1)$$

In this series of tests, the measured crack widths were available, and therefore the measured crack widths were used to obtain the unbonded length of the bar at the crack using Eq. (1). The yield strain was used as a reasonable assumption for the strain in the reinforcement bar to calculate unbonded length.[24,25]

The strains listed across the top of the specimens in Fig. 10 (shown in red) were calculated using the unbonded length corresponding to the crack width at the last load stage at the intersection of the crack and the transverse reinforcement for each transverse bar that crosses the critical crack. For the failure span of HTS4, the strain shown at the top of the beam was obtained for the failure crack rather than the critical crack as determined at the last load stage. The values show that almost every transverse reinforcement bar in the shear span of the members yielded prior to reaching the peak load. For some bars near the ends of the critical crack—that is, near the flexural compression region and loading plate or near the support plate—the strains are lower and may not reach the yield strain. This is as an expected result, because at these locations, the deformations in the members, and therefore crack widths and demand on the transverse reinforcement, are small. Near the center of the shear span, some distance away from the support and loading plates, the strains in the transverse reinforcement that cross the critical crack are large and exceed the yield strain of the reinforcement.

The strains calculated using a gauge length of 4 in. (102 mm) for HTS2 ranged between 4.6 × 10^{-3} and 22.7 × 10^{-3}, while strains calculated using the unbonded length ranged between 8.4 × 10^{-3} and 24.5 × 10^{-3}. The strains for HTS3 calculated using a gauge length of 4 in. (102 mm) ranged between 2.2 × 10^{-3} and 20.7 × 10^{-3}, while strains calculated using the unbonded length ranged between 2.9 × 10^{-3} and 18.3 × 10^{-3}. Comparing HTS2 and HTS3, there are not significant differences in the strains in transverse reinforcement crossing the critical crack. This suggests that the response of members that use stirrups compared with headed transverse bars is similar for the members tested. The strains calculated using a gauge length of 4 in. (102 mm) for HTS4 ranged between 4.3 × 10^{-3} and 21.8 × 10^{-3}, while strains calculated using the unbonded length ranged between 14.0 × 10^{-3} and 32.8 × 10^{-3}. Because HTS4 had a smaller area of transverse reinforcement compared to HTS3 and HTS4, the average transverse stiffness of the member was lower, and the strains are expected to be higher. While some of the strains in HTS4 were higher than HTS2 and HTS3, the range of strains observed were similar to those measured for HTS2 and HTS3. The strains calculated using a gauge length of 4 in. (102 mm) for HTS5 ranged between 2.6 × 10^{-3} and 26.1 × 10^{-3}, while strains calculated using the unbonded length ranged between 3.4 × 10^{-3} and 32.1 × 10^{-3}. The strains calculated using a gauge length of 4 in. (102 mm) for HTS6 ranged between 3.6 × 10^{-3} and 18.7 × 10^{-3}, while strains calculated using the unbonded length ranged between 6.4 × 10^{-3} and 30.9 × 10^{-3}.

Figure 11 shows the shear force versus the strains calculated using a gauge length of 4 in. (102 mm) and strains determined using the calculated unbonded length for the transverse reinforcement in HTS2 to HTS6. The strains were obtained for the shear reinforcement that showed the largest magnitude of that strain at the peak load. As seen in Fig. 11, the strains in members HTS2 to HTS6 reached the yield strain of the shear reinforcement bars, at 67%, 40%, 56%, 39%, and 55% of the peak shear force, respectively. For HTS1, Fig. 11 shows the strain at the crack calculated

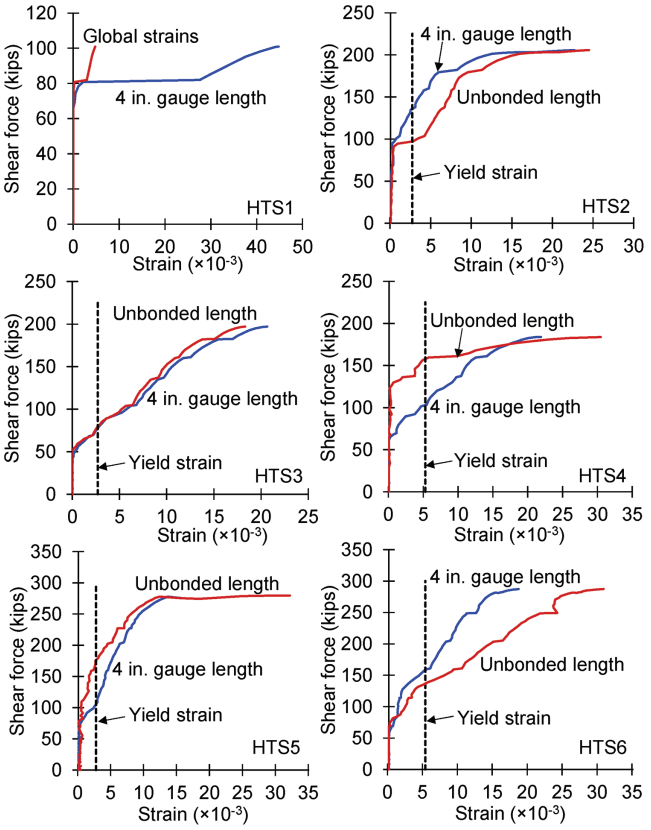

Fig. 11—Shear force versus transverse reinforcement strains. (Note: 1 in. = 25.4 mm; 1 kip = 4.45 kN.)

using a gauge length of 4 in. (102 mm) and the global strain determined at the middle of the shear span. The strain using 4 in. (102 mm) gauge length at the crack is provided for reference and comparison to other specimens. The global strain was determined over a gauge length of 36 in. (914 mm), extending nearly the full height of the beam. For HTS1, the deformations are large because minimum transverse reinforcement was not provided. For the specimens that contained transverse reinforcement, HTS2 to HTS6, a vertical dashed line indicates the yield strain of transverse reinforcement. For all specimens that include transverse reinforcement, both the strains calculated using a gauge length of 4 in. (102 mm) and strains calculated using the unbonded length, the shear reinforcement exceeded the yield strain. The maximum strain in the transverse reinforcement at the peak load using a gauge length of 4 in. (102 mm), and the maximum strain at the peak load calculated using the unbonded length are summarized in Table 3.

CONCLUSIONS AND RECOMMENDATIONS

In this study, six large-scale, shear-critical reinforced concrete deep beam experiments were examined to investigate the influence of high-strength headed reinforcing bars for use as transverse reinforcement. The transverse reinforcement arrangements investigated included Grade 60 180-degree hooked No. 4 stirrups, Grade 60 No. 4 headed bars, and Grade 80 No. 4 headed bars. The headed bars used in this study had a bearing area of four times the bar area and met the ASTM A970 Class HA standard. The stirrups used were anchored around longitudinal bars, as required by ACI 318-19. The headed bars were anchored by placing them inside of the longitudinal bars and by placing the bearing face in contact with the longitudinal reinforcement. The minimum clear cover was 2.5 in. (63.5 mm), which is theminimum clear cover required by ACI 318-19 for headed deformed bars in tension. The use of minimum transverse reinforcement in shear critical deep beams greatly improves the shear capacity and response of the members, regardless whether Grade 60 or 80 reinforcement is used and regardless if the transverse reinforcement is provided as stirrups with 180-degree bends or headed bars with bearing areas four times the bar area. The use of Grade 60 headed bars for use as transverse reinforcement in deep concrete beams performs well compared to similar members that use conventional stirrups with 180-degree hooks. The use of Grade 80 headed bars as transverse reinforcement in the HTS series of deep beam tests performs well compared to similar members that contain the same quantity of transverse reinforcement, $\rho_v f_{vy}$. For the HTS series experiments, whether Grade 60 or 80 headed reinforcement bars are used, an increase in quantity of transverse reinforcement, in terms of $\rho_v f_{vy}$ or percent quantity, results in increased shear capacity.

The results also showed that regardless whether Grade 60 or 80 reinforcement is used and regardless if the transverse reinforcement is provided as stirrups with 180-degree bends or headed bars, the transverse reinforcement yielded across the critical cracks. All the members with minimum shear reinforcement exhibited controlled distributed crack patterns. The inclusion of at least minimum reinforcement improved crack control in all cases. For the HTS series experiments, the crack widths near service loads were reasonable and the crack widths at the peak load were not excessive when transverse reinforcement, in any form, was provided.

Based on the previous conclusions determined from the research conducted, the following are several recommendations as they pertain to the design of high-strength headed reinforcing bars for use as transverse reinforcement in shear critical deep beams.

1. The ACI 318 Code should allow for the use of transverse reinforcement in concrete deep beams with yield stresses up to at least 80 ksi (552 MPa).

2. The ACI 318 Code should allow for the use of headed reinforcement bars with a bearing area of at least four times the bar area for use as transverse reinforcement.

3. The AASHTO LRFD code should allow for the use of transverse reinforcement in concrete deep beams with yield stresses up to at least 80 ksi (552 MPa).

As variables beyond those explored are modified, there may be a need to conduct further analysis or experimental studies to investigate the influence of those parameters on the shear response.

AUTHOR BIOS

ACI member **Dhanushka K. Palipana** *is a Postdoctoral Researcher at the University of Kansas, Lawrence, KS. She received her BScEng from the University of Peradeniya, Peradeniya, Sri Lanka, in 2017 and her PhD from North Carolina State University, Raleigh, NC, in 2023. She is a member of Joint ACI-ASCE Subcommittees 445-E, SOA Torsion, and 445-F, Interface Shear.*

ACI member **Giorgio T. Proestos** *is an Assistant Professor at North Carolina State University. He received his BASc in Engineering Science, his MASc, and his PhD from the University of Toronto, Toronto, ON, Canada, in 2012, 2014, and 2018, respectively. He is Secretary of Joint ACI-ASCE Committee 445, Shear and Torsion; Secretary of Joint ACI-ASCE Committee 445-F, Interface Shear; and a member of Joint ACI-ASCE Subcommittee 445-E, SOA Torsion. He received the ACI Chester Paul Seiss Award in 2018 and the ACI Design Award in 2017.*

ACKNOWLEDGMENTS

This research was funded by the Concrete Reinforcing Steel Institute Foundation and this paper is based on the final findings of the funded project. The reinforcing bars used in the construction of the test specimens was generously donated by Headed Reinforcement Corporation.

REFERENCES

1. ACI Committee 318, "Building Code Requirements for Structural Concrete (ACI 318-19) and Commentary (ACI 318R-19) (Reapproved 2022)," American Concrete Institute, Farmington Hills, MI, 2019, 624 pp.

2. Joint ACI-ASCE Committee 326. "Shear and Diagonal Tension," *ACI Journal Proceedings*, V. 59, No. 2, Feb. 1962, pp. 277-334.

3. ACI Committee 318, "Building Code Requirements for Reinforced Concrete (ACI 318-63)," American Concrete Institute, Farmington Hills, MI, 1963, 144 pp.

4. Proestos, G.; Bae, G.; Cho, J.; and Bentz, E., "Influence of High-Strength Bars on Shear Response of Containment Walls," *ACI Structural Journal*, V. 113, No. 5, Sept.-Oct. 2016, pp. 917-927. doi: 10.14359/51688750

5. Cladera, A., "Shear Design of Reinforced High-Strength Concrete Beams," PhD thesis, Universitat Politècnica de Catalunya, Barcelona, Spain, 2002, 325 pp.

6. Munikrishna, A.; Hosny, A.; Rizkalla, S.; and Zia, P., "Behavior of Concrete Beams Reinforced with ASTM A1035 Grade 100 Stirrups under Shear," *ACI Structural Journal*, V. 108, No. 1, Jan.-Feb. 2011, pp. 34-41.

7. Rogowsky, D. M., and MacGregor, J. G., "Tests of Reinforced Concrete Deep Beams," *ACI Journal Proceedings*, V. 83, No. 4, July-Aug. 1986, pp. 614-623.

8. Birrcher, D.; Tuchscherer, R.; Huizinga, M.; Bayrak, O.; Wood, S.; and Jirsa, J., "Strength and Serviceability Design of Reinforced Concrete Deep Beams," Report No. FHWA/TX-09/0-5253-1, Center of Transportation Research, The University of Texas at Austin, Austin, TX, 2009.

9. Lequesne, R. D.; O'Reilly, M.; Darwin, D.; Lepage, A.; Al-Sabawy, A.; Guillen, E.; and Spradling, D., "Use of Headed Bars as Shear Reinforcement," The University of Kansas Center for Research, Inc., Lawrence, KS, 2018, 256 pp.

10. Forest, S. B., "Anchorage of Single Leg Stirrups in Reinforced Concrete Slabs and Walls," MASc thesis, Department of Civil Engineering, University of Toronto, Toronto, ON, Canada, 2019, 253 pp.

11. Yoshida, Y., "Shear Reinforcement for Large Lightly Reinforced Concrete Members," MASc thesis, Department of Civil Engineering, University of Toronto, Toronto, ON, Canada, 2000, 160 pp.

12. Yang, Y.; Varma, A. H.; Kreger, M. E.; Wang, Y.; and Zhang, K., "Shear Strength of Reinforced Concrete Beams with T-Headed Bars for Safety Related Nuclear Structures," *Engineering Structures*, V. 230, 2021, p. 111705. doi: 10.1016/j.engstruct.2020.111705

13. Lubell, A. S.; Bentz, E. C.; and Collins, M. P., "Headed Shear Reinforcement Assemblies for One-Way Shear," *ACI Structural Journal*, V. 106, No. 6, Nov.-Dec. 2009, pp. 878-886.

14. AASHTO, "AASHTO LRFD Bridge Design Specifications and Commentary," ninth edition, American Association of State Highway Transportation Officials, Washington, DC, 2020, 1912 pp.

15. ASTM A370-21, "Standard Test Methods and Definitions for Mechanical Testing of Steel Products," ASTM International, West Conshohocken, PA, 50 pp.

16. Palipana, D. K., "Assessment of Shear Transfer Mechanisms in Reinforced Concrete Deep Beams from Experiments with Full Field-of-View Displacement Field Data," PhD thesis, North Carolina State University, Raleigh, NC, 2023. 440 pp.

17. Trandafir, A. N.; Palipana, D. K.; Proestos, G. T.; and Mihaylov, B. I., "Framework for Crack-based Assessment of Existing Lightly Reinforced Concrete Deep Beams," *ACI Structural Journal*, V. 119, No. 1, Jan. 2022, pp. 255-266.

18. Mihaylov, B. I.; Bentz, E. C.; and Collins, M. P., "Two-Parameter Kinematic Theory for Shear Behavior of Deep Beams," *ACI Structural Journal*, V. 110, No. 3, May-June 2013, pp. 447-456.

19. Kani, M. W.; Huggin, M. W.; and Wittkopp, R. R., *Kani on Shear in Reinforced Concrete*, Department of Civil Engineering, University of Toronto, Toronto, ON, Canada, 1979.

20. Palipana, D. K.; Trandafir, A. N.; Mihaylov, B. I.; and Proestos, G. T., "Framework for Quantification of Shear Transfer Mechanisms from Deep Beam Experiments," *ACI Structural Journal*, V. 119, No. 3, May 2022, pp. 53-65.

21. ACI Committee 224, "Control of Cracking in Concrete Structures (ACI 224-01) (Reapproved 2008)," American Concrete Institute, Farmington Hills, MI, 2001, 46 pp.

22. Gehri, N.; Mata-Falcón, J.; and Kaufmann, W., "Automated Crack Detection and Measurement Based on Digital Image Correlation," *Construction and Building Materials*, V. 256, Sep, 2020, pp. 1-14. doi: 10.1016/j.conbuildmat.2020.119383

23. Poldon, J. J.; Hoult, N. A.; and Bentz, E. C., "Shining a New Light on the Riddle of Shear," *Concrete International*, V. 45, No. 2, Feb. 2023, pp. 17-25.

24. Ruggeiro, D., "The Behavior of Reinforced Concrete Subjected to Reversed Cyclic Shear," PhD thesis, Department of Civil Engineering, University of Toronto, Toronto, ON, Canada, 2015, 455 pp.

25. Maekawa, K.; Pimanmas, A.; and Okamura, H., *Nonlinear Mechanics of Reinforced Concrete*, Spon Press, London, UK, 2003.

ACI in Your Classroom

Integrate ACI into your classroom!

To support future leaders, ACI has launched several initiatives to engage students in the Institute's activities and programs – select programs that may be of interest to Educators are:

- **Free student membership –** encourage students to sign up
- **Special student discounts on *ACI 318 Building Code Requirements for Structural Concrete*, *ACI 530 Building Code Requirements and Specification for Masonry Structure*, & *Formwork for Concrete* manual.**
- **Access to *Concrete International* –** free to all ACI student members
- **Access to *ACI Structural Journal* and *ACI Materials Journal* –** free to all ACI student members
- **Free sustainability resources –** free copies of Sustainable Concrete Guides provided to universities for use in the classroom
- **Student competitions –** participate in ACI's written and/or team-based competitions
- **Scholarships and fellowships –** students who win awards are provided up to $15,000 and may be offered internships and paid travel to attend ACI's conventions
- **ACI Award for University Student Activities –** receive local and international recognition for your University's participation in concrete-related activities
- **Free access to the *ACI Collection of Concrete Codes, Specifications, and Practices* –** in conjunction with ACI's chapters, students are provided free access to the online ACI Collection
- **ACI online recorded web sessions and continuing education programs –** online learning tools ideal for use as quizzes or in-class study material

https://www.concrete.org/educatorsandresearchers/aciinyourclassroom.aspx

ACI STRUCTURAL JOURNAL TECHNICAL PAPER

Title No. 121-S39

Analytical Evaluation of Deep Beams with High-Strength Headed Shear Reinforcement, Part II

by Dhanushka K. Palipana and Giorgio T. Proestos

The use of normal-strength (Grade 60) and high-strength (Grade 80) headed bars as transverse reinforcement can improve the constructability of reinforced concrete structures. However, the ACI 318-19 Code does not allow the use of headed bars as transverse reinforcement in deep beams. ACI 318-19 also does not allow engineers to take advantage of the increased yield strength of Grade 80 reinforcement for use as shear reinforcement. This paper presents an analytical evaluation of shear-critical deep beams that use high-strength headed reinforcement. Six recently conducted large-scale experiments are modeled using the two-parameter kinematic theory, the nonlinear finite element tool VecTor2, and strut-and-tie methods described in codes. The predictions are compared with experimental results. A parametric study is conducted to evaluate the influence of the quantity of transverse reinforcement and yield stress of the transverse reinforcement on the response of shear-critical deep beams.

Keywords: deep beams; finite element modeling; headed reinforcement; high strength; reinforced concrete; shear; strut-and-tie.

INTRODUCTION

Reinforced concrete deep beams have small shear span-depth ratios (a/d). ACI 318-19[1] defines deep beams as members that have a clear span (l_n) less than four times the depth of the member (h) or members that have concentrated loads within two times the depth from the face of the support. The AASHTO LRFD Bridge Design Specifications (ninth edition)[2] defines deep beams as members with an a/d of 2 or less. Unlike in slender beams, in deep beams, shear deformations become significant and plane sections do not remain plane. These shear-critical members are often heavily loaded and contain large quantities of steel reinforcement in the longitudinal and transverse directions. Reducing the reinforcement congestion in such members by using high-strength reinforcement can improve the constructability of the members due to more simplified reinforcement cages and better concrete placement. Similarly, using headed bars for the transverse reinforcement can simplify the construction of such members and reduce the development lengths in comparison to other reinforcement details.

The ACI 318-19 Code limits the maximum yield stress that can be used for shear reinforcement to 60 ksi (414 MPa). ACI 318-19 also does not allow the use of headed bars as shear reinforcement; it does, however, allow the use of headed bars for longitudinal reinforcement.

A series of tests conducted by Proestos et al.[3] on elements subjected to combinations of pure shear and biaxial stresses showed that it would be appropriate to increase the permitted yield stress of transverse reinforcement in the ACI 318 Code to 80 ksi (552 MPa). Munikrishna et al.[4] studied the behavior of slender beams with high-yield-strength stirrups. In these tests, the stirrups yielded before crushing of the compression zone. The authors also observed that the specimens with high-strength stirrups performs well compared to the specimens with lower-strength stirrups. The authors also found that beams that contain smaller amounts of high-strength stirrups can achieve similar loads to members that use larger quantities of lower-strength stirrups. A series of tests conducted on simply supported slender beams by Lee et al.[5] showed

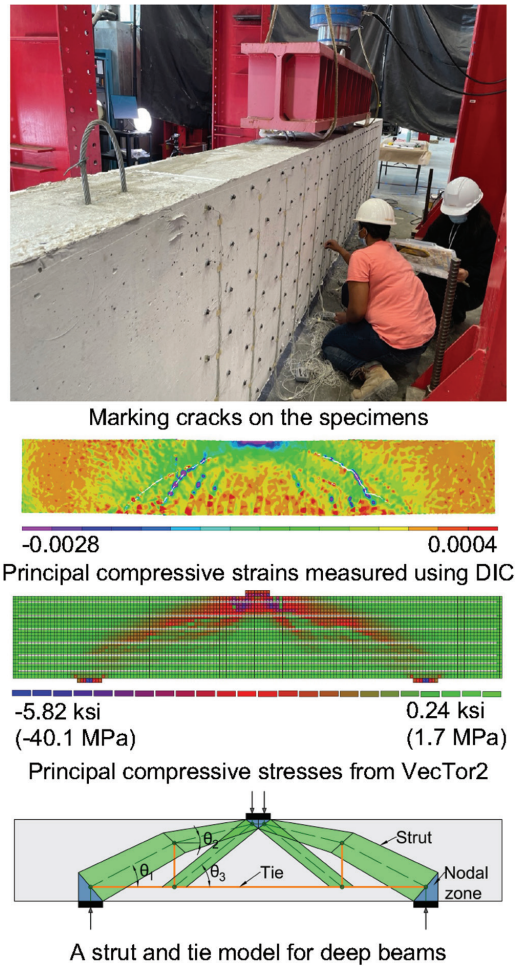

Fig. 1—Experimental and analytical evaluation of deep beams.

ACI Structural Journal, V. 121, No. 3, May 2024.
MS No. S-2023-080.R1, doi: 10.14359/51740487, received September 29, 2023, and reviewed under Institute publication policies.

that the shear strength of specimens increases approximately linearly with the quantity of reinforcement, $\rho_v f_{vy}$. The authors also observed that the shear strength of specimens increases with increasing concrete strength for constant $\rho_v f_{vy}$ values. The experiments showed that the measured maximum crack widths in specimens that contained transverse reinforcement with high yield stresses were approximately the same as the crack widths in members that contained transverse reinforcement with lower yield stresses. The authors also observed that, irrespective of the yield stress of the reinforcement, the crack widths at a specific applied load were approximately the same in all the experiments. Finally, the authors observed that even when transverse reinforcement with larger yield stresses was used, the cracks were well distributed.

The effectiveness of headed bars for use as transverse shear reinforcement in reinforced concrete beams has been studied by several researchers.[6-9] Lequesne et al.[7] conducted a series of tests on reinforced concrete beam experiments containing headed bars and found that the members performed well if sufficient anchorage was provided for the transverse bars. The authors concluded that adequate anchorage is provided when one of the following two conditions are met: 1) when the transverse reinforcement is engaged with the longitudinal bars for No. 4 or smaller bars; or 2) when the headed bars are placed inside at least one longitudinal bar and a side cover to the headed bars of at least six bar diameters is provided for No. 6 or smaller bars. Under these conditions, it was observed that the headed bars could reach their yield stress. These results also showed that when high-strength shear reinforcement replaces larger quantities of Grade 60 reinforcement, such that the $\rho_v f_{vy}$ remains unchanged, the specimens achieve the same shear strength, and there is no discernible effect on crack patterns.

This paper presents an analytical study conducted to evaluate shear-critical reinforced concrete deep beams that use high-strength headed shear reinforcement. The paper first compares different analytical methods used to predict the detailed response of six recently tested deep beam experiments. Figure 1 shows a specimen in the experimental series under load and the marking and measuring of cracks during the experiment. In this paper, the specimen behavior is modeled using the two-parameter kinematic theory (2PKT), the nonlinear finite element tool VecTor2, and strut-and-tie models from ACI 318-19, the AASHTO LRFD ninth edition, and CSA A23.3-19.[10] Figure 1 shows the principal compressive strains measured from digital image correlation (DIC), which are compared with principal compressive stresses obtained from VecTor2. Figure 1 also shows a strut-and-tie model for deep beams with transverse reinforcement. A parametric study is then conducted to evaluate the influence of the quantity of transverse reinforcement and the yield strength of the transverse reinforcement on the shear strength of deep beams. This analytical study explores the effect of a/d, transverse reinforcement yield stress (f_{vy}), transverse reinforcement quantity (ρ_v), quantity of reinforcement ($\rho_v f_{vy}$), longitudinal reinforcement quantities (ρ_l), and concrete strength (f_c') on shear performance.

RESEARCH SIGNIFICANCE

The paper conducts an analytical study of deep beams that use no shear reinforcement, normal-strength (Grade 60) reinforcement in the form of conventional stirrups, normal-strength (Grade 60) headed shear reinforcement, and high-strength (Grade 80) headed shear reinforcement. The results are compared with a recently conducted experimental program. A parametric study is conducted to evaluate the influence of quantity and yield strength of transverse reinforcement on the shear performance of deep beams. The results support liberalizing code limits on the use of high-strength headed bars as transverse reinforcement in deep beams.

EXPERIMENTAL PROGRAM

To investigate the performance of high-strength headed bars as shear reinforcement in deep beams, a series of six large-scale, shear-critical deep beam experiments, the HTS series, were recently conducted. The specimens measured 240 in. (6096 mm) long, 40 in. (1016 mm) deep, and 15 in. (381 mm) wide. The effective depth of the members, d, was 33 in. (838 mm). All six specimens contained eight No. 10 reinforcing bars for the bottom longitudinal reinforcement, which corresponds to a longitudinal reinforcement ratio (ρ_l) of 2.05%. All six specimens contained horizontally distributed reinforcement consisting of eight Grade 60 No. 4 bars spaced at 6.6 in. (167.6 mm), arranged four on each face of the specimen. These distributed bars result in a horizontal reinforcement ratio (ρ_h) of 0.40%. The transverse reinforcement was a variable in the experiments and was changed for each specimen. The different transverse reinforcement arrangements investigated included Grade 60 180-degree hooked No. 4 stirrups, Grade 60 No. 4 headed bars, and Grade 80 No. 4 headed bars.

HTS1 contained no shear reinforcement. HTS2 contained Grade 60 stirrups with 180-degree hooks spaced at 10.7 in. (272 mm) along the span. HTS3 contained Grade 60 headed bars spaced at 10.7 in. (272 mm) along the span. HTS2 and HTS3 contained a quantity of reinforcement ρ_v equal to 0.25%, which is the minimum transverse reinforcement stipulated in ACI 318-19 for deep beams ($\rho_{v,min}$ of 0.25%).[1] HTS4 was designed such that the member contained the same $\rho_v f_{vy}$ ratio as HTS3 but replaces the Grade 60 reinforcement with Grade 80 reinforcement in the transverse direction. Therefore, the amount of Grade 80 transverse reinforcement ρ_v used in HTS4 was reduced to 0.19%. HTS5 consisted of Grade 60 No. 4 headed bars for the transverse reinforcement spaced at 6.6 in. (167.6 mm), resulting in a ρ_v of 0.40%. HTS6 also contained No. 4 headed bars spaced at 6.6 in. (167.6 mm), resulting in a ρ_v of 0.40%; however, HTS6 contained Grade 80 bars. Both HTS5 and HTS6 adhere to the minimum shear reinforcement requirements, including the minimum spacing requirement that indicates the reinforcement must not be spaced more than $d/5$ or 12 in. (305 mm).[1]

The headed bars used in this series of tests consisted of a bearing area (A_{brg}) of four times the bar area (A_b) and met the ASTM A970 Class HA standard. The a/d for the six specimens examined was 2.5. In this series of tests, the a/d of the deep beams was selected to minimize the shear transmitted

by mechanisms other than the transverse reinforcement. Specifically, the specimen design was selected to minimize the shear transmitted by the critical loading zone and the shear transmitted by aggregate interlock. That is, relatively large a/d were selected so that shallower critical crack angles would form, resulting in smaller aggregate interlock forces along the cracks and smaller forces transmitted in the critical loading zone.[11-14] By selecting the specimen properties in this manner, the influence of the transverse reinforcement on member response is increased which is appropriate for this study on the influence of high-strength transverse reinforcement on deep beam behavior. Figure 2 and Table 1 provide a summary of the geometrical and reinforcement details of the experiments considered in this paper. The concrete cylinder strengths of the specimens, f_c', are also provided in Table 1. The yield stress (f_y), yield strain (ε_y), strain-hardening strain (ε_{sh}), ultimate strength (f_u), and strain at ultimate strength (ε_u) of all the reinforcement obtained following ASTM A370-21[15] are shown in Fig. 3.

The deep beam test specimens, measuring 240 in. (6096 mm) long, were supported on two 12 x 15 x 2 in. (305 x 381 x 51 mm) support plates. The support plates rested on roller supports. A loading plate measuring 12 x 15 x 3 in. (305 x 381 x 76 mm) was used in all six experiments in the series. The load was placed in the center of the span of each specimen.

DIC was used to capture the surface deformations of the specimens throughout loading on the east face of the members. On the west face of the specimens, infrared light-emitting diode (LED) markers were tracked with motion-capture cameras to obtain surface deformations. A string potentiometer was used at the midspan of the specimens. In addition to these measurement systems, video was recorded throughout loading. Local high-resolution photographs were also

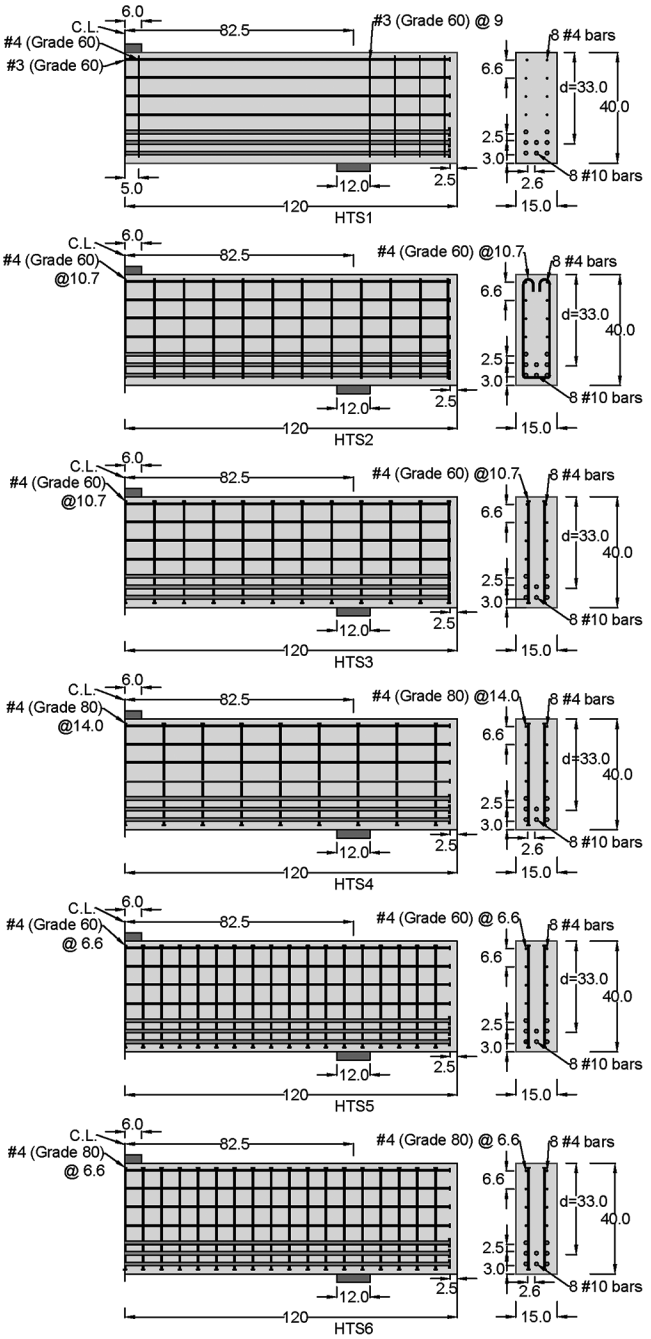

Fig. 2—Specimen geometry and reinforcement details for HTS1 to HTS6. (Note: 1 in. = 25.4 mm; 1 ksi = 6.89 MPa.)

Table 1—Summary of HTS series specimens and material properties

Specimen	f_c', ksi	f_y, ksi	ρ_v, %	f_{vy}, ksi	$\rho_v f_{vy}$, psi	Description of shear reinforcement
HTS1	5.19	87.6	—	—	—	No shear reinforcement
HTS2	4.39	87.6	0.25	69.7	174	Grade 60 180-degree hooked stirrups; resulting ρ_v of 0.25%
HTS3	4.39	87.6	0.25	69.7	174	Grade 60 headed bars; resulting ρ_v of 0.25%
HTS4	3.90	87.6	0.19	88.4	168	Grade 80 headed bars with same $\rho_v f_{vy}$ as HTS3 (ρ_v is 0.19%)
HTS5	4.66	87.6	0.40	69.7	282	Grade 60 headed bars at $d/5$ spacing; resulting ρ_v of 0.4%
HTS6	4.67	87.6	0.40	88.4	357	Grade 80 headed bars at $d/5$ spacing; resulting ρ_v of 0.4%

Note: ρ_v is shear reinforcement ratio; f_{vy} is yield stress of transverse reinforcement; 1 in. = 25.4 mm; 1 ksi = 1000 psi = 6.89 MPa.

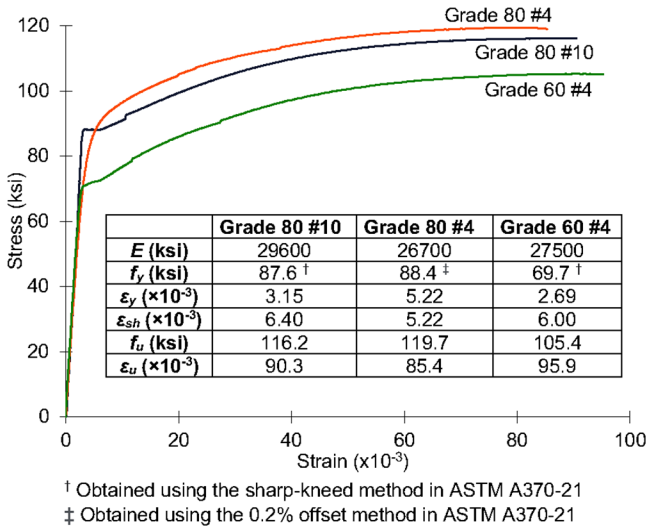

	Grade 80 #10	Grade 80 #4	Grade 60 #4
E (ksi)	29600	26700	27500
f_y (ksi)	87.6 †	88.4 ‡	69.7 †
ε_y (×10^{-3})	3.15	5.22	2.69
ε_{sh} (×10^{-3})	6.40	5.22	6.00
f_u (ksi)	116.2	119.7	105.4
ε_u (×10^{-3})	90.3	85.4	95.9

† Obtained using the sharp-kneed method in ASTM A370-21
‡ Obtained using the 0.2% offset method in ASTM A370-21

Fig. 3—Stress-versus-strain response of steel coupons and reinforcement properties. (Note: 1 ksi = 6.89 MPa.)

manually obtained to capture local observations and global observations periodically throughout the experiments. The specimens were loaded monotonically to failure at a rate of approximately 1 kip/s (4.45 kN/s).

Summary of HTS series member response

With initial loading, flexural cracks occurred at the bottom of the beams near midspan. With further loading, flexural cracks widened and propagated toward the flexural compression region. Shear cracks formed in the clear shear span between the support and loading plate. As the load increased the shear cracks extended and grew in width. Ultimately all the specimens failed in shear. Figure 4 shows a summary of the load versus displacement response for the six specimens. More details of the experimental setup, the experimental program and detailed experimental results can be found elsewhere.[11]

COMPARISON OF MEMBER RESPONSE WITH MODEL PREDICTIONS

This section compares the experimental observations with the predictions from five models. Comparisons are made with the 2PKT, the nonlinear finite element tool VecTor2, and strut-and-tie models from three codes—the ACI 318-19 Code, the AASHTO LRFD ninth edition Code, and the CSA A23.3-19 Code.

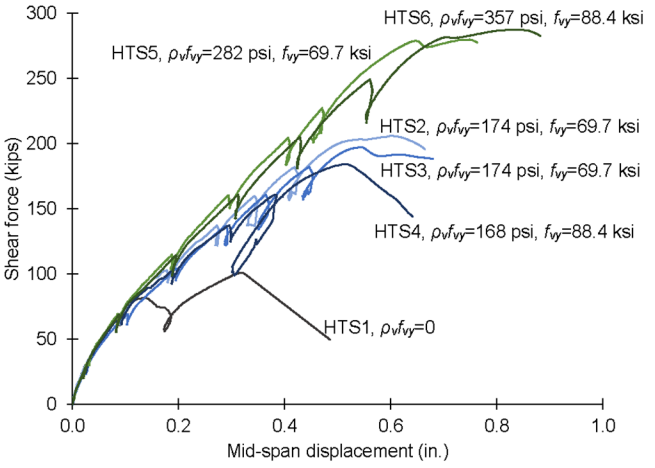

Fig. 4—Load-versus-displacement response for HTS1 to HTS6. (Note: 1 in. = 25.4 mm; 1 kip = 4.45 kN; 1 ksi = 6.89 MPa.)

2PKT

The 2PKT proposed by Mihaylov et al.[12] is a kinematic model capable of predicting the full deformation field and peak load of shear critical deep beams. The method is based on equilibrium and constitutive relationships. The response of deep beams is predicted based on two kinematic parameters: the vertical deformation of the critical loading zone (Δ_c) and the average strain in the bottom reinforcement ($\varepsilon_{t,avg}$). The 2PKT captures four shear transfer mechanisms: shear transferred in the uncracked region near the loading plate—the critical loading zone (CLZ) (V_{CLZ}), shear transferred by aggregate interlock (V_{ci}), shear transmitted in the transverse reinforcement (V_s), and shear transmitted by dowel action (V_d). Previous research has shown that the 2PKT can predict the behavior of the deep beams well. When compared to a database of 529 deep beam experiments, the method has shown to provide excellent results with a mean test to predicted ratio of 1.10 and a coefficient of variation (COV) of 13.7%.[12,16,17] Table 2 summarizes the 2PKT predictions for the HTS series of experiments examined in this paper. The predicted shear strength (V_{2PKT}) is also compared with the experimentally measured peak shear force.

For HTS1, the amount of shear carried in the CLZ accounts for 71% of the predicted shear that can be transmitted in the member, with the contributions from aggregate interlock and dowel action accounting for the balance of the predicted shear that can be transmitted. For HTS2 and HTS3, the predicted shear that is transmitted in the CLZ accounts for 35% of the total shear that can be transmitted, with 37% predicted to be carried in the transverse reinforcement. The balance is predicted to be carried through aggregate interlock and dowel action. HTS4, which uses the same $\rho_v f_{vy}$ but replaces Grade 60 reinforcement with Grade 80 reinforcement, is predicted to have a shear strength 94% of HTS2 and HTS3. The prediction captures well the reduction observed in the experimental results, indicating that the 2PKT can predict the influence of using Grade 80 reinforcement in comparison to Grade 60 reinforcement. HTS5 and HTS6 are predicted to transmit 66 kip (294 kN) of shear force in the critical loading zone. This corresponds to 30% and 28% of the predicted total shear capacity, respectively.

Table 2—Summary of shear-strength predictions

Specimen	V_{exp}, kip	V_{CLZ}, kip	V_{ci}, kip	V_s, kip	V_d, kip	V_{2PKT}, kip	$V_{STM,\ ACI}$, kip	$V_{STM,\ AASHTO}$, kip	$V_{STM,\ CSA}$, kip	V_{VT2}, kip	V_{exp}/V_{2PKT}	$V_{exp}/V_{STM,\ ACI}$	$V_{exp}/V_{STM,\ AASHTO}$	$V_{exp}/V_{STM,\ CSA}$	V_{exp}/V_{VT2}
HTS1	101	72	22	0	40	134	47	179	113	140	0.75	2.15	0.56	0.89	0.72
HTS2	206	63	19	68	31	182	241	243	169	212	1.13	0.85	0.85	1.22	0.97
HTS3	197	63	19	68	31	182	241	243	169	212	1.08	0.82	0.81	1.17	0.93
HTS4	184	57	18	63	32	171	214	224	154	198	1.08	0.86	0.82	1.19	0.93
HTS5	280	66	19	110	24	219	253	255	205	245	1.28	1.11	1.1	1.37	1.14
HTS6	288	66	18	135	19	239	253	255	224	263	1.21	1.14	1.13	1.29	1.1
										Average	1.09	1.15	0.88	1.19	0.96
										COV	16.6%	43.9%	23.8%	13.6%	15.4%

Note: 1 kip = 4.45 kN.

The amount of predicted shear that can be transmitted in the transverse reinforcement is predicted to be 110 and 135 kip (489 and 601 kN), respectively, which corresponds to 50% and 46%, respectively. These predictions indicate that the increase in strength that is obtained by replacing Grade 60 transverse reinforcement with the same quantity of Grade 80 transverse reinforcement can be quantified. Notably, unlike slender members, since the contribution of the critical loading zone significantly contributes to the total shear that can be carried, the influence of the transverse reinforcement must be considered along with the contribution of the other shear carrying mechanisms.

The average test-to-predicted ratio (V_{exp}/V_{2PKT}) determined from the 2PKT for the six experiments of the HTS series was 1.09, with a COV of 16.6%. HTS1 had the lowest V_{exp}/V_{2PKT} with a value of 0.75, and this member was also the only specimen that did not contain shear reinforcement. It should also be noted that the 2PKT sectional check was omitted in the calculations. For HTS2 to HTS6, the members that contained transverse reinforcement, all the predictions were conservative, with the V_{exp}/V_{2PKT} ranging from 1.08 to 1.28. The 2PKT predicted that all the specimens will fail in shear before the yielding of bottom longitudinal reinforcement, which is consistent with the experimental observations.

Nonlinear finite element predictions using VecTor2

The nonlinear finite element program VecTor2 was used to determine the shear capacity and full member response of the specimens. VecTor2 is a nonlinear finite element program that is based on the Modified Compression Field Theory (MCFT)[18] and the Distributed Stress Field Model (DSFM).[19] VecTor2 has been used extensively over the past decades with success in a variety of applications.[20] Additionally, because the tool is also based on the MCFT, the tool is consistent with the intent of the AASHTO LRFD and the CSA A23.3 Code. The beams were modeled using rectangular elements for the concrete and truss elements for longitudinal reinforcement. Transverse reinforcement was modelled as smeared reinforcement. All the default constitutive models were used, except the parabola constitutive model was changed to the Modified Popovics stress-strain relationship described by Collins and Mitchell.[21] The steel properties obtained from the steel coupon tests were used to model steel material behavior. Figure 5 compares the experimentally measured midspan displacement versus the applied shear force with the response predicted by VecTor2.

For all six HTS experiments, the uncracked stiffness is well predicted by VecTor2. The cracked stiffness is somewhat overpredicted for all the HTS members, regardless of whether shear reinforcement was included, the grade of transverse reinforcement used, or the anchorage detail of the transverse reinforcement. The peak load is well predicted for the series, with an average test-to-predicted ratio of 0.96 and a COV of 15.4%. VecTor2 overpredicts the response of HTS1, the member without minimum transverse reinforcement. It should be emphasized that no parameters were calibrated to develop the predictions from VecTor2. The material properties were simply input into program and the predictions were obtained. Additionally, the constitutive models were not

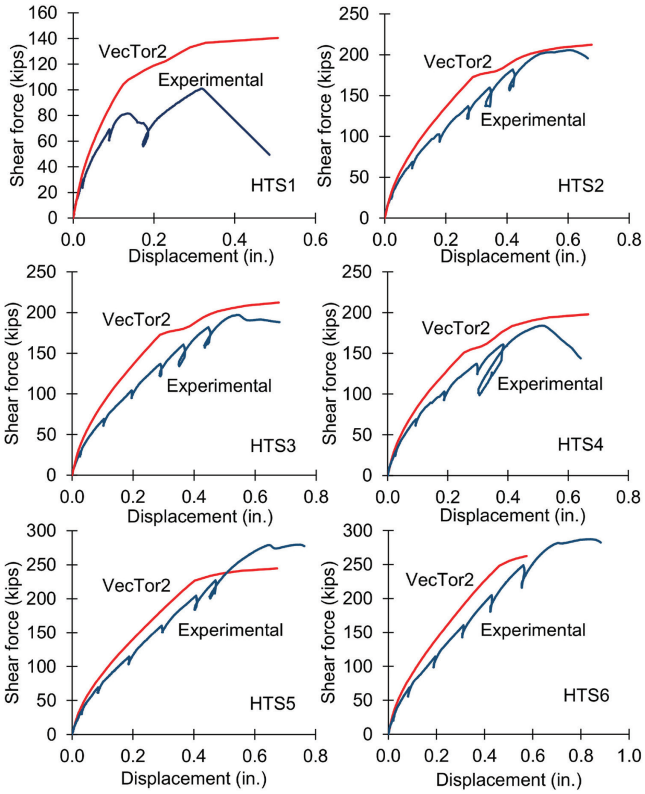

Fig. 5—VecTor2 load deformation predictions for HTS1 to HTS6. (Note: 1 in. = 25.4 mm; 1 kip = 4.45 kN.)

fit or otherwise adjusted to match the predictions with the globally observed experimental response (except, as previously noted, the only change from the default settings was that the Modified Popovics relationship was selected for use as opposed to the parabola constitutive model). Thus, while there are some discrepancies between the observed and measured response, it remains impressive that the response is well predicted without the need to calibrate results. This gives confidence the tool can be used to explore variables not directly tested in the experimental series.

In addition to predicting the shear capacity and load deformation response, VecTor2 can be used to investigate the crack patterns and stresses in the reinforcement. Because the MCFT and the DFSM are smeared, rotating crack models, VecTor2 can predict the average crack widths that occur. Figure 6 shows in red, the crack patterns predicted by VecTor2 at the peak load. Overlaid on the VecTor2 crack patterns are the experimentally determined crack patterns shown in black. Also indicated in the figure is the experimentally observed failure span and the experimentally determined critical crack marked in blue. The critical crack is the crack that has the largest crack widths in a shear span. In deep beams, this crack propagates from the inner edge of the support plate to near the loading plate. Due to the significant deformations of this crack, typically, the failure of the members occur along this crack. However, for HTS4, the failure crack differed from the critical crack identified at the final load stage prior to failure, the failure crack is marked in green.

For all the specimens, the predicted crack patterns obtained from VecTor2 match the experimentally observed crack patterns well. Both the shear and flexural cracks are

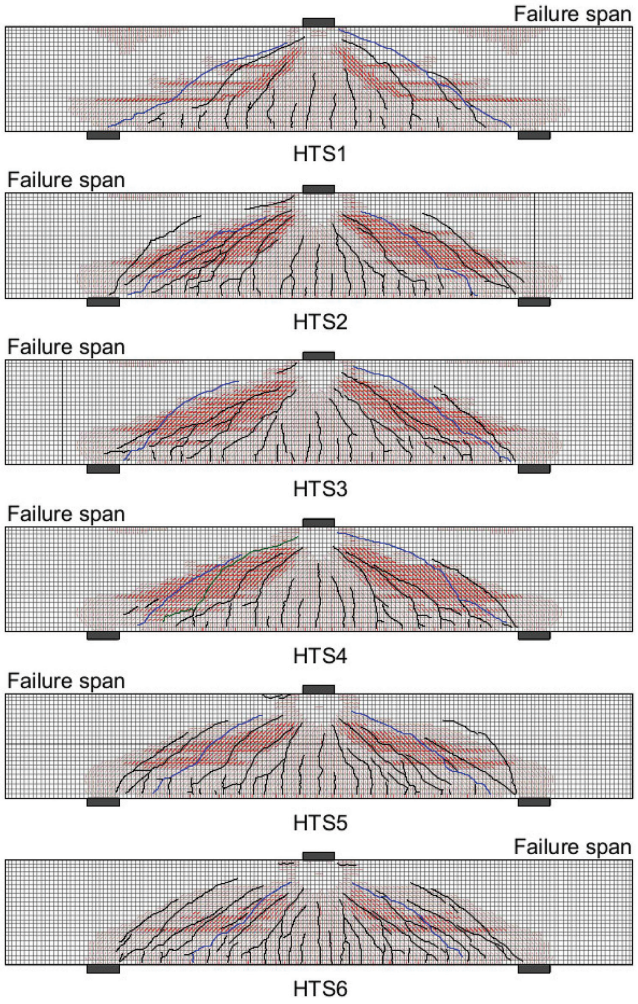

Fig. 6—Experimentally observed crack patterns and predicted crack patterns determined from VecTor2 at peak load for HTS1 to HTS6.

well predicted. As can be seen, the size of the uncracked region underneath the loading plate where the cracks terminate is also well predicted. Notably, the predicted crack angles agree well with the experimentally observed cracks.

Figure 7 compares the principal compressive strain fields obtained from the DIC data with the principal compressive stresses in the concrete determined from VecTor2. It can be seen that VecTor2 predicts the load arching from the loading plate to the support plates well and is in agreement with the measured strains. The VecTor2 models also predicts high compressive stresses near the edges of the loading plate well. Finally, there is good agreement between the experimental measurements and VecTor2 as they relate to the region of compressive straining and how that changes with the reinforcement used. The benefits of using transverse reinforcement predicted by VecTor2 are reflected in the strain field maps measured in the experiments.

The vertical strain maps obtained from the DIC system can be compared to the maps of stress in the reinforcement predicted by VecTor2; refer to Fig. 8. The comparisons can be used to evaluate whether the transverse steel is predicted to yield and if the region over which substantial straining is expected is consistent with the strains observed in the experiments. For HTS2 to HTS6, VecTor2 predicts substantial distributed yielding of the transverse reinforcement in the clear span of the members. This is the case for members reinforced with Grade 60 transverse reinforcement and Grade 80 transverse reinforcement. Yielding was also observed for members containing minimum transverse reinforcement and for members with substantially more than minimum transverse reinforcement.

Strut-and-tie modeling of HTS series

This section summarizes strut-and-tie model predictions for the HTS series of experiments. Models were developed based on ACI 318-19, the AASHTO LRFD ninth edition Code, and CSA A23.3-19. In these calculations, the ϕ factors are taken as unity to assess the efficacy of the codes in predicting the shear capacity of the members.

The strut-and-tie models developed based on the ACI 318-19 are first discussed. For HTS1, the strut-and-tie model is shown in Fig. 9(a). In this model, the applied load is divided into two-point loads at the quarter point of the loading plate. The top nodes are connected by a horizontal strut. The longitudinal steel is modeled as a tension tie at the centroid of the flexural tension reinforcement. Consistent with the ACI 318-19, the strut strength was obtained using Eq. (1) and (2). Herein, A_{cs} is the cross-sectional area of the strut and f_c' is the concrete strength. The parameter β_c was taken as 1.0. For boundary struts, β_s was taken as 1.0. For interior struts, β_s was taken as 0.4, because HTS1 did not contain minimum distributed reinforcement.

$$F_{ns} = f_{ce}A_{cs} \tag{1}$$

$$f_{ce} = 0.85\beta_c\beta_s f_c' \tag{2}$$

The strength of the tie was calculated using $A_{st}f_y$. Herein, A_{st} is the area of longitudinal reinforcement and f_y is the yield stress of longitudinal reinforcement. The longitudinal tie is located at the centroid of the longitudinal reinforcement. The strength of the nodes (blue regions in Fig. 9; full-color PDF can be accessed at www.concrete.org) was calculated using Eq. (3) and (4)

$$F_{nn} = f_{ce}A_{cz} \tag{3}$$

$$f_{ce} = 0.85\beta_c\beta_n f_c' \tag{4}$$

Herein, β_c was taken as 1.0. For the top nodes, which are bounded by struts and bearing areas, β_n was taken as 1.0. For the bottom nodes, which anchor one tie, β_n was taken as 0.8. The maximum load predicted by the model is associated with the load that just exceeds these limits. The force in the horizontal strut is taken as the maximum force it can transmit. The ultimate load is then determined based on the geometry of the model, where equilibrium is satisfied and strength limits are reached.

The strut-and-tie models for HTS2 to HTS6, which contained shear reinforcement, were refined to account for the transverse reinforcement (refer to Fig. 9(b)). In these models, half the quantity of transverse reinforcement in the

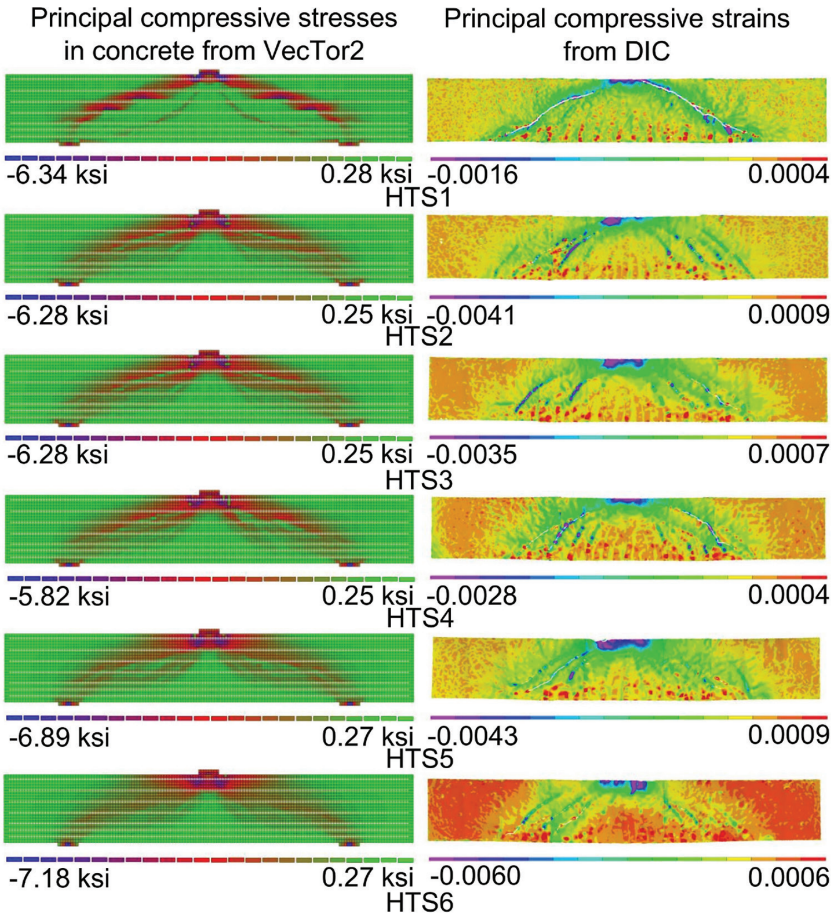

Fig. 7—Principal compressive stresses in concrete from VecTor2 (left); and principal compressive strains obtained from experiments (right).

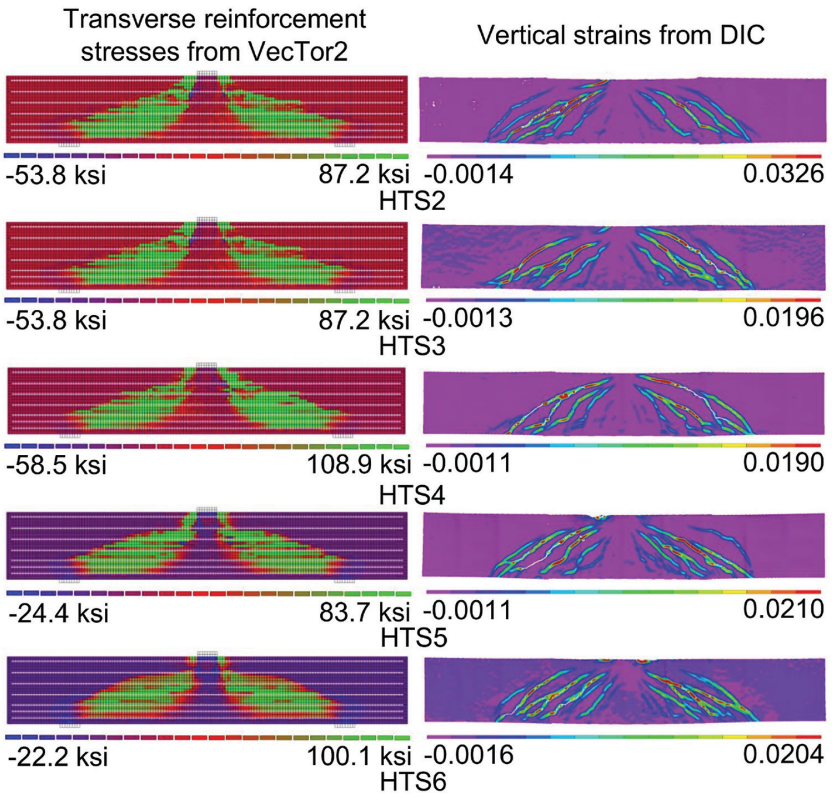

Fig. 8—Transverse steel stresses from VecTor2 (left); and vertical strains obtained using DIC data (right) for HTS2 to HTS6. (Note: 1 MPa = 0.145 ksi.)

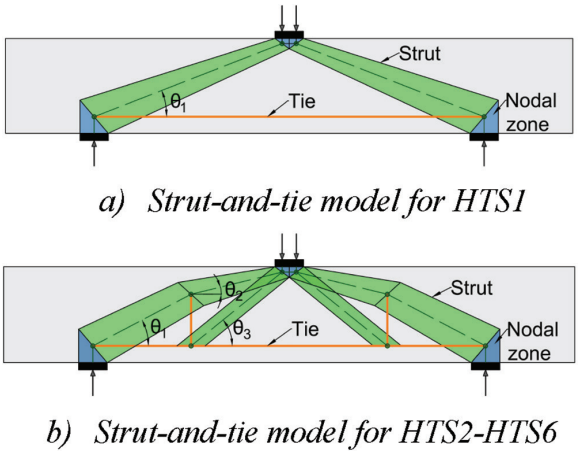

Fig. 9—HTS Series strut-and-tie models.

clear shear span was lumped at the center of the clear shear span in a vertical tie.[10,22] The force of vertical tie was taken as the yield force of transverse reinforcement considered. The strengths of the nodes, struts, and ties were determined as described previously for HTS1. For interior struts of HTS2 to HTS6, β_s was taken as 0.75, because the members contained minimum distributed reinforcement.

The same geometric arrangement for the strut-and-tie models as illustrated in Fig. 9 were used to develop predictions consistent with the AASHTO LRFD ninth edition Code, according to which nodes are characterized as: 1) CCC: nodes where three struts intersect; 2) CCT: nodes where a single tie intersects two struts; and 3) CTT: nodes where two ties intersect a concrete strut. The resistance of a nodal face is given by Eq. (5) and (6). Herein, A_{cn} is the cross-sectional area of the node face and m is the confinement factor, taken as 1.0 for the HTS series specimens. The factor v is taken as 0.45 if the structure does not contain at least the minimum crack control reinforcement ratio of 0.003 in horizontal and vertical directions. For the top CCC nodes of HTS2 to HTS6, 0.85 was used as v for the back face and the bearing face. For the bottom CCT nodes of HTS2 to HTS6, 0.75 was used as v for the back face and the bearing face. For the strut-to-node interface of the CCC and CCT nodes in HTS2 to HTS6, the v term was taken as 0.63, 0.63, 0.65, 0.62, and 0.62, respectively.

$$P_n = f_u A_{cn} \tag{5}$$

$$f_{cu} = mvf_c' \tag{6}$$

The strength of the tie is given by $A_{st}f_y$. A_{st} is the area of longitudinal reinforcement, and f_y is the yield stress of the reinforcement. The location of the longitudinal is defined at the centroid of the longitudinal reinforcement.

The load on each nodal face and in each tie must be less than the capacity limits described. The force in the horizontal strut is taken as the maximum force it can transmit. The maximum predicted load is determined based on the geometry of the model, where equilibrium is satisfied and another nodal strength limit is reached.

The same geometric arrangement of strut-and-tie models as shown in Fig. 9 was used to develop predictions consistent with the CSA A23.3-19 Code. In CSA A23.3-19, the compressive force in the strut is limited to $f_{cu}A_{cs}$. The term A_{cs} is the effective cross-sectional area of strut. The limiting compressive stress f_{cu} is calculated using Eq. (7) and (8). Herein, θ_s is the smallest angle between the strut and the adjoining ties, and ε_s is the tensile strain in the tie inclined at θ_s. This reduction in strut capacity is based on the compression softening relationship proposed by Vecchio and Collins.[18] The force in the ties cannot exceed the yield force of the reinforcement, $A_{st}f_y$.

$$f_{cu} = \frac{f_c'}{0.8 + 170\varepsilon_1} \leq 0.85f_c' \tag{7}$$

$$\varepsilon_1 = \varepsilon_s + (\varepsilon_s + 0.002)\cot^2\theta_s \tag{8}$$

To determine the maximum predicted force from the model, the force in the horizontal strut is taken as the maximum force it can transmit. The ultimate load is determined based on the geometry of the model, where equilibrium is satisfied and another strength limit is reached. For CSA A23.3-19 strut-and-tie models, the strut at the support at the intersection of the flexural tension tie is typically critical because of the compression softening effect at that location.

Table 2 summarizes the strut-and-tie model predictions determined using the ACI 318-19, the AASHTO LRFD ninth edition, and CSA A23.3-19 Codes. The table also summarizes the 2PKT and the VecTor2 predicted shear capacities.

The results indicate that beneficial effects of including transverse reinforcement can be captured by the strut-and-tie models. In particular, the results obtained give reasonable predictions for HTS2 to HTS4. The results also indicate that the strut-and-tie models can capture the increase in shear capacity that occurs when quantities above minimum shear reinforcement are provided, as can be seen in HTS5 and HTS6.

The use of strut-and-tie models to predict the capacity of the HTS series of experiments gave different results depending on the code used. The ACI 318-19 Code gave a mean test-to-predicted ratio of 1.15, with a COV of 43.9%. The lowest test-to-predicted ratio occurred for HTS3 with a value of 0.82, and the prediction for specimen HTS1 was most conservative with a test-to-predicted ratio of 2.15. AASHTO LRFD ninth edition gave a mean test-to-predicted ratio for the strut-and-tie models of 0.88 with a COV of 23.8%. The CSA A23.3-19 Code gave a mean test-to-predicted ratio of 1.19 and a COV of 13.6%. It should be noted that for HTS1, the only member without transverse reinforcement, there is a significant range of predictions. Comparing the predictions of HTS1 with other specimens, the results indicate that the inclusion of shear reinforcement improves the spread of the predictions by the models. This result is consistent with other studies in the literature.[23] Importantly, the strut-and-tie models were able to capture the beneficial effects of including shear reinforcement. Notably, the quality of the strut-and-tie model predictions was unaffected by the type of transverse reinforcement used, whether the transverse reinforcement consisted of Grade 60 or 80 reinforcement,

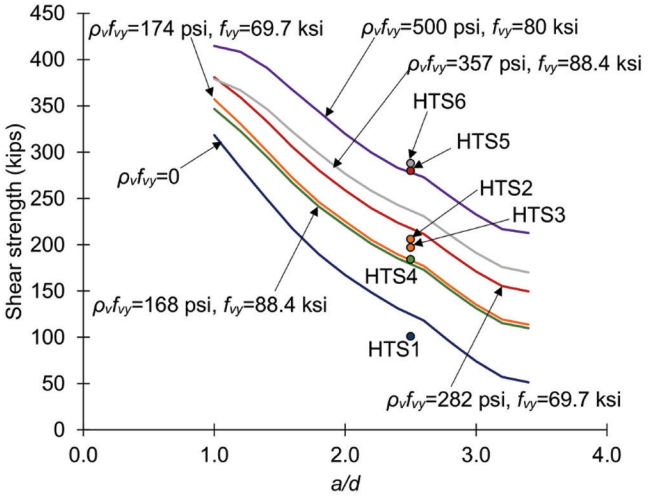

Fig. 10—Influence of a/d *on shear strength. (Note: 1 kip = 4.45 kN; 1 ksi = 6.89 MPa.)*

or whether the transverse reinforcement was anchored with stirrups or headed bars.

PARAMETRIC STUDY ON DEEP-BEAM SHEAR CAPACITY

To explore the variables that were not tested in the experimental series, a parametric study was also conducted on several variables relevant to the shear strength of deep beams. The parametric evaluations were conducted to investigate the influence of the *a*/*d*, yield stress of reinforcement, quantity of reinforcement ($\rho_v f_{vy}$), quantity of shear reinforcement (%), longitudinal reinforcement quantity, and concrete cylinder strength on the shear performance of the members. The member properties of the HTS series were used, except for the variable that is parametrically varied. For example, the average concrete strength of HTS specimens was used. The parametric study was conducted using the 2PKT because the model can capture the influence of these variables on the shear capacity and the model had a very good mean test-to-predicted ratio and COV for the HTS series. The figures in this section also include the HTS series experiments, where appropriate.

Figure 10 shows the influence of *a*/*d* on the shear response of the members predicted by the 2PKT. The figure includes the predictions for five different $\rho_v f_{vy}$ values that were selected to match the $\rho_v f_{vy}$ values used in the HTS experimental series. One additional line corresponding to a yield stress of the reinforcement of 80 ksi (552 MPa) and a $\rho_v f_{vy}$ value of 500 psi (3.45 MPa) is included. Figure 10 also shows the experimentally observed shear strengths for the HTS series of experiments. It should be noted that the 2PKT predictions are not limited to the sectional capacity of the equivalent slender member for these predictions. That is, as the *a*/*d* increase beyond approximately 2.5 or 3, the response of the members may be governed by slender beam action. The predictions from the sectional shear equations may give higher predicted shear strengths than the 2PKT, and it would be appropriate to use those values. Therefore, the predictions provided in Fig. 10 represent a lower limit on the predicted strength.

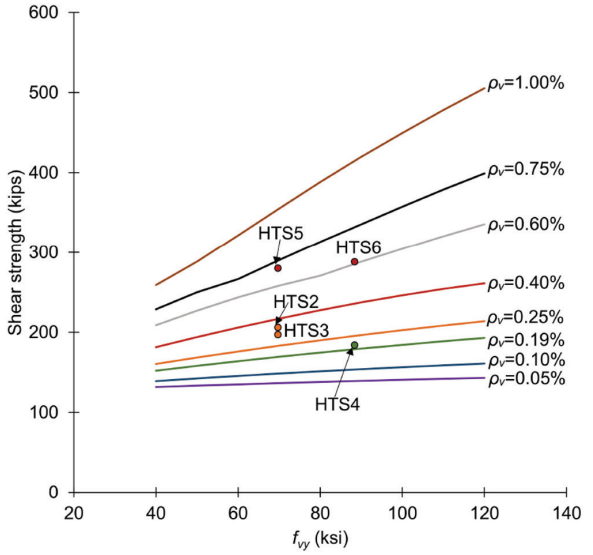

Fig. 11—Influence of f_{vy} *on shear strength. (Note: 1 kip = 4.45 kN; 1 ksi = 6.89 MPa.)*

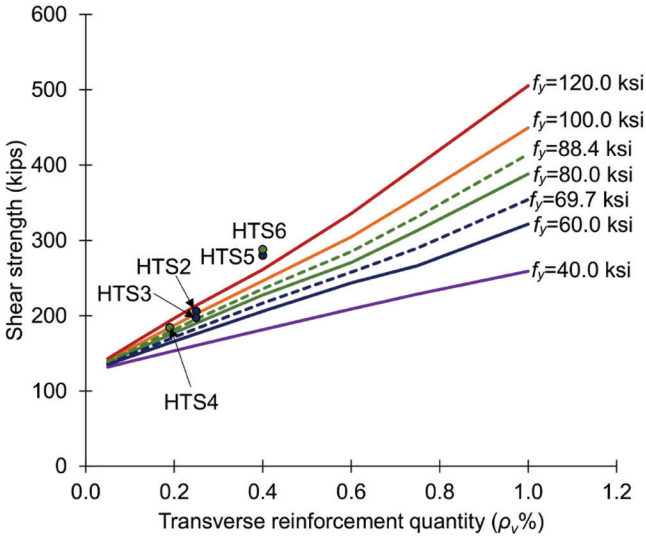

Fig. 12—Influence of ρ_v *on shear strength. (Note: 1 kip = 4.45 kN; 1 ksi = 6.89 MPa.)*

Figure 11 shows the effect of the yield stress of the transverse reinforcement on the predicted shear strength for members with different quantities of transverse reinforcement. The figure shows the predicted response for yield stresses of the reinforcement ranging from 40 to 120 ksi (276 to 827 MPa) and for quantities of transverse reinforcement ranging from 0.05 to 1.0%.

Figure 12 shows the influence of quantity of transverse reinforcement, in terms of percent, on the shear strength of the member for quantities of transverse reinforcement ranging from 0.05% to 1.0%. The figure shows the predicted influence for members that contain transverse steel reinforcement with yield stresses ranging from 40 to 120 ksi (276 to 827 MPa).

Figure 13 also shows the influence of the quantity of shear reinforcement in terms of $\rho_v f_{vy}$ on shear capacity. The figure shows the predicted capacity of members ranging from 0 to 500 psi (0 to 3.45 MPa) and also plots several lines

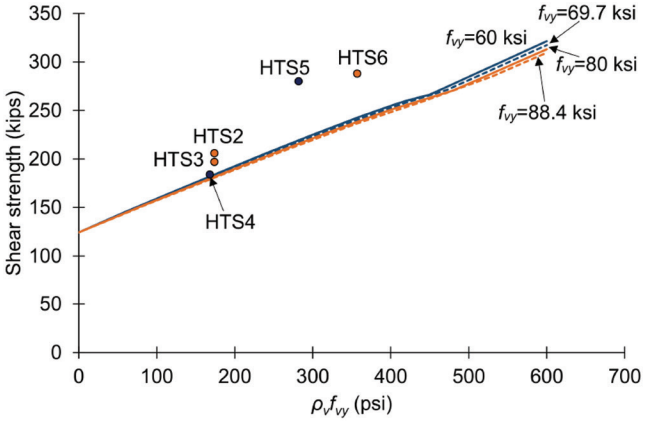

Fig. 13—Influence of $\rho_v f_{vy}$ on shear strength for different reinforcement yield stresses. (Note: 1 kip = 4.45 kN; 1 ksi = 6.89 MPa.)

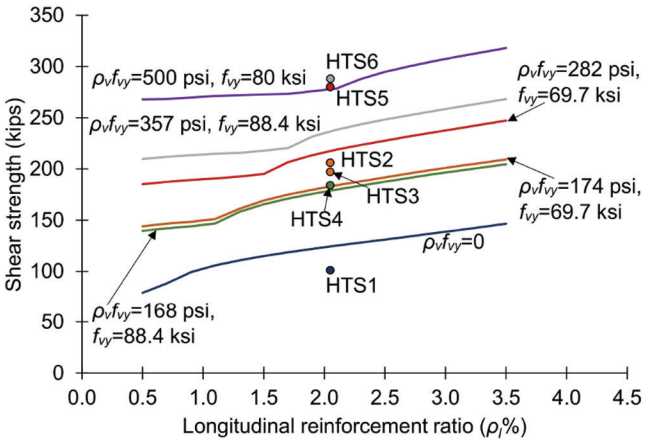

Fig. 14—Influence of longitudinal reinforcement quantity (ρ_l %) on shear strength. (Note: 1 kip = 4.45 kN; 1 ksi = 6.89 MPa.)

corresponding to the predictions of members using steel yield stresses ranging from 40 to 120 ksi (276 to 827 MPa). The results indicate that while the total quantity of reinforcement included in terms of $\rho_v f_{vy}$ is important, there is a relatively minor influence of the yield stress of the reinforcement on the ultimate capacity for the members investigated.

The influence of the longitudinal reinforcement quantity on the shear strength is shown in Fig. 14. The figure shows the predictions for the quantity of reinforcement that range from 0.5 to 3.5%. As expected, while there is a predicted influence, the shear strength is less sensitive to this parameter than to parameters such as the transverse reinforcement.

Finally, the influence of the concrete cylinder strength on the shear capacity is shown in Fig. 15. The figure shows the predicted shear strength for concrete strengths ranging from 2.5 to 12 ksi (17.2 to 82.7 MPa). Several predictions corresponding to different quantities of transverse reinforcement are plotted.

The results show that the shear strength decreases with increasing a/d. Larger shear reinforcement quantities give larger shear strength for a specific a/d. For a given ρ_v, the shear strength of the specimens increases with increasing yield strength of the transverse reinforcement. For very

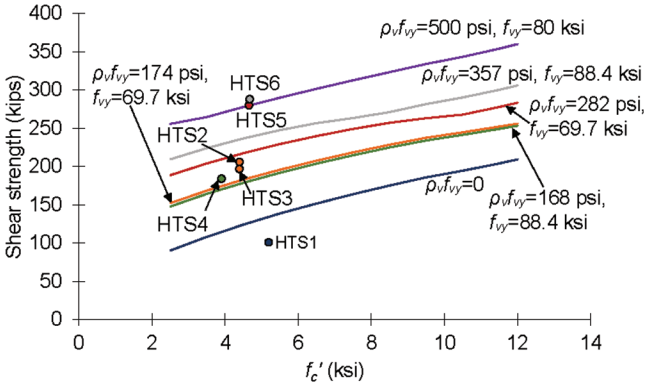

Fig. 15—Influence of f_c' on shear strength. (Note: 1 kip = 4.45 kN; 1 ksi = 6.89 MPa.)

small ρ_v such as 0.05%, the increase of shear strength can be insignificant, even if shear reinforcement with very large yield strength such as 120 ksi (827 MPa) is used. Increases in $\rho_v f_{vy}$ increases the shear strength of deep beam members. This increase is approximately linear for the specimens and range of values explored. Increases in longitudinal reinforcement ratio results in higher strengths. This effect is less significant than increases to transverse reinforcement quantities. The shear strength of the deep beams examined, also increases with increasing concrete strength.

CONCLUSIONS AND RECOMMENDATIONS

The paper presents an analytical evaluation of deep beams that use no shear reinforcement, normal-strength (Grade 60) conventional stirrups, normal-strength (Grade 60) headed shear reinforcement and high-strength (Grade 80) headed shear reinforcement. The results are compared with the experimental results of a recently conducted experimental program, the HTS series. The numerical studies were conducted using the Two-Parameter Kinematic Theory (2PKT), the nonlinear finite element program VecTor2, and strut-and-tie models from the ACI 318-19 Code, the AASHTO LRFD ninth edition Code, and the CSA A23.3-19 Code. To further complement the experimental work and existing literature, the 2PKT was used to conduct a parametric study to investigate the influence of various parameters on the shear strength of members with similar properties to the HTS series.

The 2PKT was able to predict the shear capacity with a mean test-to-predicted ratio of 1.09 and a coefficient of variation (COV) of 16.6% and is capable of capturing the response of deep beams reinforced with high-strength reinforcement. The 2PKT predicted that all the specimens will fail in shear before the yielding of bottom longitudinal reinforcement and that the transverse reinforcement is predicted to yield at failure. This is consistent with the experimental observations.

The nonlinear finite element program VecTor2 was able to predict the shear capacity of the HTS series of tests with a mean test-to-predicted ratio of 0.96 and a COV of 15.4%. VecTor2 can capture the response of deep beams reinforced with high-strength reinforcement. The VecTor2 models also predicted the shear and flexural cracks well. Comparing the predicted principal compressive stresses in the concrete with

the principal compressive strains measured in the experiments, illustrates that VecTor2 predicts the compression fields in the experiments well and captures the influence of reinforcement on member response. VecTor2 predicted yielding of transverse reinforcement in the clear spans of the members. This agreed well with the strain measurements observed in the experiments.

The use of strut-and-tie models to predict the capacity of the HTS series of experiments gave different results depending on the method used. The ACI 318-19 Code gave a mean test-to-predicted ratio of 1.15 with a COV of 43.9%. AASHTO LRFD gave a mean test-to-predicted ratio for the strut-and-tie models of 0.88 with a COV of 23.8%. The CSA A23.3-19 Code gave a mean test-to-predicted ratio of 1.19 with a COV of 13.6%. The strut-and-tie models were able to capture the beneficial effects of including shear reinforcement. Additionally, the quality of the strut-and-tie model predictions were unaffected by the type of transverse reinforcement used, whether the transverse reinforcement consisted of Grade 60 or 80 reinforcement, or whether the transverse reinforcement was anchored with stirrups or headed bars. Thus, the use of strut-and-tie design provisions can be used in the design of members that use Grade 60 or Grade 80 reinforcement anchored with conventional stirrups with 180-degree bends or with headed bars.

A parametric study was conducted to explore influence of shear span-depth ratio (a/d), transverse reinforcement yield stress (f_{vy}), transverse reinforcement quantity (ρ_v), quantity of reinforcement ($\rho_v f_{vy}$), longitudinal reinforcement quantity (ρ_l) and concrete strength (f_c') on shear strength. The parametric study corroborates the findings of the experimental program and demonstrates that while reinforcement yield stresses corresponding to Grade 60 and 80 steels were experimentally investigated, the conclusions of this research likely extend to steel reinforcement yield stresses beyond 80 ksi (552 MPa). The results certainly extend to steel transverse reinforcement yield stresses of 88.4 ksi (610 MPa), which is the measured yield stress of the Grade 80 reinforcement used in the HTS series of experiments.

Based on the previous conclusions determined from the research conducted, the following are several recommendations as they pertain to the design of high-strength headed reinforcing bars for use as transverse reinforcement in shear-critical deep beams.

1. The ACI 318 Code should allow for the use of transverse reinforcement in concrete deep beams with yield stresses of at least 80 ksi (552 MPa).

2. The ACI 318 Code should allow for the use of headed reinforcement bars with a bearing area of at least four times the bar area for use as transverse reinforcement.

3. The AASHTO LRFD Code should allow for the use of transverse reinforcement in concrete deep beams with yield stresses of at least 80 ksi (552 MPa).

These recommendations are based on the literature reviewed, the experimental series conducted, and numerical studies conducted. As variables beyond those explored are modified, there may be a need to conduct further analysis or experimental studies to investigate the influence of those parameters on the shear response.

AUTHOR BIOS

ACI member **Dhanushka K. Palipana** *is a Postdoctoral Researcher at the University of Kansas, Lawrence, KS. She received her BScEng from the University of Peradeniya, Peradeniya, Sri Lanka, in 2017 and her PhD from North Carolina State University, Raleigh, NC, in 2023. She is a member of Joint ACI-ASCE Subcommittees 445-E, SOA Torsion, and 445-F, Interface Shear.*

ACI member **Giorgio T. Proestos** *is an Assistant Professor at North Carolina State University. He received his BASc in Engineering Science, his MASc, and his PhD from the University of Toronto, Toronto, ON, Canada, in 2012, 2014, and 2018, respectively. He is Secretary of Joint ACI-ASCE Committee 445, Shear and Torsion; Secretary of Joint ACI-ASCE Committee 445-F, Interface Shear; and a member of Joint ACI-ASCE Subcommittee 445-E, SOA Torsion. He received the ACI Chester Paul Seiss Award in 2018 and the ACI Design Award in 2017.*

ACKNOWLEDGMENTS

This research was funded by the Concrete Reinforcing Steel Institute Foundation and this paper is based on the final findings of the funded project. The reinforcing bars used in the construction of the test specimens was generously donated by Headed Reinforcement Corporation.

REFERENCES

1. ACI Committee 318, "Building Code Requirements for Structural Concrete (ACI 318-19) and Commentary (ACI 318R-19) (Reapproved 2022)," American Concrete Institute, Farmington Hills, MI, 2019, 624 pp.

2. AASHTO, "AASHTO LRFD Bridge Design Specifications and Commentary," ninth edition, American Association of State Highway Transportation Officials, Washington, DC, 2020, 1912 pp.

3. Proestos, G.; Bae, G.; Cho, J.; and Bentz, E., "Influence of High-Strength Bars on Shear Response of Containment Walls," *ACI Structural Journal*, V. 113, No. 5, Sept.-Oct. 2016, pp. 917-927. doi: 10.14359/51688750

4. Munikrishna, A.; Hosny, A.; Rizkalla, S.; and Zia, P., "Behavior of Concrete Beams Reinforced with ASTM A1035 Grade 100 Stirrups under Shear," *ACI Structural Journal*, V. 108, No. 1, Jan.-Feb. 2011, pp. 34-41.

5. Lee, J.; Choi, I.; and Kim, S., "Shear Behavior of Reinforced Concrete Beams with High-Strength Stirrups," *ACI Structural Journal*, V. 108, No. 5, Sept.-Oct. 2011, pp. 620-629.

6. Yoshida, Y., "Shear Reinforcement for Large Lightly Reinforced Concrete Members," MASc thesis, Department of Civil Engineering, University of Toronto, Toronto, ON, Canada, 2000, 160 pp.

7. Lequesne, R. D.; O'Reilly, M.; Darwin, D.; Lepage, A.; Al-Sabawy, A.; Guillen, E.; and Spradling, D., "Use of Headed Bars as Shear Reinforcement," The University of Kansas Center for Research, Inc., Lawrence, KS, 2018, 256 pp.

8. Forest, S. B., "Anchorage of Single Leg Stirrups in Reinforced Concrete Slabs and Walls," MASc thesis, Department of Civil Engineering, University of Toronto, Toronto, ON, Canada, 2019, 253 pp.

9. Yang, Y.; Varma, A. H.; Kreger, M. E.; Wang, Y.; and Zhang, K., "Shear Strength of Reinforced Concrete Beams with T-Headed Bars for Safety Related Nuclear Structures," *Engineering Structures*, V. 230, 2021, p. 111705. doi: 10.1016/j.engstruct.2020.111705

10. CSA A23.3-19, "Design of Concrete Structures," CSA Group, Toronto, ON, Canada, 2019, 301 pp.

11. Palipana, D. K., "Assessment of Shear Transfer Mechanisms in reinforced Concrete Deep Beams from Experiments with Full Field-of-View Displacement Field Data," PhD thesis, North Carolina State University, Raleigh, NC, 2023. 440 pp.

12. Mihaylov, B. I.; Bentz, E. C.; and Collins, M. P., "Two-Parameter Kinematic Theory for Shear Behavior of Deep Beams," *ACI Structural Journal*, V. 110, No. 3, May-June 2013, pp. 447-456.

13. Trandafir, A. N.; Palipana, D. K.; Proestos, G. T.; and Mihaylov, B. I., "Framework for Crack-Based Assessment of Existing Lightly Reinforced Concrete Deep Beams," *ACI Structural Journal*, V. 119, No. 1, Jan. 2022, pp. 255-266.

14. Palipana, D. K.; Trandafir, A. N.; Mihaylov, B. I.; and Proestos, G. T., "Framework for Quantification of Shear Transfer Mechanisms from Deep Beam Experiments," *ACI Structural Journal*, V. 119, No. 3, May 2022, pp. 53-65.

15. ASTM A370-21, "Standard Test Methods and Definitions for Mechanical Testing of Steel Products," ASTM International, West Conshohocken, PA, 50 pp.

16. Proestos, G. T.; Palipana, D. K.; and Mihaylov, B. I., "Evaluating the Shear Resistance of Deep Beams Loaded or Supported by Wide Elements," *Engineering Structures*, V. 226, 2021, p. 111368. doi: 10.1016/j.engstruct.2020.111368

17. Palipana, D. K., and Proestos, G. T., "Large-Scale Shear Critical Reinforced Concrete Deep Beam Experiments Monitored with Full Field of View Digital Image Correlation Equipment," *26th International Conference on Structural Mechanics in Reactor Technology (SMiRT-26)*, Berlin/Potsdam, Germany, 2022.

18. Vecchio, F. J., and Collins, M. P., "The Modified Compression-Field Theory for Reinforced Concrete Elements Subjected to Shear," *ACI Structural Journal*, V. 83, No. 2, Mar.-Apr. 1986, pp. 219-231.

19. Vecchio, F. J., "Disturbed Stress Field Model for Reinforced Concrete: Implementation," *Journal of Structural Engineering*, ASCE, V. 127, No. 1, 2001, pp. 12-20. doi: 10.1061/(ASCE)0733-9445(2001)127:1(12)

20. Wong, P. S.; Vecchio, F. J.; and Trommels, H., "VecTor2 & FormWorks User's Manual," second edition, Toronto, ON, Canada, 2013.

21. Collins, M. P., and Mitchell, D., *Prestressed Concrete Structures*, Response Publication, Canada, 1997, 766 pp.

22. Joint ACI-ASCE Committee 445, "Strut-and-Tie Method Guidelines for ACI 318-19—Guide (ACI PRC-445-21)," American Concrete Institute, Farmington Hills, MI, 2021, 88 pp.

23. Li, Y.; Chen, H.; Yi, W.; Peng, F.; Li, Z.; and Zhou, Y., "Effect of Member Depth and Concrete Strength on Shear Strength of RC Deep Beams without Transverse Reinforcement," *Engineering Structures*, V. 241, 2021, p. 112427. doi: 10.1016/j.engstruct.2021.112427

ACI STRUCTURAL JOURNAL TECHNICAL PAPER

Title No. 121-S40

Seismic Performance of Gravity-Load-Designed Beam-Column Joints with Strain-Hardened Cementitious Composite

by B.S. Sindu and Saptarshi Sasmal

Beam-column (BC) joints are crucial components for ensuring the safety of structures during earthquakes. Various standards/codes (Eurocode 8, ACI 352R-02, and IS 13920:1993) prescribe special reinforcement detailing at the joint region to improve the seismic performance. Although extremely important, execution of the same is challenging due to heavy reinforcement congestion. In this regard, an attempt has been made in this study to develop a strain-hardened, high-performance cementitious composite (SHCC) with improved tension-related performance for seismic-resistant BC joints, which can potentially reduce the reinforcement demand. The efficacy of SHCC in improving the gravity-load-designed (GLD) BC joints without any additional reinforcement required for ductile detailing is investigated. Full-scale BC joint specimens were developed and subjected to reversed cyclic loading, and the critical seismic performance—such as hysteresis behavior, damage pattern, energy dissipation, shear deformation, and strength/stiffness degradation—were evaluated and compared with GLD specimens with normal concrete. It is observed that the GLD specimens with SHCC at the joint region showed remarkable performance. Without any additional confinement in the joint region, energy dissipation is doubled (100%), and shear deformation is only 40% of the GLD under the same drift demand. The findings of this study will help in developing seismic-resistant BC joints with the minimum reinforcement.

Keywords: beam-column (BC) joint; energy dissipation; hysteresis behavior; seismic upgradation; strain-hardened cementitious composite (SHCC).

INTRODUCTION

The structural integrity of framed reinforced concrete (RC) structures is primarily governed by the performance of the beam-column (BC) joints.[1,2] Utmost care has to be taken to appropriately design the BC joints to meet their functional requirements (to transfer vertical loads from beams and slabs to columns), strength requirements (to withstand vertical loads such as dead load, live load, and so on), and ductility requirements (to undergo inelastic deformation without significant reduction in load-carrying capacity during wind and seismic lateral loads).[1-3] Severe earthquakes in the past have shown that most multi-story buildings were severely damaged/completely collapsed due to the sudden shear failure of the rigid BC joints, causing huge losses to human lives and the economy.[4,5] Most existing RC structures have been designed only to withstand gravity loads, and hence, their performance becomes questionable during earthquakes. To prevent this brittle failure that causes devastating effects and to offer confinement to the concrete in the plastic hinge region, additional transverse reinforcements are suggested.[6-8] Most countries have improved their design codes to include clauses for ductile design and special detailing of BC joints to improve their ductility and offer seismic resistance. Though the addition of transverse reinforcements and special detailing improve the seismic resistance of the joints, the inherent weakness of concrete being brittle leads to the spalling of concrete at the joint region and prevents the joint from being able to withstand further deformation. Also, due to the strain incompatibility between steel and concrete, at higher drift ratios, interfacial slip occurs and leads to deterioration of the bond between them, leading to the failure of the joint.[9] The special and stringent reinforcement detailing also causes difficulty in the fabrication of reinforcement cages and consolidation of concrete at that region, leading to a vulnerable joint.[10]

To overcome these issues, attempts are being made to use fiber-reinforced concrete (FRC)/advanced cementitious composites at joint regions to reduce the reinforcement requirement. FRC possesses high strength, ductility, toughness, and damage-tolerant capabilities and can undergo deformation even after attaining peak load (improved post-peak behavior).[11-13] The presence of fibers controls the damage propagation by arresting the cracks and enables a better bond with the reinforcement, thereby improving the joint performance. The use of FRC in joint regions has proven to increase the shear strength, ductility, energy dissipation capacity, and reduce the reinforcement requirement. The specimens also demonstrated limited/stable damage progression and had inelastic deformation capabilities.[14,15] Attempts were also made to develop BC joints with FRC consisting of hybrid fibers to take advantage of each type of fiber. It was demonstrated that using FRC with hybrid fibers improved the hysteresis behavior, energy dissipation capacity, displacement ductility index, and showed a stable degradation in strength and stiffness.[16-19] However, increased fiber content causes workability issues, segregation, and balling of concrete. In the meantime, the performance of concrete with less fiber content is found to be ineffective due to the inadequacy of fiber in improving the material properties to the desired level.

ACI Structural Journal, V. 121, No. 3, May 2024.
MS No. S-2023-090.R2, doi: 10.14359/51740484, received September 18, 2023, and reviewed under Institute publication policies.

A superior alternative to FRC is high-performance cementitious composites (HPCCs), which are highly workable due to the absence of coarse aggregates and the inclusion of additives such as silica fume and fly ash at their optimum dosages.[20-22] Strain-hardened cementitious composite (SHCC) is a type of HPCC with high tensile strength (>4 MPa [0.58 ksi]) and large strain capacity (3 to 7%) that exhibits multiple microcracks (rather than the formation of a single macrocrack) and possesses strain-hardening behavior (increase in stress after peak stress), as opposed to the strain-softening behavior exhibited by FRC.[23-25] Because this type of remarkable and unconventional characteristic is achieved through meticulous engineering, SHCC is also termed as engineered cementitious composite (ECC). The large strain capacity and tolerance to damage make SHCC an ideal candidate for developing seismic-resistant BC joints. The incorporation of SHCC improved the ultimate strength, ductility, energy dissipation capacity, damage tolerance of the joint, and the maximum joint shear stress was found to be much below the seismic code recommendations (ACI 318-19).[20,26,27] The use of SHCC reduced the requirement of transverse reinforcements in beams, columns, and the joint region,[17,28] thereby improving the ease of fabrication without compromising the ductile behavior. Fischer and Li[29] carried out exhaustive experimental investigations on ECC BC joint specimens with different parameters, such as the percentage of transverse reinforcement and surface coating of fiber-reinforced polymer (FRP) reinforcements (ribbed or sanded), and demonstrated that FRP-reinforced ECC BC joints showed stable hysteresis behavior with minimum residual deflection and gradual damage progression, in comparison to normal concrete joints. SHCC is also a suitable candidate for seismic rehabilitation of existing structures. Due to the high-performance characteristics, jacketing can be done with a very thin SHCC panel and without additional stirrups, as opposed to normal concrete jacketing, therefore staying within the original structural dimensions.[30-32] Upgradation with SHCC is beneficial for existing structures with poor concrete quality or damaged/deteriorated substrate as it can overcome the debonding issues encountered by the conventional techniques involving FRP wrapping.[10] However, to achieve the appropriate performance, the concrete should be easily flowable and penetrate the existing reinforcements without any segregation.[33] Though extensive work has been carried out in the past, a holistic study of the development of easily workable SHCC and the design of BC joints (without additional transverse reinforcements) with the plastic hinge at a defined location in the beam pertaining to the needs of seismic-resistant structures has not yet been achieved.

In view of this, this study aims to develop easily workable SHCC, which can be used to develop seismic-resistant BC joints. The novelty of the present study lies in developing suitable material with strain-hardening properties for the BC joints, which are generally subjected to high shear during seismic loading. The present study has underlined two aspects: 1) without any additional confinement or special ductile detailing, the developed material can enable the BC joints to perform excellently under seismic loading; and 2) for conventional design with ductile detailing where congestion of reinforcement is always an issue, to ensure proper concrete compaction, the developed material will be a potential solution. Then, the efficacy of SHCC is evaluated by incorporating it in the joint region of a full-scale BC joint specimen where the reinforcements were provided according to the gravity load design (GLD) only. The reversed cyclic loading test with increasing drift ratios is carried out on the GLD-SHCC specimen (reinforcements pertaining to GLD with SHCC at the joint region), and its shear capacity, energy dissipation capabilities, damage tolerance, and seismic resistance are evaluated. The responses obtained from the specimen(s) with SHCC are also quantitatively compared with those of normal concrete GLD specimens.

RESEARCH SIGNIFICANCE

Reinforcement congestion and improper concreting due to difficulty in compaction are the two major challenges in the construction of seismic-resistant, framed RC structures. To overcome this issue, an attempt has been made in this study to develop an easily workable SHCC that can impart seismic resistance to the GLD structures. Performance in terms of hysteresis behavior, damage progression, strength/stiffness degradation, energy dissipation, shear deformation, and so on of full-scale BC joints is evaluated under reversed cyclic loading. The study suggests that the scheme will be useful for both new construction with less reinforcement and for upgrading existing GLD structures.

EXPERIMENTAL INVESTIGATION

Development of SHCC

The material constituents used for SHCC are cement (ordinary portland cement [OPC], Grade 53), silica fume, silica sand, polyvinyl alcohol (PVA) fibers, water, and high-range water-reducing admixture (HRWRA). The mixture proportions for developing the SHCC are cement, silica fume, and silica sand in the ratio of 1:0.7:0.7, with a water-binder ratio (w/b) (by weight) of 0.25 along with PVA fibers of 2% by volume of the dry mixture (cement, silica fume, and silica sand). The PVA fibers used in this study have a length of 8 mm (0.315 in.) and diameter of 40 μm (0.0016 in.) with a tensile strength and elastic modulus of 1600 MPa (232.06 ksi) and 41 GPa (5946.55 ksi). Measured quantities of cement, silica fume, and silica sand were mixed thoroughly in a concrete mixer. Then water with HRWRA was added to this mixture and mixed for 2 minutes. PVA fibers were added slowly to this mixture and mixed at 198 rpm for 5 minutes (Fig. 1). More details about the development of SHCC can be found elsewhere.[21,34,35]

Flow properties of SHCC

Proper concreting in the joint region is very important for proper load transfer from beams to columns and for withstanding the lateral loads experienced by the structure. However, due to practical difficulties, in most cases, concreting is poorly done at the joint regions with very little or no compacting. This challenge has been addressed in this study by developing highly flowable SHCC that requires minimal/no external compaction (self-consolidating concrete) at the joint region. Tests have been carried out

(results are presented in Table 1) to ascertain the flow characteristics, such as filling ability, passing ability, viscosity, and segregation resistance, as per the EFNARC[36] guidelines, and it has been observed that the SHCC developed in the present study meets the code recommendations for self-consolidating concrete. Figures 1(a) and (b) show the flowable nature of the developed SHCC.

Mechanical properties of SHCC

Tension-related properties of SHCC were evaluated in a high-precision, servo-hydraulic universal testing machine (UTM). Direct tension tests were carried out on a dog-bone-shaped specimen of dimensions 30 x 12.5 mm (1.18 x 0.49 in.) (as shown in Fig. 2(a)). The gauge length was kept at 80 mm (3.15 in.). An in-house fabricated fixture was used to hold the specimen while testing to prevent gripping failure. Two linear variable displacement transformers (LVDTs) (front and back) were attached to the specimen to measure the axial elongation. The test was carried out in a displacement control mode at a rate of 0.05 mm/min (0.002 in./min). Flexure and fracture tests were carried out on prism specimens of dimensions 40 x 40 x 160 mm (1.57 x 1.57 x 6.30 in.) (as shown in Fig. 2(b) and (c)). Specimens were subjected to three-point bending in a displacement control mode. The deflection of the specimens at midspan was recorded through an LDVT. For fracture tests, a notch of 2 mm (0.079 in.) thickness was created at the center of the specimen for a depth of 12 mm (0.47 in.). Two knife edges were pasted at the bottom of the specimen adjacent to the notch on both sides. A crack mouth opening displacement (CMOD) gauge was affixed to the knife edges to record the CMOD. Six specimens of each type were tested to determine the properties.

Figure 3(a) shows the stress versus strain response obtained from direct tension tests. The strain data presented in this figure are calculated from the elongation recorded in

(a) (b)

Fig. 1—(a) Flowable nature of SHCC; and (b) J-ring test to evaluate the self-consolidation of SHCC.

Table 1—Flow properties of SHCC

Test parameter	Test method	Measured value	Code recommendations
Filling ability	Slump flow	D_s = 795 mm	650 to 800 mm
	T_{50} slump flow	T_{50} = 2.75 seconds	2 to 5 seconds
	V-funnel	T = 10 seconds	6 to 12 seconds
Passing ability	J-ring	$H_2 - H_1$ = 6.75 mm	0 to 10 mm
	U-box	$(H_2 - H_1)$ = 0 mm	0 to 30 mm
	L-box	H_2/H_1 = 0.94	0.8 to 1.0
Segregation resistance	V-funnel	$T_{5minutes}$ = 12 seconds	T to $(T + 3)$ seconds

Note: D_s is final average diameter of mixture in slump flow test; T_{50} is time taken for SHCC to reach 500 mm spread circle in slump flow test; T is time taken for SHCC to get discharged fully in V-funnel test; $T_{5minutes}$ is time taken for SHCC to get discharged fully after allowing it to stand for 5 minutes in V-funnel test; 1 mm = 0.039 in.

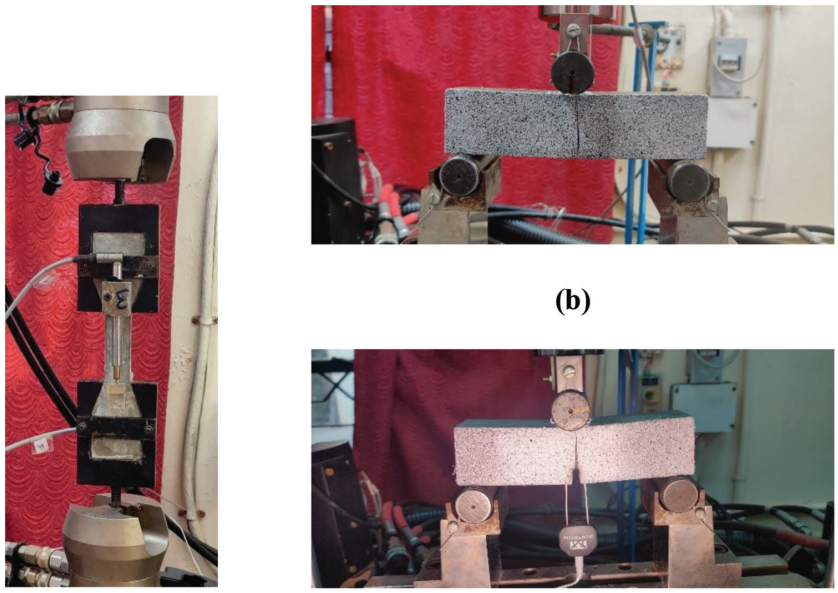

(a) (b) (c)

Fig. 2—Experimental test setup to determine mechanical properties of SHCC: (a) direct tension test; (b) flexure test; and (c) fracture test.

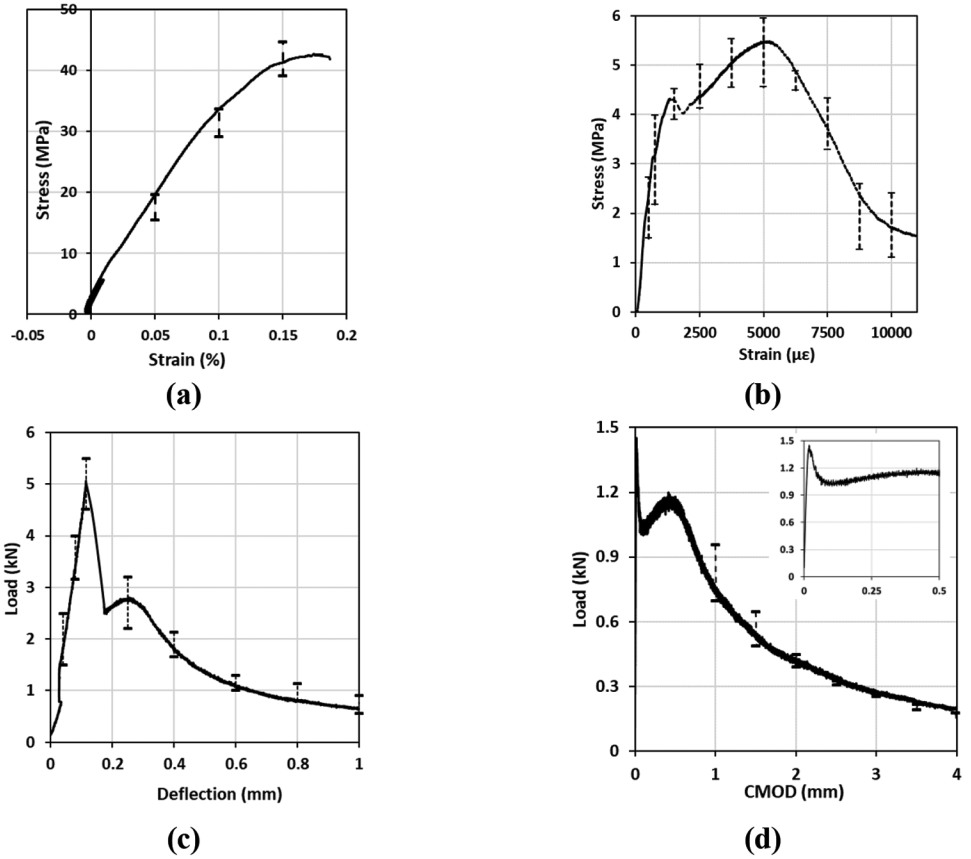

Fig. 3—(a) Stress-versus-strain response obtained from cylinder compression test; (b) stress-versus-strain response obtained from direct tension test; (c) load-versus-deflection response obtained from flexure test; and (d) load-versus-CMOD response obtained from fracture test. (Note: 1 MPa = 0.145 ksi; 1 kN = 0.225 kip; 1 mm = 0.039 in.)

Table 2—Mechanical properties of SHCC and reference concrete mixture

Test	Property	SHCC	Normal concrete
Cylinder compression	Compressive strength	43 MPa (6.24 ksi)	35 MPa (5.08 ksi)
	Elastic modulus	64 GPa (9.28 × 10^3 ksi)	23 GPa (3.34 × 10^3 ksi)
Direct tension	Tensile strength	5.49 MPa (0.80 ksi)	3.5 MPa (0.51 ksi)
	Strain capacity (considering 40% residual strength)	9000 με	—
Flexure	Flexural strength	17.58 MPa (2.55 ksi)	5.9 MPa (0.86 ksi)
	Energy dissipation capacity	1.68 × 10^{-3} J (0.00124 ft·lb)	—
Fracture	Fracture energy	1453.30 J/m^2 (0.69 ft·lb/in.^{2})	268.75 J/m^2 (0.13 ft·lb/in.^{2})

the LVDTs. The stress-strain response of SHCC shows the promising strain-hardening behavior post the pseudo-yield strength. This phenomenon is observed due to the formation of chemical bonds in addition to the mechanical bonds formed between the fiber and the matrix, causing efficient crack bridging and multiple cracking (when a crack forms, fibers in the matrix bridge the crack, causing the formation of cracks at the adjacent location and closing the current active crack). This process delays the failure of the composite, leading to improved strain capacity. The strain capacity (considering 40% residual strength) of SHCC developed in this study is found to be 9000 με with an ultimate strength of 5.49 MPa (0.80 ksi).

From the load-versus-deflection response (Fig. 3(b)) obtained from flexure tests, the strain-hardening phenomenon can be observed after the sudden drop in load from the peak load. The observed strain-hardening phenomenon is due to the crack bridging by the PVA fibers, which form the chemical bonds in addition to the mechanical bonds with the surrounding cementitious matrix. This strain-hardening behavior is also responsible for the high energy dissipation capacity (1.68 × 10^{-3} J [0.00124 lb·ft]) of SHCC. Similar behavior can also be witnessed in the load versus CMOD response obtained from the fracture tests. Table 2 presents the mechanical properties of SHCC determined from the compression, direct tension, flexure, and fracture tests. From the mechanical tests carried out on hardened SHCC, it has been found that the fracture energy of the developed material is 1453.30 J/m^2 (0.69 ft·lb/in.^{2}) (compared to 268.75 J/m^2 [0.13 ft·lb/in.^{2}] for reference concrete used in the present study and also 50 to 150 J/m^2 [0.024

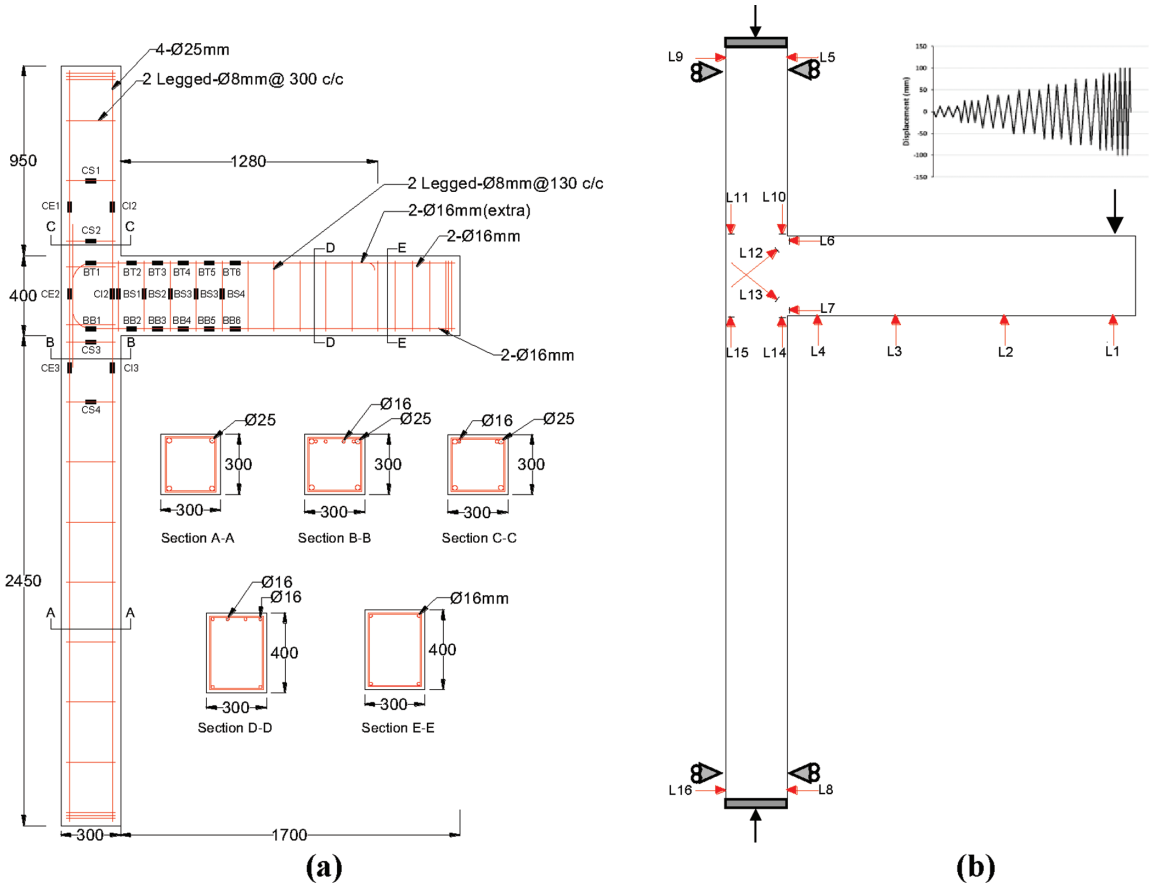

Fig. 4—(a) Geometry and reinforcement details of BC joint specimen considered in this study along with strain gauge locations; and (b) LVDTs placed for measuring beam deflection (L1 to L4), joint rotation (L6, L7, L10, L11, L14, and L15), shear deformation (L12 and L13), and column buckling (L5, L8, L9, and L16). (Note: 1 mm = 0.039 in.)

to 0.071 ft·lb in.^{2}] for normal concrete with compressive strength of 30 to 70 MPa [4.35 to 10.15 ksi][37]).

SHCC FOR SEISMIC UPGRADATION OF BEAM-COLUMN JOINTS

Beam-column joint specimen details

The performance of SHCC with high strain capacity, energy dissipation capacity, and fracture energy in enhancing the hysteresis performance of GLD BC joints is investigated in detail. A full-scale exterior BC joint with the beam cross section of 400 x 300 mm (15.75 x 11.81 in.) and column cross section of 300 x 300 mm (11.81 x 11.81 in.) is considered for this purpose. The dimensions of the members and reinforcements provided are based on the design of a typical exterior BC joint of a three-bay, three-story RC framed building for the maximum bending moment under different load combinations (dead load, superimposed dead load, and live load) as per the codal provisions. More details on the analysis and design can be found elsewhere.[38] The disposition of the member length of the subassemblage (the BC joint with the appropriate length of beam and upper/lower columns) is done in such a way as to maintain the joint shear and joint face moments obtained from the numerical analysis of the full structure. The details of the specimen geometry, including the reinforcement details, are provided in Fig. 4. Steel reinforcements with a yield strength of 500 MPa (Fe 500) (72.52 ksi) were used in this study. Four 25 mm (0.98 in.) diameter bars were provided as main reinforcements in columns, along with two-legged 8 mm (0.31 in.) diameter stirrups with a spacing of 300 mm (11.81 in.) center-to-center. Two 16 mm (0.63 in.) diameter bars were provided as reinforcements in both the top and bottom of the beams, with an additional two 16 mm (0.63 in.) diameter bars at the top. Two-legged 8 mm (0.31 in.) diameter stirrups were placed at a spacing of 130 mm (5.12 in.) center-to-center. All the main reinforcements from the beams were extended for a length of 525 mm (20.67 in.) in the columns. The reinforcement details at different sections are also shown in Fig. 4.

To reduce the complexities involved in providing reinforcements as per ductile detailing, an attempt has been made to use SHCC in the GLD BC subassemblage, which can withstand the seismic load without any intervention on the reinforcement detailing just by replacing the concrete in the joint portion with ductile SHCC. To quantitatively determine the enhancement in properties due to SHCC, two types of specimens are considered in this study: one with normal concrete (properties provided in Table 2) throughout, and the other with SHCC in the joint region.

Initially, a reinforcement cage was made ready with the detailing shown in Fig. 5(a). Strain gauges were pasted on the reinforcements in the joint region to get a complete picture of the strain distribution in this localized area. The reinforcement cage was then placed in the steel mold with appropriate cover thickness. For the reference specimen, normal

(a) (b)

Fig. 5—(a) Reinforcement cage as per requirements of GLD (inset picture shows strain gauges pasted in joint region); and (b) seismically upgraded GLD BC joint subassemblages (by providing SHCC at joint region).

concrete with a mixture of cement to fine aggregate to coarse aggregate in the ratio of 1:2.25:2.35 is used. For developing the GLD specimen with SHCC at the joint region, wooden planks were used as separators between normal concrete and SHCC. A portion of normal concrete was filled near the joint portion to hold the wooden planks sturdily. Then, the joint portion was filled with SHCC. Finally, concrete was filled in the remaining portion, and the surface was finished smoothly. The curing of the specimens was carried out for 28 days using wet gunny bags.

Test protocol and instrumentation details

To assess the seismic performance of the joint, specimens were subjected to reversed cyclic loading in a displacement control mode. The specimen was laid on the floor, and the tip of the beam was subjected to load in the horizontal direction using a computer-controlled servo-hydraulic actuator. To allow rotation of the specimen and movement of the actuator, rollers were placed below the specimen and the actuator. The tests were carried out while the column was under a constant axial load to replicate the phenomenon observed in the actual structure. The axial load of 300 kN (67.44 kip) was applied using a hydraulic jack at one end of the column while rigidly supporting the other end. Load cells were placed on both ends of the column (between the column end and hydraulic jack and between the other column end and bulkhead) to monitor the axial force applied while testing.

Reversed cyclic loading was applied in terms of drift ratio, which is the measure of displacement with respect to the free length of the beam.

$$\text{Drift ratio (\%)} = \frac{\Delta l}{L} \cdot 100 \quad (1)$$

where Δl is the applied displacement at the tip of the beam (mm); and L is the free length of the beam (from the column face) (mm).

The displacement time history adopted in this study is presented in the inset graph in Fig. 6. The displacements are applied in the increments of 12.5 mm (0.49 in.) (drift ratio of 0.735%). To get a stabilized response (crack stabilization), at each drift ratio, three load cycles were applied. The response of the specimen during the loading cycles was monitored using LVDTs. Four LVDTs were mounted along the length of the beam at each of the L4 locations, starting from L1 at the tip of the beam up to L4 near the column face, to measure the beam deflection. To capture the joint rotation, six LVDTs were placed near the joint: two at the beam end (L6 and L7), two at the edge of the top column (L10 and L11), and two at the edge of the bottom column (L14 and L15). To capture the joint shear deformation, two LVDTs (L12 and L13) were placed in the joint region in a diagonal fashion, as shown in Fig. 6. The test arrangement, along with the hydraulic jack and instrumentation setup, is shown in Fig. 6.

RESULTS AND DISCUSSION

The responses of the GLD specimen and seismically upgraded GLD specimen with SHCC at the joint region (GLD-SHCC) under reversed cyclic loading are analyzed in detail to evaluate the efficacy of SHCC in improving the seismic resistance of the BC joint.

Hysteresis behavior

The load versus displacement responses (measured from the actuator) of the GLD and GLD-SHCC specimens are presented in Fig. 7. It can be observed that both the load-carrying capacity and the deformability are high in the case of the GLD specimen with the SHCC joint. In both cases (GLD and GLD-SHCC), the load-carrying capacity is higher during loading in the negative direction (causing tension in the beam top) than the load-carrying capacity in the positive direction (causing tension in the beam bottom). In the GLD specimen, peak load was attained at 37.5 mm (1.48 in.) displacement during loading in the negative direction. However, for the displacement levels from 25 to 50 mm (0.98 to 1.97 in.), the load-carrying capacity remained almost stable. Due to a further increase in drift demand (displacement), major cracks started to appear, and the load-carrying capacity of the specimen started decreasing.

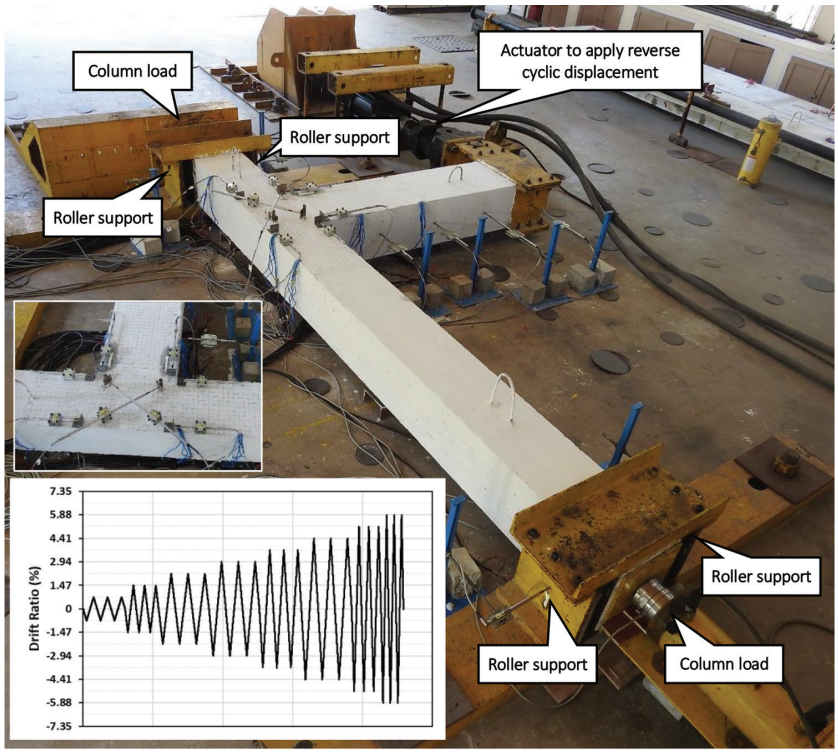

Fig. 6—Test arrangement for investigating efficacy of BC joint subassemblages under reversed cyclic loading (inset picture shows LVDT arrangements in joint region); and (inset graph) displacement (in terms of drift) time history applied at tip of beam.

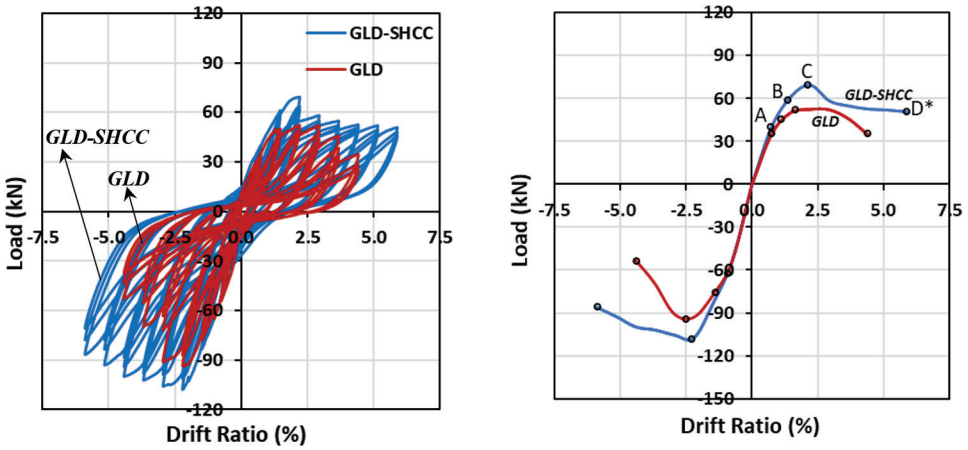

Fig. 7—(a) Hysteresis behavior of GLD and GLD-SHCC specimens under reversed cyclic loading; and (b) envelope curve of load-versus-displacement response. (Note: 1 kN = 0.225 kip.)

During the loading in the positive direction, the peak load is also attained at 37.5 mm (1.48 in.) displacement. On further increase in displacement, the load-carrying capacity drops drastically. Hence, the application of reversed cyclic loading was stopped at 75 mm (2.95 in.) displacement (corresponding to a drift ratio of 4.41%).

In the GLD-SHCC specimen, during the loading in the negative direction, the peak load was attained at 37.5 mm (1.48 in.) displacement. On further increase in displacement, the load-carrying capacity dropped suddenly by approximately 16%; thereafter, the reduction remained very low/stable. During the loading in the positive direction, the peak load was attained at 37.5 mm (1.48 in.) displacement, and with a further increase in displacement up to 100 mm (3.94 in.), the load-carrying capacity reduced in a stable manner, with the final reduction of approximately 20% of peak load. Because 100 mm (3.94 in.) displacement (corresponding to the drift ratio of 5.88%) is very high for seismic-resistant structures, reversed cyclic loading on the GLD-SHCC specimen was stopped at that displacement demand. The load-carrying capacity of GLD-SHCC is found to be 32.57% higher (during loading in the negative direction) and 15.32% higher (during loading in the positive direction) than the GLD specimen. Though the improvement

level is less at peak load on the negative side, at 75 mm (2.95 in.) displacement, the load capacity is improved by 89.26% due to the replacement of normal concrete in the joint region with SHCC. However, on the positive side, at 75 mm (2.95 in.) displacement level, the improvement in load capacity is by 52.75%.

Damage progression with increase in drift demand

The crack development/damage pattern of GLD and GLD-SHCC specimens is monitored for different displacement levels (drift ratios) during positive and negative displacement cycles. There is a significant difference in the crack pattern between GLD and GLD-SHCC specimens, indicating the change in the mode of failure between the two specimens. The crack patterns of the GLD and GLD-SHCC specimens at different drift demands are presented in Fig. 8.

The crack pattern of the GLD specimen after three reversed loading cycles with drift ratios of 0.74 and 1.47% shows uniformly spaced flexural cracks in both the top and bottom of the beam adjacent to the joint region. A few horizontal cracks developed near the joint region in the bottom column. Additionally, a few diagonal cracks were also formed parallel to the L12 LVDT. Further, after two sets of reversed cyclic loading with drift ratios of 2.21 and 2.95%, the previously developed diagonal crack widened along with the formation of another wide diagonal crack perpendicular to it, creating an X-shaped crack pattern. In addition, a wide vertical crack developed parallel to the column exterior face at approximately 50 mm (1.97 in.) away from the column face and at the interior column face in the region connected to the beam. Further, after another two sets of reversed cyclic loading cycles with drift ratios of 3.69 and 4.43%, the earlier developed diagonal and vertical cracks further widened; thus, a drastic reduction in the strength and stiffness of the specimen was observed. A large number of equally spaced horizontal cracks formed along the length of the bottom column. Many new diagonal cracks and their branches also developed in the joint region. Spalling of concrete was observed near the X-shaped diagonal crack and between the diagonal and vertical cracks. Upon further loading until failure, most parts of the concrete in the joint region from the column external face to the intersection of the X-shaped crack wedged out, creating a wide V-shaped failure, as shown in Fig. 9(a).

The GLD-SHCC specimen also exhibited uniformly spaced flexural cracks in both the top and bottom of the beam adjacent to the joint region at initial drift cycles, and equally spaced horizontal cracks in the column. The major difference is that there were a greater number of flexural cracks in the top of the beam than in the bottom of the beam, leaving some of the top cracks up to the midheight of the beam, whereas, in the GLD specimen, all the top flexural cracks were connected. The horizontal cracks formed in the column were more closely spaced and for a much longer column length. One X-shaped crack formed from two diagonal cracks was present in addition to another diagonal crack parallel to the L12 LVDT. After two sets of reversed cyclic loading with drift ratios of 2.21 and 2.95%, a significant vertical crack formed at the inner face of the column in the region connecting to the beam. The widening of diagonal cracks did not occur in the GLD-SHCC specimen; instead, many new diagonal cracks formed, forming multiple X-type cracks. Many new horizontal cracks developed in the column exterior face, reducing the spacing between the cracks. Further, under increased drift demand, that is, drift ratios of 3.69 and 4.43%, one diagonal crack (parallel to the L13 LVDT) widened along with the vertical crack formed in the column inner face. This is in addition to the formation of a large number of fine horizontal cracks in the column external face, making the spacings between them very small (≈10 to 25 mm [0.39 to 0.98 in.]). Because the damage to the GLD-SHCC specimen was less, it was subjected to higher loading. After two sets of reversed loading cycles with drift ratios of 5.17 and 5.88%, two diagonal cracks parallel to the L12 LVDT (perpendicular to the previously developed diagonal crack) were found to widen further. Additionally, multiple new fine cracks and crack branches were formed in the beam, column, and joint region. This is the signature nature of SHCC material: it is capable of forming multiple crack paths due to the crack bridging by the PVA fibers; in contrast, in normal concrete, once a crack is formed, it widens, and failure takes place. Another interesting fact is that no spalling of concrete was observed even after the displacement level of 100 mm (3.94 in.) (drift of 5.88%). The specimen was subjected to monotonic loading up to 120 mm (4.72 in.) displacement, and the test was stopped. The final damage pattern of the specimen is shown in Fig. 9(b). The crack bridging by the well-distributed PVA fibers can also be witnessed in this figure.

Development of strain in reinforcements

Strain development along the beam longitudinal reinforcement, starting from the column face toward the loading point at the beam bottom (BB2 to BB6) in both the GLD and GLD-SHCC specimens, is presented in Fig. 10(a) and (b), respectively, for different drift ratios. From the figures, it can be observed that the strain distribution in the GLD and GLD-SHCC specimens is different. In the GLD specimen, the maximum strain develops closer to the column face, and as the distance from the column face increases, the strain monotonically decreases. The yielding of reinforcement near the BC interface starts after the drift ratio of 1.47% (witnessed by the reinforcement strain greater than 2500 με). Once the yielding of reinforcement started, the zone became weak, causing further deterioration in that area. However, in the case of the GLD-SHCC specimen, strain development seems to be constant along a certain portion of the beam, depicting distributed regions of distress. The yielding of reinforcement near the BC interface of the GLD-SHCC specimen also started after the drift ratio of 1.47%. A further increase in drift ratio increased the strain in the joint region, and the strain gauge was subsequently damaged (found from the received strain data). An interesting phenomenon observed in the GLD-SHCC specimen is that the yielding of reinforcement occurred even far away from the face of the column. The constant strain above 2500 με from 200 to 600 mm (7.87 to 23.62 in.) from the face of the column indicates that the damage is not concentrated at

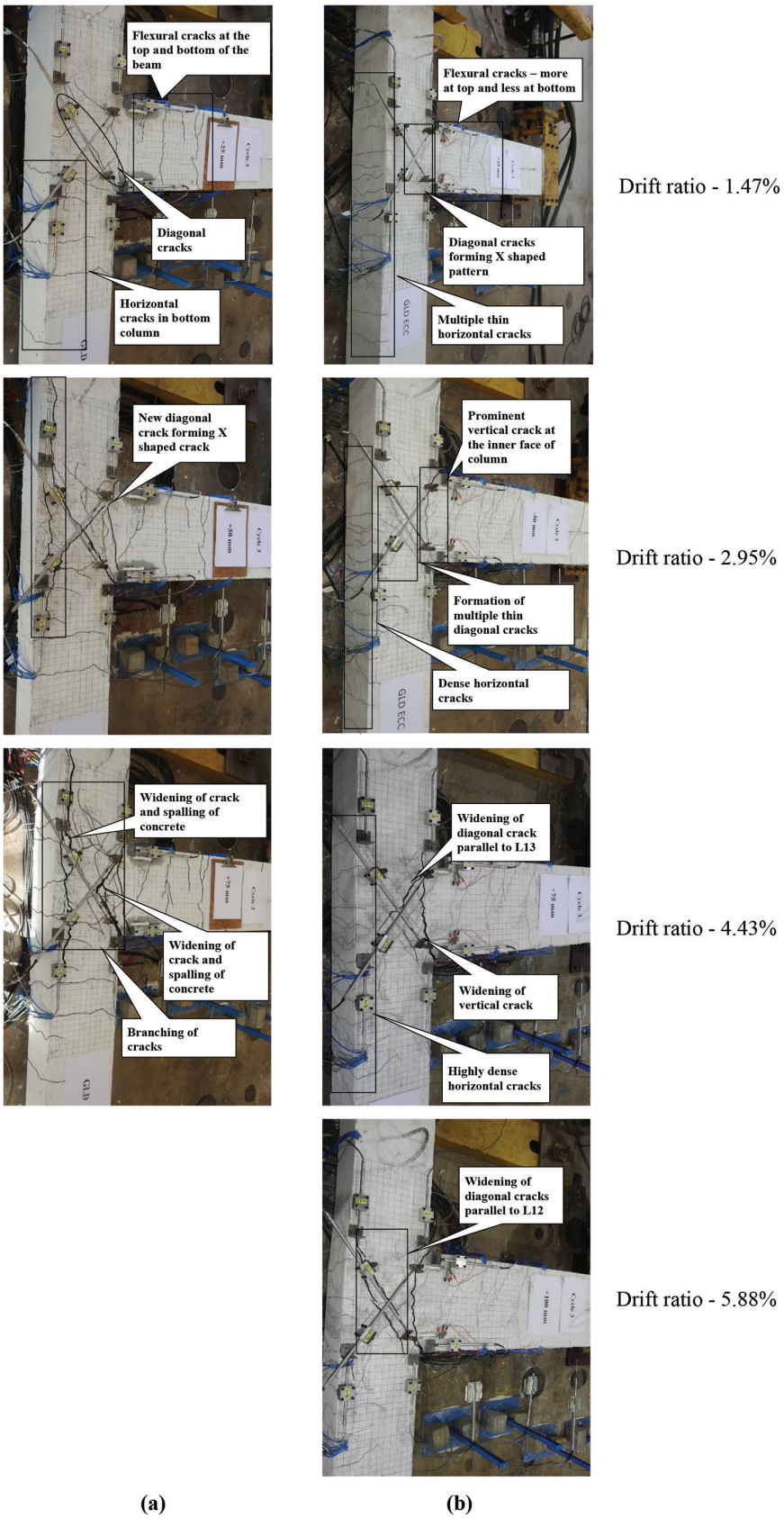

Fig. 8—Damage pattern of: (a) GLD; and (b) GLD-SHCC specimens during different displacement levels.

a particular location and is distributed, thereby increasing the capacity of the joint. The same can also be witnessed in Fig. 10(b). Multiple damage sites also pave the way for higher energy dissipation capacity of the component. It should be mentioned that the replacement of concrete in the joint portion with SHCC shifted the plastic hinge formation away from the column face and led to the development of a long plastic hinge zone (rather than at a concentrated

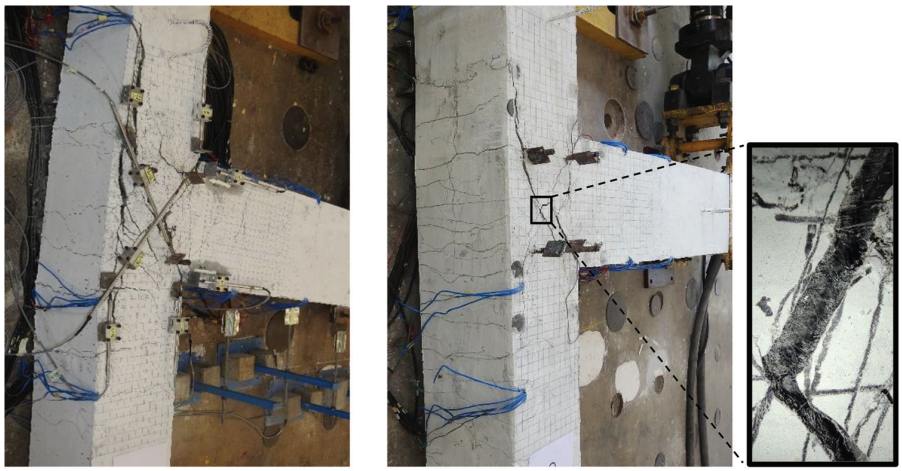

(a) (b)

Fig. 9—Final damage pattern of: (a) GLD; and (b) GLD-SHCC specimens.

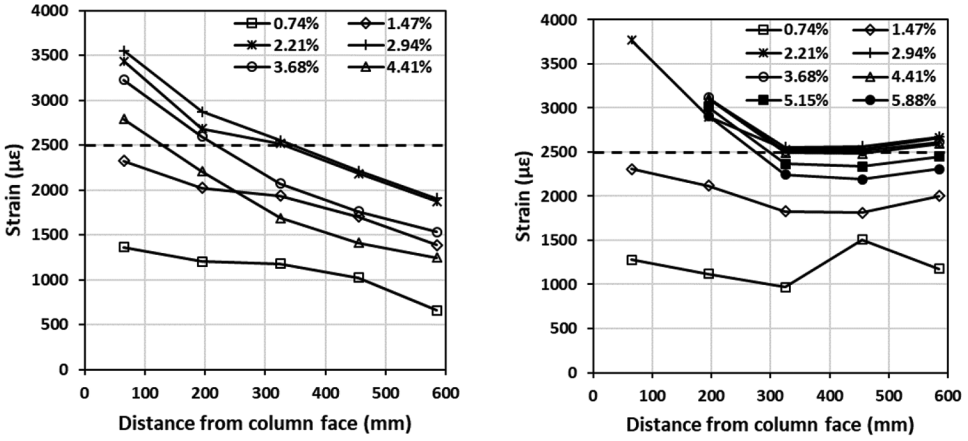

(a) (b)

Fig. 10—Strain development at beam bottom during different drift ratios: (a) GLD; and (b) GLD-SHCC specimens.

location) in the beam, which is very favorable behavior to prevent collapse of multi-story buildings.

Strength and stiffness degradation

The strength degradation of the GLD and GLD-SHCC specimens for different displacement levels (drift ratios) during positive and negative load cycles is presented in Fig. 11(a). The strength of the GLD specimen during the positive load cycle is 52.23 kN (11.74 kip), and during the negative load cycle is 93.4 kN (21 kip). During both cycles (positive and negative), the specimen attains its strength at 37.5 mm (1.48 in.) displacement (2.21% drift ratio). When the displacement level was increased to 50 mm (1.97 in.) (2.95% drift ratio), the strength reduced nominally (less than 3%). On a further increase in displacement, the strength dropped drastically. For a drift ratio of 4.43%, the reduction in strength amounts to 34% and 43% during the positive and negative load cycles, respectively. The strength of the GLD-SHCC specimen is 69.24 kN (15.57 kip) during the positive cycle and 107.71 kN (24.21 kip) during the negative cycle. Similar to the GLD specimen, the specimen attains its strength at 37.5 mm (1.48 in.) displacement in both the positive and negative load cycles. The degradation in strength of the GLD-SHCC specimen was initially very high (16% for a drift ratio of 2.95%), which stabilized later. The maximum degradation in strength for a drift ratio of 5.89% is very low (20% during negative displacement and 27% during positive displacement). The most interesting phenomenon observed from the plot is the steep and linear degradation of strength in the case of the GLD specimen compared to the nonlinear degradation of strength in the GLD-SHCC specimen. A change in the slope of the strength degradation curve is observed at a drift ratio of 4.43% in the GLD-SHCC specimen, with degradation happening at a reduced pace during positive displacement and at a faster pace during negative displacement beyond that.

Similar to strength degradation, the stiffness of the specimen also degraded during reversed cyclic loading with increased displacement levels. The stiffness degradation of the BC specimen is evaluated in terms of secant stiffness (slope of one complete reversed loading cycle, as shown in the inset figure in Fig. 11(b). The stiffness degradation of

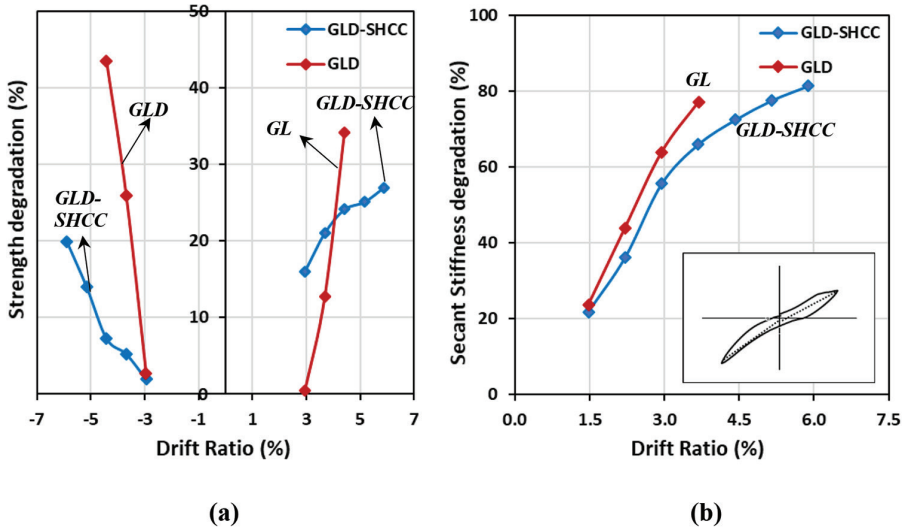

Fig. 11—(a) Strength degradation; and (b) secant stiffness degradation of GLD and GLD-SHCC specimens under reversed cyclic loading.

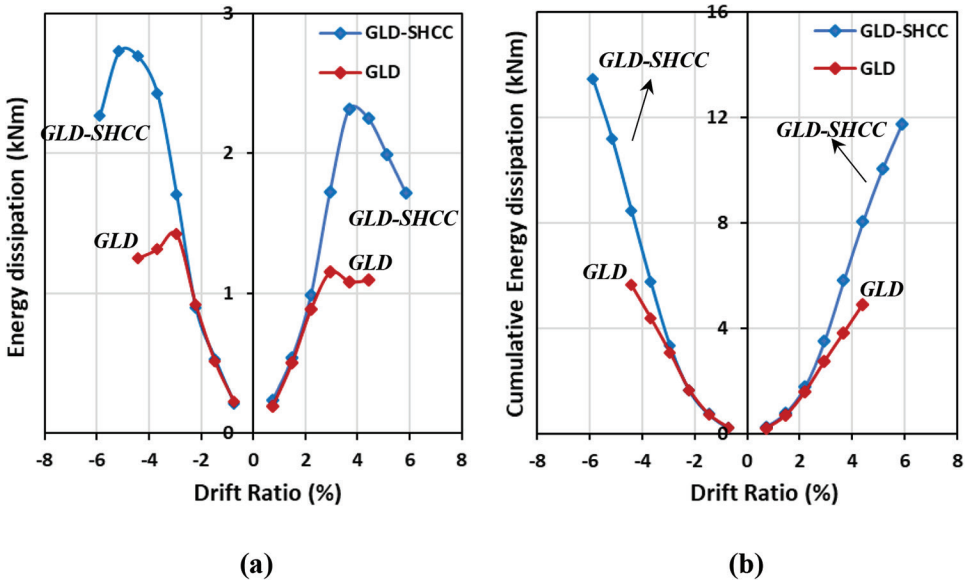

Fig. 12—(a) Energy dissipated; and (b) cumulative energy dissipated by GLD and GLD-SHCC specimens during reversed cyclic loading. (Note: 1 kN·m = 737.56 lb·ft.)

both the GLD and GLD-SHCC specimens started at a drift ratio of 1.5%. The stiffness degradation of the GLD and GLD-SHCC specimens was almost similar up to a drift ratio of 3%, with the GLD showing a slightly higher degradation than the GLD-SHCC specimen. However, after a drift ratio of 3%, the stiffness degradation of the GLD-SHCC specimen slowed down drastically (this can be interpreted from the change in slope of Fig. 11(b)). However, in the case of the GLD specimen, the rate of stiffness degradation is very minor. At a drift ratio of 3.68%, the stiffness degradation of the GLD specimen was 16.88% higher than the GLD-SHCC specimen. The maximum degradation in stiffness of 77% is observed in the GLD specimen at a drift ratio of 3.68%. A similar level of stiffness degradation takes place in the GLD-SHCC specimen at a drift ratio of 5.15%.

Energy dissipation

Energy dissipation capacity is a key property that dictates the performance of the BC joint under seismic loading. It is a measure of the area under the load-displacement curve. The higher the energy dissipation capacity, the higher the chances of the joint to withstand seismic events, which eventually averts the collapse of structures. Figure 12(a) shows the energy dissipated by the GLD and GLD-SHCC specimens during positive and negative drift scenarios. During the initial stages (up to a drift ratio of 2.21%), the energy dissipated by the GLD and GLD-SHCC specimens is nearly the same. However, during higher drift ratios, the energy dissipation capacity of the GLD-SHCC specimen is very high compared to the GLD specimen. At a drift ratio of 2.94%, the energy dissipated by the GLD-SHCC specimen is 50% higher than the GLD specimen during positive drift and 20% higher during negative drift. Beyond this displacement level, the ability of the GLD specimen to dissipate energy reduced

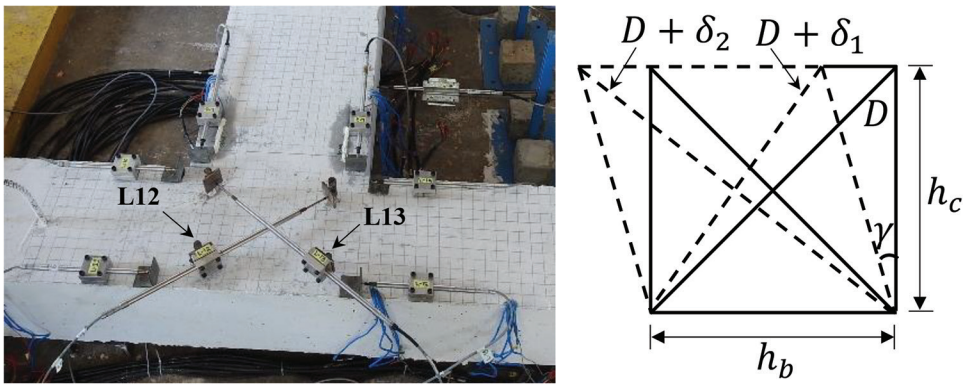

(a) (b)

Fig. 13—(a) Instrumentation for measuring joint shear deformation; and (b) schematic representation of joint distortion.

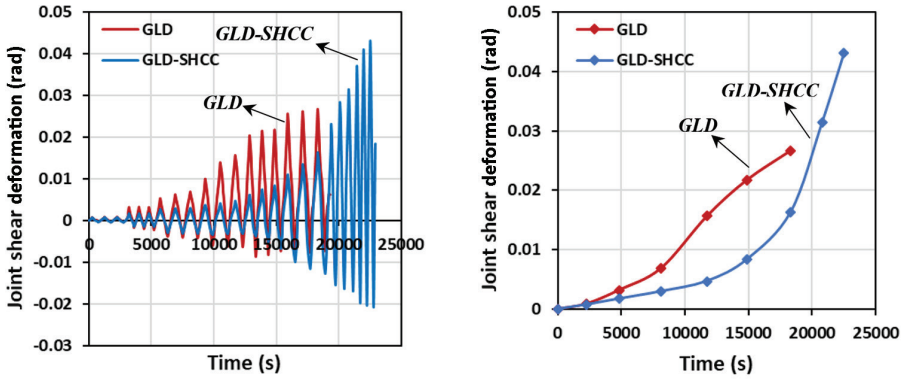

(a) **(b)**

Fig. 14—(a) Joint shear deformation of GLD and GLD-SHCC specimens; and (b) envelope of positive shear deformation.

owing to higher deterioration of the specimen. However, in the case of the GLD-SHCC specimen, the ability to dissipate energy reduced after a drift ratio of 3.68% during positive displacement and 5.15% during negative displacement. The cumulative energy dissipated (Fig. 12(b)) by the GLD-SHCC specimen is 64% higher than the GLD specimen up to a drift ratio of 4.41% during positive displacement and 50% higher during negative displacement. The cumulative energy dissipated by the GLD-SHCC specimen up to 100 mm (3.94 in.) displacement (5.88% drift ratio) is 11.76 and 13.45 kN·m (8373.73 and 9920.21 lb·ft) during positive and negative displacement cycles.

Shear deformation

Shear deformation/distortion of BC joints is an important aspect to consider during the seismic design of structures. As per the guidelines of FEMA 273,[39] the allowable limits for joint shear distortion in terms of the shear angle (γ) is 0.005 rad at peak strength and 0.01 rad at the collapse stage. To determine the shear angle of the BC joint, the deformation measurements from two diagonal LVDTs (L12 and L13) were used (shown in Fig. 13(a)). The shear angle (the angle between the undistorted and distorted joints) (Fig. 13(b)) was calculated using the procedure established in Sasmal et al.,[40] according to which

$$\gamma = \frac{(2D + \delta_1 + \delta_2)(\delta_2 - \delta_1)}{4h_c h_b} \quad (2)$$

where h_b is the depth of the beam (400 mm [15.75 in.]); h_c is the width of the column (300 mm [11.81 in.]); and D is the diagonal length (500 mm [19.69 in.]). After deformation, the diagonal lengths get altered to ($D + \delta_1$) and ($D + \delta_2$). The deformation of diagonals δ_1 and δ_2 are obtained from LVDTs L12 and L13, respectively. The shear angle thus obtained for the GLD and GLD-SHCC specimens is presented in Fig. 14(a), and the envelope of positive shear deformation is presented in Fig. 14(b). From the figure, it can be identified that the shear deformation of the GLD specimen is much higher than that of the GLD-SHCC specimen. The allowable shear deformation at the collapse of 0.01 rad was reached in the GLD specimen at a drift ratio of 2.94%, during which the GLD-SHCC specimen had undergone deformation of only 0.0027 rad (72.73% less). This allowable collapse level deformation was achieved by the GLD-SHCC specimen at a drift ratio of 4.41% (50% higher drift ratio than GLD). The maximum shear deformation experienced by the GLD specimen is 0.027 rad at a drift ratio of 4.41%, and in the case of the GLD-SHCC specimen, it is 0.043 rad at a drift ratio of 5.58%.

Displacement ductility

The displacement ductility of the BC joints is determined using the method suggested in the literature.[41,42] From the envelope curve of the hysteresis load versus displacement response, points corresponding to first concrete cracking (A), steel yielding (B), maximum stress (C), and joint failure (D) are determined (as shown in Fig. 7(b)). The points corresponding to the first change in stiffness denote concrete cracking, and the second change in stiffness denotes reinforcement yielding. The displacement ductility is determined from the ratio of displacements at joint failure and reinforcement yielding (Δ_u/Δ_y). In the GLD-SHCC specimen, the point D is marked with the asterisk as it does not correspond to actual failure (instead, the test was halted due to excessive displacement). Accordingly, the displacement ductility of the GLD specimen was found to be 3.75, and the GLD-SHCC specimen was found to be greater than 5.

CONCLUSIONS

The development of a novel strain-hardened cementitious composite (SHCC) with high tensile properties and self-consolidating capabilities and the application of the developed material for seismic-resistant beam-column (BC) joints with the minimum reinforcement are discussed in the present study. The technique for developing less congested joints with SHCC can be used to develop congestion-free joints with seismic-resistant capabilities. Material-level tests were carried out to evaluate the primary tensile properties of SHCC and its ability for self-consolidation. Then, component-level reversed cyclic loading tests were carried out to demonstrate the seismic-resistant capabilities of the newly developed BC joints (gravity load-designed [GLD] specimens with SHCC at the joint region: GLD-SHCC). Some of the key conclusions drawn from this study include:

1. From the material-level tests carried out on SHCC, it has been found that its tensile strength is 5.49 MPa (0.80 ksi), its energy dissipation capacity is 1.68×10^{-3} J (0.00124 ft·lb), and its fracture energy is 1453.30 J/m^2 (0.69 ft·lb/in.^{2}). It also possessed the capabilities required for self-consolidating concrete as per the code recommendations.

2. The hysteresis behavior of the GLD-SHCC specimen showed improved load-carrying capacity and deformability compared to GLD. The load-carrying capacity of GLD-SHCC is 32.57% higher than GLD in the positive direction and 15.32% higher in the negative direction. The GLD specimen could not withstand the drift demand of more than 2.95% (with reasonable strength degradation) due to high damage at this displacement level. However, the GLD-SHCC specimen could be displaced up to 5.88% drift with minimum damage (fewer adverse cracks and less strength/stiffness degradation).

3. The damage pattern of the GLD specimen showed a brittle shear failure with an X-shaped crack pattern at the joint, and a significant amount of spalling of concrete was observed. However, in the GLD-SHCC specimen, the damage was distributed with finer cracks, and the plastic hinge zone was away from the column face and for a longer portion of the beam.

4. The degradation in strength and stiffness is also considerably less in the GLD-SHCC specimen than in the GLD specimen. The maximum degradation in stiffness of 77% was observed in the GLD specimen at a drift ratio of 3.68%. A similar level of stiffness degradation happened in the GLD-SHCC specimen at a much higher drift ratio (5.15%).

5. The cumulative energy dissipated by GLD-SHCC is greater than 10 kN·m (7375.62 lb·ft), which is more than double that of the GLD specimen. Similarly, the maximum shear deformation experienced by the GLD specimen is 0.027 rad, and, in the case of the GLD-SHCC specimen, it is 0.043 rad. The displacement ductility of the GLD specimen is 3.75, and the GLD-SHCC specimen is greater than 5. These three performance characteristics are crucial for the joints to possess seismic resistance.

To summarize, it was identified that the BC joints studied here with highly workable SHCC at the joint zone can significantly improve the seismic resistance of GLD BC joints and reduce the need for providing transverse reinforcements, making construction more practical and feasible. The present study provides new information on the potential use of flowable strain-hardened cement-based composite in BC joints in seismic-prone areas without the requirement of additional reinforcement at the joint region.

AUTHOR BIOS

B.S. Sindu *is a Principal Scientist in the Special and Multifunctional Structures Laboratory (SMSL) at CSIR-Structural Engineering Research Centre (CSIR-SERC), Chennai, Tamil Nadu, India. Her research interests include nano-engineering of cementitious composites, mechanics of materials, strain-hardened cementitious composites, multiscale modeling, and smart composites.*

Saptarshi Sasmal *is a Chief Scientist and Head of SMSL at CSIR-SERC. His research interests include computational mechanics, nanoindentation, wave propagation techniques, integrity assessment and structural health monitoring, innovative and smart cementitious composites, and composite systems.*

ACKNOWLEDGMENTS

The authors duly acknowledge the help received from the technical staff members of the Special and Multifunctional Structures Laboratory (SMSL) of CSIR-SERC while carrying out the experimental investigations.

REFERENCES

1. Calvi, G. M.; Magenes, G.; and Pampanin, S., "Relevance of Beam-Column Joint Damage and Collapse in RC Frame Assessment," *Journal of Earthquake Engineering*, V. 6, No. sup001, 2002, pp. 75-100. doi: 10.1080/13632460209350433

2. Sasmal, S.; Novák, B.; Rmanjaneyulu, K.; Roehm, C.; Srinivas, V.; Lakshmanan, N.; and Iyer, N. R., "Upgradation of Gravity Load Designed Subassemblages Subjected to Seismic Type Loading," *Composite Structures*, V. 93, No. 6, May 2011, pp. 1561-1573. doi: 10.1016/j.compstruct.2011.01.001

3. Suryanto, B.; Tambusay, A.; Suprobo, P.; Bregoli, G.; and Aitken, M. W., "Seismic Performance of Exterior Beam-Column Joints Constructed with Engineered Cementitious Composite: Comparison with Ordinary and Steel Fibre Reinforced Concrete," *Engineering Structures*, V. 250, Jan. 2022, Article No. 113377. doi: 10.1016/j.engstruct.2021.113377

4. AbdelAleem, B. H., and Hassan, A. A. A., "Effect of Combining Steel Fibers with Crumb Rubber on Enhancing the Behavior of Beam-Column Joints under Cyclic Loading," *Engineering Structures*, V. 182, Mar. 2019, pp. 510-527. doi: 10.1016/j.engstruct.2018.12.089

5. Esmaeeli, E.; Barros, J. A. O.; Sena-Cruz, J.; Fasan, L.; Li Prizzi, F. R.; Melo, J.; and Varum, H., "Retrofitting of Interior RC Beam–Column Joints Using CFRP Strengthened SHCC: Cast-in-Place Solution," *Composite Structures*, V. 122, Apr. 2015, pp. 456-467. doi: 10.1016/j.compstruct.2014.12.012

6. Lowes, L. N., and Altoontash, A., "Modeling Reinforced-Concrete Beam-Column Joints Subjected to Cyclic Loading," *Journal of Structural*

Engineering, ASCE, V. 129, No. 12, Dec. 2003, pp. 1686-1697. doi: 10.1061/(ASCE)0733-9445(2003)129:12(1686)

7. Murty, C. V. R.; Rai, D. C.; Bajpai, K. K.; and Jain, S. K., "Effectiveness of Reinforcement Details in Exterior Reinforced Concrete Beam-Column Joints for Earthquake Resistance," *ACI Structural Journal*, V. 100, No. 2, Mar.-Apr. 2003, pp. 149-156.

8. Engindeniz, M.; Kahn, L. F.; and Zureick, A.-H., "Repair and Strengthening of Reinforced Concrete Beam-Column Joints: State of the Art," *ACI Structural Journal*, V. 102, No. 2, Mar.-Apr. 2005, pp. 187-197.

9. Filiatrault, A.; Pineau, S.; and Houde, J., "Seismic Behavior of Steel-Fiber Reinforced Concrete Interior Beam-Column Joints," *ACI Structural Journal*, V. 92, No. 5, Sept.-Oct. 1995, pp. 543-552.

10. Del Vecchio, C.; Di Ludovico, M.; Balsamo, A.; and Prota, A., "Seismic Retrofit of Real Beam-Column Joints Using Fiber-Reinforced Cement Composites," *Journal of Structural Engineering*, ASCE, V. 144, No. 5, May 2018, p. 04018026. doi: 10.1061/(ASCE)ST.1943-541X.0001999

11. Banthia, N., and Gupta, R., "Hybrid Fiber Reinforced Concrete (HyFRC): Fiber Synergy in High Strength Matrices," *Materials and Structures*, V. 37, No. 10, Dec. 2004, pp. 707-716. doi: 10.1007/BF02480516

12. Afroughsabet, V.; Biolzi, L.; and Ozbakkaloglu, T., "High-Performance Fiber-Reinforced Concrete: A Review," *Journal of Materials Science*, V. 51, No. 14, July 2016, pp. 6517-6551. doi: 10.1007/s10853-016-9917-4

13. Abbas, A. A.; Syed Mohsin, S. M.; and Cotsovos, D. M., "Seismic Response of Steel Fibre Reinforced Concrete Beam-Column Joints," *Engineering Structures*, V. 59, Feb. 2014, pp. 261-283. doi: 10.1016/j.engstruct.2013.10.046

14. Abbass, W.; Khan, M. I.; and Mourad, S., "Evaluation of Mechanical Properties of Steel Fiber Reinforced Concrete with Different Strengths of Concrete," *Construction and Building Materials*, V. 168, Apr. 2018, pp. 556-569. doi: 10.1016/j.conbuildmat.2018.02.164

15. Alaee, P., and Li, B., "High-Strength Concrete Exterior Beam-Column Joints with High-Yield Strength Steel Reinforcements," *Engineering Structures*, V. 145, Aug. 2017, pp. 305-321. doi: 10.1016/j.engstruct.2017.05.024

16. Röhm, C.; Novák, B.; Sasmal, S.; Karusala, R.; and Srinivas, V., "Behavior of Fibre Reinforced Beam-Column Subassemblages under Reversed Cyclic Loading," *Construction and Building Materials*, V. 36, Nov. 2012, pp. 319-329. doi: 10.1016/j.conbuildmat.2012.04.114

17. Zhang, R.; Matsumoto, K.; Hirata, T.; Ishizeki, Y.; and Niwa, J., "Application of PP-ECC in Beam-Column Joint Connections of Rigid-Framed Railway Bridges to Reduce Transverse Reinforcements," *Engineering Structures*, V. 86, Mar. 2015, pp. 146-156. doi: 10.1016/j.engstruct.2015.01.005

18. Siva Chidambaram, R., and Agarwal, P., "Seismic Behavior of Hybrid Fiber Reinforced Cementitious Composite Beam–Column Joints," *Materials and Design*, V. 86, Dec. 2015, pp. 771-781. doi: 10.1016/j.matdes.2015.07.164

19. Zainal, S. M. I. S.; Hejazi, F.; and Rashid, R. S. M., "Enhancing the Performance of Knee Beam-Column Joint Using Hybrid Fibers Reinforced Concrete," *International Journal of Concrete Structures and Materials*, V. 15, No. 1, Dec. 2021, Article No. 20. doi: 10.1186/s40069-021-00457-w

20. Said, S. H., and Abdul Razak, H., "Structural Behavior of RC Engineered Cementitious Composite (ECC) Exterior Beam-Column Joints under Reversed Cyclic Loading," *Construction and Building Materials*, V. 107, Mar. 2016, pp. 226-234. doi: 10.1016/j.conbuildmat.2016.01.001

21. Sindu, B. S., and Sasmal, S., "On the Development and Studies of Nano- and Micro-Fiber Hybridized Strain Hardened Cementitious Composite," *Archives of Civil and Mechanical Engineering*, V. 19, No. 2, June 2019, pp. 348-359. doi: 10.1016/j.acme.2018.11.008

22. Emara, M.; Mohamed, H. A.; Rizk, M. S.; and Hu, J. W., "Behavior of ECC Columns Confined Using Steel Wire Mesh under Axial Loading," *Journal of Building Engineering*, V. 43, Nov. 2021, Article No. 102809. doi: 10.1016/j.jobe.2021.102809

23. Li, M., and Li, V. C., "Rheology, Fiber Dispersion, and Robust Properties of Engineered Cementitious Composites," *Materials and Structures*, V. 46, No. 3, Mar. 2013, pp. 405-420. doi: 10.1617/s11527-012-9909-z

24. Ranade, R.; Zhang, J.; Lynch, J. P.; and Li, V. C., "Influence of Micro-Cracking on the Composite Resistivity of Engineered Cementitious Composites," *Cement and Concrete Research*, V. 58, Apr. 2014, pp. 1-12. doi: 10.1016/j.cemconres.2014.01.002

25. Sindu, B. S.; Thirumalaiselvi, A.; and Sasmal, S., "Investigations on Fracture Related Properties of Strain Hardened Concrete Using Digital Image Correlation and Acoustic Emission Techniques," *European Journal of Environmental and Civil Engineering*, V. 26, No. 14, 2022, pp. 6807-6829. doi: 10.1080/19648189.2021.1962411

26. Dehghani, A.; Mozafari, A. R.; and Aslani, F., "Evaluation of the Efficacy of Using Engineered Cementitious Composites in RC Beam-Column Joints," *Structures*, V. 27, Oct. 2020, pp. 151-162. doi: 10.1016/j.istruc.2020.05.045

27. Zhang, X., and Li, B., "Seismic Performance of RC Beam–Column Joints Constructed with Engineered Cementitious Composites," *Journal of Structural Engineering*, ASCE, V. 146, No. 12, Dec. 2020, p. 04020271. doi: 10.1061/(ASCE)ST.1943-541X.0002824

28. Parra-Montesinos, G., and Wight, J. K., "Seismic Response of Exterior RC Column-to-Steel Beam Connections," *Journal of Structural Engineering*, ASCE, V. 126, No. 10, Oct. 2000, pp. 1113-1121. doi: 10.1061/(ASCE)0733-9445(2000)126:10(1113)

29. Fischer, G., and Li, V. C., "Deformation Behavior of Fiber-Reinforced Polymer Reinforced Engineered Cementitious Composite (ECC) Flexural Members under Reversed Cyclic Loading Conditions," *ACI Structural Journal*, V. 100, No. 1, Jan.-Feb. 2003, pp. 25-35.

30. Shannag, M. J.; Barakat, S.; and Abdul-Kareem, M., "Cyclic Behavior of HPFRC-Repaired Reinforced Concrete Interior Beam-Column Joints," *Materials and Structures*, V. 35, No. 6, July 2002, pp. 348-356. doi: 10.1007/BF02483154

31. Khan, M. I.; Al-Osta, M. A.; Ahmad, S.; and Rahman, M. K., "Seismic Behavior of Beam-Column Joints Strengthened with Ultra-High Performance Fiber Reinforced Concrete," *Composite Structures*, V. 200, Sept. 2018, pp. 103-119. doi: 10.1016/j.compstruct.2018.05.080

32. Sharma, R., and Bansal, P. P., "Behavior of RC Exterior Beam Column Joint Retrofitted Using UHP-HFRC," *Construction and Building Materials*, V. 195, Jan. 2019, pp. 376-389. doi: 10.1016/j.conbuildmat.2018.11.052

33. Rai, T.; Mukharjee, B. B.; and Barai, S. V., "Beam-Column Joints Made of Self-Compacting Concrete Containing Recycled Coarse Aggregates and Nano-Silica," *International Journal of Sustainable Materials and Structural Systems*, V. 4, No. 1, 2020, pp. 91-104. doi: 10.1504/IJSMSS.2020.106420

34. Sindu, B. S., and Sasmal, S., "Multi-Scale Abridged Cement Composite with Enhanced Mechanical Properties," *ACI Materials Journal*, V. 117, No. 4, July 2020, pp. 105-117.

35. Sindu, B. S., and Sasmal, S., "Pseudo-Ductile Cementitious Composites by Hierarchical Crack Bridging," *ACI Materials Journal*, V. 119, No. 1, Jan. 2022, pp. 145-158.

36. EFNARC, "Specification and Guidelines for Self-Compacting Concrete," European Federation for Specialist Construction Chemicals and Concrete Systems, Flums, Switzerland, 2002, 32 pp.

37. Ghiassi, B.; Soltani, M.; and Rahnamaye Sepehr, S., "Micromechanical Modeling of Tension Stiffening in FRP-Strengthened Concrete Elements," *Journal of Composite Materials*, V. 52, No. 19, Aug. 2018, pp. 2577-2596. doi: 10.1177/0021998317751248

38. Ramanjaneyulu, K.; Novák, B.; Sasmal, S.; Roehm, C.; Lakshmanan, N.; and Iyer, N. R., "Seismic Performance Evaluation of Exterior Beam-Column Subassemblages Designed According to Different Codal Recommendations," *Structure and Infrastructure Engineering*, V. 9, No. 8, 2013, pp. 817-833. doi: 10.1080/15732479.2011.625954

39. FEMA 273, "NEHRP Guidelines for the Seismic Rehabilitation of Buildings," Federal Emergency Management Agency, Washington DC, 1997, 435 pp.

40. Sasmal, S.; Ramanjaneyulu, K.; Novák, B.; and Lakshmanan, N., "Analytical and Experimental Investigations on Seismic Performance of Exterior Beam-Column Subassemblages of Existing RC-Framed Building," *Earthquake Engineering & Structural Dynamics*, V. 42, No. 12, Oct. 2013, pp. 1785-1805. doi: 10.1002/eqe.2298

41. Park, R., and Paulay, T., "Behaviour of Reinforced Concrete External Beam-Column Joints under Cyclic Loading," *Proceedings of the Fifth World Conference on Earthquake Engineering (5WCEE)*, V. 1, Rome, Italy, 1973, pp. 772-781.

42. Corinaldesi, V.; Letelier, V.; and Moriconi, G., "Behaviour of Beam-Column Joints Made of Recycled-Aggregate Concrete under Cyclic Loading," *Construction and Building Materials*, V. 25, No. 4, Apr. 2011, pp. 1877-1882. doi: 10.1016/j.conbuildmat.2010.11.072

ACI STRUCTURAL JOURNAL TECHNICAL PAPER

Title No. 121-S41

Shear Behavior of Precast Concrete Box Culverts Reinforced with Glass Fiber-Reinforced Polymer Bars under Concentrated Load

by Ahmed Elnady, Salaheldin Mousa, and Brahim Benmokrane

This research evaluated the structural behavior of precast concrete box culverts (PCBCs) reinforced with glass fiber-reinforced polymer (GFRP) bars, both experimentally and theoretically. Four full-scale specimens with a span of 1500 mm (59.06 in.), a rise of 1500 mm (59.06 in.), and a joint length of 1219 mm (48 in.) were prepared, along with one specimen with a span of 1800 mm (70.87 in.). Four specimens were reinforced with GFRP bars, and one specimen with steel bars as a reference. The PCBCs were tested up to failure under a concentrated load over a contact area of 250 x 600 mm (9.8 x 23.6 in.) on the top slab. The load plate simulated the footprint of the truck wheel load (87.5 kN [19.67 kip] CL-625 truck) according to the Canadian Highway Bridge Design Code. The investigated test parameters were the longitudinal reinforcement stiffness (GFRP versus steel), the longitudinal GFRP reinforcement ratios, specimen clear span, and slab thickness. Two-way shear failure was observed in all the tested specimens as a result of the concentrated load acting on the top slab. The test results revealed that increasing the longitudinal reinforcement ratio, as well as increasing the top-slab thickness, resulted in higher load-carrying capacity, lower deflection, and lower concrete and reinforcement strains. The experimental shear strengths were compared to the values predicted using current code provisions for two-way shear resistance equations. The results show that the punching-shear resistance equation in CSA S806-12 provided good yet conservative predictions of the shear capacity of the PCBCs' top slab. The Canadian Highway Bridge Design Code does not provide an equation for two-way shear design of FRP-reinforced concrete members. The two-way shear equation available for steel-reinforced concrete members was modified to take into account the characteristics of FRP bars. The modified equation produced predictions consistent with the experimental results. Moreover, the findings of this study demonstrate the feasibility and effectiveness of using GFRP bars as internal reinforcement for PCBCs as an alternative to steel bars.

Keywords: design codes; experimental and analytical studies; failure mode and cracking pattern; glass fiber-reinforced polymer (GFRP) reinforcement; load-deflection behavior; precast concrete box culverts (PCBCs); punching-shear resistance; reinforced concrete; strains.

INTRODUCTION

The culvert is a water structure used to convey drainage or stormwater along roadways, railways, or any other crossing where it intersects with the direction of water flow. The box culvert is the most popular shape in field applications and is usually used as a single or multicell culvert (Kim and Yoo 2005). Culvert construction can be cast-in-place or involve precast units. There are some advantages of using precast concrete box culverts (PCBCs) over in-place construction, including higher quality control, higher concrete strength, uniform structure parts, lower cost, and shorter installation time. The culvert is a buried structure surrounded by soil, and consequently, it is subjected to aggressive environments that expose the structure to high moisture, chlorides, and salt content. The flowing waters may contain acids, alkalies, industrial waste, or chemicals. In addition, there is a risk of exposure to deicing salts, especially in North America. This exposure impacts the structure's durability and leads to corrosion of the steel reinforcement. Corrosion of steel reinforcement is one of the causes of the deterioration of concrete structures, thereby reducing the expected lifetime (Capozucca 1995; Chang and Seo 2012). Corrosion of steel reinforcing bars is a primary concern with infrastructure as it leads to costly repairs and rehabilitation (Angst 2018). Using fiber-reinforced polymer (FRP) is one of the most effective alternative solutions for reinforcing bars in concrete structures, especially when steel corrosion is a major concern (Gudonis et al. 2013). FRP is considered a high-performance material with many advantages compared to steel, including a weight of approximately one-quarter that of steel, corrosion resistance, high tensile strength, high mechanical performance, low maintenance costs, and easy installation (Benmokrane and Rahman 1998; Mufti et al. 2005; Ahmed et al. 2020). Concrete structures reinforced with FRP bars have been used in a wide range of structures in the United States and Canada (Benmokrane et al. 2004, 2021a). FRP reinforcement has recorded tangible successes in the areas of parking garages, tunneling, marine structures, water tanks, and highway bridges (El-Salakawy et al. 2003, 2005; Benmokrane et al. 2006, 2007, 2016; Mohamed and Benmokrane 2014, 2015; ACI Committee 440 2015; Caratelli et al. 2017; Ahmed et al. 2017, 2020; Hosseini et al. 2023; Idemudia et al. 2023). Glass FRP (GFRP) bars have been one of the most popular types of FRP reinforcing bars in the last few decades. GFRP bars are characterized by high tensile strength and high corrosion resistance compared to steel bars (Jabbar and Farid 2018; Benmokrane et al. 2021b).

Steel-reinforced concrete box culverts have been the topic of significant research efforts over the last two decades. Experimental and finite element analyses have

ACI Structural Journal, V. 121, No. 3, May 2024.

MS No. S-2023-102.R1, doi: 10.14359/51740488, received December 20, 2023, and reviewed under Institute publication policies.

been performed on the shear behavior of the top slab of standard sizes of steel-reinforced concrete box culverts as per ASTM C1433-03 (Garg and Abolmaali 2006). The effect of different parameters, including culvert size and loading locations, on the shear capacity of steel-reinforced concrete box culverts has been studied (McGrath et al. 2005; Garg and Abolmaali 2006, 2009; Garg et al. 2007; Abolmaali and Garg 2008a,b). These studies have significantly improved the knowledge about how box culvert concrete structures should be analyzed and designed. Although the shear behavior of steel-reinforced concrete box culverts has been thoroughly studied, knowledge concerning the shear behavior of PCBCs with GFRP reinforcement is still in its early stages and has been dealt with in limited projects. Recently, Hassanli et al. (2022) studied the structural behavior of the inverted U-shaped concrete culvert reinforced with GFRP bars and shear reinforcement in the top slab. The tests were performed according to AS 1597.1-2010 under vertical loading. The load location was varied with three different cases: lateral load applied, no lateral load applied and walls restrained, and no lateral load applied and walls unrestrained. Punching-shear failure was observed in all the specimens with acceptable load-carrying capacity. It was concluded that the serviceability limit states (deflection and crack width) governed the design.

The box culvert is structurally analyzed as a rigid frame using the moment distribution method to obtain the final moment distribution at joints using the relative stiffness of the slabs and walls (Ahmed and Alarabi 2011; Kolate et al. 2014). Concrete box culverts are subjected to different types of loads, including dead loads, permanent loads, water loads, earth loads, live loads, and vertical surcharge loads (AASHTO 2018; CSA S6:19). When the fill height above the top slab is 0.6 m (23.62 in.) or more, a uniform distribution of the wheel load through the fill is considered. Otherwise, the wheel load is applied to the top slab with the specified wheel footprint with no distribution through the fill (AASHTO 2018; CSA S6:19). The vicinity of a concentrated load on a slab, such as with bridges and culverts, is evaluated for two-way shear (ACI Committee 318 2019).

The shear strength of FRP-reinforced concrete slabs has been reported in the literature (Matthys and Taerwe 2000; Ospina et al. 2003; El-Sayed et al. 2005; Hassan et al. 2013; Nguyen-Minh and Rovňák 2013). The results indicated that increasing the longitudinal FRP reinforcement ratio increased the punching-shear capacity, decreased the reinforcement strains, and achieved lower deflection values. Bouguerra et al. (2011) studied the punching-shear capacity of FRP-reinforced concrete bridge deck slabs with different thicknesses. The punching-shear capacity of the tested slabs was directly proportional to the slab thickness, and the measured strains were affected inversely by the slab thickness and the longitudinal reinforcement ratio. Kurtoğlu et al. (2023) investigated the punching-shear strength of GFRP-reinforced slabs with different slab thicknesses. They concluded that increasing the slab thickness by 20% resulted in 50% higher punching-shear capacity with higher pre- and post-cracking stiffness.

FRP-reinforced concrete box culvert design is not included in the current design codes (AASHTO 2018; CSA S6:19). There are no research results in the literature on the shear behavior of GFRP-reinforced PCBCs, which is the motivation of the current study. This research is part of an ongoing research program in the Department of Civil and Building Engineering at the University of Sherbrooke, in which the shear behavior of full-scale FRP-reinforced PCBCs is investigated with different culvert spans, loading locations, FRP reinforcing bar types, longitudinal FRP reinforcement ratios, concrete compressive strengths, and test bedding materials.

RESEARCH SIGNIFICANCE

Over the last two decades, outstanding research has been conducted on steel-reinforced concrete box culverts. Few research articles and discussions have been published on FRP-reinforced concrete culverts. So far, this study is the first experimental program aimed at providing experimental data on the shear strength and behavior of full-scale concrete box culvert units reinforced with GFRP bars under truck wheel loading in terms of various parameters. The findings will help implement the use of GFRP bars in concrete box culverts, which can be an innovative solution to the corrosion problem in buried structure applications. This study also provides analysis to determine the effects of the longitudinal GFRP reinforcement ratio, reinforcement stiffness (steel versus GFRP), and culvert size on the shear strength of the top slab. The experimental data and theoretical study provide the evidence required to include design provisions in the updated "AASHTO LRFD Bridge Design Guide Specifications for GFRP-Reinforced Concrete" (AASHTO 2018) and the Canadian Highway Bridge Design Code (CSA S6:19) for the use of GFRP bars as internal reinforcement in PCBCs under traffic loads.

EXPERIMENTAL INVESTIGATION

Test matrix and specimen details

A total of five full-scale PCBC specimens reinforced with GFRP or steel bars were constructed and tested up to failure under vertical loading. Four specimens were reinforced with GFRP bars with longitudinal reinforcement ratios ranging from 0.66 to 1.67%; one specimen was reinforced with steel bars as a reference. Table 1 presents the test matrix, specimen ID, dimensions, concrete strength, and reinforcement details of the specimens. Each specimen was identified with a unique three-part ID. The first part indicates the number of longitudinal bars per layer in each slab or wall. This is followed by the letter G or S identifying the type of reinforcing bar: G for GFRP and S for steel. The last part indicates the clear span: S1 for 1500 mm (59.06 in.) and S2 for 1800 mm (70.87 in.). Specimens 6-G-S1, 9-G-S1, 12-G-S1, and 6-S-S1 had a clear span of 1500 mm (59.06 in.) and a rise of 1500 mm (59.06 in.) with a joint length of 1219 mm (48 in.). The top and bottom slabs as well as the side walls were 150 mm (5.91 in.) thick. The haunch dimensions were equal to the wall thickness in both directions: 150 mm (5.91 in.). Specimen 6-G-S2 had a clear span of 1800 mm (70.87 in.) and a rise of 1500 mm (59.06 in.) with a joint length of 1219 mm (48.00 in.). The thickness of the top

Table 1—Dimensions, reinforcement, and concrete strength of tested specimens

Specimen ID	Span, mm	Rise, mm	t slab/wall, mm	t haunch, mm	d, mm	Reinforcement type	Transverse reinforcement	Longitudinal reinforcement		Concrete strength		
								Reinforcement	ρ_f, %	n^*	COV, %	f_c', MPa
6-G-S1	1500	1500	150	150	117	GFRP	No. 4 @ 292 mm	No. 5 @ 233 mm	0.83	6	8.2	38
9-G-S1	1500	1500	150	150	117	GFRP	No. 4 @ 292 mm	No. 5 @ 146 mm	1.25	6	8.8	44.9
12-G-S1	1500	1500	150	150	117	GFRP	No. 4 @ 292 mm	No. 5 @ 106 mm	1.67	6	5.6	41.4
6-G-S2	1800	1500	180	180	147	GFRP	No. 4 @ 292 mm	No. 5 @ 233 mm	0.83	6	3.1	43.1
6-S-S1	1500	1500	150	150	117	Steel	10M @ 292 mm	15M @ 292 mm	0.66	6	2.7	45.1

*n is number of tested concrete cylinders for each test specimen.

Note: 1 mm = 0.0394 in.; 1 MPa = 0.145 ksi.

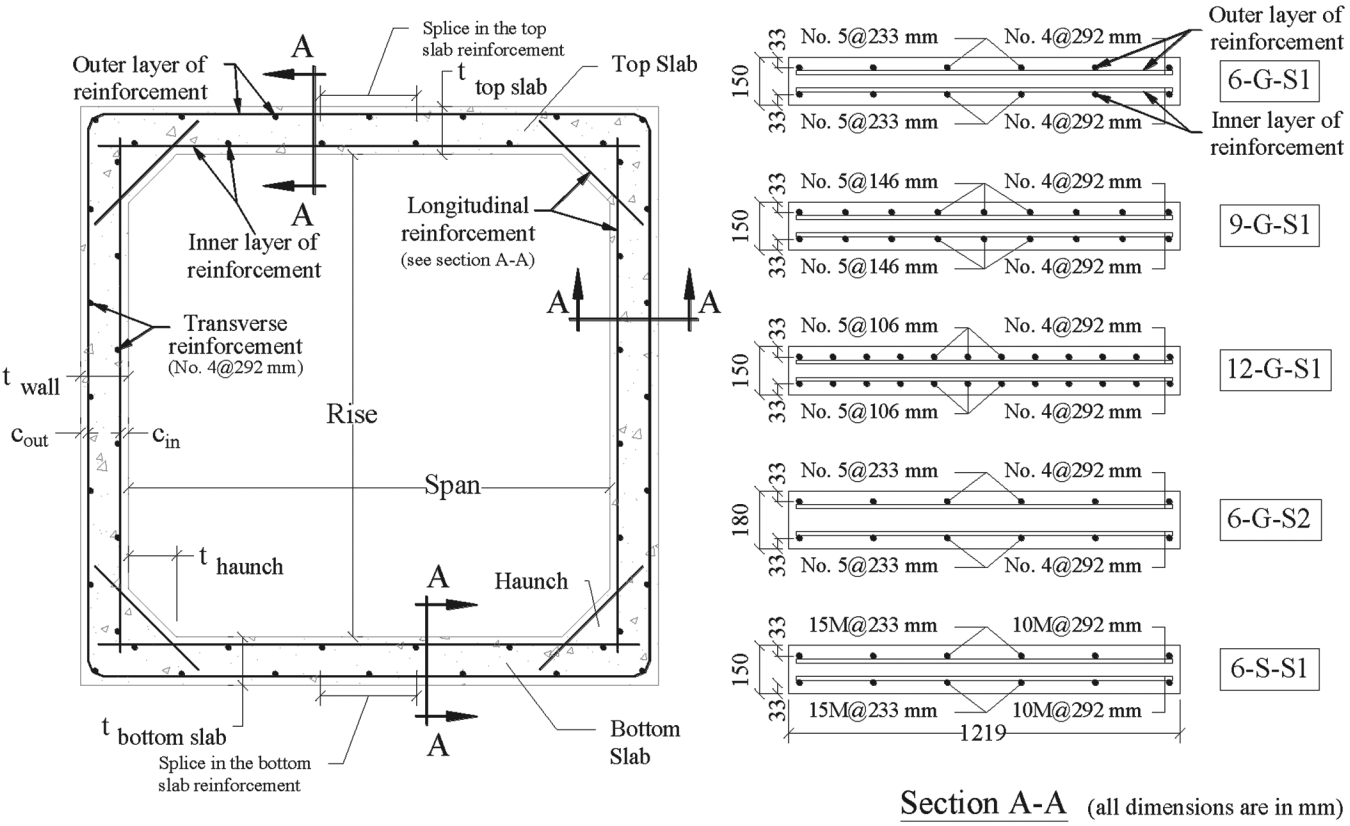

Fig. 1—Dimensions and reinforcement details of specimens. (Note: 1 mm = 0.0394 in.)

slab, bottom slab, and side walls was 180 mm (7.09 in.). The haunch dimensions were equal to the wall thickness in both directions: 180 mm (7.09 in.). The inner and outer concrete covers (c_{in} and c_{out}) were kept constant at 35 mm (1.4 in.) for all the specimens. Figure 1 shows the concrete dimensions and the reinforcement details of the PCBCs. Each specimen in this study had two layers of reinforcement as outer and inner layers of reinforcement per slab or wall. Each layer consisted of longitudinal reinforcement, parallel to the traffic direction, and transverse reinforcement, perpendicular to the traffic direction, without shear reinforcement. Three different longitudinal GFRP reinforcement ratios were used to reinforce the specimens in the slabs, walls, and haunches to investigate the effects of the longitudinal reinforcement ratio (refer to Fig. 1, Section A-A). The longitudinal reinforcement ratio of 0.83% was used in specimen 6-G-S1 and consisted of six No. 5 longitudinal GFRP bars at 233 mm (9.17 in.) in outer and inner layers of reinforcement per slab or wall. The other two longitudinal reinforcement ratios (1.25% and 1.67%) were used for specimens 9-G-S1 and 12-G-S1, respectively, and consisted of nine and 12 No. 5 GFRP longitudinal bars at 146 and 106 mm (5.75 and 4.17 in.) in outer and inner layers of reinforcement per slab or wall, respectively. Specimen 6-G-S2 was reinforced with six No. 5 GFRP longitudinal bars at 233 mm (9.17 in.) in the outer and inner layers of reinforcement per slab or wall, with a longitudinal reinforcement ratio of 0.66%. All the GFRP specimens had No. 4 GFRP bars at 292 mm (11.50 in.) as transverse reinforcement in outer and inner layers of reinforcement per slab or wall. Steel-reinforced specimen 6-S-S1 had six 15M steel longitudinal bars at 233 mm (9.17 in.) in outer and inner layers of reinforcement per slab or wall with a longitudinal reinforcement ratio of 0.83%; 10M steel bars at 292 mm (11.50 in.) were used as transverse reinforcement

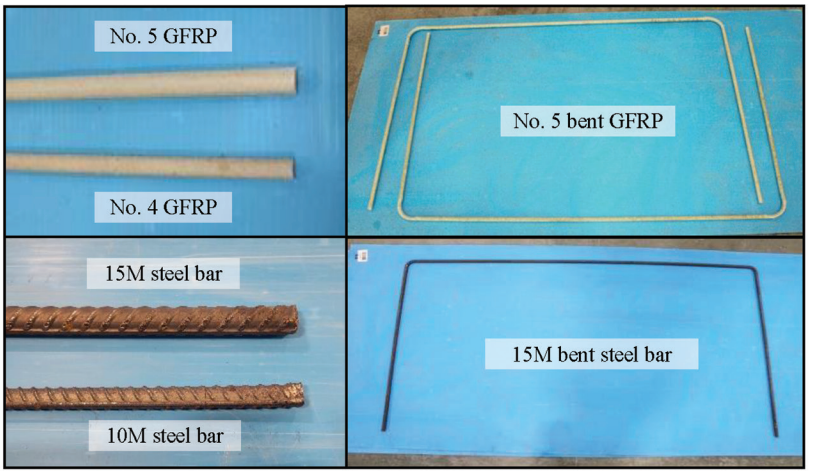

(a)

(b)

(c)

Fig. 2—(a) GFRP bars and steel bars; (b) GFRP and steel cages; and (c) PCBC specimen fabrication.

in outer and inner layers per slab or wall (refer to Fig. 1, Section A-A).

Materials

Sand-coated No. 5 and No. 4 GFRP bars were used to reinforce the GFRP specimens (6-G-S1, 9-G-S1, 12-G-S1, and 6-G-S2) in the longitudinal and transverse directions, respectively. The GFRP straight and bent bars were manufactured with a boron-free glass fiber content of 84.7% and 72.0% (by weight), respectively, in a vinyl ester resin. The ultimate tensile strength (f_{fu}) and modulus of elasticity (E_f) of the longitudinal and bent GFRP bars were determined according to CSA S806-12 (Annex C) and CSA S807:19 (Annex E), as reported by the manufacturer. The transverse shear strength of the GFRP bars was determined according to ASTM D7617/D7617M-11(2017), as reported by the manufacturer. The steel-reinforced specimen (6-S-S1) was reinforced with 15M and 10M deformed steel bars in the longitudinal and transverse directions, respectively, as shown in Fig. 2(a). Table 2 provides the mechanical properties of the GFRP and steel bars.

The PCBC specimens were cast with normalweight concrete in Saint-Hyacinthe, QC, Canada, with a target 28-day compressive strength of 40 MPa (5.80 ksi). Six

Table 2—Material properties of GFRP and steel reinforcing bars

GFRP reinforcement								
Bar No.	d_{bar}, mm	A_{bar}*, mm^2	$A_{im.}$†, mm^2	E_f, GPa	f_{fu}, MPa	f_{fu}, MPa (bent bar)	ε_{fu}, %	Transverse shear tensile strength, MPa
GFRP (straight bars)								
No. 4	13.0	127	146	60.7	1391	—	2.29	238
No. 5	15.0	198	236	63.7	1403	—	2.20	236
GFRP (bent bars)								
No. 5	15.0	198	232	50.6	1169	637	2.31	233
Steel								
Bar size	d_{bar}, mm	A_{bar}*, mm^2		E_s, GPa	F_y, MPa		ε_y, %	
10M	11.3	71		200	460		0.23	
15M	16.0	198		200	460		0.23	

*Nominal bar cross-sectional area.

†Immersed cross-sectional area.

Note: 1 mm = 0.0394 in.; 1 mm^2 = 0.00155 in.^{2}; 1 MPa = 0.145 ksi.

standard concrete cylinders measuring 100 x 200 mm (3.94 x 7.87 in.) per specimen were collected during casting to measure the compressive strength of each specimen. The concrete compressive strength (f_c') was determined on the day of testing of each specimen, as presented in Table 1.

Specimen fabrication

Figure 2(b) shows the assembled GFRP and steel PCBC cages at the University of Sherbrooke's Centre de mise à l'échelle laboratory (CME). The cages were prepared and then shipped to the precast concrete producer for casting. Wooden formwork was carefully fabricated to suit the different dimensions of the specimens. Figure 2(c) shows the casting and demolding of the PCBC specimens. After curing, the PCBC specimens were shipped to the University of Sherbrooke's structural laboratory for testing.

Test setup and instrumentation

The test setup was designed and fabricated at the structural laboratory of the University of Sherbrooke in accordance with CSA S6:19. The tested specimens were placed directly on the laboratory's rigid floor. A standard steel load plate measuring 250 x 600 mm (9.8 x 23.6 in.) was used to simulate a CL-625 truck wheel footprint. CSA S6:19 presents the CL-625 truck axle and wheel loads with a total load of 625 kN (140.51 kip). The maximum wheel load of 87.5 kN (19.67 kip) was used in this study for comparison with the experimental results. The load plate was placed on the top slab to simulate a wheel load on a box culvert with less than 0.6 m (23.62 in.) depth of earth fill above the top slab, as illustrated in CSA S6:19. The load-plate location shown in Fig. 3 was chosen to generate the maximum shear stresses at the most expected critical location for the truck wheel above the top slab of the box culvert structure. It was located at the edge of the joint length and along the span at a distance d (critical shear location) between the edge of the load plate and the tip of the right haunch. The load plate was attached to a 1000 kN (224.8 kip) hydraulic actuator mounted to a steel frame. A 20 mm (0.79 in.) thick layer of rubber was placed between the load plate and the concrete surface for a uniform load distribution over the loading area. The load was applied at a displacement-controlled rate of 0.3 mm/min (0.01 in./min) during the testing of the specimens. Figure 3 shows the details of the test setup.

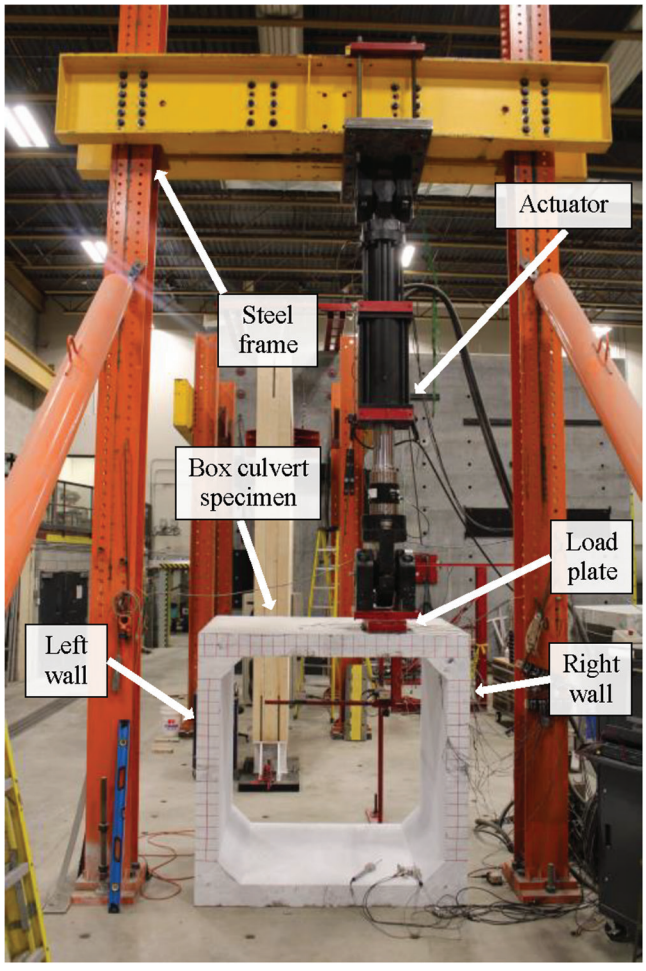

Fig. 3—Test setup.

For each specimen, 10 electrical resistance strain gauges with a gauge length of 6 mm (0.24 in.) and a gauge

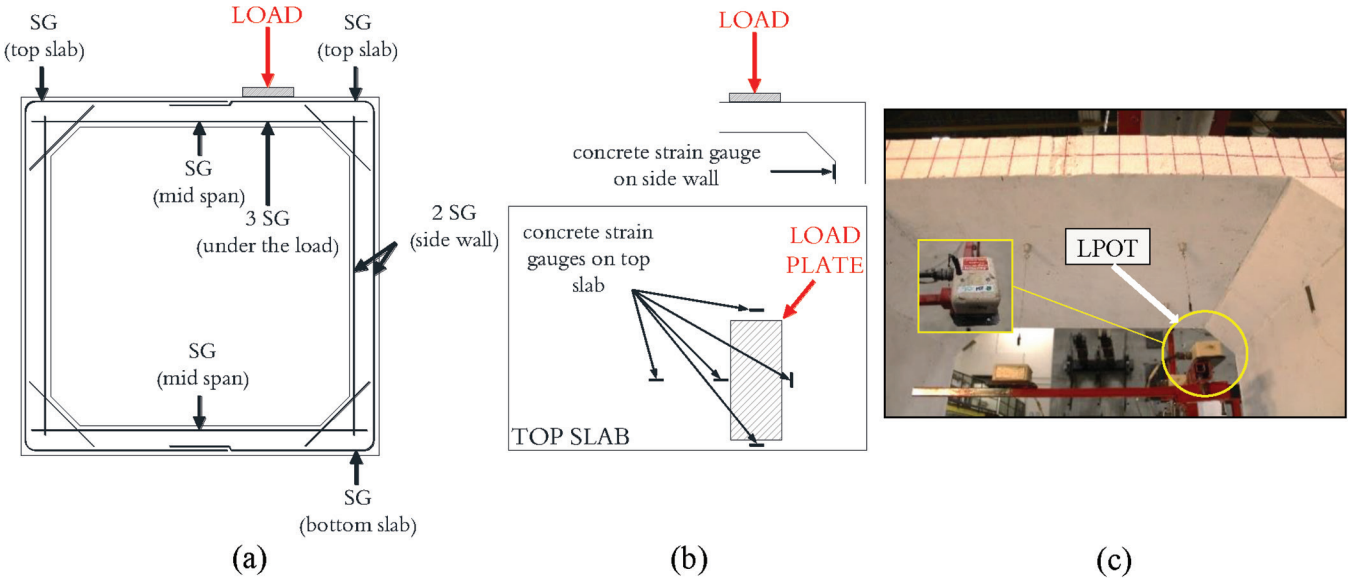

Fig. 4—PCBC instrumentation: (a) strain gauges on longitudinal bars; (b) concrete strain gauges; and (c) LPOTs.

resistance of 120 ± 0.5 Ω were attached to the GFRP and steel bars during cage preparation. The strain gauges were distributed on each specimen cage at the maximum tension and compression locations and directly under the load plate to measure strain in the longitudinal reinforcing bars. On the top slab, as in Fig. 4(a), six strain gauges (SGs) were distributed as follows; a) two SGs on the outer layer of longitudinal reinforcement above the right and left walls; b) three SGs on the inner layer of longitudinal reinforcement under the center of the loading area, which were used for validation; and c) one SG on the inner layer of longitudinal reinforcement at midspan. On the right wall, two SGs were attached to the outer and inner layers of the longitudinal reinforcement at midheight. Moreover, two SGs were attached to the bottom slab on the outer and inner layers of longitudinal reinforcement under the right wall and at midspan, respectively. The concrete compressive strains were measured with five SGs (wire SGs using a polyester resin backing) with a gauge length of 60 mm (2.36 in.) and a gauge resistance of 120 ± 0.5Ω, glued to the top surface (compression side) of the top slab before testing. Additionally, one SG was placed on the inside face of the right wall (refer to Fig. 4(b)). The top slab's deflection was captured with linear potentiometers (LPOTs) at midspan and below the load-plate location, and the lateral displacement of the vertical walls was captured at midspan (refer to Fig. 4(c)). The crack propagation line was marked by drawing a line parallel to the observed crack, and the corresponding load was written beside the end of the crack to indicate the crack propagation (refer to Fig. 5). An automatic data acquisition system monitored by a computer was used to record the readings of the LPOTs, SGs, and load cells.

TEST RESULTS AND OBSERVATIONS

This section presents the failure mode and cracking patterns, load-deflection behavior, and the concrete and reinforcing bar strains during the testing of the PCBCs. It also summarizes the effect of changing the longitudinal reinforcement type, longitudinal GFRP reinforcement ratio, clear span, and the top-slab thickness on the tested PCBCs. In this section, the calculated design factored load P_{fact} was calculated according to CSA S6:19. The design factored load was calculated as 1.4 × 1.7 × 87.5 kN (19.67 kip) = 208.25 kN (46.14 kip), where 1.4 is the dynamic load factor, 1.7 is the live-load combination factor, and 87.5 kN (19.67 kip) is the maximum design truck wheel load (87.5 kN CL-625 truck).

Failure mode and cracking pattern

Flexural cracks appeared first for all specimens on the bottom surface of the top slab (tension side) directly under the load location. The first crack (cracking load) appeared at an average load of 55 kN (12.36 kip) for all the specimens, except 6-G-S2, in which the first crack appeared at a load of 64 kN (14.39 kip). Linear propagation of the first flexural cracks parallel to the supporting walls increased as the load increased. At higher loadings, flexural cracks started to initiate and propagate on the outside surface of the right wall, followed by flexural cracks on the left wall, as shown in Table 3. In Specimens 6-G-S1, 9-G-S1, 12-G-S1, 6-G-S2, and 6-S-S1, diagonal flexural cracks appeared on the bottom surface of the top slab and propagated diagonally up to loads of 305, 285, 206, 229, and 320 kN (68.57, 64.07, 46.31, 51.48, and 71.94 kip), respectively. Negative flexural cracks appeared on the top slab's top surface at the supports due to the framing action on the box culvert. Table 3 presents the first negative crack load. At loads of 154, 158, 160, 230, and 142 kN (34.62, 35.52, 35.97, 51.71, and 31.92 kip), flexural cracks initiated from the bottom surface of the top slab and propagated vertically on the edge of the slab in Specimens 6-G-S1, 9-G-S1, 12-G-S1, 6-G-S2, and 6-S-S1, respectively. These flexural cracks propagated diagonally toward the load-plate location as shear cracks appeared on the edge of the top slab at loads of 175, 201, 210, 279, and 276 kN (39.34, 45.19, 47.21, 62.72, and 62.05 kip), respectively. At an advanced stage of loading prior to failure, diagonal shear cracks were observed on the edge of the top slab that could be characterized as wide and clear cracks, as shown in Fig. 5. The specimens failed with the wide shear cracks on the edge of the top slab and were accompanied by diagonal

Table 3—Experimental test results of tested specimens

Specimen ID	First flexural crack*, kN	First negative flexural crack†, kN	First crack on walls (right/left)‡, kN	First shear crack§, kN	Ultimate failure load, kN	Mode of failure	Ultimate deflection, mm
6-G-S1	55	233	105/130	277	365.6	TSF	22.68
9-G-S1	55	162	135/160	375	391.6	TSF	20.16
12-G-S1	55	196	206/196	312	431.6	TSF	19.25
6-G-S2	64	190	135/146	385	477.1	TSF	20.53
6-S-S1	56	310	204/240	250	290‖/459.9#	TSF	20.01

*Crack on bottom surface of top slab.

†Crack on top surface of top slab.

‡Cracks on outside face of side walls.

§Shear crack appeared on edge side of top slab.

‖Steel bars yielding load.

#Ultimate failure load.

Note: TSF is two-way shear failure; 1 kN = 0.225 kip; 1 mm = 0.0394 in.

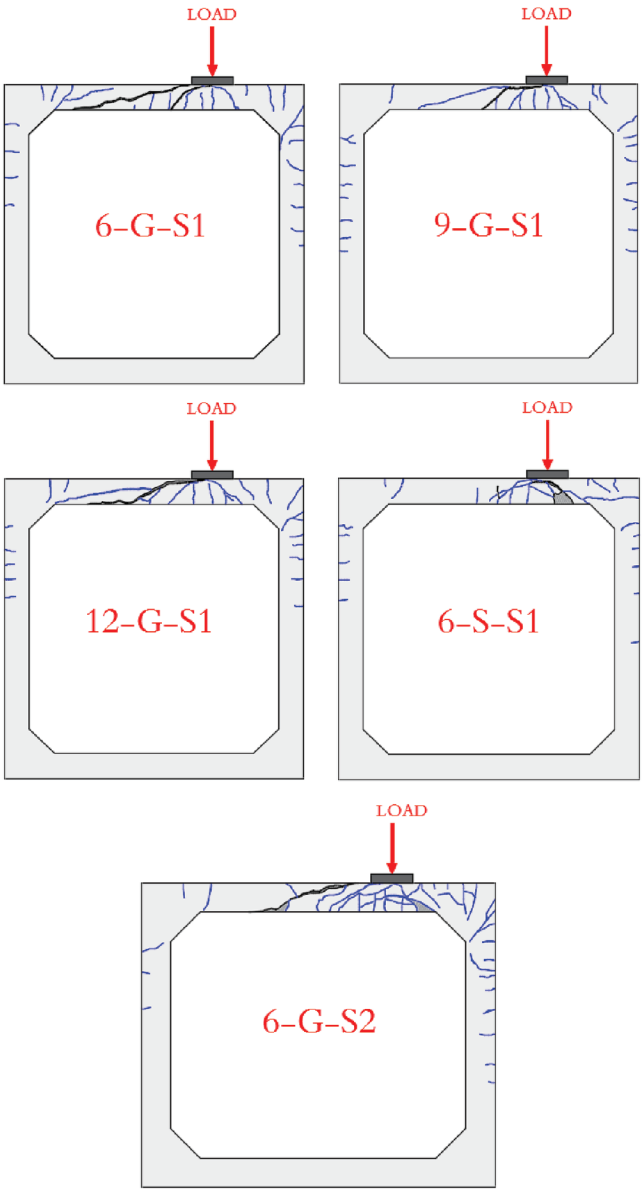

Fig. 5—Cracking pattern of specimens at failure before releasing load.

flexural cracks on the bottom surface of the top slab. The ultimate failure loads were 366, 392, 432, 477, and 460 kN (82.2, 88, 97, 107.3, and 103.4 kip) for Specimens 6-G-S1, 9-G-S1, 12-G-S1, 6-G-S2, and 6-S-S1, respectively. The ultimate failure load values ranged from 1.76 to 2.29 times the factored design load of 208.25 kN (46.14 kip) given in CSA S6:19. Table 3 summarizes the load associated with the different cracking patterns of the tested PCBC specimens.

Figure 5 shows a truncated cone shape of the shear failure of the tested specimens. Figure 6 shows the cracking patterns at failure for all the specimens. Two-way shear failure was observed on the inside face of the top slab. It was considered the typical mode of failure for all the tested specimens. The two-way shear behavior mainly resulted from the concentrated load acting on the top slab of the PCBCs. ACI 318-19 states that the concentrated loads create local moments and shear that might cause one-way slabs to have two-way behavior. This coincides with the observed mode of failure of the tested specimens in this study. In addition, it is in agreement with the results reported by Hassanli et al. (2022) for GFRP-reinforced inverted U-shaped culverts under concentrated loading. It should be mentioned that no penetration of the load plate into the concrete was observed for any of the PCBCs tested in this study.

Regardless of longitudinal reinforcement ratio and type, the cracking loads were almost similar for the specimens with a 150 mm (5.91 in.) top-slab thickness, with an average of 55 kN (12.36 kip). It increased to 64 kN (14.39 kip) in Specimen 6-G-S2 with a thicker top slab of 180 mm (7.09 in.). Higher load-carrying capacities were obtained by specimens with higher axial reinforcement stiffness or greater top-slab thickness, which coincides with Hassan et al. (2013).

Load-deflection behavior of specimens

Figure 7 shows the top slab's deflection measured under the center of the load plate versus the applied loads for the tested specimens. The load-deflection curves of all the GFRP-reinforced specimens were almost bilinear. The pre-cracking behavior was almost similar to the cracking load representing the behavior of the uncracked slab using the gross moment of inertia of the concrete section. The post-cracking

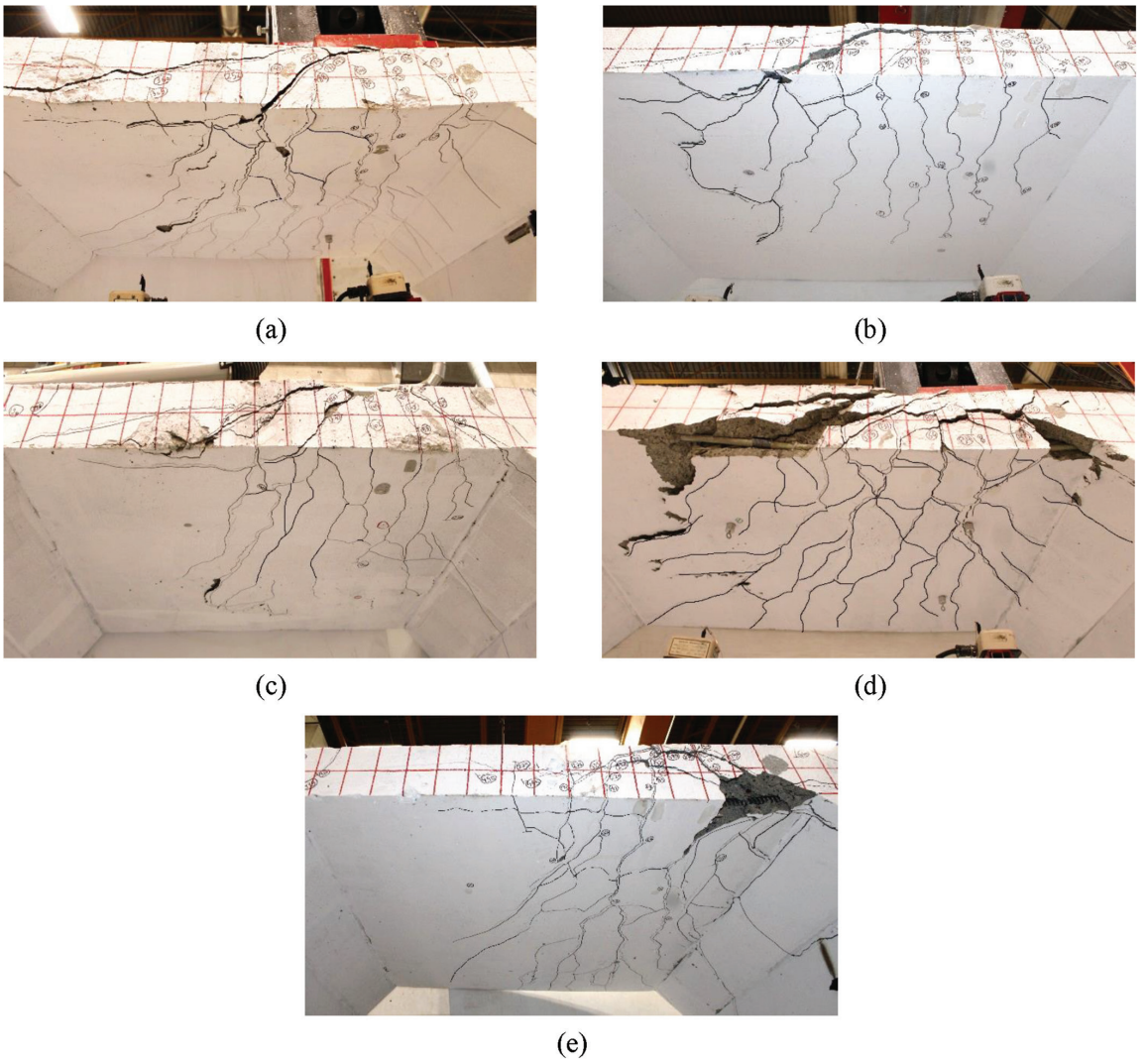

Fig. 6—Diagonal cracks on top slab's bottom surface of GFRP-reinforced specimens: (a) 6-G-S1; (b) 9-G-S1; (c) 12-G-S1; (d) 6-G-S2; and (e) steel-reinforced specimen 6-S-S1.

stage represents the cracked slab with reduced moment of inertia. At this stage, specimen behavior was influenced by the axial reinforcement stiffness, which is a function of the modulus of elasticity E_f and area A_f of the reinforcing bars. The steel-reinforced specimen had linear load-deflection behavior prior to yielding at 290 kN (65.19 kip). At the same loading level, Specimen 6-S-S1 had higher rigidity than its counterpart 6-G-S1. After the yield point of the longitudinal reinforcing bars on the tension side of the top slab, it exhibited a yield plateau with a decrease in stiffness, followed by a gradual decrease in the overall stiffness of the specimen. Table 3 presents the ultimate deflection values corresponding to the ultimate failure loads.

At the same loading level, Specimens 9-G-S1 and 12-G-S1, with higher longitudinal reinforcement ratios, had lower deflection values and higher rigidity than Specimen 6-G-S1. In addition, Specimen 6-G-S2, with a thicker top slab, exhibited higher rigidity and lower deflection than Specimen 6-G-S1. Furthermore, Specimen 6-S-S1 showed higher rigidity, prior to the steel bars yielding, than its counterpart 6-G-S1.

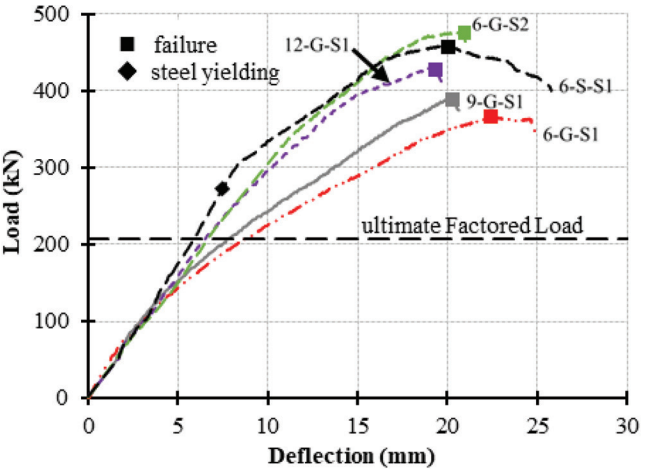

Fig. 7—Load-deflection relationship for tested specimens. (Note: 1 kN = 0.225 kip.)

Strains in concrete and longitudinal reinforcement

Figure 8(a) presents the load versus concrete strain readings measured on the top surface of concrete of the top slab (compression side) around the load. Low concrete strains

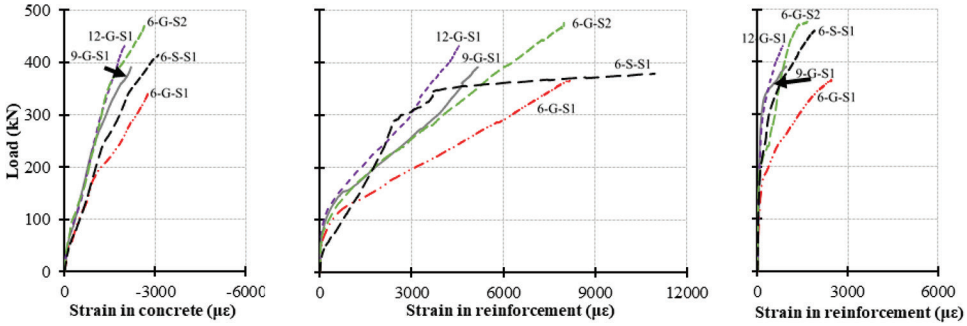

Fig. 8—Load-strain relationships: (a) concrete compressive strains; (b) tensile reinforcement strains under load; and (c) outer reinforcement strains at supports. (Note: 1 kN = 0.225 kip.)

for all specimens were measured before cracking, ranging between –109 and –197 με. Specimen 6-G-S1 showed concrete strains similar to that of its counterpart 6-S-S1 up to 45% of the ultimate load. Then it had higher concrete compressive strains, as shown in Fig 8(a). The maximum measured concrete compressive strains were –2753, –2837, –1982, –2644, and –3105 με for Specimens 6-G-S1, 9-G-S1, 12-G-S1, 6-G-S2, and 6-S-S1, respectively. The measured strains for all the GFRP-reinforced specimens were within the specified crushing failure limit in ACI CODE-440.11-22 (–3000 με) and CSA S806-12 (–3500 με), while they exceeded the design limit in ACI 318-19 (–3000 με) for steel-reinforced Specimen 6-S-S1. It should be mentioned that the concrete SGs in Specimen 6-G-S1 were damaged at a load of 341.6 kN (76.79 kip) (93% of total load), as were those in specimen 6-S-S1 at a load of 415 kN (93.92 kip) (90% of total load).

Figure 8(b) shows the load versus tensile strains in the bottom longitudinal bars of the top slab directly under the load plate. From the load-strain relationship, the tensile strain readings for the GFRP bars were observed to be very low prior to the initiation of the first crack. After the first flexural crack occurred, the strains in the GFRP-reinforced specimens increased linearly up to failure. The maximum tensile strain readings in the GFRP-reinforced specimens were 8165, 5160, 4540, and 7980 με for Specimens 6-G-S1, 9-G-S1, 12-G-S1, and 6-G-S2, respectively. The maximum GFRP tensile strain reading (8165 με) represents 37% of the characteristic tensile strength, indicating that the failure was not caused by GFRP bars rupturing. On the other hand, the steel-reinforced specimen showed a yield plateau of tensile steel bars, resulting in a rapid increase in the tensile strain readings up to failure. The steel bars yielded at approximately 2480 με, at a load of 290 kN (65.19 kip) (63% of the ultimate failure load). Thereafter, the tensile SG stopped recording at a load of 379 kN (85.20 kip) (82% of the ultimate failure load) with a tensile strain of 10,948 με. Figure 8(c) plots the load versus tensile strains in the outer reinforcing bars of the top slab in the negative moment zone at the supports. It shows that the outer reinforcing bars in all the specimens were under tension as a result of the framing action on the box culvert structure. The maximum measured strain in the GFRP-reinforced specimens was 2459 με, representing 11% of the characteristic tensile strength of the GFRP bars. The axial reinforcement stiffness and the top-slab thickness affected the measured strains.

Influence of longitudinal reinforcement type

While Specimens 6-G-S1 and 6-S-S1 had the same longitudinal reinforcement ratio (0.83%), Specimen 6-S-S1 had higher axial reinforcement stiffness due to the steel bars having a higher modulus of elasticity (E_s = 200 GPa [29,000 ksi]) than the GFRP bars (E_f = 63.7 GPa [9239 ksi]). Before cracking occurred, the initial stiffness was not significantly affected by the axial reinforcement stiffness, as shown in Fig. 7. After cracking, the behavior of the two specimens differed, and the stiffness of specimens at this stage was dependent on the axial stiffness of the reinforcing bars. It led to higher deflection and lower load-carrying capacity in the GFRP-reinforced specimen. According to the load-deflection relationship of the two specimens presented in Fig. 7, the steel-reinforced specimen's post-cracking stiffness was 2.93 times greater than that of the GFRP-reinforced specimen. This value is approximately equivalent to the ratio of the modulus of elasticity of steel bars to that of GFRP bars. At the same loading level, Specimen 6-S-S1 had higher rigidity and lower deflection values than 6-G-S1. In addition, it had higher loading capacity than specimen 6-G-S1. Thus, Specimen 6-G-S1 had 20.5% lower load-carrying capacity and 13.3% higher ultimate deflection than its counterpart Specimen 6-S-S1. Specimen 6-G-S1 exhibited linear-elastic behavior after the first crack up to failure. In contrast, Specimen 6-S-S1 had linear stiffness up to the yielding of the steel bars at a load of 290 kN (65.19 kip) and then exhibited a yield plateau after 2480 με up to failure. Consequently, Specimen 6-S-S1 failed as the result of two-way shear failure initiated by steel yielding.

Influence of longitudinal reinforcement ratio

Three longitudinal reinforcement ratios of 0.83%, 1.25%, and 1.67% were used for the GFRP-reinforced specimens. The load-carrying capacity increased as the longitudinal reinforcement ratio increased, enhancing the tested specimens' stiffness and decreasing top-slab deflection. Increasing the longitudinal reinforcement ratio in Specimens 9-G-S1 and 12-G-S1 increased their load-carrying capacity by 7% and 17%, respectively, and decreased the top-slab ultimate deflection under the load by 8% and 14%, respectively. Moreover, given the same load level, increasing the

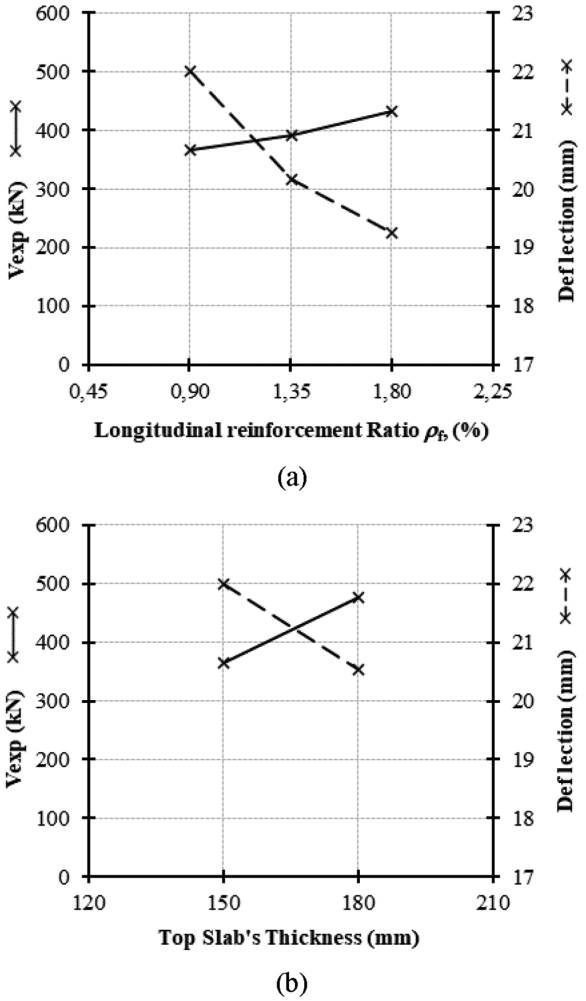

Fig. 9—Experimental load capacity versus: (a) longitudinal reinforcement ratio; and (b) top-slab thickness. (Note: 1 kN = 0.225 kip; 1 mm = 0.0394 in.)

longitudinal reinforcement ratio decreased the concrete strains by 38% and 48%, respectively, and the reinforcement strains by 42% and 55%, respectively. The experimental load capacity versus the longitudinal reinforcement ratio relationship in Fig. 9(a) shows that the load-carrying capacity positively correlates with the longitudinal reinforcement ratio, while the top-slab deflection negatively correlates with the longitudinal GFRP reinforcement ratio. Changing the reinforcement ratio significantly impacted the load-carrying capacity, emphasizing the importance of considering the reinforcement ratio in the calculations.

Influence of clear span length and top-slab thickness

The clear span and slab thickness of Specimen 6-G-S2 were increased to 1800 and 180 mm (70.87 and 7.09 in.), respectively. Specimens 6-G-S1 and 6-G-S2 both had the same axial reinforcement stiffness and GFRP reinforcement type. Increasing the top-slab thickness increased the load-carrying capacity by approximately 30% and decreased the ultimate deflection by 7%. Moreover, it lowered the neutral-axis location and increased the depth of the uncracked concrete contribution to resist shear stresses, as attested by Specimen

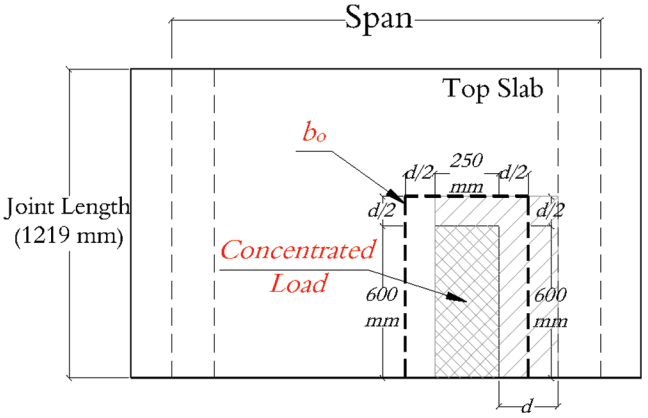

Fig. 10—Effective perimeter around concentrated load at top slab. (Note: 1 mm = 0.0394 in.)

6-G-S2, which had a cracking load 16% higher than that of Specimen 6-G-S1. Specimen 6-G-S2 had 50% and 33% lower concrete and reinforcement strains, respectively, at the same load level as Specimen 6-G-S1. In the two-way action, increasing the slab thickness increased the surface area that resisted the two-way shear action, which yields higher punching-shear capacity with flatter shear cracks (Hassan et al. 2013). The experimental load-carrying capacity versus the slab thickness relationship in Fig. 9(b) shows that the load-carrying capacity positively correlates with the slab thickness. In contrast, the top-slab deflection negatively correlates with the top-slab thickness.

THEORETICAL STUDY

This section presents a theoretical study to evaluate the accuracy of two-way shear equations in design codes to predict the shear capacity of the top slab of PCBCs reinforced with GFRP bars under a truck wheel load. In this section, the effective perimeter of the critical section around the load is computed at a distance of $d/2$ away from the concentrated load, as shown in Fig. 10. Table 4 presents a comparison between the experimental shear failure load and the predicted two-way shear resistances of the top slab of the tested specimens. Figure 11 presents the ratio V_{exp}/V_{pred} from different provisions versus the longitudinal reinforcement ratio for the GFRP-reinforced specimens.

Background of two-way shear design equations

Several two-way shear design equations for FRP-reinforced concrete elements have been integrated into North America's various design codes. Two-way shear equations in the design codes ACI CODE-440.11-22 (ACI Committee 440 2022), AASHTO LRFD, and CSA S806-12 were assessed by comparing their predictions to the experimental results. In addition to the provisions mentioned previously, a modification has been made to the two-way shear equation for steel-reinforced concrete members in CSA S6:19 to account for the axial stiffness of FRP reinforcement.

ACI CODE-440.11 (2022)—ACI CODE-440.11-22 specifies the stress corresponding to nominal two-way shear strength provided by the concrete v_c of GFRP-reinforced concrete slabs, as presented in Eq. (1). The nominal shear

Table 4—Comparison of experimental and predicted shear capacities of GFRP specimens

Specimen ID	Failure load (V_{exp}), kN	ACI CODE-440.11-22		AASHTO LRFD		CSA S806-12		CSA S6:19 (modified)	
		V_{pred}, kN	V_{exp}/V_{pred}	V_{pred}, kN	V_{exp}/V_{pred}	V_{pred}, kN	V_{exp}/V_{pred}	V_{pred}, kN	V_{exp}/V_{pred}
6-G-S1	365.6	175.4	2.08	174.7	2.09	275.3	1.33	354.0	1.03
9-G-S1	391.6	220.3	1.78	219.5	1.78	333.1	1.18	428.5	0.91
12-G-S1	431.6	244.3	1.77	243.4	1.77	356.9	1.21	459.0	0.94
6-G-S2	477.1	205.5	2.32	212.4	2.25	346.1	1.38	445.2	1.07
Average		—	1.99	—	1.97	—	1.27	—	0.99
Standard deviation		—	0.27	—	0.23	—	0.10	—	0.07
COV, %		—	13.43	—	11.86	—	7.55	—	7.55

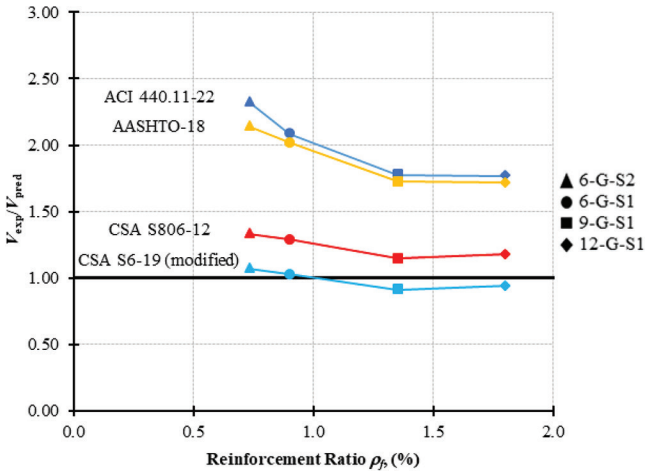

Fig. 11—Comparison of experimental to predicted results.

strength provided by concrete V_c can be calculated with Eq. (2)

$$v_c = 10\lambda_s k_{cr}\sqrt{f_c'} \geq 1.6\lambda_s\sqrt{f_c'}, \text{ psi} \quad (1 \text{ psi} = 0.00689 \text{ MPa}) \tag{1}$$

$$V_c = v_c(b_o d), \text{ kip} \quad (1 \text{ kip} = 4.448 \text{ kN}) \tag{2}$$

where λ_s is the size effect factor; k_{cr} is the ratio of the elastic cracked transformed section neutral-axis depth to the effective depth; f_c' is the compressive strength of concrete ($\sqrt{f_c'} \leq 100$ psi [0.689 MPa]); d is the effective depth calculated from the concrete compression side to the center of the GFRP longitudinal tension reinforcement; and b_o is the perimeter of the critical shear section and is computed at a distance of $d/2$ from the concentrated load edge. The term λ_s can be calculated from Eq. (3) for the case of $A_{fv} < A_{fv,min}$, which is a function of the transverse shear reinforcement area. The term k_{cr} can be calculated from Eq. (4) as a function of the longitudinal reinforcement ratio ρ_f and the modular ratio n_f.

$$\lambda_s = \sqrt{\frac{2}{1 + \left(\frac{d}{10}\right)}} \leq 1.0 \tag{3}$$

$$k_{cr} = \sqrt{2\rho_f n_f + (\rho_f n_f)^2} - \rho_f n_f \tag{4}$$

AASHTO (2018)—For two-way action, the punching-shear resistance of the concrete V_c in GFRP-reinforced concrete slabs without shear reinforcement can be calculated with Eq. (5).

$$V_c = 0.316k\sqrt{f_c'}b_{o;0.5d}d_v, \text{ kip} \quad (1 \text{ kip} = 4.448 \text{ kN}) \tag{5}$$

The term k can be calculated with Eq. (4).

CSA S806 (2012)—According to CSA S806-12, the punching-shear resistance V_c of FRP concrete slabs can be calculated as the smallest value in Eq. (6), (7), and (8)

$$V_c = \left(1 + \frac{2}{\beta_c}\right)\left[0.028\lambda\phi_c(E_f\rho_f f_c')^{\frac{1}{3}}\right]b_{o;0.5d}d \tag{6}$$

$$V_c = \left[\left(\frac{\alpha_s d}{b_o}\right) + 0.19\right]0.147\lambda\phi_c(E_f\rho_f f_c')^{\frac{1}{3}}b_{o;0.5d}d \tag{7}$$

$$V_c = 0.056\lambda\phi_c(E_f\rho_f f_c')^{\frac{1}{3}}b_{o;0.5d}d \tag{8}$$

where β_c is the ratio of the long side to the short side of the concentrated load; λ is the factor for concrete density (λ = 1.0 for normal-density concrete); ϕ_c is the resistance factor for concrete; and α_s is 3 for the edge column or concentrated load.

CSA S6 (2019) (modified)—In CSA S6:19, the available two-way shear action equation is for steel-reinforced slabs, walls, or footings. The concrete resistance V_c to the two-way shear action can be calculated with Eq. (9)

$$V_c = \phi_c f_{cr} b_{o;0.5d} d \tag{9}$$

where f_{cr} is the concrete cracking strength ($f_{cr} = 0.4\sqrt{f_c'} \leq$ 3.2 MPa [464.12 psi] for normal-density concrete).

Equation (9) has been modified by directly implementing the FRP axial stiffness ($\rho_f E_f$) and the shear span-depth ratio (a/d) and is presented as shown in Eq. (10). The modified equation (Eq. (10)) was used for the calculations in this study and referred to as "CSA S6-19 (modified)," as shown in Fig. 11

$$V_c = 0.066\phi_c(\rho_f E_f f_c' d/a)^{1/3} b_{o;0.5d} d \tag{10}$$

where a is the distance between the tip of the haunch and the edge of the load plate. The coefficient (0.066) was determined based on the conducted regression analysis using the experimental database presented in this study.

Comparison between experimental and theoretical results

The shear capacities of the PCBCs' top slab were compared to the predictions using the two-way shear action equations mentioned herein. In all the analyses, the material resistance, concrete density, and member safety factors were taken as equal to unity. Table 4 gives the experimental-to-predicted shear ratios (V_{exp}/V_{pred}) of the tested specimens. Figure 11 plots the V_{exp}/V_{pred} from different provisions against the longitudinal GFRP reinforcement ratios. Based on the results in Table 4, it can be concluded that the CSA S806-12 punching-shear equation yielded good yet conservative prediction values, with an average V_{exp}/V_{pred} of 1.27 ± 0.10 and a coefficient of variation (COV) of 7.55%. The ACI CODE-440.11-22 and AASHTO LRFD equations provided very conservative predictions, with an average V_{exp}/V_{pred} of 1.99 ± 0.27 and 1.97 ± 0.23 and a COV of 13.43% and 11.86%, respectively. For the modified equation of CSA S6:19, this direct insertion of the FRP axial stiffness and the load location into the equation yielded the closest predictions to the experimental shear capacities, with an average V_{exp}/V_{pred} of 0.99 ± 0.07 and a COV of 7.55%, as presented in Table 4.

Based on the results in Table 4, two-way shear equations can be used to predict the shear capacity of the PCBCs' top slabs subjected to a concentrated load over a part of the entire width. In addition, it can be explained by the two-way shear failure of the tested specimens. The CSA S806-12 punching-shear equation gave good yet conservative predictions. The modified CSA S6:19 two-way shear equation provided the predictions the most consistent with the experimental results.

CONCLUSIONS

This paper reported on the structural behavior and shear strength of full-scale precast concrete box culverts (PCBCs) reinforced with glass fiber-reinforced polymer (GFRP) bars both experimentally and theoretically under CSA S6:19 truck wheel loading. The CL-625 truck wheel load was simulated with a 250 x 600 mm (9.8 x 23.6 in.) load plate located at the edge of the joint length and at a distance d along the span between the edge of the load plate and the tip of the right haunch. Based on the experimental results and the theoretical study presented in this paper, the following conclusions can be drawn:

1. The failure of the GFRP-reinforced PCBCs was two-way shear failure of the top slab, while the steel-reinforced concrete specimen failed as the result of two-way shear failure of the top slab after the yielding of the steel tension reinforcement in the top slab. No signs of penetration of the load plate into the concrete were observed during specimen loading.

2. All the GFRP-reinforced PCBCs exceeded the ultimate factored live load (208.25 kN = 1.4 × 1.7 × 87.5 kN [46.14 kip]) as per CSA S6:19, and the first shear crack was observed at a range of 133% to 184% of the ultimate factored live load.

3. Based on the test results, the failure of the GFRP-reinforced PCBCs was not triggered by GFRP bar rupture or concrete crushing. The maximum tensile strain (8165 με) achieved by the GFRP-reinforced specimens at failure represents 37% of the ultimate tensile strain of the GFRP bars.

4. The maximum compressive concrete strain at failure for the GFRP-reinforced concrete specimens was less than the specified design limits in ACI CODE-440.11-22 (–3000 με) and CSA S806-12 (–3500 με), while it exceeded the design limit in ACI 318-19 for the steel-reinforced Specimen 6-S-S1.

5. Changing the longitudinal GFRP reinforcement ratio significantly affected the load-carrying capacity of the tested specimens. This highlights the vital role of the direct implementation of the reinforcement ratio in calculating the two-way shear capacity, as carried out in the modified equation (Eq. (10)).

6. Increasing the clear span length and the top-slab thickness by 20% for Specimen 6-G-S2 increased the load-carrying capacity by 30% and decreased the top slab's ultimate deflection by 7%. Moreover, it increased the cracking load by 16%. Specimen 6-G-S2 had lower concrete and reinforcement strains than the counterpart Specimen 6-G-S1.

7. The experimental-to-predicted ratio of the two-way shear capacity indicates good yet conservative predictions for CSA S806-12. On the other hand, ACI CODE-440.11-22 and AASHTO LRFD yielded very conservative predictions of the two-way shear capacity. The two-way shear equation available for steel-reinforced concrete members in CSA S6:19 was modified to consider the FRP bars' axial stiffness ($\rho_f E_f$). The modified equation produced accurate predictions, with an average V_{exp}/V_{pred} of 0.99 ± 0.07 and a coefficient of variation (COV) of 7.55%.

8. The experimental findings were the first of their kind on the applicability of using GFRP as internal reinforcement for PCBCs under truck wheel loading. These experimental results can be considered in upcoming provisions of ACI CODE-440.11 and CSA S6 codes for using GFRP bars as internal reinforcement for PCBC applications. Furthermore, research is required using numerical analysis as a complementary approach to further enhance the understanding of member behavior.

AUTHOR BIOS

Ahmed Elnady *is a Doctoral Candidate in the Department of Civil and Building Engineering at the University of Sherbrooke, Sherbrooke, QC, Canada. He received his BSc and MSc in civil engineering from the Faculty of Engineering, Benha University, Benha, Egypt. His research interests include the use of fiber-reinforced polymers (FRPs) in reinforced concrete structures.*

Salaheldin Mousa *is a Research Associate in the Department of Civil and Building Engineering at the University of Sherbrooke, where he also received his PhD. He received his BSc and MSc from the Faculty of Engineering at Shoubra, Benha University. His research interests include the use of FRPs in reinforced concrete structures.*

Brahim Benmokrane, *FACI, is a Professor in the Department of Civil and Building Engineering at the University of Sherbrooke, Tier-1 Canada Research Chair in Advanced Composite Materials for Civil Structures,*

NSERC Senior Research Chair in FRP Reinforcement for Concrete Infrastructure, and Director of the University of Sherbrooke Research Center on Structural FRP Composite Materials for Concrete Structures (CRUSMAC). He is a member of ACI Committees 435, Deflection of Concrete Building Structures, and 440, Fiber-Reinforced Polymer Reinforcement, and ACI Subcommittees 440-E, FRP-Professional Education; 440-F, FRP-Repair-Strengthening; 440-H, FRP-Reinforced Concrete; 440-I, FRP-Prestressed Concrete; 440-K, FRP-Material Characteristics; and 440-L, FRP-Durability. He received the ACI Arthur J. Boase Award in 2022. His research interests include the development of FRP reinforcement for concrete structures and their durability, structural performance, and field applications.

ACKNOWLEDGMENTS

The authors wish to acknowledge the financial support of the Natural Sciences and Engineering Research Council of Canada (NSERC Alliance), the Tier-1 Canada Research Chair in Advanced Composite Materials for Civil Structures, and the Fonds de recherche du Québec – Nature et technologies (FRQNT). The authors are grateful to the precast company (Sym-Tech Béton Préfabriqué, Saint-Hyacinthe, QC, Canada) and the GFRP bar manufacturer (Pultrall Inc., Thetford Mines, QC, Canada) for their involvement in this project, and to the technical staff of the structural lab in the Department of Civil and Building Engineering at the University of Sherbrooke.

REFERENCES

AS 1597.1-2010, 2010, "Precast Reinforced Concrete Box Culverts, Part 1: Small Culverts (Not Exceeding 1200 mm Span and 1200 mm Height)," Standards Australia, Sydney, NSW, Australia, 44 pp.

AASHTO, 2018, "AASHTO LRFD Bridge Design Guide Specifications for GFRP-Reinforced Concrete," second edition, American Association of State Highway and Transportation Officials, Washington, DC.

Abolmaali, A., and Garg, A., 2008a, "Shear Behavior and Mode of Failure for ASTM C1433 Precast Box Culverts," *Journal of Bridge Engineering*, ASCE, V. 13, No. 4, pp. 331-338. doi: 10.1061/(ASCE)1084-0702(2008)13:4(331)

Abolmaali, A., and Garg, A. K., 2008b, "Effect of Wheel Live Load on Shear Behavior of Precast Reinforced Concrete Box Culverts," *Journal of Bridge Engineering*, ASCE, V. 13, No. 1, pp. 93-99. doi: 10.1061/(ASCE)1084-0702(2008)13:1(93)

ACI Committee 318, 2019, "Building Code Requirements for Structural Concrete (ACI 318-19) and Commentary (ACI 318R-19) (Reapproved 2022)," American Concrete Institute, Farmington Hills, MI, 624 pp.

ACI Committee 440, 2015, "Guide for the Design and Construction of Structural Concrete Reinforced with Fiber-Reinforced Polymer (FRP) Bars (ACI 440.1R-15)," American Concrete Institute, Farmington Hills, MI, 88 pp.

ACI Committee 440, 2022, "Building Code Requirements for Structural Concrete Reinforced with Glass Fiber-Reinforced Polymer (GFRP) Bars—Code and Commentary (ACI CODE-440.11-22)," American Concrete Institute, Farmington Hills, MI, 260 pp.

Ahmed, A.; Guo, S.; Zhang, Z.; Shi, C.; and Zhu, D., 2020, "A Review on Durability of Fiber Reinforced Polymer (FRP) Bars Reinforced Seawater Sea Sand Concrete," *Construction and Building Materials*, V. 256, Article No. 119484. doi: 10.1016/j.conbuildmat.2020.119484

Ahmed, A. O. M., and Alarabi, E., 2011, "Development Formulation for Structural Design of Concrete Box Culverts," *Practice Periodical on Structural Design and Construction*, ASCE, V. 16, No. 2, pp. 48-55. doi: 10.1061/(ASCE)SC.1943-5576.0000075

Ahmed, E. A.; Benmokrane, B.; and Sansfaçon, M., 2017, "Case Study: Design, Construction, and Performance of the La Chancelière Parking Garage's Concrete Flat Slabs Reinforced with GFRP Bars," *Journal of Composites for Construction*, ASCE, V. 21, No. 1, p. 05016001. doi: 10.1061/(ASCE)CC.1943-5614.0000656

Angst, U. M., 2018, "Challenges and Opportunities in Corrosion of Steel in Concrete," *Materials and Structures*, V. 51, No. 1, Article No. 4. doi: 10.1617/s11527-017-1131-6

ASTM C1433-03, 2003, "Standard Specification for Precast Reinforced Concrete Box Sections for Culverts, Storm Drains, and Sewers," ASTM International, West Conshohocken, PA, 16 pp.

ASTM D7617/D7617M-11(2017), 2017, "Standard Test Method for Transverse Shear Strength of Fiber-Reinforced Polymer Matrix Composite Bars," ASTM International, West Conshohocken, PA, 12 pp.

Benmokrane, B.; El-Salakawy, E.; El-Gamal, S.; and Goulet, S., 2007, "Construction and Testing of an Innovative Concrete Bridge Deck Totally Reinforced with Glass FRP Bars: Val-Alain Bridge on Highway 20 East," *Journal of Bridge Engineering*, ASCE, V. 12, No. 5, Sept.-Oct., pp. 632-645. doi: 10.1061/(ASCE)1084-0702(2007)12:5(632)

Benmokrane, B.; El-Salakawy, E.; Desgagné, G.; and Lackey, T., 2004, "FRP Bars for Bridges," *Concrete International*, V. 26, No. 8, Aug., pp. 84-90.

Benmokrane, B.; El-Salakawy, E.; El-Ragaby, A.; and Lackey, T., 2006, "Designing and Testing of Concrete Bridge Decks Reinforced with Glass FRP Bars," *Journal of Bridge Engineering*, ASCE, V. 11, No. 2, pp. 217-229. doi: 10.1061/(ASCE)1084-0702(2006)11:2(217)

Benmokrane, B.; Mohamed, H.; and Ahmed, E., 2016, "Recent Developments of FRP Bars as Internal Reinforcement in Concrete Structures & Field Applications," *Proceeding of the Fourth International Conference on Sustainable Construction Materials and Technologies (SCMT4)*, Las Vegas, NV, Aug. 7-11, 10 pp.

Benmokrane, B.; Mohamed, H. M.; Mousa, S.; Elsafty, A.; and Nolan, S., 2021a, "Design, Construction, Testing, and Behavior of Driven Precast Concrete Piles Reinforced with GFRP Bars and Spirals," *Journal of Bridge Engineering*, ASCE, V. 26, No. 8, p. 04021050. doi: 10.1061/(ASCE)BE.1943-5592.0001755

Benmokrane, B.; Mousa, S.; Mohamed, K.; and Sayed-Ahmed, M., 2021b, "Physical, Mechanical, and Durability Characteristics of Newly Developed Thermoplastic GFRP Bars for Reinforcing Concrete Structures," *Construction and Building Materials*, V. 276, Article No. 122200. doi: 10.1016/j.conbuildmat.2020.122200

Benmokrane, B., and Rahman, H., eds., 1998, *Durability of Fiber Reinforced Polymer (FRP) Composites for Construction: Proceedings of the First International Conference (CDCC'98)*, Sherbrooke, QC, Canada, 665 pp.

Bouguerra, K.; Ahmed, E. A.; El-Gamal, S.; and Benmokrane, B., 2011, "Testing of Full-Scale Concrete Bridge Deck Slabs Reinforced with Fiber-Reinforced Polymer (FRP) Bars," *Construction and Building Materials*, V. 25, No. 10, pp. 3956-3965. doi: 10.1016/j.conbuildmat.2011.04.028

CSA S6:19, 2019, "Canadian Highway Bridge Design Code," CSA Group, Toronto, ON, Canada.

CSA S807:19, 2019, "Specification for Fibre-Reinforced Polymers," CSA Group, Toronto, ON, Canada.

CSA S806-12, 2012, "Design and Construction of Building Structures with Fibre-Reinforced Polymers (Reaffirmed in 2021)," CSA Group, Toronto, ON, Canada.

Capozucca, R., 1995, "Damage to Reinforced Concrete Due to Reinforcement Corrosion," *Construction and Building Materials*, V. 9, No. 5, pp. 295-303. doi: 10.1016/0950-0618(95)00033-C

Caratelli, A.; Meda, A.; Rinaldi, Z.; Spagnuolo, S.; and Maddaluno, G., 2017, "Optimization of GFRP Reinforcement in Precast Segments for Metro Tunnel Lining," *Composite Structures*, V. 181, pp. 336-346. doi: 10.1016/j.compstruct.2017.08.083

Chang, K., and Seo, D., 2012, "Behavior of One-Way Concrete Slabs Reinforced with GFRP Bars," *Journal of Asian Architecture and Building Engineering*, V. 11, No. 2, pp. 351-358. doi: 10.3130/jaabe.11.351

El-Salakawy, E.; Benmokrane, B.; and Desgagné, G., 2003, "Fibre-Reinforced Polymer Composite Bars for the Concrete Deck Slab of Wotton Bridge," *Canadian Journal of Civil Engineering*, V. 30, No. 5, pp. 861-870. doi: 10.1139/l03-055

El-Salakawy, E.; Benmokrane, B.; El-Ragaby, A.; and Nadeau, D., 2005, "Field Investigation on the First Bridge Deck Slab Reinforced with Glass FRP Bars Constructed in Canada," *Journal of Composites for Construction*, ASCE, V. 9, No. 6, Dec., pp. 470-479. doi: 10.1061/(ASCE)1090-0268(2005)9:6(470)

El-Sayed, A.; El-Salakawy, E.; and Benmokrane, B., 2005, "Shear Strength of One-Way Concrete Slabs Reinforced with Fiber-Reinforced Polymer Composite Bars," *Journal of Composites for Construction*, ASCE, V. 9, No. 2, pp. 147-157. doi: 10.1061/(ASCE)1090-0268(2005)9:2(147)

Garg, A. K., and Abolmaali, A., 2006, "Shear Behavior of Small Span Single and Double Precast Reinforced Concrete Box Culverts," *Pipelines 2006: Service to the Owner: Proceedings of the Pipeline Division Specialty Conference*, A. Atalah and A. Tremblay, eds., Chicago, IL, July 30-Aug. 2, pp. 1-12.

Garg, A. K., and Abolmaali, A., 2009, "Finite-Element Modeling and Analysis of Reinforced Concrete Box Culverts," *Journal of Transportation Engineering*, ASCE, V. 135, No. 3, pp. 121-128. doi: 10.1061/(ASCE)0733-947X(2009)135:3(121)

Garg, A. K.; Abolmaali, A.; and Fernandez, R., 2007, "Experimental Investigation of Shear Capacity of Precast Reinforced Concrete Box Culverts," *Journal of Bridge Engineering*, ASCE, V. 12, No. 4, pp. 511-517. doi: 10.1061/(ASCE)1084-0702(2007)12:4(511)

Gudonis, E.; Timinskas, E.; Gribniak, V.; Kaklauskas, G.; Arnautov, A. K.; and Tamulėnas, V., 2013, "FRP Reinforcement for Concrete Structures: State-of-the-Art Review of Application and Design," *Engineering Structures and Technologies*, V. 5, No. 4, pp. 147-158. doi: 10.3846/2029882X.2014.889274

Hassan, M.; Ahmed, E.; and Benmokrane, B., 2013, "Punching-Shear Strength of Normal and High-Strength Two-Way Concrete Slabs Reinforced

with GFRP Bars," *Journal of Composites for Construction*, ASCE, V. 17, No. 6, p. 04013003. doi: 10.1061/(ASCE)CC.1943-5614.0000424

Hassanli, R.; Youssf, O.; Manalo, A.; Najafgholipour, M. A.; Elchalakani, M.; del Rey Castillo, E.; and Lutze, D., 2022, "An Experimental Study of the Behavior of GFRP-Reinforced Precast Concrete Culverts," *Journal of Composites for Construction*, ASCE, V. 26, No. 5, p. 04022043. doi: 10.1061/(ASCE)CC.1943-5614.0001224

Hosseini, S. M.; Mousa, S.; Mohamed, H.; and Benmokrane, B., 2023, "Application of GFRP Bars in Precast Concrete Tunnel Lining Segments," *8th International Conference on Advanced Composite Materials in Bridges and Structures*, B. Benmokrane, K. Mohamed, A. Farghaly, and H. Mohamed, eds., Sherbrooke, QC, Canada, pp. 187-195.

Idemudia, D.; Newhook, J.; and Oudah, F., 2023, "Design and Performance of GFRP Reinforced Bridge Decks in Nova Scotia—Preliminary Analysis," *8th International Conference on Advanced Composite Materials in Bridges and Structures*, B. Benmokrane, K. Mohamed, A. Farghaly, and H. Mohamed, eds., Sherbrooke, QC, Canada, pp. 61-68.

Jabbar, S. A., and Farid, S. B. H., 2018, "Replacement of Steel Rebars by GFRP Rebars in the Concrete Structures," *Karbala International Journal of Modern Science*, V. 4, No. 2, pp. 216-227. doi: 10.1016/j.kijoms.2018.02.002

Kim, K., and Yoo, C. H., 2005, "Design Loading on Deeply Buried Box Culverts," *Journal of Geotechnical and Geoenvironmental Engineering*, ASCE, V. 131, No. 1, pp. 20-27. doi: 10.1061/(ASCE)1090-0241(2005)131:1(20)

Kolate, N.; Mathew, M.; and Mali, S., 2014, "Analysis and Design of RCC Box Culvert," *International Journal of Scientific and Engineering Research*, V. 5, No. 12, pp. 36-40.

Kurtoğlu, A. E.; Bilgehan, M.; Gülşan, M. E.; and Çevik, A., 2023, "Experimental and Theoretical Investigation of the Punching Shear Strength of GFRP-Reinforced Two-Way Slabs," *Structural Engineering International*, V. 33, No. 3, pp. 379-388. doi: 10.1080/10168664.2022.2093689

Matthys, S., and Taerwe, L., 2000, "Concrete Slabs Reinforced with FRP Grids. II: Punching Resistance," *Journal of Composites for Construction*, ASCE, V. 4, No. 3, pp. 154-161. doi: 10.1061/(ASCE)1090-0268(2000)4:3(154)

McGrath, T. J.; Liepins, A. A.; and Beaver, J. L., 2005, "Live Load Distribution Widths for Reinforced Concrete Box Sections," *6th International Bridge Engineering Conference: Reliability, Security, and Sustainability in Bridge Engineering*, Boston, MA, July 17-20, pp. 99-108.

Mohamed, H. M., and Benmokrane, B., 2014, "Design and Performance of Reinforced Concrete Water Chlorination Tank Totally Reinforced with GFRP Bars: Case Study," *Journal of Composites for Construction*, ASCE, V. 18, No. 1, p. 05013001. doi: 10.1061/(ASCE)CC.1943-5614.0000429

Mohamed, H. M., and Benmokrane, B., 2015, "Make the Case: The Use of FRP Bars for Soft-Eyes in Construction of Tunnels," *Tunnels and Tunnelling, The Official Publication of the Tunnelling Association of Canada*, Dec.-Jan., pp. 35-40.

Mufti, A.; Onofrei, M.; Benmokrane, B.; Banthia, N.; Boulfiza, M.; Newhook, J.; Bakht, B.; Tadros, G.; and Brett, P., 2005, "Durability of GFRP Reinforced Concrete in Field Structures," *7th International Symposium on Fiber-Reinforced Polymer (FRP) Reinforcement for Concrete Structures (FRPRCS-7)*, SP-230, C. K. Shield, J. P. Busel, S. L. Walkup, and D. D. Gremel, eds., American Concrete Institute, Farmington Hills, MI, pp. 1361-1377.

Nguyen-Minh, L., and Rovňák, M., 2013, "Punching Shear Resistance of Interior GFRP Reinforced Slab-Column Connections," *Journal of Composites for Construction*, ASCE, V. 17, No. 1, pp. 2-13. doi: 10.1061/(ASCE)CC.1943-5614.0000324

Ospina, C. E.; Alexander, S. D. B.; and Cheng, J. J. R., 2003, "Punching of Two-Way Concrete Slabs with Fiber-Reinforced Polymer Reinforcing Bars or Grids," *ACI Structural Journal*, V. 100, No. 5, Sept.-Oct., pp. 589-598.

ACI STRUCTURAL JOURNAL TECHNICAL PAPER

Title No. 121-S42

Cyclic Behavior of Beams with Double-Perimeter and Continuous-Stirrup Hoops

by Yu-Chen Ou, Hermawan Sutejo, Jyun-Lin Huang, and Sheng-I Yen

Two types of hoop layouts, double-perimeter hoops (DPH) and continuous-stirrup hoops (CSH), were examined in this research for beams of special moment frames. Compared to conventional hoops (CH), the DPH and CSH have the advantage of better constructability. Full-scale beam specimens—specimen CH as a control specimen and specimens DPH and CSH as test specimens—were tested using lateral cyclic loading to examine their seismic performance. Test results showed that although specimen DPH violated the Code requirement for the number and spacing of laterally supported longitudinal bars, the specimen still exhibited seismic performance sufficient for beams of special moment frames. Specimen CSH showed better seismic performance than the control specimen (CH). The better performance of CSH was mainly attributed to the better concrete confinement and reinforcing bar buckling restraint ability of the intermediate hoops of the CSH than the intermediate stirrups of the CH.

Keywords: closed stirrups; deformation capacity; energy dissipation; hoops; plastic hinge region; reinforced concrete beams; reinforcement buckling; special moment frames.

INTRODUCTION

It is stated in ACI 318-19[1] that in the potential plastic hinge region of beams of special moment frames, transverse reinforcement should be provided in the form of hoops. The spacing of the hoops should not exceed $d/4$, 150 mm (6 in.), and $6d_b$ for Grade 420 MPa (60 ksi) longitudinal bars. Moreover, every corner and alternate longitudinal bar closest to the tension and compression faces should be laterally supported by transverse reinforcement. In addition, the spacing of the laterally supported longitudinal bars (h_x) should not be more than 350 mm (14 in.). These requirements are intended to provide good concrete confinement to increase concrete strength and deformation capacities and to provide sufficient lateral support for longitudinal bars to prevent premature buckling in compression.

To improve the constructability, the hoop is allowed to be formed by a U-stirrup having seismic hooks at both ends and closed by a crosstie. A typical transverse reinforcement layout used in Taiwan that satisfies the aforementioned requirements is shown in Fig. 1(a). This layout is referred to as conventional hoops (CH) herein and consists of a perimeter stirrup and an intermediate stirrup. Both stirrups have seismic hooks at the ends. The two stirrups are closed by a crosstie on the top. The construction proceeds in the following steps (Fig. 2): a) placing the two top-corner longitudinal bars and then installing the perimeter stirrups with the hooks of the stirrups hanging on the two top longitudinal bars; b) placing the two bottom-corner longitudinal bars; c) placing the two intermediate top longitudinal bars and then installing the intermediate stirrups hanging on the two longitudinal bars; d) placing the rest of the bottom longitudinal bars; e) placing the rest of the top longitudinal bars; and f) placing the crossties to close the stirrups. All reinforcing bars were secured together in place by tie wire. Note that the aforementioned construction is conducted on site after the floor and beam formwork is set. Thus, the space for beam reinforcement work is limited as reinforcing bars can only be placed from the top side of the beam. The intermediate stirrups further increase the difficulty of bar placement and limit the space for bar tying. As a result, many construction companies in Taiwan are reluctant to construct intermediate stirrups. If the shear design requires four legs of stirrups, two pieces of perimeter stirrups would be used instead of intermediate stirrups, as shown in Fig. 1(b). This type of transverse reinforcement is referred to as double-perimeter hoops (DPH) herein. The construction of DPH proceeds in the following steps (Fig. 3): a) placing the two top-corner longitudinal bars and then installing the perimeter stirrups (two in a set) with the hooks of the stirrups hanging on the two top longitudinal bars; b) placing all the bottom longitudinal bars; c) placing the rest of the top longitudinal bars; and d) placing the crossties to close the stirrups. Because there is no interference from the intermediate stirrups, the space for the placement and tying of reinforcing bars is maximized, and construction time is reduced. The DPH can satisfy the requirements for shear and the maximum spacing between hoops. However, they often fail to satisfy the requirements that every alternate longitudinal bar should be laterally supported, and often violate the maximum h_x requirement (350 mm [14 in.]).

The requirement that every alternate longitudinal bar needs to be laterally supported is mainly intended to reduce the buckling tendency of longitudinal bars in compression. The maximum h_x requirement is primarily to ensure confinement effectiveness by limiting the span of confined concrete arches.[2] These requirements were originally developed for columns[3,4] and first appeared in ACI 318-63.[5] These requirements were extended to the plastic hinge region of beams of special moment frames in ACI 318-83.[6] In ACI 318-14, the requirements were made stricter by requiring lateral support

ACI Structural Journal, V. 121, No. 3, May 2024.
MS No. S-2023-105.R1, doi: 10.14359/51740485, received November 26, 2023, and reviewed under Institute publication policies.

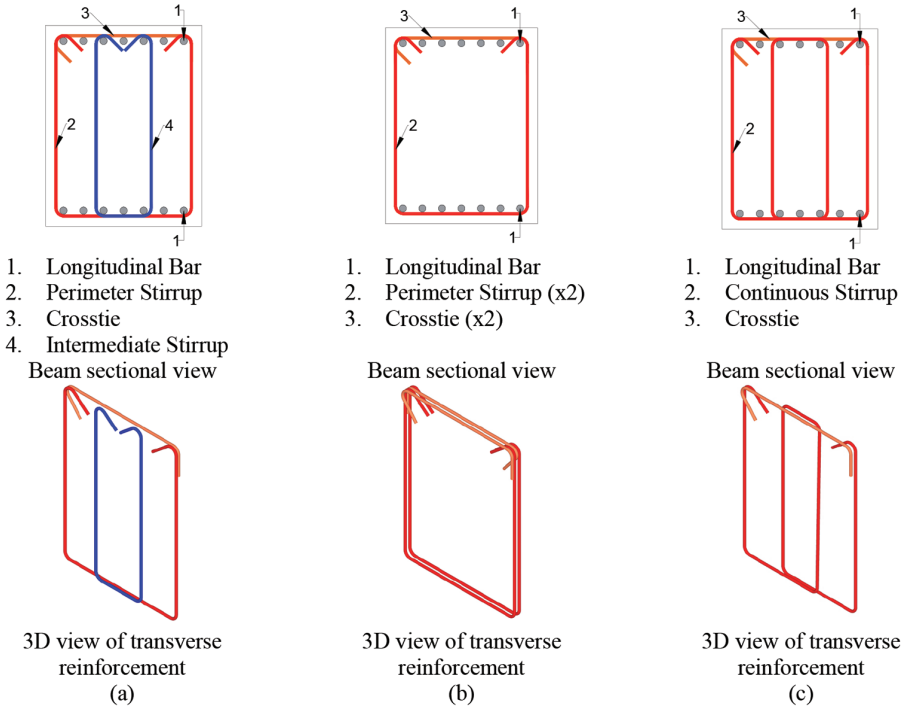

Fig. 1—Transverse reinforcement layouts: (a) CH; (b) DPH; and (c) CSH.

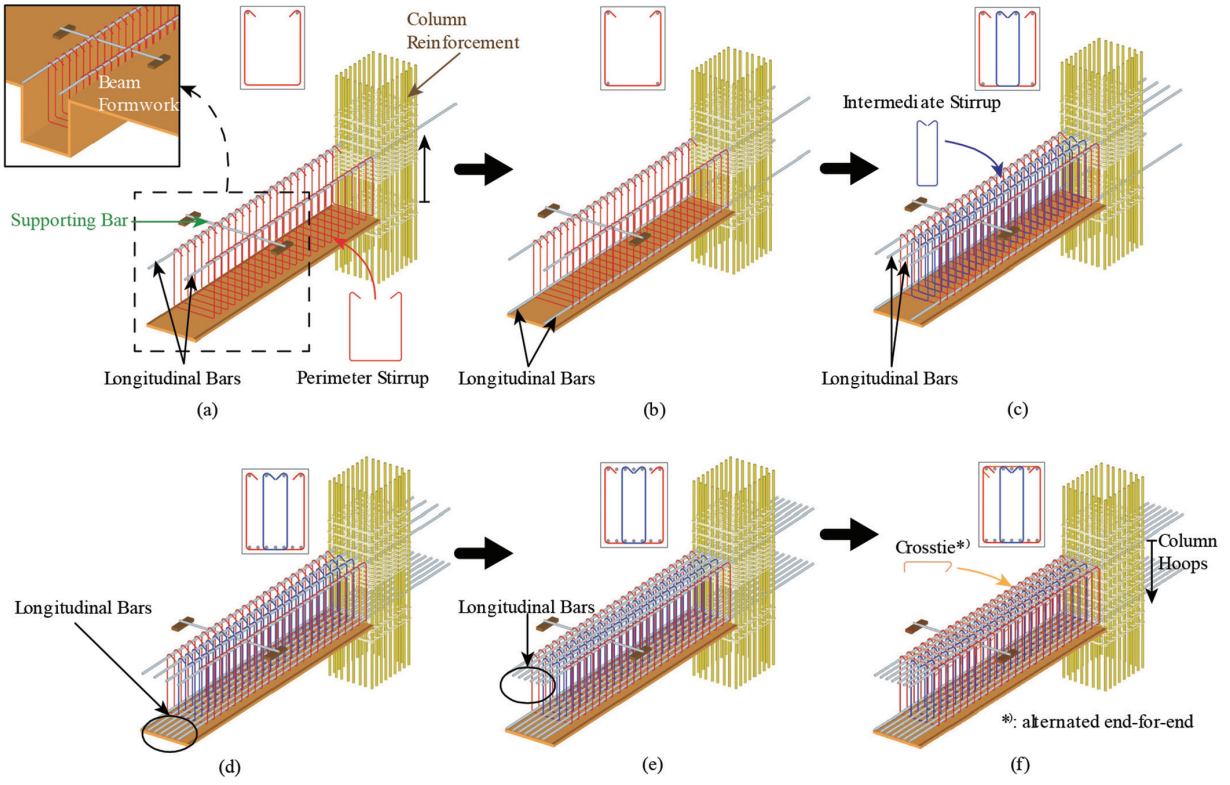

Fig. 2—Construction procedure for CH.

for every longitudinal bar and limiting h_x to 200 mm (8 in.) for the plastic hinge region of the columns of special moment frames when $P_u > 0.3A_g f_c'$ or $P_u > 70$ MPa (10,000 psi). This change is mainly based on the research by Elwood et al.[7,8]

Compared with the abundant test data on columns, no tests to the authors' knowledge were conducted to examine the effect of the number and spacing of laterally supported longitudinal bars on the seismic behavior of beams. Visnjic et al.[9] examined the effect of hoop spacing on the seismic performance of large beams. As a result of this research, one of the upper limits of the hoop spacing, 305 mm (12 in.), was reduced to 152 mm (6 in.) in ACI 318-11[10] to delay the buckling of longitudinal bars of large beams. Note that in Visnjic et al.'s study, the number and spacing of laterally supported longitudinal bars satisfy the Code requirements. Beams are typically subjected to a negligible or small axial

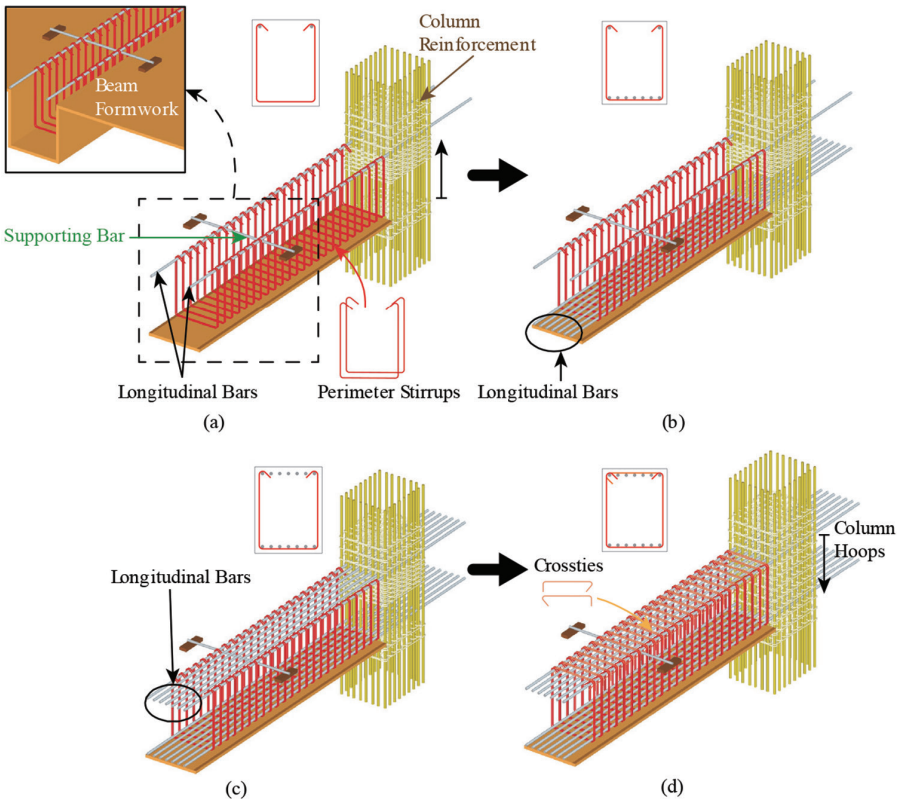

Fig. 3—Construction procedure for DPH.

compressive load of less than $0.1A_g f_c'$. Some engineers argue that the Code requirements for the number and spacing of laterally supported longitudinal bars in the potential plastic hinge region may be relaxed, provided that the spacing of hoops satisfies the Code requirement. Therefore, the first objective of this research was to examine this possibility by comparing the seismic performance of a beam with the CH (Fig. 1(a)) and the DPH (Fig. 1(b)). The second objective of this research was to examine the seismic performance of a beam with the proposed continuous-stirrup hoops (CSH), as shown in Fig. 1(c). The proposed hoops improve the constructability of the transverse reinforcement and satisfy the Code requirement for the number and spacing of laterally supported longitudinal bars.

Continuous-stirrup hoops

As shown in Fig. 1(c), each set of CSH consists of a single-bar continuous stirrup with seismic hooks at both ends and a crosstie to close the continuous stirrup. The continuous stirrup runs continuously to form a perimeter stirrup and an intermediate hoop. The construction of the hoops proceeds in the following steps (Fig. 4): a) placing the two top-corner longitudinal bars and then placing all the continuous stirrups near the column side with the hooks of the stirrups hanging on the two longitudinal bars; b) placing the bottom and then the top longitudinal bars within the intermediate hoops of the continuous stirrups; c) moving the continuous stirrups one by one to their design locations; d) placing the rest of the bottom and top longitudinal bars; and e) placing the crossties to close the stirrups. Compared to the CH (Fig. 1(a)), the CSH have the advantage of reducing installation time as the intermediate hoop is installed together with the perimeter stirrup.

The use of beam continuous-hoop reinforcement, in which the transverse reinforcement of the entire beam is formed by one continuously wound bar, to increase the constructability of beam transverse reinforcement has been examined in several previous studies.[11-16] Tests conducted using monotonic and cyclic loading have shown beams with continuous-hoop reinforcement can have better structural performance than beams with conventional transverse reinforcement.[15] However, such continuous-hoop reinforcement does not have the intermediate hoop required in this research.

RESEARCH SIGNIFICANCE

The intermediate stirrups of CH in beams of special moment frames often cause construction difficulty. Two types of hoop layouts (DPH and CSH) with better constructability than the CH were proposed in this research to address the issue. Results of tests using full-scale specimens showed that beams with the proposed hoop layouts could develop sufficient seismic performance for use in special moment frames.

EXPERIMENTAL PROGRAM

Specimen design

Three full-scale beam specimens were tested in this research. The beams were designed based on applicable provisions of beams of special moment frames of ACI 318-19.[1] The dimensions and reinforcement details of the specimens are shown in Fig. 5. The material properties of the specimens are listed in Table 1. Specimen CH had the conventional hoops (CH), as shown in Fig. 1(a), as transverse reinforcement and served

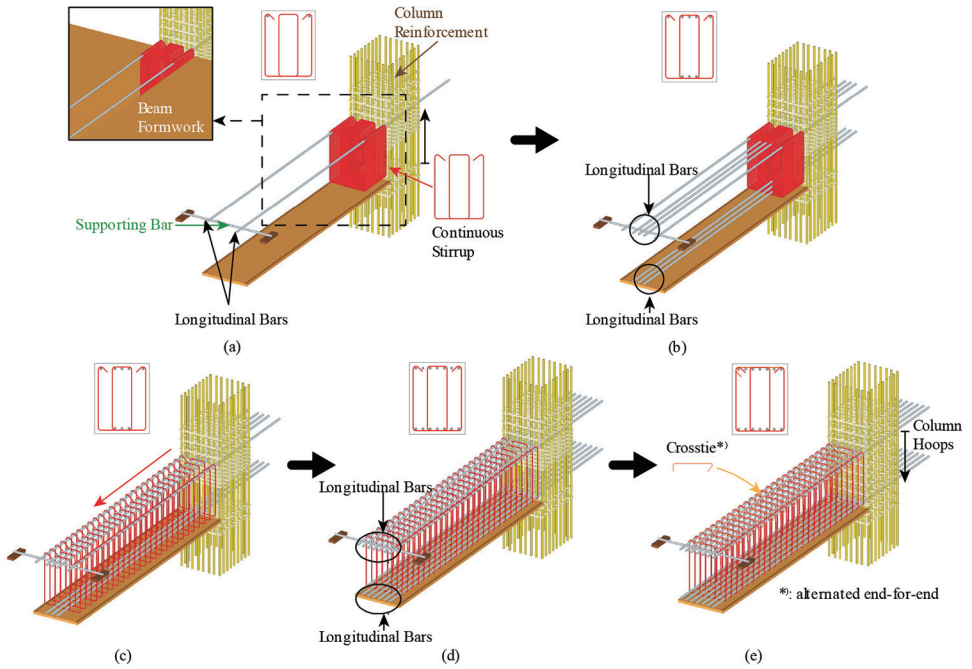

Fig. 4—Construction procedure for CSH.

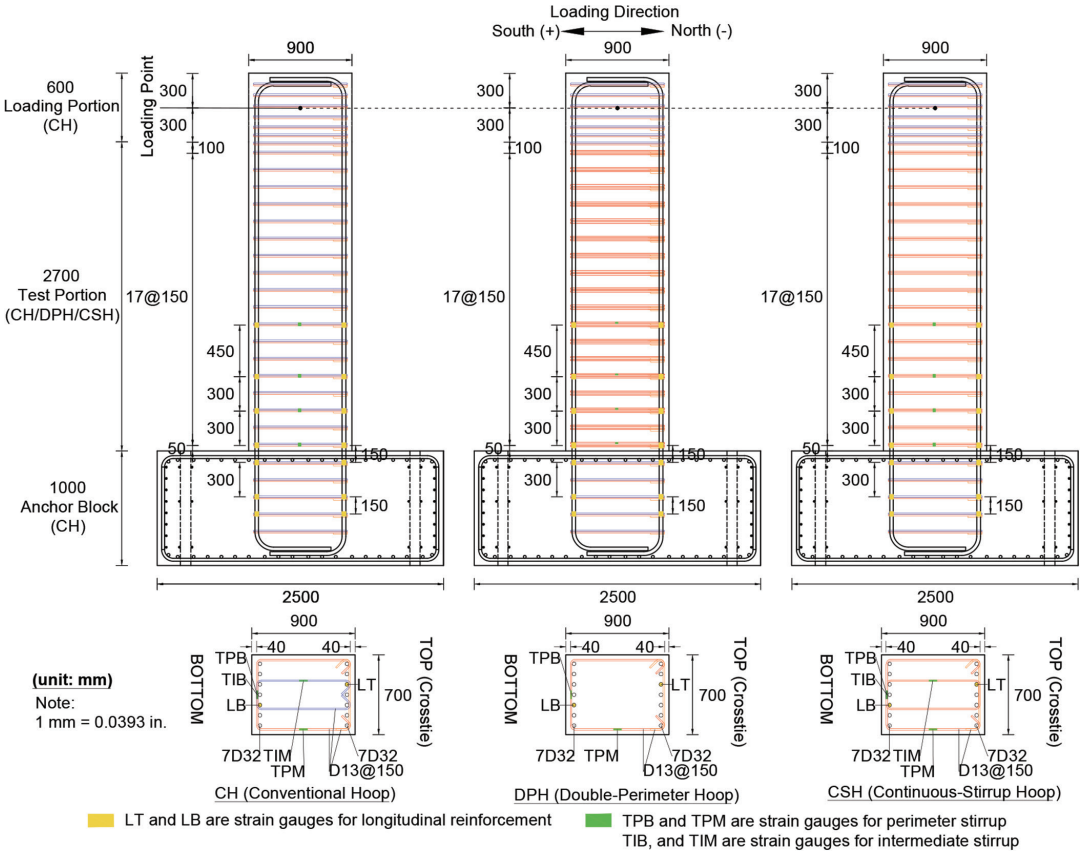

Fig. 5—Specimen design.

as a control specimen. Specimen DPH was designed with the double-perimeter hoops (DPH), as shown in Fig. 1(b), as transverse reinforcement, and specimen CSH had the continuous-stirrup hoops (CSH), as shown in Fig. 1(c), as transverse reinforcement. Figures 6(a) to (c) show the photos of the top side view of the reinforcing bar cages, and Fig. 6(d) to (f) show the top-corner view of the reinforcing bar cages. For specimen DPH, the central five top and bottom longitudinal bars did not have lateral support from the seismic hooks of transverse reinforcement, which violated the Code requirement that every alternate longitudinal bar should be laterally supported. Moreover, the h_x of the DPH was 562 mm (22.13 in.), which violated the maximum h_x requirement (350 mm [14 in.]). Comparing the seismic behavior of specimens

Table 1—Material properties

Specimen	Concrete		Longitudinal reinforcement				Perimeter hoop			Intermediate stirrup or hoop		
	f_{cs}', MPa	f_c', MPa	f_{yls}, MPa	f_{yl}, MPa	f_{ul}, MPa	ρ_l, %	f_{yps}, MPa	f_{yp}, MPa	f_{up}, MPa	f_{yis}, MPa	f_{yi}, MPa	f_{ui}, MPa
CH	35	51.7	420	462	669	0.98 (7D32)	420	474	666	420	474	666
DPH		49.5								—		
CSH		48.7								420	474	666

Note: 1 MPa = 0.145 ksi.

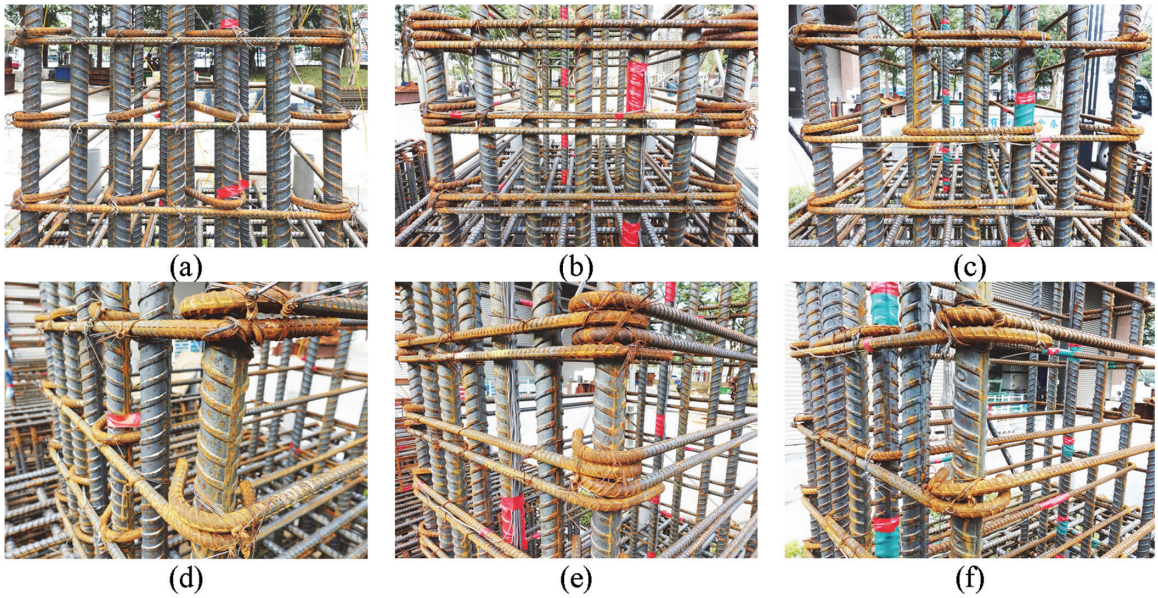

Fig. 6—Photos of reinforcing bar cages: top side view of specimens (a) CH, (b) DPH, and (c) CSH; and top-corner side view of specimens (d) CH, (e) DPH, and (f) CSH.

DPH and CH would reveal the effect of violating the aforementioned Code requirements on the seismic performance of the beam. Furthermore, comparing the seismic behavior of specimens CSH and CH would reveal the seismic performance of the CSH.

All the specimens had the same beam cross-sectional dimensions of 700 x 900 mm (27.6 x 35.4 in.) (width x height). The thickness of the concrete cover was 40 mm (1.57 in). Normalweight concrete with a specified compressive strength (f_{cs}') of 35 MPa (5.076 ksi) was used for all the specimens. SD 420W steel deformed bars, which have a material specification similar to ASTM A706 Grade 60 deformed bars,[17] were used for all longitudinal and transverse reinforcing bars. These cross-sectional dimensions and material strengths are typical for beams at the lower stories of 15-story buildings with a span length of approximately 8 to 9 m (26.2 to 29.5 ft) in the Taipei region of Taiwan.

For all the specimens, the distance from the loading point to the beam fixed end was 3000 mm (118.11 in.). The resulting shear span-effective depth ratio (a/d) was 3.6, falling into the category of slender beams. The beam was designed with seven D32 (a diameter of 32 mm [1.27 in.]) longitudinal bars on the top and bottom sides of the cross section. The top and bottom sides of the cross section are also referred to as the north and south sides (refer to Fig. 5), respectively. The seven D32 bars resulted in a longitudinal tension reinforcement ratio (ρ_l) of 0.98%. The transverse reinforcement of the beam was designed so that the shear demand (V_u) calculated based on $1.25f_{yls}$ was close to the design shear strength (ϕV_n) to critically evaluate the seismic performance of the beams. Moreover, the spacing of hoops needs to satisfy the maximum spacing requirement ($d/4$, 150 mm [6 in.], and $6d_b$) for the potential plastic hinge region. Considering these requirements and using D13 (a diameter of 13 mm [0.5 in.]) reinforcing bars, the spacing of the transverse reinforcement was determined to be 150 mm (5.91 in.). This resulted in a shear demand-capacity ratio ($V_u/\phi V_n$) of 0.85 to 0.87.

Test setup and instrumentation

The specimens were tested in an upright, cantilever fashion, as shown in Fig. 7. The end block of the specimen was fixed to the strong floor by post-tensioning. Lateral cyclic loading satisfying ACI 374.1-05[18] was applied to the free end of the specimen beam. The loading was displacement-controlled to drift levels of 0.25, 0.375, 0.5, 0.75, 1.0, 1.5, 2.0, 3.0, 4.0, 5.0, 6.0, 7.0, and 8.0%. Positive loading was defined as laterally pulling the beam so that the top side of the beam (north side) was in tension and the bottom side (south side) was in compression. Each drift level was repeated in three cycles to observe the degradation of strength and stiffness in each drift level. The test was conducted until the load dropped to less than 50% of the peak load.

Strain gauges were installed on the transverse and longitudinal reinforcement, as shown in Fig. 5, to measure the

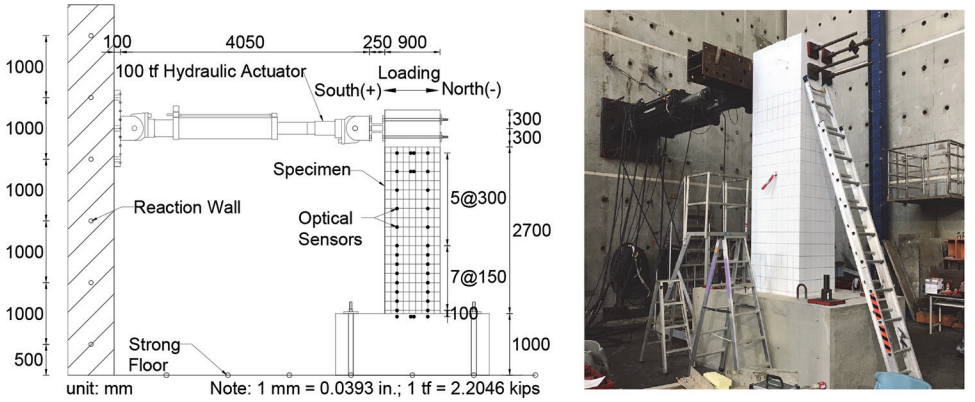

Fig. 7—(a) Test setup; and (b) photo of test setup.

induced strain in the reinforcement. Optical sensors were attached to the east face of the specimen. These sensors allowed an optical receiver to track their space coordinates during testing. These coordinate data were used to calculate the deformations of the beam, including curvature and shear strains.

TEST RESULTS AND DISCUSSION

Damage process

For all three specimens, flexural cracks first appeared at 0.25% drift. At 0.375% drift, some flexural cracks started to turn inclined to become flexural-shear cracks. The extent, number, and width of the cracks increased with increasing drift levels. At the end of the first cycle of 3% drift loading, extensive flexural and flexural-shear cracks were observed for all three specimens. No significant differences in behavior were found between the three specimens.

After the first cycle of the 4% drift loading, significant differences in behavior appeared between the three specimens. The differences mainly occurred around the top side of the beam (north side). Note that crossties were used on this side. The differences can be observed from the east side view of the specimen (the side face of the beam), as shown in Fig. 8(a) to (c), and the north side view of the specimen (the top face of the beam), as shown in Fig. 8(d) to (f), for specimens CH, DPH, and CSH, respectively. Specimen CH showed clear bulging on the north face, likely due to the pushing from the concrete expansion and buckling of longitudinal bars in compression. Specimen DPH exhibited extensive concrete spalling, exposing buckled longitudinal bars and loosened crossties (popping out from the 90-degree end). Specimen CSH showed damage less severe than the other two beams. No significant bulging nor spalling of concrete was observed. The damage condition of specimen CSH demonstrated that the intermediate hoops of specimen CSH were more effective in confining concrete and restraining the buckling of longitudinal bars than the conventional intermediate stirrups of specimen CH. The intermediate hoops of specimen CSH are formed by one continuous bar and hence can provide better restraint to longitudinal bars within the hoop than the conventional intermediate stirrups. Specimen DPH showed the most severe damage. This was true despite two crossties being used for each set of DPH. In contrast, one crosstie was used for each set of CH and CSH. It appeared that the crossties alone could not effectively restrain the buckling of the central five longitudinal bars at 4% drift. As a result, specimen DPH showed a significant drop in the lateral load at the peak negative 4% drift when the top side of the beam was in compression. Hence, in the negative drift loading, specimen DPH reached the peak applied load at 3% drift, earlier than the other two specimens.

The damage around the bottom side (south side) of the beam was generally less than that around the top side for all three specimens. This was because crossties were not used for the bottom sides, and the lateral support of all the supported bottom longitudinal bars was provided by the corners of hoops or stirrups rather than seismic hooks. The three specimens did not show significant differences in damage around the bottom side of the beam, although specimen DPH did show slightly more severe bulging than the other two specimens (Fig. 8(b)). The lateral load was still increasing for all three specimens in the positive loading direction when the bottom side of the beam was in compression.

After the first cycle of 5% drift, severe damage involving concrete spalling, longitudinal bar buckling, and loosening of crossties and stirrup hooks could be observed around the top side of the beam (north side) for all three specimens, as shown in Fig. 9. At this drift and in the negative loading direction when the top side of the beam was in compression, specimens CH and CSH showed a significant drop in the lateral load. Therefore, in the negative loading direction, both specimens reached their peak lateral load at 4% drift. A comparison of the damage conditions showed that specimen DPH showed the worst buckling behavior. The top five central longitudinal bars buckled almost uniformly outward (Fig. 9(h)). These bars were only restrained from buckling by crossties, which tended to pop out from the 90-degree end once the cover concrete spalled. Only the two top-corner longitudinal bars were better restrained by the seismic hooks of the perimeter stirrups. For specimen CSH, the top five longitudinal bars, including the two top-corner bars and the three bars within the intermediate hoops, were effectively restrained to resist buckling (Fig. 9(i)). In contrast, for specimen CH, four top longitudinal bars, including the two top-corner bars and the two bars laterally supported by the seismic hooks of the intermediate stirrups, were effectively

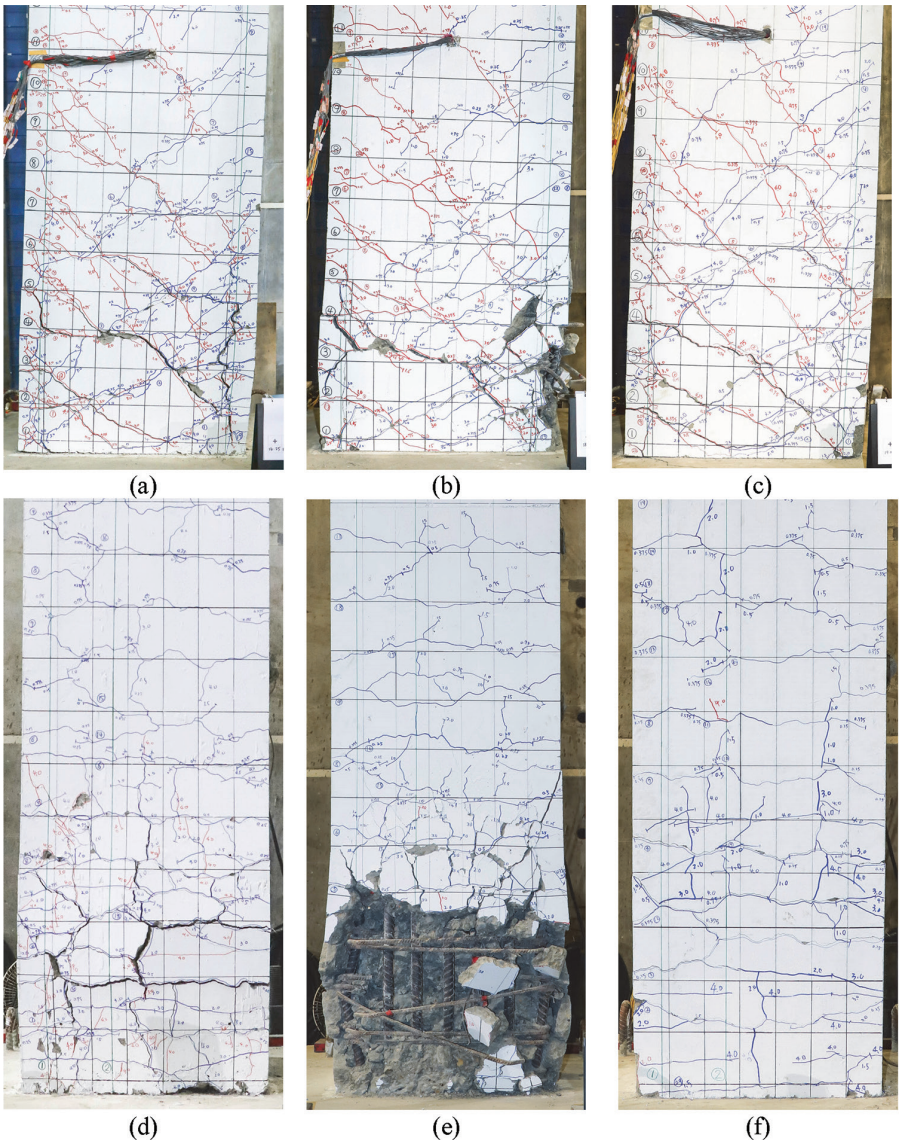

Fig. 8—Damage condition after first cycle of 4% drift on east face (side face) of beam near fixed end for specimens (a) CH, (b) DPH, and (c) CSH; and on north face (top face) of beam for specimens (d) CH, (e) DPH, and (f) CSH.

restrained from buckling (Fig. 9(g)). Therefore, specimen CSH, with one more longitudinal bar effectively restrained than specimen CH and better restraint ability of intermediate hoops than the intermediate stirrups of specimen CH, showed a smaller extent of concrete damage and less severity of buckling of longitudinal bars than specimen CH.

The damage around the bottom side of the beam was again less severe than that around the top side for all three specimens (Fig. 9(a) to (c)) after the first cycle of 5% drift. Specimen DPH showed severe concrete spalling around the bottom side. The lateral load in the positive loading direction dropped significantly at 5% drift compared to the previous drift. Hence, the peak lateral load in the positive loading direction of specimen DPH occurred at 4% drift. The damage condition of specimen CH around the bottom side was better than that of specimen DPH. Only some bulging of cover concrete was observed. However, the lateral load still started to drop at this drift ratio. Thus, the lateral load in the positive loading direction of specimen CH also reached the peak at 4% drift. In contrast, the lateral load was still increasing for specimen CSH in the positive loading direction. It started to drop at 6% drift, later than the other two beams.

The testing of specimens CH, DPH, and CSH was terminated after the second cycle of 6% drift, the second cycle of 5% drift, and the second cycle of 6% drift when the negative load dropped to 27%, 15%, and 25% the peak value, respectively. No fracture of longitudinal and transverse reinforcing bars was observed at the end of the test for specimens CH and DPH, as shown in Fig. 10(a) and (b), respectively. In contrast, for specimen CSH, fractures of longitudinal and transverse reinforcing bars were observed, as shown in Fig. 10(c). This indicates that the stresses of reinforcing bars in specimen CSH were better developed due to better restraint from the intermediate hoops of the CSH than the other two specimens.

Hysteretic behavior

The lateral load and displacement relationships (hysteretic behavior) of specimens CH, DPH, and CSH are shown in Fig. 11(a) to (c), respectively. The envelope responses of

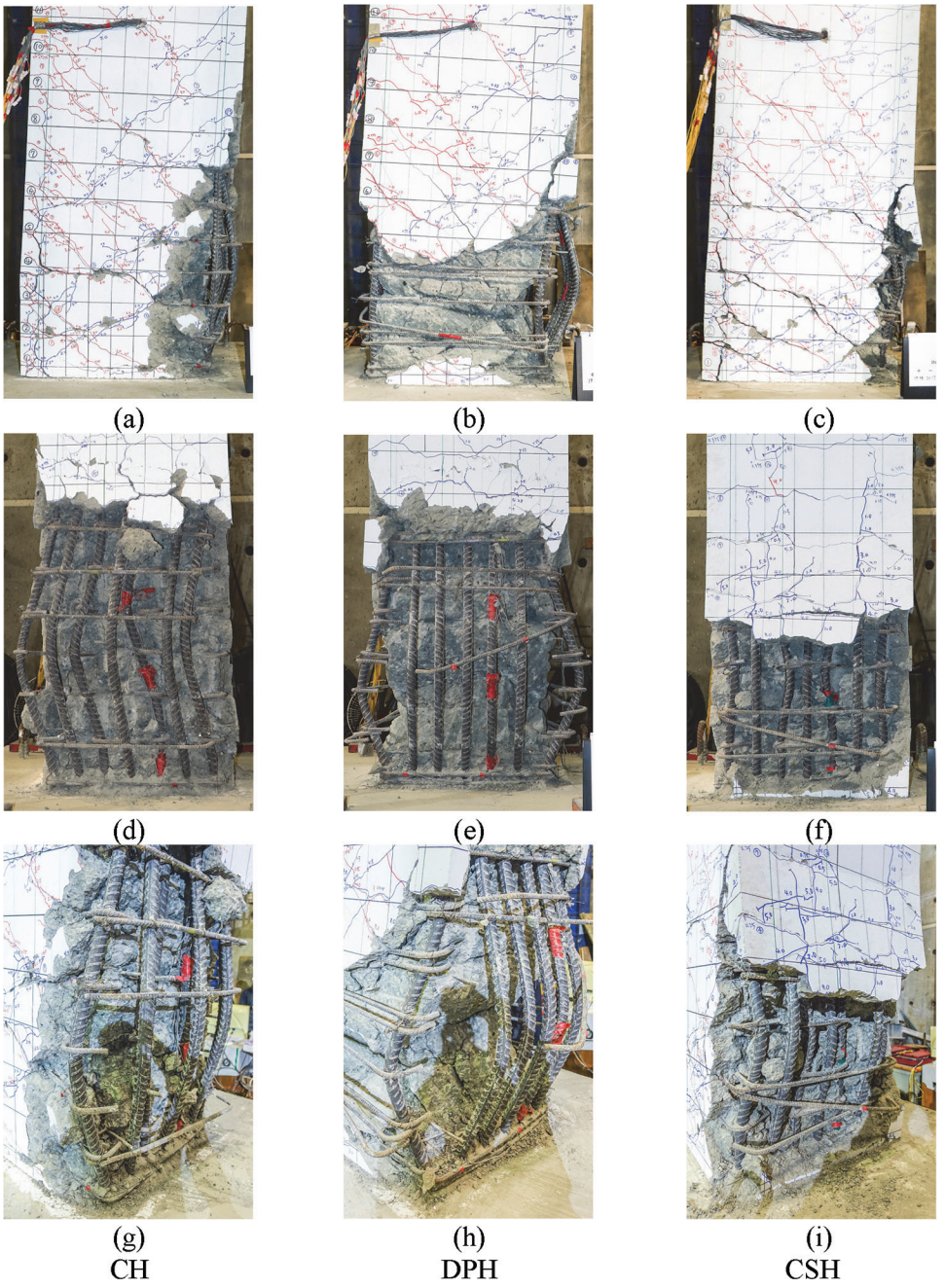

Fig. 9—Damage condition after first cycle of 5% drift on east face (side face) of beam near fixed end for specimens (a) CH, (b) DPH, and (c) CSH; on north face (top face) of beam for specimens (d) CH, (e) DPH, and (f) CSH; and at northeast corner for specimens (g) CH, (h) DPH, and (i) CSH.

all three specimens are compared in Fig. 11(d). To evaluate the ductility (μ) and plastic drift capacity (Δ_p) of the beam, the envelope responses of all three specimens were idealized using the bilinear model from FEMA 356.[19] The bilinear model has two linear segments. The first segment passes through the envelope response at approximately 60% of the yield load ($0.6V_y$) and ends at the yield point. The second segment starts from the yield point and ends at the ultimate drift (Δ_u). The second segment is assumed to have zero stiffness. The Δ_u is defined as the drift when the lateral load drops to 80% of the peak value on the descending branch of the envelope response. The yield point was selected so that the area covered under the bilinear model would be close to the area under the envelope response curve. The μ is defined as the ratio of Δ_u to the drift of the yield point (Δ_y), and the plastic drift (Δ_p) is defined as Δ_u minus Δ_y. The bilinear model parameters and the measured peak lateral load of each specimen are listed in Table 2.

All specimens showed similar hysteretic behavior when the drift did not exceed 4% and 3% in the positive and negative loading directions, respectively. Some pinching was observed for each specimen. The pinching was likely due to shear and/or bond deterioration. Specimen DPH reached the peak load in the positive direction at 4% drift, the same as the control specimen (CH). However, the strength degradation after the peak load of specimen DPH was more severe than

Fig. 10—Close view of reinforcement damage of specimens: (a) CH; (b) DPH; and (c) CSH.

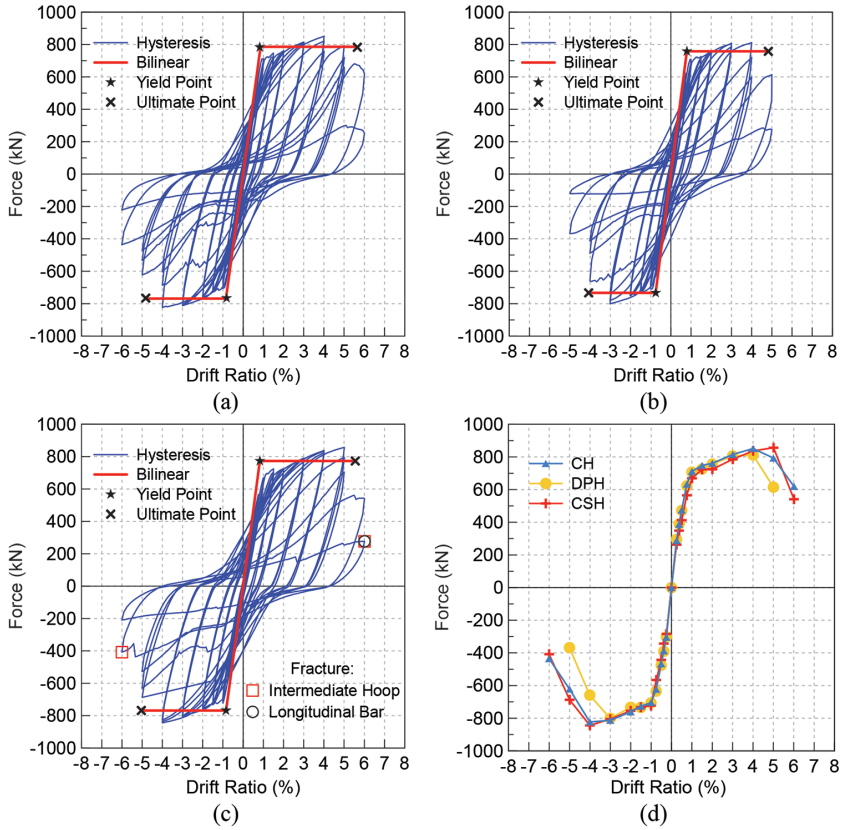

Fig. 11—Hysteretic behavior of specimens: (a) CH; (b) DPH; (c) CSH; and (d) envelope responses of all specimens. (Note: 1 kN = 0.2248 kip.)

that of specimen CH. In the negative direction, specimen DPH reached the peak load at 3% drift, earlier than specimen CH. As a result, the average Δ_u, Δ_p, and μ of specimen DPH were 4.5%, 3.7%, and 5.8, respectively, which were 14%, 16%, and 5% lower than the average Δ_u, Δ_p, and μ of 5.2%, 4.4%, and 6.1 of specimen CH, respectively. As stated previously, the lower drift and ductility capacities of specimen DPH were mainly due to the lack of lateral support to the central five longitudinal bars, leading to earlier and more extensive buckling of the bars in compression. However, specimen DPH still exhibited drift and ductility capacities higher than typically required for beams of special moment frames—for example, 3.5%.[18]

Specimen CSH reached the peak load in the positive loading direction at 5% drift, which is 1% drift later than specimen CH. However, after the peak load, the strength of specimen CSH degraded faster than CH. This was due to the fracture of the longitudinal bars in specimen CSH, resulting from a better restraint by the CSH than the CH. In the negative loading direction, specimen CSH reached the peak load at 4% drift, the same as specimen CH, and showed a slightly lower strength degradation in the beginning than specimen CH but later accelerated due to fracture of the longitudinal bars. The average Δ_u, Δ_p, and μ of specimen CSH were 5.3%, 4.5%, and 6.3, respectively, which were 2%, 2%, and 3% higher than those of specimen CH, respectively. The better

Table 2—Drift capacity and strength ratio

Specimen	Loading direction	Δ_y, %	Δ_u, %	μ	Δ_p, %	V_y, kN	V_{max}, kN	M_{test}, kN·m	M_n, kN·m	M_{test}/M_n	ξ_{eq} 4%, %
CH	(+)	0.86	5.65	6.57	4.79	786	851	2554	1857	1.38	18.80
	(–)	0.85	4.82	5.65	3.97	769	823	2469	1857	1.33	
	Avg.	0.86	5.24	6.11	4.38	777	837	2511	1857	1.35	
DPH	(+)	0.79	4.82	6.09	4.03	758	812	2436	1857	1.31	18.38
	(–)	0.75	4.07	5.42	3.32	734	801	2403	1857	1.29	
	Avg.	0.77	4.45	5.76	3.68	746	806	2419	1857	1.30	
CSH	(+)	0.83	5.55	6.71	4.72	734	857	2570	1857	1.38	20.03
	(–)	0.85	5.04	5.94	4.19	758	844	2533	1857	1.36	
	Avg.	0.84	5.30	6.32	4.46	746	850	2551	1857	1.37	

Note: 1 kN = 0.2248 kip; 1 kN·m = 0.7376 kip·ft.

performance of specimen CSH in drift and ductility capacities was not so significant compared with damage control, as shown in the previous section. However, the beneficial effect of the CSH on the drift and ductility capacities could still be observed.

Also listed in Table 2 is the ratio of the measured average moment strength (M_{test}) to the nominal moment strength (M_n) calculated based on ACI 318-19[1] with actual material strengths. The M_{test}/M_n of specimen DPH was 1.3. Although it is 4% lower than that of specimen CH, it is 30% higher than M_n. This and the observations from the drift and ductility capacities stated earlier showed that despite the lower lateral support to the central five longitudinal bars on the top and bottom sides of the beam of specimen DPH, the specimen still exhibited strength and deformation sufficient for beams of special moment frames. The M_{test}/M_n of specimen CSH was 1.37, which was 1% higher than that of specimen CH. The strength capacity of specimen CSH was similar to specimen CH.

Curvature, bar slip, and shear strain

The curvature, including bar slip and shear strain distributions for each specimen, were calculated based on the space coordinate measurements of the optical sensors attached to the east face of the specimen. Figures 12(a) to (c) show the distributions of the curvature, including the contribution from the bar slip, and Fig. 12(d) to (f) show the distributions of the shear strain. Beam level zero in Fig. 12 represents the fixed end of the beam. Note that the curvature value at beam level zero was mainly due to the contribution from the bar slip. Because the sensors were removed at 4% drift to protect them from being damaged by the severe concrete cracking and spalling occurring at that drift, the curvature and shear strain data were only available up to 3% drift.

It can be seen from Fig. 12 that specimen DPH showed a length with large curvatures of approximately 725 mm (28.54 in.) and a length of large shear strains of approximately 1025 mm (40.35 in.) from the fixed end at 3% drift. These were larger by 26% and 17% than the corresponding lengths observed in specimen CH, approximately 575 and 875 mm (22.64 and 34.45 in.), respectively. This indicated more extensive damage in specimen DPH than CH at 3% drift. However, this more extensive damage at 3% drift did not cause a significant difference in the visual damage and hysteretic behavior, as presented in previous sections.

For specimen CSH, the lengths with large curvatures and shear strains at 3% drift were approximately 575 and 875 mm (22.64 and 34.45 in.), the same as those of specimen CH at the same drift. These observations were consistent with the previous observations on damage and hysteretic behavior in which the two specimens showed similar behavior at 3% drift.

Figure 13 shows the percentage contributions of the curvature, bar slip, and shear strain to the lateral displacement of the beam for each specimen. The lateral displacement due to bar slip was calculated from the curvature value at beam level zero and that due to curvature from the rest of the measured curvatures. For specimens CH, DPH, and CSH at 3% drift, the curvature and bar slip contributed to 85.05, 84.94, and 86.87%, and shear strains contributed to 14.95, 15.06, and 13.13% of the lateral displacement, respectively. All three specimens showed flexural-dominated behavior, with a flexural contribution of more than 85% of the total lateral displacement. The CSH controlled shear deformations better than the other two specimens. The shear strain of specimen CSH at 3% drift was lower by 12% than specimen CH. Specimen DPH showed a very similar level of shear strain at 3% drift to specimen CH.

Energy dissipation

The energy dissipation capacity was assessed using the equivalent damping ratio (ξ_{eq}), as defined in Eq. (1). The ξ_{eq} was calculated for each cycle of the hysteretic response. The average value of the three cycles of each drift level is shown in Fig. 14. Similar values of ξ_{eq} were observed between the three specimens when the drift was equal to or less than 3%. At 4% drift, the ξ_{eq} of specimen DPH started to decrease. The ξ_{eq} was 18.38%, lower by 2% than specimen CH, which was 18.80%. In contrast, the ξ_{eq} of specimen CSH was still increasing. The ξ_{eq} was 20.03%, higher by 7% than specimen CH. At 5% drift, specimen DPH failed, and hence the ξ_{eq} was not shown in the figure. At this drift, the ξ_{eq} of specimen CSH was 18.50%, higher by 39% than specimen CH.

$$\xi_{eq} = \frac{1}{4\pi}\left(\frac{E_D}{E_S}\right) \quad (1)$$

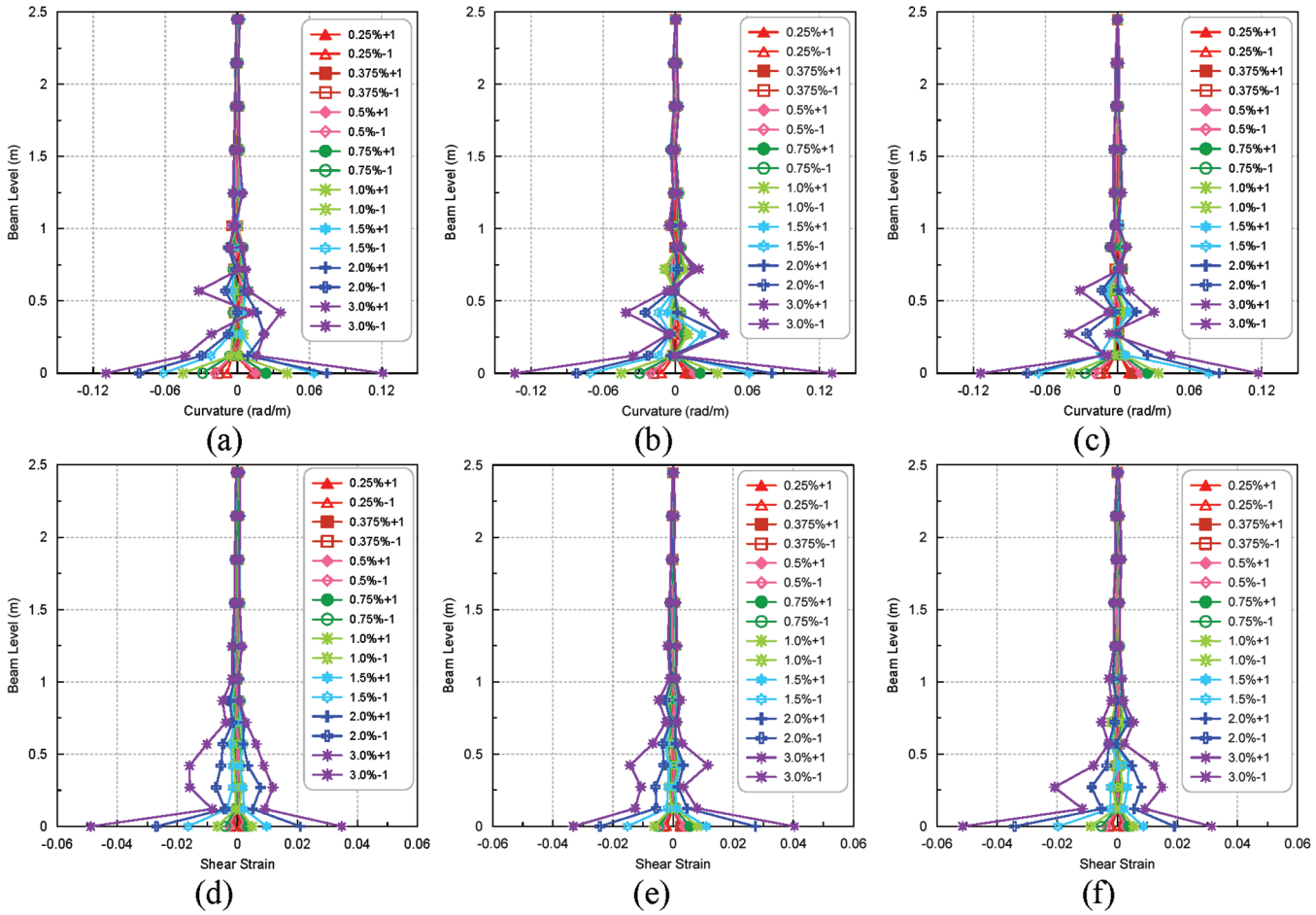

Fig. 12—Curvature distributions of specimens: (a) CH; (b) DPH; and (c) CSH; and shear strain distributions of specimens: (d) CH; (e) DPH; and (f) CSH. (Note: 1 mm = 0.0393 in.)

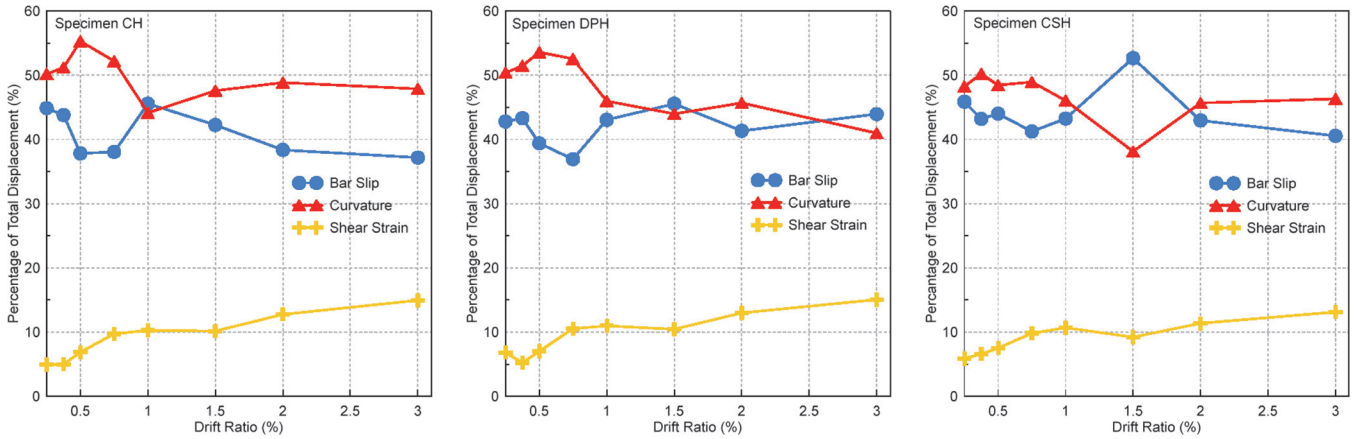

Fig. 13—Percentage contributions of curvature, bar slip, and shear strain to lateral displacement of beam.

From the previous comparison, it can be seen that specimen DPH showed a similar energy dissipation to specimen CH up to 4% drift, which is typically considered sufficient for beams of special moment frames, as stated previously. The lack of lateral support to the central five longitudinal bars on the top and bottom sides of the beam had a significant adverse effect on the energy dissipation only when the drift reached 5%. Specimen CSH showed an energy dissipation capacity superior to specimen CH, starting from 4% drift. This again indicated the better confinement and restraint effect of the CSH than the CH.

Strain gauge analysis

The strain responses of the beam top and bottom longitudinal reinforcing bars from gauges LT, located 350 mm (13.78 in.) from the fixed end of the beams, and gauges LB, located 50 mm (1.97 in.) from the fixed end of the beams, are shown in Fig. 15(a) and (b), respectively. The locations of gauges LT and LB in the beam cross section are shown

in Fig. 5. The responses of specimen CSH at the drifts of 0.375 to 0.5% were lost and hence are not shown. All the specimens showed tensile yielding of longitudinal reinforcing bars at approximately 1% drift, consistent with the yield drift shown in Table 2. No significant differences were observed between the specimens. This is mainly because the strain responses were available only up to 1.5% drift. The damages of the specimens were still minor at this drift ratio.

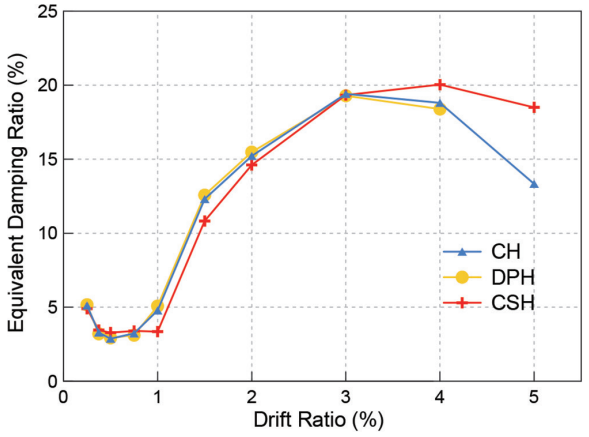

Fig. 14—Equivalent damping ratio.

The strain responses of the perimeter stirrups from gauges TPM, located 350 mm (13.78 in.) from the fixed end of the beams, are shown in Fig. 15(c). The perimeter stirrups of all the specimens developed strains much higher than the yield strain, indicating that the perimeter stirrups with seismic hooks at both ends in these specimens were effectively used to resist cyclic shear and provide restraint to corner longitudinal bars and confinement to concrete. The strain responses of the intermediate stirrups (specimen CH) and intermediate hoops (specimen CSH) from gauges TIM, located 350 mm (13.78 in.) from the fixed end of the beams, are shown in Fig. 15(d). Specimen DPH did not have intermediate stirrups or hoops and hence was not included in the comparison. It can be seen that the strains of the intermediate hoops of specimen CSH were initially similar to those of the intermediate stirrups of specimen CH but were much higher at high drifts. This observation was consistent with the damage observation stated previously, in which the intermediate hoops of specimen CSH showed fracture while the intermediate stirrups of specimen CH did not. This again showed that the intermediate hoops made of a continuous bar could be better mobilized to resist shear, buckling of longitudinal bars, and concrete expansion than the intermediate stirrups with seismic hooks at both ends. The seismic hooks tended

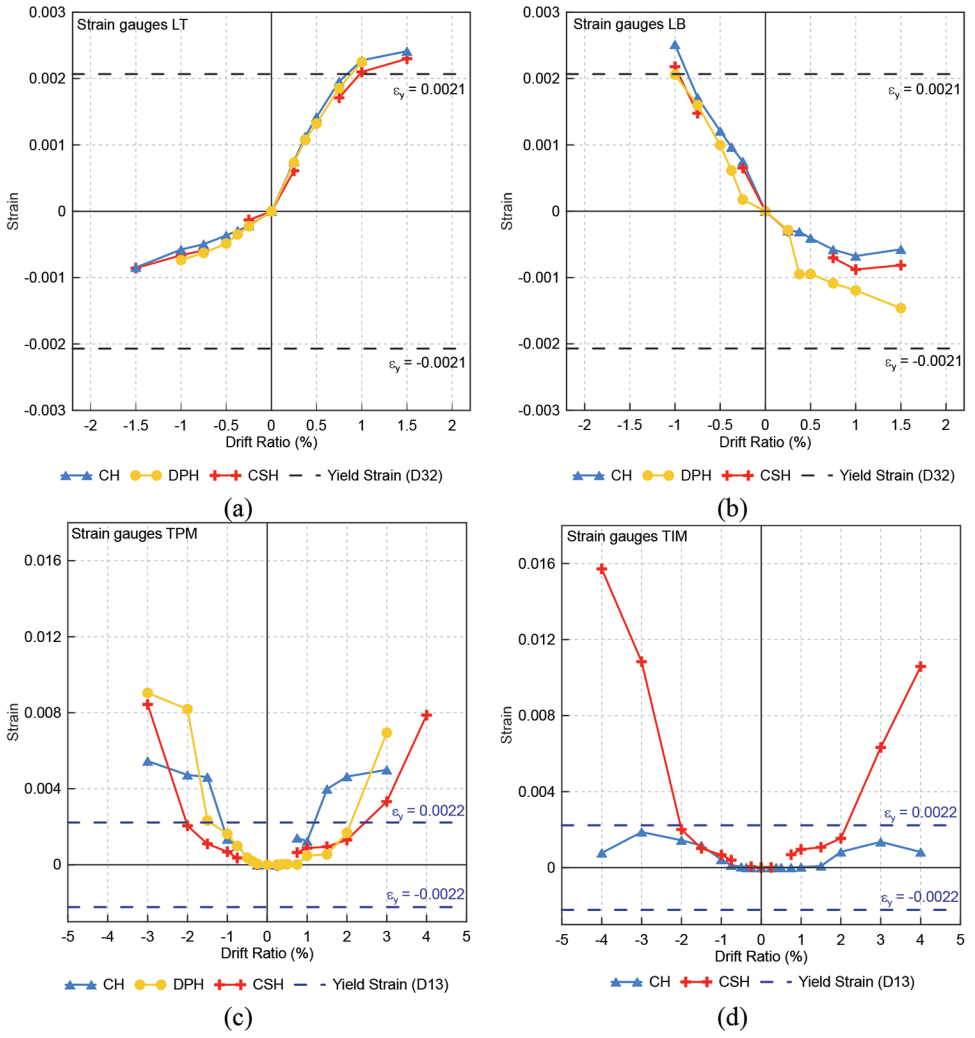

Fig. 15—Envelope responses of strain gauges: (a) LT; (b) LB; (c) TPM; and (d) TIM.

to be pushed out after spalling of cover concrete, as shown in Fig. 9(g). In contrast, the intermediate hoops did not have this problem and hence performed better than the intermediate stirrups.

CONCLUSIONS

Two types of hoop layouts, double-perimeter hoops (DPH) and continuous-stirrup hoops (CSH), with better constructability than conventional hoops (CH), were proposed in this research for the potential plastic hinge region of beams of special moment frames. Three full-scale beam specimens were tested to examine their seismic performance. Specimen CH was designed with conventional hoops and served as a control specimen. Specimens DPH and CSH were designed with double-perimeter hoops and continuous-stirrup hoops, respectively. The DPH used in specimen DPH violated the Code requirements for the number and spacing of laterally supported longitudinal bars in the potential plastic hinge region. Specimens CH and CSH conformed to the Code requirements using intermediate stirrups and hoops, respectively. The following conclusions can be drawn based on the test observations and analysis. Due to budget constraints, only a limited number of specimens were investigated. Care should be taken when extending the interpretation of the test results of this research to beams with different design parameters, such as different longitudinal compression to tension reinforcement ratios, the presence of a slab, and so on.

1. Specimen DPH showed Δ_u, Δ_p, and μ of 4.5%, 3.7%, and 5.8, which were 14%, 16%, and 5% lower than those of specimen CH, respectively. The lower deformation capacities of specimen DPH were mainly due to the fewer laterally supported longitudinal bars. This caused earlier and more extensive buckling of longitudinal bars and more severe concrete damage, particularly near the top side of the beam, where crossties were used. Despite this, the deformation capacities of specimen DPH were still higher than typically required for beams of special moment frames. The M_{test}/M_n and ξ_{eq} at 4% drift of specimen DPH were 1.3 and 18.38%, which were 4% and 2% lower than those of specimen CH, respectively. Furthermore, the DPH showed a similar ability to control the shear deformation of the beam to specimen CH. Despite violating the Code requirements for the number and spacing of laterally supported longitudinal bars, specimen DPH still possessed sufficient strength, deformation, and energy dissipation required for beams of special moment frames. Note that this conclusion is likely only applicable to cases similar to or less critical than specimen DPH, which had 29% of longitudinal bars (two out of seven bars) laterally supported by a seismic hook or the corner of a hoop and the maximum h_x of 562 mm (22.13 in.). A further reduction in the number and increase in the spacing of laterally supported longitudinal bars is expected to decrease the seismic performance.

2. Specimen CSH showed Δ_u, Δ_p, μ, and M_{test}/M_n of 5.3%, 4.5%, 6.3, and 1.37, which were 2%, 2%, 3%, and 1% higher than those of specimen CH, respectively. The ξ_{eq} of specimen CSH were 20.03% and 18.50% at 4% and 5% drift, which were 7% and 39% higher than those of specimen CH, respectively. The shear strain of specimen CSH at 3% drift was 12% lower than that of specimen CH. The better performance of specimen CSH was attributed to the better concrete confinement and reinforcing bar buckling restraint ability of the intermediate hoops (made of a continuous bar) of the CSH than the intermediate stirrups of the CH. The top central three longitudinal bars in CSH were better restrained from buckling than those of CH. The damage severity and extent of specimen CSH were less for a given drift than specimen CH. The proposed CSH can increase the constructability and seismic performance of beams of special moment frames.

AUTHOR BIOS

ACI member **Yu-Chen Ou** *is a Distinguished Professor in the Department of Civil Engineering at National Taiwan University, Taipei, Taiwan. He received his PhD from the State University of New York at Buffalo, Buffalo, NY. He is President of the ACI Taiwan Chapter. His research interests include reinforced concrete structures, earthquake engineering, and bridge engineering.*

ACI member **Hermawan Sutejo** *is a PhD Candidate in the Department of Civil Engineering at National Taiwan University, where he received his master of science in civil engineering. His research interests include earthquake-resistant reinforced concrete structures and finite element modeling of reinforced concrete members.*

Jyun-Lin Huang *is a Civil Engineer. He received his master of science in civil engineering from National Taiwan University.*

Sheng-I Yen *is the Vice President of the Technical Division at Chien Kuo Construction Co., Ltd., in Taipei, Taiwan. He received his PhD from National Yang Ming Chiao Tung University, Hsinchu, Taiwan.*

ACKNOWLEDGMENTS

The authors would like to thank the financial support from Chien Kuo Construction Co., Ltd., and the National Science and Technology Council (NSTC) of Taiwan under Contract No. 109-2221-E-002-003-MY3, and the National Center for Research on Earthquake Engineering (NCREE) of Taiwan for experimental facilities and personnel.

NOTATION

A_g	=	gross area of concrete section
a	=	shear span of beam
d	=	distance from extreme compression fiber to centroid of longitudinal tension reinforcement
d_b	=	nominal diameter of bar and wire
E_D	=	total energy dissipated in isolation system per displacement cycle
E_S	=	effective strain energy
f_c'	=	actual compressive strength of concrete
f_{cs}'	=	specified compressive strength of concrete
f_{ui}	=	ultimate strength of intermediate hoops or stirrups
f_{ul}	=	ultimate strength of longitudinal reinforcement
f_{up}	=	ultimate strength of perimeter hoops
f_{yi}	=	actual yield strength of intermediate hoops or stirrups
f_{yis}	=	specified yield strength of intermediate hoops or stirrups
f_{yl}	=	actual yield strength of longitudinal reinforcement
f_{yls}	=	specified yield strength of longitudinal reinforcement
f_{yp}	=	actual yield strength of perimeter hoops
f_{yps}	=	specified yield strength of perimeter hoops
h_x	=	maximum center-to-center spacing of longitudinal bars laterally supported by corners of crossties or hoop legs around perimeter of column or wall boundary element
M_n	=	beam nominal moment capacity
M_{test}	=	beam maximum moment from testing
P_u	=	factored axial force
V_{max}	=	maximum test lateral force
V_n	=	nominal shear strength
V_u	=	factored shear force at section
V_y	=	lateral force of yield point
Δ_p	=	plastic drift
Δ_u	=	ultimate drift
Δ_y	=	yield drift
ε_y	=	yield strain of reinforcement

ϕ = strength reduction factor, 0.75 for shear
μ = ductility
ρ_l = longitudinal tension reinforcement ratio
ξ_{eq} = equivalent viscous damping ratio

REFERENCES

1. ACI Committee 318, "Building Code Requirements for Structural Concrete (ACI 318-19) and Commentary (ACI 318R-19) (Reapproved 2022)," American Concrete Institute, Farmington Hills, MI, 2019, 624 pp.

2. Mander, J. B.; Priestley, M. J. N.; and Park, R., "Theoretical Stress-Strain Model for Confined Concrete," *Journal of Structural Engineering*, ASCE, V. 114, No. 8, Sept. 1988, pp. 1804-1826. doi: 10.1061/(ASCE)0733-9445(1988)114:8(1804)

3. Pfister, J. F., "Influence of Ties on the Behavior of Reinforced Concrete Columns," *ACI Journal Proceedings*, V. 61, No. 5, May 1964, pp. 521-538.

4. DeGagné, B.; Erdogmus, E.; and Savage, J., "Longitudinal Bar Spacing and Intermediate Ties," *Concrete International*, V. 38, No. 5, May 2016, pp. 43-46.

5. ACI Committee 318, "Building Code Requirements for Reinforced Concrete (ACI 318-63)," American Concrete Institute, Farmington Hills, MI, 1963, 144 pp.

6. ACI Committee 318, "Building Code Requirements for Reinforced Concrete (ACI 318-83)," American Concrete Institute, Farmington Hills, MI, 1983, 111 pp.

7. Elwood, K. J.; Maffei, J.; Riederer, K. A.; and Telleen, K., "Improving Column Confinement: Part 1: Assessment of Design Provisions," *Concrete International*, V. 31, No. 11, Nov. 2009, pp. 32-39.

8. Elwood, K. J.; Maffei, J.; Riederer, K. A.; and Telleen, K., "Improving Column Confinement: Part 2: Proposed New Provisions for the ACI 318 Building Code," *Concrete International*, V. 31, No. 12, Dec. 2009, pp. 41-48.

9. Visnjic, T.; Antonellis, G.; Panagiotou, M.; and Moehle, J. P., "Large Reinforced Concrete Special Moment Frame Beams under Simulated Seismic Loading," *ACI Structural Journal*, V. 113, No. 3, May-June 2016, pp. 469-480.

10. ACI Committee 318, "Building Code Requirements for Structural Concrete (ACI 318-11) and Commentary (ACI 318R-11)," American Concrete Institute, Farmington Hills, MI, 2011, 503 pp.

11. Kang, S.-M.; Park, S.-W.; Jang, S.-W.; Jin, J.-M.; Eom, T.-S.; and Park, H.-G., "Constructability and Economic Evaluation of Continuous Hoop Reinforcement Method," *Journal of the Korea Institute of Building Construction*, V. 13, No. 3, 2013, pp. 291-305.

12. Chalioris, C. E., and Karayannis, C. G., "Experimental Investigation of RC Beams with Rectangular Spiral Reinforcement in Torsion," *Engineering Structures*, V. 56, Nov. 2013, pp. 286-297. doi: 10.1016/j.engstruct.2013.05.003

13. De Corte, W., and Boel, V., "Effectiveness of Spirally Shaped Stirrups in Reinforced Concrete Beams," *Engineering Structures*, V. 52, July 2013, pp. 667-675. doi: 10.1016/j.engstruct.2013.03.032

14. Karayannis, C. G., and Chalioris, C. E., "Shear Tests of Reinforced Concrete Beams with Continuous Rectangular Spiral Reinforcement," *Construction and Building Materials*, V. 46, Sept. 2013, pp. 86-97. doi: 10.1016/j.conbuildmat.2013.04.023

15. Shahrooz, B. M.; Forry, M. L.; Anderson, N. S.; Bill, H. L.; and Doellman, A. M., "Continuous Transverse Reinforcement—Behavior and Design Implications," *ACI Structural Journal*, V. 113, No. 5, Sept.-Oct. 2016, pp. 1085-1094. doi: 10.14359/51689154

16. Bill, H. L.; Miller, M. L.; Doellman, A. M.; and Shahrooz, B. M., "Evaluation of Continuous Transverse Reinforcement," *Concrete International*, V. 35, No. 11, Nov. 2013, pp. 49-55.

17. ASTM A706/A706M-14, "Standard Specification for Deformed and Plain Low-Alloy Steel Bars for Concrete Reinforcement," ASTM International, West Conshohocken, PA, 2014, 7 pp.

18. ACI Committee 374, "Acceptance Criteria for Moment Frames Based on Structural Testing and Commentary (ACI 374.1-05) (Reapproved 2019)," American Concrete Institute, Farmington Hills, MI, 2005, 9 pp.

19. FEMA 356, "Prestandard and Commentary for the Seismic Rehabilitation of Buildings," Federal Emergency Management Agency, Washington, DC, 2000, 518 pp.

ACI STRUCTURAL JOURNAL TECHNICAL PAPER

Title No. 121-S43

Modeling of Glass Fiber-Reinforced Polymer-Reinforced Squat Walls under Lateral Loading

by Ju-Hyung Kim, Yail J. Kim, and Hong-Gun Park

This paper presents mechanics-based modeling approaches to understand the shear behavior of squat walls reinforced with glass fiber-reinforced polymer (GFRP) bars when subjected to lateral loading. The applicability of design provisions in published specifications is examined using collated laboratory test data, resulting in the need for developing revised guidelines. Analytical studies are undertaken to evaluate the effects of reinforcement type on the response of load-bearing walls and to establish failure criteria as a function of various stress states in constituents. Obvious distinctions are noticed in the behavior of squat walls with steel and GFRP reinforcing bars owing to their different reinforcing schemes, tension-stiffening mechanisms, and material properties. Newly proposed equations outperform existing ones in terms of predicting the shear capacity of GFRP-reinforced squat walls. Furthermore, based on geometric and reinforcing attributes, a novel determinant index is derived for the classification of structural walls into squat and slender categories, which overcomes the limitations of prevalent methodologies based solely on aspect ratio. A practical method is suggested to adjust the failure mode of walls with GFRP reinforcing bars, incorporating a characteristic reinforcement ratio.

Keywords: failure mode; glass fiber-reinforced polymer (GFRP); modeling; shear; squat wall.

INTRODUCTION

Shear walls are indispensable for a building structure to accommodate lateral loads. Improper designs accelerate the deterioration of load-bearing members and bring about serviceability problems such as excessive sidesway.[1] Placing shear walls in the right locations ensures the stability of building frames,[2] and the large wall stiffness controls the horizontal displacement of constituents within an acceptable limit stipulated in specifications.[3] When subjected to lateral loading, both ends of a wall (typically called boundary elements with concentrated reinforcing bars) carry tension and compression forces.[4] These elements, which are essential if the maximum compression stress near the end of a wall exceeds a certain limit,[5] are instrumental in resisting load reversals and inhibiting unanticipated buckling.[6] Depending upon aspect ratio (h_w/l_w, where h_w and l_w are the height and length of a wall, respectively), shear walls are categorized as squat and slender; however, no absolute demarcation is available from a behavioral perspective: a ratio between $h_w/l_w = 1.0$ and 2.0 often plays a role as a bifurcation point.[7-9] Among other particulars, the shear strength coefficient (α_c) of structural walls in ACI 318-19[5] may fulfill the demand for practical guidance ($\alpha_c = 3.0$ for $h_w/l_w \leq 1.5$, 2.0 for $h_w/l_w \geq 2.0$, and a linearly interpolated value for $1.5 < h_w/l_w < 2.0$ in U.S. customary units). These classifications can be interpreted in a way that an aspect ratio is reasonably taken to be below 1.5 for squat walls and a ratio between 1.5 and 2.0 indicates a transition from squat to slender walls.

The application of non-metallic reinforcement has become commonplace around the globe[10]; accordingly, a building code with glass fiber-reinforced polymer (GFRP) reinforcing bars (ACI CODE-440.11-22[11]) was recently published to direct practicing engineers. While high strength, light weight, nonmagnetic composition, and low maintenance are some of the many advantages that GFRP composites offer, corrosion resistance is the most notable benefit when incorporated in concrete structures.[12] On the use of GFRP reinforcement for shear walls, a consensus has not yet been made. Some researchers argue that technical evidence is insufficient for field application[13]; by contrast, others claim that the non-yielding nature of GFRP with a low elastic modulus improves the seismic performance of concrete members.[14,15] As far as GFRP-reinforced squat walls are concerned, limited research has been reported and only a few experimental papers are available.[8,16] Further studies are thus necessary to understand the behavior of squat walls with GFRP reinforcing bars and to expand the applicable boundary of these nontraditional construction materials.

This paper discusses an analytical model to examine the response of GFRP-reinforced squat walls under lateral loading. With the aim of overcoming the limitations of technical findings from test data,[8,16] detailed mechanics are accounted for and design recommendations are elaborated. In addition, an alternative expression is suggested to identify a behavioral threshold between squat and slender walls, which is not simply reliant on an aspect ratio.

RESEARCH SIGNIFICANCE

The design of shear walls is empirical and heavily relies on practitioners' experience without systematic derivations.[17,18] Notwithstanding the broad adoption of GFRP reinforcement in concrete members, little is known about its use in squat walls. Because the failure mechanism of squat walls differs from that of slender walls (that is, the former tends to fail in shear, accompanied by diagonal tension cracks,

ACI Structural Journal, V. 121, No. 3, May 2024.
MS No. S-2023-172.R1, doi: 10.14359/51740489, received November 22, 2023, and reviewed under Institute publication policies.

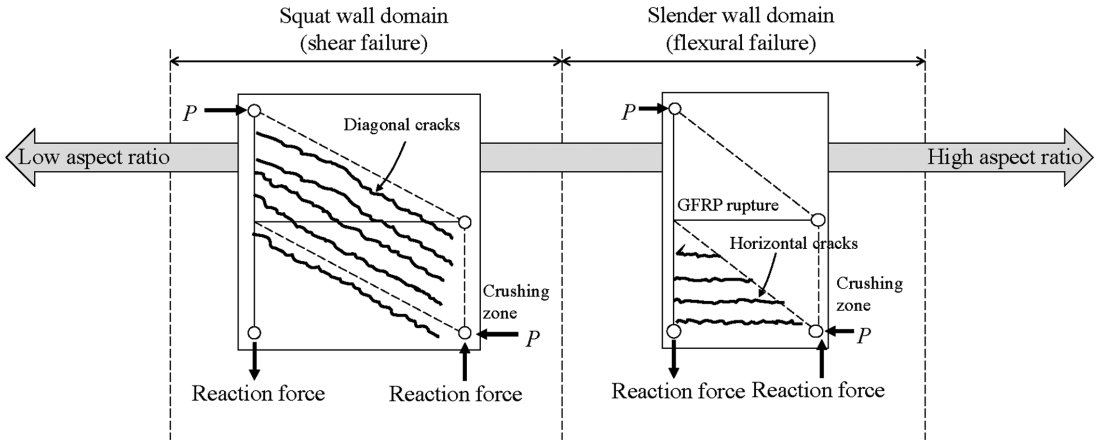

Fig. 1—Conceptual failure modes of GFRP-reinforced concrete walls.

whereas the latter fails in flexure[1]), archetypal methods that are predicated upon ductile responses cannot be applied. Furthermore, in view of deficient ductility in squat walls, attention should be paid to how premature shear failure can be precluded by employing adequate technical approaches. A refined mechanics-based model is developed to elucidate the intrinsic behavior of squat walls with GFRP reinforcing bars, leading to the proposal of practical design equations.

BACKGROUND

Expository discussions are presented with regard to the shear behavior of GFRP-reinforced concrete walls. Codified design provisions are reviewed and evaluated using test data, including a comparative analysis that investigates functional differences between squat walls with steel and GFRP reinforcing bars.

Potential failure modes

As conceptually visualized in Fig. 1, a GFRP-reinforced concrete wall may fail in flexure, shear, or a combination thereof. For instructional purposes, the load path of the wall is approximated with idealized joints connecting compression and tension segments (dotted and solid lines in Fig. 1, respectively). When the wall's aspect ratio is lower than a certain limit, its failure is governed by compression struts parallel to diagonal tension cracks in the web and by the crushing of the end zone (the squat wall domain in Fig. 1). If an aspect ratio is higher than the limit, the wall tends to bend like a cantilever fixed at the base and horizontal cracks formed within the tension zone; eventually, it fails by either the rupture of GFRP or the crushing of the concrete (the slender wall domain in Fig. 1). Contingent upon the properties of wall structures, a transition between these two scenarios can be seen.

Design method

Because the design of squat walls with GFRP reinforcement has not been fully documented in published specifications, the coalescence of ACI 440.1R-15,[12] ACI 318-19,[5] and ACI 440.11-22[11] may be used. The nominal shear capacity of a wall (V_n) is expressed as[5,11]

$$V_n = V_c + V_f \le V_{n,max} \tag{1}$$

$$V_{n,max} = k_1 f_c'^{0.5} d t_w = k_2 f_c'^{0.5} l_w t_w \tag{2}$$

where V_c and V_f are the nominal shear resistance of the concrete and reinforcement, respectively; k_1 and k_2 are empirical constants (k_1 = 10 and k_2 = 8 for U.S. customary units and k_1 = 0.83 and k_2 = 0.66 for metric units[5]); t_w and l_w are the thickness and length of the wall, respectively; and d is the effective depth ($d = 0.8l_w$).[11] The individual components of Eq. (1) are provided by[11,12]

$$V_c = k_3 f_c'^{0.5} t_w k d = k_4 f_c'^{0.5} k l_w t_w \tag{3}$$

$$k = \sqrt{2\rho_f n_f + (\rho_f n_f)^2} - \rho_f n_f \tag{4}$$

$$V_f = A_{fv} f_{fv} d/s = \rho_h f_{fv} l_w t_w \tag{5}$$

$$f_{fv} = \Omega E_f \le f_{fb} \tag{6}$$

where k_3 and k_4 are empirical constants (k_3 = 5 and 0.4 and k_4 = 4 and 0.32 for U.S. customary and metric units, respectively[11]); ρ_f is the reinforcement ratio ($\rho_f = A_{fv}/(bd)$, in which A_{fv} is the cross-sectional area of the shear reinforcement and b is the width of the wall); n_f is the modular ratio ($n_f = E_f/E_c$, in which E_f and E_c are the elastic moduli of the GFRP and concrete, respectively); s is the center-to-center spacing of the reinforcing bars; f_{fb} is the design strength of the bent stirrup made of GFRP; and Ω is the strain limit of the reinforcement (Ω = 0.004).[12]

Appraisal

Existing test data—Figure 2(a) shows a ratio between the experimental and nominal shear capacities of GFRP-reinforced squat walls (V_{test} and V_n, respectively). The properties of test specimens excerpted from Table 1 are as follows[8]: aspect ratio (h_w/l_w) = 0.68 and 1.14, compressive strength of concrete (f_c') = 33 to 40 MPa (4790 to 5800 psi), tensile strength of GFRP (f_{fu}; f_{uh} and f_{uv} for horizontal and vertical reinforcing bars in Table 1, respectively) = 1022 to 1100 MPa (148 to 160 ksi), and horizontal and vertical reinforcement ratios (ρ_h and ρ_v, respectively) = 0.38% to 0.7%. The specimens with h_w/l_w = 1.33 in Table 1 were excluded due to a low reinforcement ratio in the boundary element (ρ_{be} =

Table 1—Summary of existing test programs on GFRP-reinforced squat walls

No.	Reference	Specimen	h_w, mm	l_w, mm	h_w/l_w	t_w, mm	l_{be}, mm	f_c', MPa	f_{uh}, MPa	f_{uv}, MPa	f_{ul}, MPa	f_{ut}, MPa	ρ_h, %	ρ_v, %	ρ_{be}, %	ρ_l, %	$N/(A_g f_c')$, %	V_{test}, kN	Drift*, %	Failure mode
1	Arafa et al.[19]	G4-250	2000	1500	1.33	200	200	35	1372	1372	1020	1065	0.51	0.59	1.43	0.89	0	678	2.65	Flexure
2	Arafa et al.[19]	G4-160	2000	1500	1.33	200	200	35	1372	1372	1020	1065	0.79	0.59	1.43	0.89	0	708	2.80	Flexure
3	Arafa et al.[19]	G4-80	2000	1500	1.33	200	200	40	1372	1372	1020	1065	1.58	0.59	1.43	0.89	0	912	2.75	Flexure
4	Arafa et al.[19]	G6-80	2000	1500	1.33	200	200	41	1372	1372	1020	1065	3.56	0.59	1.43	0.89	0	935	2.90	Flexure
5	Arafa et al.[20]	G4	2000	1500	1.33	200	200	40	1372	1372	1020	1065	1.58	0.59	1.43	0.89	0	740	2.60	Flexure
6	Shabana et al.[8]	MSQ1	1600	1400	1.14	150	225	40	1100	1100	1100	1022	0.38	0.5	4.48	5.0	7.5	561	1.13	Shear
7	Shabana et al.[8]	MSQ2	1600	1400	1.14	150	225	39	1022	1100	1100	1022	0.38	0.5	4.48	5.0	15.0	590	1.17	Shear
8	Shabana et al.[8]	MSQ3	1600	1400	1.14	150	225	37	1022	1100	1100	1022	0.63	0.5	4.48	5.0	7.5	683	1.54	Shear
9	Shabana et al.[8]	MSQ4	1600	1400	1.14	150	225	37	1022	1100	1100	1022	0.63	0.7	4.48	5.0	7.5	732	1.81	Shear
10	Shabana et al.[8]	SSQ1	950	1400	0.68	150	225	35	1022	1100	1100	1022	0.38	0.5	4.48	5.0	7.5	1071	1.00	Shear
11	Shabana et al.[8]	SSQ3	950	1400	0.68	150	225	33	1022	1100	1100	1022	0.63	0.5	4.48	5.0	7.5	1102	1.10	Shear

*Lateral drift at failure.

Note: h_w is wall height; l_w is wall length; t_w is wall thickness; b_{be} is boundary element width; f_c' is concrete compressive strength; f_{uh} is tensile strength of web horizontal GFRP reinforcing bar; f_{uv} is tensile strength of web vertical GFRP bar; $f_{u,be}$ is tensile strength of GFRP reinforcing bar in boundary elements; ρ_h is web horizontal reinforcement ratio; ρ_v is web vertical reinforcement ratio; ρ_{be} is vertical reinforcement ratio in boundary elements; $N/(A_g f_c')$ is axial load ratio applied to top of wall; V_{test} is experimental capacity. 1 mm = 0.0394 in.; 1 MPa = 145 psi.

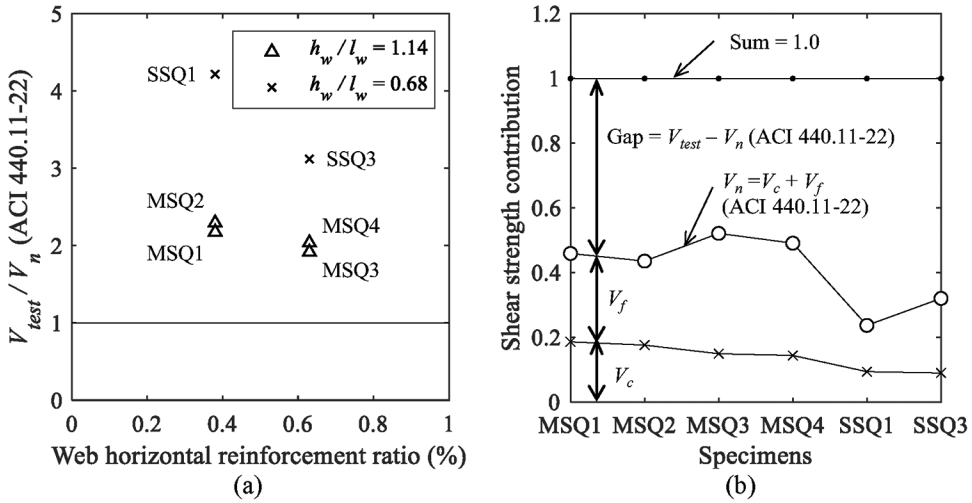

Fig. 2—ACI design approach for GFRP-reinforced concrete walls with an aspect ratio of less than 1.5: (a) shear capacity; and (b) contribution of components.

1.43%), which will be accounted for in a subsequent section. Although the number of test specimens in Fig. 2(a) is insufficient to render conclusive information, owing to a lack of available data, it is substantiated that Eq. (1) underestimated the capacity of the walls; especially, significant conservatism was noticed ($V_{test}/V_n > 3.0$) when the aspect ratio was $h_w/l_w = 0.68$. These discrepancies are ascribed to the fact that the expression of V_c in Eq. (1) was empirically calibrated using flexure-shear-combined responses alongside large diagonal tension cracks[12]; on the contrary, the shear-dominated behavior of the squat walls with a low aspect ratio entailed narrow inclined cracks parallel to the compression struts (Fig. 1). Accordingly, an improvement is required to better predict the capacity of squat walls with GFRP reinforcing bars, which can avert the placement of unnecessary shear reinforcement.

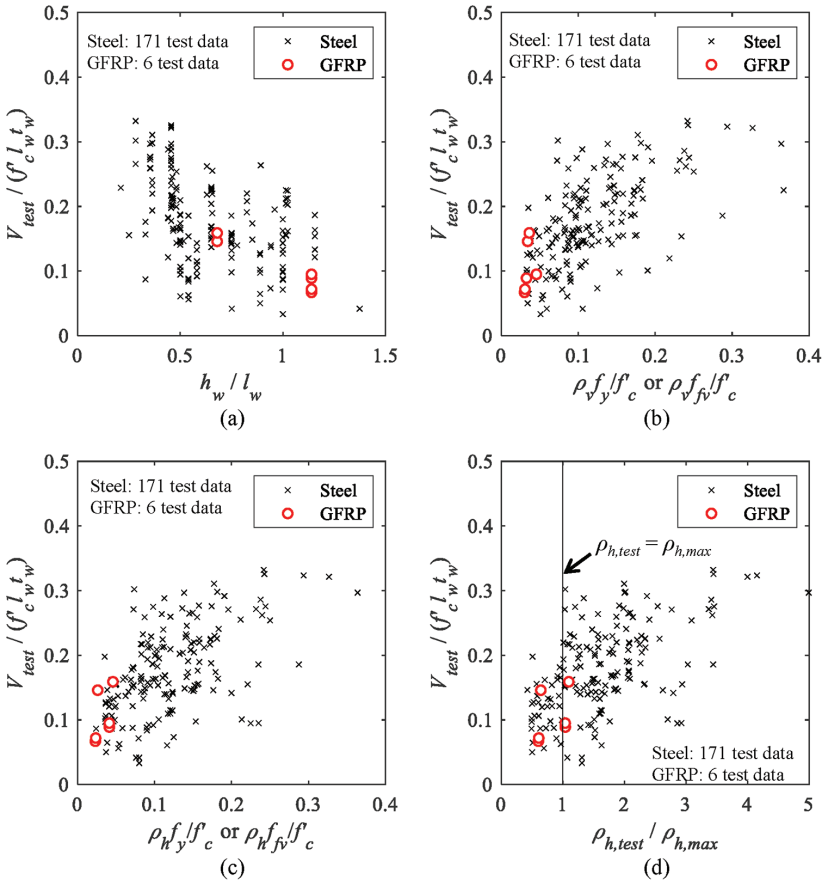

Fig. 3—Comparison of steel- and GFRP-reinforced squat walls: (a) aspect ratio; (b) normalized horizontal reinforcement ratio in web; (c) normalized vertical reinforcement ratio in web; and (d) ratio between horizontal reinforcement ratio and maximum reinforcement ratio.

The portion of the concrete and GFRP resistance (Eq. (3) and (5), respectively) is allocated in Fig. 2(b). For consistency, the allowable strain limit of $\Omega = 0.004$ was employed to calculate V_f in all specimens. The gap between the test and prediction spanned from 0.48 to 0.76 and the degree of margin ($V_{test} - V_n$) was apparent when the aspect ratio dropped to $h_w/l_w = 0.68$ (the SSQ series). This tendency again confirms that the design approach of ACI CODE-440.11-22[11] does not cover GFRP-reinforced concrete squat walls.

Comparison against steel reinforcement—To figure out behavioral differences between GFRP and steel reinforcing bars in squat walls, a comparative assessment was made. For steel-reinforced walls, a total of 171 test data were collated from literature[21-51] with the succeeding properties (those of GFRP-reinforced walls were delineated in the preceding section): h_w/l_w = 0.21 to 1.5; f_c' = 20 to 70 MPa (2900 to 10,150 psi); ρ_h and ρ_v = 0.25% to 2.8%; and f_y = 284 to 750 MPa (41 to 109 ksi), in which f_y is the yield strength of the reinforcing bars. Figure 3 graphs the test capacities of the walls, which were normalized by the cross-sectional area and concrete strength ($f_c' l_w t_w$) to accommodate variable geometric and material properties, as a function of primary design parameters. While the normalized capacities of both steel and GFRP cases decreased with an increase in the aspect ratio (Fig. 3(a)), their response range differed in the ordinate: $0.03 \le V_{test}/(f_c' l_w t_w) \le 0.33$ for steel and $0.07 \le V_{test}/(f_c' l_w t_w) \le 0.16$ for GFRP. Analogous patterns were noted for the normalized horizontal reinforcement ratios ($\rho_h f_y/f_c'$ for steel and $\rho_h f_{fv}/f_c'$ for GFRP) and vertical reinforcement ratios ($\rho_v f_y/f_c'$ for steel and $\rho_v f_{fv}/f_c'$ for GFRP) given in Fig. 3(b) and (c), respectively. These distinct ranges of wall capacities, depending upon the reinforcement type, can be explained by deriving the maximum horizontal reinforcement ratio ($\rho_{h,max}$) when the shear capacity of the walls ($V_{n\text{-}wall}$) is equivalent to their shear-strength limit ($V_{n,max}$, Eq. (2)), which represents the most critical state in a squat wall system: diagonal tension failure equals web-crushing.

The $V_{n\text{-}wall}$ expressions for the steel- and GFRP-reinforced concrete walls are attained from ACI 318 (Eq. (7))[5] and ACI CODE-440.11-22 (Eq. (1))[11]

$$V_{n\text{-}wall} = (\alpha_c \lambda f_c'^{0.5} + \rho_h f_{yh}) l_w t_w \tag{7}$$

where α_c is the shear strength coefficient (α_c = 3.0 and 0.25 for U.S. customary and metric units, respectively, for an aspect ratio of $h_w/l_w \le 1.5$); and λ is the concrete strength factor (λ = 1.0 for ordinary concrete). After setting Eq. (7) = Eq. (2) and Eq. (1) = Eq. (2) for steel and GFRP-reinforced concrete walls, respectively, the horizontal reinforcement ratio (ρ_h) is solved, which is equivalent to the maximum reinforcement ratio of each instance ($\rho_{h,max}$)

$$\rho_{h,max} = \psi_1 \frac{f_c'^{0.5}}{f_{yh}} \text{ for steel reinforcement} \tag{8}$$

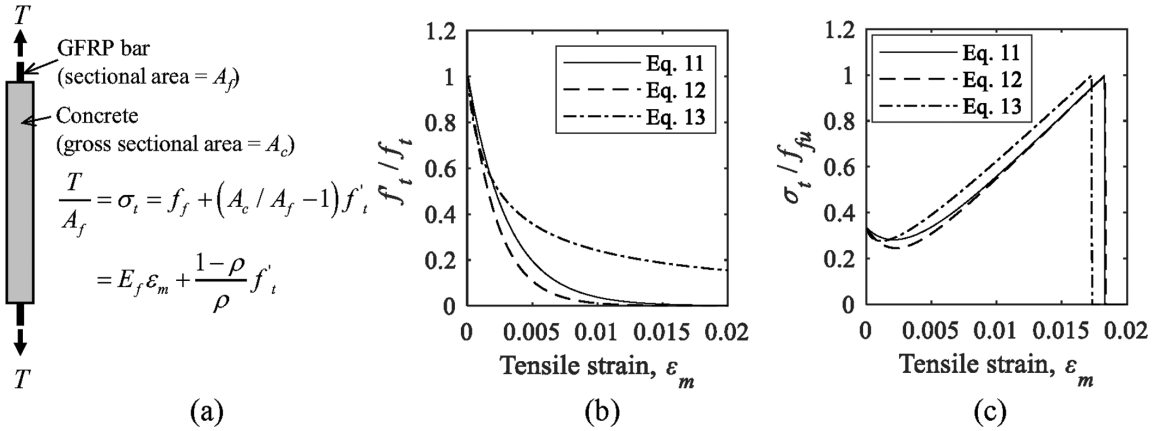

Fig. 4—Tension stiffening of GFRP-reinforced concrete: (a) schematic representation; (b) progressive reduction of tensile stress in concrete; and (c) strain-dependent response.

$$\rho_{h,max} = (\psi_2 - \psi_3 k)\frac{f_c'^{0.5}}{f_{fv}} \text{ for GFRP reinforcement} \quad (9)$$

where ψ_1, ψ_2, and ψ_3 are constants ($\psi_1 = 5$, $\psi_2 = 8$, and $\psi_3 = 4$ for U.S. customary units and $\psi_1 = 0.41$, $\psi_2 = 0.66$, and $\psi_3 = 0.34$ for metric units). As demonstrated in Fig. 3(d), the majority of reinforcement ratios in the steel-reinforced walls (136 specimens or 80% of the entire samples) exceeded the maximum ratio ($\rho_{h,max}$); contrarily, most ratios of walls with GFRP were close to or less than the maximum ratio. These observations clarify that the amount of reinforcing bars was generally greater in the steel-reinforced walls than their GFRP counterparts, which was related to the high strength of GFRP, and that the contribution of these reinforcing bars to the shear capacity of the walls was dissimilar, justifying the need for an independent design approach pertaining to GFRP-reinforced squat walls.

MODELING

To comprehend the ramifications of steel and GFRP reinforcing bars for the shear behavior of reinforced concrete squat walls, a twofold analytical model is formulated at the element and structural levels. This section outlines an overview of modeling processes along with implementation steps and verification against test data.

Element level

Framework—A unit square panel[52] represented shear-loaded wall elements with steel and GFRP reinforcing bars. The panel concrete had a tensile strength of $f_t = 1.8$ MPa (260 psi), resulting from $f_c' = 30$ MPa (4350 psi),[53] and was orthogonally reinforced with reinforcing bars at a reinforcement ratio of $\rho = 0.25\%$ to 3.0%. The lower bound of the ratio conformed to the requirement of ACI 318-19,[5] while the upper bound enveloped the ratios of the experimental specimens presented in Fig. 3. The yield and ultimate strengths of the steel and GFRP reinforcing bars were $f_y = 420$ MPa (60 ksi) and $f_{fu} = 1100$ MPa (160 ksi) with elastic moduli of $E_s = 200$ GPa (29,000 ksi) and $E_f = 60$ GPa (8700 ksi), respectively. The stress-strain behavior of the panel was computed as per the procedure of the Modified Compression Field Theory,[53] incorporating tension-stiffening that realistically considered interactions between the concrete and reinforcing bars.

Tension stiffening—A schematic representation of the tension-stiffening mechanism is shown in Fig. 4(a). The tensile stress of the reinforced concrete segment (σ_t) is calculated by the summation of reinforcing bar stresses inside the concrete (f_f) and the surrounding concrete ($(A_c/A_f - 1)f_t'$, in which A_c and A_f are the cross-sectional areas of the concrete and reinforcing bar, respectively, and f_t' is the stress of the concrete with tensioning-stiffening)

$$\sigma_t = E_f \varepsilon_m + \frac{1-\rho}{\rho} f_t' \quad (10)$$

where ε_m is the tensile strain of the reinforced concrete. For the representation of tension stiffening in GFRP-reinforced concrete, three candidate expressions were chosen[54-56]

$$f_t' = f_t \exp\left[-1100(\varepsilon_m - \varepsilon_{cr})\left(\frac{E_f}{200{,}000}\right)\right] \quad (11)$$

$$f_t' = f_t \exp\left[-1500(\varepsilon_m - \varepsilon_{cr})\left(\frac{E_f}{200{,}000}\right)\right] \quad (12)$$

$$f_t' = f_t / \left(1 + \beta_1(\varepsilon_m - \varepsilon_{cr})\left[\left(\frac{E_f}{200{,}000}\right)\right]^{\gamma}\right) \quad (13)$$

where ε_{cr} is the concrete strain at cracking; and β_1 and γ are the tension-stiffening constants ($\beta_1 = 1400$ and $\gamma = 0.8$, 1.0, and 1.5 for ribbed, sand-coated, and helically wrapped GFRP bars, respectively[56]). As plotted in Fig. 4(b) and (c), the downward propensity of Eq. (11) and (12) was alike, whereas Eq. (13) overestimated the tension-stiffening effect. Given the marginal tension stiffening of GFRP-reinforced concrete members,[57] Eq. (12) was used in this study. For the occasion of steel-reinforced concrete, the tension-stiffening model of Vecchio and Collins[53] was adopted

$$f_t' = f_t/(1 + (200\varepsilon_m)^{0.5}) \quad (14)$$

Constitutive relationship—Figures 5(a) and (b) reveal the stress-strain relationship of the steel-and GFRP-reinforced

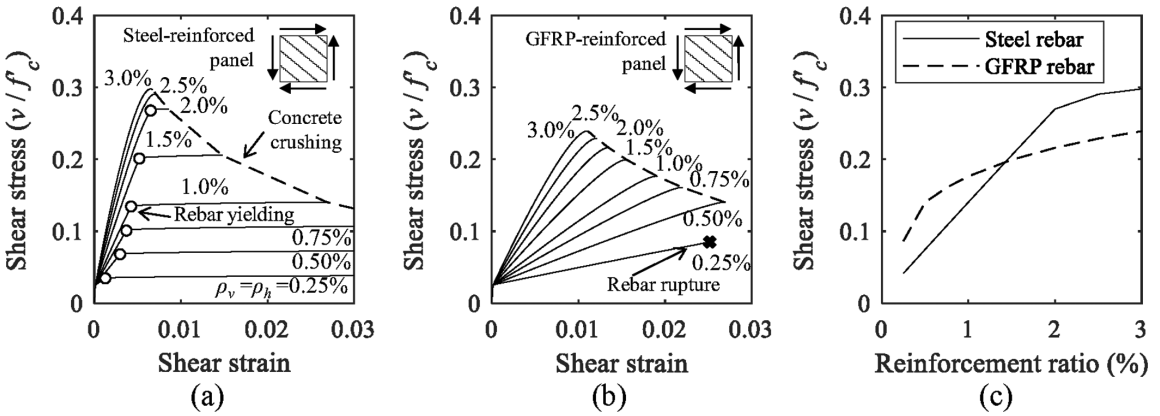

Fig. 5—Element-level shear behavior: (a) steel-reinforced concrete panel; (b) GFRP-reinforced concrete panel; and (c) comparison of maximum shear stresses.

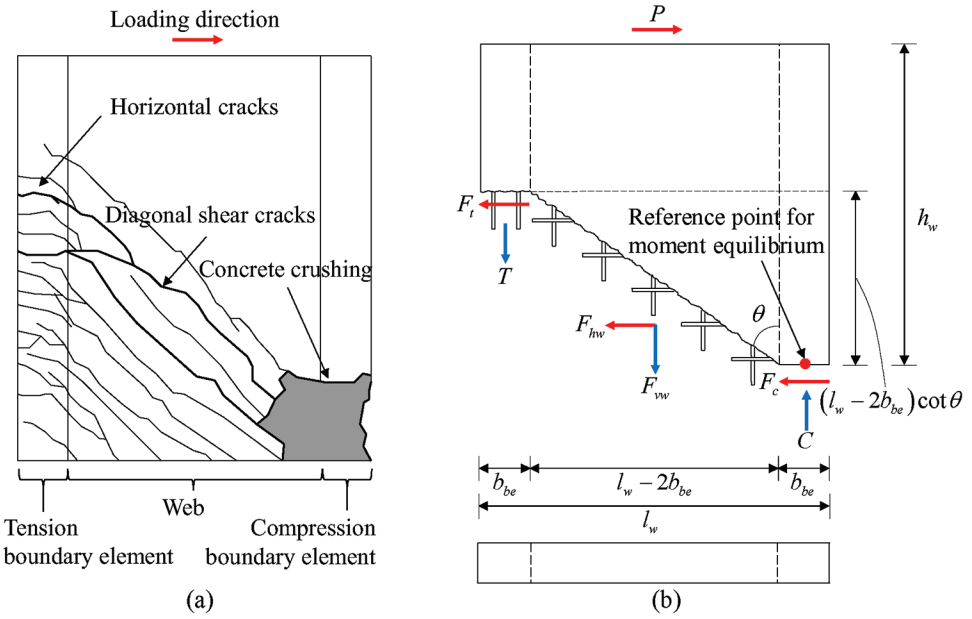

Fig. 6—Analytical model: (a) test observation; and (b) simplified free body diagram.

concrete panels loaded in shear, respectively. To focus on the disparity of these reinforcing bar types, the average stress values (v) in the ordinate were normalized by the concrete strength (f_c'). The failure of the steel-reinforced panel was attributed to the yielding of the reinforcing bars combined with the crushing of the concrete (Fig. 5(a)), except for the heavily reinforced panel having $\rho \geq 2.5\%$ that failed without yielding. On the GFRP-reinforced panel (Fig. 5(b)), concrete crushing was responsible for the failure, with the exception of the lightly reinforced panel ($\rho = 0.25\%$). The low elastic modulus of GFRP caused much increase in strain under the same stress level, compared with the steel-reinforced case. Shown in Fig. 5(c) is a compilation of the maximum shear stresses with the reinforcement ratio of the panels. The reinforcing bar types obviously influenced the shear capacity of the panels, which reemphasizes the necessity of a customized model for GFRP-reinforced squat walls.

Structural level

Derivation—A simplified free-body diagram of a failed squat wall (Fig. 6(a)) is illustrated in Fig. 6(b). In compliance with ACI 374.2R-13,[58] the wall is loaded laterally and force equilibrium is achieved

$$P = F_t + F_{hw} + F_c \tag{15}$$

$$C = T + F_{vw} \tag{16}$$

$$P = T\frac{l_w - b_{be}}{h_w} + F_{hw}\frac{l_w - 2b_{be}}{2h_w}\cot\theta + F_{vw}\frac{l_w - b_{be}}{2h_w} \tag{17}$$

where P is the applied load; F_t and F_c are the resultant forces of the tension and compression boundary elements, respectively; F_{hw} and F_{vw} are the resultant forces of the web in the horizontal and vertical directions, respectively; C and T are the resistance of the boundary elements in compression and tension, respectively; l_w and h_w are the length and height of the wall, respectively; b_{be} is the width of the boundary element; and θ is the crack angle in degrees. Because the dowel action of GFRP reinforcing bars is negligible in a cracked plane,[12] the F_t term in Eq. (15) can be ignored. The

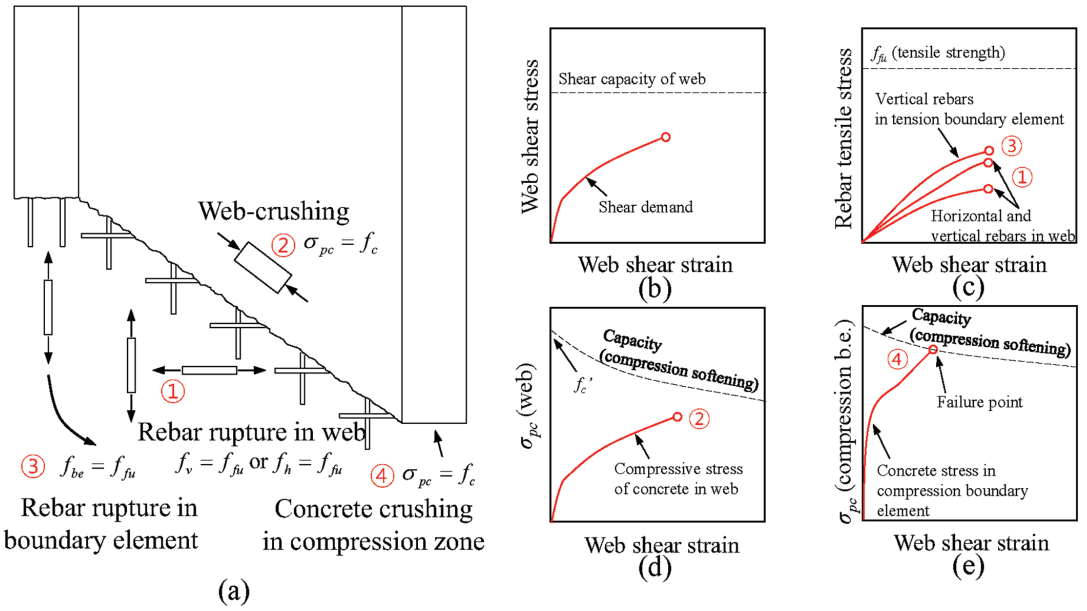

Fig. 7—Potential failure modes: (a) components; (b) stress-stain in web; (c) reinforcing bar stresses in web and tension boundary element; (d) concrete stress in web; and (e) concrete stress in compression boundary element.

horizontal force in the compression boundary element (F_c) is then obtained by combining Eq. (15) and (17)

$$F_c = P - F_{hw} = T\frac{l_w - b_{be}}{h_w} + F_{vw}\frac{l_w - b_{be}}{2h_w} + F_{hw}\left(\frac{l_w - 2b_{be}}{2h_w}\cot\theta - 1\right) \quad (18)$$

The organizational format of Eq. (18) explains the load-bearing mechanism of the squat wall in Fig. 1, corroborated by the failure pattern of test specimens No. 6 to 11 in Table 1: the horizontal force (F_c) in Fig. 6(b) would increase with an increase in the aspect ratio of the web (related to $h_w/(l_w - 2b_e)$ and $h_w/(l_w - b_e)$) and the vertical reinforcement in the web and the tension boundary element (concerned with F_{vw} and T). Likewise, Eq. (18) can account for the failure mode of the slender wall in Fig. 1: the F_c term decreases when the contribution of the vertical bars (F_{vw}) declines, which allows the progression of horizontal cracks along the web (that is, a precluded development of diagonal tension cracks). The linear elastic nature of GFRP reinforcing bars yields the succeeding expressions

$$F_{hw} = \rho_h E_f \varepsilon_h (l_w - 2b_e) t_w \cot\theta = \rho_h E_f \varepsilon_h A_{web} \cot\theta \quad (19)$$

$$F_{hv} = \rho_v E_f \varepsilon_v (l_w - 2b_e) t_w = \rho_v E_f \varepsilon_v A_{web} \quad (20)$$

$$T = \rho_{be} E_f \varepsilon_{be} b_{be} t_w = \rho_{be} E_f \varepsilon_{be} A_{be} = \rho_{be} E_f \varepsilon_v A_{be} \quad (21)$$

where ρ_h and ρ_v are the horizontal and vertical reinforcement ratios of the web, respectively; ρ_{be} is the reinforcement ratio of the boundary element; and ε_h, ε_v, and ε_{be} are the strains of the horizontal and vertical reinforcing bars and the boundary element, respectively. Because the web of a laterally loaded squat wall is subjected to uniform shear stress distributions,[59] the strain of the vertical reinforcing bars along the cracked plane (ε_v) may be equated with that of the boundary element (ε_{be}) transmitting axial forces (Fig. 6(b)). This approximation ($\varepsilon_v = \varepsilon_{be}$) is supported by experimentally measured strains.[8]

Failure criteria—Figure 7(a) depicts the possible failure modes of the squat wall model. The following is a succinct description of the individual cases.

1. *Rupture of GFRP reinforcing bars in the web*: When the stress of the vertical and horizontal reinforcing bars (f_v and f_h, respectively) is greater than the tensile strength of GFRP (f_{fu}), the reinforcing bars rupture. Contemplating that reinforcing bar strains at peak drift ratios in squat walls are generally smaller than the ultimate strain of commercially available GFRP reinforcing bars,[8,12] the occurrence of this failure mode may be uncommon.

2. *Web crushing*: Crushing failure of concrete in the web takes place if the principal compressive stress (σ_{pc}) reaches the softened concrete strength (f_c)

$$f_c = f_c' / (0.8 + 170\varepsilon_{pt}) \quad (22)$$

where ε_{pt} is the principal tensile strain of the concrete. Equation (22)[60] denotes the degradation of concrete with an increase in the maximum normal strain when subjected to mechanical loading; in other words, the shear deformation of the web under the lateral load (Fig. 6) raises the principal strain, thereby weakening the concrete resistance without regard to the type of reinforcement. As such, Eq. (22) can be used for both steel- and FRP-reinforced concrete members.[61]

3. *Rupture of GFRP reinforcing bars in the tension boundary element*: Reinforcing bars will rupture when their stress (f_{be}) equals the tensile strength (f_{fu}), which depends upon the amount of longitudinal reinforcing bars in the tension boundary element. Conventionally speaking, the tension boundary element of a shear wall transmits axial forces[62]; thus, stress interactions between normal and inclined components are negligible.

4. *Concrete crushing in the compression boundary element*: The combined shear and compression forces in

the compression boundary element at the reference point associated with moment equilibrium (Fig. 6(b)) increase concrete stresses and prompt crushing failure ($\sigma_{pc} = f_c$). This failure type is frequently observed in squat walls tested in laboratories.[8,16]

The notional explication of these failure modes is provided in Fig. 7(b) to (e). When the squat wall is loaded laterally, the stress and strain of the web increase in a steady manner (Fig. 7(b)). The stress states of the reinforcing bars and concrete in the web and the boundary elements are computed as detailed in the previous section, and those are compared against the aforementioned failure criteria. The shear deformation of the web causes the elongation of the horizontal and vertical reinforcing bars (Fig. 7(c)) as well as the compression of the concrete (Fig. 7(d)). The lateral load also exerts axial tension and compression to the boundary elements (Fig. 7(c) and (e)). As drawn in Fig. 7(e), the shear-compression-combined action in the compression boundary element augments the concrete stress and can accelerate the development of the principal stress, resulting in the crushing of the concrete that is reported in laboratory research.[8,16]

Implementation—The previously described model is solved with a procedure recapitulated in Fig. 8. Numerical iterations are necessary to determine the failure mode and load-bearing capacity of the squat wall:

Step 1: The geometric and material properties of the wall structure are collected as input parameters, including concrete and GFRP reinforcing bars

Step 2: An initial shear strain in the web (γ) is assumed with a small fraction of the concrete cracking strain (γ = 0.0005 was chosen for the present study). Afterward, in accordance with the Modified Compression Field Theory,[53] the constituent strains of the concrete (ε_{pt} and ε_{pc}, in which ε_{pc} is the strain corresponding to the principal compressive stress σ_{pc}) and GFRP (ε_h and ε_v) are calculated. Each of the four possible failure modes defined earlier is checked, belonging to the assumed shear strain.

Step 3: Upon obtaining the strains in the web from Step 2, the forces in the boundary elements are computed (C, F_c, and T in Eq. (16), (18), and (21), respectively). For the failure of the tension boundary element, the tensile force T is compared with the ultimate capacity of the reinforcing bar ($\rho_{be} f_{fu} b_{be} t_w$). Regarding the compression boundary element, the maximum shear stress attained from the Modified Compression Field Theory involving the compression force C is multiplied by the cross-sectional area of the boundary element to ascertain the horizontal resistance F_c, which is evaluated against the shear strength of the element.

Step 4: The stresses and resultant forces from Step 3 are appraised per the criteria established in Fig. 7(a). If a failure condition is not satisfied, the shear strain γ is increased ($\gamma_{i+1} = \gamma_i + \Delta\gamma$) and Steps 2 through 4 are repeated until a specific failure mode is found. Next, the nominal capacity of the squat wall (V_n) is quantified.

Verification—The proposed approach is validated employing the test data enumerated in Table 1. As witnessed in the laboratory, the predicted failure mode of the squat wall specimens was concrete crushing in the compression boundary element (Fig. 7(a)). Figure 9(a) assesses the predictability of the nominal shear capacity (V_n). The capacity ratio of V_{test}/V_n varied from 0.82 to 1.16, with a mean and standard deviation of 1.002 and 0.134, respectively. On the strain of the horizontal GFRP reinforcing bars in the web at the specimens' peak loads, the theoretical values were comparable to the measured strain range.[8] The strain limit of 0.004 in ACI.440.1R-15[12] served as the lower bound of the experimental strains (Fig. 9(b)), implying that this limit should be kept in the design of GFRP-reinforced squat walls.

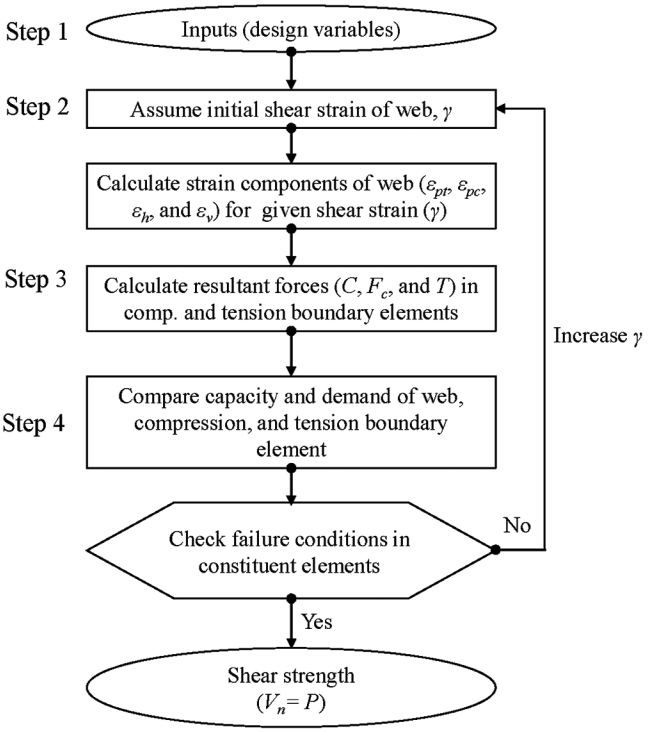

Fig. 8—Flowchart for implementation of proposed model.

DESIGN RECOMMENDATIONS

In an effort to improve the prediction of shear capacity in GFRP-reinforced walls, rational recommendations are made. Additionally, a new classification is proposed to definitize the taxonomy of squat and slender walls with an emphasis on not only wall geometries but also other attributes such as reinforcement ratios.

Proposed revision

The shear capacity of the squat wall is composed of F_c and F_{hw} (Eq. (18)). From a traditional design standpoint,[5,11,12] the F_c and F_{hw} terms can be regarded as V_c and V_f in Eq. (1), respectively. Given that the shear-resisting mechanism of the compression boundary element (Fig. 6(b)) differs from the mechanism of conventional reinforced concrete beams accompanying dowel action and aggregate interlock, the existing expression of V_c needs to be revised. Figure 10 instantiates a relationship between the capacity ratio of V_{test}/V_n and the proportion of the concrete strength ($\alpha f_c'$, where α is the fraction factor): conforming to the recommendation of prior research,[63] the shear stress range of the walls at failure was represented by $\alpha f_c'$ with an upper limit of $0.3 f_c'$. For comparison, the V_c term in Fig. 10(a) was set to be a product of the proportional stress and the cross-sectional area of

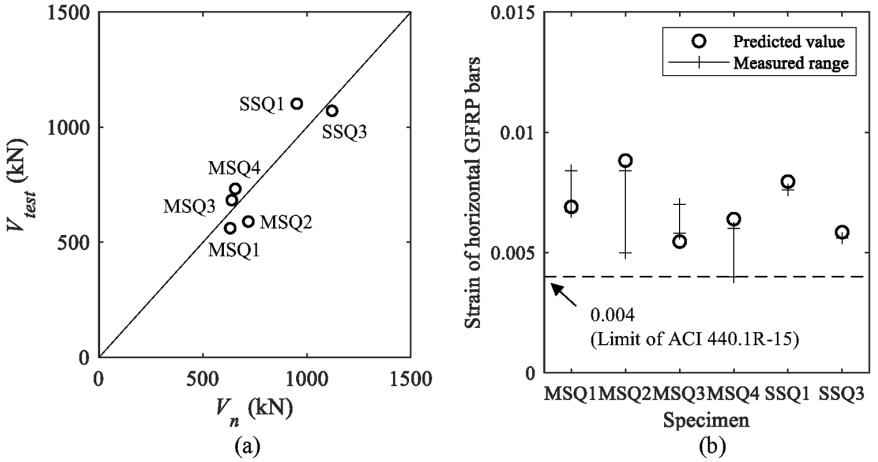

Fig. 9—Validation of proposed model: (a) shear capacity; and (b) strain of horizontal reinforcing bars at peak load. (Note: 1 kN = 0.225 kip.)

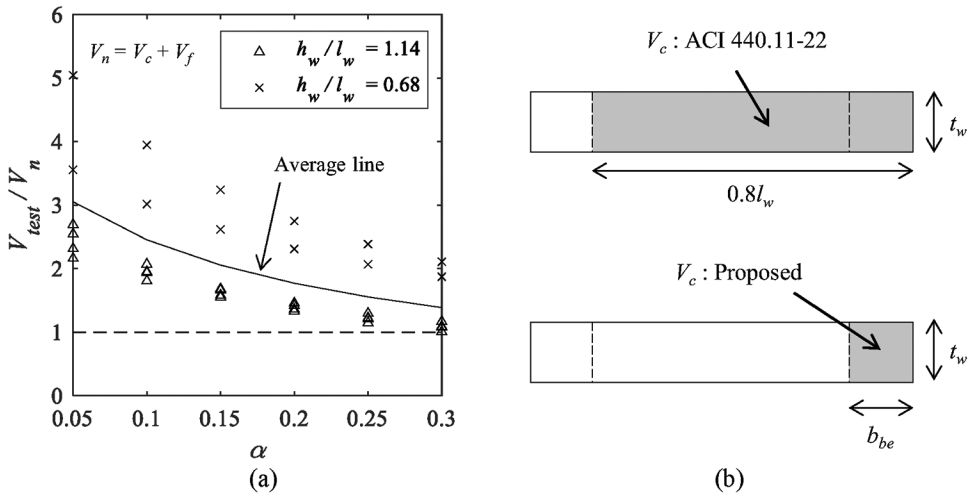

Fig. 10—Sensitivity analysis of stress fraction factor: (a) variation; and (b) effective cross-sectional area for shear resistance of concrete.

the compression boundary element ($V_c = \alpha f_c' b_{be} t_w$). Within the scope of interest ($0.05 \le \alpha \le 0.3$), the capacity ratio gradually diminished with the fraction factor. The extent of discrepancy in the ratio was the least at $\alpha = 0.3$ and the corresponding average value of $V_{test}/V_n = 1.39$ was less than the value of 2.45 at $\alpha = 0.1$ ($0.1f_c'$ is equivalent to the current design expression of ACI 440.11-22[11]). The enhanced capacity ratio with $\alpha = 0.3$ is attributed to the fact that the shear stress of $0.3f_c'$ generated higher resistance relative to the stress stemming from ACI 440.11-22[11] and that the use of the compression boundary element ($b_{be}t_w$, Fig. 10(b)) in the cracked squat wall (Fig. 6) was more realistic than the use of the entire web in the existing design approaches.[5,11] Consequently, Eq. (23) is suggested for Eq. (1)

$$V_c = 0.3f_c' b_{be} t_w = 0.3f_c' \beta l_w t_w \tag{23}$$

where β is the area ratio of the boundary element to the wall ($\beta = (b_{be}t_w)/(l_w t_w)$). The nominal shear resistance of the squat wall is, therefore, written in conjunction with Eq. (5) and (23)

$$V_n = V_c + V_f = 0.3f_c'\beta l_w t_w + (0.004E_f)A_{fv}d/s \le k_2 f_c'^{0.5} l_w t_w \tag{24}$$

It should be noted that the allowable strain limit of $\Omega = 0.004$ in Eq. (6) was not modified as articulated in the Verification section.

Determination of failure modes

Unlike the traditional definition of squat walls based only on an aspect ratio, a new criterion may be established by manipulating the analytical model to encompass the unique features of GFRP-reinforced concrete walls. This attempt imparts technical merits because the reinforcing schemes of shear walls with steel and GFRP reinforcing bars are not the same. Rearranging Eq. (18) to (21) yields Eq. (25), which manifests the strains of the horizontal and vertical GFRP reinforcing bars (ε_h, ε_v, and ε_{be})

$$F_c = \rho_{be}E_f\varepsilon_{be}A_{be}\frac{l_w - b_{be}}{h_w} + \rho_v E_f \varepsilon_v A_{web}\frac{l_w - b_{be}}{2h_w} + \rho_h E_f \varepsilon_h A_{web}\cot\theta\left(\frac{l_w - 2b_{be}}{2h_w}\cot\theta - 1\right) \tag{25}$$

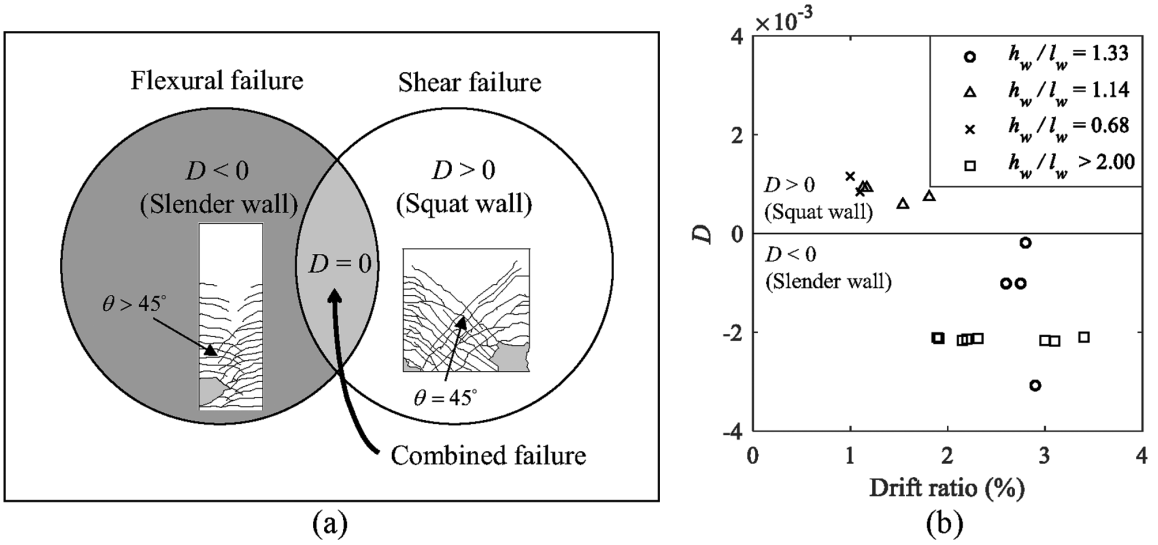

Fig. 11—Determination of failure modes: (a) Venn diagram; and (b) experimental verification.

where A_{be} and A_{web} are the cross-sectional areas of the boundary element and the web, respectively ($A_{be} = b_{be}t_w$ and $A_{web} = (l_w - 2b_{be})t_w$). Aligning with the cracked web of the squat wall shown in Fig. 6, the angle θ may be assumed to be 45 degrees and the strain compatibility condition ($\cot^2\theta = (\varepsilon_h+\varepsilon_{pc})/(\varepsilon_v+\varepsilon_{pc})$ in Vecchio and Collins[53]) enables

$$\varepsilon_\eta = (\varepsilon_v + \varepsilon_{pc})\cot\theta^2 - \varepsilon_{pc} = \varepsilon_v \tag{26}$$

Taking the previously discussed uniform stress distribution of $\varepsilon_v = \varepsilon_{be}$ and the strain limit of 0.004 stipulated in ACI 440.1R-15,[12]

$$\varepsilon_\eta = \varepsilon_v = \varepsilon_{be} = 0.004 \tag{27}$$

Then, Eq. (25) is restated as

$$F_c = 0.25\begin{pmatrix}\rho_{be}f_{fu}A_{be}\dfrac{l_w - b_{be}}{h_w} + \rho_v f_{fu}A_{web}\dfrac{l_w - b_{be}}{2h_w} + \\ \rho_h f_{fu}A_{web}\left(\dfrac{l_w - 2b_{be}}{2h_w} - 1\right)\end{pmatrix} \tag{28}$$

Dividing Eq. (28) by $f_{fu}A_w$, in which A_w is the gross cross-sectional area of the wall ($A_w = l_w t_w = A_{web} + 2A_{be}$), provides a failure determinant index (D)

$$D = \frac{F_c}{f_{fu}A_w} = 0.25\begin{pmatrix}\rho_{be}\dfrac{A_{be}}{A_w}\dfrac{l_w - b_{be}}{h_w} + \rho_v\dfrac{A_{web}}{A_w}\dfrac{l_w - b_{be}}{2h_w} + \\ \rho_h\dfrac{A_{web}}{A_w}\left(\dfrac{l_w - 2b_{be}}{2h_w} - 1\right)\end{pmatrix} \tag{29}$$

If this nondimensional index is positive ($D > 0$), the equilibrium condition depicted in Fig. 6(b) is satisfied; scilicet, the direction of the resultant force in the compression boundary element (F_c) is opposite to the applied load P. On the other hand, if the index is negative ($D < 0$), the direction of these forces is the same; hence, the assumed crack angle of θ = 45 degrees in Eq. (26) and (29) becomes invalid and the angle has to be increased to comply with the equilibrium condition (θ > 45 degrees). In that circumstance, the crack pattern of the wall conforms to the archetypal pattern of a slender wall (Fig. 11(a), inset). Equation (30) is thus adduced to discern the failure mode of structural walls with GFRP reinforcement

$$\begin{aligned} D > 0 &\rightarrow \text{squat walls with shear failure} \\ D = 0 &\rightarrow \text{transition with combined shear-flexural failure} \\ D < 0 &\rightarrow \text{slender walls with flexural failure} \end{aligned} \tag{30}$$

Allowing for the constituent terms in Eq. (29), GFRP-reinforced concrete walls with an aspect ratio of less than $h_w/l_w = 1.5$ can demonstrate flexural failure such as in the case of the slender category if their reinforcement ratios (ρ_{be}) are sufficiently low to precipitate horizontal tensile cracks. For instance, Fig. 11(b) displays the failure mode of the laboratory-tested squat walls listed in Table 1 as well as that of slender walls possessing aspect ratios greater than $h_w/l_w = 2.0$.[64,65] The specimens with an aspect ratio of $h_w/l_w = 0.68$ and 1.14 and a reinforcement ratio of $\rho_{be} = 4.48$ failed in shear ($D > 0$), whereas the specimens with $h_w/l_w = 1.33$ were positioned in the $D < 0$ domain, which matches the flexural failure observed in the laboratory and proves that the aspect ratio of structural walls is not the only factor that divides the boundary between the squat and slender categories.

Vertical reinforcement in boundary elements

A characteristic reinforcement ratio in the boundary elements ($\rho_{be,c}$) may be derived from the failure determinant function, which serves as a medium to adjust the failure mode of GFRP-reinforced concrete walls. At $D = 0$ in Eq. (29), the characteristic reinforcement ratio is specified to be

$$\rho_{be,c} = \left(\rho_h\left(\frac{2h_w - l_w + 2b_{be}}{2(l_w - b_{be})}\right) - 0.5\rho_v\right)\frac{(l_w - 2b_{be})t_w}{b_{be}t_w} \tag{31}$$

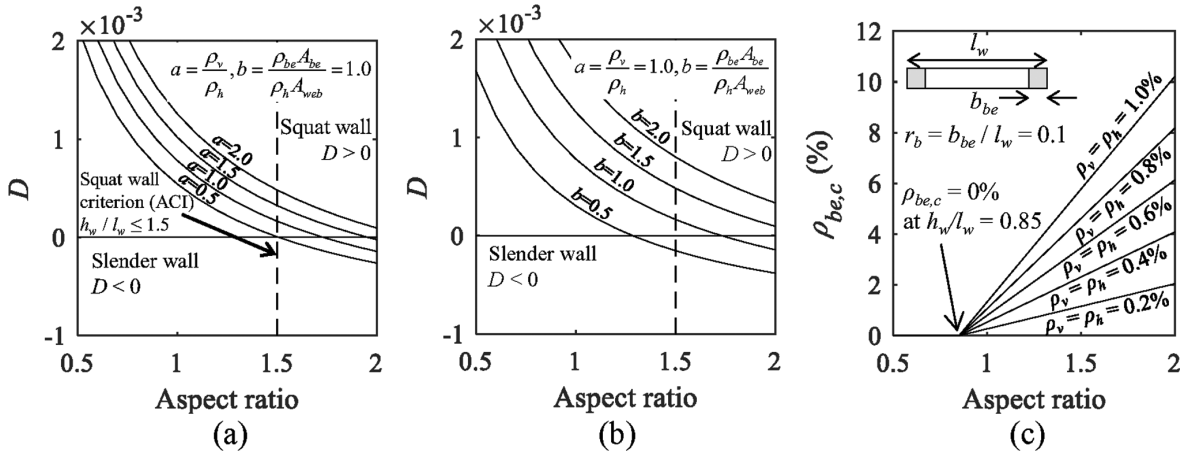

Fig. 12—Parametric analysis: (a) vertical reinforcement ratio in web; (b) longitudinal reinforcement ratio in boundary elements; and (c) characteristic vertical reinforcement ratio in boundary elements.

Equation (31) is a demarcation that apprehends whether a wall with GFRP reinforcing bars potentially fails in shear or flexure. If a reinforcement ratio in the boundary elements is greater than the characteristic ratio ($\rho_{be,c} < \rho_{be}$), shear dominates as in the failure of a squat wall. For an engineering project, practitioners can tailor ρ_{be} to accomplish an intended failure of the subject wall. A concise version of Eq. (31) is offered by letting $r_b = b_{be}/l_w$ and $a_r = h_w/l_w$ under a usual reinforcing scheme of $\rho_h = \rho_v$ in the web

$$\rho_{be,c} = \rho_h\left(\frac{a_r - 1 + 1.5\,r_b}{1 - r_b}\right)(1/r_b - 2) \qquad (32)$$

Parametric studies

The implications of geometric and reinforcing configurations for the failure of GFRP-reinforced concrete walls are visible in Fig. 12(a) through (c). A typical wall was selected (Specimen No. 8 in Table 1) for parametric investigations and its properties were used as the defaults, unless otherwise stated. Figure 12(a) exhibits the influence of a relative amount in placing vertical and horizontal reinforcing bars (ρ_v/ρ_h). With the increased aspect ratio, the determinant index (D) dwindled and the failure mode of the wall tended to shift from shear to flexure. The response curves were also affected by the vertical reinforcement ratio ρ_v. Specifically, the placement of more vertical reinforcing bars retarded the transition of the failure mode because the shear friction of the wall ascended, so the load-bearing mechanism of the squat wall was preserved. The transformational threshold of $D = 0$ that distinguishes the failure mode of the walls enveloped aspect ratios from $h_w/l_w = 1.5$ to 2.0. This finding explicates the reason why a single aspect ratio was not suited for defining a limit between squat and slender walls, which was inconclusively argued in the structural concrete community.[7-9] The reinforcement ratio of the boundary elements (ρ_{be}) was influential in altering the failure mode of the walls (Fig. 12(b)). Even though the variation trend of D was similar to the case of Fig. 12(a), the impact of ρ_{be} was prominent in comparison with ρ_v; namely, depending upon the value of ρ_{be}, a GFRP-reinforced concrete wall with $h_w/l_w > 2.0$ can still fail in shear as in the occasion of a squat wall. The growth of the characteristic reinforcement ratio ($\rho_{be,c}$) comprising a representative boundary element size of $r_b = 0.1$ is plotted in Fig. 12(c). The elevated slope of the characteristic ratio ($\rho_{be,c}$) with the reinforcement ratios of the web (ρ_v and ρ_h) points out that the balanced failure condition of the wall ($D = 0$) necessitated more reinforcing bars as its aspect ratio rose, reaffirming the significance of GFRP amounts in classifying squat and slender walls. It is, however, worth noting that the reliance of the web reinforcement ratios disappeared when the aspect ratio was below $h_w/l_w = 0.85$: the structural member was sorted into a squat wall that failed in shear, regardless of the reinforcement ratios.

SUMMARY AND CONCLUSIONS

This paper has dealt with mechanics-based analytical modeling to construe the shear behavior of glass fiber-reinforced polumer (GFRP)-reinforced squat walls when subjected to lateral loading. Through a rigorous review of existing design articles in tandem with experimental data, the limitations of current specifications were explored and the need for developing amended guidelines arose. Two-phase examinations, from local and global points of view, bring to light the influence of reinforcement type on the response of squat walls and their failure criteria as regards various stress states in structural components. A rational design proposal was made, coupled with a novel determinant index assorting load-bearing walls into squat and slender categories. Moreover, a characteristic reinforcement was rendered to assist engineering professionals in allocating architectural elements. The following are concluded:

- The provisions of ACI CODE-440.11-22[11] underestimated the shear capacity of GFRP-reinforced squat walls, particularly noticeable when an aspect ratio was as low as $h_w/l_w = 0.68$, owing to the empirical nature of the equations originating from flexure-shear-combined responses.
- The behavioral differences of squat walls with steel and GFRP reinforcing bars were evident in terms of failure characteristics and shear stress developments. The

source of these discrepancies was reinforcing amounts, tension-stiffening mechanisms, and material properties.
- The mechanics-based model ameliorated the accuracy of predicting the shear capacity of GFRP-reinforced squat walls and led to the derivation of revised expressions, constituted with the cross-sectional area of the compression boundary element and the maximum allowable reinforcing bar strain of 0.004.
- Contrary to the prevalent methodologies relying on ambiguous aspect ratios, the determinant index demystified the classification of squat walls by using the geometric and reinforcing attributes of the walls.
- The suggested characteristic reinforcement ratio would facilitate the adjustment of failure modes in GFRP-reinforced concrete walls involving an aspect ratio greater than $h_w/l_w = 0.85$, below which shear would be the dominant failure mode irrespective of reinforcing schemes in the boundary elements.

AUTHOR BIOS

Ju-Hyung Kim *is a Postdoctoral Fellow in the Department of Civil Engineering at the University of Colorado Denver, Denver, CO. He received his BE, MS, and PhD from the Department of Architecture and Architectural Engineering at Seoul National University, Seoul, South Korea. His research interests include seismic design, performance evaluation, and statistical analysis of reinforced concrete structures.*

Yail J. Kim, *FACI, is President of the Bridge Engineering Institute, An International Technical Society, and a Professor in the Department of Civil Engineering at the University of Colorado Denver. He is Chair of ACI Subcommittee 440-I, FRP-Prestressed Concrete; past Chair of ACI Committee 345, Bridge Construction and Preservation; and a member of ACI Committees 342, Evaluation of Concrete Bridges and Bridge Elements; 377, Performance-Based Structural Integrity & Resilience of Concrete Structures; 440, Fiber-Reinforced Polymer Reinforcement; and Joint ACI-ASCE Committee 343, Concrete Bridge Design. He received the ACI Chester Paul Siess Award for Excellence in Structural Research in 2019. His research interests include advanced composite materials for rehabilitation, structural informatics, complex systems, and science-based structural engineering including statistical, interfacial, and quantum physics.*

Hong-Gun Park, *FACI, is a Professor in the Department of Architecture & Architectural Engineering at Seoul National University. He received his BE and MS in architectural engineering from Seoul National University and his PhD in civil engineering from the University of Texas at Austin, Austin, TX. His research interests include numerical analysis, earthquake design of reinforced concrete, and composite structures.*

ACKNOWLEDGMENTS

This research is in part supported by the U.S. Department of Transportation through the Mountain-Plains Consortium, for which the authors are grateful. Technical contents presented herein are based on the opinion of the writers, and do not necessarily represent those of others.

REFERENCES

1. Nawy, E. G., *Reinforced Concrete: A Fundamental Approach*, Pearson, Upper Saddle River, NJ, 2008.

2. Robazza, B. R.; Yang, T. Y.; Brzev, S.; Elwood, K. J.; Anderson, D. L.; and McEwen, W., "Response of Slender Reinforced Masonry Shear Walls with Flanged Boundary Elements under In-Plane Lateral Loading: An Experimental Study," *Engineering Structures*, V. 190, 2019, pp. 389-409. doi: 10.1016/j.engstruct.2019.04.035

3. Xu, G., and Li, A., "Research on the Response of Concrete Cavity Shear Wall under Lateral Load," *Structural Design of Tall and Special Buildings*, V. 28, No. 3, 2019, p. e1577. doi: 10.1002/tal.1577

4. Zhang, J.; Li, X.; Cao, W.; and Yu, C., "Seismic Behavior of Composite Shear Walls Incorporating High-Strength Materials and CFST Boundary Elements," *Engineering Structures*, V. 220, 2020, p. 110994. doi: 10.1016/j.engstruct.2020.110994

5. ACI Committee 318, "Building Code Requirements for Structural Concrete (ACI 318-19) and Commentary (ACI 318R-19) (Reapproved 2022)," American Concrete Institute, Farmington Hills, MI, 2019, 624 pp.

6. Parra, P. F., and Moehle, J. P., "Effects of Strain Gradients in the Onset of Global Buckling in Slender Walls Due to Earthquake Loading," *Bulletin of Earthquake Engineering*, V. 18, No. 7, 2020, pp. 3205-3221. doi: 10.1007/s10518-020-00821-3

7. Zhou, Y.; Zheng, S.; Chen, L.; Long, L.; and Wang, B., "Experimental Investigation into the Seismic Behavior of Squat Reinforced Concrete Walls Subjected to Acid Rain Erosion," *Journal of Building Engineering*, V. 44, 2021, p. 102899. doi: 10.1016/j.jobe.2021.102899

8. Shabana, I.; Farghaly, A. S.; and Benmokrane, B., "Effect of Axial Load and Web Reinforcement Ratio on Seismic Behavior of Glass Fiber-Reinforced Polymer-Reinforced Concrete Squat Walls," *ACI Structural Journal*, V. 118, No. 4, July 2021, pp. 109-121.

9. Hosseini, S. M.; Yekrangnia, M.; and Vatani Oskouei, A., "Effect of Spiral Transverse Bars on Structural Behavior of Concrete Shear Walls Reinforced with GFRP Bars," *Journal of Building Engineering*, V. 55, 2022, p. 104706. doi: 10.1016/j.jobe.2022.104706

10. Nanni, A.; De Luca, A.; and Zadeh, H. J., *Reinforced Concrete with FRP Bars: Mechanics and Design*, CRC Press, Boca Raton, FL, 2014.

11. ACI Committee 440, "Building Code Requirements for Structural Concrete Reinforced with Glass Fiber-Reinforced Polymer (GFRP) Bars—Code and Commentary (ACI CODE-440.11-22)," American Concrete Institute, Farmington Hills, MI, 2022, 260 pp.

12. ACI Committee 440, "Guide for the Design and Construction of Structural Concrete Reinforced with Fiber-Reinforced Polymer (FRP) Bars (ACI 440.1R-15)," American Concrete Institute, Farmington Hills, MI, 2015, 88 pp.

13. Belay, A., and Wondimu, T., "Seismic Performance Evaluation of Steel and GFRP Reinforced Concrete Shear Walls at High Temperature," *Journal of Engineering and Applied Sciences (Asian Research Publishing Network)*, V. 70, 2023, p. 4

14. Mohamed, N.; Farghaly, A. S.; Benmokrane, B.; and Neale, K. W., "Flexure and Shear Deformation of GFRP-Reinforced Shear Walls," *Journal of Composites for Construction*, ASCE, V. 18, No. 2, 2014, p. 04013044. doi: 10.1061/(ASCE)CC.1943-5614.0000444

15. Ghazizadeh, S., and Cruz-Noguez, C. A., "Damage-Resistant Reinforced Concrete Low-Rise Walls with Hybrid GFRP-Steel Reinforcement and Steel Fibers," *Journal of Composites for Construction*, ASCE, V. 22, No. 2, 2018, p. 04018002. doi: 10.1061/(ASCE)CC.1943-5614.0000834

16. Shabana, I.; Farghaly, A. S.; and Benmokrane, B., "Earthquake Response of GFRP-Reinforced Concrete Squat Walls with Aspect Ratio of 1.14 and 0.68," *Engineering Structures*, V. 252, 2022, p. 113556. doi: 10.1016/j.engstruct.2021.113556

17. Deger, Z. T., and Basdogan, C., "Empirical Expressions for Deformation Capacity of Reinforced Concrete Structural Walls," *ACI Structural Journal*, V. 116, No. 6, Nov. 2019, pp. 53-61. doi: 10.14359/51716806

18. Siam, A.; Ezzeldin, M.; and El-Dakhakhni, W., "Machine Learning Algorithms for Structural Performance Classifications and Predictions: Application to Reinforced Masonry Shear Walls," *Structures*, V. 22, 2019, pp. 252-265. doi: 10.1016/j.istruc.2019.06.017

19. Arafa, A.; Farghaly, A. S.; and Benmokrane, B., "Effect of Web Reinforcement on the Seismic Response of Concrete Squat Walls Reinforced with Glass-FRP Bars," *Engineering Structures*, V. 174, 2018, pp. 712-723. doi: 10.1016/j.engstruct.2018.07.092

20. Arafa, A.; Farghaly, A. S.; and Benmokrane, B., "Experimental Behavior of GFRP-Reinforced Concrete Squat Walls Subjected to Simulated Earthquake Load," *Journal of Composites for Construction*, ASCE, V. 22, No. 2, 2018, p. 04018003. doi: 10.1061/(ASCE)CC.1943-5614.0000836

21. Architectural Institute of Japan, "Load-Deflection Characteristics of Nuclear Reactor Building Structures: Parts 8-9-10," *Summaries of Technical Papers, Structural Division*, V. 58, 1985. (in Japanese)

22. AIJ, "Load-Deflection Characteristics of Nuclear Reactor Building Structures: Parts 37-38-39-40," *Summaries of Technical Papers of Annual Meeting, B, Structures I*, Architectural Institute of Japan, Tokyo, Japan, 1985. (in Japanese)

23. Architectural Institute of Japan, "Load-Deflection Characteristics of Nuclear Reactor Building Structures: Parts 21-22," *Summaries of Technical Papers, Structural Division*, V. 59, 1986. (in Japanese)

24. AIJ, 1986b. "Load-Deflection Characteristics of Nuclear Reactor Building Structures: Parts 59-60-61," *Summaries of Technical Papers of Annual Meeting, B, Structures I*, Architectural Institute of Japan, Tokyo, Japan, 1986. (in Japanese)

25. AIJ, "Load-Deflection Characteristics of Nuclear Reactor Building Structures: Parts 62-63," *Summaries of Technical Papers of Annual Meeting, B, Structures I*, Architectural Institute of Japan, Tokyo, Japan, 1986. (in Japanese)

26. Antebi, J.; Utku, S.; and Hansen, R. J., "The Response of Shear Walls to Dynamic Loads," Massachusetts Institute of Technology, Cambridge, MA, 1960.

27. Bouchon, M.; Orbovic, N.; and Foure, N., "Tests on Reinforced Concrete Low-Rise Shear Walls under Static Cyclic Loading," *Proceedings of the Thirteenth World Conference on Earthquake Engineering*, Vancouver, BC, Canada, 2004, pp. 1-10.

28. Gao, X., "Framed Shear Walls under Cyclic Loading," PhD dissertation, University of Houston, Houston, TX, 1999.

29. Hidalgo, P. A.; Jordan, R. M.; and Martinez, M. P., "An Analytical Model to Predict the Inelastic Seismic Behavior of Shear Wall, Reinforced Concrete Structures," *Engineering Structures*, V. 24, No. 1, 2002, pp. 85-98. doi: 10.1016/S0141-0296(01)00061-X

30. Hirosawa, M., "Past Experimental Results on Reinforced Concrete Shear Walls and Analysis on Them," Building Research Institute, Ministry of Construction, Tokyo, Japan, 1975, 277 pp. (in Japanese)

31. Kabeyasawa, T., and Somaki, T., "Reinforcement Details for Reinforced Concrete Shear Walls with Thick Panel," *Transactions of the Japan Concrete Institute*, V. 7, 1985, pp. 369-372. (in Japanese)

32. Kim, J.-H., and Park, H.-G., "Shear and Shear-Friction Strengths of Squat Walls with Flanges," *ACI Structural Journal*, V. 117, No. 6, Nov. 2020, pp. 269-280. doi: 10.14359/51728075

33. Kim, S.-H., and Park, H.-G., "Shear Strength of Reinforced Concrete Wall with 700 MPa Shear Reinforcement," *ACI Structural Journal*, V. 118, No. 2, Mar. 2021, pp. 167-181.

34. Kim, J.-H., and Park, H.-G., "Shear Strength of Flanged Squat Walls with 690 MPa Reinforcing Bars," *ACI Structural Journal*, V. 119, No. 2, Mar. 2022, pp. 209-220.

35. Liu, X.; Burgueno, R.; Egleston, E.; and Hines, E. M., "Inelastic Web Crushing Performance Limits of High-Strength-Concrete Structural Wall-Single Wall Test Program," Report No. CEE-RR-2009/03, Michigan State University, East Lansing, MI, 2009.

36. Luna, B. N.; Rivera, J. P.; and Whittaker, A. S., "Seismic Behavior of Low-Aspect Ratio Reinforced Concrete Shear Walls," *ACI Structural Journal*, V. 112, No. 5, Sept.-Oct. 2015, pp. 593-604. doi: 10.14359/51687709

37. Maier, J., and Thurlimann, B., 1985, "Bruchversuche an stahlbetonscheiben," Institut für Baustatik und Konstruktion, Eidgenössische Technische Hochschule (ETH) Zürich, Switzerland, 130 pp. (in German)

38. Massone, L. M.; Orakcal, K.; and Wallace, J. W., "Modeling of Squat Structural Walls Controlled by Shear," *ACI Structural Journal*, V. 106, No. 5, Sept.-Oct. 2009, pp. 646-655.

39. Mo, Y. L., and Chan, J., "Behavior of Reinforced-Concrete Framed Shear Walls," *Nuclear Engineering and Design*, V. 166, No. 1, 1996, pp. 55-68. doi: 10.1016/0029-5493(96)01244-7

40. Mohammadi-Doostdar, H., "Behavior and Design of Earthquake Resistant Low-Rise Shear Walls," University of Ottawa, Ottawa, ON, Canada, 1994.

41. Oesterle, R. G.; Aristizabal-Ochoa, J. D.; Fiorato, A. E.; Russell, H. G.; and Corely, W. G., 1979, "Earthquake Resistant Structural Walls-Tests of Isolated Walls-Phase II," Construction Technology Laboratories, Portland Cement Association, Skokie, IL.

42. Ogata, K., and Kabeyasawa, T., "Experimental Study on the Hysteretic Behavior of Reinforced Concrete Shear Walls under the Loading of Different Moment-to-Shear Ratios," *Transactions of the Japan Concrete Institute*, V. 6, 1984, pp. 717-724.

43. Park, H.-G.; Baek, J.-W.; Lee, J.-H.; and Shin, H.-M., "Cyclic Loading Tests for Shear Strength of Low-Rise Reinforced Concrete Walls with Grade 550 MPa Bars," *ACI Structural Journal*, V. 112, No. 3, May-June 2015, pp. 299-310. doi: 10.14359/51687406

44. Pilette, F. C., "Behavior of Earthquake Resistant Squat Shear Walls," MS thesis, University of Ottawa, Ottawa, ON, Canada, 1987.

45. Rothe, D., "Untersuchugen zum nichtlinearen Verhalten von stahlbeton wandschieben unter erdebenbeanspruchung," PhD dissertation, Fachbereich Konstruktiver Ingenieurbau, der Technischen Hochschule Darmstadt, Darmstadt, Germany, 1992, 161 pp. (in German)

46. Saito, H.; Kikuchi, R.; Kanechika, M.; and Okamoto, K., "Experimental Study on the Effect of Concrete Strength on Shear Wall Behavior," *Proceedings of the Tenth International Conference on Structural Mechanics in Reactor Technology*, Anaheim, CA, 1989.

47. Salonikios, T. N.; Kappos, A. J.; Tegos, I. A.; and Penelis, G. G., "Cyclic Load Behavior of Low-Slenderness Reinforced Concrete Walls: Design Basis and Test Results," *ACI Structural Journal*, V. 96, No. 4, July-Aug. 1999, pp. 649-660.

48. Sato, S.; Ogata, Y.; Yoshizaki, S.; Kanata, K.; Yamaguchi, T.; Nakayama, T.; Inada, Y.; and Kadoriku, J., "Behavior of Shear Wall Using Various Yield Strength of Reinforcing Bar, Part 1: An Experimental Study," *Proceedings of the Tenth International Conference on Structural Mechanics in Reactor Technology*, Anaheim, CA, 1989.

49. Seki, M.; Kobayashi, J.; Shibata, A.; Kubo, T.; Taira, T.; and Akino, K., "Restoring Force Verification Test on RC Shear Wall," *Proceedings of the Thirteenth International Conference on Structural Mechanics in Reactor Technology*, Porto Alegre, Brazil, 1995.

50. Synge, A. J., "Ductility of Squat Shear Walls," Report No. 80-8, University of Canterbury, Christchurch, New Zealand, 1980.

51. Teng, S., and Chandra, J., "Cyclic Shear Behavior of High Strength Concrete Structural Walls," *ACI Structural Journal*, V. 113, No. 6, Nov.-Dec. 2016, pp. 1335-1345. doi: 10.14359/51689158

52. Vecchio, F. J.; Collins, M. P.; and Aspiotis, J., "High-Strength Concrete Elements Subjected to Shear," *ACI Structural Journal*, V. 91, No. 4, July-Aug. 1994, pp. 423-433.

53. Vecchio, F. J., and Collins, M. P., "The Modified Compression Field Theory for Reinforced Concrete Elements Subjected to Shear," *ACI Journal Proceedings*, V. 83, No. 2, Mar.-Apr. 1986, pp. 219-231.

54. Bischoff, P. H., and Paixao, R., "Tension Stiffening and Cracking of Concrete Reinforced with Glass Fiber Reinforced Polymer (GFRP) Bars," *Canadian Journal of Civil Engineering*, V. 31, No. 4, 2004, pp. 579-588. doi: 10.1139/l04-025

55. Miglietta, P. C.; Grasselli, G.; and Bentz, E. C., "Finite/Discrete Element Model of Tension Stiffening in GFRP Reinforced Concrete," *Engineering Structures*, V. 111, 2016, pp. 494-504. doi: 10.1016/j.engstruct.2015.12.037

56. Kharal, Z., and Sheikh, S., "Tension Stiffening and Cracking Behavior of Glass Fiber- Reinforced Polymer-Reinforced Concrete," *ACI Structural Journal*, V. 114, No. 2, Mar.-Apr. 2017, pp. 299-310. doi: 10.14359/51689420

57. Razaqpur, A. G.; Svecova, D.; and Cheung, M. S., "Rational Method for Calculating Deflection of Fiber-Reinforced Polymer Reinforced Beams," *ACI Structural Journal*, V. 97, No. 1, Jan.-Feb. 2000, pp. 175-183.

58. ACI Committee 374, "Guide for Testing Reinforced Concrete Structural Elements under Slowly Applied Simulated Seismic Loads (ACI 374.2R-13)," American Concrete Institute, Farmington Hills, MI, 2013, 18 pp.

59. Moehle, J., *Seismic Design of Reinforced Concrete Buildings*, McGraw-Hill Education, New York, 2015.

60. Collins, M. P.; Mitchell, D.; Adebar, P.; and Vecchio, F. J., "A General Shear Design Method," *ACI Structural Journal*, V. 93, No. 1, Jan.-Feb. 1996, pp. 36-45.

61. Rafi, M. M.; Nadjai, A.; and Ali, F., "Analytical Modeling of Concrete Beams Reinforced with Carbon FRP Bars," *Journal of Composite Materials*, V. 41, No. 22, 2007, pp. 2675-2690. doi: 10.1177/0021998307078728

62. Wight, J. K., *Reinforced Concrete: Mechanics and Design*, Pearson, Hoboken, NJ, 2015.

63. Nagasaka, T.; Fukuyama, H.; and Tanigaki, M., "Shear Performance of Concrete Beams Reinforced with FRP Stirrups," *Fiber-Reinforced-Plastic Reinforcement for Concrete Structures*, SP-138, American Concrete Institute, Farmington Hills, MI, 1993, pp. 789-811.

64. Hassanein, A.; Mohamed, N.; Farghaly, A. S.; and Benmokrane, B., "Modeling of Hysteretic Response for Concrete Shear Walls Reinforced with Glass Fiber-Reinforced Polymer Bars," *ACI Structural Journal*, V. 116, No. 6, Nov. 2019, pp. 17-29. doi: 10.14359/51716798

65. Mohamed, N.; Farghaly, A. S.; Benmokrane, B.; and Neale, K. W., "Experimental Investigation of Concrete Shear Walls Reinforced with Glass Fiber–Reinforced Bars under Lateral Cyclic Loading," *Journal of Composites for Construction*, ASCE, V. 18, No. 3, 2014, p. A4014001. doi: 10.1061/(ASCE)CC.1943-5614.0000393

CALL FOR ACTION

ACI Invites You To...

Share your expertise

Do you have EXPERTISE in any of these areas?

- BIM
- Chimneys
- Circular Concrete Structures Prestressed by Wrapping with Wire and Strand
- Circular Concrete Structures Prestressed with Circumferential Tendons
- Concrete Properties
- Demolition
- Deterioration of Concrete in Hydraulic Structures
- Electronic Data Exchange
- Insulating Concrete Forms, Design, and Construction
- Nuclear Reactors, Concrete Components
- Pedestal Water Towers
- Pipe, Cast-in-Place
- Strengthening of Concrete Members
- Sustainability

Then become a REVIEWER for the *ACI Structural Journal* or the *ACI Materials Journal*.

Become a Reviewer for the ACI Journals

How to become a Reviewer:

1. Go to: **http://mc.manuscriptcentral.com/aci**;
2. Click on "Create Account" in the upper right-hand corner; and
3. Enter your E-mail/Name, Address, User ID and Password, and Area(s) of Expertise.

Update your Manuscript Central user account information

Did you know that the database for MANUSCRIPT CENTRAL, our manuscript submission program, is separate from the ACI membership database?

How to update your user account:

1. Go to **http://mc.manuscriptcentral.com/aci**;
2. Log in with your current User ID & Password; and
3. Update your E-mail/Name, Address, User ID and Password, and Area(s) of Expertise.

QUESTIONS?

E-mail any questions to Journals.Manuscripts@concrete.org.

American Concrete Institute

Always advancing

ACI STRUCTURAL JOURNAL TECHNICAL PAPER

Title No. 121-S44

Reliability-Based Code Development for Carbon Fiber-Reinforced Polymer-Strengthened Circular Reinforced Concrete Columns

by Juscelina Rosiane Ferreira, Peterson Araújo Quadros, and Sofia Maria Carrato Diniz

Concrete confinement using fiber-reinforced polymers (FRPs) has been vastly used for strengthening of reinforced concrete (RC) columns. The strengthening of RC columns belongs to the realm of existing structures, which has been recognized as distinct from the design of new structures. Code development efforts for the strengthening of RC columns should follow a reliability-based framework similar to the one used in the code development for new structures. In this process, a number of additional issues arise: the mechanical model of FRP confinement representing existing RC columns, the statistical description of the design variables, and the target reliability to be attained. In this study, the reliability levels of 288 axially loaded, FRP-RC short columns of circular cross sections, strengthened according to ACI 440 guidelines, are assessed. Monte Carlo simulation is used in the probabilistic description of column strength and computation of the probability of failure. An FRP confinement model that explicitly accounts for the presence of transversal steel and attendant model errors associated to the estimation of ultimate stress and ultimate strain are used in the computation of the FRP-RC column capacity. The values of the reliability index are in the range of 3.92 to 4.61, satisfying the target reliability suggested for both new and existing structures. The research findings presented herein provide further support for the efforts of ACI Committee 440 in the development of standards related to the FRP strengthening of RC columns.

Keywords: carbon fiber-reinforced polymer (CFRP) confinement; circular cross sections; design codes; existing structures; reinforced concrete (RC); reliability index; short columns; strengthening.

INTRODUCTION

All over the world, it has been recognized that the problem of strengthening of existing structures is of paramount importance. For instance, according to the 2021 ASCE Report Card for America's Infrastructure (ASCE 2021), "42% of all bridges are at least 50 years old, and 46,154, or 7.5% of the nation's bridges, are considered structurally deficient." As a result, different techniques for the strengthening of structural elements have been investigated and used in practice; among them, strengthening of reinforced concrete (RC) columns by concrete confinement using fiber-reinforced polymers (FRP) has been largely used.

Research on concrete confinement as a means to increase concrete strength and ductility dates back to the 1920s. Following those initial steps, concrete confinement was used with steel as the confining media (Saatcioglu and Razvi 1992; Diniz and Frangopol 1997b). Extensive research on FRP confinement efficiency has demonstrated that the use of composites as confining media, particularly carbon FRP (CFRP), can further improve concrete strength gains and consequently RC column capacity, thus making FRP confinement an efficient technique for the strengthening of RC columns.

The efficiency of concrete confinement, as compared to concrete confined by steel spirals/hoops, may be largely increased by using a technique that creates an almost uniform lateral pressure by a high-strength material such as FRP. Regarding FRP types, CFRP and glass FRP (GFRP) have been considered for the confinement of RC columns; however, construction, durability, and long-term performance favor the use of CFRP over GFRP in practical applications (ACI Committee 440 2017; Micelli and Modarelli 2013). Concrete confinement is most efficient in the absence of a strain gradient in the column cross section—that is, in the case of axially loaded columns. Consequently, most of the literature on FRP-RC columns has been dedicated to such condition (Ferreira et al. 2018). Regarding cross-sectional geometry, it has been largely recognized that the confinement mechanisms in circular and square (or rectangular) cross sections present significant differences. In the case of circular cross sections, confinement by continuous FRP wrapping introduces a uniform lateral pressure, thus allowing considerable increase in column strength and ductility (if adequate confinement is provided). For square (or rectangular) cross sections, FRP confinement is less effective than for circular sections due to the presence of unconfined regions far from the corners (Micelli and Modarelli 2013). In this light, use of CFRP for the confinement of concrete is most effective in the strengthening of axially loaded, circular RC columns.

For design purposes, an adequate estimation of the axial load capacity of an FRP-strengthened RC column is required. To this end, a distinction shall be made between FRP-wrapped plain concrete cylinders (herein denoted as FRP-confined concrete [FRP-CC]) and FRP-strengthened RC columns (FRP-RC columns). In FRP-CC, a uniform lateral pressure acts along the length of the cylinder, thus representing ideal conditions for confinement efficiency. In the case of existing RC columns of circular cross sections,

ACI Structural Journal, V. 121, No. 3, May 2024.
MS No. S-2023-175.R2, doi: 10.14359/51740490, received December 20, 2023, and reviewed under Institute publication policies.

the interaction between the FRP jacket and the steel cage (transversal and longitudinal steel) may be either beneficial or detrimental. The presence of transversal and longitudinal reinforcements disturbs the uniform lateral pressure created by the FRP confinement (Ferreira and Diniz 2018). On the other hand, FRP confinement in RC columns provides additional restraining for longitudinal steel bars, postponing buckling especially for large spacings between steel hoops/spirals. However, if stiffness of the external FRP jacketing is not enough to counteract buckling of longitudinal steel bars, stress concentrations in the FRP can occur, causing its premature failure and a reduction in efficiency of the FRP confinement (Pellegrino and Modena 2010).

The importance of accounting for the existing lateral steel reinforcement in the estimation of the total confinement effects on the strength and ductility of FRP-RC columns has been recognized in some studies (Eid and Paultre 2008; Wang et al. 2012). The existing transversal steel, in isolation, may not be sufficient to develop the required strength and ductility levels; nevertheless, it is the joint behavior of two confining materials (FRP and steel) that shall be addressed. Failure to account for the FRP-steel interaction may result in costly repairs or even demolition (Ferreira and Diniz 2018).

A number of models have been proposed for circular FRP-CC; for instance, Ozbakkaloglu et al. (2013) reported 88 models for FRP-confined concrete. On the other hand, few models have been suggested for FRP-RC columns (Chastre and Silva 2010; Eid and Paultre 2008; Lee et al. 2010; Pellegrino and Modena 2010; Shirmohammadi et al. 2015).

In this study, Monte Carlo simulation (Ang and Tang 1984) is used in the reliability assessment of FRP-RC short circular columns under axial loading. Two hundred eighty-eight CFRP-RC columns, strengthened according to ACI 440.2R-17, for the ultimate limit state of axial compression are selected. An FRP-confinement model that explicitly accounts for the transversal steel (Ferreira and Diniz 2018) is used in the computation of the FRP-RC column capacity. The attendant statistical description of the model errors associated to the estimation of ultimate stress, ξ_f, and ultimate strain, ξ_ε, are used. The probability distributions of the basic random variables involved in the problem are summarized, and a rigorous numerical procedure for the computation of the column resistance is implemented. The influences of the variables live-to-dead load ratio, column diameter, unconfined concrete compressive strength, longitudinal steel ratio, confinement level of transversal steel, and FRP confinement level on the reliability of CFRP-RC columns are also evaluated.

RESEARCH SIGNIFICANCE

The use of relatively new materials, assessment of existing structures, and use of strengthening and repair techniques have been major developments in current code development initiatives. This is clearly seen in different initiatives around the globe, such as the development of the "Repair Code" (ACI Committee 562 2016), the publication of ACI CODE-440.11-22 (ACI Committee 440 2022), the revision of the *fib* Model Code (*fib* 2020), and the revision of ISO 19338 (2014). Furthermore, the implementation of reliability methods for the design of new structures and the assessment of existing structures has gained widespread acceptance (Ghosn et al. 2016). The problem of FRP strengthening of existing RC columns incorporates all these issues and their corresponding challenges, thus granting a careful consideration of the code development in this area.

A number of the variables involved in FRP-RC column resistance and column loading are uncertain; consequently, the reliability of circular FRP-RC columns can be established only in probabilistic terms. To this end, structural reliability methods (Ang and Tang 1984) are needed in the definition of the implicit safety levels in a given design recommendation. This is a basic requirement in code calibration procedures in current semi-probabilistic code formats (Diniz 2008). Moreover, the FRP strengthening of RC columns belongs to the realm of existing structures, which has been recognized as distinct from the design of new structures. In this light, a number of issues arise in code development for the strengthening of RC columns.

First, code development for the strengthening of RC columns should follow a reliability-based framework similar to the one used for new structures. While such a framework is well documented for ACI 318 (Nowak and Szerszen 2003; Szerszen and Nowak 2003), important information is lacking in the case of ACI 440.2R-17. For instance, in ACI 440.2R-17, it is mentioned that "FRP-related reduction factors were calibrated to produce reliability indexes typically above 3.5." Nevertheless, no reference is made to a research that would support such a claim. Additionally, considering the broad scope of ACI 440.2R-17 as related to strengthening of beams and columns, it is not clear if 3.5 is the assumed target reliability index for FRP-RC columns.

Second, for the scrutiny of the guidelines in ACI 440.2R-17 and verification of alignment with other international documents, a clear presentation of the assumptions and methods used in the reliability analysis process is needed. While the FRP confinement model used in the development of the guidelines is presented in ACI 440.2R-17, other important information (statistical description of the basic variables, the range of variables considered, and the structural reliability method used in the analysis) is missing.

Third, as previously mentioned, the joint behavior of transversal steel/FRP as occurs in the strengthening of existing RC columns may be either detrimental or beneficial. However, the FRP confinement model used in ACI 440.2R-17 does not account for such interaction and this may impact the safety levels resulting in the corresponding reliability assessment.

Fourth, few studies have addressed the reliability evaluation of FRP-RC columns (Val 2003; Zou and Hong 2011; Casas and Chambi 2014; Wang and Ellingwood 2015; Baji 2017). Nevertheless, no explicit consideration has been made with respect to the effects of the amount of transversal steel and the joint behavior of steel/FRP as confining media on FRP-RC column performance.

Fifth, the statistical description of the basic variables shall include both inherent and epistemic uncertainties. For instance, Wang and Ellingwood (2015) observed that the variability of the FRP ultimate strength is highly dependent on the degree of quality control in the application process.

Regarding epistemic uncertainties, their statistical descriptions are highly dependent on the quality of the database used in the assessment of a given model and may have a significant impact on the resulting reliability levels (Ribeiro et al. 2016; Ferreira and Diniz 2018).

Sixth, in semi-probabilistic code formats, the target reliability index is satisfied in an average sense. In this way, it is important to recognize those conditions that would result in safety levels much lower or much higher than the target value. In the former case, this would translate in less-than-expected safety levels, and in the latter, more expensive repairs (and potential significant impacts on economic activities or demolition).

All the aforementioned issues are dealt with in the research presented herein. A rigorous reliability-based framework is used in the treatment of the FRP strengthening of RC columns and the attendant code development issues.

DESIGN OF FRP-CONFINED RC COLUMNS BY ACI 440

According to ACI 440.2R-17, the nominal axial compressive strength, P_n, of a nonslender FRP-confined RC column is given by Eq. (1) and (2), for members with existing steel spirals and stirrups, respectively

$$\phi P_n = 0.85\phi[0.85f_{cc}(A_g - A_{sL}) + f_{yL}A_{sL}] \quad (1)$$

$$\phi P_n = 0.80\phi[0.85f_{cc}(A_g - A_{sL}) + f_{yL}A_{sL}] \quad (2)$$

where ϕ is the strength reduction factor (0.75 for spirals and 0.65 for ties); f_{cc} is the ultimate compressive stress of confined concrete; A_g is the gross area of concrete section; A_{sL} is the total area of longitudinal steel reinforcement; and f_{yL} is the specified yield strength of longitudinal steel reinforcement.

The ultimate stress of confined concrete, f_{cc}, is calculated by

$$f_{cc} = f_c' + 3.3\psi_f\kappa_a f_{lF} \quad (3)$$

where f_c' is the unconfined cylinder compressive strength of concrete; ψ_f is an additional reduction factor, taken as 0.95; κ_a is the geometry efficiency factor (equal to 1.0 for circular sections); and f_{lF} is the lateral confining pressure provided by the FRP.

The pressure f_{lF} is obtained by the balance of forces in the cross section; it is a function of the column diameter D, number of layers of FRP n, thickness of each layer t, FRP confinement efficiency coefficient k_F (taken as 0.55), and ultimate tensile stress in the FRP jacket f_F

$$f_{lF} = \frac{2nt\,k_F}{D}f_F \quad (4)$$

FRP ultimate tensile stress is the strength given by the manufacturer, f_F^*, reduced by an environmental reduction factor C_E, which depends on the fiber type (carbon, aramid, or glass) and exposure condition. For CFRP, the values of the environmental reduction factor C_E are 0.95, 0.85, and 0.85 for interior, exterior, or aggressive environment conditions, respectively.

DETAILS OF SELECTED COLUMNS

Two hundred eighty-eight axially loaded, short circular CFRP-RC columns were selected for analysis, corresponding to 48 cross sections, subject to three different dead-to-live load ratios, in two sets of spirals and tied RC columns. It is assumed that these columns were initially designed according to ACI 318-14 (ACI Committee 318 2014), and due to further increases in loading conditions, they were strengthened according to ACI 440.2-17. All columns have concrete cover c equal to 40 mm and carbon fiber thickness t equal to 0.128 mm. Further details of the column cross sections are presented in Table 1.

Each cross section is identified by a group of five letters and numbers. The first group is related to the column diameter, where D1 corresponds to 300 mm and D2 to 400 mm. The second group stands for the unconfined concrete compressive strength f_c'. In this notation, F1 and F2 correspond to 20 and 35 MPa, respectively. Lower-strength concretes were considered because they are representative of columns requiring strengthening measures. Additionally, there is ample evidence that confinement strengthening is more effective for lower strength concretes (Diniz and Frangopol 1997b; Saatcioglu and Razvi 1992). The third group is related to the longitudinal steel ratio, with L1 and L2 corresponding to 1% and 2%, respectively. The fourth group is related to the confinement index of transversal steel, $I_{se} = k_s f_{ls}/f_c'$, with T1, T2, and T3, corresponding to low ($0 < I_{se} < 0.05$), medium ($0.05 < I_{se} < 0.20$), and high confinement ($I_{se} > 0.20$), respectively, according to Cusson and Paultre (1995). The fifth group is related to the CFRP confinement index, $I_{Fe} = k_F f_{lFe}/f_c'$, with C1 and C2 representing low ($I_{Fe} = 0.08$) and high ($I_{Fe} = 0.16$) confinement, respectively. I_{Fe} equal to 0.08 is the minimum level of confinement required to assure a non-descending branch in the stress-strain curve (ACI 440.2-17). Transversal steel diameter and spacing, and FRP plies were calculated to attain the above target confinement indexes.

Following ACI 440.2-17, the effectiveness coefficient of FRP confinement, k_F, is taken as 0.55, and the coefficient of steel confinement, k_s, is obtained by Eq. (5) and (6) for hoops and spirals, respectively

$$k_s = \frac{\left(1 - \frac{s'}{2D_c}\right)^2}{1 - \rho_{cc}} \quad (5)$$

$$k_s = \frac{1 - \frac{s'}{2D_c}}{1 - \rho_{cc}} \quad (6)$$

where ρ_{cc} is the volumetric ratio of longitudinal reinforcement relative to the confined core; s' is the internal vertical spacing of spirals or stirrups; and D_c is the diameter of the confined concrete core.

The lateral confining pressure due to the action of transversal steel f_{ls} is a function of the diameter of the confined

Table 1—Details of selected column cross sections

Cross section							Transversal steel*						
No.	ID	D, mm	f_c', MPa	f_{cm}, MPa	Longitudinal steel*		No.	s, mm	ρ_{sw}, %	I_{se}†	n	ρ_F, %	I_{Fe}‡
1	D1F1L1T1C1	300	20	23.1	6	No. 4	No. 3	200	0.65	0.02	1	0.17	0.07
2	D1F1L1T1C2	300	20	23.1	6	No. 4	No. 3	200	0.65	0.04	2	0.34	0.14
3	D1F1L1T2C1	300	20	23.1	6	No. 4	No. 3	100	1.30	0.09	1	0.17	0.07
4	D1F1L1T2C2	300	20	23.1	6	No. 4	No. 3	100	1.30	0.11	2	0.34	0.14
5	D1F1L1T3C1	300	20	23.1	6	No. 4	No. 3	50	2.59	0.23	1	0.17	0.07
6	D1F1L1T3C2	300	20	23.1	6	No. 4	No. 3	50	2.59	0.25	2	0.34	0.14
7	D1F1L2T1C1	300	20	23.1	7	No. 5	No. 3	200	0.65	0.02	1	0.17	0.07
8	D1F1L2T1C2	300	20	23.1	7	No. 5	No. 3	200	0.65	0.04	2	0.34	0.14
9	D1F1L2T2C1	300	20	23.1	7	No. 5	No. 3	100	1.30	0.09	1	0.17	0.07
10	D1F1L2T2C2	300	20	23.1	7	No. 5	No. 3	100	1.30	0.11	2	0.34	0.14
11	D1F1L2T3C1	300	20	23.1	7	No. 5	No. 3	50	2.59	0.23	1	0.17	0.07
12	D1F1L2T3C2	300	20	23.1	7	No. 5	No. 3	50	2.59	0.26	2	0.34	0.14
13	D1F2L1T1C1	300	35	41.1	6	No. 4	No. 3	110	1.08	0.04	2	0.34	0.08
14	D1F2L1T1C2	300	35	41.1	6	No. 4	No. 3	110	1.08	0.05	4	0.68	0.16
15	D1F2L1T2C1	300	35	41.1	6	No. 4	No. 3	60	2.16	0.10	2	0.34	0.08
16	D1F2L1T2C2	300	35	41.1	6	No. 4	No. 3	60	2.16	0.12	4	0.68	0.16
17	D1F2L1T3C1	300	35	41.1	6	No. 4	No. 3	30	4.32	0.24	2	0.34	0.08
18	D1F2L1T3C2	300	35	41.1	6	No. 4	No. 3	30	4.32	0.25	4	0.68	0.16
19	D1F2L2T1C1	300	35	41.1	7	No. 5	No. 3	110	1.08	0.04	2	0.34	0.08
20	D1F2L2T1C2	300	35	41.1	7	No. 5	No. 3	110	1.08	0.05	4	0.68	0.16
21	D1F2L2T2C1	300	35	41.1	7	No. 5	No. 3	60	2.16	0.10	2	0.34	0.08
22	D1F2L2T2C2	300	35	41.1	7	No. 5	No. 3	60	2.16	0.12	4	0.68	0.16
23	D1F2L2T3C1	300	35	41.1	7	No. 5	No. 3	30	4.32	0.24	2	0.34	0.08
24	D1F2L2T3C2	300	35	41.1	7	No. 5	No. 3	30	4.32	0.25	4	0.68	0.16
25	D2F1L1T1C1	400	20	23.1	7	No. 5	No. 3	140	0.64	0.04	2	0.26	0.11
26	D2F1L1T1C2	400	20	23.1	7	No. 5	No. 3	140	0.64	0.05	3	0.38	0.16
27	D2F1L1T2C1	400	20	23.1	7	No. 5	No. 3	70	1.27	0.11	2	0.26	0.11
28	D2F1L1T2C2	400	20	23.1	7	No. 5	No. 3	70	1.27	0.12	3	0.38	0.16
29	D2F1L1T3C1	400	20	23.1	7	No. 5	No. 3	30	2.54	0.25	2	0.26	0.11
30	D2F1L1T3C2	400	20	23.1	7	No. 5	No. 3	30	2.54	0.26	3	0.38	0.16
31	D2F1L2T1C1	400	20	23.1	12	No. 5	No. 3	140	0.64	0.04	2	0.26	0.11
32	D2F1L2T1C2	400	20	23.1	12	No. 5	No. 3	140	0.64	0.06	3	0.38	0.16
33	D2F1L2T2C1	400	20	23.1	12	No. 5	No. 3	70	1.27	0.11	2	0.26	0.11
34	D2F1L2T2C2	400	20	23.1	12	No. 5	No. 3	70	1.27	0.13	3	0.38	0.16
35	D2F1L2T3C1	400	20	23.1	12	No. 5	No. 3	30	2.54	0.26	2	0.26	0.11
36	D2F1L2T3C2	400	20	23.1	12	No. 5	No. 3	30	2.54	0.27	3	0.38	0.16
37	D2F2L1T1C1	400	35	41.1	7	No. 5	No. 4	140	1.13	0.04	3	0.38	0.09
38	D2F2L1T1C2	400	35	41.1	7	No. 5	No. 4	140	1.13	0.06	5	0.64	0.15
39	D2F2L1T2C1	400	35	41.1	7	No. 5	No. 4	70	2.26	0.12	3	0.38	0.09
40	D2F2L1T2C2	400	35	41.1	7	No. 5	No. 4	70	2.26	0.13	5	0.64	0.15
41	D2F2L1T3C1	400	35	41.1	7	No. 5	No. 4	30	4.52	0.26	3	0.38	0.09
42	D2F2L1T3C2	400	35	41.1	7	No. 5	No. 4	30	4.52	0.27	5	0.64	0.15
43	D2F2L2T1C1	400	35	41.1	12	No. 5	No. 4	140	1.13	0.05	3	0.38	0.09

Table 1 (cont.)—Details of selected column cross sections

Cross section							Transversal steel*							
No.	ID	D, mm	f_c', MPa	f_{cm}, MPa	Longitudinal steel*		No.	s, mm	ρ_{sw}, %	I_{se}†	n	ρ_F, %	I_{Fe}‡
44	D2F2L2T1C2	400	35	41.1	12	No. 5	No. 4	140	1.13	0.06	5	0.64	0.15
45	D2F2L2T2C1	400	35	41.1	12	No. 5	No. 4	70	2.26	0.12	3	0.38	0.09
46	D2F2L2T2C2	400	35	41.1	12	No. 5	No. 4	70	2.26	0.13	5	0.64	0.15
47	D3F2L2T3C1	400	35	41.1	12	No. 5	No. 4	30	4.52	0.26	3	0.38	0.09
48	D4F2L2T3C2	400	35	41.1	12	No. 5	No. 4	30	4.52	0.27	5	0.64	0.15

*No. 3 = 9.525 mm; No. 4 = 12.7 mm; No. 5 = 15.875 mm.

†k_s is from Eq. (5) and (6).

‡k_F = 0.55.

core D_c, bar area $A_{s\phi}$, steel stress f_{sw} (assumed as the yield strength f_y), and the spacing of transversal steel s, given by

$$f_{ls} = \frac{2A_{s\phi}}{sD_c} f_{sw} \tag{7}$$

RELIABILITY BASES FOR FRP-RC COLUMNS

In this study, Monte Carlo simulation is used in the probabilistic description of column resistance and computation of probabilities of failure (and attendant reliability indexes) for the 288 CFRP-RC columns. To this end, a computational procedure, the program RACOL-FRP, was implemented in MATLAB software (Ferreira 2017). The computation of the CFRP-RC column strength uses the Lee et al. (2010) model for the calculation of the strength and deformability of CFRP-confined concrete. This model takes into account the confinement provided by both the transversal steel and the FRP jacket as occurs in actual FRP-RC columns. In Monte Carlo simulation, the following information is required: 1) the probability distributions of all random variables involved in the problem; and 2) the deterministic relationship for the computation of the quantities of interest—that is, column resistance and column probability of failure.

Statistical description of basic variables

So far, the most important application of FRP jacketing has been in the strengthening of existing RC columns. As pointed out by Melchers (2001), safety evaluation of existing structures is distinct from that related to safety implementation in the design of new ones. While design codes for new structures allow for uncertainties in the design and construction processes, much of what was initially uncertain no longer are in a finished structure. This would translate into the challenge of obtaining statistics that would describe material properties in the existing structure—for example, concrete compressive strength—as well as load statistics compatible with the revised design service life of the column. Additionally, such statistics, as well as the target reliability index (from the viewpoint of existing structures), are still open and controversial issues.

In this light, even though equivalent material properties have been suggested to be used in conjunction with deterministic safety checking (ACI Committee 562 2016; Bartlett and MacGregor 1995), the problem of the target reliability index to be used in the safety assessment of existing structures still remains. For instance, ISO 13822 (2010) suggests that lower target reliability levels for existing structures may be used if they can be justified on the basis of socio-economic criteria. Considering that a goal of the research reported herein is the evaluation of the efficiency of the strengthening process itself, this limitation may be circumvented by using a common basis of the design of new structures. As such, all the statistics reported herein are consistent with new structures.

In this study, the following variables are assumed as random: diameter of the column D; concrete cover c; unconfined concrete compressive strength f_c'; mechanical properties of steel (Young's modulus E_s, yield strength f_y, ultimate strength f_{su}, strain at the onset of the strain-hardening ε_{sh}, and ultimate strain ε_{su}); ultimate tensile strength of fibers in the FRP composite f_F; model errors associated with the ultimate stress of confined concrete ξ_f; and ultimate strain ξ_ε; dead load DL; and live load LL.

According to ACI 318, for $f_c' \leq 35$ MPa, the required average compressive strength, f_{cm}, is given by

$$f_{cm} = \frac{f_c'}{1 - 1.34\text{COV}} \tag{8}$$

where COV is coefficient of variation.

Regarding model errors, Ferreira and Diniz (2018) evaluated the performance of representative models addressing the behavior of circular CFRP-RC columns—that is, accounting for the joint behavior of FRP/transversal steel. Ultimate conditions were checked against a large experimental database comprising 151 CFRP-confined RC columns. A statistical analysis was performed to describe the random variables "model error" associated to ultimate stress ξ_f and ultimate strain ξ_ε. The Lee et al. (2010) model displays a bias close to unit and the smallest COV among the investigated models, for both ultimate stress and ultimate strain predictions. Table 2 summarizes the statistics of the random variables associated to the CFRP-RC column resistance.

Load effect statistics are obtained using the procedure described in Diniz and Frangopol (1997a) by assuming that design strength, R_d, exactly matches the design load, S_d

$$R_d = \phi P_n = S_d \tag{9}$$

Design strength ϕP_n of the CFRP-confined column is computed by the ACI 440.2-17 approach, using either Eq. (1) (spirals) or Eq. (2) (hoops), assuming that column characteristics (material properties, geometry, and so on) are

Table 2—Statistics of basic variables related to column resistance

Variable		Mean value	SD	COV	Distribution	Reference
Dimensions	Δ_D, mm	+1.52*	6.35	—	Normal	Mirza and MacGregor (1979a)
	Δ_C, mm	+8.13*	4.32	—	Normal	
Concrete compressive strength	f_{cs}' = 20 MPa	23.1	2.31	0.10	Lognormal	Diniz and Frangopol (1997a); Nowak and Szerszen (2003)
	f_{cs}' = 35 MPa	41.1	4.11	0.10	Lognormal	
Longitudinal steel properties	f_y = 420 MPa	489.3	24.47	0.05	Lognormal	Nowak and Szerszen (2003)
	f_{su}, MPa	714	59.3	0.083	Lognormal	Mirza and MacGregor (1979b)
	ε_{sh}	0.015	0.004	0.266	Normal	
	ε_{su}	0.15	0.03	0.20	Normal	
	E_s, GPa	200	6.6	0.033	Normal	
Transversal steel yield strength	f_y = 420 MPa	489.3	24.47	0.05	Lognormal	
CFRP fibers' tensile strength	f_F, MPa	3500	175	0.15	Weibull	Wang and Yang (2010)
Model errors	ξ_f	0.94	0.22	0.23	Normal	Ferreira and Diniz (2018)
	ξ_ε	0.77	0.41	0.54	Lognormal	

Table 3—Statistics of random variables associated with loads

Variable		Mean value	COV	Distribution	Reference
Dead load	F_{DL}, kN	Refer to Eq. (11)	0.10	Normal	Galambos et al. (1982)
Live load	F_{LL}, kN	Refer to Eq. (11)	0.25	Type I	

known *a priori*. It is considered that only dead and live loads act on the column (Diniz and Frangopol 1998)

$$S_d = 1.2F_{DL}^* + 1.6F_{LL}^* \quad (10)$$

where F_{DL}^* and F_{LL}^* are the nominal dead and live loads, respectively.

Galambos et al. (1982) suggested the values of 1.05 and 1.0 for the ratios of mean to nominal load μ_{DL}/F_{DL}^* and μ_{LL}/F_{LL}^*, respectively, thus resulting in

$$S_d = 1.143\mu_{DL} + 1.6\mu_{LL} \quad (11)$$

Mean values μ_{DL} and μ_{LL} can be easily found by computing the design load, S_d, corresponding to a given cross-section geometry and materials and assuming the dead-to-live load ratio $r = \mu_{DL}/\mu_{LL}$ (r = 0.5, 1.0, and 2.0 in this study). Statistics of dead and live loads (COV and type of distribution) are presented in Table 3. These statistics for live loads are consistent with a reference period of 50 years, commonly used in the design of new structures; however, in the case of existing structures, different reference periods may be required.

The following variables were assumed as deterministic: number of longitudinal bars n_L; diameter of longitudinal and transversal steel bars (ϕ_L and ϕ_w, respectively); transversal steel spacing s; FRP number of plies n; FRP elastic modulus E_F; and thickness of each FRP ply t.

Performance function

The safety of a structural component is ensured when its resistance R is sufficient to withstand the load effects S throughout its service life. The safety margin is given by $g(\boldsymbol{X}) = R - S$, where in the case of axially loaded CFRP-RC columns, R corresponds to the column resistance P_R, and S corresponds to the load effects—that is, the acting load, P_A. Considering that the acting load P_A is the sum of dead and live loads, $P_A = F_{DL} + F_{LL}$, then the performance function is given by

$$g(P_R, F_{DL}, F_{LL}) = P_R - F_{DL} - F_{LL} \quad (12)$$

The condition $g(P_R, F_{DL}, F_{LL}) = 0$ represents the limit state that separates the safe and failure regions. The resistance P_R of the confined column, in its turn, is obtained by

$$P_R = \alpha f_{cc\_up}(A_g - A_{sL}) + f_{sL}A_{sL} \quad (13)$$

where f_{cc_up} is the random variable corresponding to the compressive strength of the confined concrete, based on the Lee et al. model, corrected by the corresponding model errors; A_g is the random variable corresponding to the gross area of the cross section; A_{sL} is the total cross-sectional area of the longitudinal steel bars (deterministic); f_{sL} is the random variable corresponding to the stress in the steel longitudinal reinforcement, as given by the Park and Paulay (1975) stress-strain model; and α is a factor that takes into account the effects of accidental eccentricities, assumed as 0.85 (spirals) and 0.80 (hoops) for consistency with ACI 440.2R-17.

In Eq. (13), the random variables f_{cc_up} and f_{sL} are obtained by a strain-compatibility procedure described in the following section.

MONTE CARLO SIMULATION OF COLUMN RESISTANCE

Program RACOL-FRP contains a module for the simulation of 1,000,000 realizations of the column resistance for each of the 96 CFRP-RC selected column cross sections. This module uses the statistical description of the variables

related to column resistance (Table 2) and a strain-compatibility procedure for the computation of f_{cc_up} and f_{sL} in Eq. (13). To this end, the Lee et al. (2010) and Park and Paulay (1975) models are used for concrete confined strength and steel stress, respectively. The main features of the Lee et al. model are summarized as follows.

Lee et al. model

The stress-strain (f_c-ε_c) diagram proposed by Lee et al. (2010) is characterized by three branches. The first branch represents unconfined concrete behavior, ending at the point (f_c', ε_c'); the second accounts for the simultaneous confining effect of FRP and transversal steel, ending at (f_{cs}, ε_{cs}) which represents the yield strength of transversal steel; and in the third branch, the lateral pressure exerted by the transversal steel, f_{ls}, remains constant while the FRP lateral confining pressure, f_{lF}, increases up to the failure of the column represented by the ultimate conditions (f_{cc}, ε_{cc}). The three branches are given by

$$f_c = E_c\varepsilon_c + (f_c' - E_c\varepsilon_{c0})\left(\frac{\varepsilon_c}{\varepsilon_c'}\right)^2 \text{ for } 0 \le \varepsilon_c \le \varepsilon_c' \quad (14a)$$

$$f_c = f_c' + (f_{cs} - f_c')\left(\frac{\varepsilon_c - \varepsilon_c'}{\varepsilon_{cs} - \varepsilon_c'}\right)^{0.7} \text{ for } \varepsilon_c' \le \varepsilon_c \le \varepsilon_{cs} \quad (14b)$$

$$f_c = f_{cs} + (f_{cc} - f_{cs})\left(\frac{\varepsilon_c - \varepsilon_{cs}}{\varepsilon_{cc} - \varepsilon_{cs}}\right)^{0.7} \text{ for } \varepsilon_{cs} \le \varepsilon_c \le \varepsilon_{cc} \quad (14c)$$

where E_c is the elastic modulus of concrete, $E_c = 4700\sqrt{f_c'}$ (f_c' in MPa); f_c' and ε_c' are the axial compressive strength of unconfined concrete and the corresponding axial strain, respectively; and f_{cs} and ε_{cs} are the stress and strain corresponding to steel yielding, given by Eq. (15) and (16), respectively

$$\begin{aligned} f_{cs} &= 0.95 f_{cc} \quad \text{for } f_{lF} \ge f_{ls} \\ f_{cs} &= 0.867 f_{cc} \quad \text{for } f_{lF} < f_{ls} \end{aligned} \quad (15)$$

$$\begin{aligned} \varepsilon_{cs} &= \varepsilon_{cc}\left(0.85 + 0.03\frac{f_{lF}}{f_{ls}}\right) \quad \text{for } f_{lF} \ge f_{ls} \\ \varepsilon_{cs} &= 0.7\,\varepsilon_{cc} \quad \text{for } f_{lF} < f_{ls} \end{aligned} \quad (16)$$

where f_{cc} and ε_{cc} are the peak axial compressive stress of confined concrete and the corresponding axial strain, given by Eq. (17) and (18), respectively

$$f_{cc} = f_c' + 2(f_{ls} + f_{lF}) \quad (17)$$

$$\varepsilon_{cc} = \varepsilon_c'\left[1.75 + 5.25\left(\frac{k_s f_{ls} + f_{lF}}{f_c'}\right)\left(\frac{\varepsilon_F}{\varepsilon_c'}\right)^{0.45}\right] \quad (18)$$

where ε_F is the ultimate tensile strain in the FRP.

The effectiveness coefficient of transversal steel confinement k_s is given by

$$k_s = 2 - (f_{lF}/f_{ls}) \text{ for } f_{lF} \le f_{ls}; \text{ and } k_s = 1 \text{ for } f_{lF} > f_{ls} \quad (19)$$

Deterministic procedure for computation of column resistance

The deterministic procedure for the computation of column resistance is based on a strain-compatibility approach using Eq. (13) (refer to Fig. 1). It starts with the calculation of the ultimate conditions for the confined concrete (f_{cc} and ε_{cc}) according to the Lee et al. model; these values are then adjusted by the corresponding model errors (ξ_f and ξ_ε), resulting in f_{cc_A} and ε_{cc_A}. In the sequence, the strain compatibility between confined concrete and longitudinal steel is verified. If ε_{cc_A} is less than steel ultimate strain ε_{su}, the strain in the longitudinal steel is taken as the confined concrete strain ε_{cc_A}, and the corresponding steel stress value, f_{sL}, is updated from the corresponding stress-strain curve (Park and Paulay model). If ε_{cc_A} is larger than ε_{su}, steel stress f_{sL} is the ultimate stress f_{su}, concrete strain is taken as the ultimate steel strain ε_{su}, and the corresponding value of the stress of confined concrete is updated from the Lee et al. stress-strain curve. Finally, the updated compatible values for the confined concrete strength, f_{cc_up}, and for the stress in the longitudinal steel, f_{sL}, are then used in Eq. (13).

Statistics of column resistance

For each column, 1,000,000 realizations of the column resistance were simulated. The histogram corresponding to column series 32 with spirals (D2F1L2T1C2) (with a superimposed Normal distribution) is displayed in Fig. 2. Table 4 presents the mean, standard deviation (SD), and COV of the simulated column resistance, nominal resistance P_n, and ratios $\mu P_R/P_n$ for the CFRP-RC spiral columns. The nominal resistance, P_n, is calculated according to Eq. (1) (spirals) or Eq. (2) (hoops). The ratios $\mu P_R/P_n$ are displayed in graphical form in Fig. 3 as a function of the steel confinement level for different combinations of longitudinal steel ratios and FRP-confinement levels. From this figure, it is seen that the ratio $\mu P_R/P_n$ increases as the steel confinement level increases; for example, these ratios are 3.89, 4.27, and 5.03 for columns D1F1L1T1C1, D1F1L1T2C1, and D1F1L1T3C1, respectively. This effect is more pronounced for the combinations of lower longitudinal steel ratios (L1) and higher FRP-confinement level (C2). From the results shown in Table 4, it is observed that the ratios $\mu P_R/P_n$ are in the range of 3.61 to 5.29, demonstrating that, for all analyzed columns, the simulated mean resistance, μP_R, is much higher than the corresponding nominal resistance, P_n. Regarding the COV, it is reasonably high, in the range of 0.22 to 0.24.

RELIABILITY ANALYSIS

In this research, Monte Carlo simulation is used in the computation of probabilities of failure (and corresponding reliability indexes) of the 288 selected CFRP-RC columns. The results from this technique depend on the number of samples used, with increased accuracy as the sample size increases. The error can be calculated by Eq. (20) (Ang and Tang 1984), where P_F is the failure probability and n_s is the sample size (number of simulations used)

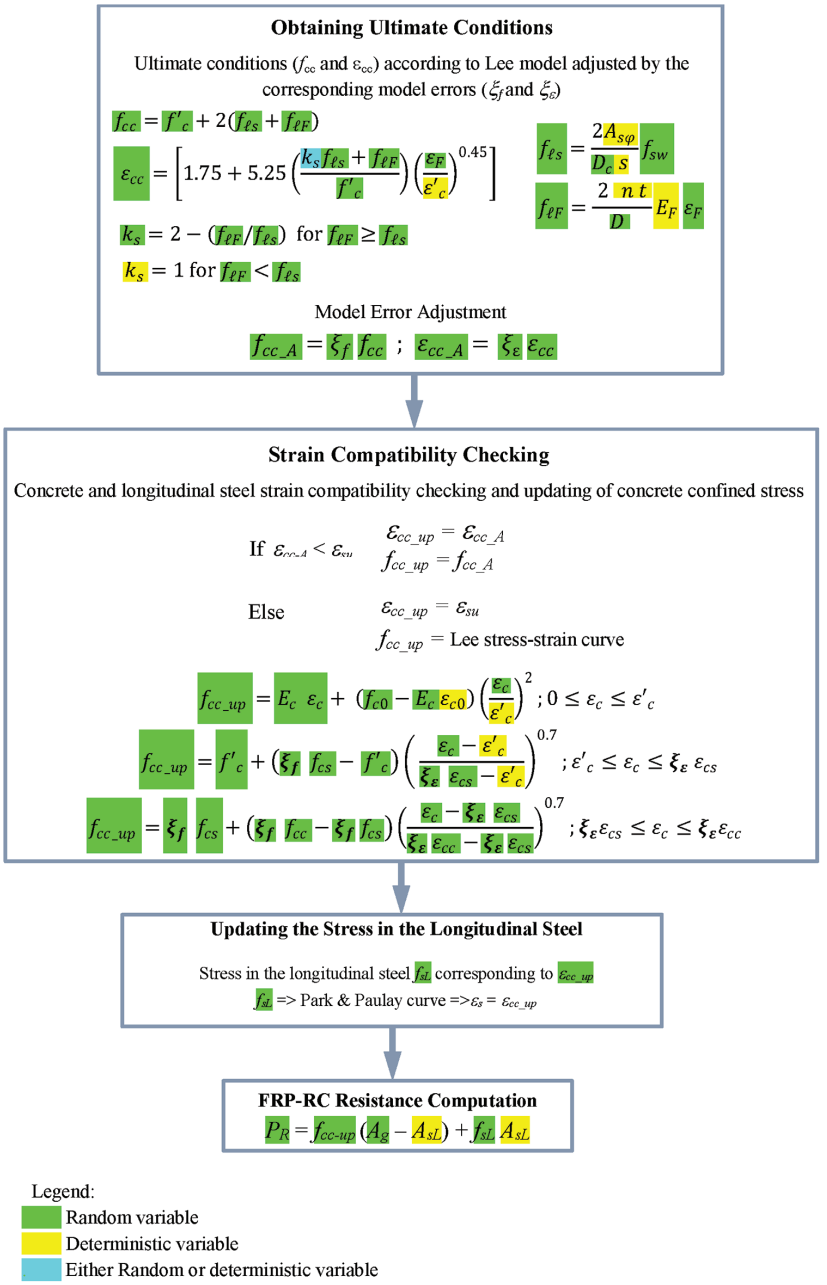

Fig. 1—Flowchart of deterministic procedure for computation of axial column resistance.

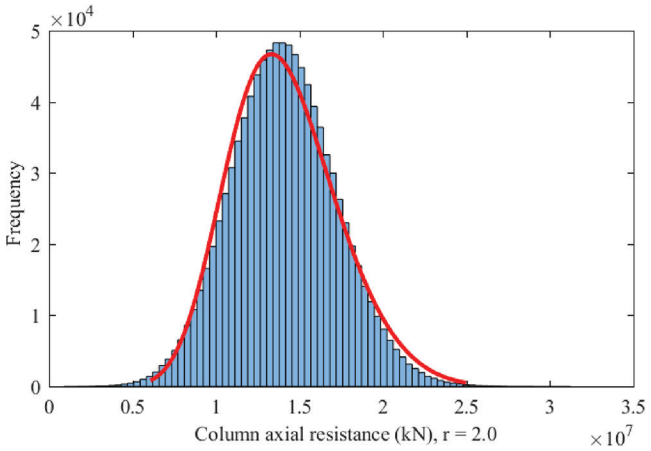

Fig. 2—Histogram of axial resistance P_R*, column series 32 with spirals (with superimposed Normal distribution).*

$$\% \text{ error} = 200\sqrt{\frac{1 - P_F}{n_s P_F}} \quad (20)$$

Szerszen and Nowak (2003) recommend a target reliability index of $\beta_T = 4.0$ for RC columns, which corresponds to $P_F = 3.2 \times 10^{-5}$. For this failure probability, and 1,000,000 simulations, the resulting percentage error is approximately 35%, which translates in a reliability index in the range of 3.9 to 4.1.

Program RACOL-FRP (Ferreira 2017) uses the flowchart shown in Fig. 4. In the calculation of the failure probability, a sample of possible outcomes of the safety margin is simulated according to the corresponding performance function. For each column, the load statistics together with column resistance statistics generated in the previous section are used in Eq. (12). The number of unsatisfactory performances ($g(\boldsymbol{X}) < 0$), n_u, is counted, and failure probability, P_F, is

Table 4—Statistics of column resistance P_R, nominal resistance P_n, and ratio $\mu P_R/P_n$ for 144 selected columns with spirals

Cross section							Cross section						
No.	ID	μP_R, kN	SD, kN	COV	P_n, kN	$\mu P_R/P_n$	No.	ID	μP_R, kN	SD, kN	COV	P_n, kN	$\mu P_R/P_n$
1	D1F1L1T1C1	6316.6	1454.5	0.23	1625.6	3.89	25	D2F1L1T1C1	12,138.2	2788.6	0.23	3068.1	3.96
2	D1F1L1T1C2	7400.0	1718.5	0.23	1813.1	4.08	26	D2F1L1T1C2	13,580.8	3146.1	0.23	3318.0	4.09
3	D1F1L1T2C1	6937.1	1591.6	0.23	1625.6	4.27	27	D2F1L1T2C1	13,194.0	3021.7	0.23	3068.1	4.30
4	D1F1L1T2C2	8020.5	1855.4	0.23	1813.1	4.42	28	D2F1L1T2C2	14,636.6	3378.4	0.23	3318.0	4.41
5	D1F1L1T3C1	8178.1	1871.3	0.23	1625.6	5.03	29	D2F1L1T3C1	15,305.5	3495.3	0.23	3068.1	4.99
6	D1F1L1T3C2	9261.5	2134.0	0.23	1813.1	5.11	30	D2F1L1T3C2	16,748.1	3850.2	0.23	3318.0	5.05
7	D1F1L2T1C1	6628.7	1451.4	0.22	1836.8	3.61	31	D2F1L2T1C1	12,629.9	2783.3	0.22	3400.9	3.71
8	D1F1L2T1C2	7709.1	1714.8	0.22	2022.6	3.81	32	D2F1L2T1C2	14,068.9	3140.1	0.22	3648.8	3.86
9	D1F1L2T2C1	7247.5	1588.1	0.22	1836.8	3.95	33	D2F1L2T2C1	13,683.0	3015.7	0.22	3400.9	4.02
10	D1F1L2T2C2	8327.9	1851.3	0.22	2022.6	4.12	34	D2F1L2T2C2	15,122.0	3371.8	0.22	3648.8	4.14
11	D1F1L2T3C1	8485.0	1866.9	0.22	1836.8	4.62	35	D2F1L2T3C1	15,789.2	3488.0	0.22	3400.9	4.64
12	D1F1L2T3C2	9565.4	2129.1	0.22	2022.6	4.73	36	D2F1L2T3C2	17,228.2	3842.3	0.22	3648.8	4.72
13	D1F2L1T1C1	11,092.8	2628.2	0.24	2721.1	4.08	37	D2F2L1T1C1	20,215.1	4763.8	0.24	4931.9	4.10
14	D1F2L1T1C2	13,259.6	3160.5	0.24	3096.1	4.28	38	D2F2L1T1C2	23,100.3	5472.3	0.24	5431.7	4.25
15	D1F2L1T2C1	12,126.9	2856.5	0.24	2721.1	4.46	39	D2F2L1T2C1	22,092.0	5178.2	0.23	4931.9	4.48
16	D1F2L1T2C2	14,293.8	3388.1	0.24	3096.1	4.62	40	D2F2L1T2C2	24,977.2	5885.7	0.24	5431.7	4.60
17	D1F2L1T3C1	14,195.2	3321.6	0.23	2721.1	5.22	41	D2F2L1T3C1	25,845.8	6020.8	0.23	4931.9	5.24
18	D1F2L1T3C2	16,362.1	3850.9	0.24	3096.1	5.28	42	D2F2L1T3C2	28,731.0	6725.2	0.23	5431.7	5.29
19	D1F2L2T1C1	11,391.6	2621.4	0.23	2922.5	3.90	43	D2F2L2T1C1	20,686.6	4752.7	0.23	5249.9	3.94
20	D1F2L2T1C2	13,552.4	3152.6	0.23	3294.1	4.11	44	D2F2L2T1C2	23,564.6	5459.8	0.23	5745.7	4.10
21	D1F2L2T2C1	12,422.8	2849.0	0.23	2922.5	4.25	45	D2F2L2T2C1	22,558.8	5166.0	0.23	5249.9	4.30
22	D1F2L2T2C2	14,583.6	3379.5	0.23	3294.1	4.43	46	D2F2L2T2C2	25,436.8	5872.2	0.23	5745.7	4.43
23	D1F2L2T3C1	14,485.4	3312.8	0.23	2922.5	4.96	47	D2F2L2T3C1	26,303.2	6006.6	0.23	5249.9	5.01
24	D1F2L2T3C2	16,646.2	3841.0	0.23	3294.1	5.05	48	D2F2L2T3C2	29,181.2	6709.6	0.23	5745.7	5.08

obtained by the ratio n_u/n_s (n_s = 1,000,000). The reliability index β is obtained by the equation $\beta = -\Phi^{-1}(P_F)$, where Φ^{-1} is the inverse standard Normal distribution.

Figures 5 and 6 present the histograms of the acting loads, P_A, and safety margins, respectively, for spiral columns 32 (r = 0.5, 1.0, and 2.0). From Fig. 5, it can be observed that as the dead-to-live load ratio increases, the asymmetry of the corresponding histogram becomes less pronounced, with a shorter upper tail. This influences the histogram of the resulting safety margin depicted in Fig. 6 for the assumed load ratios. For each histogram a superimposed Normal distribution is presented in Fig. 6, showing that as the load ratio increases, the asymmetry of the corresponding histogram of the safety margin decreases.

RELIABILITY RESULTS AND DISCUSSION

The probabilities of failure (and corresponding reliability indexes) associated to the 144 CFRP-RC spiral columns are presented in Table 5; a summary of these data for the 288 CFRP-RC columns (spirals and hoops) are shown in Tables 6(a) and (b). Reliability indexes are in the range 3.92 ($P_F = 4.5 \times 10^{-5}$) to 4.61 ($P_F = 2.0 \times 10^{-6}$); the minimum reliability index occurs in just two out of the 288 analyzed columns. In all other cases, the obtained reliability indexes are very close to or above the target suggested by Szerszen and Nowak (2003) (β_T = 4.0 for new structures). For all analyzed columns, reliability indexes are considerably higher than the target value in ACI 440.2-17 (β_T = 3.5 for existing structures).

While the largest probability of failure is approximately 22 times the smallest, it translates into a much smaller range in terms of the reliability index (3.92 to 4.61). Columns 14 (D1F2L1T1C2, r = 2.0, spirals) and 11 (D1F1L2T3C1, r = 0.5, hoops) present the smallest and the largest values of β (and consequently, the largest and smallest failure probability), respectively. The higher reliability indexes obtained for columns with hoops are due to the smaller ϕ factors associated to such columns.

The influence of the variables load ratio r, column diameter D, unconfined concrete compressive strength f_c', longitudinal steel ratio ρ_{sL}, steel confinement level I_{se}, and CFRP confinement level I_{Fe} on the reliability of CFRP-RC columns is evaluated. Figures 7, 8, and 9 present the probability of failure, P_F, as a function of the steel confinement level for different combinations of the parameters D, f_c', ρ_{sl}, and CFRP confinement level for the CFRP-RC columns

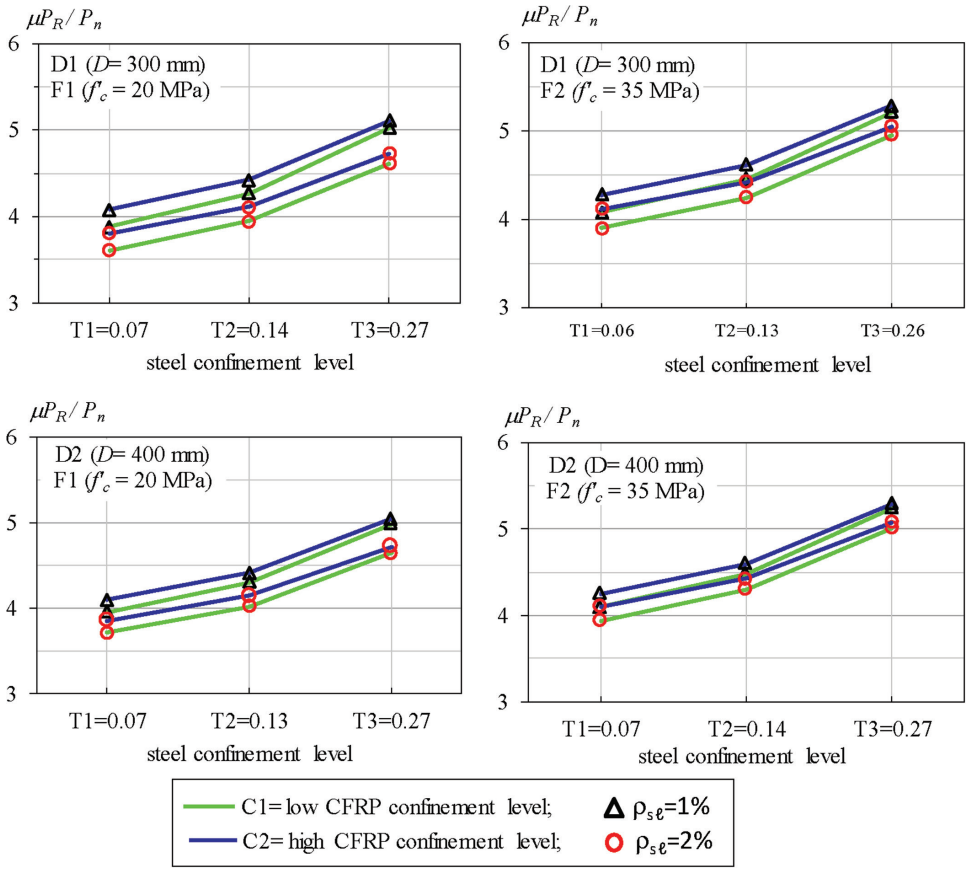

Fig. 3—Ratio between mean simulated column resistance μP_R *and nominal resistance* P_n *for 48 analyzed column cross sections with spirals.*

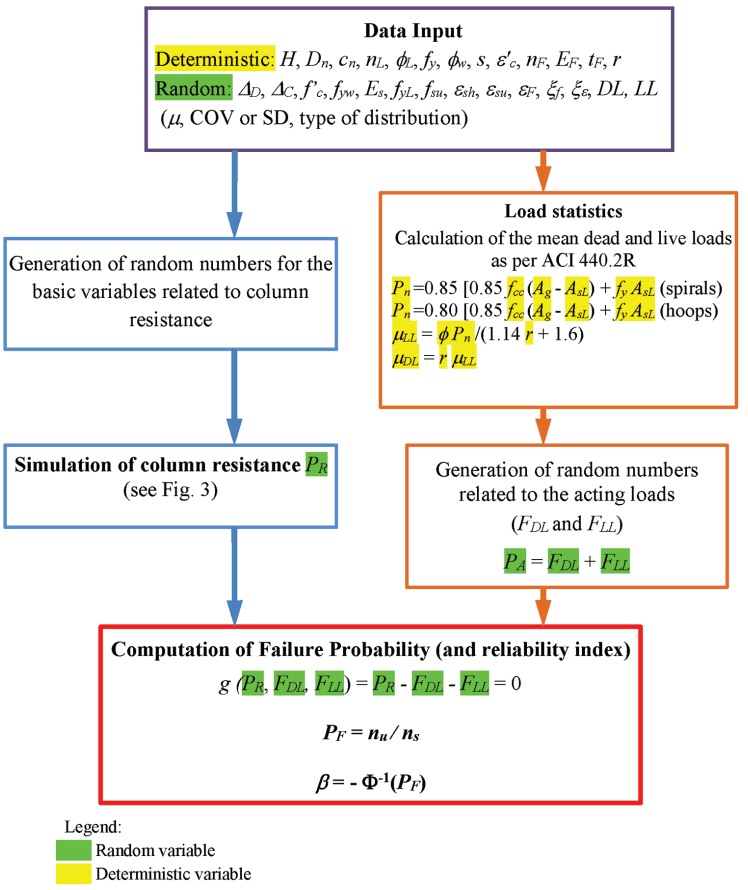

Fig. 4—Flowchart of safety assessment of FRP-RC columns, program RACOL-FRP.

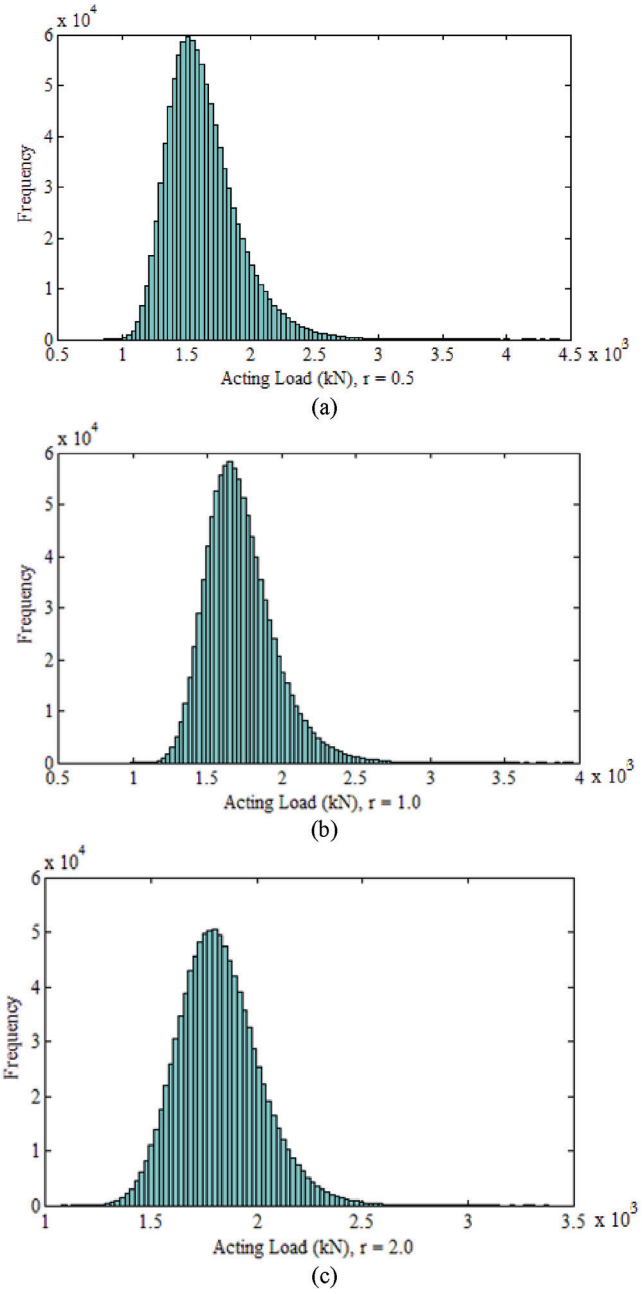

Fig. 5—Histogram of acting load P_A*, column series 32 (spirals): (a)* r = *0.5; (b)* r = *1.0; and (c)* r = *2.0.*

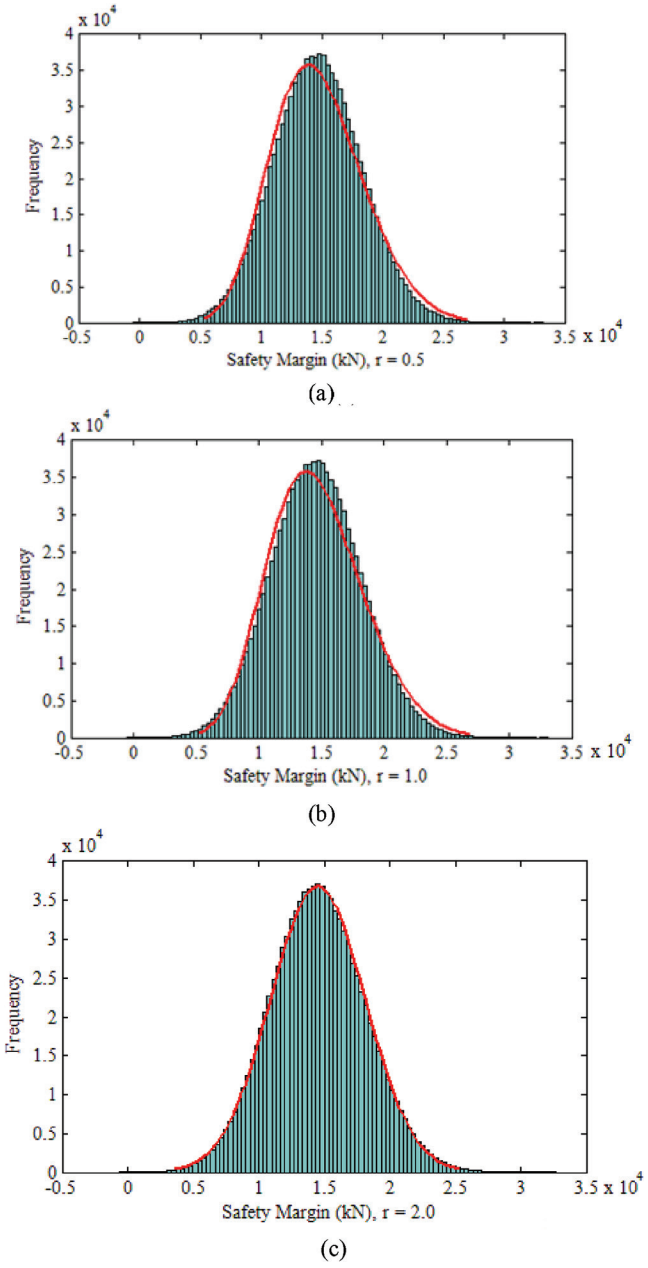

Fig. 6—Histogram of safety margin of column 32 series (spirals) with superimposed Normal distribution: (a) r = *0.5; (b)* r = *1.0; and (c)* r = *2.0.*

(spirals), corresponding to the load ratios r = 0.5, 1.0, and 2.0, respectively.

From the results obtained, it can be observed that the load ratio, r, has a slight influence on the probability of failure, P_F. Additionally, for each load ratio, it is seen that column diameter, D, has little impact on the resulting column reliability. With respect to concrete compressive strength, columns with the smallest unconfined concrete compressive strength (f_c' = 20 MPa) resulted in the smallest failure probabilities. This is consistent with the higher efficiency of confinement for lower-strength concretes (Diniz and Frangopol 1997b; Saatcioglu and Razvi 1992). Regarding the influence of the longitudinal steel ratio ρ_{sL}, it was observed that failure probability decreases as ρ_{sL} increases. This influence of ρ_{sL} could be expected due to the smaller variability of the longitudinal steel (COV = 0.05) as compared to the assumed concrete compressive strength variability (COV = 0.10).

Regarding the confinement level provided by the transversal steel I_{se}, it was found that in most cases, there is a tendency of a decrease in the failure probability with an increase in the steel confinement level, thus representing a beneficial effect of the transversal steel on the reliability of the CFRP-RC column. The levels of steel confinement used in the selected columns are either less or at most equal to the minimum suggested by ACI 318 for concrete confinement. The ACI 440.2R-17 confinement model does not consider steel confinement effects, while this effect is incorporated in the Lee et al. model. As for the FRP confinement level, the results indicate that, all other parameters remaining the same,

Table 5—Failure probability and corresponding reliability index of 144 FRP-RC columns with spirals

Cross section		Load ratio = 0.5		Load ratio = 1.0		Load ratio = 2.0		Cross section		Load ratio = 0.5		Load ratio = 1.0		Load ratio = 2.0	
No.	ID	P_F	β	P_F	β	P_F	β	No.	ID	P_F	β	P_F	β	P_F	β
1	D1F1L1T1C1	1.0×10^{-5}	4.26	1.3×10^{-5}	4.21	1.4×10^{-5}	4.19	25	D2F1L1T1C1	9.0×10^{-6}	4.29	1.3×10^{-5}	4.21	1.7×10^{-5}	4.14
2	D1F1L1T1C2	2.2×10^{-5}	4.09	2.9×10^{-5}	4.02	3.4×10^{-5}	3.98	26	D2F1L1T1C2	2.1×10^{-5}	4.10	2.4×10^{-5}	4.07	3.3×10^{-5}	3.99
3	D1F1L1T2C1	8.0×10^{-6}	4.31	1.0×10^{-5}	4.26	1.5×10^{-5}	4.17	27	D2F1L1T2C1	8.0×10^{-6}	4.31	1.3×10^{-5}	4.21	1.3×10^{-5}	4.21
4	D1F1L1T2C2	1.7×10^{-5}	4.14	2.3×10^{-5}	4.08	2.4×10^{-5}	4.07	28	D2F1L1T2C2	1.8×10^{-5}	4.13	2.2×10^{-5}	4.09	2.5×10^{-5}	4.06
5	D1F1L1T3C1	6.0×10^{-6}	4.38	9.0×10^{-6}	4.29	1.2×10^{-5}	4.22	29	D2F1L1T3C1	7.0×10^{-6}	4.34	8.0×10^{-6}	4.31	1.1×10^{-5}	4.24
6	D1F1L1T3C2	1.3×10^{-5}	4.21	1.8×10^{-5}	4.13	1.8×10^{-5}	4.13	30	D2F1L1T3C2	1.2×10^{-5}	4.22	1.6×10^{-5}	4.16	1.9×10^{-5}	4.12
7	D1F1L2T1C1	4.0×10^{-6}	4.47	4.0×10^{-6}	4.47	3.0×10^{-6}	4.53	31	D2F1L2T1C1	5.0×10^{-6}	4.42	5.0×10^{-6}	4.42	5.0×10^{-6}	4.42
8	D1F1L2T1C2	6.0×10^{-6}	4.38	1.1×10^{-5}	4.24	1.4×10^{-5}	4.19	32	D2F1L2T1C2	9.0×10^{-6}	4.29	1.3×10^{-5}	4.21	1.9×10^{-5}	4.12
9	D1F1L2T2C1	3.0×10^{-6}	4.53	3.0×10^{-6}	4.53	3.0×10^{-6}	4.53	33	D2F1L2T2C1	4.0×10^{-6}	4.47	4.0×10^{-6}	4.47	3.0×10^{-6}	4.53
10	D1F1L2T2C2	6.0×10^{-6}	4.38	9.0×10^{-6}	4.29	1.5×10^{-5}	4.17	34	D2F1L2T2C2	7.0×10^{-6}	4.34	1.0×10^{-5}	4.26	1.5×10^{-5}	4.17
11	D1F1L2T3C1	2.0×10^{-6}	4.61	3.0×10^{-6}	4.53	2.0×10^{-6}	4.61	35	D2F1L2T3C1	3.0×10^{-6}	4.53	4.0×10^{-6}	4.47	4.0×10^{-6}	4.47
12	D1F1L2T3C2	7.0×10^{-6}	4.34	7.0×10^{-6}	4.34	1.0×10^{-5}	4.26	36	D2F1L2T3C2	7.0×10^{-6}	4.34	8.0×10^{-6}	4.31	1.0×10^{-5}	4.26
13	D1F2L1T1C1	1.8×10^{-5}	4.13	2.3×10^{-5}	4.08	2.6×10^{-5}	4.05	37	D2F2L1T1C1	1.8×10^{-5}	4.13	2.3×10^{-5}	4.08	2.4×10^{-5}	4.07
14	D1F2L1T1C2	3.5×10^{-5}	3.98	3.6×10^{-5}	3.97	4.4×10^{-5}	3.92	38	D2F2L1T1C2	3.4×10^{-5}	3.98	3.8×10^{-5}	3.96	4.5×10^{-5}	3.92
15	D1F2L1T2C1	1.6×10^{-5}	4.16	1.9×10^{-5}	4.12	2.1×10^{-5}	4.10	39	D2F2L1T2C1	1.6×10^{-5}	4.16	1.7×10^{-5}	4.14	2.1×10^{-5}	4.10
16	D1F2L1T2C2	2.9×10^{-5}	4.02	3.4×10^{-5}	3.98	3.4×10^{-5}	3.98	40	D2F2L1T2C2	2.8×10^{-5}	4.03	2.9×10^{-5}	4.02	3.6×10^{-5}	3.97
17	D1F2L1T3C1	1.3×10^{-5}	4.21	1.4×10^{-5}	4.19	1.6×10^{-5}	4.16	41	D2F2L1T3C1	1.3×10^{-5}	4.21	1.3×10^{-5}	4.21	1.5×10^{-5}	4.17
18	D1F2L1T3C2	1.7×10^{-5}	4.14	2.1×10^{-5}	4.10	2.8×10^{-5}	4.03	42	D2F2L1T3C2	1.8×10^{-5}	4.13	2.1×10^{-5}	4.10	2.5×10^{-5}	4.06
19	D1F2L2T1C1	8.0×10^{-6}	4.31	1.2×10^{-5}	4.22	1.8×10^{-5}	4.13	43	D2F2L2T1C1	8.0×10^{-6}	4.31	1.3×10^{-5}	4.21	1.6×10^{-5}	4.16
20	D1F2L2T1C2	2.0×10^{-5}	4.11	2.3×10^{-5}	4.08	3.3×10^{-5}	3.99	44	D2F2L2T1C2	2.3×10^{-5}	4.08	2.6×10^{-5}	4.05	3.3×10^{-5}	3.99
21	D1F2L2T2C1	8.0×10^{-6}	4.31	8.0×10^{-6}	4.31	1.3×10^{-5}	4.21	45	D2F2L2T2C1	8.0×10^{-6}	4.31	1.2×10^{-5}	4.22	1.4×10^{-5}	4.19
22	D1F2L2T2C2	1.9×10^{-5}	4.12	2.5×10^{-5}	4.06	2.5×10^{-5}	4.06	46	D2F2L2T2C2	1.7×10^{-5}	4.14	2.1×10^{-5}	4.10	2.4×10^{-5}	4.07
23	D1F2L2T3C1	6.0×10^{-6}	4.38	9.0×10^{-6}	4.29	1.0×10^{-5}	4.26	47	D2F2L2T3C1	8.0×10^{-6}	4.31	8.0×10^{-6}	4.31	1.0×10^{-5}	4.26
24	D1F2L2T3C2	1.4×10^{-5}	4.19	1.7×10^{-5}	4.14	2.0×10^{-5}	4.11	48	D2F2L2T3C2	1.1×10^{-5}	4.24	1.6×10^{-5}	4.16	1.8×10^{-5}	4.13

Table 6(a)—Summary of statistics of failure probability P_F and reliability index β for 144 selected columns with spirals

	Failure probability P_F			Reliability index β		
Statistics	$r = 0.5$	$r = 1.0$	$r = 2.0$	$r = 0.5$	$r = 1.0$	$r = 2.0$
Mean	1.6×10^{-5}	2.0×10^{-5}	2.4×10^{-5}	4.18	4.13	4.08
Minimum	6.0×10^{-6}	6.0×10^{-6}	7.0×10^{-6}	3.98	3.96	3.92
Maximum	3.5×10^{-5}	3.8×10^{-5}	4.5×10^{-5}	4.38	4.38	4.34

Table 6(b)—Summary of statistics of failure probability P_F and reliability index β for 144 selected columns with hoops

	Failure probability P_F			Reliability index β		
Statistics	$r = 0.5$	$r = 1.0$	$r = 2.0$	$r = 0.5$	$r = 1.0$	$r = 2.0$
Mean	9.3×10^{-6}	1.1×10^{-5}	1.4×10^{-5}	4.31	4.27	4.23
Minimum	2.0×10^{-6}	3.0×10^{-6}	2.0×10^{-6}	4.12	4.07	4.05
Maximum	1.9×10^{-5}	2.4×10^{-5}	2.6×10^{-5}	4.61	4.53	4.61

with few exceptions, failure probabilities are approximately the same for the two levels of CFRP considered herein.

In this study, a large number of data points (288) representing different parameters (unconfined concrete compressive strength, amount of longitudinal steel, FRP confinement level, and so on) were considered. The results obtained indicate important trends in the safety levels that could be expected in the CFRP-strengthening of RC columns. Nevertheless, one must bear in mind that different results may be obtained for conditions outside the range of variables and the statistical descriptions used in this research.

Finally, yet importantly, it is emphasized that the reliability results obtained represent notional values aimed at allowing a comparison between safety levels associated with design of new structures and assessment of existing ones. To this end, the statistical description of the random variables considered in this study were consistent with new structures. In the case of existing structures, significant differences in the statistical description of the attendant variables may occur.

SUMMARY AND CONCLUSIONS

The research presented herein was aimed at the code development for fiber-reinforced polymer (FRP)-strengthened reinforced concrete (RC) columns. It was shown that the problem at hand incorporates a number of challenges, thus granting a careful consideration within a reliability-based framework. By developing a rigorous reliability assessment on a large number of FRP-RC columns, representing a wide range of parameters, and strengthened

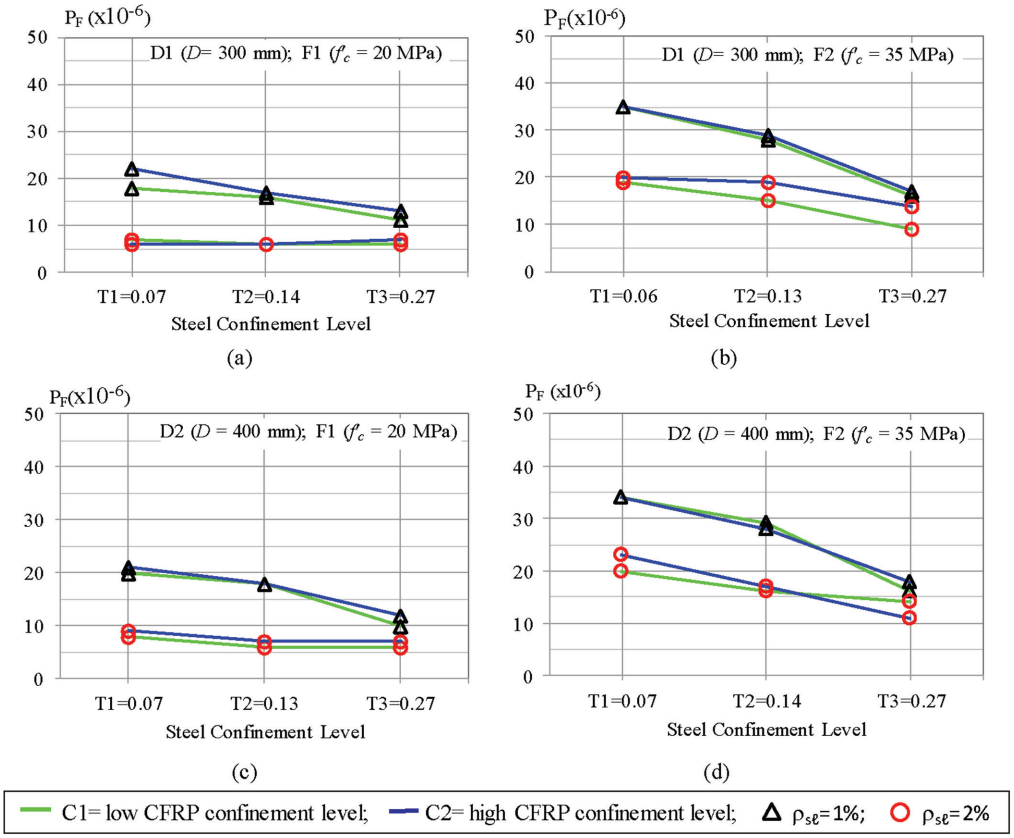

Fig. 7—Probability of failure as function of I_{se} *for different combinations of* D, f_c', ρ_{sl}, *and CFRP confinement level, columns with spirals* (r = 0.5).

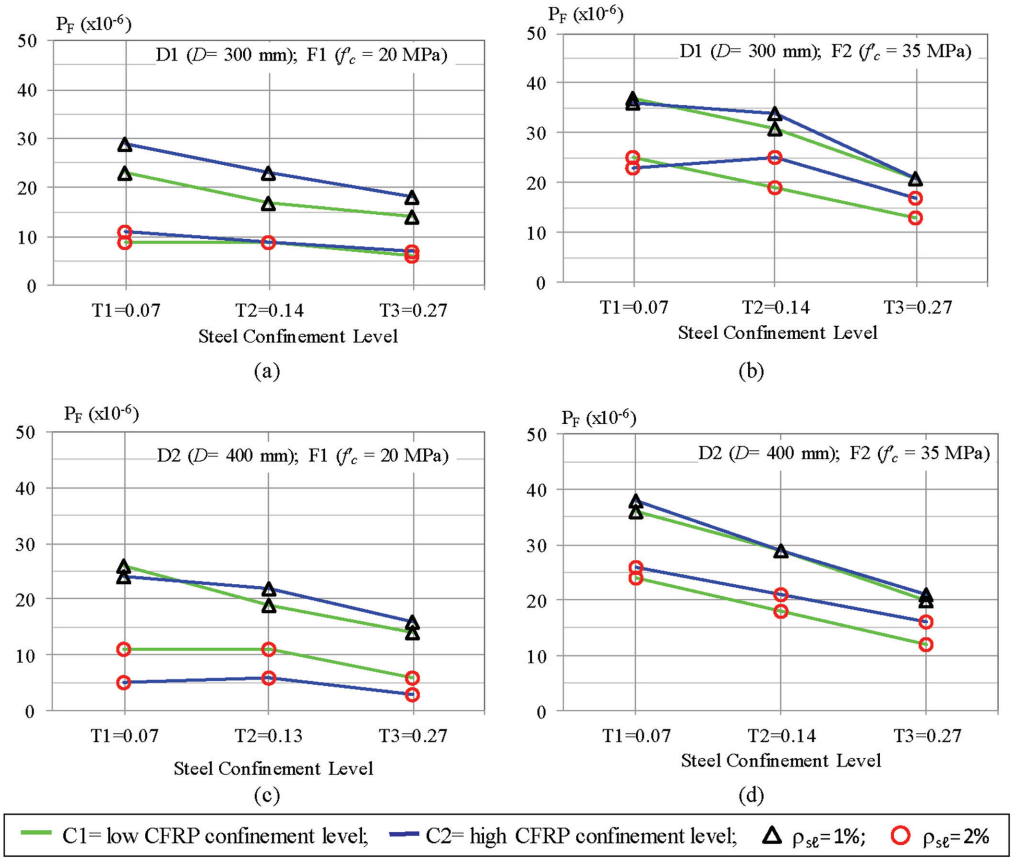

Fig. 8—Probability of failure as function of I_{se} *for different combinations of* D, f_c', ρ_{sl}, *and CFRP confinement level, columns with spirals* (r = 1.0).

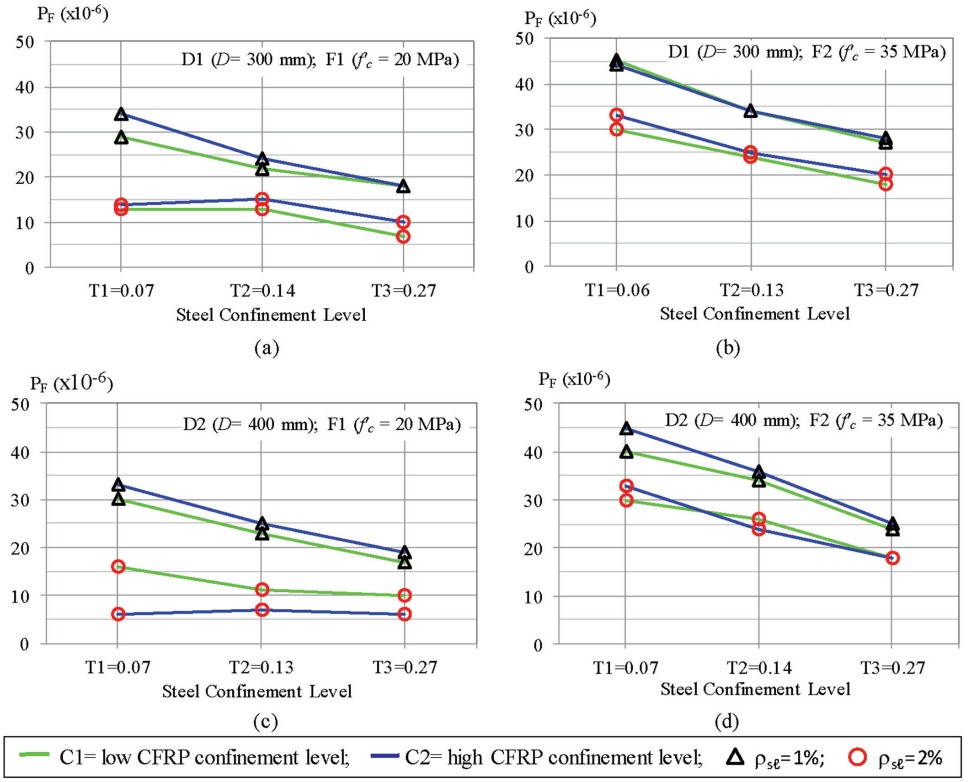

Fig. 9—Probability of failure as function of I_{se} *for different combinations of* D, f_c', ρ_{sl}, *and CFRP confinement level, columns with spirals* (r = 2.0).

according to ACI 440.2R-17, this research sheds new light on the adequacy of such guidelines.

In this work, the safety assessment of short circular RC columns confined by CFRP, with respect to the ultimate limit state, has been performed. Two hundred eighty-eight axially loaded CFRP-RC short columns, strengthened according to ACI 440.2R-17, were evaluated. The joint behavior of transversal steel/FRP, as occurs in the strengthening of existing RC columns, was investigated within a probabilistic framework, using a confinement model that represents the steel/FRP interaction.

A computational procedure using Monte Carlo simulation was developed as part of this research. It incorporates a module for the simulation of the statistics of column resistance and another for the generation of the statistics of the acting loads which depend on the strengthening design procedure—for example, ACI 440.2R-17. Special attention was given to the statistics of the basic variables to be used in each module.

The influence of the variables load ratio r, column diameter D, unconfined concrete compressive strength f_c', longitudinal steel ratio ρ_{sL}, steel confinement level I_{se}, and FRP confinement level I_{Fe} on the resulting safety levels of CFRP-RC columns was evaluated. It was concluded that:

- An increase in the load ratio resulted in a slight increase in the failure probability.
- Column diameter has a negligible impact on column reliability.
- For the analyzed columns and the recommendations of ACI 440.2R-17, the most influential variables are f_c', ρ_{sL}, and I_{Fe}.
- Smaller unconfined concrete compressive strengths and larger longitudinal steel ratios have a positive effect on column safety.
- The interaction between transversal steel/FRP in providing concrete confinement has a beneficial effect to the column safety. It is emphasized that the amount of carbon FRP (CFRP) confinement in the CFRP-RC columns was such that an ascending branch in the stress-strain curve of the confined concrete would be obtained. There is a slight tendency of an increase in the reliability index (and consequently a decrease in the failure probability) with an increase in the steel confinement ratio. While this increase may not be significant in the case of new structures, it may have an important impact on the performance of an existing structure.
- All other parameters remaining the same, reliability indexes are similar for the two levels of FRP confinement considered.

Most importantly, regarding the safety levels implicit in ACI 440.2R-17, it is shown that reliability indexes, β, are higher than the target values for new structures (β = 4.0 [Szerszen and Nowak 2003]), and considerably higher than the target for existing structures (β = 3.5, as suggested in ACI 440.2R-17). The reliability indexes obtained are in the range of 3.92 to 4.61, while failure probabilities are in the range of 2×10^{-6} to 4.5×10^{-5}. However, it is noted that the largest failure probability is 22.5 times the smallest; this is a limitation of the semi-probabilistic design formats currently in use.

It is largely accepted that the target reliability for existing structures may be smaller than those of new

structures (Steenbergen et al. 2015); $\beta_T = 3.5$ as mentioned in ACI 440.2-17 reflects this trend. In this sense, the results obtained suggest that current design procedures in ACI 440.2R-17 are conservative and a code calibration procedure could be undertaken for more economical FRP strengthening of RC columns. Nevertheless, it must be emphasized that the target reliability index to be used in the safety assessment of existing structures is still an open issue. More research related to the statistics of in-place material properties (for both concrete and FRP), load effects associated to the revised design service life of the strengthened column, and target reliability for existing structures are required.

The research presented in this paper has been limited to the FRP strengthening of axially loaded RC columns. As such, the results obtained correspond to the cases where FRP strengthening would be most effective, and consequently providing an upper bound for the corresponding safety levels. Currently, additional research is being performed by the authors addressing the more general problem of FRP strengthening of eccentrically loaded RC columns.

AUTHOR BIOS

Juscelina Rosiane Ferreira *is an Associate Professor at the State University of Minas Gerais, João Monlevade, Brazil. She received her BSc in civil engineering in 2006 from Federal University of Viçosa, Viçosa, Brazil; her MSc in civil engineering in 2009 from State University of Northern Rio de Janeiro, Rio de Janeiro, Brazil; and her PhD in structural engineering in 2017 from Federal University of Minas Gerais. Her research interests include reinforced concrete structures, structural reliability, probabilistic methods, and strengthening of structures using fiber-reinforced polymer (FRP).*

Peterson Araújo Quadros *is a PhD Candidate at the Federal University of Minas Gerais, Belo Horizonte, Brazil. He received his BSc in civil engineering from the State University of Minas Gerais in 2006 and his MSc in structural engineering from the Federal University of Minas Gerais in 2014. His research interests include sustainability, design, and repair of concrete structures and structural reliability.*

Sofia Maria Carrato Diniz, *FACI, is a Professor of structural engineering, Department of Structural Engineering, Federal University of Minas Gerais. She received her BSc in civil engineering in 1979 and her MSc in nuclear engineering in 1988 from the Federal University of Minas Gerais, and her PhD in civil engineering from the University of Colorado Boulder, Boulder, CO, in 1994. She is a past Chair (2004 to 2010) and member of ACI Committee 348, Structural Reliability and Safety. Her research interests include structural safety and reliability, durability, service life prediction, and design and repair of reinforced concrete structures.*

ACKNOWLEDGMENTS

The authors would like to thank CAPES (Coordenação de Aperfeiçoamento de Pessoal de Nível Superior) and CNPq (Conselho Nacional de Desenvolvimento Científico e Tecnológico) for the financial support provided.

REFERENCES

ACI Committee 318, 2014, "Building Code Requirements for Reinforced Concrete (ACI 318-14) and Commentary (ACI 318R-14)," American Concrete Institute, Farmington Hills, MI, 520 pp.

ACI Committee 440, 2017, "Guide for the Design and Construction of Externally Bonded FRP Systems for Strengthening Concrete Structures (ACI 440.2R-17)," American Concrete Institute, Farmington Hills, MI, 112 pp.

ACI Committee 440, 2022, "Building Code Requirements for Structural Concrete Reinforced with Glass Fiber-Reinforced Polymer (GFRP) Bars—Code and Commentary (ACI CODE-440.11-22)," American Concrete Institute, Farmington Hills, MI, 260 pp.

ACI Committee 562, 2016, "Code Requirements for Assessment, Repair, and Rehabilitation of Existing Concrete Structures (ACI 562-16) and Commentary," American Concrete Institute, Farmington Hills, MI, 88 pp.

Ang, A. H.-S., and Tang, W. H., 1984, *Probability Concepts in Engineering Planning and Design: Decision, Risk, and Reliability*, John Wiley & Sons, Inc., New York.

ASCE, 2021, "ASCE 2021 Report Card for America's Infrastructure," American Society of Civil Engineers, Reston, VA, https://infrastructurereportcard.org/cat-item/bridges-infrastructure/. (last accessed Apr. 1, 2024)

Baji, H., 2017, "Calibration of the FRP Resistance Reduction Factor for FRP-Confined Reinforced Concrete Building Columns," *Journal of Composites for Construction*, ASCE, V. 21, No. 3, p. 04016107. doi: 10.1061/(ASCE)CC.1943-5614.0000769

Bartlett, F. M., and MacGregor, J. G., 1995, "Equivalent Specified Concrete Strength from Core Test Data," *Concrete International*, V. 17, No. 3, Mar., pp. 52-58.

Casas, J. R., and Chambi, J. L., 2014, "Partial Safety Factors for CFRP-Wrapped Bridge Piers: Model Assessment and Calibration," *Composite Structures*, V. 118, pp. 267-283. doi: 10.1016/j.compstruct.2014.07.032

Chastre, C., and Silva, M. A. G., 2010, "Monotonic Axial Behavior & Modelling of RC Circular Columns Confined with CFRP," *Engineering Structures*, V. 32, No. 8, pp. 2268-2277. doi: 10.1016/j.engstruct.2010.04.001

Cusson, D., and Paultre, P., 1995, "Stress-Strain Model for Confined High-Strength Concrete," *Journal of Structural Engineering*, ASCE, V. 121, No. 3, pp. 468-477. doi: 10.1061/(ASCE)0733-9445(1995)121:3(468)

Diniz, S. M. C., 2008, "Structural Reliability: Rational Tools for Design Code Development," *Structures Congress 2008: Crossing Borders*, American Society of Civil Engineers, Reston, VA.

Diniz, S. M. C., and Frangopol, D. M., 1997a, "Reliability Bases for High-Strength Concrete Columns," *Journal of Structural Engineering*, ASCE, V. 123, No. 10, pp. 1375-1381. doi: 10.1061/(ASCE)0733-9445(1997)123:10(1375)

Diniz, S. M. C., and Frangopol, D. M., 1997b, "Strength and Ductility Simulation of High-Strength Concrete Columns," *Journal of Structural Engineering*, ASCE, V. 123, No. 10, pp. 1365-1374. doi: 10.1061/(ASCE)0733-9445(1997)123:10(1365)

Diniz, S. M. C., and Frangopol, D. M., 1998, "Reliability Assessment of High-Strength Concrete Columns," *Journal of Engineering Mechanics*, ASCE, V. 124, No. 5, pp. 529-536. doi: 10.1061/(ASCE)0733-9399(1998)124:5(529)

Eid, R., and Paultre, P., 2008, "Analytical Model for FRP-Confined Circular Reinforced Concrete Columns," *Journal of Composites for Construction*, ASCE, V. 12, No. 5, pp. 541-552. doi: 10.1061/(ASCE)1090-0268(2008)12:5(541)

Ferreira, J. R., 2017, "Reliability of Short Circular RC Columns Confined by FRP," PhD thesis, Federal University of Minas Gerais, Belo Horizonte, Brazil.

Ferreira, J. R., and Diniz, S. M. C., 2018, "Model Uncertainty in the Estimation of the Resistance of Circular Reinforced Concrete Columns Confined by Carbon Fiber Reinforced Polymer," *Structure and Infrastructure Engineering*, V. 14, No. 1, pp. 68-88. doi: 10.1080/15732479.2017.1328447

Ferreira, J. R.; Quadros, P. A.; and Diniz, S. M. C., 2018, "Extending the Life-Cycle of Reinforced Concrete Columns by FRP Strengthening," *Structures Congress 2018: Bridges, Transportation Structures, and Nonbuilding Structures*, American Society of Civil Engineers, Reston, VA.

fib, 2020, *Model Code 2020*, International Federation for Structural Concrete, Lausanne, Switzerland.

Galambos, T.; Ellingwood, B.; MacGregor, J.; and Cornell, A., 1982, "Probability Based Load Criteria: Assessment of Current Design Practice," *Journal of Structural Division*, ASCE, V. 108, No. 5, pp. 959-977.

Ghosn, M.; Frangopol, D. M.; McAllister, T. P.; Shah, M.; Diniz, S. M. C.; Ellingwood, B. R.; Manuel, L.; Biondini, F.; Catbas, N.; Strauss, A.; and Zhao, X. L., 2016, "Reliability-Based Performance Indicators for Structural Members," *Journal of Structural Engineering*, ASCE, V. 142, No. 9, p. 04016002. doi: 10.1061/(ASCE)ST.1943-541X.0001546

ISO 13822:2010, 2010, "Basis for Design of Structures – Assessment of Existing Structures," International Organization for Standardization, Geneva, Switzerland.

ISO 19338:2014, 2014, "Performance and Assessment Requirements for Design Standards on Structural Concrete," International Organization for Standardization, Geneva, Switzerland.

Lee, J. Y.; Yi, C. K.; Jeong, H. S.; Kim, S. W.; and Kim, J. K., 2010, "Compressive Response of Concrete Confined with Steel Spirals and FRP Composites," *Journal of Composite Materials*, V. 44, No. 4, pp. 481-504. doi: 10.1177/0021998309347568

Melchers, R. E., 2001, "Assessment of Existing Structures-Approaches and Research Needs," *Journal of Structural Engineering*, ASCE, V. 127, No. 4, pp. 406-411. doi: 10.1061/(ASCE)0733-9445(2001)127:4(406)

Micelli, F., and Modarelli, R., 2013, "Experimental and Analytical Study on Properties Affecting the Behaviour of FRP-Confined Concrete," *Composites. Part B, Engineering*, V. 45, No. 1, pp. 1420-1431. doi: 10.1016/j.compositesb.2012.09.055

Mirza, S. A., and MacGregor, J. G., 1979a, "Variations in the Dimensions of Reinforced Concrete Members," *Journal of the Structural Division*, ASCE, V. 105, No. 4, pp. 751-766. doi: 10.1061/JSDEAG.0005132

Mirza, S. A., and MacGregor, J. G., 1979b, "Variability of Mechanical Properties of Reinforcing Bars," *Journal of the Structural Division*, ASCE, V. 105, No. 5, pp. 921-937. doi: 10.1061/JSDEAG.0005146

Nowak, A., and Szerszen, M., 2003, "Calibration of Design Code for Buildings (ACI 318): Part 1—Statistical Models for Resistance," *ACI Structural Journal*, V. 100, No. 3, May-June, pp. 377-382.

Ozbakkaloglu, T.; Lim, J. C.; and Vincent, T., 2013, "FRP-Confined Concrete in Circular Sections: Review and Assessment of Stress–Strain Models," *Engineering Structures*, V. 49, pp. 1068-1088. doi: 10.1016/j.engstruct.2012.06.010

Park, R., and Paulay, T., 1975, *Reinforced Concrete Structures*, John Wiley & Sons, Inc., New York.

Pellegrino, C., and Modena, C., 2010, "Analytical Model for FRP Confinement of Concrete Columns with and without Internal Steel Reinforcement," *Journal of Composites for Construction*, ASCE, V. 14, No. 6, pp. 693-705. doi: 10.1061/(ASCE)CC.1943-5614.0000127

Ribeiro, A. B.; Calixto, J. M. F.; and Diniz, S. M. C., 2016, "Assessment of Epistemic Uncertainties in the Shear Strength of Slender Reinforced Concrete Beams," *Engineering Structures*, V. 116, pp. 140-147. doi: 10.1016/j.engstruct.2016.02.045

Saatcioglu, M., and Razvi, S., 1992, "Strength and Ductility of Confined Concrete," *Journal of Structural Engineering*, ASCE, V. 118, No. 6, pp. 1590-1607. doi: 10.1061/(ASCE)0733-9445(1992)118:6(1590)

Shirmohammadi, F.; Esmaeily, A.; and Kiaeipour, Z., 2015, "Stress-Strain Model for Circular Concrete Columns Confined by FRP and Conventional Lateral Steel," *Engineering Structures*, V. 84, pp. 395-405. doi: 10.1016/j.engstruct.2014.12.005

Steenbergen, R. D. J. M.; Sýkora, M.; Diamantidis, D.; Holický, M.; and Vrouwenvelder, T., 2015, "Economic and Human Safety Reliability Levels for Existing Structures," *Structural Concrete*, V. 16, No. 3, pp. 323-332. doi: 10.1002/suco.201500022

Szerszen, M., and Nowak, A., 2003, "Calibration of Design Code for Buildings (ACI 318): Part 2—Reliability Analysis and Resistance Factors," *ACI Structural Journal*, V. 100, No. 3, May-June, pp. 383-391.

Val, D. V., 2003, "Reliability of Fiber-Reinforced Polymer-Confined Reinforced Concrete Columns," *Journal of Structural Engineering*, ASCE, V. 129, No. 8, pp. 1122-1130. doi: 10.1061/(ASCE)0733-9445(2003)129:8(1122)

Wang, N., and Ellingwood, B. R., 2015, "Limit State Design Criteria for FRP Strengthening of RC Bridge Components," *Structural Safety*, V. 56, pp. 1-8. doi: 10.1016/j.strusafe.2015.03.004

Wang, W., and Yang, W., 2010, "Statistical Studies on Material Behavior of CFRP Sheets under Uniaxial Loads and its Application in Reliability Analysis," 5th International Conference on FRP Composites in Civil Engineering, CICE, Beijing, China.

Wang, Z.; Wang, D.; Smith, S. T.; and Lu, D., 2012, "Experimental Testing and Analytical Modeling of CFRP-Confined Large Circular RC Columns Subjected to Cyclic Axial Compression," *Engineering Structures*, V. 40, pp. 64-74. doi: 10.1016/j.engstruct.2012.01.004

Zou, Y., and Hong, H. P., 2011, "Reliability Assessment of FRP-Confined Concrete Columns Designed for Buildings," *Structure and Infrastructure Engineering*, V. 7, No. 3, pp. 243-258. doi: 10.1080/15732470802416998

ACI STRUCTURAL JOURNAL TECHNICAL PAPER

Title No. 121-S45

Experimental Behavior of Concrete Corbels Reinforced with Glass Fiber-Reinforced Polymer Headed-End Bars

by Matthew N. Allen and Ehab F. El-Salakawy

Glass fiber-reinforced polymer (GFRP) reinforcement is a proven noncorrodible alternative to conventional steel reinforcement. Over the past two decades, a deliberate effort has been put toward developing a comprehensive set of design provisions, culminating in the release of ACI CODE-440.11-22. Absent from this Code is the strut-and-tie method commonly used in short shear-span applications due to uncertainty in GFRP-reinforced concrete (RC) behavior. Corbels are short shear-span, shear-controlled elements used to transfer vertical and horizontal loads to columns or walls. This study presents the results of 10 full-scale corbel specimens with varying reinforcement ratios and shear span-depth ratios to better understand the behavior of GFRP-RC corbels under monotonic loading. The results indicate that the cracking behavior, strain development, deflection, capacity, and mode of failure are all dependent on the presence of secondary reinforcement and the shear span-depth ratio. The thermoplastic headed-end bars used were found to be a viable anchorage method.

Keywords: code provisions; corbel; diagonal cracking; glass fiber-reinforced polymer (GFRP); headed bars; reinforced concrete (RC); secondary reinforcement; shear strength; strut-and-tie.

INTRODUCTION

Steel-reinforced concrete (RC) corbels are structural elements commonly found in bridges, parking structures, and industrial buildings. Corbels are cantilevered members that are characterized by a low shear span-depth ratio (a/d). Corbels are used to transfer vertical and horizontal loads from one structural element to another, typically from beams or slabs to columns or walls. Figure 1 provides photos of two common applications of concrete corbels, including a single-sided corbel in a bridge and a double-sided corbel in a parking structure. It is well understood that steel reinforcement is prone to corrosion under harsh environmental conditions, especially those with heavy chloride exposure. Corrosion negatively impacts the durability, strength, serviceability, and appearance of concrete structures.

Glass fiber-reinforced polymer (GFRP) reinforcement is a proven alternative to steel reinforcement. GFRP bars are noncorrodible and have a higher strength-to-weight ratio than conventional mild steel. Glass fibers are preferred over carbon and aramid in structural applications due to their cost-effectiveness and increased deformability. There are distinct mechanical property differences when comparing GFRP to steel, including a lower elastic modulus, linear-elastic behavior up to failure, and uniaxial properties due to the pultrusion manufacturing process. The lower elastic modulus leads to higher strains, wider cracks, and lower compressive strut efficiency factors. The uniaxial properties cause GFRP bars to be weak in shear, with reduced dowel action and transverse strength. As a result, weaker shear resistance is expected in GFRP-RC corbels due to these mechanical property differences.

Discontinuity or disturbance regions ("D-regions") are discrete locations in a structure where the fundamental flexural theory assumption of "plane sections remain plane" no longer applies. Shear forces are then carried by strut or arching action. Deep beams, corbels, or locations within one member depth of a load or support are examples of D-regions. The high degree of shear stress governs the behavior, meaning corbels cannot be designed by a conventional linear analysis. As such, alternative design methods, such as shear friction or the strut-and-tie model (STM), were developed. Shear friction is an empirical-based corbel design procedure proposed by Mattock et al.[1] that is valid for a/d less than 1.0. Alternatively, the STM is a versatile design tool without a/d limitations that has gained widespread use after the hallmark paper published by Schlaich et al.[2]

The shear behavior of steel-RC corbels has been investigated extensively. Several parametric relationships have been preestablished for steel-RC corbels. An increase in the shear span-depth ratio results in a decrease in corbel shear capacity, while an increase in the main tie reinforcement ratio results in an increase in corbel shear capacity.[1,3,4] The presence of secondary reinforcement decreases crack widths, increases corbel shear capacity, and leads to a more ductile failure.[5-7] Currently, there are limited formal studies available for GFRP-RC corbels outside of the paper published by Abu-Obaida et al.[8] As previously noted, these parametric relationships must be validated for GFRP-RC structures due to the lower elastic modulus, linear-elastic behavior, and uniaxial properties.

Steel-RC corbels often use welded connections or bent bars embedded into columns or walls to develop the main tie reinforcement. GFRP bars usually require a longer development length than steel, cannot be welded, and have reduced strength at bends. The anisotropic nature of GFRP leads to an approximately 35 to 70% loss in bent strength capacity compared to straight bars.[9-11] Headed-end bars are a feasible alternative to hooked or bent bars in applications with limited space for bar development, such as corbels.

ACI Structural Journal, V. 121, No. 3, May 2024.
MS No. S-2023-181.R1, doi: 10.14359/51740491, received November 13, 2023, and reviewed under Institute publication policies.

(a) (b)

Fig. 1—Common applications of concrete corbels: (a) bridge pier bearing seat (single corbel); and (b) parking structure (double corbel).

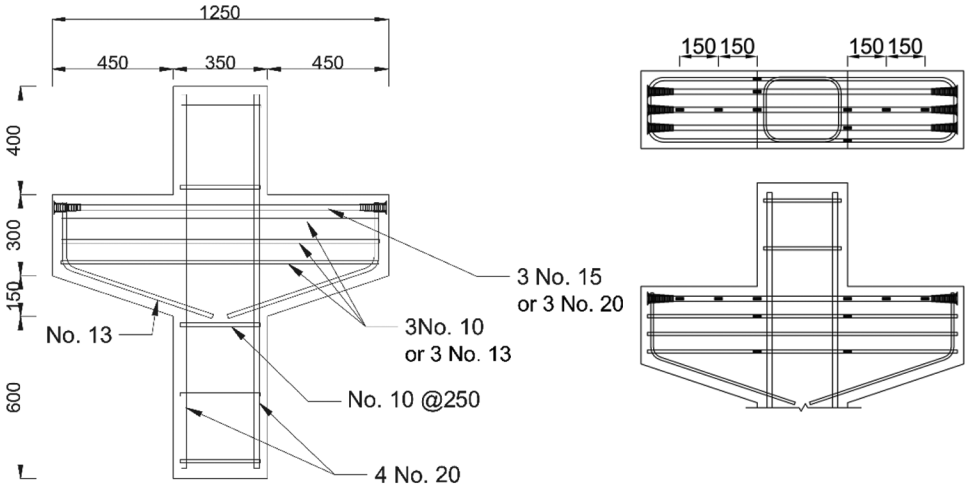

(a) (b)

Fig. 2—Details of test specimens: (a) geometry and reinforcement (GFRP-RC shown, steel-RC similar); and (b) strain gauge layout. (Note: 1 mm = 0.0394 in.)

A study by Yang et al.[12] found that headed bars provided excellent end anchorage for steel-RC corbels, leading to a higher load-carrying capacity, stiffness, and ductility. For GFRP-RC structures, recent studies have also verified the use of thermoplastic headed ends with rounded grooves.[13-15] The headed-end GFRP bars evaluated by Benmokrane et al.[14] were found to have a pullout capacity of 90% greater than the equivalent straight bars. It is worth noting that there are currently no codified parameters that govern the qualification of GFRP headed-end bars.

RESEARCH SIGNIFICANCE

The shear behavior of steel-RC corbels has been investigated extensively. Currently, ACI CODE-440.11-22[16] does not address the design of GFRP-RC corbels due to a lack of research, while CSA S806:12[17] and CSA S6:19[18] provide STM provisions adapted directly from the steel-RC CSA A23.3:19[19] code. GFRP-RC corbels are expected to perform differently from steel-RC corbels due to the GFRP material properties—specifically, the lower elastic modulus, linear-elastic behavior, and uniaxial properties. Experimental investigation is necessary to develop an understanding of GFRP-RC corbels under monotonic loading. This study presents findings on the mode of failure, crack widths, strains, deflection, and load-carrying capacity.

DESCRIPTION OF SPECIMENS AND TEST PROGRAM

Test specimens

Ten full-scale RC specimens were constructed and tested to investigate the behavior of corbels under monotonic loading. A double-corbel and column geometry was selected to resemble a common corbel application in practice. The concrete specimens had tapered corbels with a height of 450 mm (17.72 in.) at the corbel-column interface and 300 mm (11.81 in.) at the free end. The corbels had a width of 300 mm (11.81 in.) and a length of 450 mm (17.72 in.). The a/d used were 0.33 and 0.66, corresponding to a 134 and 268 mm (5.28 and 10.55 in.) shear span, respectively. The column geometry was 350 x 300 mm (13.78 x 11.81 in.) with

Table 1—Properties of test specimens

Series	Corbel ID	Main tie reinforcement			Secondary reinforcement			Shear span-depth ratio a/d	Concrete strength f_c', MPa
		Bar type	ρ_t, %	ρ_t/ρ_b	Bar type	ρ_s, %	ρ_s/ρ_b		
A	S-15-10-33	3 15M	0.50	0.14	3 10M	0.50	0.15	0.33	43.9
	G-15-0-33	3 No. 15	0.50	2.53	—	—	—	0.33	36.9
	G-15-10-33	3 No. 15	0.50	2.53	3 No. 10	0.35	1.26	0.33	36.7
	G-20-0-33	3 No. 20	0.71	3.23	—	—	—	0.33	37.2
	G-20-13-33	3 No. 20	0.71	3.23	3 No. 13	0.63	2.26	0.33	40.5
B	S-15-10-66	3 15M	0.50	0.14	3 10M	0.50	0.15	0.66	44.6
	G-15-0-66	3 No. 15	0.50	2.53	—	—	—	0.66	36.1
	G-15-10-66	3 No. 15	0.50	2.53	3 No. 10	0.35	1.26	0.66	38.4
	G-20-0-66	3 No. 20	0.71	3.23	—	—	—	0.66	41.9
	G-20-13-66	3 No. 20	0.71	3.23	3 No. 13	0.63	2.26	0.66	35.6

Note: 1 MPa = 0.14504 ksi.

upper and lower column stub heights of 600 and 400 mm (23.62 and 15.75 in.), respectively, as shown in Fig. 2. The concrete geometry remained constant for all test specimens.

Two steel-RC corbels were prepared as reference specimens to their GFRP-RC counterparts. The remaining eight GFRP-RC corbels were constructed with a combination of the following parameters: main tie reinforcement ratio, secondary reinforcement ratio, and a/d. The main tie reinforcement was three 15M (16.0 mm [0.63 in.] diameter), No. 15 (15.9 mm [0.63 in.] diameter), or No. 20 (19.0 mm [0.75 in.] diameter) bars. The secondary reinforcement was three 10M (11.3 mm [0.44 in.] diameter), No. 10 (9.5 mm [0.37 in.] diameter), or No. 13 (12.7 mm [0.50 in.] diameter) bars. The secondary reinforcement consisted of horizontal closed stirrups equally spaced below the main tie reinforcement. Four specimens were prepared without any secondary reinforcement to evaluate their parametric significance on GFRP-RC corbel behavior. No vertical secondary reinforcement was used in this study following the special provisions for brackets and corbels in Clause 8.6.5 of CSA S806:12.[17] The column reinforcement was four 20M (19.5 mm [0.77 in.] diameter) or No. 20 (19.0 mm [0.75 in.] diameter) bars with 10M (11.3 mm [0.44 in.] diameter) or No. 10 (9.5 mm [0.37 in.] diameter) closed stirrups for steel- and GFRP-RC specimens respectively, distributed equally along the column height. The corbels were designed in accordance with CSA S806:12[17] and CSA S6:19[18] for GFRP and CSA A23.3:19[19] and ACI 318-19[20] for steel.

Table 1 introduces the corbel naming convention used in this study. The specimens were divided into Series A for an a/d of 0.33 and Series B for an a/d of 0.66. Individual specimens were assigned a corbel ID comprising four distinct parts. The first letter (S or G) denotes the reinforcement material type as steel or GFRP. The second index (15 or 20) specifies the nominal diameter of the main tie reinforcement in mm. The third index (0, 10, or 13) specifies the nominal diameter of the secondary reinforcement in mm. The fourth and final index (33 or 66) provides the a/d, presented as a percentage, used during testing. For example, corbel ID G-15-10-33 was the specimen constructed with GFRP reinforcement, No. 15 main tie bars, No. 10 secondary bars, and was tested at an a/d of 0.33. Reinforcement ratios ρ_t and ρ_s were provided for the main tie and secondary reinforcement configurations, respectively. The reinforcement ratios are also presented after normalization by the balanced reinforcement ratio, ρ_b. The steel-RC configurations were under-reinforced, with ρ/ρ_b values less than 1.0, while the GFRP-RC configurations were over-reinforced, with ρ/ρ_b values greater than 1.0.

Materials

Concrete was provided by a local ready mixed supplier following performance specifications. The concrete mixture was normalweight with a target 28-day strength of 35 MPa (5.0 ksi), nominal maximum aggregate size of 20 mm (0.79 in.), and target slump of 140 mm (5.51 in.). Standard 100 x 200 mm (3.94 x 7.87 in.) concrete cylinders were cast and tested in accordance with CSA A23.1:19/CSA A23.2:19.[21] Cylinder testing occurred immediately prior to the testing of each specimen. The concrete compressive strength results are presented in Table 1. The specimens were cast in the horizontal position using wooden formwork.

Two materials were used as internal reinforcement: conventional mild steel bars and sand-coated GFRP pultruded bars. The physical and mechanical properties of each bar diameter are presented in Table 2. The GFRP properties of each unique lot number (bar size, grade, and manufacturing run) were determined by a third-party laboratory in accordance with CSA S806:12,[17] CSA S807:19,[22] ACI 440.3R-12,[23] ASTM D570-22,[24] ASTM D2584-18,[25] ASTM D3418-21,[26] and ASTM D5117-17,[27] as applicable.

The steel main tie reinforcement had 50 x 50 x 12 mm (1.97 x 1.97 x 0.47 in.) steel plates welded at each end to facilitate bar development and prevent any potential anchorage losses. Welding was completed in accordance with CSA W59-18.[28] The GFRP headed ends were made of a thermoplastic vinyl-ester resin reinforced with short E-glass fibers, cast to the end of the bars at high temperatures. Rounded grooves were provided along the inner side of the headed-end profile to improve the mechanical interlock, as shown in Fig. 3. The headed end had an approximate length of 100 mm (3.94 in.) and a maximum outer diameter

Table 2—Mechanical properties of reinforcement

Bar type	Nominal diameter, mm	Nominal area, mm^2	Modulus of elasticity, GPa	Yield/tensile strength, MPa	Yield/ultimate strain, %
10M	11.3	100	200	460	0.230
15M	16.0	200	200	450	0.225
20M	19.5	300	200	450	0.225
No. 10	9.5	71* (82)†	54.3‡	1199	2.21§
No. 13	12.7	127* (153)†	54.7‡	1209	2.21§
No. 15	15.9	199* (236)†	64.5	1580	2.45§
No. 20	19.0	285* (336)†	62.9	1465	2.33§

*Nominal area as per CSA S807:19.

†Measured area as per Annex A of CSA S806:12.

‡Measured as per Annex C of CSA S806:12.

§Calculated using modulus of elasticity and tensile strength as per Annex C of CSA S806:12.

Note: 1 mm = 0.0394 in.; 1 mm^2 = 0.00155 $in.^2$; 1 GPa = 145.04 ksi; 1 MPa = 0.14504 ksi.

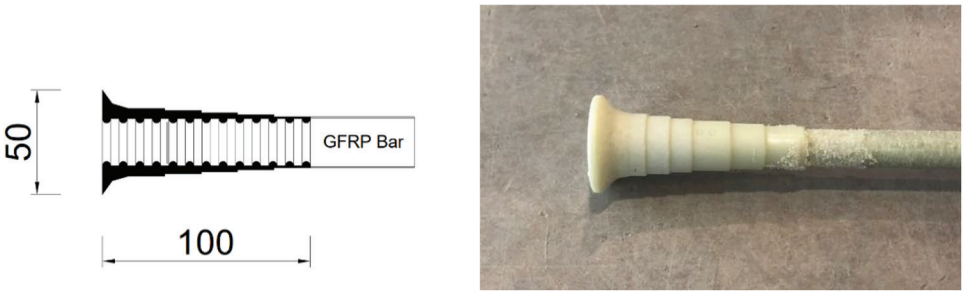

Fig. 3—Headed-end bars. (Note: 1 mm = 0.0394 in.)

Table 3—GFRP anchor head properties

Bar type	Load at break, kN	Slip at 100 kN, mm
No. 15	114.9 ± 7.5	0.43 ± 0.05
No. 20	197.7 ± 9.4	0.27 ± 0.05

Note: 1 kN = 0.2248 kip; 1 mm = 0.0394 in.

of 50 mm (1.97 in.). The load at break and slip at 100 kN (22.48 kip) for the No. 15 and No. 20 headed-end bars are provided in Table 3.

Instrumentation

Three types of instrumentation were used to record real-time data on the structural response to load: electrical strain gauges, performance indicator (PI) gauges, and linear variable displacement transducers (LVDTs). Electrical strain gauges were installed on the main tie reinforcement at the column-corbel interface, 150 and 300 mm (5.91 and 11.81 in.) offset from the interface. The two strain gauges nearest to the interface were used to capture the maximum bar strain. The strain gauge furthest from the interface was used to assess strain development near the headed ends and anchorage performance. Multiple strain gauges were installed at the same offset from the interface to provide redundancy at critical locations. Similarly, strain gauges were installed at the column-corbel interface along the top and bottom horizontal secondary reinforcement. Four 200 mm (7.87 in.) long PI gauges were mounted to the vertical concrete face to record concrete crack widths. Two PI gauges were installed near the column-corbel bearing surface interface for flexural cracks, and two were installed halfway along the inclined strut for diagonal cracks. Two LVDTs were attached to the lower column stubs to measure vertical displacement. The instrumentation was connected to a data acquisition (DAQ) system monitored by a computer.

Test setup and procedure

Figure 4 shows the schematic drawing and photo of the test setup. White paint was applied to the concrete to provide contrast for a 75 x 75 mm (2.95 x 2.95 in.) grid and crack pattern markings. The double corbels were inverted so that load could be applied with a single high-capacity piston from a 5000 kN (1124 kip) capacity hydraulic machine. Load was monotonically applied at a displacement-controlled rate of 0.5 mm/min (0.020 in./min) and was continuously monitored and held at critical points to mark crack patterns. Tests were terminated once the load dropped by at least 25% of the peak load. The high-capacity pistons transferred the load through a spherical head, a 300 x 350 x 25 mm (11.81 x 13.78 x 0.98 in.) steel bearing plate, and a 6 mm (0.24 in.) elastomeric bearing pad at the upper column stub. Each corbel bearing face was supported by 300 x 150 x 50 mm (11.81 x 5.91 x 1.97 in.) steel plates with a roller on one side and pinned support with an electrical-resistance compression load cell on the other. The load was then transferred through concrete support blocks and distributed into the laboratory strong floor.

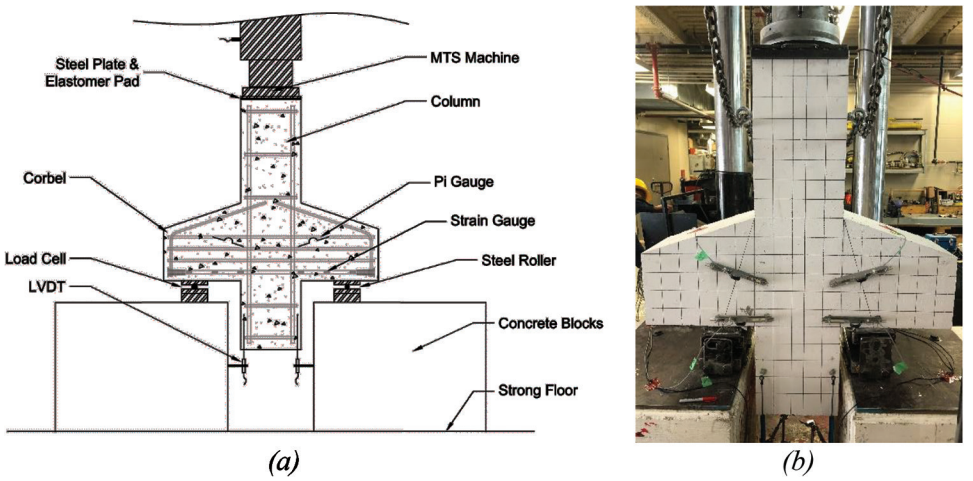

Fig. 4—Details of test setup: (a) test setup schematic; and (b) test setup photo.

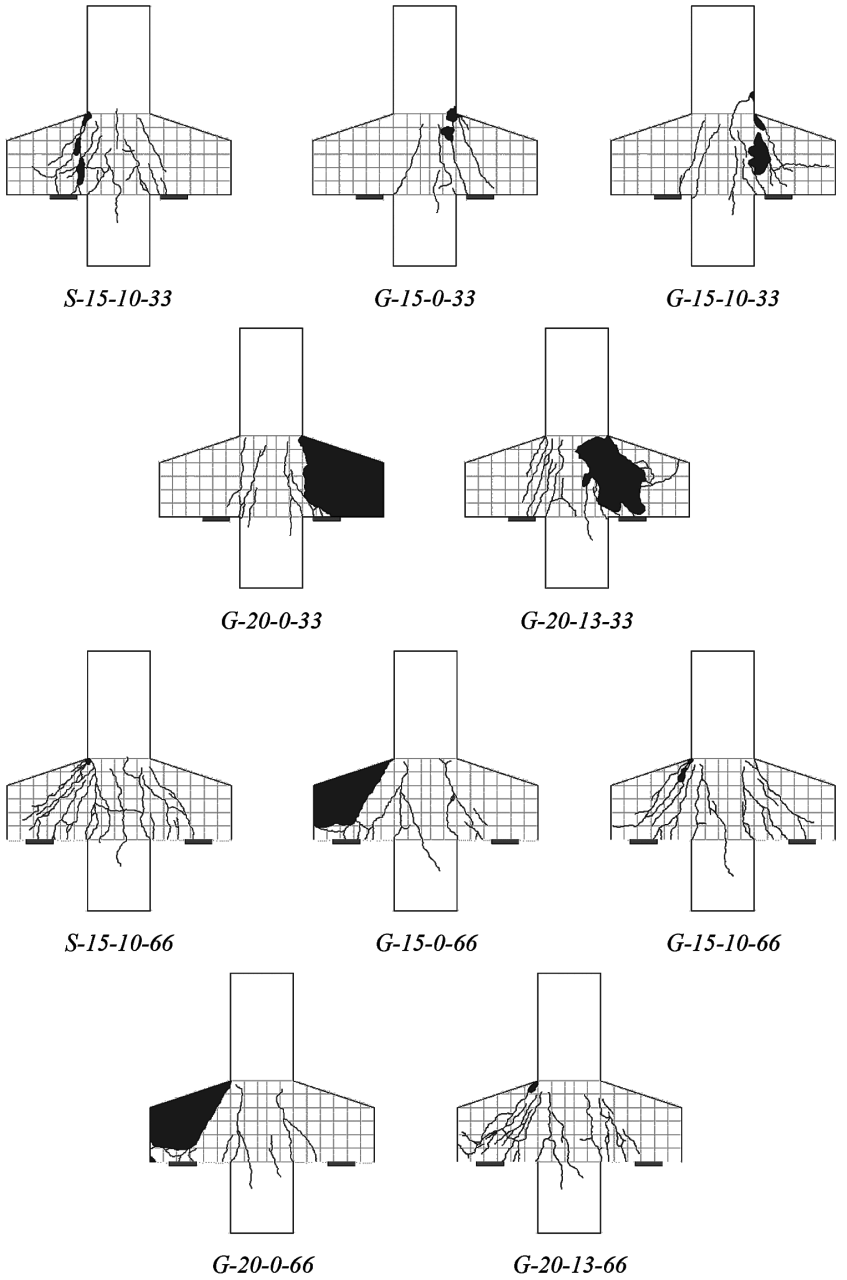

Fig. 5—Crack patterns at ultimate load.

TEST RESULTS AND DISCUSSION

General behavior and mode of failure

The corbel specimens were monotonically loaded until failure. The general behavior was characterized by marking crack patterns at regular intervals, photos of any observable deterioration, and photos at failure. Figure 5 presents the crack patterns at ultimate load, which was documented for one vertical face on each specimen. The initiation of crack development was consistent for all specimens in this study. The initial cracks were flexural in nature, forming at the column-corbel interface. The flexural cracks propagated vertically throughout the corbel height. After considerable load gain, diagonal cracks started to form near the center of the corbel height. The orientation of diagonal cracks closely followed the theoretical inclined struts, which matches the flow of stresses idealized in STM models. The appearance of initial cracking did not seem to be influenced by the proportioning of the main tie or secondary reinforcements.

Generally, the specimens with secondary reinforcement were able to continually carry load after the formation of diagonal strut cracks. Specimens without secondary reinforcement showed limited resiliency and commonly displayed brittle, abrupt failures. The specimens with secondary reinforcement were able to achieve an increased number of crack formations prior to failure. This relationship is shown in the G-20-13-66 specimen, which had a high degree of flexural and diagonal strut cracking compared to G-20-0-66, which was only able to form a few flexural cracks prior to failure.

The shaded gray regions represent an area that was either spalled, delaminated, or fully sheared from the rest of the column-corbel specimen. For example, G-20-13-33 experienced concrete cover spalling throughout the diagonal strut due to a high concentration of cracking, compared to G-15-0-66 and G-20-0-66, which both had wide shear cracks, leading to large masses of concrete fully dislodged from the unreinforced web of the corbel at failure. The wide shear cracks on G-15-0-66 and G-20-0-66 followed the theoretical diagonal strut until it intersected the main tie reinforcement, where the crack changed directions and projected out horizontally toward the free end of the corbel. This behavior was not present in any of the corbel specimens with secondary reinforcement due to the restraining action of the distributed bar.

Four modes of failure were observed, as shown in Fig. 6: tie yielding (TY) (steel-RC corbel), diagonal-compression (DC), flexural-compression (FC), and diagonal splitting (SP). The GFRP modes of failure were consistent with those presented in Abu-Obaida et al.[8] TY consists of extensive flexural cracking until yielding of the main tie steel reinforcement in tension. DC is characterized by both flexural and diagonal strut cracks developing prior to failure of the diagonal compression strut. FC consists of wide flexural cracking followed by crushing of concrete in the diagonal strut near the compression face. Finally, SP is the most undesirable mode of failure, in which a wide crack parallel to the diagonal strut forms in a sudden, brittle manner. Specimens that exhibited signs of SP include G-20-0-33, G-15-0-66, G-20-0-66, and G-20-13-66. These results suggest that the likelihood of SP is increased in specimens without secondary reinforcement and higher a/d. TY was only noted for S-15-10-66. Signs of DC were observed in all $a/d = 0.33$ specimens. FC was exhibited in all specimens with $a/d = 0.66$ and secondary reinforcement, including S-15-10-66, G-15-10-66, and G-20-13-66. The specimens with increased main tie and secondary reinforcement ratios generally had the same mode of failure as their counterpart specimens.

Crack width

PI gauges were mounted near the column-corbel interface and halfway along the inclined strut to monitor flexural and diagonal crack widths, respectively. Figure 7 presents the load-flexural crack width and load-diagonal strut crack width relationships. Flexural cracks were the first to form and generally developed at a higher intensity than the diagonal strut cracks. The steel-RC specimens displayed narrower crack widths at equivalent loads to their GFRP-RC counterparts. This trend was expected due to the modulus of elasticity differences between the two materials. One notable exception to this trend was S-15-10-66 prior to failure, where the steel began to yield and permitted the rapid development of flexural cracks and crack width openings. The presence of secondary reinforcement had a negligible influence on flexural cracking. This relationship was evaluated at the corbel service load and ultimate load. Service loads in this study were estimated as 60% of the nominal design strength in the steel-RC specimens using the actual yield strength of steel, which resulted in 665 kN (149.50 kip) for $a/d = 0.33$ and 415 kN (93.30 kip) for $a/d = 0.66$. The flexural crack widths at service loads were 0.97 and 1.08 mm (0.038 and 0.043 in.) with and without secondary reinforcement, respectively. Similarly, the flexural crack widths at failure were 1.98 and 1.99 mm (0.078 and 0.079 in.) with and without secondary reinforcement, respectively. This was anticipated because flexural crack widths initiate at the tension face of the corbels, intersecting the main tie reinforcement first before propagating toward the secondary reinforcement.

The failure of every GFRP-RC specimen was controlled by the diagonal strut crack development.

The development of diagonal strut cracks varied for each specimen. Five of the 10 specimens exhibited no diagonal strut cracks under service loads, while the remaining specimens had narrow crack widths of less than approximately 0.25 mm (0.010 in.). For G-15-0-66 and G-20-0-66, the corbels failed immediately after the strut crack was initiated, displaying a sudden and brittle failure, which is not desirable. This contrasts with G-15-10-66 and G-20-13-66, where appreciable load gain was achieved after the strut crack opened by redistributing stress to the secondary reinforcement. The presence of secondary reinforcement helped confine concrete cracks, carry compressive stresses, resist transverse tensile stresses, and mitigate brittle failures. The specimens with secondary reinforcement developed 3.5 times greater strut crack widths at failure than those without secondary reinforcement.

The difference between G-15-0-66 and G-15-10-66 demonstrates the effect of secondary reinforcement on concrete crack widths. Crack widths were consistently less for the specimen with secondary reinforcement at comparable loads

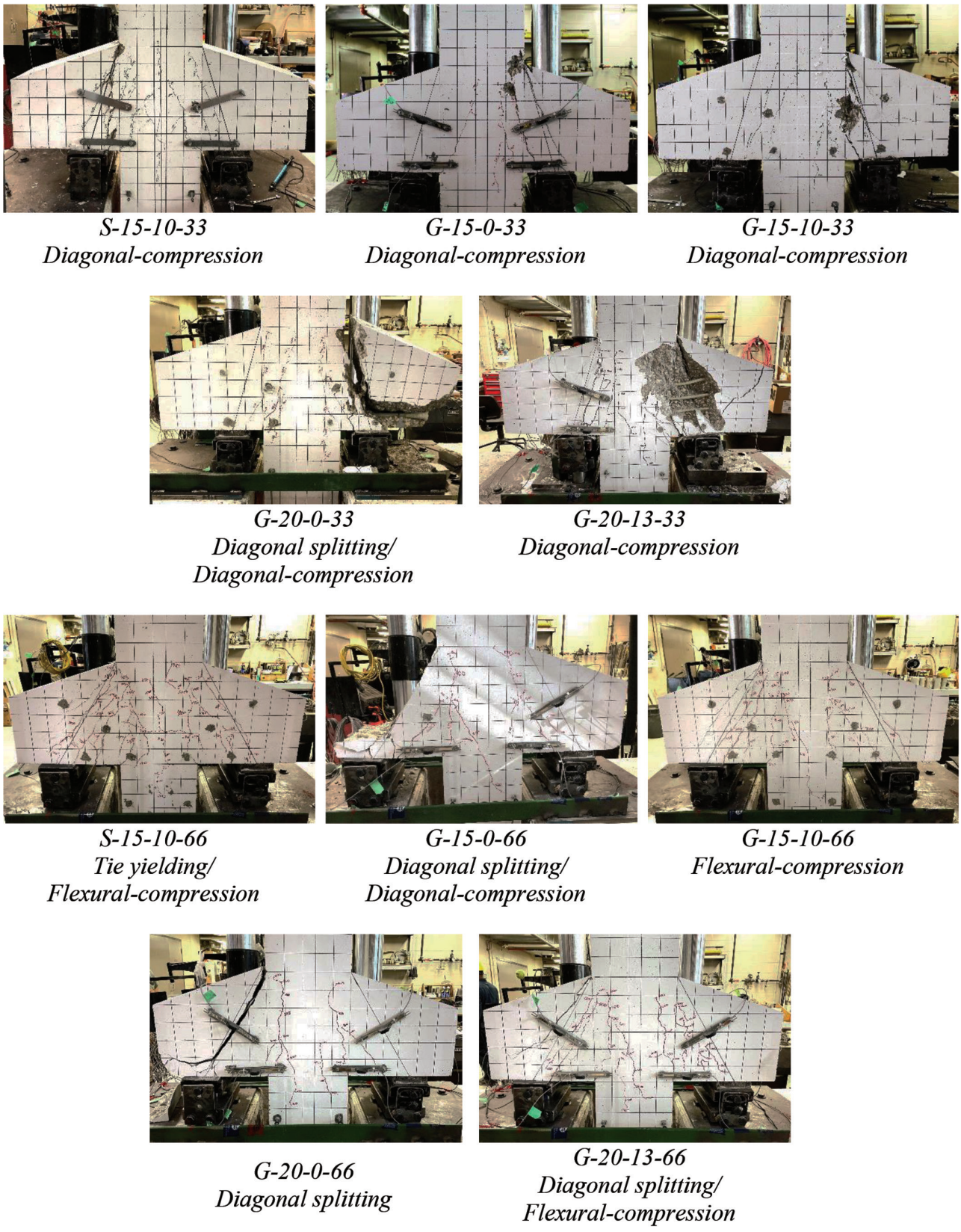

Fig. 6—Common modes of failure.

due to the dowel action and clamping stresses. As expected, an increase in crack width was positively correlated with a decrease in corbel capacity due to increasing the *a*/*d*. For example, G-15-0-33 had approximately 41% larger capacity and 48% less flexural crack width than G-15-0-66. This relationship is primarily attributed to the slope angle of the struts, which is critical to shear-controlled elements like corbels. The corbel capacity reduction is also contributed to by the reduced aggregate interlocking action across the shear plane, resulting from increased crack widths.

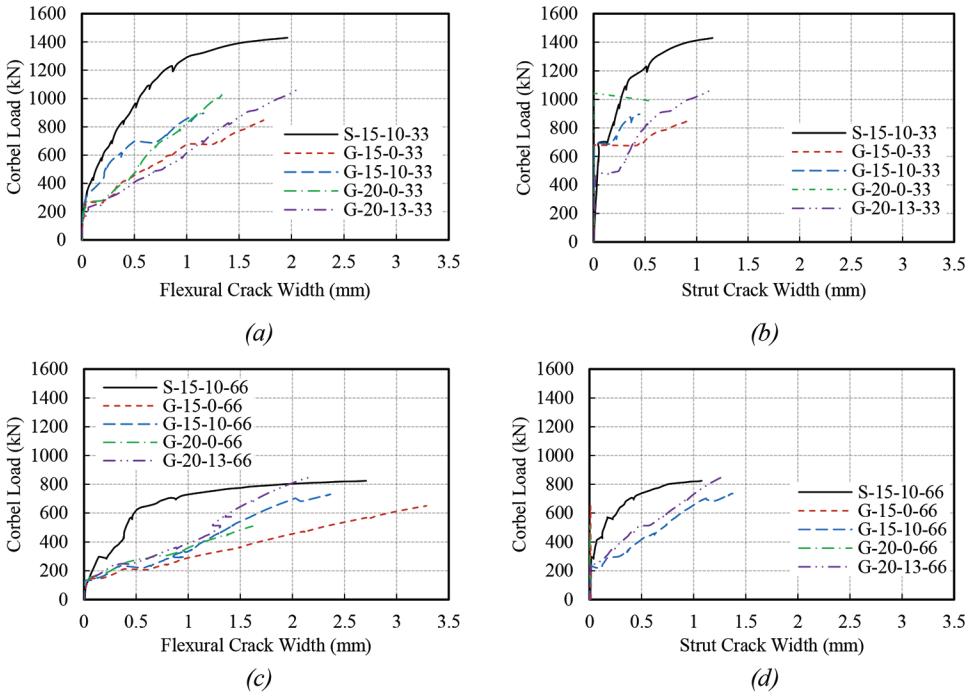

Fig. 7—Load-crack width relationship: (a) flexural cracking for a/d *= 0.33; (b) strut cracking for* a/d *= 0.33; (c) flexural cracking for* a/d *= 0.66; and (d) strut cracking for* a/d *= 0.66. (Note: 1 kN = 0.225 kip; 1 mm = 0.0394 in.)*

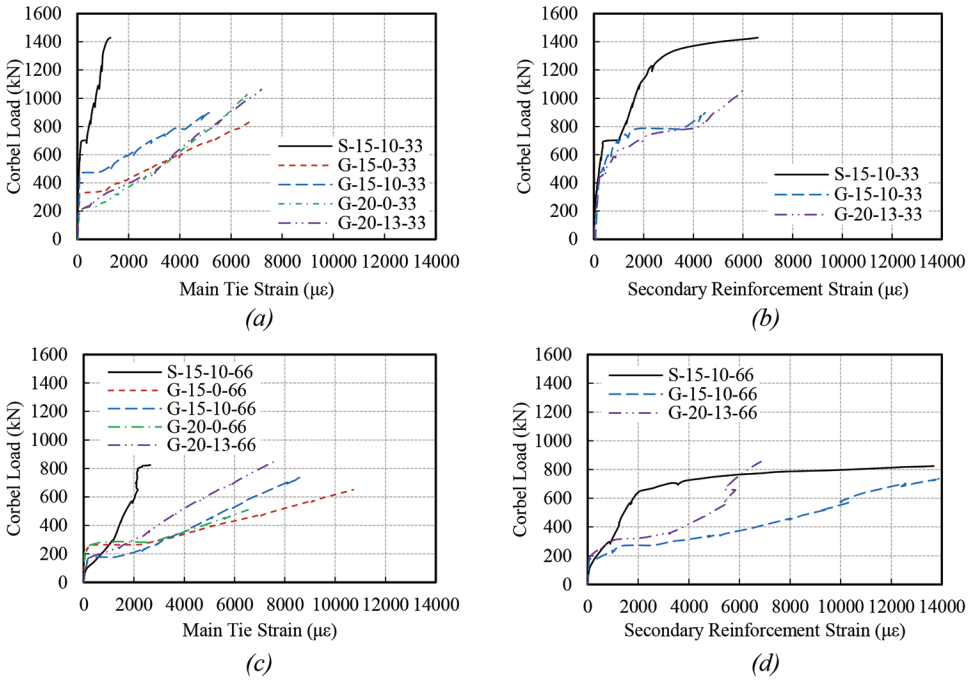

Fig. 8—Load-strain relationship in reinforcing bars: (a) main tie reinforcement for a/d *= 0.33; (b) secondary reinforcement for* a/d *= 0.33; (c) main tie reinforcement for* a/d *= 0.66; and (d) secondary reinforcement for* a/d *= 0.66.*

The two shear span-depth ratios, and the corresponding slope angle of the struts, had a considerable influence on crack development. The specimens with a/d = 0.66 had approximately 47% higher flexural crack width at failure than a/d = 0.33. This trend is logical given that there is a positive correlation between a/d and the magnitude of flexural stresses. Similarly, the development of initial diagonal strut cracking was impacted by a/d. Specimens with a/d = 0.33 showed an initial diagonal strut crack at 752 kN (169.06 kip) on average compared to 416 kN (93.52 kip) for a/d = 0.66, corresponding to an approximately 45% reduction.

Strains in reinforcement

Figure 8 presents the load-strain relationship in the reinforcing bars. The maximum strain readings for the a/d = 0.33 specimens consistently occurred at the corbel-column interface, while this reading in the a/d = 0.66 specimens occurred at either the interface or 150 mm (5.91 in.) offset

from the interface. The strain readings presented for the secondary reinforcement were taken as the maximum of the top or bottom of the three secondary stirrups recorded at the interface.

The main tie strains were negligible until the flexural cracking load, where a sharp increase in strain occurred as stress was transferred into the reinforcement. The main tie strains for the GFRP-RC specimens progressed linearly until failure, while the secondary strains exhibited a more sporadic strain progression due to the close relationship with the diagonal cracking. The strains in the steel-RC specimens developed at a slower rate than their GFRP-RC counterparts due to the higher modulus of elasticity. For example, S-15-10-33 had a maximum main tie strain of 1640 με (round off strains to the nearest 10) compared to 5160 με for G-15-10-33, despite S-15-10-33 achieving a higher capacity of 1432 kN (321.93 kip) compared to 897 kN (201.65 kip) for G-15-10-33. The main tie strain in S-15-10-66 exceeded the yield point prior to failure. The secondary reinforcement in both steel-RC specimens, S-15-10-33 and S-15-10-66, reached the yield point and deformed continuously prior to failure without meaningful load gain. The maximum GFRP strain in this study was 13,870 με in the G-15-0-66 secondary reinforcement, which is still well below the 22,100 με ultimate strain for No. 10 bars and represents approximately 63% use.

Specimens G-15-0-66 and G-15-10-66 showed a similar load-strain response. The addition of secondary reinforcement in G-15-10-66 led to a slightly higher corbel capacity and lower main tie strain at equivalent loads to G-15-0-66. Specimen G-15-0-66 had relatively higher strains than G-15-10-66 at comparable loads due to tensile stresses being isolated to the main tie reinforcement, whereas G-15-10-66 had secondary reinforcement to redistribute stress to as cracks developed. The a/d = 0.66 specimens without secondary reinforcement, G-15-0-66 and G-20-0-66, developed main tie strains more rapidly than their equivalent specimens with secondary reinforcement. This can be attributed to the secondary reinforcement aiding with stress redistribution, reducing the amount of stress isolated to the main tie reinforcement. This relationship was less identifiable for the a/d = 0.33 specimens.

The two shear span-depth ratios affected the strain development in the main tie and secondary reinforcements. The specimens with a/d = 0.66 developed main tie strains that were 30% higher on average than a/d = 0.33. Similarly, the specimens with a/d = 0.66 developed secondary reinforcement strains that were 102% higher on average than a/d = 0.33. This relationship agrees with the flexural crack width trend identified earlier and is once again attributed to the positive correlation between a/d, the slope angle of the strut, and the magnitude of flexural stresses. The presence of secondary reinforcement had a marginal impact on the main tie strain at failure. Specimens with secondary reinforcement had an average main tie strain of 7150 με compared to 7750 με for specimens without secondary reinforcement, corresponding to an 8.3% increase.

Anchorage of headed-end bars

Strain gauges were installed along the main tie reinforcement and near the headed ends to evaluate the dissipation of stresses and anchorage performance. Figure 9 shows the strain profiles for select specimens. The peak strain readings occurred at the column-corbel interface, identified as a distance along a corbel length of 0 mm (0 in.), for all specimens shown except G-15-0-66, where the strains at 150 mm (5.91 in.) offset from the interface were greatest. Each of the specimens was efficient in dissipating strains prior to the strain gauge nearest to the headed ends, which is identified as 300 mm (11.81 in.) offset from the interface. Strains recorded near the headed end were generally less than 1500 με. The maximum strain that developed near the headed ends was in G-15-10-66, with 5010 με at failure. This corresponds to a load of 64.4 kN (14.48 kip) in the headed end, which is considerably less than the tested load of 114.9 kN (25.83 kip) at break previously presented in Table 3.

The required development length was calculated in accordance with CSA S806:12[17] using experimental strains ranging from 300 to 640 mm (11.81 to 25.20 in.). The available development length without bending measured from the column-corbel interface is only 410 mm (16.14 in.), indicating that mechanical anchorage is necessary to develop the ultimate strength of the reinforcing bars. The headed ends used in this study were efficient in carrying the necessary tensile stresses to develop the peak corbel load without premature failure. No indications of slippage in the headed ends or insufficient reinforcement anchorage were observed at failure.

There were instances of headed-end bars experiencing fracture after the peak load. However, these were not classified as anchorage failures as they were due to the primary diagonal shear crack propagating horizontally toward the outer corbel face after intersecting the main tie reinforcement. The shear plane then applied prying action to the headed-end rounded grooves, leading to the fracture. Figure 10 displays photos of the headed ends post-failure. Specimens G-15-0-66, G-20-0-33, and G-20-13-33 each experienced some degree of headed-end fracture at failure, whereas G-20-0-66 shows the three headed ends still intact after failure.

Load-deflection response

Two LVDTs were mounted at the lower column stub to measure deflection. The average of the two LVDT values was plotted against corbel load in Fig. 11. For the GFRP-RC specimens, the load-deflection relationship progressed relatively linear until cracking, where a reduction in stiffness was observed. This relationship was evident for each of the a/d = 0.66 specimens, where a reduction in slope occurred at approximately 200 kN (44.96 kip). The presence of secondary reinforcement did not appear to influence the linear deflection behavior. The two steel-RC specimens, S-15-10-33 and S-15-10-66, experienced a steady load-deflection increase until approximately 80% of the ultimate load, where deflection began to increase rapidly relative to the corbel load. This effect is clearly displayed by S-15-10-66, where the main tie and secondary reinforcements both

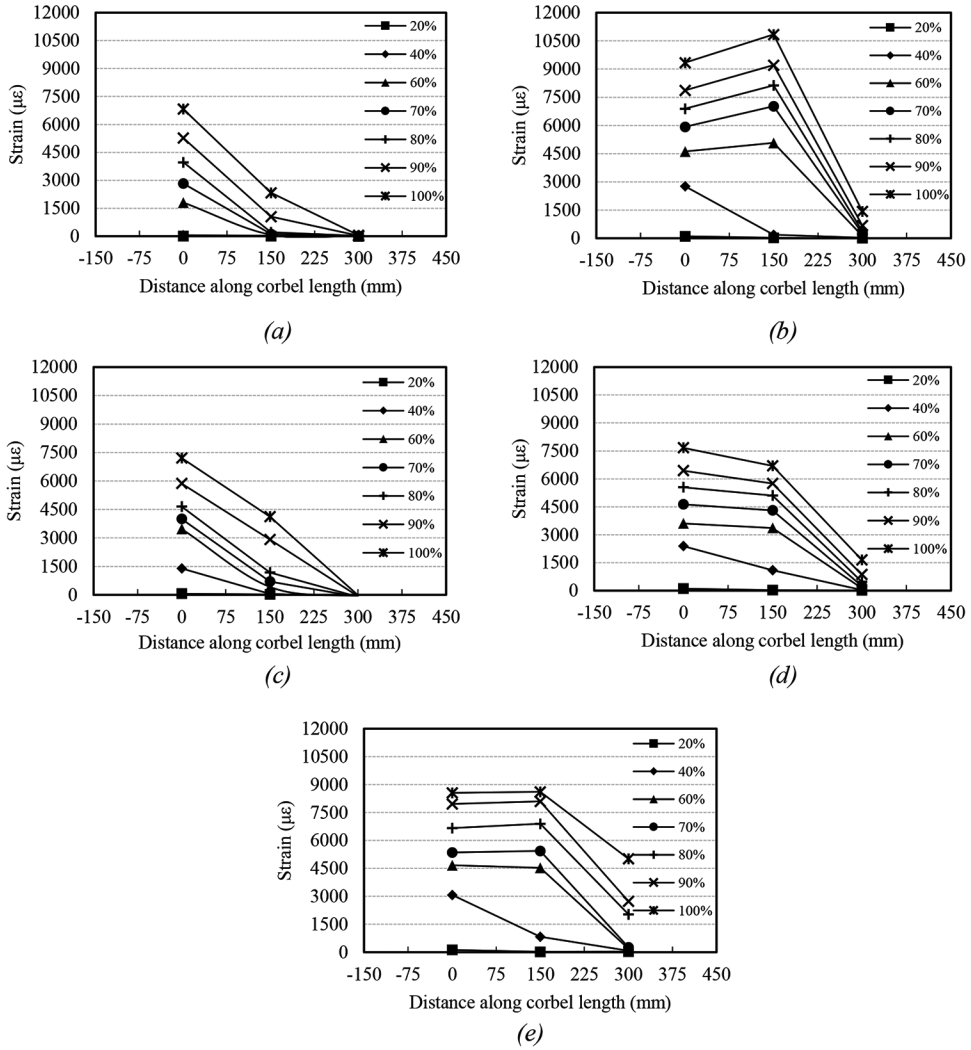

Fig. 9—Strain profiles for selected specimens: (a) G-15-0-33; (b) G-15-0-66; (c) G-20-13-33; (d) G-20-13-66; and (e) G-15-10-66.

yielded and continually increased in strain while the load remained relatively constant. Generally, the main tie stiffness is understood to have the greatest influence on the deflection of corbels. This suggests that the GFRP-RC specimens should have a higher deflection at equivalent loads to their steel-RC counterparts due to the difference in modulus of elasticity. The $a/d = 0.66$ specimens with GFRP recorded deflection readings that were consistently higher than S-15-10-66 after the initial cracks developed. However, the $a/d = 0.33$ specimens with GFRP-RC displayed comparable deflection to S-15-10-33 until failure with no discernable trends. Overall, the $a/d = 0.66$ specimens had approximately 29% greater deflection than $a/d = 0.33$. This was expected due to the increased strut inclination and flexural stresses as the shear span-depth ratio increases. The specimens with secondary reinforcement achieved a maximum deflection of 21% greater than those without secondary reinforcement. The secondary reinforcement provided clamping forces and redistributed stress from diagonal strut cracks, leading to a higher capacity and corresponding deflection.

Load-carrying capacity

Table 4 summarizes the experimental capacities and test results for each corbel. V_u represents the ultimate capacity of the governing corbel, which was equal to the load cell reading for a pinned-support corbel failure or the total actuator load less the load cell reading for a roller-support corbel failure. ε_t and ε_s provide the maximum strains for the main tie and secondary reinforcements, respectively. Δ provides the deflection, while $w_{cr\text{-}flex}$ and $w_{cr\text{-}dia}$ represent the flexural and diagonal strut crack widths, respectively; each of these parameters is provided at the corbel service load and ultimate load. The final column classifies each corbel as one of the following modes of failure: TY for a tie-yielding failure (steel-RC), DC for a diagonal-compression failure, FC for a flexural-compression failure, and SP for a diagonal splitting failure, as previously discussed herein.

Figure 12 presents the relationship between the load capacity and shear span-depth ratio. Each pair of corbels with identical reinforcement were plotted in tandem. The line connecting each corbel pair visually links the $a/d = 0.33$ and $a/d = 0.66$ data points. It is not intended to suggest a linear relationship for all intermediate shear span-depth ratios. The decreasing slope of the plots represents a negative correlation

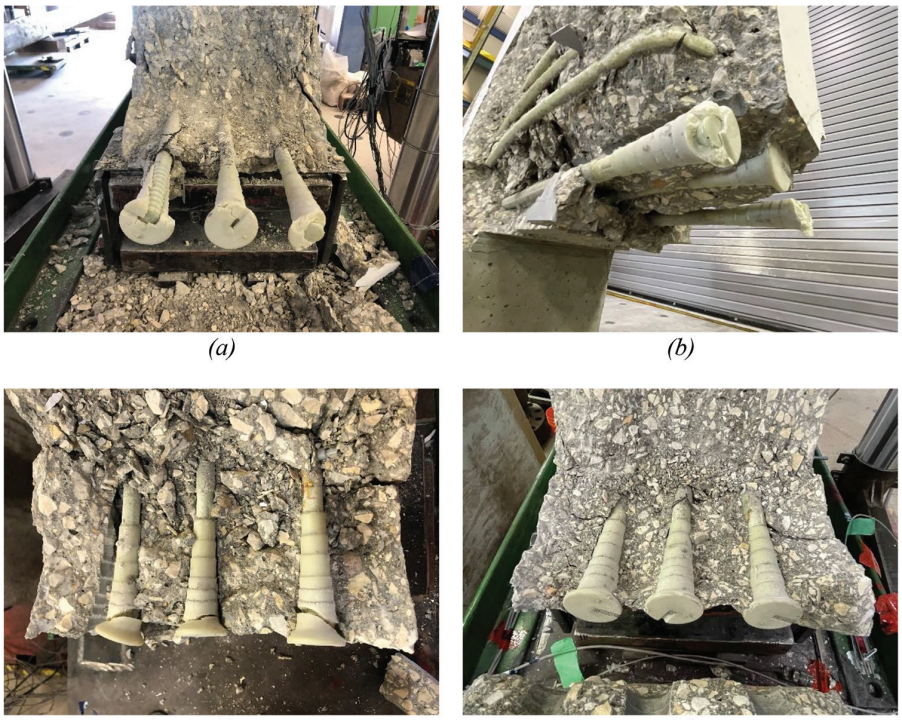

Fig. 10—Common headed ends post-failure: (a) G-20-0-33; (b) G-20-13-33; (c) G-15-0-66; and (d) G-20-0-66.

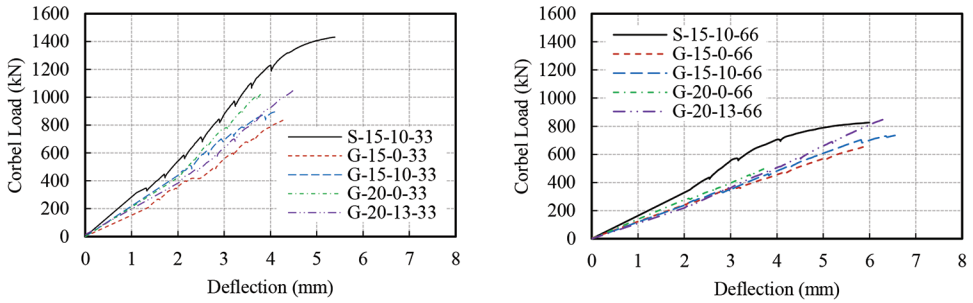

Fig. 11—Load-deflection relationship: (a) a/d *= 0.33; and (b)* a/d *= 0.66.*

between load capacity and shear span-depth ratio, with a/d = 0.33 specimens having approximately 47% higher shear capacity than a/d = 0.66. The specimens with increased main tie and secondary reinforcement ratios, G-20-13-33 and G-20-13-66, had a less pronounced influence on load capacity, reaching a 17% higher shear capacity on average than their counterpart specimens, G-15-10-33 and G-15-10-66. The presence of secondary reinforcement was found to have a similar influence on load capacity, with secondary reinforcement achieving a 16% higher shear capacity on average than those without secondary reinforcement. The steel-RC specimens achieved a higher shear capacity than their equivalent GFRP-RC counterparts. Specimen S-15-10-33 had a shear capacity of 1432 kN (321.93 kip) compared to 897 kN (201.65 kip) for G-15-10-33. The shear capacity difference was not as substantial for the a/d = 0.66 pair, with 826 kN (185.69 kip) for S-15-10-66 and 736 kN (165.46 kip) for G-15-10-66, which can be attributed to the increasing tensile stresses and main tie use as the shear span-depth ratio increases.

CONCLUSIONS

Based on the test results of the 10 full-scale corbels presented herein, the following conclusions can be drawn:

1. The cracking behavior of the glass fiber-reinforced polymer (GFRP)-reinforced concrete (RC) specimens closely resembled the steel-RC control specimens. Flexural cracks were the first to form near the column-corbel interface, followed by diagonal cracks near the center of the corbel height.

2. Four modes of failure were observed in this study: tie yielding (TY) (steel-RC), diagonal-compression (DC), flexural-compression (FC), and diagonal splitting (SP). All the GFRP-RC specimens had a concrete-controlled brittle shear failure through diagonal strut cracking. DC was the most common mode of failure observed. The likelihood of the most undesirable and brittle mode of failure, SP, was increased in specimens without secondary reinforcement at the higher shear span-depth ratio (a/d) of 0.66.

3. The parametric performance of corbel specimens was dependent on the a/d. The specimens with an a/d of 0.66

Table 4—Experimental capacities and summary of test results

Series	Corbel ID	V, kN	ε_t, με	ε_s, με	Δ, mm		$w_{cr\text{-}flex}$, mm		$w_{cr\text{-}dia}$, mm		Failure mode
		Ult.			Serv.	Ult.	Serv.	Ult.	Serv.	Ult.	
A	S-15-10-33	1432	1640	6770	2.36	5.39	0.26	1.96	0.05	1.15	DC
	G-15-0-33	845	6880	—	3.34	4.31	0.62	1.73	0.00	0.91	DC
	G-15-10-33	897	5160	4420	2.82	4.15	0.53	1.26	0.00	0.47	DC
	G-20-0-33	1042	6730	—	2.65	3.84	0.70	1.33	0.00	0.00*	SP/DC
	G-20-13-33	1062	7210	6030	2.87	4.55	1.07	2.05	0.36	1.13	DC
B	S-15-10-66	826	2400	14,010	2.40	5.99	0.37	2.71	0.07	1.08	TY/FC
	G-15-0-66	656	10,840	—	3.57	5.90	1.78	3.29	0.00	0.00*	SP/DC
	G-15-10-66	736	8580	13,870	3.46	6.56	1.18	2.39	0.50	1.37	FC
	G-20-0-66	509	6540	—	3.13	3.81	1.21	1.62	0.00	0.00*	SP
	G-20-13-66	854	7660	6850	3.34	6.37	1.09	2.20	0.33	1.30	SP/FC

*Specimens in which failure occurred immediately following first diagonal strut crack.

Note: V is ultimate capacity of corbel; ε_t is strain in main tie reinforcement; ε_s is strain in secondary reinforcement; Δ is deflection; $w_{cr\text{-}flex}$ is flexural crack width; $w_{cr\text{-}strut}$ is diagonal strut crack width; DC is diagonal-compression failure; SP is diagonal splitting failure; TY is tie-yielding failure; FC is flexural-compression failure. Quantitative results are provided at corbel service load (Serv.) and ultimate load (Ult.). 1 kN = 0.2248 kip; 1 mm = 0.0394 in.

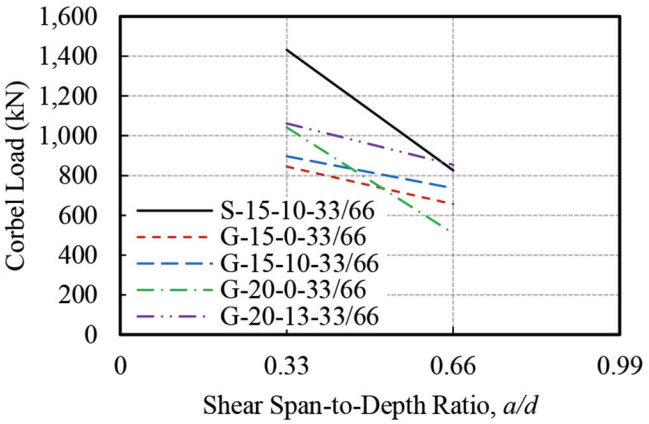

Fig. 12—Load capacity-shear span-depth ratio relationship.

exhibited approximately 47% greater flexural crack widths, 45% lower strut cracking load, 30% higher main tie strains, 102% higher secondary reinforcement strains, 29% greater deflection, and 32% lower shear capacity than their a/d = 0.33 counterpart specimens.

4. The GFRP-RC specimens with secondary reinforcement developed narrower crack widths at equivalent loads, comparable main tie strains, approximately 21% greater deflection, and 16% higher shear capacity than the identical specimens without secondary reinforcement. The presence of secondary reinforcement improved serviceability performance and allowed resilient load gain after strut cracking.

5. The two steel-RC specimens in this study achieved a shear capacity of approximately 60% and 12% higher than their GFRP-RC counterparts for a/d = 0.33 and a/d = 0.66, respectively. The steel-RC specimens displayed narrower crack widths at equivalent loads to their GFRP-RC counterparts. This relationship was expected and can be attributed to the difference in the modulus of elasticity of the materials.

6. The GFRP reinforcement developed the necessary tensile strains with considerable reserve capacity from the undesirable brittle nature of GFRP rupture. The maximum strain observed in the experimental program was 13,870 με, compared to the 22,100 με ultimate strain, representing 63% use of the GFRP bars.

7. The thermoplastic headed ends used in this study provided sufficient anchorage to develop the necessary main tie tensile stresses. The peak corbel load was reached without any indications of slippage or premature failure. Strain readings near the headed ends were used to verify the dissipation of stresses and confirm bar development. The maximum strain recorded near the headed ends was 5010 με. This corresponds to a load of 64.4 kN (14.48 kip), which is considerably less than the tested load of 114.9 kN (25.83 kip) at break of the headed ends.

AUTHOR BIOS

ACI member **Matthew N. Allen** *is a Master's Student in the Department of Civil Engineering at the University of Manitoba, Winnipeg, MB, Canada. He is also a Structural Engineer-in-Training with Dillon Consulting Limited. He received his BSc from the University of Manitoba in 2020. He is the recipient of the 2021 ACI Foundation Don Marks Memorial Fellowship. His research interests include the design of bridge structures, large-scale testing, fiber-reinforced polymers (FRPs), and strut-and-tie modeling of deep or irregular concrete elements.*

Ehab F. El-Salakawy, *FACI, is a Professor in the Department of Civil Engineering at the University of Manitoba. He is a member of ACI Committee 440, Fiber-Reinforced Polymer Reinforcement. He received the ACI Mete A. Sozen Award for Excellence in Structural Research in 2020. His research interests include the design, construction, durability, large-scale testing, and rehabilitation of reinforced concrete structures using FRP reinforcement.*

ACKNOWLEDGMENTS

The authors would like to express their sincere gratitude to the ACI Foundation, the Natural Sciences and Engineering Research Council of Canada (NSERC), and the University of Manitoba Graduate Fellowship (UMGF) for financial support. The GFRP reinforcement was generously provided by Pultrall Inc. The valuable assistance received from C. Klowak, S. Abraha, and D. Szara, as a part of the W.R. McQuade Structures Laboratory technical staff, is greatly appreciated.

REFERENCES

1. Mattock, A. H.; Chen, K. C.; and Soongswang, K., "The Behavior of Reinforced Concrete Corbels," *PCI Journal*, V. 21, No. 2, Mar.-Apr. 1976, pp. 52-77. doi: 10.15554/pcij.03011976.52.77

2. Schlaich, J.; Schäfer, K.; and Jennewein, M., "Toward a Consistent Design of Structural Concrete," *PCI Journal*, V. 32, No. 3, May-June 1987, pp. 74-150. doi: 10.15554/pcij.05011987.74.150

3. Fattuhi, N. I., "Strength of SFRC Corbels Subjected to Vertical Load," *Journal of Structural Engineering*, ASCE, V. 116, No. 3, Mar. 1990, pp. 701-718. doi: 10.1061/(ASCE)0733-9445(1990)116:3(701)

4. Dawood, A. A.; Kadhum, A. K.; and Abdul-Razzaq, K. S., "Strength of Reinforced Concrete Corbels – A Parametric Study," *International Journal of Civil Engineering and Technology (IJCIET)*, V. 9, No. 11, Nov. 2018, pp. 2274-2288.

5. Kriz, L. B., and Raths, C. H., "Connections in Precast Concrete Structures–Strength of Corbels," *PCI Journal*, V. 10, No. 1, Feb. 1965, pp. 16-61. doi: 10.15554/pcij.02011965.16.61

6. Solanki, H., and Sabnis, G. M., "Reinforced Concrete Corbels — Simplified," *ACI Structural Journal*, V. 84, No. 5, Sept.-Oct. 1987, pp. 428-432.

7. Campione, G.; La Mendola, L.; and Mangiavillano, M. L., "Steel Fiber-Reinforced Concrete Corbels: Experimental Behavior and Shear Strength Prediction," *ACI Structural Journal*, V. 104, No. 5, Sept.-Oct. 2007, pp. 570-579.

8. Abu-Obaida, A.; El-Ariss, B.; and El-Maaddawy, T., "Behavior of Short-Span Concrete Members Internally Reinforced with Glass Fiber-Reinforced Polymer Bars," *Journal of Composites for Construction*, ASCE, V. 22, No. 5, Oct. 2018, p. 04018038.

9. Jeremic, N., and Sheikh, S. A., "Performance of Glass Fiber-Reinforced Polymer Bent Bars," *ACI Structural Journal*, V. 118, No. 2, Mar. 2021, pp. 273-285.

10. Johal, K. S., "Investigation of Creep Rupture Phenomenon in Glass Fibre Reinforced Polymer (GFRP) Stirrups," master's thesis, University of Toronto, Toronto, ON, Canada, 2016, 146 pp.

11. Vint, L., and Sheikh, S., "Investigation of Bond Properties of Alternate Anchorage Schemes for Glass Fiber-Reinforced Polymer Bars," *ACI Structural Journal*, V. 112, No. 1, Jan.-Feb. 2015, pp. 59-68.

12. Yang, J.-M.; Lee, J.-H.; Yoon, Y.-S.; Cook, W. D.; and Mitchell, D., "Influence of Steel Fibers and Headed Bars on the Serviceability of High-Strength Concrete Corbels," *Journal of Structural Engineering*, ASCE, V. 138, No. 1, Jan. 2012, pp. 123-129. doi: 10.1061/(ASCE)ST.1943-541X.0000427

13. Mohamed, A. M.; Mahmoud, K.; and El-Salakawy, E. F., "Behavior of Simply Supported and Continuous Concrete Deep Beams Reinforced with GFRP Bars," *Journal of Composites for Construction*, ASCE, V. 24, No. 4, Aug. 2020, p. 04020032. doi: 10.1061/(ASCE)CC.1943-5614.0001039

14. Benmokrane, B.; Mohamed, H. M.; Manalo, A.; and Cousin, P., "Evaluation of Physical and Durability Characteristics of New Headed Glass Fiber–Reinforced Polymer Bars for Concrete Structures," *Journal of Composites for Construction*, ASCE, V. 21, No. 2, Apr. 2017, p. 04016081.

15. Johnson, D. T., and Sheikh, S. A., "Performance of Bent Stirrup and Headed Glass Fibre Reinforced Polymer Bars in Concrete Structures," *Canadian Journal of Civil Engineering*, V. 40, No. 11, Nov. 2013, pp. 1082-1090. doi: 10.1139/cjce-2012-0522

16. ACI Committee 440, "Building Code Requirements for Structural Concrete Reinforced with Glass Fiber-Reinforced Polymer (GFRP) Bars—Code and Commentary (ACI CODE-440.11-22)," American Concrete Institute, Farmington Hills, MI, 2022, 260 pp.

17. CSA S806:12 (R2021), "Design and Construction of Building Structures with Fibre-Reinforced Polymers," CSA Group, Toronto, ON, Canada, 2021, 201 pp.

18. CSA S6:19, "Canadian Highway Bridge Design Code," CSA Group, Toronto, ON, Canada, 2019, 1182 pp.

19. CSA A23.3:19, "Design of Concrete Structures," CSA Group, Toronto, ON, Canada, 2019, 301 pp.

20. ACI Committee 318, "Building Code Requirements for Structural Concrete (ACI 318-19) and Commentary (ACI 318R-19) (Reapproved 2022)," American Concrete Institute, Farmington Hills, MI, 2019, 624 pp.

21. CSA A23.1:19/CSA A23.2:19, "Concrete Materials and Methods of Concrete Construction/Test Methods and Standard Practices for Concrete," CSA Group, Toronto, ON, Canada, 2019, 882 pp.

22. CSA S807:19, "Specification for Fibre-Reinforced Polymers," CSA Group, Toronto, ON, Canada, 2019, 67 pp.

23. ACI Committee 440, "Guide Test Methods for Fiber-Reinforced Polymer (FRP) Composites for Reinforcing or Strengthening Concrete and Masonry Structures (ACI 440.3R-12)," American Concrete Institute, Farmington Hills, MI, 2012, 23 pp.

24. ASTM D570-22, "Standard Test Method for Water Absorption of Plastics," ASTM International, West Conshohocken, PA, 2022, 4 pp.

25. ASTM D2584-18, "Standard Test Method for Ignition Loss of Cured Reinforced Resins," ASTM International, West Conshohocken, PA, 2018, 3 pp.

26. ASTM D3418-21, "Standard Test Method for Transition Temperatures and Enthalpies of Fusion and Crystallization of Polymers by Differential Scanning Calorimetry," ASTM International, West Conshohocken, PA, 2021, 8 pp.

27. ASTM D5117-17, "Standard Test Method for Dye Penetration of Solid Fiberglass Reinforced Pultruded Stock," ASTM International, West Conshohocken, PA, 2017, 4 pp.

28. CSA W59-18 (R2023), "Welded Steel Construction," CSA Group, Toronto, ON, Canada, 2018, 549 pp.

ARE YOU A RESEARCHER?

SIGN UP FOR ORCID TODAY!

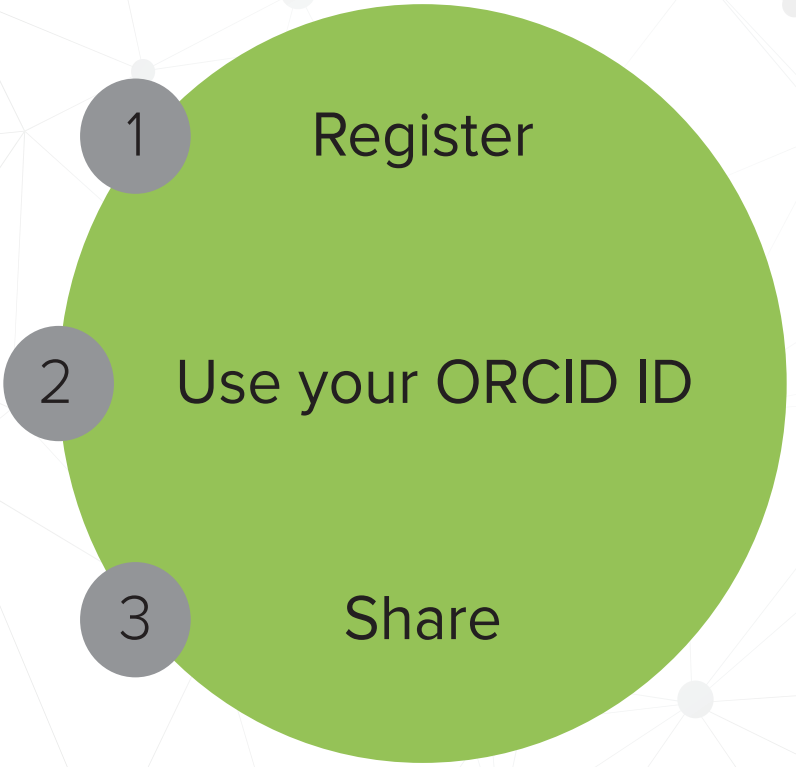

ORCID provides a digital identifier that distinguishes you from every other researcher and, through integration in key research workflows such as manuscript and grant submission, supports automated linkages between you and your professional activities, ensuring that your work is recognized.

ORCID services are FREE and it's as easy as **1-2-3**.

WWW.ORCID.ORG

NEW Symposium Publications from ACI

SP-345: Materials, Analysis, Structural Design and Applications of Textile Reinforced Concrete/Fabric Reinforced Cementitious Matrix

Several state-of-the-art sessions on textile-reinforced concrete/fabric-reinforced cementitious matrix (TRC/FRCM) were organized by ACI Committee 549 in collaboration with RILEM TC MCC during the ACI Fall 2019 Convention in Cincinnati, OH, and the ACI Virtual Technical Presentations in June 2020. The forum provided a unique opportunity to collect information and present knowledge in the field of TRC and FRCM as sustainable construction materials.

Available in PDF format: $69.50
(FREE to ACI members)

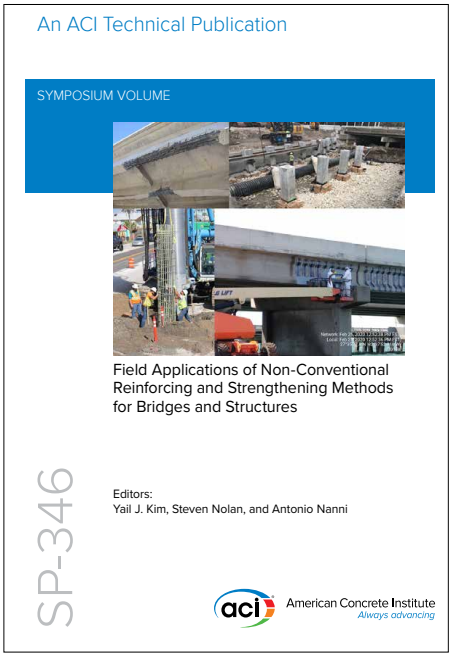

SP-346: Field Applications of Non-Conventional Reinforcing and Strengthening Methods for Bridges and Structures

A sustainable built environment requires a comprehensive process from material selection through to reliable management. Although traditional materials and methods still dominate the design and construction of our civil infrastructure, nonconventional reinforcing and strengthening methods for concrete bridges and structures can address the functional and economic challenges facing modern society.

Available in PDF format: $69.50
(FREE to ACI members)

American Concrete Institute
+1.248.848.3700 • www.concrete.org

NEW Symposium Publications from ACI

SP-347: Recent Developments in High Strain Rate Mechanics and Impact Behavior of Concrete

This Symposium Volume reports on the latest developments in the field of high-strain-rate mechanics and behavior of concrete subject to impact loads. This effort supports the mission of ACI Committee 370, Blast and Impact Load Effects, to develop and disseminate information on the design of concrete structures subjected to impact, as well as blast and other short-duration dynamic loads.

Available in PDF format: $69.50
(ACI members: $39.00) ($30.50 savings)

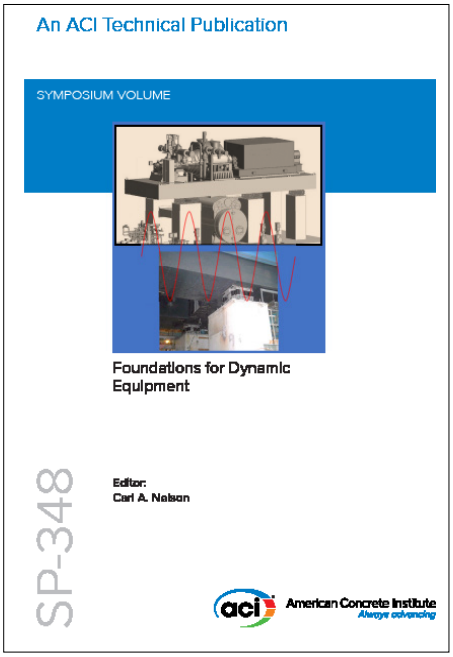

SP-348: Foundations for Dynamic Equipment

This special publication grew out of the Technical Session titled “Application of ACI 351-C Report on Dynamic Foundations,” held at the ACI Spring 2019 Convention in Québec City, Québec. Following this event, ACI Committee 351 decided to undertake a special publication with contributions from those session participants willing to develop their presentations into full-length papers. Three papers included in the current publication were contributed by these presenters and their coauthors, with six additional papers provided by others.

Available in PDF format: $69.50
(ACI members: $39.00) ($30.50 savings)

American Concrete Institute
+1.248.848.3700 • www.concrete.org

ACI STRUCTURAL JOURNAL

The American Concrete Institute (ACI) is a leading authority and resource worldwide for the development and distribution of consensus-based standards and technical resources, educational programs, and certifications for individuals and organizations involved in concrete design, construction, and materials, who share a commitment to pursuing the best use of concrete.

Individuals interested in the activities of ACI are encouraged to explore the ACI website for membership opportunities, committee activities, and a wide variety of concrete resources. As a volunteer member-driven organization, ACI invites partnerships and welcomes all concrete professionals who wish to be part of a respected, connected, social group that provides an opportunity for professional growth, networking, and enjoyment.

American Concrete Institute